V/STOL DYNAMICS AND AEROELASTIC ROTOR-AIRFRAME TECHNOLOGY

Volume II. Description and Correlation of New Methodologies

H. R. ALEXANDER
A. K. AMOS
F. J. TARZANIN
R. B. TAYLOR
THE BOEING COMPANY, VERTOL DIVISION

FOREWORD

This report was prepared by The Boeing Company, Vertol Division of Philadelphia, Pennsylvania, for the Aerospace Dynamics Branch, Vehicle Dynamics Division, Air Force Flight Dynamics Laboratory, Wright-Patterson Air Force Base, Ohio, under Contract F33615-71-C-1310. This research is part of a continuing effort to develop new and improved techniques for defining dynamic and aeroelastic phenomena for rotor/propeller-powered V/STOL flight vehicles under the Air Force Systems Command's exploratory development program. This contract was initiated under Project 1370, "Dynamic Problems in Military Flight Vehicles," Task 137005, "Prediction and Control of Flight Vehicle Vibration." Mr. A. R. Basso of the Aerospace Dynamics Branch was the Project Engineer.

The final report is presented in three volumes. The first volume contains a state-of-the-art review of stability and blade vibratory loads in V/STOL aircraft. The second volume contains the development of the analytical methods, the correlation of analytical results with experimental data, and the results of parametric investigations. The third volume contains a user's guide to the digital computer programs including input and output formats. The third volume is not being distributed; however, it is available upon request from the Air Force Flight Dynamics Laboratory/FYS, Wright-Patterson Air Force Base, Ohio 45433.

Mr. H. R. Alexander was The Boeing Company, Vertol Division Project Engineer.

This report covers work conducted from February 1971 through February 1972. The manuscript was released by the authors in February 1972 for publication as an AFFDL Technical Report.

This Technical Report has been reviewed and is approved.

Walter J. Mykytow

WALTER J. MYKYTOW
Assistant for Research and Technology
Vehicle Dynamics Division

ABSTRACT

The blade loads analysis calculates rotor blade flapwise, chordwise, and torsional deflections and loads, together with rotor performance, control system forces, and vibratory hub loads. Articulated and hingeless rotors with 2 to 9 blades and large twist may be analyzed. The blades may be of arbitrary planform, twist, and radial variation in airfoil section.

The analysis considers coupled flapwise-chordwise-torsion deflections of the rotor blades. Boundary conditions for either articulated or hingeless rotors are applied and the solution is obtained by expanding the variables in a 10-harmonic Fourier series.

Airload calculations include the effects of airfoil section geometry, compressibility, stall, 3-dimensional flow, unsteady aerodynamics, and nonuniform inflow. The unsteady aerodynamic loads are calculated by modifying the static loads resulting from the airfoil tables to include Theodorsen's shed wake function, dynamic stall effects based on oscillating airfoil data, and yawed flow across the blade.

The nonuniform inflow calculations are based on a tip and root vortex trailed from each blade. The vortex wake is assumed to be rigid and to drift relative to the hub with a constant resultant velocity composed of thrust-induced uniform downwash and the aircraft airspeed.

The upgraded aeroelastic stability analyses handle all the classical mechanisms of instability such as whirl flutter, air and ground resonance, and aeromechanical instability. Additional phenomena dealt with include individual blade flutter resulting from pitch-lag-flap coupling which may occur when rotor blades are deflected under load; limit-cycle wing-rotor flutter caused by a similar mechanism; and the effect on aeroelastic behavior of rotor tilt to the free stream.

In the area of rotor loads, correlation of prop/rotor and helicopter rotor loads test data has been made with the fully coupled rotor loads analysis. Predictions are made for alternating blade loads and steady in-plane hub moments for prop/rotors and for alternating blade loads, pitch link loads, and airloads for helicopters.

In the area of aeroelastic stability, phenomena beyond the scope of analysis with previous stability methodology are investigated and stability trends associated with certain sensitive parameters are presented. These include the influence of blade frequencies, blade deflections and thrust, and advance ratio. Parametric behavior of propeller-rotor static derivatives is presented. An unexpected discovery of this study was

the sensitivity of the rotor derivatives to blade lead-lag motion when the frequency of this mode is near 1 per rev. This result was subsequently confirmed by test and adds substantially to our understanding of the influence of large propeller-rotors on static divergence and flying qualities.

The impact of the new prediction capabilities and possible refinement or development of design criteria through use of the analysis are discussed.

TABLE OF CONTENTS

	Page
Part I. New Methodology for Aeroelastic Stability Analysis	1
INTRODUCTION	3
SCOPE OF ANALYSIS	3
FEATURES OF ANALYSIS	3
LIMITATIONS OF ANALYSIS	4
SYSTEM DEFINITION	5
STRUCTURAL IDEALIZATION	5
MATHEMATICAL MODELING	8
COORDINATE SYSTEMS AND TRANSFORMATIONS	9
FIXED-COORDINATE SYSTEM	9
SPATIAL COORDINATES IN AIRFRAME SUBSYSTEM	9
SPATIAL COORDINATES IN ROTOR SUBSYSTEM	13
SPATIAL COORDINATES IN LANDING GEAR SUBSYSTEM	23
ANALYTICAL METHODS	24
LAGRANGIAN FORMULATION OF STABILITY EQUATIONS	24
KINETIC ENERGY TERMS	26
EXTERNAL LOAD TERMS	29
STRAIN ENERGY AND DISSIPATION TERMS	37
RESULTANT EQUATIONS AND SOLUTION	41
Part II. Aeroelastic Stability Analysis Correlation and Trend Studies	43
INTRODUCTION	45
AEROELASTIC STABILITY CORRELATION	45
CORRELATION WITH 1/10-SCALE TILT-ROTOR DYNAMIC MODEL	45
ONERA 13-FOOT-DIAMETER PROPELLER	45
MODEL 160 TILT-ROTOR 1/22-SCALE DYNAMICALLY SIMILAR MODEL	45
ROTOR DERIVATIVE TREND STUDIES AND CORRELATION	46
STABILITY TREND STUDIES	46
ROTOR DERIVATIVE TREND STUDIES	47
ROTOR LOADS	47
AEROELASTIC STABILITY: CORRELATION AND TREND STUDIES	55
CORRELATION	55
TREND STUDIES	57

	Page
ROTOR DERIVATIVE TREND STUDIES	71
ROTOR DERIVATIVE SENSITIVITY TO ADVANCE RATIO, FLAP FREQUENCY, AND LOCK NUMBER	71
ROTOR DERIVATIVE SENSITIVITY TO LEAD-LAG NATURAL FREQUENCY	71
Part III. New Methodology for Aeroelastic Prop/Rotor Loads Analysis	77
INTRODUCTION	79
HISTORY OF DEVELOPMENT	81
PROGRAM FLOW DIAGRAM	83
DYNAMIC ANALYSIS	88
BLADE IDEALIZATION	88
DYNAMIC BLADE RESPONSE	91
AERODYNAMIC ANALYSIS	100
AIRLOADS	100
DEVELOPMENT OF THE THEORY	100
METHOD OF CALCULATION	109
NONUNIFORM DOWNWASH	111
Part IV. Prop/Rotor Loads Analysis Correlation	121
INTRODUCTION	123
PROP/ROTOR LOADS CORRELATION	124
INTRODUCTION	124
CORRELATION RESULTS	124
HELICOPTER LOADS CORRELATION	184
INTRODUCTION	184
CORRELATION RESULTS	184
Part V. Impact and Potential of New Methods	291
IMPACT OF NEW METHODOLOGY ON PREDICTION CAPABILITY	293
AEROELASTIC STABILITY	293
ROTOR LOADS	293
POTENTIAL EFFECTS OF NEW CAPABILITY ON DESIGN PRACTICE AND CRITERIA	296
AEROELASTIC STABILITY	296
ROTOR LOADS	296
REFERENCES	297
BIBLIOGRAPHY	300

LIST OF ILLUSTRATIONS

Figure		Page
1	Typical Landing Gear Representation	6
2	Schematic Diagram of Rotor Hub Showing Blade Mount Eccentricities	7
3	Aircraft Coordinate Axes (Fixed-Coordinate System)	10
4	Local Coordinate Axes for Typical Segment of Various Airframe Components	11
5	Rotor and Aircraft Coordinate Axes	14
6	Shaft and Disc Coordinate Systems	15
7	Rotating and Nonrotating Coordinate Systems	17
8	Blade Normal Section and Local Blade Coordinate Systems	17
9	Aerodynamic Parameters at a Typical Blade Section	32
10	Model 160 1/10-Scale V/STOL Tilt-Rotor Dynamically Similar Model	48
11	NASA Ames and AARL 13-Foot Fiberglass Performance Model Rotor	49
12	Model 160 1/22-Scale Dynamically Similar V/STOL Tilt-Rotor Model	50
13	Mathematical Model for Rotor Derivative Parametric Trend Studies	51
14	Model 213 1/9-Scale Dynamically Similar V/STOL Tilt/Stowed-Rotor Conversion Model . . .	52
15	Model 170 1/3-Scale Dynamically Similar V/STOL Wing and Rotor Model	53
16	Model 160 1/10-Scale Performance Model	54
17	Model 160 1/10-Scale Tilt-Rotor Dynamically Similar Full-Span Model Correlation	59

Figure		Page
18	Model 160 1/10-Scale Tilt-Rotor Dynamically Similar Semi-Span Model Correlation	60
19	Blade Flutter Correlation 13' Diameter Rotor Performance Test (ONERA 1968)	61
20	Model 160 1/22-Scale Dynamically Similar V/STOL Tilt-Rotor Model Correlation Torsionally Stiff Wing Spar	62
21	Model 160 1/22-Scale Dynamically Similar V/STOL Tilt-Rotor Model Correlation Torsionally Weak Wing Spar	63
22	Model 213 1/9-Scale Conversion Model - 85 Ft/Sec Derivative Variation with RPM	64
23	M213 1/9-Scale Conversion Model - 141 Ft/Sec Derivative Variation With RPM	65
24	Calculated Pitch-Lag-Flap Flutter Boundaries for a Preliminary Design Blade	66
25	Blade Flutter Sensitivity to Changes in Lead-Lag Frequency Ratio and Thrust	67
26	Individual Blade Flutter Sensitivity to Torsional Natural Frequency	68
27	Sensitivity of Wing/Rotor Pitch-Lag-Flap Flutter to Precone Angle and Thrust	69
28	Sensitivity of Wing/Rotor Pitch-Lag-Flap Flutter to Drag Offset and Thrust	70
29	Variation of Rotor Derivatives With Flap Frequency. Lag Frequency High	73
30	Effect of Lock Number on Rotor Derivatives for Flap Frequency Ratios $n\beta$ = 1.1, 1.2, 1.6, and 2.0	74
31	Variation of Normal and Side Force Derivatives with Lag Frequency Ratio	75
32	Variation of Hub Pitching and Yawing Moment Derivatives with Lag Frequency Ratio	76
33	Flow Chart for Rotor Loads Program	84

Figure		Page
34	Schematic Diagram of Nonuniform Downwash Routine for Normal Conditions	85
35	Comparison of Actual Blade and Idealized Blade	89
36	Spanwise Variation of Blade Physical Properties	90
37	Coupled Flap-Lag-Torsion Matrix Sequence . . .	96
38	Shed Wake Assumptions	101
39	Engineering Approximation Accounting for Yawed Flow	103
40	Typical Oscillating Airfoil Test Data for Vertol 23010-1.58 Airfoil	104
41	The Dynamic C_L Calculation in Stall Is Dependent on the Dynamic Stall Delay	107
42	The Dynamic C_M in Stall Is Dependent on the Dynamic Stall Delay	107
43	Comparison of Test and Theoretical Dynamic C_L and C_M for a Condition Below Stall, at Stall, and Beyond Stall	110
44	Effect of Downwash	113
45	Calculation of Trailed Vortex Strength	114
46	Vortex Vector Diagram	116
47	1/3-Scale LIT Blade, Predicted and Measured Alternating Flap Bending in Hover Due to Cyclic Pitch	130
48	1/3-Scale LIT Blade, Predicted and Measured First- and Second-Harmonic Flap Bending in Hover Due to Cyclic Pitch	131
49	1/3-Scale LIT Blade, Predicted and Measured Flap Bending Waveform in Hover for 8 Degrees Cyclic Pitch	132
50	1/3-Scale LIT Blade, Predicted and Measured Alternating Chord Bending in Hover Due to Cyclic Pitch	133

Figure		Page
51	1/3-Scale LIT Blade, Predicted and Measured First- and Second-Harmonic Chord Bending in Hover Due to Cyclic Pitch	134
52	1/3-Scale LIT Blade, Predicted and Measured Chord Bending Waveform in Hover for 8 Degrees Cyclic Pitch	135
53	1/3-Scale LIT Blade, Predicted and Measured Alternating Torsion in Hover Due to Cyclic Pitch	136
54	1/3-Scale LIT Blade, Predicted and Measured Torsional Waveform in Hover for 8 Degrees Cyclic Pitch	137
55	1/3-Scale LIT Blade, Predicted and Measured Steady Rotor Pitching Moment in Hover Due to Cyclic Pitch	138
56	1/3-Scale LIT Blade, Predicted and Measured Steady Rotor Yawing Moment in Hover Due to Cyclic Pitch	139
57	Model 160 Performance Model, Predicted and Measured Alternating Flap Bending Moment in Hover for 3 Degrees Cyclic Pitch	140
58	Model 160 Performance Model, Predicted and Measured First- and Second-Harmonic Flap Bending Moment in Hover for 3 Degrees Cyclic Pitch	141
59	Model 160 Performance Model, Predicted and Measured Flap Bending Waveform in Hover for 3 Degrees Cyclic at 2,300 RPM	142
60	Model 160 Performance Model, Predicted and Measured Alternating Chord Bending Moment in Hover for 3 Degrees Cyclic Pitch	143
61	Model 160 Performance Model, Predicted and Measured First- and Second-Harmonic Chord Bending Moment in Hover for 3 Degrees Cyclic Pitch	144
62	Model 160 Performance Model, Predicted and Measured Chord Bending Waveform in Hover for 3 Degrees Cyclic at 2,300 RPM	145

Figure		Page
63	Model 160 Performance Model, Predicted and Measured Blade Torsional Waveform in Hover for 3 Degrees Cyclic at 2,300 RPM	146
64	Model 160 Performance Model, Predicted and Measured Alternating Torsion in Hover for 3 Degrees Cyclic Pitch	147
65	Model 160 Performance Model, Predicted and Measured Steady Rotor Pitching Moment in Hover for 3 Degrees Cyclic Pitch	148
66	Model 160 Performance Model, Predicted and Measured Alternating Flap Bending Moment in Hover for 3 Degrees Cyclic Pitch	149
67	1/3-Scale LIT Blade, Predicted and Measured Alternating Flap Bending Due to Rotor Angle of Attack in Cruise	152
68	1/3-Scale LIT Blade, Predicted and Measured Alternating Chord Bending Due to Rotor Angle of Attack in Cruise	153
69	1/3-Scale LIT Blade, Predicted and Measured Alternating Torsion Due to Rotor Angle of Attack in Cruise	154
70	1/3-Scale LIT Blade, Predicted and Measured First- and Second-Harmonic Flap Bending Due to Rotor Angle of Attack in Cruise	155
71	1/3-Scale LIT Blade, Predicted and Measured First- and Second-Harmonic Chord Bending Due to Rotor Angle of Attack in Cruise	156
72	1/3-Scale LIT Blade, Predicted and Measured Flap Bending Waveform for 5.1 Degrees Angle of Attack in Cruise	157
73	1/3-Scale LIT Blade, Predicted and Measured Chord Bending Waveform for 5.1 Degrees Angle of Attack in Cruise	158
74	1/3-Scale LIT Blade, Predicted and Measured Torsional Waveform for 5.1 Degrees Angle of Attack in Cruise	159
75	1/3-Scale LIT Blade, Predicted and Measured Steady Rotor Pitching Moment Due to Rotor Angle of Attack in Cruise	160

Figure		Page
76	1/3-Scale LIT Blade, Predicted and Measured Steady Rotor Yawing Moment Due to Rotor Angle of Attack in Cruise	161
77	Model 213 1/9-Scale Conversion Model, Predicted and Measured First- and Second-Harmonic Flap Bending at 0.125R Due to Rotor Angle of Attack in Cruise	164
78	Model 213 1/9-Scale Conversion Model, Predicted and Measured Flap Bending Waveform at 0.125R for 2.26 Degrees Rotor Angle of Attack in Cruise	165
79	Model 213 1/9-Scale Conversion Model, Predicted and Measured First- and Second-Harmonic Chord Bending at 0.125R Due to Rotor Angle of Attack in Cruise	166
80	Model 213 1/9-Scale Conversion Model, Predicted and Measured Chord Bending Waveform at 0.125R for 2.26 Degrees Rotor Angle of Attack in Cruise	167
81	Model 213 1/9-Scale Conversion Model, Predicted and Measured Alternating Torsion at 0.150R Due to Rotor Angle of Attack in Cruise	168
82	Model 213 1/9-Scale Conversion Model, Predicted and Measured Steady Rotor Pitching Moment Due to Rotor Angle of Attack in Cruise	169
83	Model 213 1/9-Scale Conversion Model, Predicted and Measured Steady Rotor Yawing Moment Due to Rotor Angle of Attack in Cruise	170
84	1/3-Scale Lit Blade, Predicted and Measured Effect of Cyclic Pitch on Alternating Flap Bending in Transition	173
85	1/3-Scale LIT Blade, Predicted and Measured First- and Second-Harmonic Flap Bending Due to Pitch in Transition	174
86	1/3-Scale LIT Blade, Predicted and Measured Flap Bending Waveform for 0 Degrees Cyclic Pitch in Transition	175

Figure		Page
87	1/3-Scale LIT Blade, Predicted and Measured Alternating Chord Bending Due to Cyclic Pitch in Transition	176
88	1/3-Scale LIT Blade, Predicted and Measured First- and Second-Harmonic Chord Bending Due to Cyclic Pitch in Transition	177
89	1/3-Scale LIT Blade, Predicted and Measured Chord Bending Waveform for 0 Degrees Cyclic Pitch in Transition	178
90	1/3-Scale LIT Blade, Predicted and Measured Alternating Torsion Due to Cyclic Pitch in Transition	179
91	1/3-Scale LIT Blade, Predicted and Measured Torsional Waveform for 0 Degrees Cyclic Pitch in transition	180
92	1/3-Scale LIT Blade, Predicted and Measured Rate of Change of Steady Rotor Pitching Moment With Cyclic in Transition	181
93	1/3-Scale LIT Blade, Predicted and Measured Rate of Change of Steady Rotor Yawing Moment With Cyclic in Transition	182
94	1/3-Scale LIT Blade, Predicted and Measured Total Steady Rotor In-Plane Hub Moment With Cyclic in Transition	183
95	CH-47C Aft Rotor, Predicted and Measured Alternating Pitch Link Loads With Airspeed . .	189
96	CH-47C Aft Rotor Pitch Link Load Amplitude Distribution for 114 Data Cycles at 123 Knots	190
97	CH-47C With Advanced-Geometry Blades, Aft Rotor Predicted and Measured Alternating Pitch Link Loads With Airspeed	191
98	Model 347 With CH-47C Blades, Aft Rotor Predicted and Measured Alternating Pitch Link Loads With Airspeed	192
99	CH-47C Aft Rotor, Predicted and Measured Pitch Link Load Waveform at 111 Knots	193

Figure		Page
100	CH-47C Aft Rotor, Predicted and Measured Pitch Link Waveform at 123 Knots	194
101	CH-47C Aft Rotor, Predicted and Measured Pitch Link Load Waveform at 133 Knots	195
102	CH-47C With Advanced-Geometry Blades, Aft Rotor Predicted and Measured Pitch Link Waveform at 117 Knots	196
103	CH-47C With Advanced-Geometry Blades, Aft Rotor Predicted and Measured Pitch Link Waveform at 126 Knots	197
104	CH-47C With Advanced-Geometry Blades, Aft Rotor Predicted and Measured Pitch Link Waveform at 132 Knots	198
105	Model 347 With CH-47C Blades, Aft Rotor Predicted and Measured Pitch Link Load Waveform at 122 Knots	199
106	Model 347 With CH-47C Blades, Aft Rotor Predicted and Measured Pitch Link Load Waveform at 140 Knots	200
107	Model 347 With CH-47C Blades, Aft Rotor Predicted and Measured Pitch Link Load Waveform at 152 Knots	201
108	CH-47C Forward Rotor, Predicted and Measured Alternating Pitch Link Loads With Airspeed	202
109	CH-47C Forward Rotor, Predicted and Measured Pitch Link Load Waveform at 111 Knots	203
110	CH-47C Forward Rotor, Predicted and Measured Pitch Link Load Waveform at 123 Knots	204
111	CH-47C Forward Rotor, Predicted and Measured Pitch Link Load Waveform at 133 Knots	205
112	CH-47C With Advanced-Geometry Blades, Forward Rotor Predicted and Measured Alternating Pitch Link Loads with Airspeed . .	206

Figure		Page
113	CH-47C With Advanced-Geometry Blades, Forward Rotor Predicted and Measured Pitch Link Waveform at 117 Knots	207
114	CH-47C With Advanced-Geometry Blades, Forward Rotor Predicted and Measured Pitch Link Waveform at 126 Knots	208
115	CH-47C With Advanced-Geometry Blades, Forward Rotor Predicted and Measured Pitch Link Waveform at 132 Knots	209
116	Model 347 With CH-47C Blades, Forward Rotor Predicted and Measured Alternating Pitch Link Loads With Airspeed	210
117	Model 347 With CH-47C Blades, Forward Rotor Predicted and Measured Pitch Link Load Waveform at 122 Knots	211
118	Model 347 With CH-47C Blades, Forward Rotor Predicted and Measured Pitch Link Load Waveform at 140 Knots	212
119	Model 347 With CH-47C Blades, Forward Rotor Predicted and Measured Pitch Link Load Waveform at 152 Knots	213
120	CH-47C L-01, Predicted Flap Bending Moment Mode Shapes in a Vacuum at 230 RPM	216
121	CH-47C Aft Rotor, Predicted and Measured Alternating Flap Bending Moment at V = 111 Knots	217
122	CH-47C Aft Rotor, Predicted and Measured Alternating Flap Bending Moment at V = 123 Knots	218
123	CH-47C Aft Rotor, Predicted and Measured Alternating Flap Bending Moment at V = 133 Knots	219
124	CH-47C With Advanced-Geometry Blades, Aft Rotor Predicted and Measured Alternating Flap Bending Moment at 100 Knots	220
125	CH-47C With Advanced-Geometry Blades, Aft Rotor Predicted and Measured Alternating Flap Bending Moment at 117 Knots	221

Figure		Page
126	CH-47C With Advanced-Geometry Blades, Aft Rotor Predicted and Measured Alternating Flap Bending Moment at 126 Knots	222
127	CH-47C With Advanced-Geometry Blades, Aft Rotor Predicted and Measured Alternating Flap Bending Moment at 132 Knots	223
128	Model 347 With CH-47C Blades, Aft Rotor Predicted and Measured Alternating Flap Bending Moment at V = 87 Knots	224
129	Model 347 With CH-47C Blades, Aft Rotor Predicted and Measured Alternating Flap Bending Moment at V = 122 Knots	225
130	Model 347 With CH-47C Blades, Aft Rotor Predicted and Measured Alternating Flap Bending Moment at V = 140 Knots	226
131	Model 347 With CH-47C Blades, Aft Rotor Predicted and Measured Alternating Flap Bending Moment at V = 152 Knots	227
132	CH-47C Forward Rotor, Predicted and Measured Alternating Flap Bending Moment at V = 111 Knots	228
133	CH-47C Forward Rotor, Predicted and Measured Alternating Flap Bending Moment at V = 123 Knots	229
134	CH-47C Forward Rotor, Predicted and Measured Alternating Flap Bending Moment at V = 133 Knots	230
135	CH-47C With Advanced-Geometry Blades, Forward Rotor Predicted and Measured Alternating Flap Bending Moment at 100 Knots	231
136	CH-47C With Advanced-Geometry Blades, Forward Rotor Predicted and Measured Alternating Flap Bending Moment at 117 Knots	232
137	CH-47C With Advanced-Geometry Blades, Forward Rotor Predicted and Measured Alternating Flap Bending Moment at 126 Knots	233

Figure		Page
138	CH-47C With Advanced-Geometry Blades, Forward Rotor Predicted and Measured Alternating Flap Bending Moment at 132 Knots	234
139	Model 347 With CH-47C Blades, Forward Rotor Predicted and Measured Alternating Flap Bending Moment at V = 87 Knots	235
140	Model 347 With CH-47C Blades, Forward Rotor Predicted and Measured Alternating Flap Bending Moment at V = 122 Knots	236
141	Model 347 With CH-47C Blades, Forward Rotor Predicted and Measured Alternating Flap Bending Moment at V = 140 Knots	237
142	Model 347 With CH-47C Blades, Forward Rotor Predicted and Measured Alternating Flap Bending Moment at V = 152 Knots	238
143	CH-47C Aft Rotor, Predicted and Measured Alternating Chord Bending Moment at V = 111 Knots	242
144	CH-47C Aft Rotor, Predicted and Measured Alternating Chord Bending Moment at V = 123 Knots	243
145	CH-47C Aft Rotor, Predicted and Measured Alternating Chord Bending Moment at V = 133 Knots	244
146	CH-47C With Advanced-Geometry Blades, Aft Rotor Predicted and Measured Alternating Chord Bending Moment at 100 Knots	245
147	CH-47C With Advanced-Geometry Blades, Aft Rotor Predicted and Measured Alternating Chord Bending Moment at 117 Knots	246
148	CH-47C With Advanced-Geometry Blades, Aft Rotor Predicted and Measured Alternating Chord Bending Moment at 126 Knots	247
149	CH-47C With Advanced-Geometry Blades, Aft Rotor Predicted and Measured Alternating Chord Bending Moment at 132 Knots	248

Figure		Page
150	Model 347 With CH-47C Blades, Aft Rotor Predicted and Measured Alternating Chord Bending Moment at V = 87 Knots	249
151	Model 347 With CH-47C Blades, Aft Rotor Predicted and Measured Alternating Chord Bending Moment at V = 122 Knots	250
152	Model 347 With CH-47C Blades, Aft Rotor Predicted and Measured Alternating Chord Bending Moment at V = 140 Knots	251
153	Model 347 With CH-47C Blades, Aft Rotor Predicted and Measured Alternating Chord Bending Moment at V = 152 Knots	252
154	Model 347 With CH-47C Blades, Aft Rotor Predicted and Measured Chord Bending Waveform at 152 Knots	253
155	CH-47C Rotor Blade Lag Damper Force Versus Piston Velocity	254
156	CH-47C L-01, Predicted Chord Bending Moment Mode Shapes in a Vacuum at 230 RPM . .	255
157	CH-47C Forward Rotor, Predicted and Measured Alternating Chord Bending Moment at V = 111 Knots	256
158	CH-47C Forward Rotor, Predicted and Measured Alternating Chord Bending Moment at V = 123 Knots	257
159	CH-47C Forward Rotor, Predicted and Measured Alternating Chord Bending Moment at V = 133 Knots	258
160	CH-47C With Advanced-Geometry Blades, Forward Rotor Predicted and Measured Alternating Chord Bending Moment at 100 Knots	259
161	CH-47C With Advanced-Geometry Blades, Forward Rotor Predicted and Measured Alternating Chord Bending Moment at 117 Knots	260

Figure		Page
162	CH-47C With Advanced-Geometry Blades, Forward Rotor Predicted and Measured Alternating Chord Bending Moment at 126 Knots	261
163	CH-47C With Advanced-Geometry Blades, Forward Rotor Predicted and Measured Alternating Chord Bending Moment at 132 Knots	262
164	Model 347 With CH-47C Blades, Forward Rotor Predicted and Measured Alternating Chord Bending Moment at V = 87 Knots	263
165	Model 347 With CH-47C Blades, Forward Rotor Predicted and Measured Alternating Chord Bending Moment at V = 122 Knots	264
166	Model 347 With CH-47C Blades, Forward Rotor Predicted and Measured Alternating Chord Bending Moment at V = 140 Knots	265
167	Model 347 With CH-47C Blades, Forward Rotor Predicted and Measured Alternating Chord Bending Moment at V = 152 Knots	266
168	Model 347 With CH-47C Blades, Forward Rotor Predicted and Measured Chord Bending Waveform at 152 Knots	267
169	CH-34 Predicted and Measured Lift/Unit Span at 0.55R at 110 Knots	270
170	CH-34 Predicted and Measured Lift/Unit Span at 0.75R at 110 Knots	271
171	CH-34 Predicted and Measured Lift/Unit Span at 0.85R at 110 Knots	272
172	CH-34 Predicted and Measured Lift/Unit Span at 0.95R at 110 Knots	273
173	CH-34 Predicted and Measured Lift/Unit Span at 0.99R at 110 Knots	274
174	CH-34 Predicted and Measured Lift/Unit Span at 0.55R at 110 Knots	275
175	CH-34 Predicted and Measured Lift/Unit Span at 0.75R at 110 Knots	276

Figure		Page
176	CH-34 Predicted and Measured Lift/Unit Span at 0.85R at 110 Knots	277
177	CH-34 Predicted and Measured Lift/Unit Span at 0.95R at 110 Knots	278
178	CH-34 Predicted and Measured Lift/Unit Span at 0.99R at 110 Knots	279
179	CH-34 Predicted and Measured Lift/Unit Span at 0.55R at 150 Knots	280
180	CH-34 Predicted and Measured Lift/Unit Span at 0.75R at 150 Knots	281
181	CH-34 Predicted and Measured Lift/Unit Span at 0.85R at 150 Knots	282
182	CH-34 Predicted and Measured Lift/Unit Span at 0.95R at 150 Knots	283
183	CH-34 Predicted and Measured Lift/Unit Span at 0.99R at 150 Knots	284
184	CH-34 Predicted and Measured Lift/Unit Span at 0.55R at 175 Knots	285
185	CH-34 Predicted and Measured Lift/Unit Span at 0.75R at 175 Knots	286
186	CH-34 Predicted and Measured Lift/Unit Span at 0.85R at 175 Knots	287
187	CH-34 Predicted and Measured Lift/Unit Span at 0.95R at 175 Knots	288
188	CH-34 Predicted and Measured Lift/Unit Span at 0.99R at 175 Knots	289

LIST OF TABLES

Table		Page
I	Summary of Prop/Rotor Models Used for Correlation	125
II	Summary of Test Conditions of Prop/Rotor Models Used for Correlation	126
III	Summary of Prop/Rotor Model Test Data Used for Correlation	126
IV	Summary of Helicopters and Flight Conditions Used for Correlation	185
V	Summary of Helicopter Test Data Used for Correlation	185
VI	Summary of Prop/Rotor Bending Moment Correlation Results	295

LIST OF SYMBOLS

A	acceleration vector; rotor disc area, square feet
$AC_{1, 2, 3, 4}$	damping coefficients of landing gear dashpot elements
$AK_{1, 2, 3, 4}$	spring rates of landing gear stiffness elements
a	centrifugal force along pitch axis; lift curve slope, nondimensional
ay	centrifugal force perpendicular to pitch axis
{B}	root column matrix
b	blade identification; blade number; distance from pitch axis to pitch link perpendicular to pitch link; semichord length of airfoil section
C	coriolis force in the lag direction due to blade flap motion
{C}	tip column matrix
C_D	aerodynamic drag coefficient
C_L	aerodynamic lift coefficient
C_M	aerodynamic pitching moment coefficient
C_T	thrust coefficient, thrust/ρ AV_T, nondimensional
C_β, C_ζ	viscous damping coefficient at flap and lag pin, respectively
c	vortex identification
$\bar{c}$	mean chord of blade, feet
c_o	chord width
D	drag force parallel to the relative wind
[D]	transfer matrix across blade station

$[E]$	transfer matrix across elastic beam
e_o	hub offset at center of rotation
e_x	blade drag offset, nondimensional
e_β	flap pin offset from center of rotation measured along pitch axis
$[F]$	transfer matrix across force
F_x	longitudinal force due to flap foreshortening
$\overline{F}_x$	longitudinal coriolis force due to blade lag motion
F_{xF}, F_{yF}, F_{zF}	fixed-system hub forces
F_{xR}, F_{yR}, F_{zR}	rotating hub forces
f_x	component of thrust in disc plane parallel to pitch axis
f_r, f_y, f_z	blade root forces
g	acceleration due to gravity
H	blade element drag force in disc plane
$\dot{h}$	velocity of airfoil section normal to resultant airstream velocity locally
I_b	blade moment of inertia about center of rotation, slugs per square foot
I_β	flap inertia
I_θ	pitch inertia
I_ζ	lag inertia
i	rotor shaft angle
i_N	nacelle tilt angle from horizontal cruise position, degrees
K_β, K_ζ	clockspring rate at blade flap and lag pin, respectively
L	distance from flap to lag hinge; lift force perpendicular to the relative wind

l_n	distance along blade from station n to station n + 1
M	aerodynamic pitching moment; Mach number; blade mass
[M]	transfer matrix across mass
M_x	blade pitching moment
M_y	blade flapping moment
M_z	blade lag moment
M_{XF}, M_{YF}, M_{ZF}	fixed-system hub moments
M_{XR}, M_{YR}, M_{ZR}	rotating hub moments
m	blade station mass
m_x, m_y, m_z	blade root moments
N_C	wing chordwise bending frequency, per rev
N_P	wing torsion frequency, per rev
N_{R1}	0.86 per rev
N_{R2}	1.2 per rev
N_{R3}	6.0 per rev
N_V	wing vertical bending frequency, per rev
N_β	blade flapping frequency, per rev
N_ζ	blade lead-lag frequency, per rev
N_θ	blade torsion or pitch frequency, per rev
n	station identification
nc, ns	Fourier coefficient
P	aerodynamic force perpendicular to chord line
P_o	tilt angle of rotor shaft axis relative to aircraft longitudinal axis

P_{FS}, P_R, P_T, P_W	tilt angles of various airframe segments relative to aircraft longitudinal axis
Q	aerodynamic moment at aerodynamic center
q	Fourier coefficient; dynamic pressure, $1/2\rho V^2$, pounds per square foot
R	dissipation function; blade radius, feet
r	blade segment location along axis of blade measured from hub center; distance from lag hinge to blade particle
S	speed of sound
[S]	spring matrix in coupled flap-pitch or lag damper matrix in uncoupled lag
T	kinetic energy; thrust (perpendicular to disc plane)
U	strain energy; resultant airspeed at a blade segment; total velocity of blade particle
U_P	airspeed component normal to U_T but lying in a blade normal section; vertical component of total velocity (parallel to shaft axis)
U_T	airspeed component parallel to rotor disc; tangential component of total velocity (in disc plane)
u_i	generalized coordinate
u_{oi}	steady-state component of generalized coordinate
V_T	tipspeed, feet per second
V_X, V_Y, V_Z	aircraft speed components in fixed coordinate system
$\bar{V}_X$, $\bar{V}_Y$, $\bar{V}_Z$	components of induced velocity in rotating disc coordinate system
V_y	blade shear in lag direction
V_z	blade shear in flap direction

$\bar{V}_1$	blade velocity in hover
$\bar{V}_2$	induced velocity
v_o	downwash velocity
W_e	virtual work of external forces
x_n	distance from rotor center to blade particle
y	flexible deflection in lag direction of pitch axis (positive forward)
$\bar{y}$	mass offset from the pitch axis (positive aft)
z	flexible deflection in the flap direction of the pitch axis (positive up)
α	aerodynamic angle of attack
β	blade flap angle measured from disc plane; precone angle, degrees
Γ	vortex strength
γ	steady-state blade geometric pitch angle including collective pitch, geometric twist, and elastic twist; blade Lock number, $\rho a \bar{c} R^4 / I_b$, nondimensional
ΔD	drag force on airfoil segment
$\Delta H, \Delta T, \Delta M$, etc.	blade station aerodynamic loads
ΔL	lift force on airfoil segment
ΔM	pitching moment on airfoil segment
$\Delta\varepsilon$	distance from pitch axis forward to aerodynamic center nondimensionalized to blade chord
ε	distance from the midchord forward to the pitch axis nondimensionalized to blade chord
ζ_x	lag component of steady-state blade segment deflection
ζ_z	flap component of steady-state blade segment deflection

ζ_y	radial shortening at blade segment under steady state
η_{xj}	lag component of jth blade mode shape
η_{zj}	flap component of jth blade mode shape
η_{yj}	radial shortening corresponding to jth blade mode shape
$\overline{\eta}_{jk}$	radial shortening accompanying jth and kth modes acting simultaneously
θ	pitch angle measured from pitch axis
θ_{TE}	pitch component of rotor disc teeter angle
θ_{75}	blade collective pitch setting at 0.75R, degrees
λ	nondimensional downwash velocity; inflow ratio; advance ratio, axial speed/tipspeed, nondimensional
μ	advance ratio
ξ	lag angle measured from pitch axis
ρ	mass density of air, slugs per cubic foot
ρ_m	mass density of structural components
σ	rotor solidity, total blade area divided by disc area, nondimensional
ϕ	induced angle
$\{\phi_{df}\}_j$	vector of displacement components associated with jth airframe mode shape
$\{\phi_{rf}\}_j$	vector of rotational components associated with jth airframe mode shape
ψ	blade azimuth position
ψ_{TE}	yaw component of rotor disc teeter angle
Ω	rotor angular velocity, rpm
$\omega_A(j)$	modal frequency of jth airframe mode
$\omega_B(j)$	modal frequency of jth blade mode

Part I. New Methodology for Aeroelastic Stability Analysis

A. K. Amos

INTRODUCTION

SCOPE OF ANALYSIS

The new methodology has been developed to provide significant improvements in areas where existing tools have not been particularly successful in the prediction or correlation of aeroelastic instability behavior (1). It also provides greater capability and flexibility in the representation of rotor, airframe/empennage, and landing gear structural interactions and is therefore applicable to entire aircraft systems. These include configurations such as tilt-rotor and tilt-wing V/STOL designs and single-rotor as well as tandem-rotor helicopters. Flight conditions of such systems ranging from hover through transition to cruise are accommodated, along with ground effects involving landing gear dynamics. System features included in the analysis are:

- Large-diameter rotors with flexible blades
- Airframe structure with flexible aerodynamic lifting surfaces
- Landing gear with linear viscoelastic properties.

Starting with a description of the system and flight conditions and using basic aeroelastic properties of the system and environment as supplied, the analysis establishes a number of possible states of perturbation about steady flight conditions and the inherent stability of each.

FEATURES OF ANALYSIS

The analysis provides for large aeroelastic steady deflections of the rotor blades, which may include mechanical precone and static droop. These deflections are one source of kinematic and dynamic couplings between blade bending and blade torsional vibrations. The effects of these couplings on the stability of the system have been discussed in Reference 1. Their inclusion in the analysis represents a significant advance in the state of the art.

Lumped mass and inertia representation and modal synthesis of the system perturbations from steady state form the basis of the analysis. Fully coupled pitch-flap-lag blade modes are provided for. The aerodynamics of the rotor blades and airframe lifting surfaces are based on two-dimensional quasi-steady theories, but with provision for reducing the blade aerodynamics to a steady (or static) formulation. The air inflow through the rotor disc is treated very generally, providing for any inclination from axial to purely tangential. This

eliminates one of the most serious application restrictions inherent in existing analyses.

LIMITATIONS OF ANALYSIS

The consideration of steady blade deflections is limited to collective effects only; i.e., cyclic blade deflections are assumed negligible. Cyclic perturbations are considered, however. The blade aerodynamic treatment does not account for stall effects, although provision is made for the use of experimentally determined lift curve slope values.

SYSTEM DEFINITION

STRUCTURAL IDEALIZATION

The entire system is partitioned structurally into three subsystems: rotor, airframe, and landing gear. Each subsystem is made up of a number of available components which serve as building blocks for defining particular problems during actual application of the analysis.

The landing gear subsystem has four possible oleo-tire assembly units. Each is idealized as a rigid mass supported by a number of linear springs and dashpots as shown in Figure 1. The springs and dashpots represent the oleo and tire viscoelasticity. The point P lies in and has compatible displacements with the airframe subsystem; it is, however, isolated rotationally from the airframe. The mass has an independent translational freedom parallel to the Z axis (Figure 1). In the other two coordinate directions it follows rigidly the translations of point P.

Two general configuration rotors are provided for in the rotor subsystem. They can be particularized to tandem-rotor helicopter, tilt-rotor, tilt-wing, and conventional propeller-driven aircraft configurations; or to a single-rotor helicopter system by retaining only one of the two. Each rotor consists of three or more blades attached to a central hub. The hub is mounted to a rotating shaft which is encased in a nacelle or pylon structure as illustrated in Figure 2. The hub and shaft combination is isolated from the nacelle/pylon in rotation about the shaft axis. Additionally, the hub is free to teeter in pitch and yaw relative to the nacelle/pylon.

The blades are mounted to the hub with variable offsets from the hub center of rotation as illustrated in Figure 2. Each blade is flexible in both bending and torsion and is idealized as a slender elastic beam. Its steady-state configuration is characterized by possibly large deflections in flap, lead-lag, and pitch, including geometric twist and collective pitch setting. The hub freedoms of motion are made up of (1) all translations of the nacelle/pylon structure at its interface with the hub; (2) nacelle/pylon rotations other than that about the shaft axis; and (3) teetering and shaft axis rotational freedoms of the hub. The blade kinematics are separated into rigid components arising from the hub motions and elastic deformations relative to the hub.

The following components constitute the airframe subsystem: two wings, two tails, one fin, and two nacelle/pylon structures. The wings, tails, and fin are each considered as a two-dimensional lifting surface. Each is idealized as a finite-element aeroelastic system.

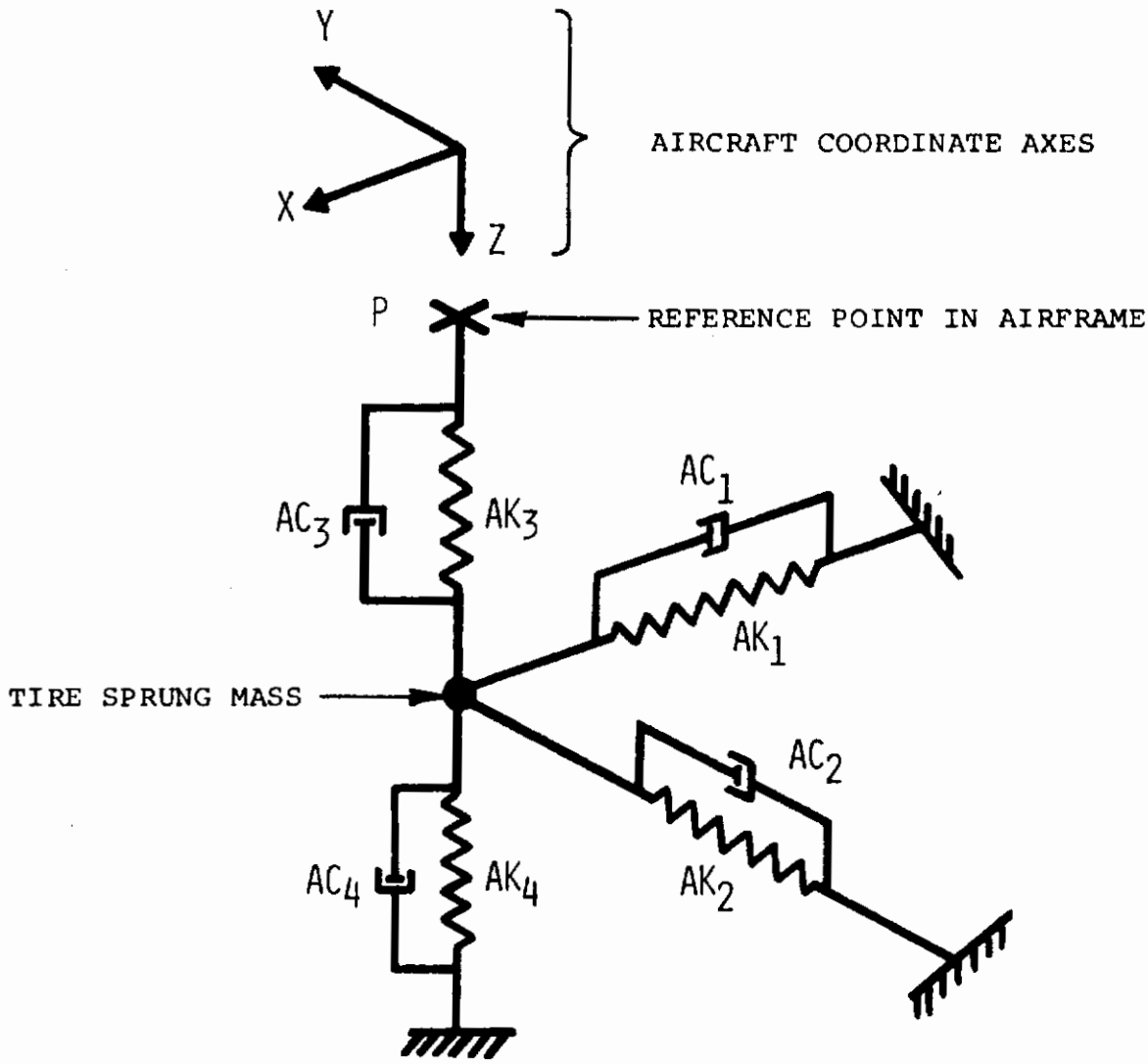

Figure 1. Typical Landing Gear Representation

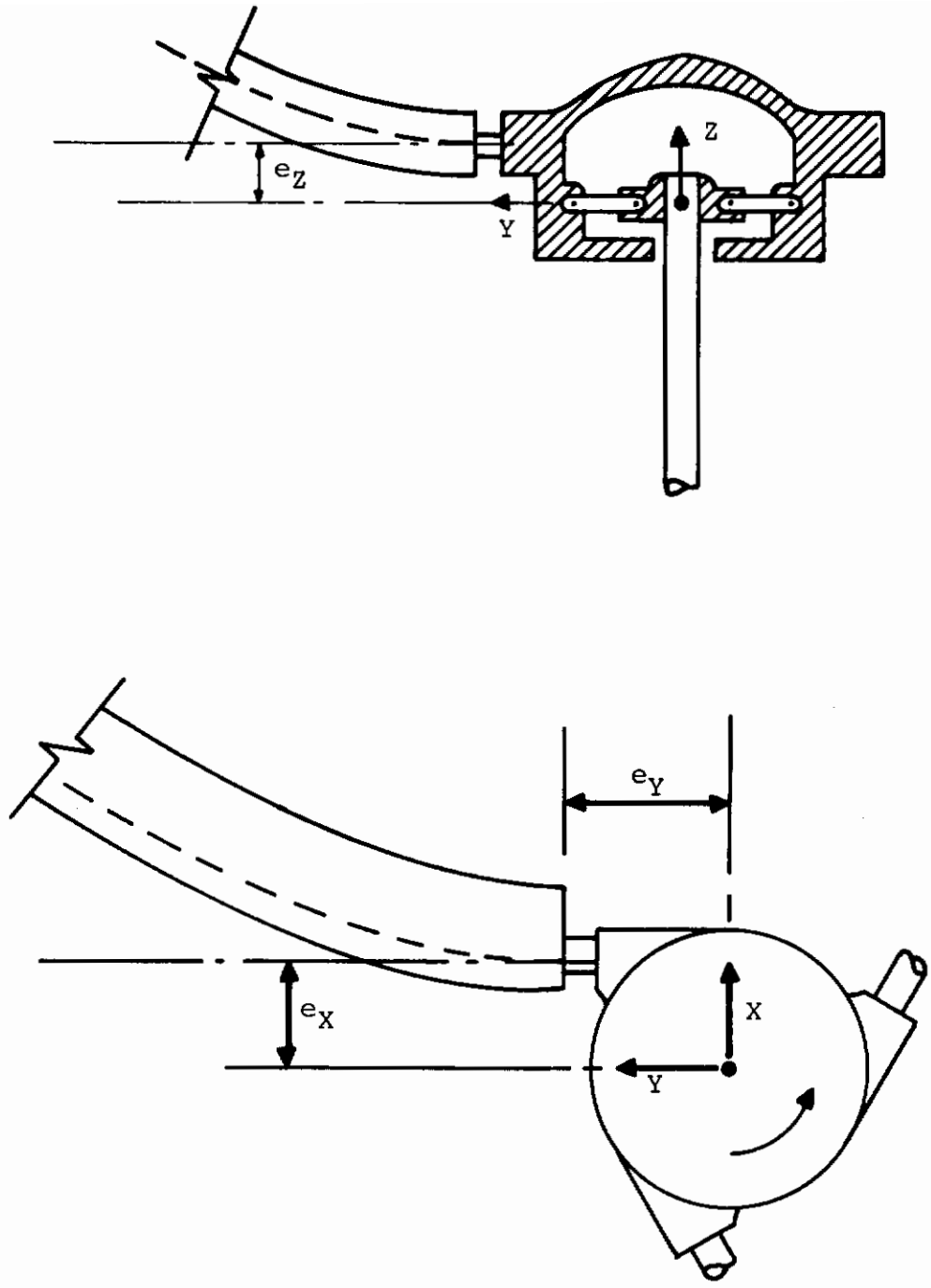

Figure 2. Schematic Diagram of Rotor Hub Showing Blade Mount Eccentricities

MATHEMATICAL MODELING

The mathematical model of the system envisions the aircraft in its steady-state configuration as fixed in space with the air streaming past it. A set of coordinates fixed to the aircraft in the steady state is therefore also fixed in space.

The structural idealization of the landing gears also defines the mathematical model of the subsystem. In the airframe and rotor subsystems, the mathematical model is derived from a finite-element discretization of the individual components. The inertial and aerodynamic properties of the elements are lumped at representative points or sections and the elastic properties are averaged between adjacent elements. As an alternative to considering the actual elastic properties, the model postulates the existence of characteristic functions or modes which reflect the inertial and elastic properties of the finite-element system. The kinematic freedoms of the finite elements are therefore represented by modal synthesis, employing modal freedoms as generalized coordinates.

COORDINATE SYSTEMS AND TRANSFORMATIONS

FIXED-COORDINATE SYSTEM

A system of orthogonal coordinates is established in space such that the X axis is coincident with the steady-state longitudinal axis of the aircraft. The origin is located at some convenient location along this axis. The Z axis is such that it would represent a vertically downward direction, if the aircraft were in level flight. Figure 3 illustrates the fixed-coordinate system.

SPATIAL COORDINATES IN AIRFRAME SUBSYSTEM

Each finite element of the airframe components is associated with a reference point whose spatial coordinates in the fixed-coordinate system under steady state are represented by the vector $\{X_{FR}\}_o$. A local coordinate system is defined with origin at the reference point under steady-state conditions. Transformation from the local to the fixed-coordinate systems is represented by the matrix $[T_{AF}]$.

Figure 4 illustrates the local axes for typical elements of the various airframe components. Except for the fin element, each local system shown represents a rotation of the fixed system through a pitch angle about the Y axis. The coordinate transformation is thus given generally by

$$[T_{AF}] = \begin{bmatrix} \cos P, & 0, & \sin P \\ 0 \ , & 1, & 0 \\ -\sin P, & 0, & \cos P \end{bmatrix} \qquad (1)$$

where $P = P_W$ for wing element
$= P_{FS}$ for fuselage element
$= P_T$ for tail element
$= 0$ for fin element

Under perturbations, the reference point is displaced and rotated relative to its steady-state location. These are represented in the local coordinate system by the displacement vector $\{d_R\}$ and the rotation vector $\{\theta_R\}$.

The spatial coordinate vector of the reference point in a perturbed configuration is thus given in the fixed-coordinate system by

$$\{X_{FR}\} = \{X_{FR}\}_o + [T_{AF}]\{d_R\}. \qquad (2)$$

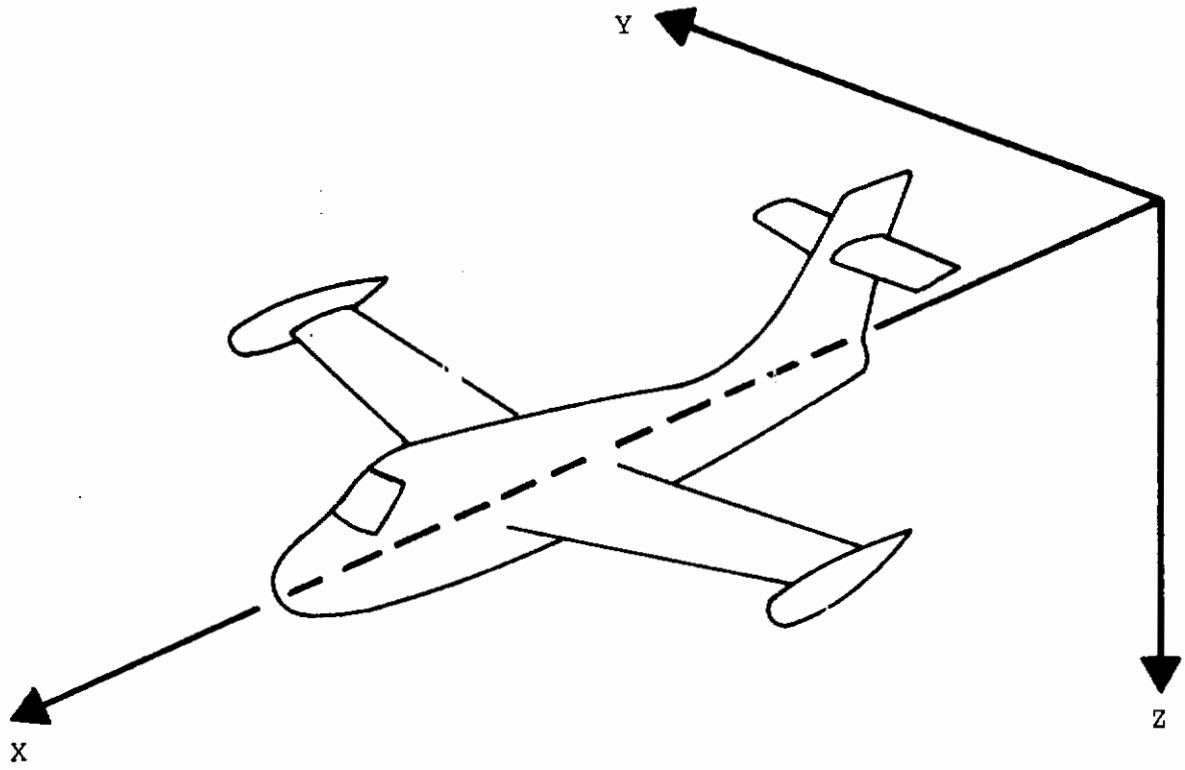

Figure 3. Aircraft Coordinate Axes (Fixed-Coordinate System)

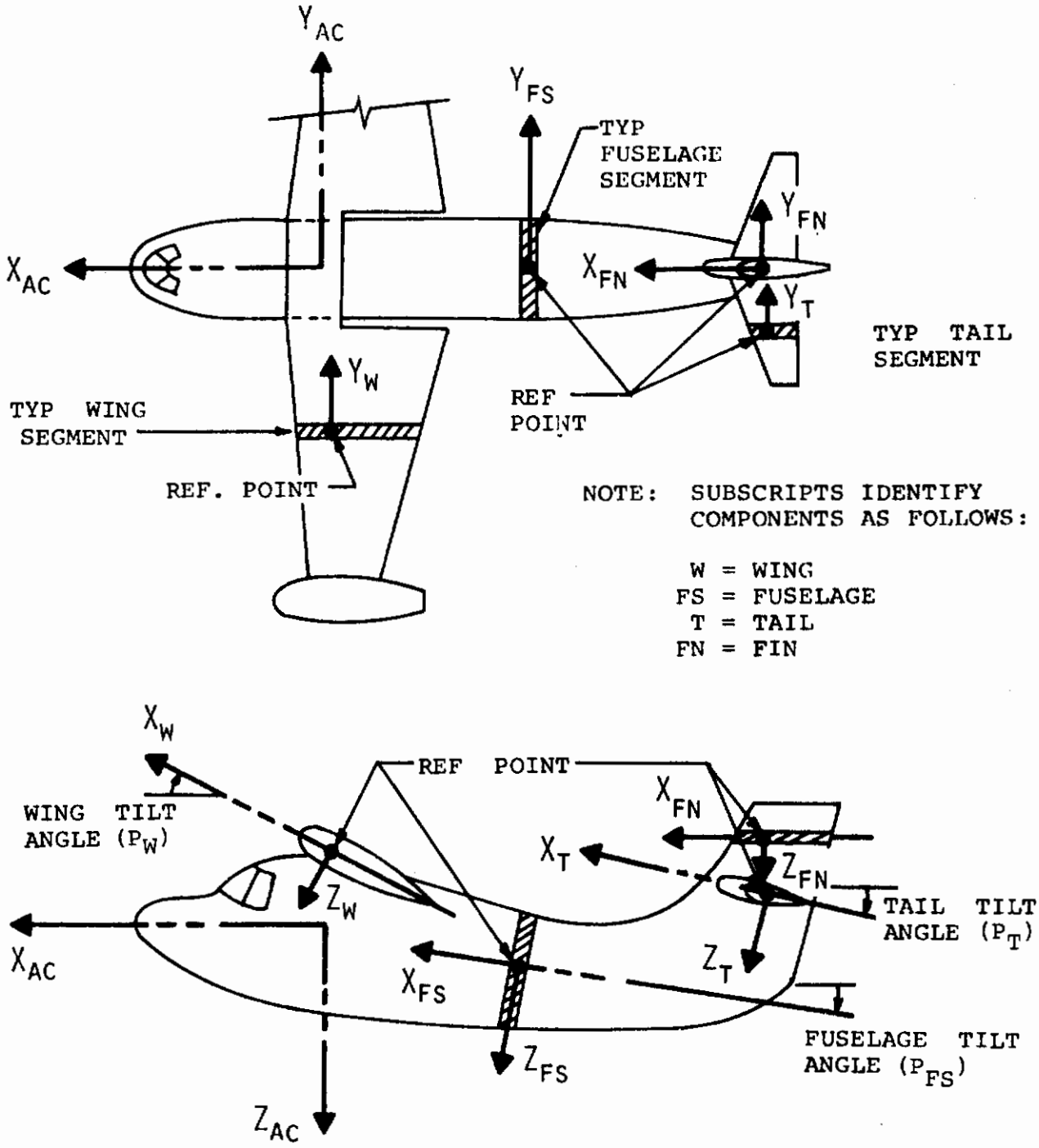

Figure 4. Local Coordinate Axes for Typical Segment of Various Airframe Components

Consider now a point A in the element whose coordinates relative to the reference point under steady-state conditions is given in the local coordinate system by the vector $\{\lambda_A\}$. Its perturbed spatial coordinate vector in the fixed system is

$$\{X_{FA}\} = \{X_{FR}\}_o + [T_{AF}](\{d_R\} + [T_{\theta R}]\{\lambda_A\}) \tag{3}$$

where $[T_{\theta R}] = \begin{bmatrix} 1 , & -\theta_{RZ}, & \theta_{RY} \\ \theta_{RZ}, & 1 , & -\theta_{RX} \\ -\theta_{RY}, & \theta_{RX} & 1 \end{bmatrix}$. (4)

See Reference 2 for derivation of transformation.

Modal synthesis of the displacement and rotation vectors $\{d_R\}$ and $\{\theta_R\}$ is expressed by

$$\{d_R\} = \sum_j \{\phi_{df}\}_j \, q_{Aj}$$

$$\{\theta_R\} = \sum_j \{\phi_{rf}\}_j \, q_{Aj} \tag{5}$$

where $\{\phi_{df}\}_j$ is a vector of the displacement components and $\{\phi_{rf}\}_j$ is a vector of the rotational components of the jth airframe mode specified at the reference point.

Variations of the spatial coordinates with the modal freedoms can now be established as below:

$$\{X_{FR}\}_{,j} = \frac{\partial\{X_{FR}\}}{\partial q_{Aj}} = [T_{AF}] \{\phi_{df}\}_j$$

$$\{X_{FA}\}_{,j} = \frac{\partial\{X_{FA}\}}{\partial q_{Aj}} = [T_{AF}](\{\phi_{df}\}_j + [T_{\theta R}]_{,j}\{\lambda_A\}) \tag{6}$$

where $[T_{\theta R}]_{,j} = \frac{\partial}{\partial q_{Aj}} [T_{\theta R}] = \begin{bmatrix} 0 , & -\phi_{rfj}(3), & \phi_{rfj}(2) \\ \phi_{rfj}(3), & 0 , & -\phi_{rfj}(1) \\ \phi_{rfj}(2), & \phi_{rfj}(1), & 0 \end{bmatrix}$ (7)

SPATIAL COORDINATES IN ROTOR SUBSYSTEM

Figure 5 shows the rotor shaft axis in relation to the fixed coordinate system under steady-state conditions. The hub location on this axis is used to establish the origin of a steady-state shaft coordinate system as shown in Figure 6. The coordinate transformation from this system to the fixed system is represented by $[T_p]$ given by

$$[T_p] = \begin{bmatrix} -\sin P_o, & 0, & \cos P_o \\ 0, & 1, & 0 \\ -\cos P_o, & 0, & -\sin P_o \end{bmatrix} . \qquad (8)$$

In a perturbed configuration, the hub is displaced and rotated relative to its steady-state location. These are represented by a displacement vector $\{d_H\}$ and a rotation vector $\{\theta_H\}$ referenced to the steady-state shaft coordinate system.

A perturbed shaft coordinate system is now defined with its origin at the perturbed hub location and representing a rotation of the steady-state shaft system through the rotation vector $\{\theta_H\}$. The transformation between the perturbed and steady-state shaft coordinate systems is

$$[T_w] = \begin{bmatrix} 1, & -\theta_{HZ}, & \theta_{HY} \\ \theta_{HZ}, & 1, & -\theta_{HX} \\ -\theta_{HY}, & \theta_{HX}, & 1 \end{bmatrix} . \qquad (9)$$

In the perturbed configuration, the hub is considered teetered so that the disc plane is not normal to the shaft axis at the hub.

A nonrotating disc coordinate system $({}^{(3)}X, {}^{(3)}Y, {}^{(3)}Z)$ is defined with its origin at the perturbed hub location and the ${}^{(3)}Z$ direction normal to the disc plane. It represents a rotation of the perturbed shaft coordinate system through a teeter angle with components Φ_{TEX} about ${}^{(4)}X$ and Φ_{TEY} about ${}^{(4)}Y$. The transformation

$$[T_{TE}] = \begin{bmatrix} \cos \Phi_{TEY}; & 1/2(\sin \Phi_{TEY})(\sin \Phi_{TEX}); & \sin \Phi_{TEY} \\ 1/2(\sin \Phi_{TEY})(\sin \Phi_{TEX}); & \cos \Phi_{TEX}; & -\sin \Phi_{TEX} \\ -\sin \Phi_{TEY}; & \sin \Phi_{TEX}; & (\cos \Phi_{TEY})(\cos \Phi_{TEX}) \end{bmatrix} \qquad (10)$$

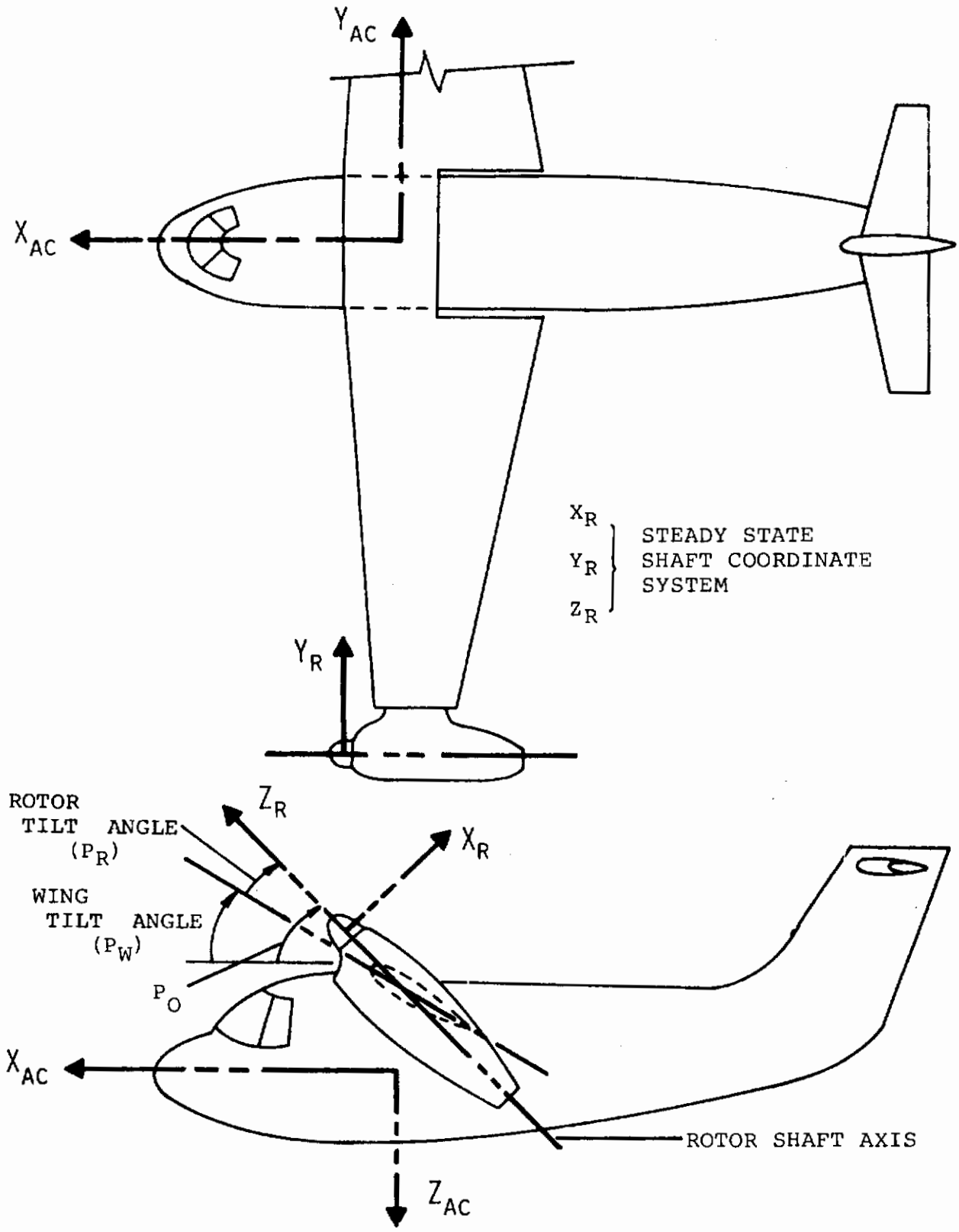

Figure 5. Rotor and Aircraft Coordinate Axes

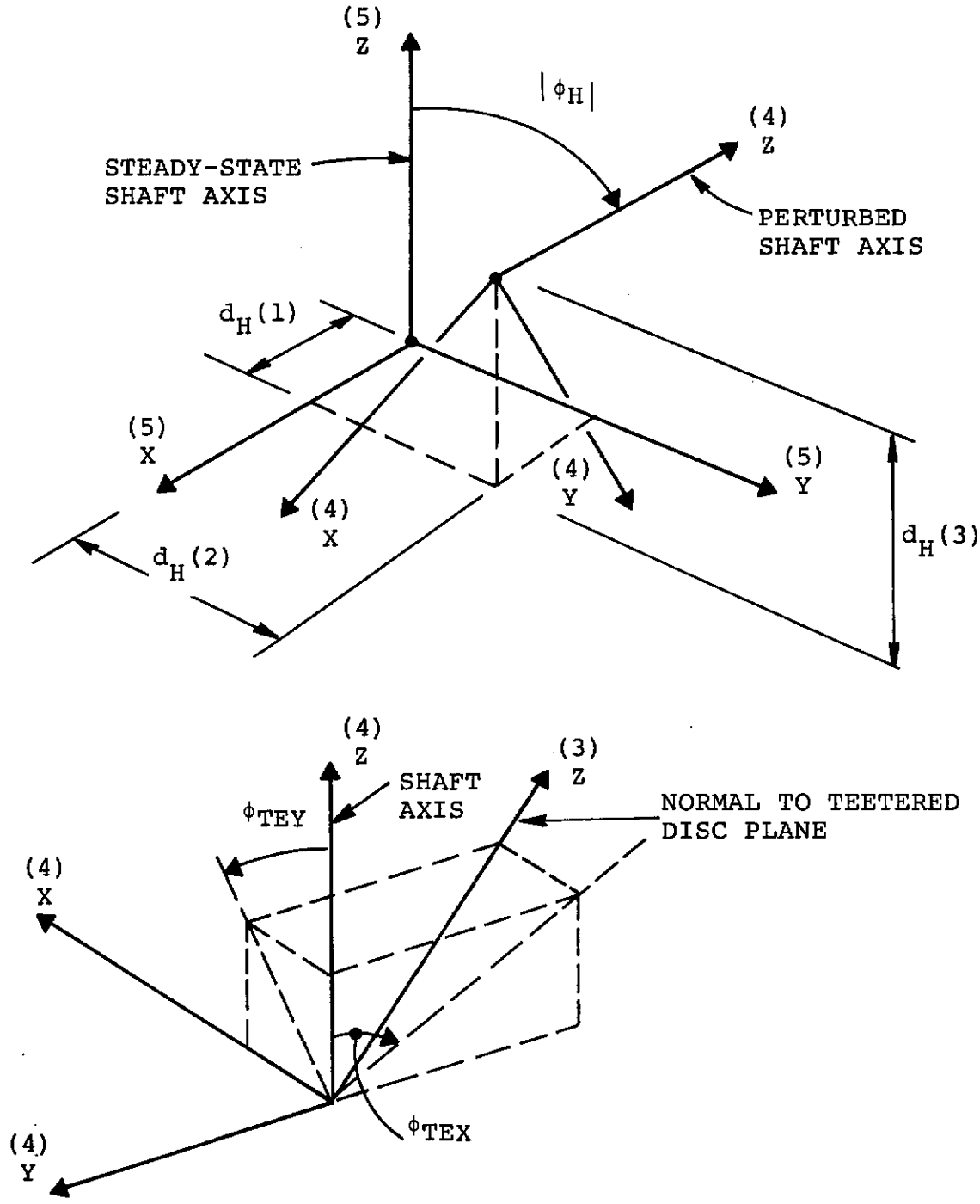

Figure 6. Shaft and Disc Coordinate Systems

relates the nonrotating disc system to the perturbed shaft coordinate system. A rotating disc coordinate system is established by rotating the nonrotating system through the azimuth angle ψ as shown in Figure 7. Transformation from rotating to nonrotating system is given by

$$[T_\psi] = \begin{bmatrix} \sin\psi & \cos\psi & 0 \\ -\cos\psi & \sin\psi & 0 \\ 0 & 0 & 1 \end{bmatrix} . \qquad (11)$$

The displacement vector $\{X_{BA}\}$ referred to the rotating disc system locates a predetermined reference point on the chord axis of a representative blade segment section. The plane of the blade section is used to define a normal blade section coordinate system as shown in Figure 8. The transformation from this to the rotating disc system is given by

$$[T_S] = \begin{bmatrix} (1-1/2\theta_L^2), & \theta_L & , -1/2\theta_L\theta_F \\ -\theta_L & , 1-1/2(\theta_L^2 + \theta_F^2), & -\theta_F \\ -1/2\theta_L\theta_F , & \theta_F & , (1-1/2\theta_F^2) \end{bmatrix} . \qquad (12)$$

A local blade coordinate system (X_B, Y_B, Z_B) with X_B parallel to the chord axis is next defined with the origin at the reference point. This represents a rotation of natural blade section coordinate system by the blade section twist angle θ_T about $Y^{(1)}$. Hence the transformation matrix

$$[T_\theta] = \begin{bmatrix} \cos\theta_T, & 0 & \sin\theta_T \\ 0 & , 1 & 0 \\ -\sin\theta_T, & 0 & \cos\theta_T \end{bmatrix} . \qquad (13)$$

Consider now a point A in the blade section with coordinates in the blade coordinate system represented by $\{\lambda_A\}$. In the normal blade section system it has coordinates represented by

$$\{X_A\}^{(1)} = [T_\theta]\{\lambda_A\} . \qquad (14)$$

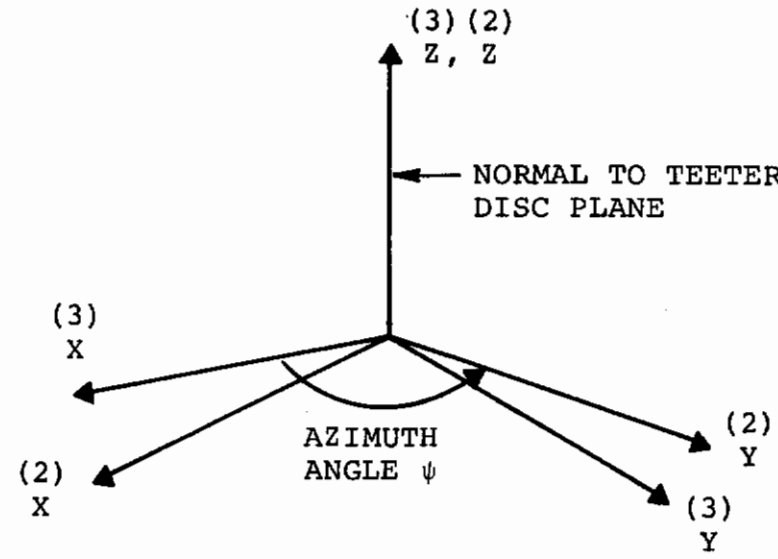

Figure 7. Rotating and Nonrotating Coordinate Systems

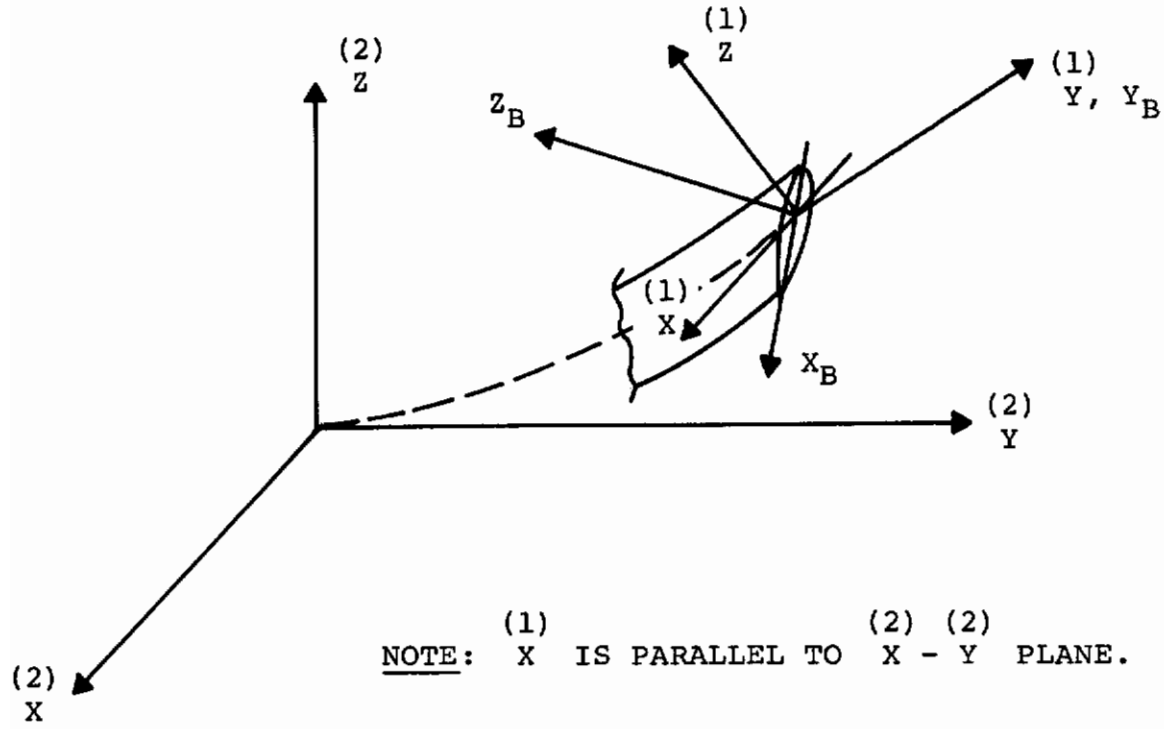

Figure 8. Blade Normal Section and Local Blade Coordinate Systems

In the other coordinate systems point A has the coordinates shown below:

Rotating Disc System:

$$\{X_A\}^{(2)} = \{X_{BA}\} + [T_s][T_\theta]\{\lambda_A\} \tag{15}$$

Nonrotating Disc System:

$$\{X_A\}^{(3)} = [T_\psi](\{X_{BA}\} + [T_s][T_\theta]\{\lambda_A\}) \tag{16}$$

Perturbed Shaft System:

$$\{X_A\}^{(4)} = [T_{TE}][T_\psi](\{X_{BA}\} + [T_s][T_\theta]\{\lambda_A\}) \tag{17}$$

Steady-State Shaft System:

$$\{X_A\}^{(5)} = \{d_H\} + [T_w][T_{TE}][T_\psi](\{X_{BA}\} + [T_s][T_\theta]\{\lambda_A\}) \tag{18}$$

Fixed System:

$$\{X_{FA}\} = [T_p](\{d_H\} + [T_w][T_{TE}][T_\psi](\{X_{BA}\} + [T_s][T_\theta]\{\lambda_A\}) \tag{19}$$

The blade coordinates are made up of steady-state and perturbation components. The latter are obtained from modal synthesis. Thus the blade twist angle is given by

$$\theta_T = (\gamma + \sum_j \theta_{Rj}\, q_{Bj})\Gamma \quad , \tag{20}$$

where γ is the net steady-state twist angle locally;

θ_{Rj} is the blade twist component of the jth blade mode. The components of $\{X_{BA}\}$ are given by

$$\begin{aligned} X_{BAX} &= (\zeta_X + \sum_j \eta_{xj}\, q_{Bj})\Gamma \\ X_{BAY} &= r - \zeta_y - \sum_j \eta_{yj}\, q_{Bj} - \sum_{jk} \bar{\eta}_{jk}\, q_{Bj}\, q_{Bk} \\ X_{BAZ} &= \zeta_z + \sum_j \eta_{zj}\, q_{Bj} \end{aligned} \tag{21}$$

Γ = +1 for clockwise rotation of the blades as viewed from the shaft side and -1 for counterclockwise rotation

where ζ_x and ζ_z are the steady-state blade deflections in lag and flap; ζ_y is the radial shortening due to the above deflections; r is the radial distance of the segment reference section; η_{xj} and η_{zj} are modal components in lag and flap, and η_{yj} and η_{jk} are modal contributions to the blade radial shortening.

The angles θ_L and θ_F are slope angles associated with the lag and flap displacement components;

$$\text{i.e.,}\quad \theta_L = X_{BAX,r} = (\zeta_{x,r} + \sum_j \eta_{x,rj}\, q_{Bj})\Gamma$$

$$\theta_F = X_{BAZ,r} = \zeta_{z,r} + \sum_j \eta_{z,rj}\, q_{Bj} \qquad (22)$$

Using equations 20 and 22 in equations 12 and 13 yields:

$$[T_\theta]_o = \begin{bmatrix} \cos\gamma & 0 & \Gamma\sin\gamma \\ 0 & 1 & 0 \\ -\Gamma\sin\gamma & 0 & \cos\gamma \end{bmatrix}$$

$$\left(\frac{\partial}{\partial q_{Bi}}[T_\theta]\right)_o \cong \begin{bmatrix} 1, & 0, & \Gamma\theta_{Ri} \\ 0, & 1, & 0 \\ -\Gamma\theta_{Ri}, & 0, & 0 \end{bmatrix}$$

$$[T_s]_o = \begin{bmatrix} (1-1/2\zeta_{x,r}^2) & ; & \Gamma\zeta_{x,r} & ; & -1/2\Gamma\zeta_{x,r}\zeta_{z,r} \\ -\Gamma\zeta_{x,r} & ; & [1-1/2(\zeta_{x,r}^2+\zeta_{z,r}^2)] & ; & -\zeta_{z,r} \\ -1/2\Gamma\zeta_{x,r}\,\zeta_{z,r} & ; & \zeta_{z,r} & ; & (1-1/2\zeta_{z,r}^2) \end{bmatrix}$$

$$\left(\frac{\partial}{\partial q_{Bi}}[T_s]\right)_o = \begin{bmatrix} -\zeta_{x,r}\,\eta_{x,ri}; & \Gamma\eta_{x,ri}; & -1/2\Gamma(\zeta_{x,r}\,\eta_{z,ri}+\zeta_{z,r}\,\eta_{x,ri}) \\ -\Gamma\eta_{x,ri}; & -(\zeta_{x,r}\,\eta_{x,ri}+\zeta_{z,r}\,\eta_{z,ri}); & -\eta_{z,ri} \\ -1/2\Gamma(\zeta_{x,r}\,\eta_{z,ri}+\zeta_{z,r}\,\eta_{x,ri}); & \eta_{z,ri}; & -\zeta_{z,r}\,\eta_{z,ri} \end{bmatrix}$$

(23)

From equation 21

$$\{X_{BA}\}_o = \begin{Bmatrix} e_x + r\zeta_x \\ r - \zeta_y \\ e_z + \zeta_z \end{Bmatrix}$$

$$\left(\frac{\partial}{\partial q_{Bi}} \{X_{BA}\}\right)_o = \begin{Bmatrix} r\eta_{xi} \\ -\eta_{yi} \\ \eta_{zi} \end{Bmatrix}$$

$$\left(\frac{\partial^2}{\partial q_{Bi}\, \partial q_{Bj}} \{X_{BA}\}\right)_o = \begin{Bmatrix} 0 \\ -\bar{n}_j k \\ 0 \end{Bmatrix} \qquad (24)$$

The azimuth angle ψ for an individual blade is

$$\psi = \psi_o + r\Omega t + q_\psi \qquad (25)$$

where q_ψ is the rotor hub rotational freedom about the shaft axis. Hence:

$$[T_\psi]_o = \begin{bmatrix} \sin(\psi_o + r\Omega t); & \cos(\psi_o + r\Omega t); & 0 \\ -\cos(\psi_o + r\Omega t); & \sin(\psi_o + r\Omega t); & 0 \\ 0 \quad ; & 0 \quad ; & 1 \end{bmatrix}$$

$$\frac{\partial}{\partial t}[T_\psi])_o = r\Omega \begin{bmatrix} \cos(\psi_o + r\Omega t); & -\sin(\psi_o + r\Omega t); & 0 \\ \sin(\psi_o + r\Omega t); & \cos(\psi_o + r\Omega t); & 0 \\ 0 \quad ; & 0 \quad ; & 0 \end{bmatrix}$$

$$\left(\frac{\partial^2}{\partial t^2}[T_\psi]\right)_o = -\Omega^2 \begin{bmatrix} \sin(\psi_o + r\Omega t); & \cos(\psi_o + r\Omega t); & 0 \\ -\cos(\psi_o + r\Omega t); & \sin(\psi_o + r\Omega t); & 0 \\ 0 \quad ; & 0 \quad ; & 0 \end{bmatrix}$$

$$\left(\frac{\partial^2}{\partial q_\psi \, \partial t}\,[T_\psi]\right)_o = -\Gamma\Omega\begin{bmatrix} \sin(\psi_o+\Gamma\Omega t); & \cos(\psi_o+\Gamma\Omega t); & 0 \\ -\cos(\psi_o+\Gamma\Omega t); & \sin(\psi_o+\Gamma\Omega t); & 0 \\ 0 \quad ; & 0 \quad ; & 0 \end{bmatrix}$$

$$\left(\frac{\partial^3}{\partial q_\psi \, \partial t^2}\,[T_\psi]\right)_o = -\Omega^2\begin{bmatrix} \cos(\psi_o+\Gamma\Omega t); & -\sin(\psi_o+\Gamma\Omega t); & 0 \\ \sin(\psi_o+\Gamma\Omega t); & \cos(\psi_o+\Gamma\Omega t); & 0 \\ 0 \quad ; & 0 \quad ; & 0 \end{bmatrix}$$

$$\left(\frac{\partial}{\partial q_\psi}\,[T_\psi]\right)_o = \begin{bmatrix} \cos(\psi_o+\Gamma\Omega t); & -\sin(\psi_o+\Gamma\Omega t); & 0 \\ \sin(\psi_o+\Gamma\Omega t); & \cos(\psi_o+\Gamma\Omega t); & 0 \\ 0 \quad ; & 0 \quad ; & 0 \end{bmatrix}$$

$$\left(\frac{\partial^2}{\partial q_\psi^2}\,[T_\psi]\right)_o = \begin{bmatrix} -\sin(\psi_o+\Gamma\Omega t); & -\cos(\psi_o+\Gamma\Omega t); & 0 \\ \cos(\psi_o+\Gamma\Omega t); & -\sin(\psi_o+\Gamma\Omega t); & 0 \\ 0 \quad ; & 0 \quad ; & 0 \end{bmatrix} \qquad (26)$$

The hub teeter angles ϕ_{TEX} and ϕ_{TEY} have steady-state and perturbation components;

i.e., $\phi_{TEX} = \psi_{TE} + q_{TEX}$

$$\phi_{TEY} = \theta_{TE} + q_{TEY} \qquad (27)$$

Substituting in equation 10,

$$[T_{TE}]_o = \begin{bmatrix} \cos\theta_{TE}; & 1/2 \sin\theta_{TE} \sin\psi_{TE}; & \sin\theta_{TE} \\ 1/2 \sin\theta_{TE} \sin\psi_{TE}; & \cos\psi_{TE}; & -\sin\psi_{TE} \\ -\sin\theta_{TE}; & \sin\psi_{TE}; & \cos\theta_{TE}\cos\psi_{TE} \end{bmatrix}$$

$$\left(\frac{\partial}{\partial q_{TEX}}\,[T_{TE}]\right)_o = [T_{TE}]_o \begin{bmatrix} 0 & 0 & 0 \\ 0 & 0 & -1 \\ 0 & 1 & 0 \end{bmatrix}$$

$$\left(\frac{\partial}{\partial q_{TEY}}\,[T_{TE}]\right)_o = [T_{TE}]_o \begin{bmatrix} 0 & 0 & 1 \\ 0 & 0 & 0 \\ -1 & 0 & 0 \end{bmatrix}$$

$$\left(\frac{\partial^2}{\partial q_{TEX}\,\partial q_{TEX}}\,[T_{TE}]\right)_o = [T_{TE}]_o \begin{bmatrix} 0 & 0 & 0 \\ 0 & -1 & 0 \\ 0 & 0 & -1 \end{bmatrix}$$

$$\left(\frac{\partial^2}{\partial q_{TEX}\,\partial q_{TEY}}\,[T_{TE}]\right)_o = [T_{TE}]_o \begin{bmatrix} 0 & 1/2 & 0 \\ 1/2 & 0 & 0 \\ 0 & 0 & 0 \end{bmatrix}$$

$$\left(\frac{\partial^2}{\partial q_{TEY}\,\partial q_{TEY}}\,[T_{TE}]\right)_o = [T_{TE}]_o \begin{bmatrix} -1 & 0 & 0 \\ 0 & 0 & 0 \\ 0 & 0 & -1 \end{bmatrix} \qquad (28)$$

The shaft perturbation displacements and rotations are represented by:

$$\{d_H\} = \sum_j \{\phi_{df}\}_j\, q_{Aj}$$

$$\{\theta_H\} = \sum_j \{\phi_{rf}\}_j\, q_{Aj} \qquad (29)$$

Therefore, from equation 9,

$$[T_w]_o = [I]$$

$$\left(\frac{\partial}{\partial q_{Ai}}\,[T_w]\right) = \begin{bmatrix} 0 & ; & -\phi_{rfi}(3); & \phi_{rfi}(2) \\ \phi_{rfi}(3); & & 0 & ; & -\phi_{rfi}(1) \\ -\phi_{rfi}(2); & & \phi_{rfi}(1); & & 0 \end{bmatrix}$$

Also, $\{d_H\}_o = \{o\}$

$$\left(\frac{\partial}{\partial q_{Ai}} \{d_H\}\right)_o = \{\phi_{df}\}_i \qquad (30)$$

SPATIAL COORDINATES IN LANDING GEAR SUBSYSTEM

The spatial coordinates of the reference point P are

$$\{X_{FP}\} = \{X_{FP}\}_o + \sum_j \{\phi_{df}\}_j q_{Aj} \quad . \qquad (31)$$

The mass point spatial coordinates are given by

$$\{X_{FH}\} = \sum_j \begin{Bmatrix} \phi df(x) \\ \phi df(y) \\ 0 \end{Bmatrix}_j q_{Aj} + \begin{Bmatrix} 0 \\ 0 \\ 1 \end{Bmatrix} q_L \quad . \qquad (32)$$

$\{\phi df\}_j$ is a vector of displacements at P due to the jth airframe mode.

q_L is the individual vertical freedom of the mass.

ANALYTICAL METHODS

LAGRANGIAN FORMULATION OF STABILITY EQUATIONS

Lagrange's equations of motion for nonconservative systems may be written as

$$\frac{d}{dt}\left(\frac{\partial T}{\partial \dot{u}_i}\right) - \frac{\partial T}{\partial u_i} + \frac{\partial U}{\partial u_i} + \frac{\partial R}{\partial \dot{u}_i} - \frac{\partial We}{\partial u_i} = 0 \quad , \tag{33}$$

where T = kinetic energy,

U = strain energy,

R = dissipation function of the system,

We = virtual work of external forces,

u_i = ith component of generalized coordinates of the system.

Application of the above to a dynamic system leads to equilibrium equations which can be represented generally by

$$F_i\ (u_j;\ \dot{u}_j;\ \ddot{u}_j,\ t) = 0 \tag{34}$$

and are generally nonlinear in the generalized coordinates.

The coordinates for an aircraft system can be separated into steady-state and perturbation components. The latter may be considered as a linear combination of known characteristic functions with their undetermined coefficients constituting the perturbation freedoms;

$$\text{i.e.,}\quad u_i = u_{oi} + \sum_k \phi_{ik}\, q_k \quad , \tag{35}$$

where u_{oi} = steady-state component of ith coordinate,

ϕ_{ik} = kth characteristic function in the ith coordinate,

qk = kth perturbation freedom.

Hence equation 34 becomes

$$F_i\ (u_{oj};\ \dot{u}_{oj};\ \ddot{u}_{oj};\ q_j;\ \dot{q}_j;\ \ddot{q}_j;\ t) = 0 \quad . \tag{36}$$

A Taylor's series expansion leads to

$$(F_i)_o + \sum_j \left[\left(\frac{\partial F_i}{\partial q_j}\right)_o q_j + \left(\frac{\partial F_i}{\partial \dot{q}_j}\right)_o \dot{q}_j + \left(\frac{\partial F_i}{\partial \ddot{q}_j}\right)_o \ddot{q}_j\right]$$

$$+ 1/2 \sum_j \sum_k \left[\left(\frac{\partial^2 F_i}{\partial q_j \partial q_k}\right)_o q_j q_k + \left(\frac{\partial^2 F_i}{\partial q_j \partial \dot{q}_k}\right)_o q_j \dot{q}_k + \left(\frac{\partial^2 F_i}{\partial \dot{q}_j \partial q_k}\right)_o \dot{q}_j q_k\right.$$

$$+ \left(\frac{\partial^2 F_i}{\partial q_j \partial \ddot{q}_k}\right)_o q_j \ddot{q}_k + \left(\frac{\partial^2 F_i}{\partial \ddot{q}_j \partial q_k}\right)_o \ddot{q}_j q_k + \left(\frac{\partial^2 F_i}{\partial \dot{q}_j \partial \dot{q}_k}\right)_o \dot{q}_j \dot{q}_k$$

$$+ \left(\frac{\partial^2 F_i}{\partial \dot{q}_j \partial \ddot{q}_k}\right)_o \dot{q}_j \ddot{q}_k + \left(\frac{\partial^2 F_i}{\partial \ddot{q}_j \partial \dot{q}_k}\right)_o \ddot{q}_j \dot{q}_k + \left.\left(\frac{\partial^2 F_i}{\partial \ddot{q}_j \partial \ddot{q}_k}\right)_o \ddot{q}_j \ddot{q}_k\right]$$

$$+ (\text{higher order derivative terms}) = 0 \quad . \tag{37}$$

The zero subscripts in the above relation indicate evaluation of the quantities involved for steady-state equilibrium conditions. These conditions are governed by the equilibrium equations

$$F_i\ (u_{oj};\ \dot{u}_{oj};\ \ddot{u}_{oj};\ t) = 0 \quad . \tag{38}$$

The remaining terms of equation 37 must then vanish to ensure equilibrium of the system in any perturbed configuration -- this is the condition for neutral stability of the steady state. Thus, when attention is focused only on small perturbations, the stability equations are given by

$$\sum_j \left[(\partial F_i/\partial \ddot{q}_j)_o \ddot{q}_j + (\partial F_i/\partial \dot{q}_j)_o \dot{q}_j + (\partial F_i/\partial q_j)_o q_j\right] = 0 \quad . \tag{39}$$

In matrix notation the above is represented by

$$[M]\{\ddot{q}\} + [C]\{\dot{q}\} + [K]\{q\} = 0 \tag{40}$$

where $M(i,j) = \dfrac{\partial F_i}{\partial \ddot{q}_j}$

$$C(i,j) = \frac{\partial F_i}{\partial \dot{q}_j}$$

$$K(i,j) = \frac{\partial F_i}{\partial q_j}$$

$\{q\}$ = vector of all system freedoms.

KINETIC ENERGY TERMS

The kinetic energy of the system is expressed generally by

$$T = 1/2 \sum^{S} \int \rho_m \{\dot{X}_F\}^T \{\dot{X}_F\} \, d\sigma \quad , \tag{41}$$

where X_F is a spatial coordinate vector of an element of mass,

ρ_m is the mass density,

$d\sigma$ is an element of volume.

The integration extends over the volume of a finite element and the summation is over the totality of elements in the system.

Time dependency of the spatial coordinates is both implicit through the perturbation freedoms (q_i) and explicit through the azimuth angle increment (Ωt) of the rotor blades;

$$\text{i.e., } \{X_F\} = \{X_F(q_i, t)\} \quad . \tag{42}$$

Hence,
$$\{\dot{X}_F\} = \frac{\partial}{\partial t}\{X_F\} + \sum_j \frac{\partial}{\partial q_j}\{X_F\} \dot{q}_j$$

$$= \{\dot{X}_F(\dot{q}_i, q_i, t)\}$$

$$\{\ddot{X}_F\} = \frac{\partial}{\partial t}\{\dot{X}_F\} + \sum_j \left(\frac{\partial}{\partial q_j}\{\dot{X}_F\} \dot{q}_j + \frac{\partial}{\partial \dot{q}_j}\{\dot{X}_F\} \ddot{q}_j\right)$$

$$= \frac{\partial^2}{\partial t^2}\{X_F\} + \sum_j \left(2\frac{\partial^2}{\partial q_j \partial t}\{X_F\} \dot{q}_j + \frac{\partial}{\partial q_j}\{X_F\} \ddot{q}_j\right)$$

$$+ \sum_j \sum_k \frac{\partial^2}{\partial q_j \partial q_k}\{X_F\} \dot{q}_j \dot{q}_k$$

$$= \{\ddot{X}_F(\ddot{q}_i, \dot{q}_i, q_i, t)\} \tag{43}$$

The following relations follow from the above results:

$$\frac{\partial}{\partial \dot{q}_j}\{\dot{X}_F\} = \frac{\partial}{\partial q_j}\{X_F\}$$

$$\frac{\partial}{\partial q_j}\{\dot{X}_F\} = \frac{\partial^2}{\partial q_j \partial t}\{X_F\} + \sum_k \frac{\partial^2}{\partial q_j \partial q_k}\{X_F\}\,\dot{q}_j \qquad (44)$$

From equation 41,

$$\frac{\partial T}{\partial \dot{q}_j} = \sum^S \int \rho_m \frac{\partial}{\partial \dot{q}_j}\{\dot{X}_F\}^T\{\dot{X}_F\}\,d\sigma$$

$$= \sum^S \int \rho_m \left[\left(\frac{\partial}{\partial q_j}\{X_F\}\right)^T\left(\frac{\partial}{\partial t}\{X_F\}\right) + \sum_k \left(\frac{\partial}{\partial q_j}\{X_F\}\right)^T \left(\frac{\partial}{\partial q_k}\{X_F\}\right)\dot{q}_k\right] d\sigma$$

$$\frac{d}{dt}\left(\frac{\partial T}{\partial \dot{q}_j}\right) = \frac{\partial}{\partial t}\left(\frac{\partial T}{\partial \dot{q}_j}\right) + \sum_k \left[\frac{\partial}{\partial q_k}\left(\frac{\partial T}{\partial \dot{q}_j}\right)\dot{q}_k + \frac{\partial}{\partial \dot{q}_k}\left(\frac{\partial T}{\partial \dot{q}_j}\right)\ddot{q}_k\right]$$

$$= \sum^S \int \rho_m \left[\left(\frac{\partial^2}{\partial q_j \partial t}\{X_F\}\right)^T\left(\frac{\partial}{\partial t}\{X_F\}\right) + \left(\frac{\partial}{\partial q_j}\{X_F\}\right)^T\left(\frac{\partial^2}{\partial t^2}\{X_F\}\right)\right.$$

$$+ \sum_k \left\{\left(\frac{\partial^2}{\partial q_j \partial t}\{X_F\}\right)^T\left(\frac{\partial}{\partial q_k}\{X_F\}\right)\dot{q}_k + 2\left(\frac{\partial}{\partial q_j}\{X_F\}\right)^T\left(\frac{\partial^2}{\partial q_k \partial t}\{X_F\}\right)\dot{q}_k\right.$$

$$\left. + \left(\frac{\partial^2}{\partial q_j \partial q_k}\{X_F\}\right)^T\left(\frac{\partial}{\partial t}\{X_F\}\right)\dot{q}_k + \left(\frac{\partial}{\partial q_j}\{X_F\}\right)^T\left(\frac{\partial}{\partial q_k}\{X_F\}\right)\ddot{q}_k\right\}$$

$$+ \sum_k \sum_l \left\{\left(\frac{\partial}{\partial q_j}\{X_F\}\right)^T\left(\frac{\partial^2}{\partial q_k \partial q_l}\{X_F\}\right) + \left(\frac{\partial^2}{\partial q_j \partial q_l}\{X_F\}\right)^T\left(\frac{\partial}{\partial q_k}\{X_F\}\right)\right\}$$

$$\left.\dot{q}_k \dot{q}_l\right] d\sigma$$

Also, $$\frac{\partial T}{\partial q_j} = \sum^{S} \int \rho_m \left(\frac{\partial}{\partial q_j}\{\dot{X}_F\}\right)^T \{\dot{X}_F\}\, d\sigma$$

$$= \sum^{S} \int \rho_m \left[\left(\frac{\partial^2}{\partial q_j \partial t}\{X_F\}\right)^T \left(\frac{\partial \{X_F\}}{\partial t}\right) + \sum_{kl}\sum \left(\frac{\partial^2}{\partial q_j \partial q_k}\{X_F\}\right)^T \right.$$

$$\left(\frac{\partial}{\partial q_l}\{X_F\}\right) \dot{q}_k \dot{q}_l + \sum_k \left\{\left(\frac{\partial}{\partial q_j \partial t}\{X_F\}\right)^T \left(\frac{\partial}{\partial q_k}\{X_F\}\right)\right.$$

$$\left.\left. + \left(\frac{\partial^2}{\partial q_j \partial q_k}\{X_F\}\right)^T \left(\frac{\partial}{\partial t}\{X_F\}\right)\right\} \dot{q}_k\right] d\sigma$$

Hence, $$\frac{d}{dt}\left(\frac{\partial T}{\partial \dot{q}_j}\right) - \frac{\partial T}{\partial q_j}$$

$$= \sum^{S} \int \rho_m \left[\left(\frac{\partial}{\partial q_j}\{X_F\}\right)^T \left(\frac{\partial^2}{\partial t^2}\{X_F\}\right) + \sum_{kl}\sum \left(\frac{\partial}{\partial q_j}\{X_F\}\right)^T \right.$$

$$\left(\frac{\partial^2}{\partial q_k \partial q_l}\{X_F\}\right) \dot{q}_k \dot{q}_l + \sum_k \left\{\left(\frac{\partial}{\partial q_j}\{X_F\}\right)^T \left(\frac{\partial}{\partial q_k}\{X_F\}\right) \ddot{q}_k \right.$$

$$\left.\left. + 2\left(\frac{\partial}{\partial q_j}\{X_F\}\right)^T \left(\frac{\partial^2}{\partial q_k \partial t}\{X_F\}\right) \dot{q}_k\right\}\right] d\sigma$$

The right-hand side of the above is now expanded in a Taylor's series about the steady-state configuration and truncated at the linear terms in the system freedoms and their time derivatives to give:

$$\frac{d}{dt}\left(\frac{\partial T}{\partial \dot{q}_j}\right) - \frac{\partial T}{\partial q_j}$$

$$= \sum^{S} \left[\sum_k \int \rho_m \left(\frac{\partial}{\partial q_j}\{X_F\}\right)^T_o \left(\frac{\partial}{\partial q_k}\{X_F\}\right)_o d\sigma\right\} \ddot{q}_k$$

$$+ 2\sum_k \left\{\int \rho_m \left(\frac{\partial}{\partial q_j}\{X_F\}\right)^T_o \left(\frac{\partial^2}{\partial q_k \partial t}\{X_F\}\right)_o d\sigma\right\} \dot{q}_k$$

$$+ \sum_k \{\int \rho_m \left[\left(\frac{\partial^2}{\partial q_j \partial q_k}\{X_F\}\right)_o^T \left(\frac{\partial^2}{\partial t^2}\{X_F\}\right)_o\right.$$

$$+ \left(\frac{\partial}{\partial q_j}\{X_F\}\right)_o^T \left(\frac{\partial^3}{\partial q_k \partial t^2}\{X_F\}\right)_o \left.\right] d\sigma\} q_k$$

$$+ \int \rho_m \left(\frac{\partial}{\partial q_j}\{X_F\}\right)_o^T \left(\frac{\partial^2}{\partial t^2}\{X_F\}\right)_o d\sigma] \qquad (45)$$

The kinetic energy contributions to the stability equations are therefore:

$$M_{KE}(i,j) = \sum^S \int \rho_m \left(\frac{\partial}{\partial q_i}\{X_F\}\right)_o^T \left(\frac{\partial}{\partial q_j}\{X_F\}\right)_o d\sigma$$

$$C_{KE}(i,j) = 2\sum^S \int \rho_m \left(\frac{\partial}{\partial q_i}\{X_F\}\right)_o^T \left(\frac{\partial^2}{\partial q_j \partial t}\{X_F\}\right)_o d\sigma$$

$$K_{KE}(i,j) = \sum^S \int \rho_m \left[\left(\frac{\partial^2}{\partial q_i \partial q_j}\{X_F\}\right)_o^T \left(\frac{\partial^2}{\partial t^2}\{X_F\}\right)_o\right.$$

$$+ \left(\frac{\partial}{\partial q_i}\{X_F\}\right)_o^T \left(\frac{\partial^3}{\partial q_j \partial t^2}\{X_F\}\right)_o \left.\right] d\sigma \qquad (46)$$

The last integral in equation 45 is the kinetic energy contribution to the steady-state equilibrium equations.

EXTERNAL LOAD TERMS

The external loads acting on any finite element of the system are represented generally by a force vector and a moment vector. The static equivalents of these at the origin of the fixed-coordinate system are denoted by $\{F_f\}$ and $\{M_F\}$. Under a virtual displacement comprising perturbations from steady state, the finite element undergoes configuration changes. The actual displacements and rotations of the element have kinematical equivalents at the origin of the fixed-coordinate system represented by $\delta\{X_F\}$ and $\delta\{\phi_F\}$. These are defined as the displacements and rotations which must be applied at the origin to produce the true deflections and rotations of the element if it were rigidly linked to the origin in the steady state.

The virtual work of the external forces on the element are then obtained as:

$$W_e = (\delta\{X_F\})^T\{F_F\} + (\delta\{\phi_F\})^T\{M_F\} \quad . \tag{47}$$

But $\delta\{X_F\} = \sum_j \left(\frac{\partial}{\partial q_j}\{X_F\}\right)_o q_j$

$$\delta\{\phi_F\} = \sum_j \left(\frac{\partial}{\partial q_j}\{\phi_F\}\right)_o q_j \quad ; \tag{48}$$

therefore, $W_e = \sum_j [(\frac{\partial}{\partial q_j}\{X_F\})_o^T\{F_F\} + (\partial/\partial q_j\{\phi_F\})_o^T\{M_F\}]\ q_j$

and $$\frac{\partial W_e}{\partial q_j} = (\frac{\partial}{\partial q_j}\{X_F\})_o^T\{F_F\} + (\frac{\partial}{\partial q_j}\{\phi_F\})_o^T\{M_F\} \quad . \tag{49}$$

If it is assumed that the forces and moments are functions of the system freedoms and their first two time derivatives,

i.e., $$\{F_F\} = \{F_F\ (q_i, \dot{q}_i, \ddot{q}_i, t)\}$$

$$\{M_F\} = M_F\ (q_i, \dot{q}_i, \ddot{q}_i, t)\} \quad , \tag{50}$$

then a Taylor's series expansion of $\partial We/\partial q_j$ yields

$$\begin{aligned}\frac{\partial We}{\partial q_j} = {} & (\frac{\partial}{\partial q_j}\{X_F\})_o^T\{F_F\}_o + (\frac{\partial}{\partial q_j}\{\phi_F\})_o^T\{M_F\}_o \\ & + \sum_k [(\frac{\partial}{\partial q_j}\{X_F\})_o^T(\frac{\partial}{\partial q_k}\{F_F\})_o + (\frac{\partial}{\partial q_j}\{\phi_F\})_o^T(\frac{\partial}{\partial q_k}\{M_F\})_o]\ q_k \\ & + \sum_k [(\frac{\partial}{\partial q_j}\{X_F\})_o^T(\frac{\partial}{\partial \dot{q}_k}\{F_F\})_o + (\frac{\partial}{\partial q_j}\{\phi_F\})_o^T(\frac{\partial}{\partial \dot{q}_k}\{M_F\})_o]\ \dot{q}_k \\ & + \sum_k [(\frac{\partial}{\partial q_j}\{X_F\})_o^T(\frac{\partial}{\partial \ddot{q}_k}\{F_F\})_o + (\frac{\partial}{\partial q_j}\{\phi_F\})_o^T(\frac{\partial}{\partial \ddot{q}_k}\{M_F\})_o]\ \ddot{q}_k \\ & + \text{higher order derivative terms.}\end{aligned} \tag{51}$$

The external load contributions to the stability equations are obtained from the above as

$$M_{EX}(i,j) = \sum^{S} [(\frac{\partial}{\partial q_i}\{X_F\})_o^T (\frac{\partial}{\partial \ddot{q}_j}\{F_F\})_o + (\frac{\partial}{\partial q_i}\{\phi_F\})_o^T (\frac{\partial}{\partial \ddot{q}_j}\{M_F\})_o]$$

$$C_{EX}(i,j) = \sum^{S} [(\frac{\partial}{\partial q_i}\{X_F\})_o^T (\frac{\partial}{\partial \dot{q}_j}\{F_F\})_o + (\frac{\partial}{\partial q_i}\{\phi_F\})_o^T (\frac{\partial}{\partial \dot{q}_j}\{M_F\})_o]$$

$$K_{EX}(i,j) = \sum^{S} [(\frac{\partial}{\partial q_i}\{X_F\})_o^T (\frac{\partial}{\partial q_j}\{F_F\})_o + (\frac{\partial}{\partial q_i}\{\phi_F\})_o^T (\frac{\partial}{\partial q_j}\{M_F\})_o] \quad . \tag{52}$$

The external loads considered in the present analysis comprise aerodynamic forces and moments on the rotor blades and on the airframe components (except fuselage). The blade aerodynamics are considered below in illustration of the external load analysis.

The aerodynamic forces and moments on a blade segment consist of a lift force ΔL, drag force ΔD, and pitching moment ΔM as shown in Figure 9.

They are expressed by

$$\Delta L = 1/2\rho U^2 (2b)\Delta r.\ C_L$$

$$\Delta D = 1/2\rho U^2 (2b)\Delta r.\ C_D$$

$$\Delta M = 1/2\rho U^2 (2b)^2 \Delta r.\ C_M \tag{53}$$

The coefficients C_L, C_D, and C_M are functions of the airspeed (U), the angle of attack (α) and its time derivatives ($\dot{\alpha}$, $\ddot{\alpha}$), the segment velocity and acceleration ($\dot{h}$, $\ddot{h}$) normal to the airstream. The airspeed and angle of attack depend on the velocity components U_T and U_P shown in Figure 9 as follows:

$$U = (U_P^2 + U_T^2)^{1/2}$$

$$\alpha = \theta_T - \tan^{-1} U_P/U_T \tag{54}$$

Hence the aerodynamic independent variables may be taken as:

$$U_T,\ U_P,\ \dot{U}_T,\ \dot{U}_P,\ \ddot{U}_T,\ \ddot{U}_P,\ \theta_T,\ \dot{\theta}_T,\ \ddot{\theta}_T,\ \dot{h},\ \ddot{h} \quad . \tag{55}$$

These in turn are functions of the system freedoms.

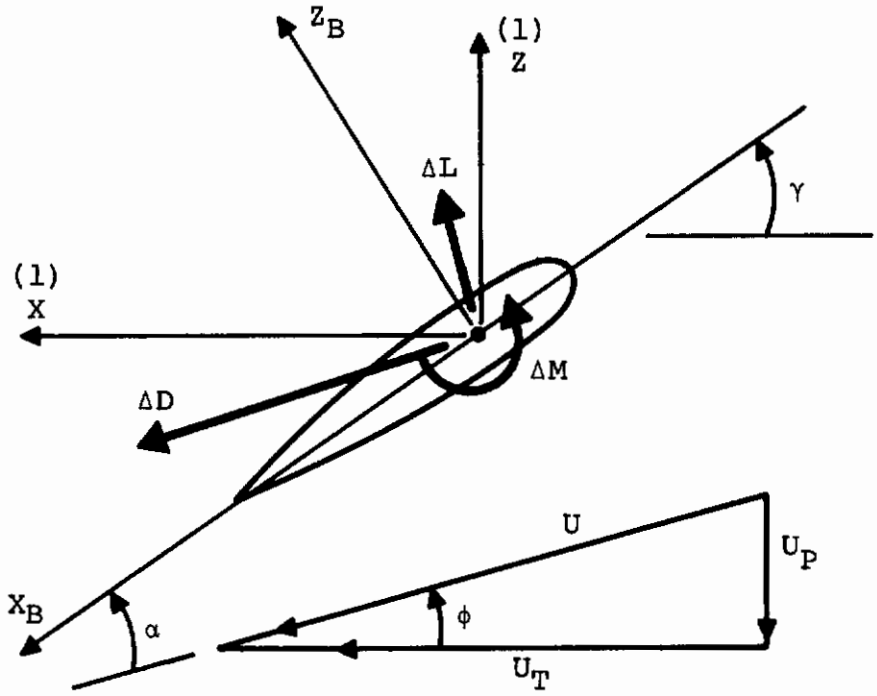

Figure 9. Aerodynamic Parameters at a Typical Blade Section

The velocity components U_T and U_P are derived from a velocity vector $\{V_B\}$;

$$\text{i.e.,} \quad \{V_B\} = \begin{Bmatrix} U_T \\ U_N \\ -U_P \end{Bmatrix} \quad , \tag{56}$$

where U_N is normal to both U_T and U_P.

The vector is made up of components from the blade rotational speed Ω, the aircraft speed with components V_X, V_Y, and V_Z in fixed-coordinate system, and induced velocities from various sources represented in the rotating disc coordinate system by

$$\{\bar{V}\} = \begin{Bmatrix} \bar{V}_X \\ \bar{V}_Y \\ \bar{V}_Z \end{Bmatrix} \quad . \tag{57}$$

It is easily shown that

$$\{V_B\} = -\Omega[T_S]^T[\hat{Z}]\overset{(2)}{\{X_A\}} - [R][T_S]^T([T_\psi]^T[T_{TE}]^T[T_P]\{V\} - \{\bar{V}\} \tag{58}$$

where $\{V\} = \begin{Bmatrix} V_X \\ V_Y \\ V_Z \end{Bmatrix}$

$$[R] = \begin{bmatrix} \Gamma & 0 & 0 \\ 0 & 1 & 0 \\ 0 & 0 & 1 \end{bmatrix}$$

Γ = +1 for clockwise rotating blades
= -1 for counterclockwise rotating blades
} as viewed from the shaft side

$$[\hat{Z}] = \begin{bmatrix} 0 & -1 & 0 \\ 1 & 0 & 0 \\ 0 & 0 & 0 \end{bmatrix}$$

This establishes the relationship between the airspeed components and the system freedoms. Equation 20 does the same for the blade twist θ_T. The blade segment velocity $\dot{h}$ is given by

$$\dot{h} = -\{L_3\}^T[T_\phi]^T[T_S]^T\overset{(2)}{(d/dt\{X_A\})} \quad , \tag{59}$$

where $\{L_3\} = \begin{Bmatrix} 0 \\ 0 \\ 1 \end{Bmatrix}$

$$[T_\phi] = \begin{bmatrix} \cos\phi, & 0, & \sin\phi \\ 0 & , 1, & 0 \\ -\sin\phi, & 0, & \cos\phi \end{bmatrix}$$

$$\phi = \tan^{-1}\frac{U_P}{U_T} \tag{60}$$

A force vector $\{F_{BA}\}$ and a moment vector $\{M_{BA}\}$ are defined in the normal blade section coordinate system from ΔL, ΔD, and ΔM as

$$\{F_{BA}\} = [T_\phi]\begin{Bmatrix} \Delta D \\ 0 \\ \Delta L \end{Bmatrix}$$

$$\{M_{BA}\} = \begin{Bmatrix} 0 \\ \Delta M \\ 0 \end{Bmatrix} \tag{61}$$

These are resolved into the fixed-coordinate system yielding

$$\{F_{FA}\} = [T_F]\{F_{BA}\}$$

$$\{M_{FA}\} = [T_F]\{M_{BA}\} \tag{62}$$

where $[T_F] = [T_P][T_W][T_{TE}][T_\psi][T_S]$. (63)

Their statical equivalents at the origin of the fixed-coordinate system are

$$\{F_F\} = \{F_{FA}\}$$

$$\{M_F\} = \{M_{FA}\} + [S_F]^T\{F_{FA}\} \tag{64}$$

where $[S_F] = [\{S_{F1}\}, \{S_{F2}\}, \{S_{F3}\}]$

$$\{S_{F1}\} = [\hat{X}]\{X_{FA}\}$$

$$\{S_{F2}\} = [\hat{Y}]\{X_{FA}\}$$

$$\{S_{F3}\} = [\hat{Z}]\{X_{FA}\}$$

and $$[\hat{X}] = \begin{bmatrix} 0 & 0 & 0 \\ 0 & 0 & -1 \\ 0 & 1 & 0 \end{bmatrix}$$

$$[\hat{Y}] = \begin{bmatrix} 0 & 0 & 1 \\ 0 & 0 & 0 \\ -1 & 0 & 0 \end{bmatrix} \quad . \tag{65}$$

Therefore, $$\left(\frac{\partial}{\partial q_j}\{F_F\}\right)_o = \left(\frac{\partial}{\partial q_j}[T_F]\right)_o \{F_{BA}\}_o$$

$$+ [T_F]_o \left(\frac{\partial}{\partial q_j}\{F_{BA}\}\right)_o \quad . \tag{66}$$

But $$\frac{\partial}{\partial q_i}\{F_{BA}\} = \left(\frac{\partial}{\partial U_T}\{F_{BA}\}\right) \cdot \frac{\partial U_T}{\partial q_j} + \left(\frac{\partial}{\partial U_P}\{F_{BA}\}\right) \cdot \frac{\partial U_P}{\partial q_j}$$

$$+ \left(\frac{\partial}{\partial \dot{U}_T}\{F_{BA}\}\right) \cdot \frac{\partial \dot{U}_T}{\partial q_j} + \left(\frac{\partial}{\partial \dot{U}_P}\{F_{BA}\}\right) \cdot \frac{\partial \dot{U}_P}{\partial q_j}$$

$$+ \left(\frac{\partial}{\partial \ddot{U}_T}\{F_{BA}\}\right) \cdot \frac{\partial \ddot{U}_T}{\partial q_j} + \left(\frac{\partial}{\partial \ddot{U}_P}\{F_{BA}\}\right) \cdot \frac{\partial \ddot{U}_P}{\partial q_j}$$

$$+ \left(\frac{\partial}{\partial \theta_T}\{F_{BA}\}\right) \cdot \frac{\partial \theta_T}{\partial q_j} + \left(\frac{\partial}{\partial \dot{h}}\{F_{BA}\}\right) \cdot \frac{\partial \dot{h}}{\partial q_j}$$

$$+ \left(\frac{\partial}{\partial \ddot{h}}\{f_{BA}\}\right) \cdot \frac{\partial \ddot{h}}{\partial q_j} \quad . \tag{67}$$

This is expressed in matrix notation by defining the 3 X 9 matrix [KF] and the nine-component vector $\{\Lambda_j\}$ as

$$[KF] = \left[\left(\frac{\partial}{\partial U_T}\{F_{BA}\}\right); \left(\frac{\partial}{\partial U_P}\{F_{BA}\}\right); \left(\frac{\partial}{\partial \dot{U}_T}\{F_{BA}\}\right); \left(\frac{\partial}{\partial \dot{U}_P}\{F_{BA}\}\right);\right.$$

$$\left(\frac{\partial}{\partial \ddot{U}_T}\{F_{BA}\}\right); \left(\frac{\partial}{\partial \ddot{U}_P}\{F_{BA}\}\right); \left(\frac{\partial}{\partial \theta_T}\{F_{BA}\}\right); \left(\frac{\partial}{\partial \dot{h}}\{F_{BA}\}\right);$$

$$\left.\left(\frac{\partial}{\partial \ddot{h}}\{F_{BA}\}\right)\right]$$

$$\{\Lambda_j\}^T = [\frac{\partial U_T}{\partial q_j}; \frac{\partial U_P}{\partial q_j}; \frac{\partial \dot{U}_T}{\partial q_j}; \frac{\partial \dot{U}_P}{\partial q_j}; \frac{\partial \ddot{U}_T}{\partial q_j}; \frac{\partial \ddot{U}_P}{\partial q_j}; \frac{\partial \theta_T}{\partial q_j}; \frac{\partial \dot{h}}{\partial q_j}; \frac{\partial \ddot{h}}{\partial q_j}] \quad . \quad (68)$$

Hence, $$\frac{\partial}{\partial q_j}\{F_{BA}\} = [KF]\{\Lambda_j\} \quad (69)$$

and $$(\frac{\partial}{\partial q_j}\{F_F\})_o = (\frac{\partial}{\partial q_j}[T_F])_o \{F_{BA}\}_o + [T_F]_o [KF]_o \{\Lambda_j\}_o \quad . \quad (70)$$

From equation 64,

$$(\frac{\partial}{\partial q_j}\{M_F\})_o = (\frac{\partial}{\partial q_j}[T_F])_o \{M_{BA}\}_o + [T_F]_o (\frac{\partial}{\partial q_j}\{M_{BA}\})_o$$

$$+ (\frac{\partial}{\partial q_j}[S_F])_o^T [T_F]_o \{F_{BA}\}_o + [S_F]_o^T (\frac{\partial}{\partial q_j}[T_F])_o \{F_{BA}\}_o$$

$$+ [S_F]_o^T [T_F]_o (\frac{\partial}{\partial q_j}\{F_{BA}\})_o \quad . \quad (71)$$

Following equation 69, $\partial/\partial q_j\{M_{BA}\}$ can be written as

$$\frac{\partial}{\partial q_j}\{M_{BA}\} = [KM]\{\Lambda_j\} \quad (72)$$

where $$[KM] = [(\frac{\partial}{\partial U_T}\{M_{BA}\}); (\frac{\partial}{\partial U_P}\{M_{BA}\}); (\frac{\partial}{\partial \dot{U}_T}\{M_{BA}\}); (\frac{\partial}{\partial \dot{U}_P}\{M_{BA}\});$$

$$(\frac{\partial}{\partial \ddot{U}_T}\{M_{BA}\}); (\frac{\partial}{\partial \ddot{U}_P}\{M_{BA}\}); (\frac{\partial}{\partial \theta_T}\{M_{BA}\});$$

$$(\frac{\partial}{\partial \dot{h}}\{M_{BA}\}); (\frac{\partial}{\partial \ddot{h}}\{M_{BA}\})] \quad . \quad (73)$$

Hence, $$\left(\frac{\partial}{\partial q_j}\{M_F\}\right)_o = \left(\frac{\partial}{\partial q_j}[T_F]\right)_o \{M_{BA}\}_o + \left(\frac{\partial}{\partial q_j}[S_F]\right)_o^T [T_F]_o \{F_{BA}\}_o$$

$$+ [S_F]_o^T \left(\frac{\partial}{\partial q_j}[T_F]\right)_o \{F_{BA}\} + ([T_F]_o [KM]_o$$

$$+ [S_F]_o^T [T_F]_o [KF]_o)\{\Lambda_j\}_o \quad . \tag{74}$$

The derivatives of $\{F_F\}$ and $\{M_F\}$ with respect to $\dot{q}_j$ and $\ddot{q}_j$ are similarly obtained as

$$\left(\frac{\partial}{\partial \dot{q}_j}\{F_F\}\right)_o = [T_F]_o [KF]_o \{\dot{\Lambda}_j\}_o$$

$$\left(\frac{\partial}{\partial \dot{q}_j}\{M_F\}\right)_o = ([T_F]_o [KM]_o + [S_F]_o^T [T_F]_o [KF]_o)\{\dot{\Lambda}_j\}_o$$

$$\left(\frac{\partial}{\partial \ddot{q}_j}\{F_F\}\right)_o = [T_F]_o [KF]_o \{\ddot{\Lambda}_j\}_o$$

$$\left(\frac{\partial}{\partial \ddot{q}_j}\{M_F\}\right)_o = ([T_F]_o [KM]_o + [S_F]_o^T [T_F]_o [KF]_o)\{\ddot{\Lambda}_j\}_o \tag{75}$$

where $$\{\dot{\Lambda}_j\}^T = \left[\frac{\partial U_T}{\partial \dot{q}_j}; \frac{\partial U_P}{\partial \dot{q}_j}; \frac{\partial \dot{U}_T}{\partial \dot{q}_j}; \frac{\partial \dot{U}_P}{\partial \dot{q}_j}; \frac{\partial \ddot{U}_T}{\partial \dot{q}_j}; \frac{\partial \ddot{U}_P}{\partial \dot{q}_j}; \frac{\partial \dot{\theta}_T}{\partial \dot{q}_j}; \frac{\partial \dot{h}}{\partial \dot{q}_j}; \frac{\partial \ddot{h}}{\partial \dot{q}_j}\right]$$

$$\{\ddot{\Lambda}_j\}^T = \left[\frac{\partial U_T}{\partial \ddot{q}_j}; \frac{\partial U_P}{\partial \ddot{q}_j}; \frac{\partial \dot{U}_T}{\partial \ddot{q}_j}; \frac{\partial \dot{U}_P}{\partial \ddot{q}_j}; \frac{\partial \ddot{U}_T}{\partial \ddot{q}_j}; \frac{\partial \ddot{U}_P}{\partial \ddot{q}_j}; \frac{\partial \ddot{\theta}_T}{\partial \ddot{q}_j}; \frac{\partial \dot{h}}{\partial \ddot{q}_j}; \frac{\partial \ddot{h}}{\partial \ddot{q}_j}\right] . \tag{76}$$

STRAIN ENERGY AND DISSIPATION TERMS

The strain energy is a function of the elasticity and the state of strain in the structural members of the system. The latter depends on the system freedoms but not on their time derivatives;

i.e., $$U = U(q_i; t) \quad . \tag{77}$$

The strain energy term in Lagrange's equations is therefore represented by the Taylor's series

$$\frac{\partial U}{\partial q_j} = \left(\frac{\partial U}{\partial q_j}\right)_o + \sum_k \left(\frac{\partial^2 U}{\partial q_j \partial q_k}\right)_o q_k + 1/2 \sum_k \sum_l \left(\frac{\partial^3 U}{\partial q_j \partial q_k \partial q_l}\right)_o q_k q_l + \text{higher order terms.} \quad (78)$$

The only contribution to the stability equations is in the stiffness matrix;

$$\text{i.e.,} \quad K_{SE}(i,j) = \left(\frac{\partial^2 U}{\partial q_i \partial q_j}\right)_o . \quad (79)$$

The dissipation function is assumed to be a function of the first time derivatives of the system freedoms,

$$R = R(\dot{q}_i, t) . \quad (80)$$

As such it contributes only to the damping coefficients in the stability equations;

$$\text{i.e.,} \quad C_{DISS}(i,j) = \left(\frac{\partial^2 R}{\partial \dot{q}_i \partial \dot{q}_j}\right)_o . \quad (81)$$

The coefficient matrices of the stability equations are seen to comprise constituents from kinetic energy, strain energy, dissipation, and external load considerations.

$$[M] = [M]_{KE} + [M]_{EX}$$

$$[C] = [C]_{KE} + [C]_{DISS} + [C]_{EX}$$

$$[K] = [K]_{KE} + [K]_{SE} + [K]_{EX} \quad (82)$$

Each of these constituents is made up of contributions from the three basic subsystems as discussed previously under kinetic energy and external loading. Separating the strain energy constituent into the subsystem contributions,

$$[K]_{SE} = [K_R]_{SE} + [K_{AF}]_{SE} + [K_{LG}]_{SE} . \quad (83)$$

The strain energy of a single landing gear (see Figure 1) is given by

$$U_{LG} = 1/2\ \{X_{FM}\}^T \begin{bmatrix} AK_1 & & \\ & AK_2, & \\ & & AK_4 \end{bmatrix} \{X_{FM}\}$$

$$+ 1/2(\{X_{FM}\} - \{X_{FP}\})^T \begin{bmatrix} o & o & \\ & & AK_3 \end{bmatrix} (\{X_{FM}\} - \{X_{FP}\}) \quad . \quad (84)$$

$$\text{Hence, } K_{LG/SE}(i,j) = \sum^G \left(\frac{\partial^2}{\partial q_i \partial q_j}\{X_{FM}\}\right)_o^T \left(\left[GK1\right]\{X_{FM}\}_o - \left[GK2\right]\{X_{FP}\}_o\right)$$

$$+ \sum^G \left(\frac{\partial^2}{\partial q_i \partial q_j}\{X_{FP}\}\right)_o^T \left(\left[GK1\right]\{X_{FP}\}_o - \left[GK2\right]\{X_{FM}\}_o\right)$$

$$+ \sum^G \left(\frac{\partial}{\partial q_i}\{X_{FM}\}\right)_o^T \left(\left[GK1\right]\left(\frac{\partial}{\partial q_j}\{X_{FM}\}\right)_o - \left[GK2\right]\right.$$

$$\left.\left(\frac{\partial}{\partial q_j}\{X_{FP}\}\right)_o\right) + \sum^G \left(\frac{\partial}{\partial q_i}\{X_{FP}\}\right)_o^T \left(\left[GK1\right]\left(\frac{\partial}{\partial q_j}\{X_{FP}\}\right)_o\right.$$

$$\left. - \left[GK2\right]\left(\frac{\partial}{\partial q_j}\{X_{FM}\}\right)_o\right) \quad (85)$$

where $\sum^G$ indicates summation over all landing gears and

$$\left[GK1\right] = \begin{bmatrix} AK_1 & & \\ & AK_2 & \\ & & AK_3 + AK_4 \end{bmatrix}$$

$$\left[GK2\right] = \begin{bmatrix} o & o & \\ & & AK_3 \end{bmatrix} \quad (86)$$

The airframe component is obtained from the modal frequencies ($\omega_A(i)$) and inertias ($M_A(i)$) using the diagonal stiffness matrix property associated with normal modes;

$$\text{i.e., } [K_{AF}]_{SE} = \left[\omega_A(i)^2 M_A(i)\right] \quad . \quad (87)$$

In the rotor subsystem, the modal stiffness is made up of the kinetic energy and strain energy constituents:

$$[K_R] = [K_R]_{KE} + [K_R]_{SE} \quad . \quad (88)$$

The kinetic energy part is of the form

$$[K_R]_{KE} = \Omega^2 [k_R] \quad .$$

The modes corresponding to a rotating blade (in vacuo) at an angular speed of Ω_{REF} are assumed to give rise to a diagonal stiffness matrix applicable to that speed;

i.e., $$[K_R]_{REF} = \left[\omega_B(i)^2 M_B(i)\right]$$

$$= \Omega^2_{REF}[k_R] + [K_R]_{SE} \quad .$$

Hence, $$[K_R]_{SE} = \left[\omega_B(i)^2 M_B(i)\right] - \Omega^2_{REF}[k_R] \tag{89}$$

where $\omega_B(i)$ is the ith rotating mode frequency of the blade measured at Ω_{REF}

$M_B(i)$ is the ith modal mass.

The constituent $[C]_{DISS}$ is separable into landing gear, airframe, and rotor contributions similar to $[K]_{SE}$. It can be shown by consideration of the dissipation functions of the landing gears that

$$\begin{aligned} C_{LG/DISS}(i,j) = & \sum^{G} \left(\frac{\partial^2}{\partial \dot{q}_i \partial \dot{q}_j}\{\dot{X}_{FM}\}\right)_o^T \left(\left[GC1\right]\{\dot{X}_{FM}\}_o - \left[GC2\right]\{\dot{X}_{FP}\}_o\right) \\ & + \sum^{G} \left(\frac{\partial^2}{\partial \dot{q}_i \partial \dot{q}_j}\{\dot{X}_{FP}\}\right)_o^T \left(\left[GC1\right]\{\dot{X}_{FP}\}_o - \left[GC2\right]\{\dot{X}_{FM}\}_o\right) \\ & + \sum^{G} \left(\frac{\partial}{\partial \dot{q}_i}\{\dot{X}_{FM}\}\right)_o^T \left(\left[GC1\right]\left(\frac{\partial}{\partial \dot{q}_j}\{\dot{X}_{FM}\}\right)_o - \left[GC2\right]\left(\frac{\partial}{\partial \dot{q}_j}\{\dot{X}_{FP}\}\right)_o\right) \\ & + \sum^{G} \left(\frac{\partial}{\partial \dot{q}_i}\{\dot{X}_{FP}\}\right)_o^T \left(\left[GC1\right]\left(\frac{\partial}{\partial \dot{q}_j}\{\dot{X}_{FP}\}\right)_o - \left[GC2\right]\left(\frac{\partial}{\partial \dot{q}_j}\{\dot{X}_{FM}\}\right)_o\right) \end{aligned} \tag{90}$$

where $$\left[GC1\right] = \begin{bmatrix} AC_1 & & \\ & AC_2 & \\ & & AC_3 + AC_4 \end{bmatrix}$$

$$\left[GC2\right] = \begin{bmatrix} o & & \\ & o & \\ & & AC_3 \end{bmatrix} \quad . \tag{91}$$

Structural damping in the airframe and rotor subsystems is specified as fractions of the critical viscous damping coefficients of the various modes.

$$\text{Hence,} \quad [C_{AF}]_{DISS} = \left[2\mu_A(i)\omega_A(i)M_A(i) \right]$$

$$[C_R]_{DISS} = \left[2\mu_B(i)\omega_B(i)M_B(i) \right] \qquad (92)$$

where $\mu_A(i)$ = fraction of critical viscous damping in ith airframe mode

$\mu_B(i)$ = fraction of critical viscous damping in ith blade mode.

RESULTANT EQUATIONS AND SOLUTION

The foregoing analytical developments establish the numerical and algebraic manipulations involved in assembling the coefficients of the stability equations. Two basic processes are involved. The first is the formation of a number of transformation matrices and vectors as defined in coordinate systems and transformations, using basic input data which defines the system and operating conditions. The second process is execution of the matrix algebra indicated in this and the previous section.

The transformations involving azimuth angle (ψ) contain trigonometric functions of the time-varying quantity (Ωt) as indicated in equation 26. The coefficients of the stability equations therefore contain these harmonic terms and are arrived at by modifying standard matrix operations to include harmonic analyses concurrently.

The solution of systems of equations with harmonic coefficients has been the subject of various publications in the past (see, for example, Reference 3). These solutions have largely been based on Floquet's theorem. The present development uses a quasi-normal mode approach which replaces individual blade modal freedoms with rotor freedoms (equivalent to tip-path-plane modal freedoms in flapping blades). The latter are further represented by a truncated general Fourier series giving rise to the so-called collective (zero-order harmonic) and cyclic (first- and higher-order harmonics) freedoms. Only the first harmonic is considered in the present treatment. References 4 and 5 contain more detailed discussion and definition of quasi-normal modes.

Part II. Aeroelastic Stability Analysis

Correlation and Trend Studies

H. R. Alexander

INTRODUCTION

AEROELASTIC STABILITY CORRELATION

Hingeless rotors, and more particularly the hingeless tilt-rotor V/STOL configuration, present a number of technical challenges which are not found in an acute form in conventional articulated rotor helicopters or aircraft powered by relatively rigid propellers with high disc loadings.

Three problem areas have been discussed in detail in Volume I and include such phenomena as whirl flutter and divergence, ground and air resonance, and aeromechanical instability. These classical stability problems have the common feature that they may be analyzed and predicted in terms of airframe degrees of freedom and a simple blade representation. Thus, whirl flutter tends to be associated with flapping motion of the blade and pitching or yawing of the hub; resonance phenomena such as ground resonance and aeromechanical instabilities may be analyzed in terms of linear hub motion in the rotor plane coupling with blade lead-lag degrees of freedom. However, experience has shown that additional instabilities may occur when the blades adopt deflection shapes under load, introducing strong coupling between pitch or torsion and lag or flap. Furthermore, such coupling mechanism may alter the blade behavior to the point where a wing-rotor instability occurs even though the blade by itself is stable.

CORRELATION WITH 1/10-SCALE TILT-ROTOR DYNAMIC MODEL

Incidents involving this type of coupling have generally been of limited amplitude. Correlation with two such incidents is presented in the next section. These occurred on the Model 160 1/10-scale dynamically similar tilt-rotor model (Figure 10).

ONERA 13-FOOT-DIAMETER PROPELLER

The blade itself may become unstable when subjected to thrust and torque conditions causing deflections which, in turn, couple the flap, lag, and torsion degrees of freedom. A correlation has been made with an incident of this type which occurred during a propeller performance test at ONERA (France), Figure 11. The blade experienced a severe instability at high advance ratio, which is predictable in terms of blade properties alone. At very low advance ratios a rather mild limit-cycle instability was experienced and in this case the blade does not go unstable by itself, but when the hub degrees of freedom are introduced the instability is obtained.

MODEL 160 TILT-ROTOR 1/22-SCALE DYNAMICALLY SIMILAR MODEL

In Volume I it was indicated that tilting the rotor in wind

tunnel tests of the Model 160 1/22-scale dynamically similar tilt-rotor (Figure 12) had produced significant and apparently contradictory shifts in the stability boundaries. The methodology previously available did not permit correlation, but application of the computer program described in Part I gives the trends experienced in test.

ROTOR DERIVATIVE TREND STUDIES AND CORRELATION

Parametric studies of rotor hub forces and moment derivatives were performed as part of the subject contract to establish the effect of selected parameters such as blade frequency and Lock number on the derivatives and therefore on the static divergence of rotor-wing systems. These initial studies were made with a simple mathematical model (Figure 13) and indicated unexpected and interesting trends in the rotor hub forces and moment derivatives when the lead-lag frequency of the blade was parametrically varied over a range including 1 per rev. Specifically, the normal force derivative C_{N_α} was observed to reach a minimum at 1 per rev and the pitching moment derivative C_{m_α} reversed sign. In a subsequent test of a dynamically similar 1/9-scale tilt/stowed-rotor conversion model (Figure 14), the rotor derivatives were carefully measured over a range of rpm in which the lead-lag mode frequency progressed from less than 1 per rev at 900 rpm to values significantly greater than 1 per rev as the rotor was feathered. The measured values demonstrated the predicted behavior trend and subsequent correlation calculations using the model properties and a method based on the stability technology outlined in Part I gave excellent agreement with test.

STABILITY TREND STUDIES

In selecting which parameters to investigate we have been guided by two considerations: (a) to use the capability provided by the new stability methodology, (b) to explore those parameters which we would intuitively expect to be critical or are known from test to be those to which instabilities are sensitive. Then we have concentrated on instability mechanisms involving blade pitch, lag, and flap degrees of freedom because the classical mechanisms are handled adequately by the previously available technology. In these areas the effect of thrust, precone, and drag offset have been investigated, along with the variation in blade torsional frequency and lead-lag frequency. As points of departure in these studies we have used existing scaled model parameters or preliminary blade design parameters. Both individual blade flutter and wing-rotor limit-cycle flutter have been studied. The results obtained suggest that further extensive studies might be usefully accomplished.

ROTOR DERIVATIVE TREND STUDIES

As mentioned earlier, rotor derivative correlation was preceded by an investigation of the influence of blade parameters such as flapping and lead-lag natural frequencies and Lock number. Some of these results were included in Volume I and are repeated here, along with the additional results for the influence of lead-lag natural frequency.

ROTOR LOADS

Part IV of this volume presents the results of the rotor loads correlation using the coupled loads analysis described in Part III. The correlation is divided into two main sections: prop/rotor loads and helicopter loads. Test data for the prop/rotor correlation were obtained from wind tunnel tests of three prop/rotor models. Photographs of the three prop/rotor wind tunnel models are shown in Figures 14, 15, and 16. These models offered a wide range of blade dynamic characteristics as well as a wide range of flight conditions and reliable test data. Alternating blade root moments as well as steady rotor in-plane moments were correlated with the loads analysis and the results are presented in Part IV. For the helicopter loads correlation, flight test data from three tandem-rotor helicopters were used: the CH-47C, the CH-47 with advanced-geometry blades, and the Model 347 with CH-47C blades. Test data from these aircraft offered correlation in predominately unstalled and predominately stalled conditions. Alternating flap and chord bending and alternating pitch link loads data were used for correlation. In addition to blade loads correlation, airloads test data obtained from a wind tunnel test of a full-scale CH-34 rotor were correlated with airloads predicted by the coupled loads analysis. Results of the helicopter correlation are presented in Part IV.

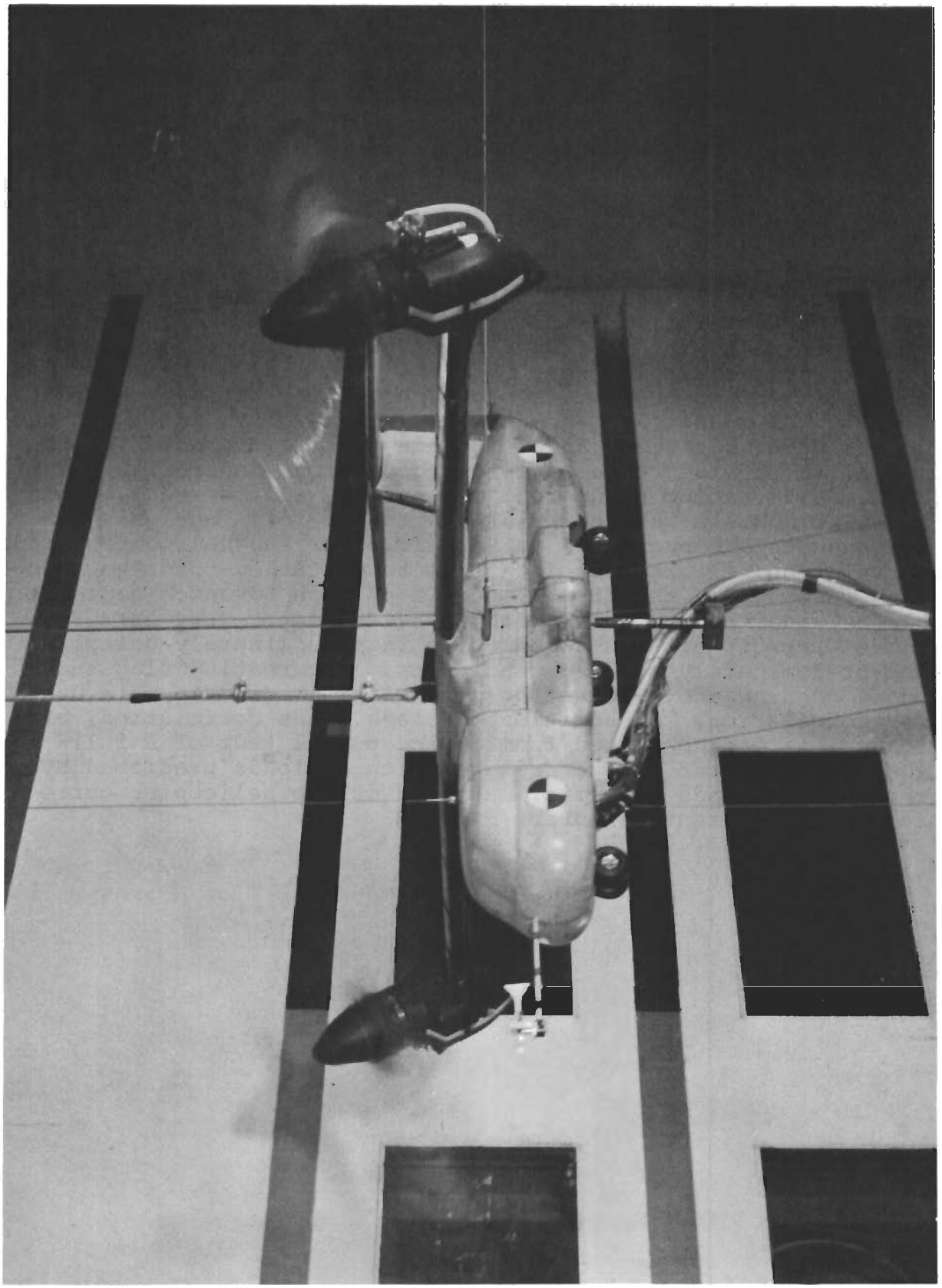

Figure 10. Model 160 1/10-Scale V/STOL Tilt-Rotor Dynamically Similar Model

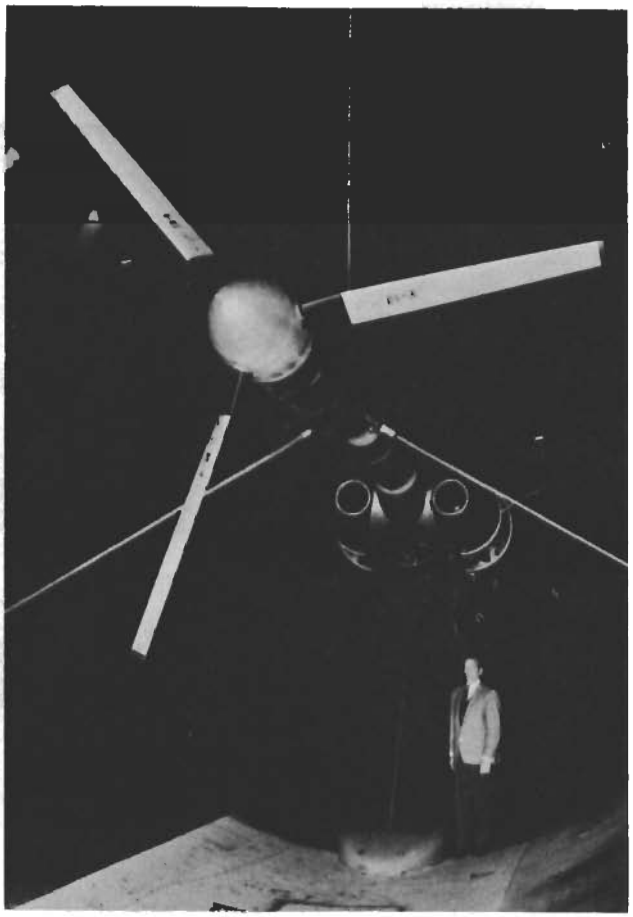

Figure 11. NASA Ames and AARL 13-Foot Fiberglass Performance Model Rotor

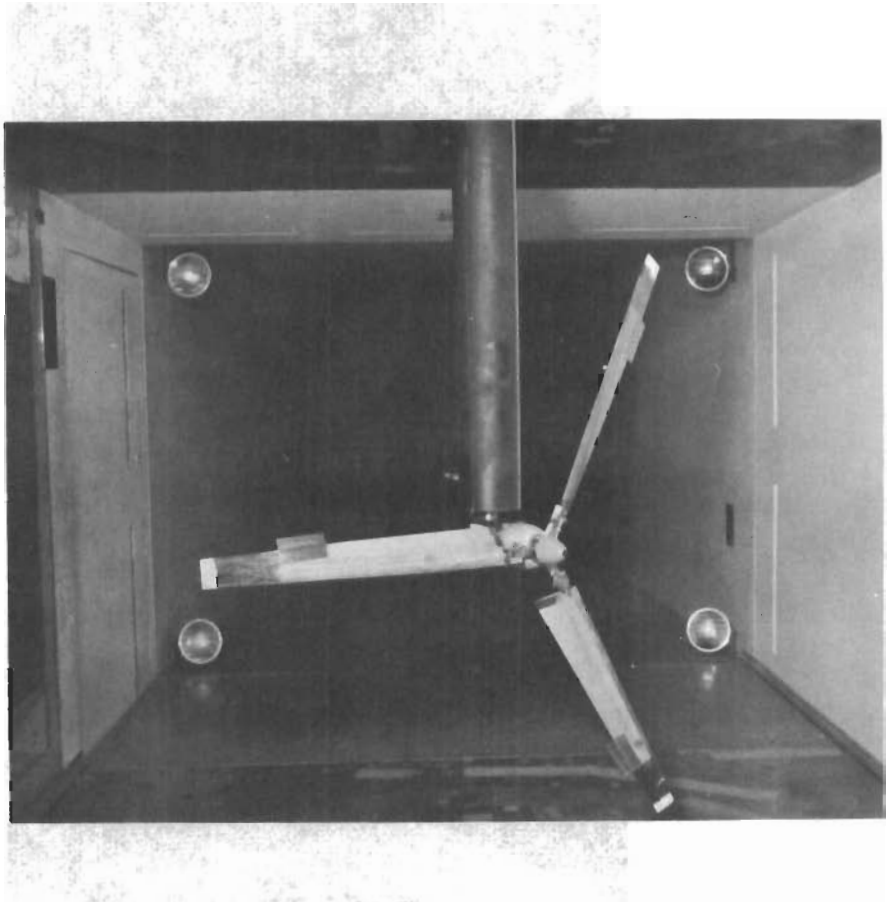

Figure 12. Model 160 1/22-Scale Dynamically Similar V/STOL Tilt-Rotor Model

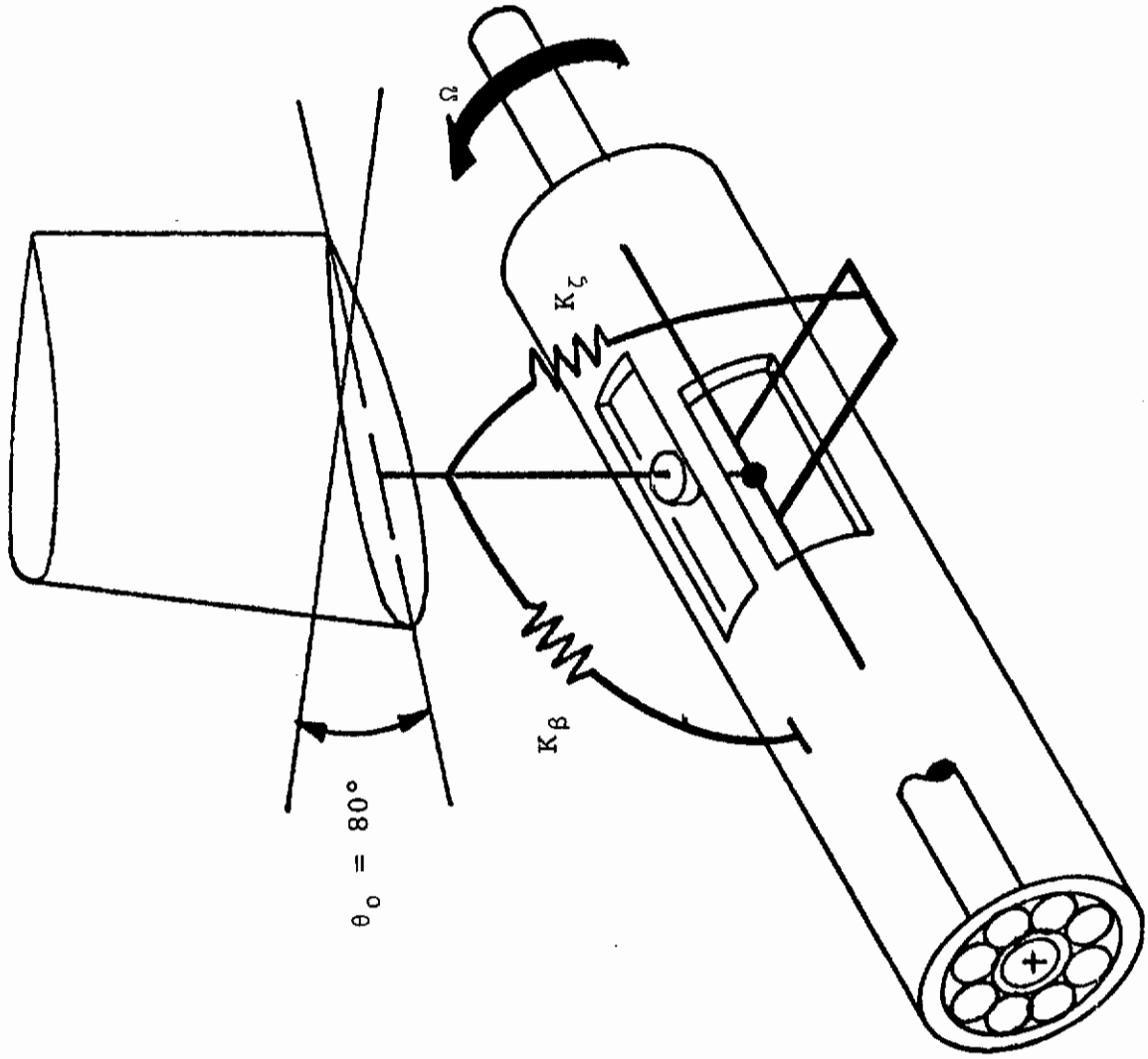

Figure 13. Mathematical Model for Rotor Derivative Parametric Trend Studies

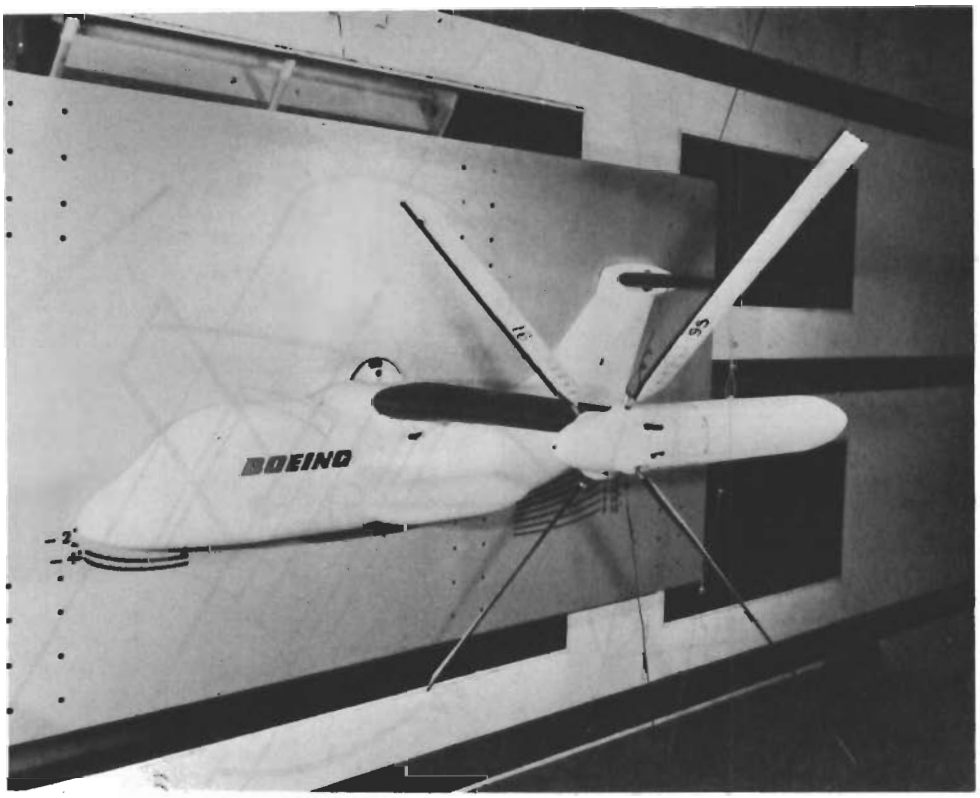

Figure 14. Model 213 1/9-Scale Dynamically Similar V/STOL Tilt/Stowed-Rotor Conversion Model

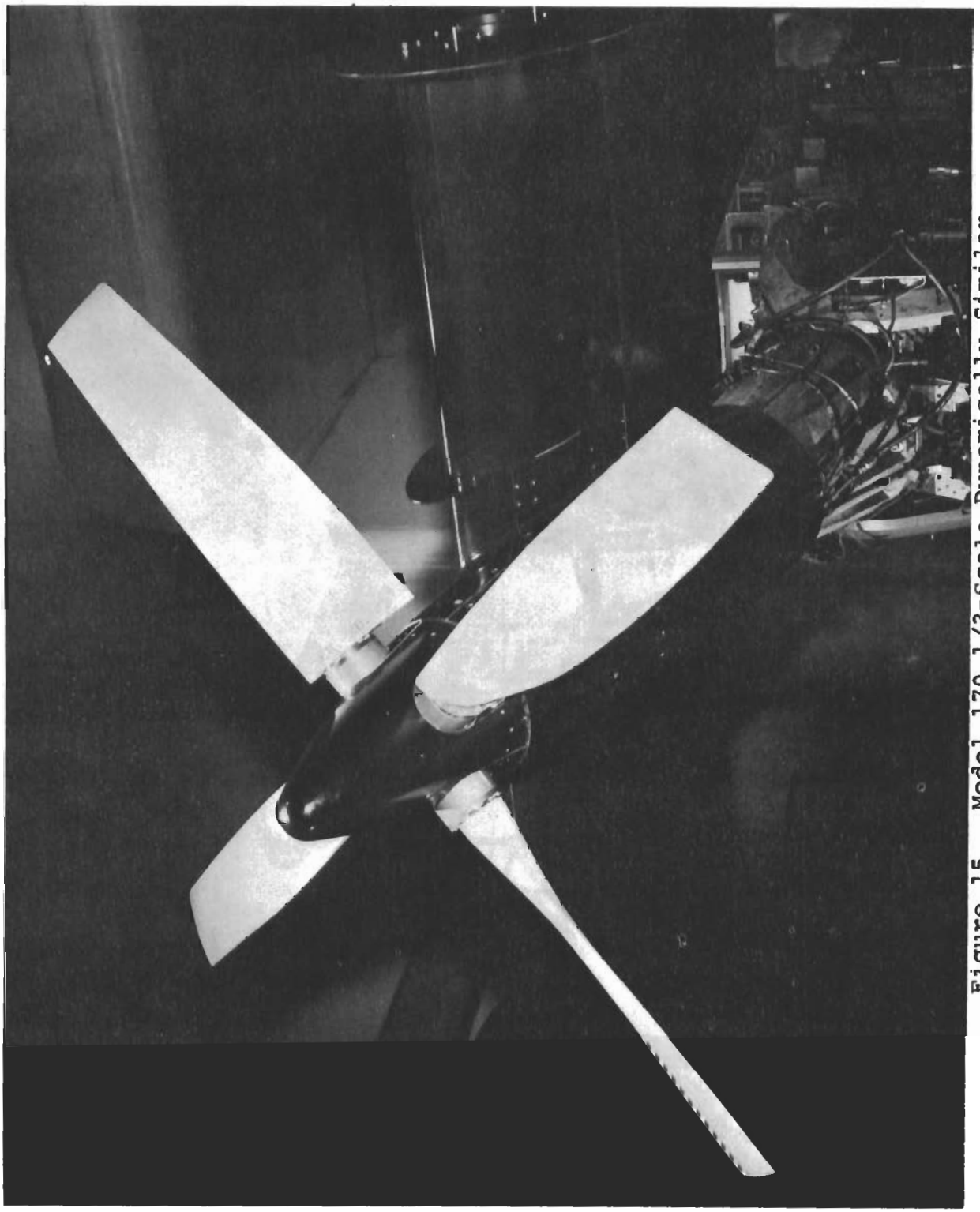

Figure 15. Model 170 1/3-Scale Dynamically Similar V/STOL Wing and Rotor Model

Figure 16. Model 160 1/10-Scale Performance Model

AEROELASTIC STABILITY: CORRELATION AND TREND STUDIES

CORRELATION

Correlation With Model 160 1/10-Scale Tilt-Rotor Dynamically Similar Full-Span Model Instability

The Model 160 1/10-scale dynamically similar full-span model was found on test to have unstable regions as indicated in Figure 17. The instability, which was limit-cycle in type, occurred when the collective pitch settings were reduced to the negative-thrust region in the q and tilt conditions being tested. The unstable mechanism involved flap, lag, and torsion motion of the blades, and the wing and rigid-body pitch degrees of freedom were also observed to participate actively. In the zero- and negative-thrust regions the blades are bent significantly away from the precone condition (5 degrees) so that strong inertial coupling exists between lead-lag blade motion and blade torsion and pitch. The C-39 program described in Part I shows successful correlation as indicated by the calculated flutter boundaries.

Correlation With the Model 160 1/10-Scale Tilt-Rotor Dynamically Similar Semi-Span Model

This model also was unstable in a limit-cycle mode involving wing bending and torsion, and blade lead-lag, flap, and torsion degrees of freedom (Figure 18). Although the model frequency parameters are rather different from those of the later full-span version, the behavior is similar. The analysis predicts the onset of instability at slightly greater negative-thrust conditions than those actually experienced. However, in view of the excellent correlation with the full-span version, it seems logical to attribute this to less precise knowledge of the earlier model parameters.

13-Foot-Diameter Fiberglass Blade Instability Correlation

During the aerodynamic performance test of a 13-foot-diameter prop-rotor conducted under NASA Contract NAS2-5025 at the ONERA facility at Modane, France, two instabilities were encountered. A violent instability occurred at a tunnel speed of 643 feet per second at 980 rpm and a low-growth-rate instability was experienced at 60 feet per second and 1,040 rpm. Correlation with each of these instabilities is shown in Figure 19. These incidents were clearly sensitive to the thrust and blade deflections combination. The blades were not scaled to any realistic full-scale design and the vibratory modes have all relatively high per-rev values. The modal deflections are highly coupled and three predominantly flexural modes occur at lower frequencies than the blade torsion mode. Thus, a minimum of four blade modes is required in any attempt at correlation.

In the high-speed case the calculated flutter boundary is plotted as a function of collective pitch and rpm. At the collective pitch of the incident, 55 degrees, the boundary is at 900 rpm or 80 rpm before the speed at which the instability was reported; that is to say, the calculation is conservative but the accuracy is within 10 percent. The low-speed incident could not be predicted in terms of blade properties alone, but when the stand modal properties were included in the calculation it seems that a very mild instability is predicted near 1,040 rpm, the rotor angular velocity at which the incident occurred.

Model 160 1/22-Scale Dyanmically Similar V/STOL Tilt-Rotor Model Correlation Study

The Model 160 1/22-scale model consisted of a nacelle and wing spar of variable stiffness and a 3-bladed, articulated, flapping rotor. Correlation with analysis was reasonably good and on the conservative side for untilted axial-flow cases, i.e., classical whirl flutter. When the nacelle was tilted relative to the wing on a wing spar relatively stiff in torsion, a significant reduction in the flutter speed was experienced as shown in Figure 20. However, with a low torsionally stiff wing spar, an increase in flutter speed was recorded as shown in Figure 21 when the nacelle and rotor were tilted. The analysis available for correlation did not address the problem of nacelle tilt and nonaxial flow through the rotor and the current study is the first attempt to correlate with this data. In Figure 20 the calculated boundaries corresponding to the test condition are shown. It is seen that the trend of a significant reduction in flutter speed with 4.5 degrees tilt of the nacelle is also in the calculated values; however, both boundaries are conservative in relation to the test data. Figure 21 shows calculated boundary as a function of tilt angle for the low torsionally stiff wing spar. This is seen to follow the test data closely, although the calculation becomes slightly unconservative at the higher tilt cases.

Correlation With Static Rotor Derivatives

Although the C-39 computer program does not compute directly the steady hub force and moment derivatives, it evaluates and prints out the partial derivative of forces in each of the rotor variables and 6 orthogonal linear and angular hub displacements. The derivatives are with respect to unit amplitude, rate, or acceleration in each of the hub displacement rotor variables. Proceeding from this information, it is relatively straightforward to compute the rotor steady response and hence rotor hub forces and moments with respect to such quantities as incremental shaft angle. This provides a convenient check on the rotor technology in cases where no instability boundaries are encountered in the test region. In such

cases the rotor hub derivatives may still be measured. In a flexible blade the dynamic response of the blade has to be computed accurately to provide the correct hub forces and moments. This correlation with static rotor derivatives goes a long way toward substantiating the accuracy of stability predictions when the onset of instability does not occur in the test range.

Correlation of this sort is shown in Figure 22. The measured derivatives were obtained from the Model 213 1/9-scale conversion model, Figure 14. The calculated values show excellent agreement with the test data. In this rotor the first natural frequency of the blade crosses 1 per rev at 500 rpm, so that the test data confirms the unexpected sensitivity in this region to blade lead-lag frequency mentioned earlier. At 85 feet per second excellent correlation is obtained when the first and second blade flexural modes are included (Figure 22). At higher advance ratios (141 feet per second) the influence of blade torsion has to be included to achieve a similar level of correlation (Figure 23).

TREND STUDIES

The preceding sections have demonstrated a substantially reliable capability to correlate with nonclassical rotor instability behavior. Selected parametric variations are now developed to gain information on the sensitivity to parameters expected to be critical.

Effect of Advance Ratio and Thrust at Constant RPM on Individual Blade Stability

In Figure 24, calculated pitch-lag-flap flutter boundaries for an individual blade are shown. These show that, for the particular design chosen for investigation, instability would occur at zero airspeed and zero thrust. As advance ratio increases the amount of negative thrust that can be tolerated also increases, but the amount of positive thrust that can be pulled without an instability is reduced at the same time.

Whether this would prove to be a problem in practice would depend on the thrust-speed schedule and also on how this behavior is modified when the rotor-to-wing dynamics are included.

Sensitivity of Blade Stability to Lead-Lag Natural Frequency

The lead-lag frequency of the blade mentioned in the preceding paragraph was varied over a range from 0.4 per rev to 1.4 per rev (baseline value 0.73). Two regions of flutter are identified as shown in Figure 25. Negative thrust is destabilizing when the lead-lag frequency is above 1 per rev and in the vicinity of the flap frequency of 1.22 per rev. Positive thrust is destabilizing for lead-lag frequencies below 1 per

rev, but below 0.6 per rev large values of negative thrust produce static divergence.

Sensitivity of Individual Blade Flutter to Blade Torsional Natural Frequency

The torsional frequency of the blade discussed in the preceding two paragraphs was varied over the range 2.0 to 6.5 per rev. It is seen in Figure 26 that in the positive-thrust regime the stability is relatively insensitive to torsional frequency. This is true down to a value of 2.2 per rev where a pitch-flap flutter boundary occurs. In the negative-thrust regime this merges into a pitch-flap divergence boundary. This suggests that individual blade flutter is relatively insensitive to variations in blade torsional frequency over practical ranges of torsional stiffness.

Sensitivity of Wing-Rotor Pitch-Lag-Flap Instabilities to Precone Angle and Thrust

For this study data pertaining to the Model 160 1/10-scale dynamically similar model was used at an advance ratio of 0.13. It was expected that significant changes would be seen in the amounts of positive and negative thrust required to produce instability when the precone angle is changed. This was found not to be the case as shown in Figure 27. Over a wide range of precone values there is remarkably little change in the thrust level required for the onset of the wing-rotor instability. This indicates that the blade deflection away from the precone position, and hence the flap-pitch and lag-pitch inertial coupling, is much less important than the magnitude of the steady aerodynamic forces (thrust and drag) on the rotor blade.

Sensitivity of Wing-Rotor Pitch-Lag-Flap Flutter to Drag Offset and Thrust

The Model 160 1/10-scale dynamically similar model was selected for study. Since the drag offset affects the blade elastic deflections, it was anticipated that a significant influence on pitch-lag-flap flutter would be demonstrated. However, a result very similar to that for precone was evaluated as shown in Figure 28. We must conclude, as in the case of precone, that the inertial coupling variations introduced by offset are much less significant than the steady blade force modal couplings.

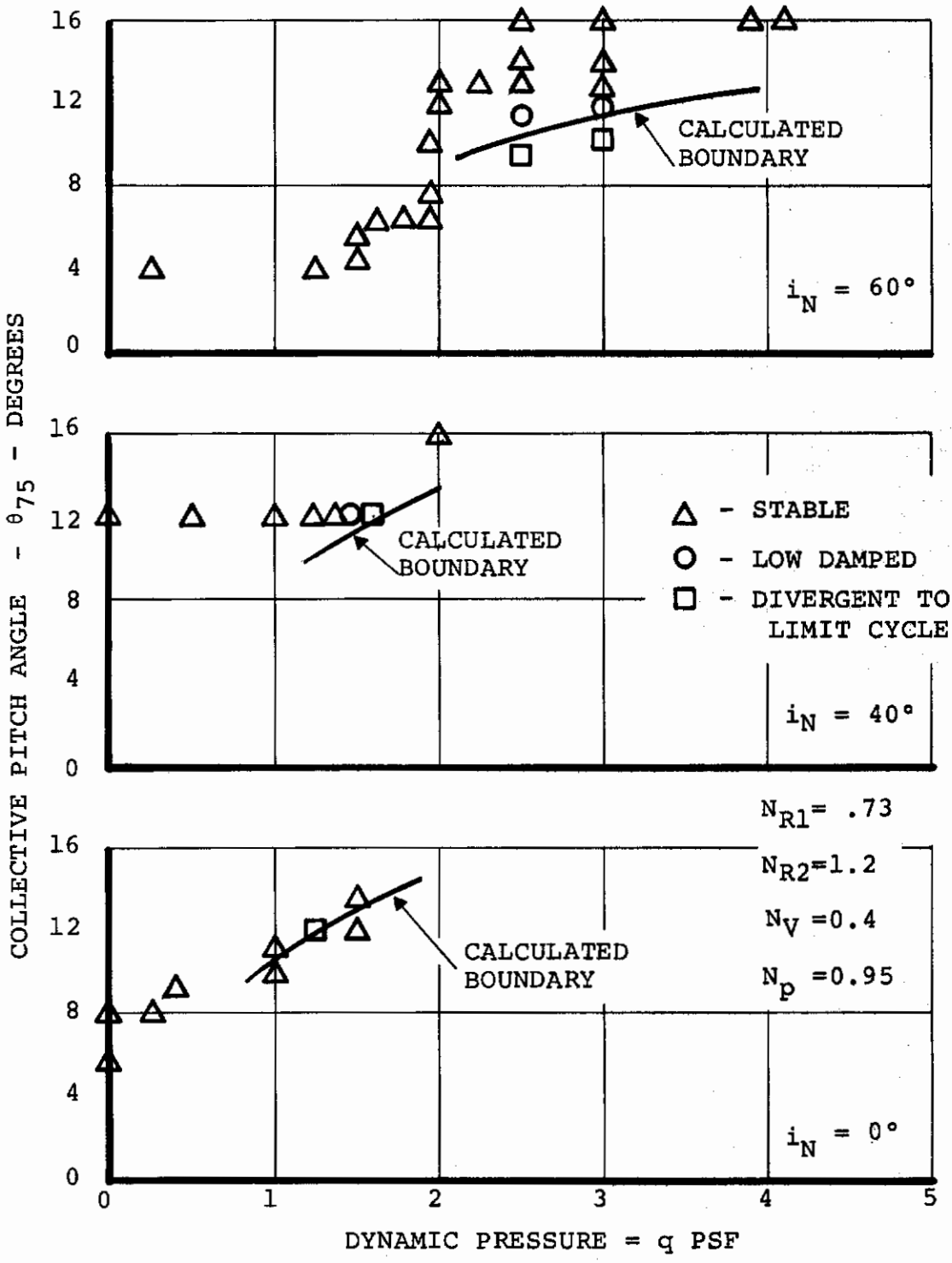

Figure 17. Model 160 1/10-Scale Tilt-Rotor Dynamically Similar Full-Span Model Correlation

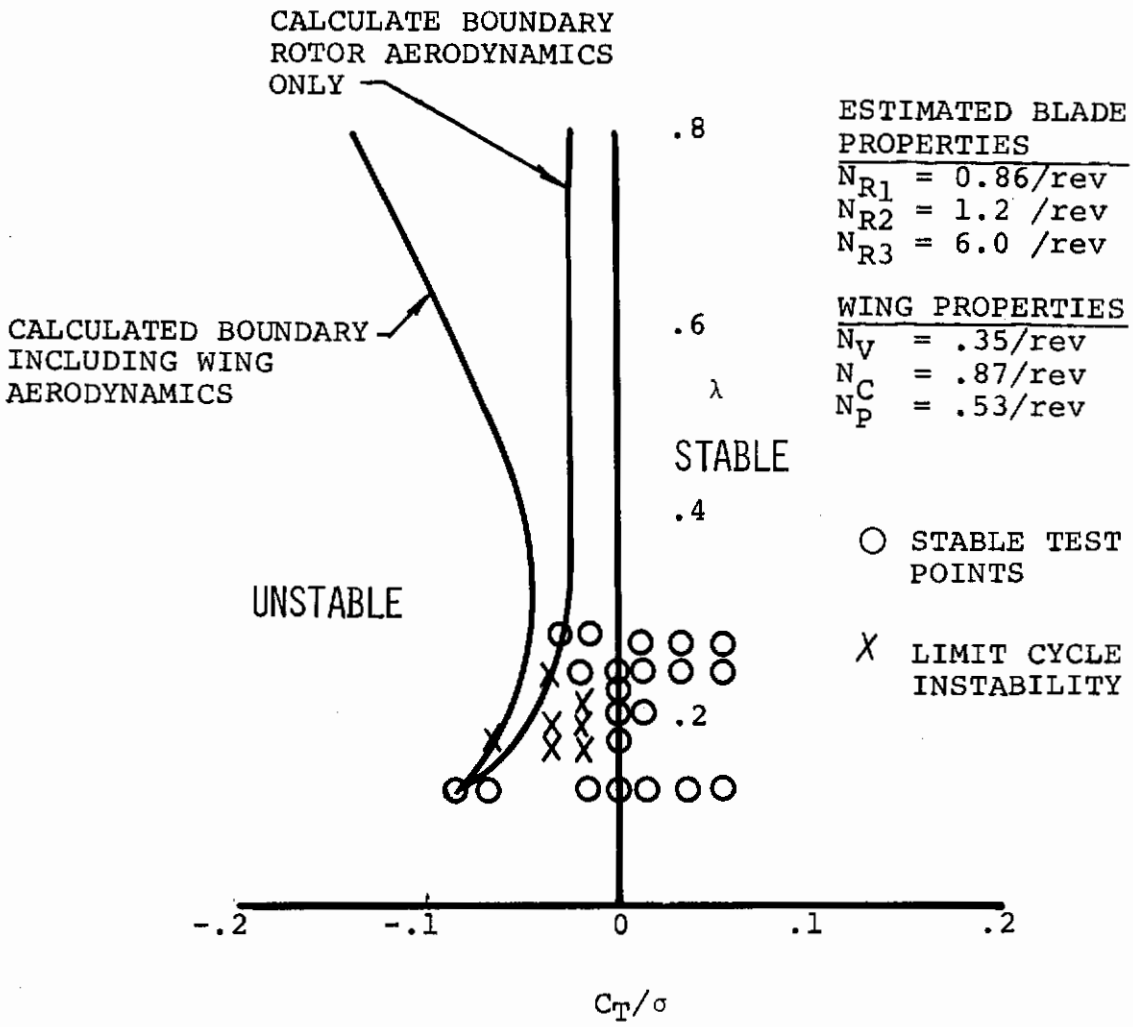

Figure 18. Model 160 1/10-Scale Tilt-Rotor Dynamically Similar Semi-Span Model Correlation

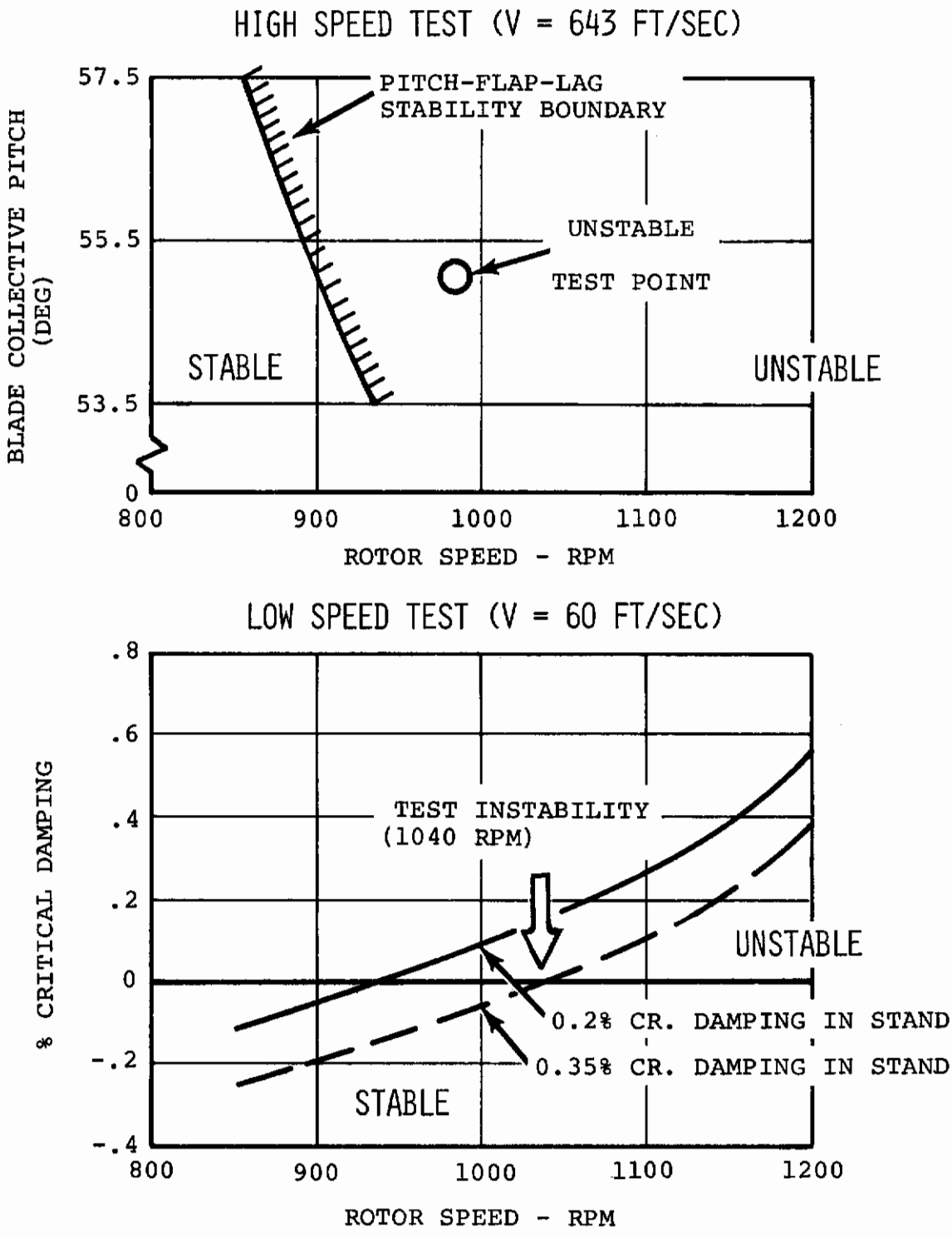

Figure 19. Blade Flutter Correlation 13' Diameter Rotor Performance Test (ONERA 1968)

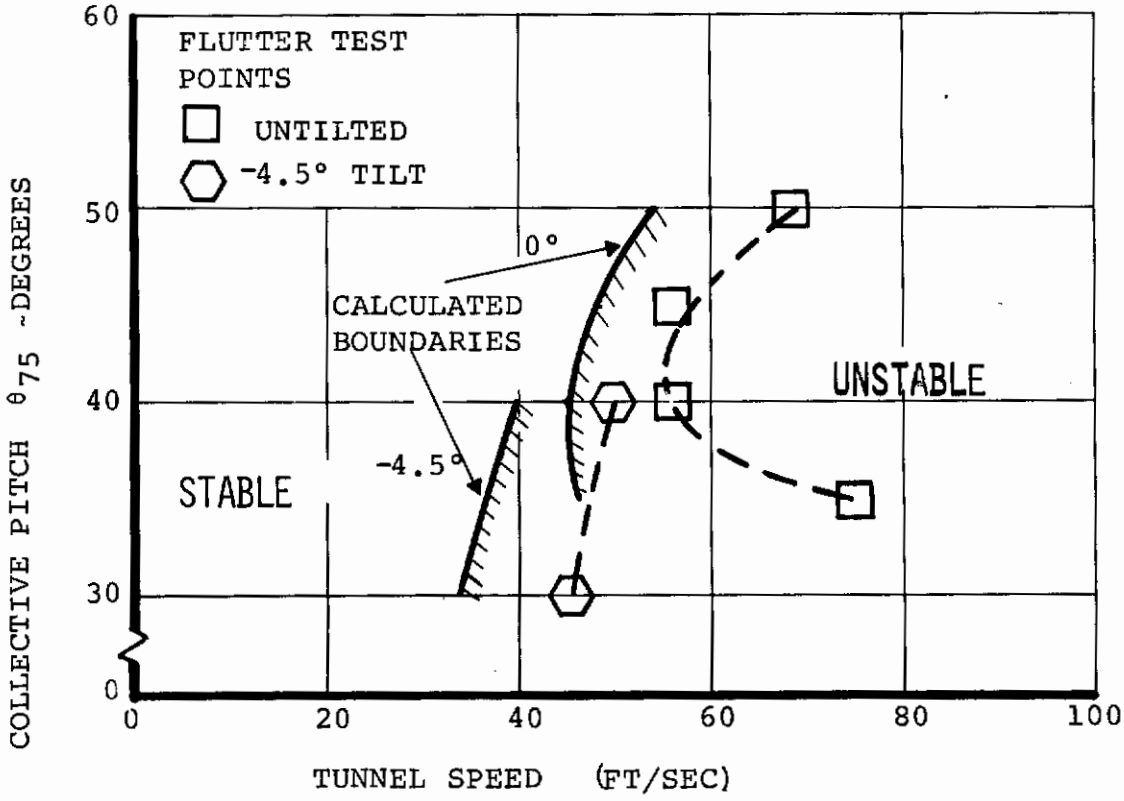

Figure 20. Model 160 1/22-Scale Dynamically Similar V/STOL Tilt-Rotor Model Correlation Torsionally Stiff Wing Spar

1/22 SCALE TILT ROTOR TEST CORRELATIONS

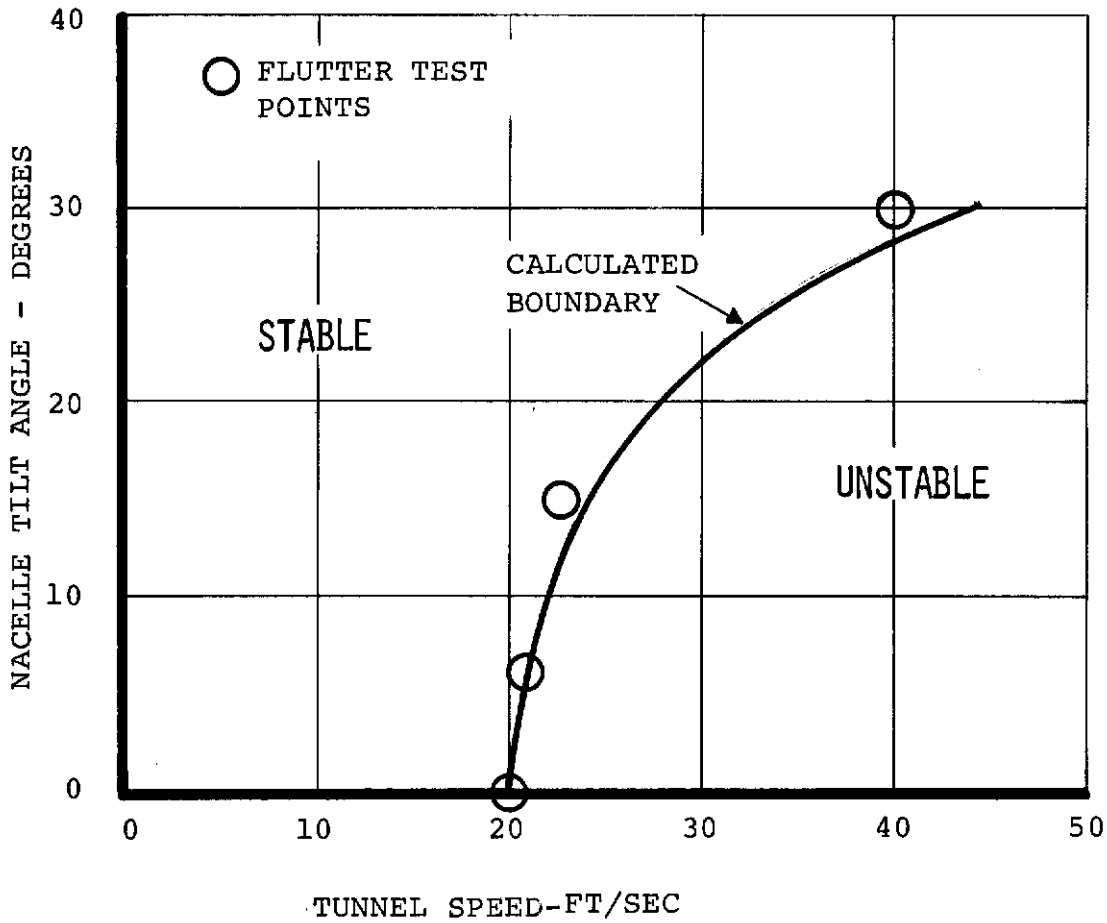

Figure 21. Model 160 1/22-Scale Dynamically Similar V/STOL Tilt-Rotor Model Correlation Torsionally Weak Wing Spar

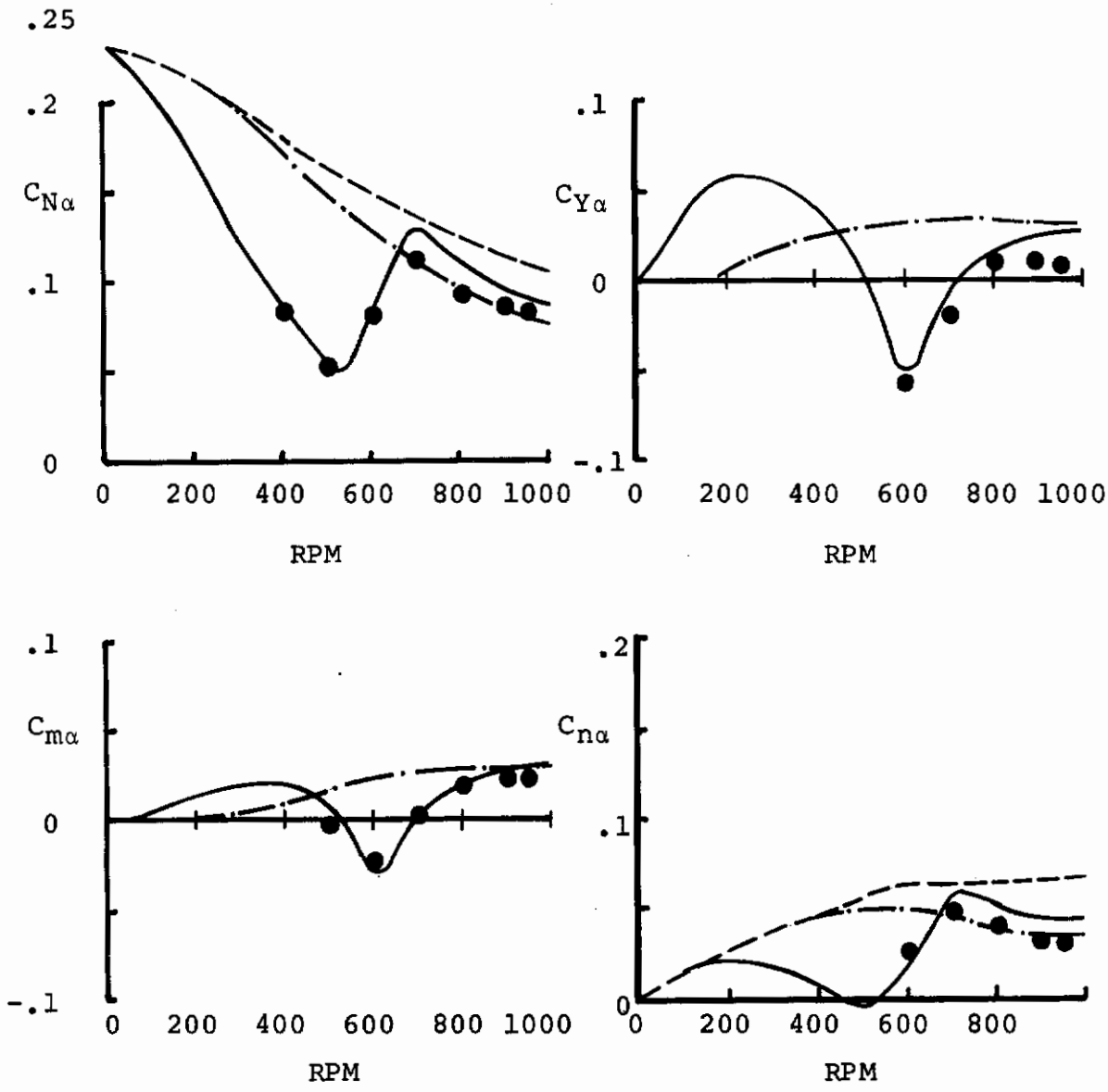

Figure 22. Model 213 1/9-Scale Conversion Model - 85 Ft/Sec Derivative Variation with RPM

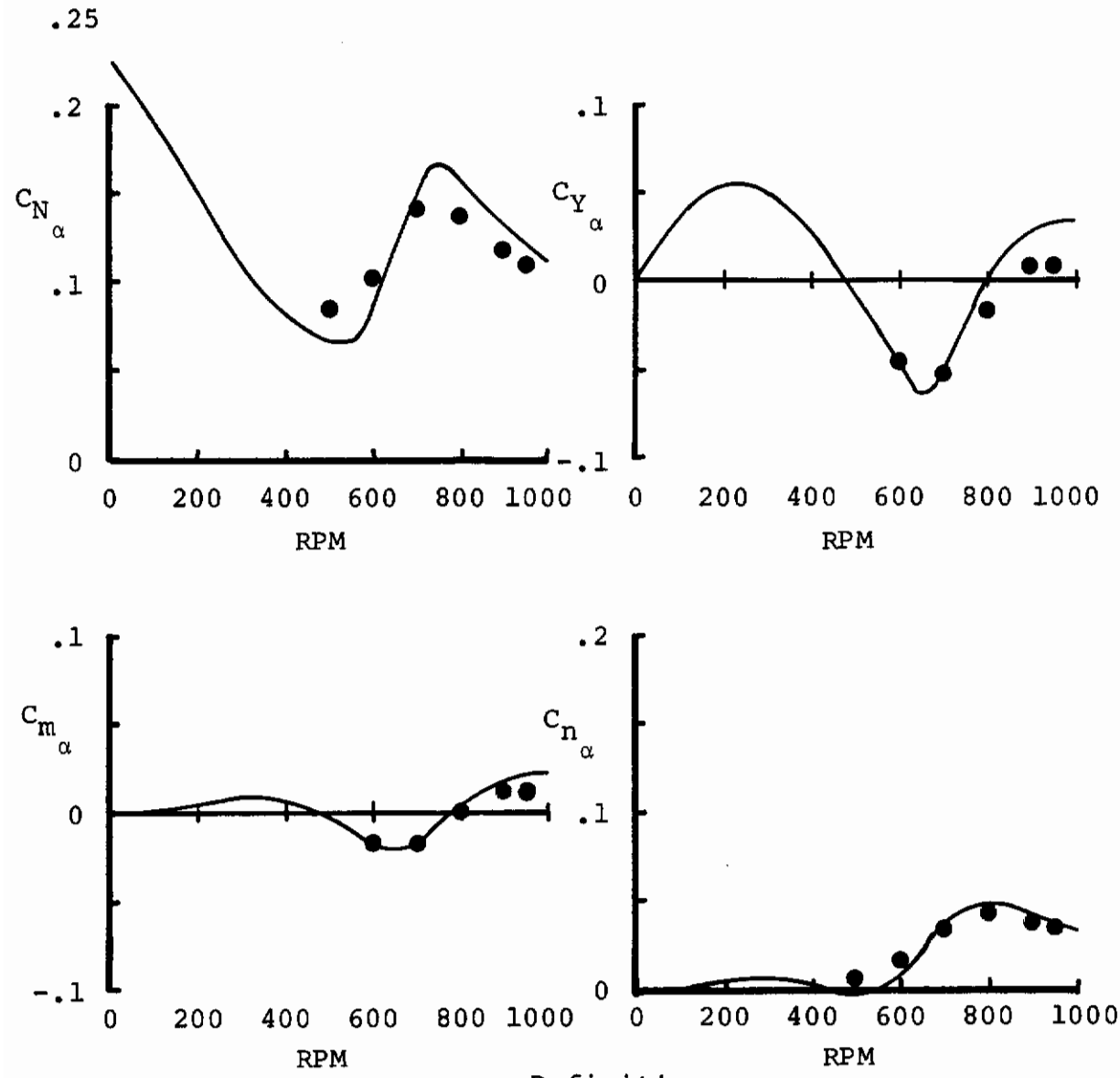

Test Points ●
Theoretical Predictions
——— Flap and Lead-Lag

$\frac{dC_L}{d\alpha} = 5.7$

Definitions

Normal Force = $1/2\rho\pi R^2V^2C_{N_\alpha}\cdot\alpha$

Side Force = $1/2\rho\pi R^2V^2C_{Y_\alpha}\cdot\alpha$

Pitching Moment = $\rho\pi R^3V^2C_{m_\alpha}\cdot\alpha$

Yawing Moment = $\rho\pi R^3V^2C_{n_\alpha}\cdot\alpha$

Figure 23. M213 1/9-Scale Conversion Model - 141 Ft/Sec Derivative Variation With RPM

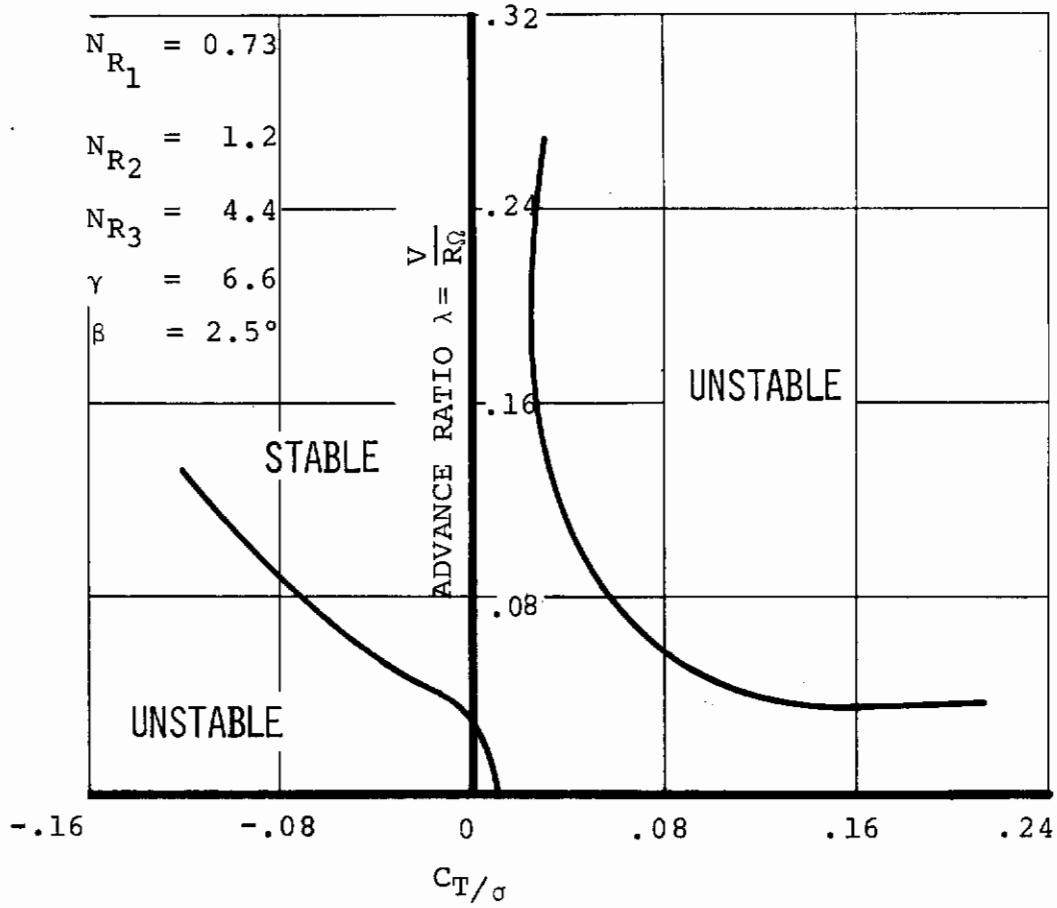

Figure 24. Calculated Pitch-Lag-Flap Flutter Boundaries for a Preliminary Design Blade

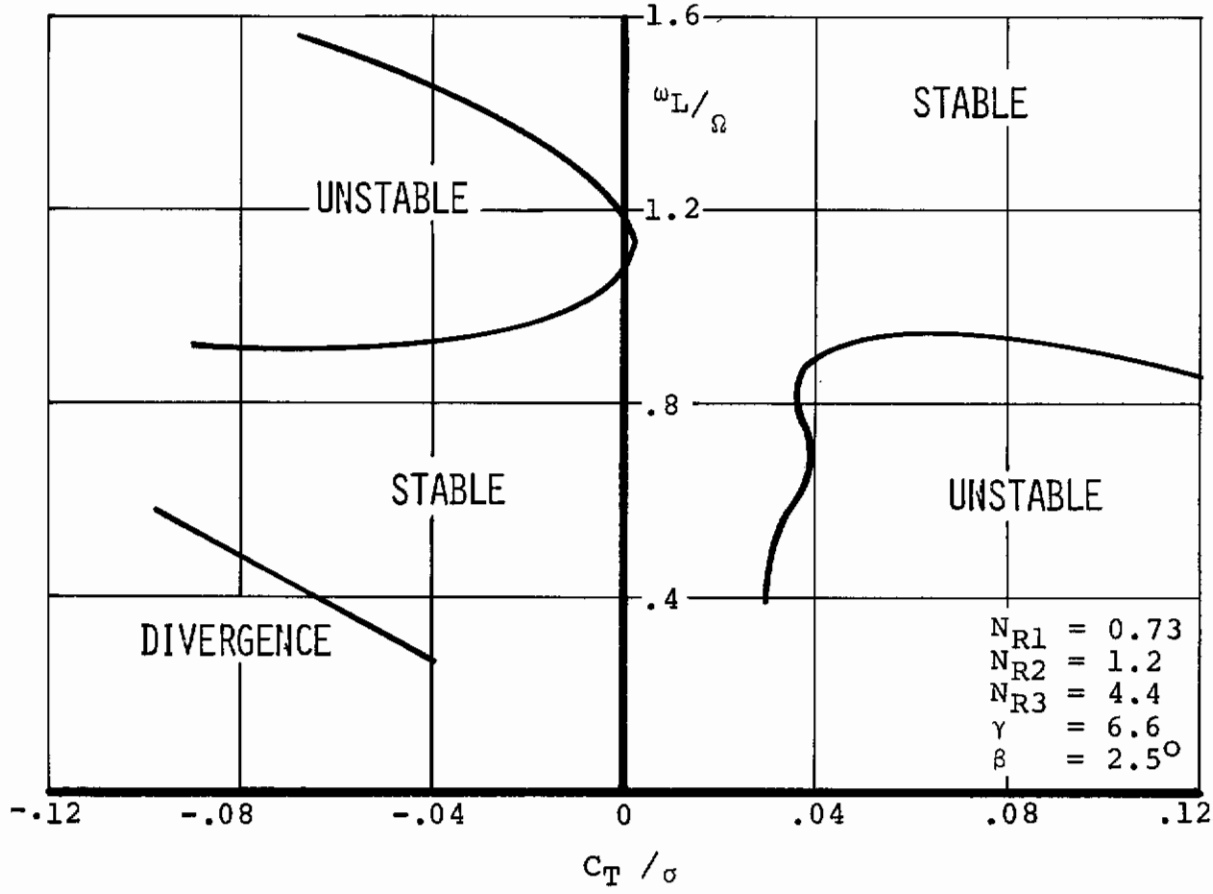

Figure 25. Blade Flutter Sensitivity to Changes in Lead-Lag Frequency Ratio and Thrust

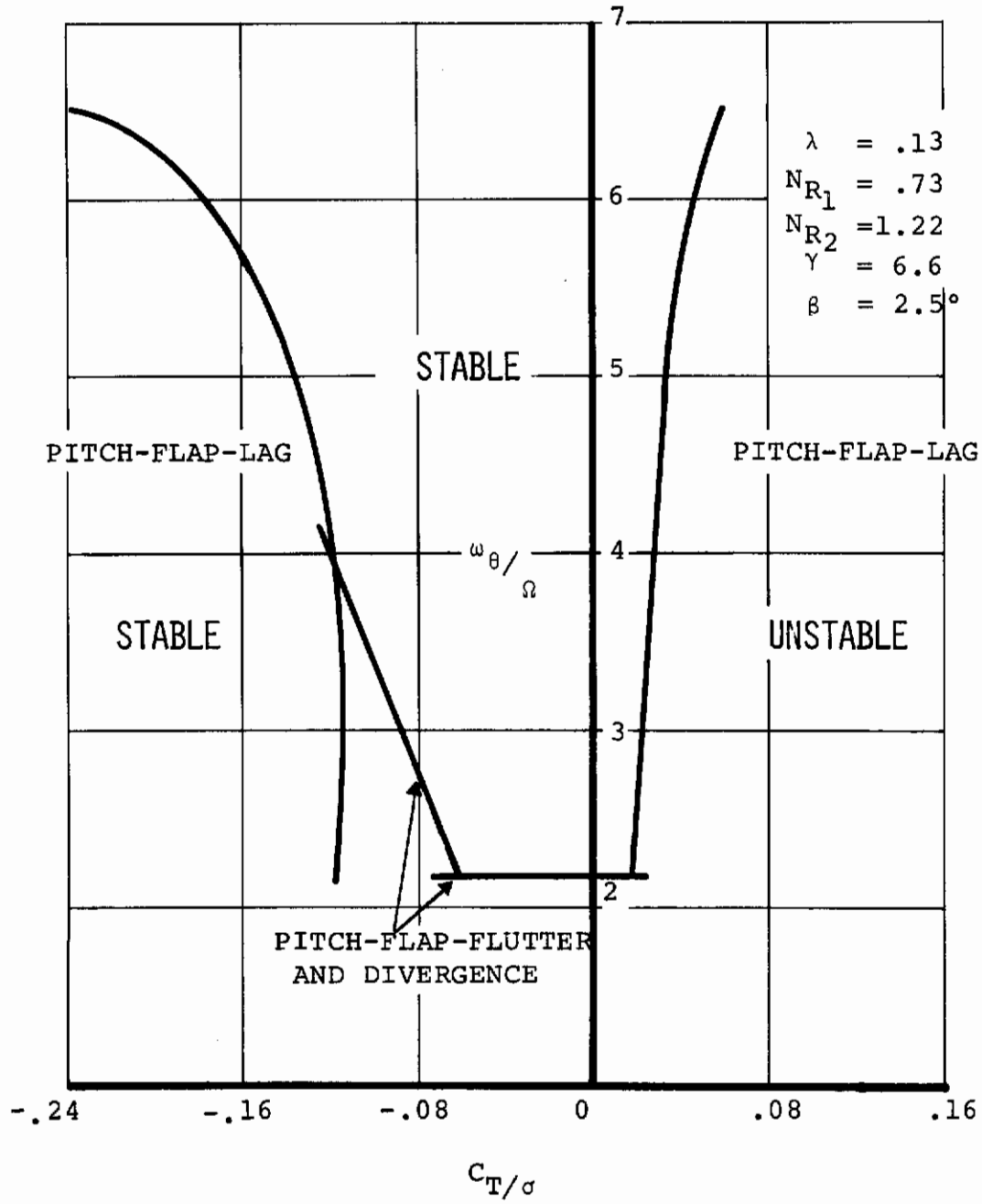

Figure 26. Individual Blade Flutter Sensitivity to Torsional Natural Frequency

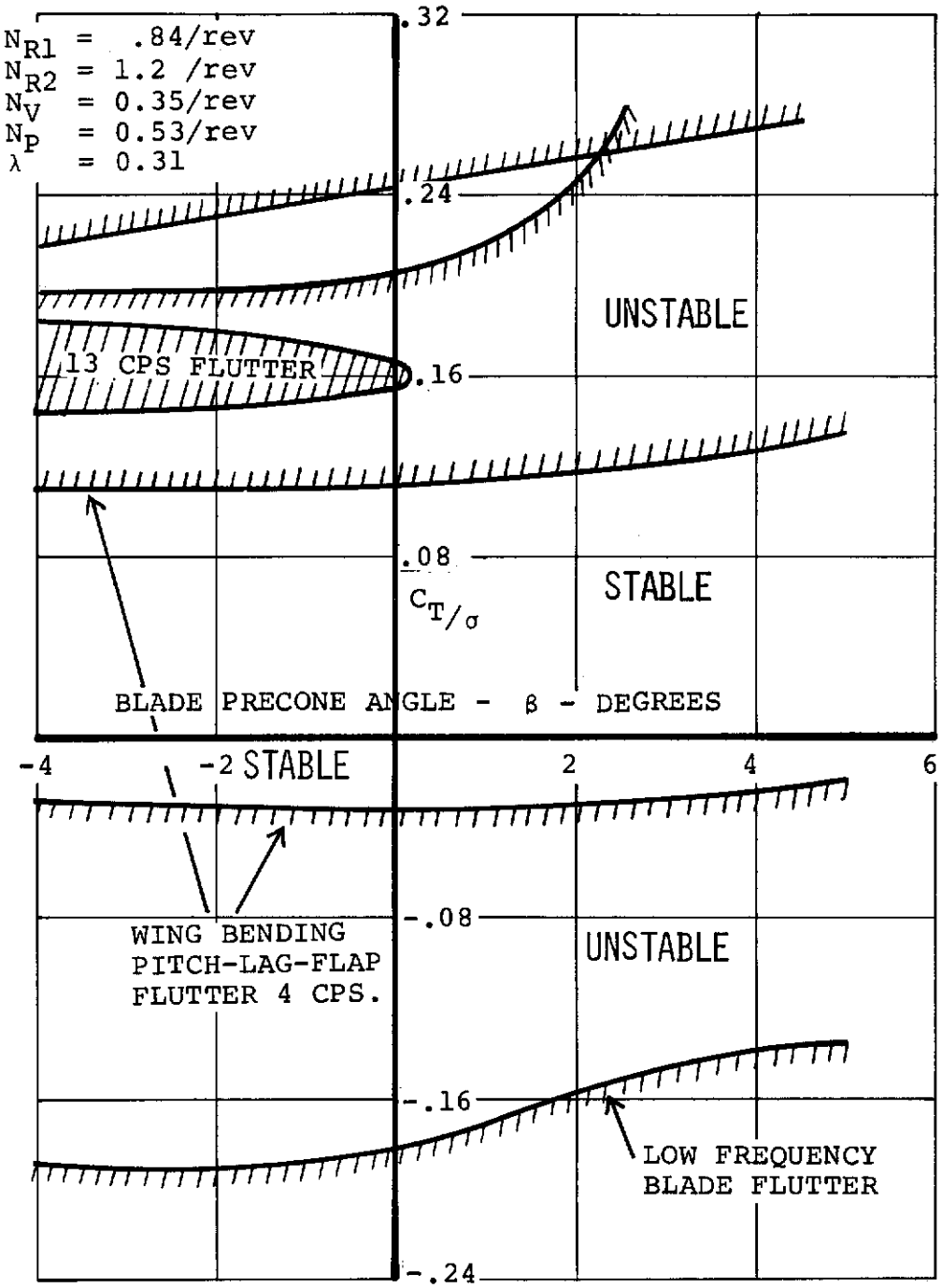

Figure 27. Sensitivity of Wing/Rotor Pitch-Lag-Flap Flutter to Precone Angle and Thrust

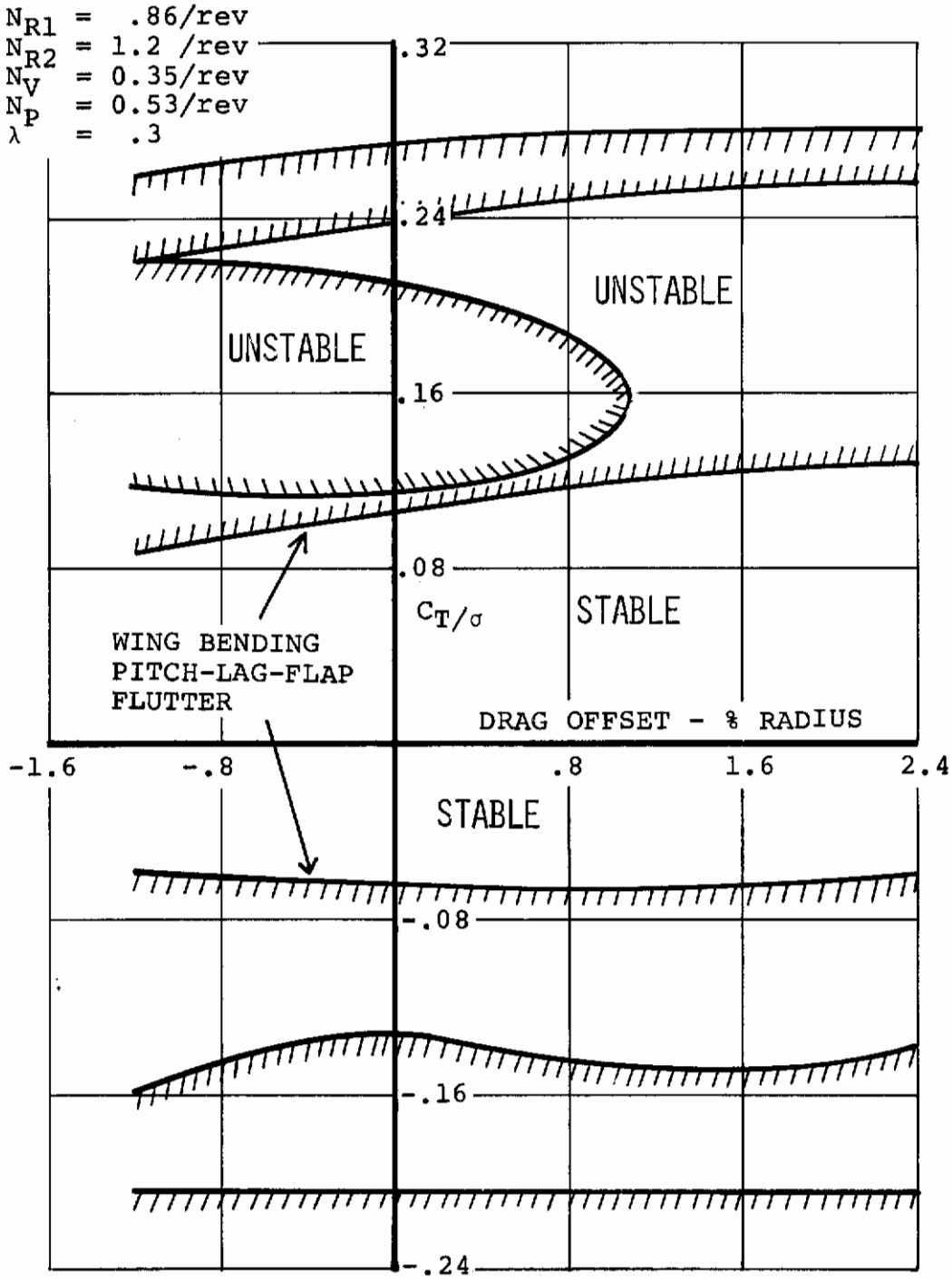

Figure 28. Sensitivity of Wing/Rotor Pitch-Lag-Flap Flutter to Drag Offset and Thrust

ROTOR DERIVATIVE TREND STUDIES

ROTOR DERIVATIVE SENSITIVITY TO ADVANCE RATIO, FLAP FREQUENCY, AND LOCK NUMBER

The static derivatives of the rotor provide a convenient means of determining the accuracy of aeroelastic blade theory. The parametric behavior of the derivatives is important in itself since the static divergence characteristics of V/STOL tilt-rotors are governed by the rotor normal force and moment derivatives. This is discussed at some length in Volume I and need not be repeated here. In view of this importance of the rotor static derivatives, studies have been accomplished investigating the effects of blade advance ratio, flap natural frequencies, lag natural frequency, and Lock number. With the exception of lead-lag natural frequency, these are discussed in Volume I. Figures 29 and 30 showing the effects of advance ratio, blade flapping frequency, and Lock number are included in this volume for ease of reference. As is noted in Figure 29, the derivatives are extremely sensitive to blade flapping frequency, particularly in the 1.2- to 1.4-per-rev range typical of propeller/rotor designs for V/STOL.

In Figure 30 some results are presented for Lock number variation. These show a significant sensitivity to Lock number, particularly in the pitching moment derivative $C_{m\alpha}$ and side force derivative $C_{y\alpha}$, where a reversal of trend is also noted as the blade frequency increases from 1.2 to 1.6 per rev.

Overall, the results indicate the need for care in the evaluation of blade parameters to be used in static and dynamic calculations involving the blade.

ROTOR DERIVATIVE SENSITIVITY TO LEAD-LAG NATURAL FREQUENCY

In the derivative studies in the preceding paragraphs the blade assumed lead-lag frequency was sufficiently high that the freedom did not affect the results. In Figures 31 and 32 the parametric behavior with lead-lag natural frequency is presented. As in the earlier work, the mathematical model of Figure 13 was used. A dramatic variation of all derivatives is noted when the lead-lag frequency is in the vicinity of one per rev. Particularly notable is the change in sign of the pitching-moment and side-force derivatives. These variations are of profound importance to the static and dynamic aeroelastic properties of rotor-powered aircraft whose designs incorporate blade in-plane frequencies below or near one per rev. The discovery of this effect is a significant new contribution to our body of knowledge of rotor system behavior.

An intuitive explanation of this sensitivity to lead-lag frequency may be given. The phase of the lead-lag motion to

one-per-rev aerodynamic forcing caused by the shaft angle α tends to increase rapidly from low value to 180 degrees as the blade passes through resonance. Then the coupling between lead-lag motion and flapping motion undergoes a change of sign as the blade lead-lag frequency traverses one per rev. In addition, the lead-lag amplitude will be magnified in this region so that the cross-couplings overcome the natural tendency of the blade to flap back (i.e., $C_{m\alpha}$ positive) with increasing shaft angle.

As noted earlier, these trends have been fully confirmed by subsequent test data and correlation.

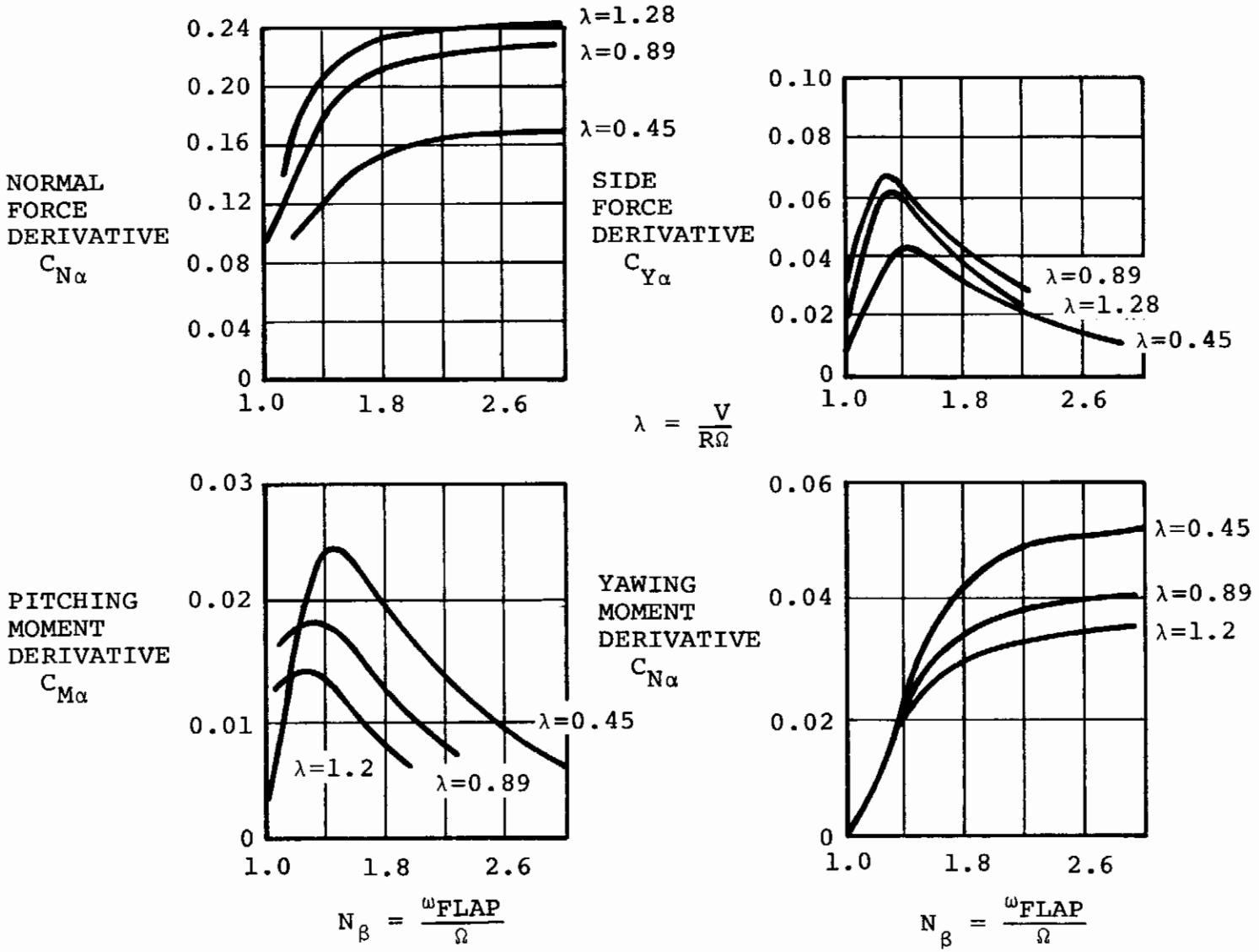

Figure 29. Variation of Rotor Derivatives With Flap Frequency. Lag Frequency High

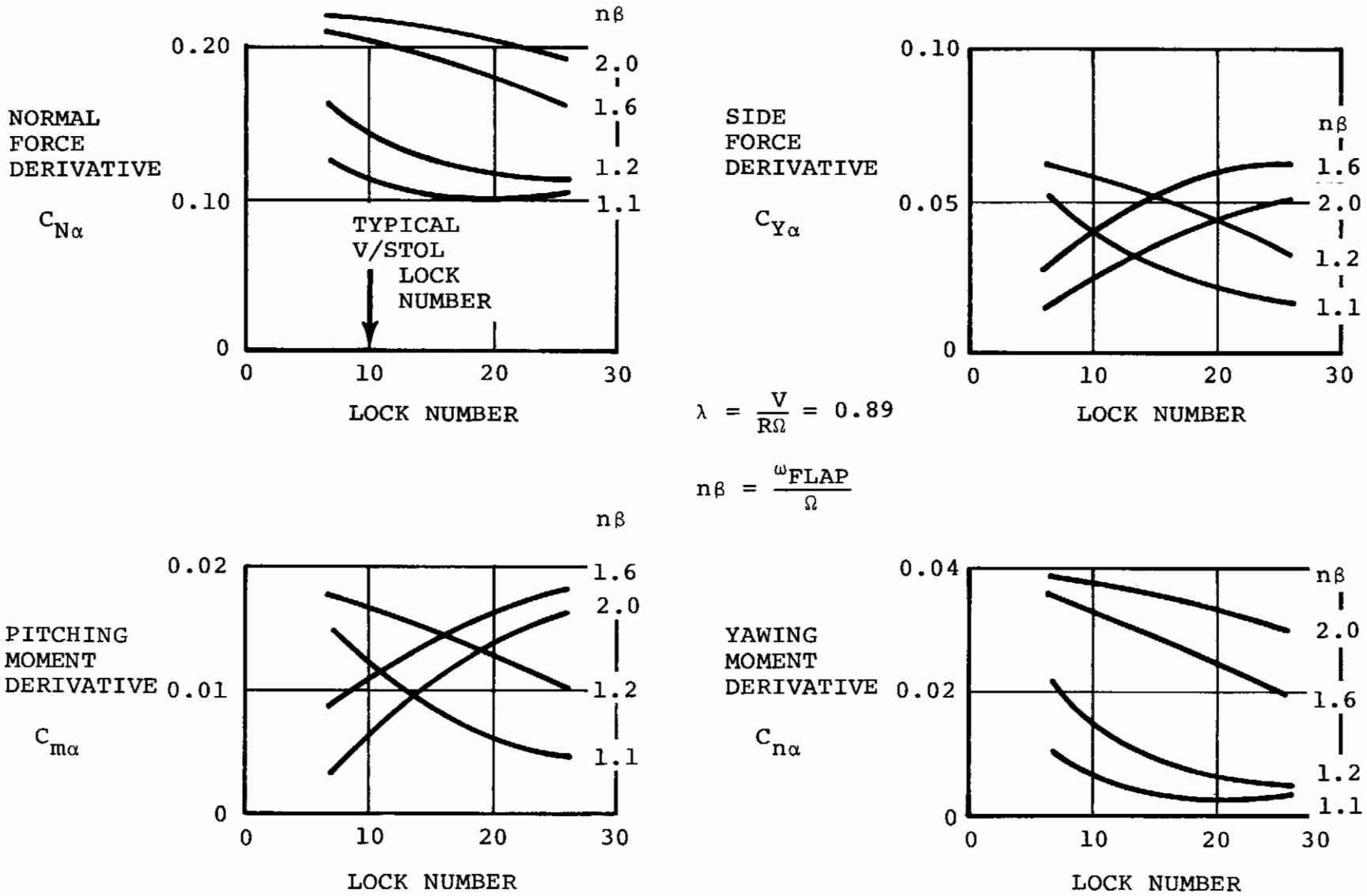

Figure 30. Effect of Lock Number on Rotor Derivatives for Flap Frequency Ratios $n\beta$ = 1.1, 1.2, 1.6, and 2.0

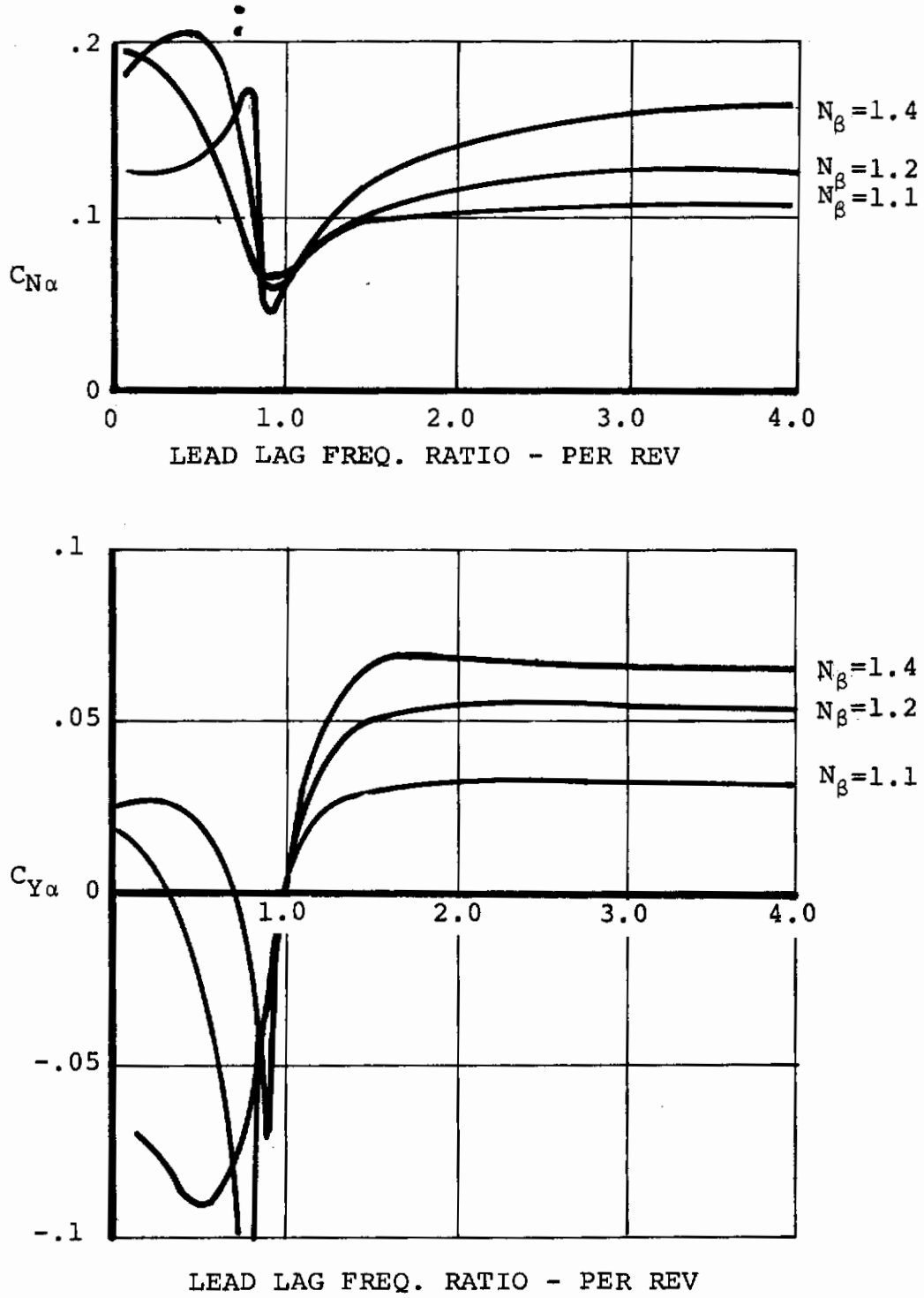

Figure 31. Variation of Normal and Side Force Derivatives with Lag Frequency Ratio

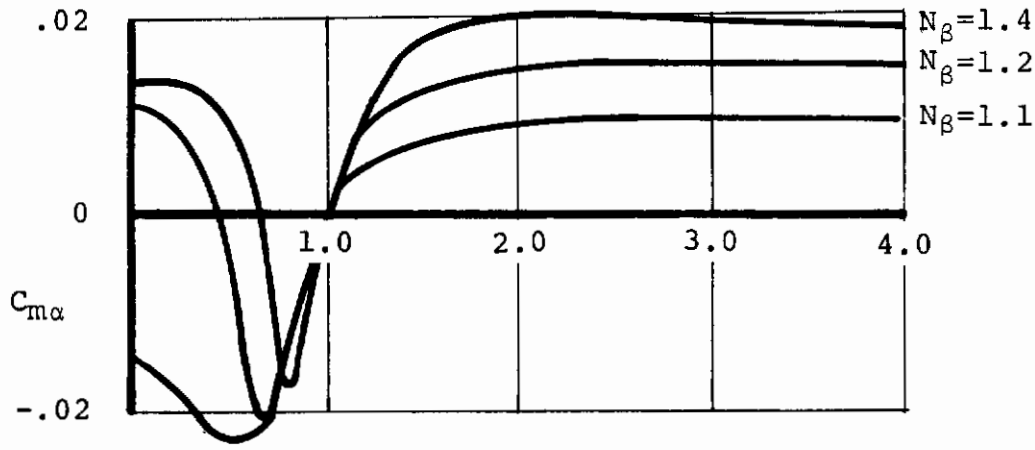

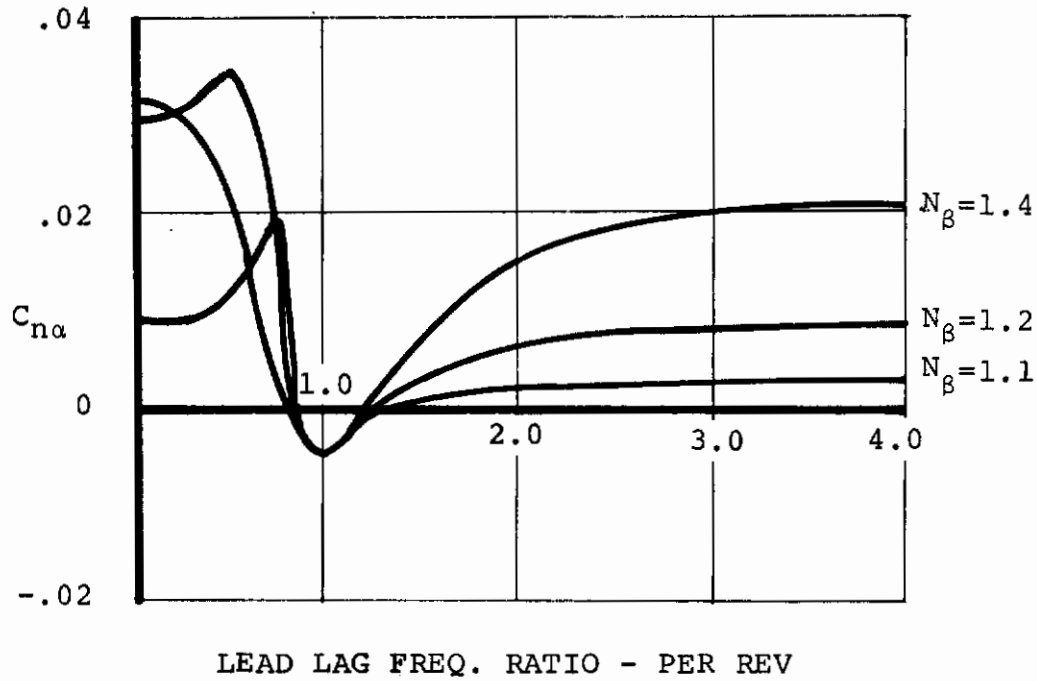

Figure 32. Variation of Hub Pitching and Yawing Moment Derivatives with Lag Frequency Ratio

Part III. New Methodology for Aeroelastic Prop/Rotor Loads Analysis

F. J. Tarzanin

INTRODUCTION

An ideally designed prop/rotor aircraft has all its structural load limits beyond the power-limited flight envelope. When structural loads limit the flight envelope, the aircraft is inefficient and costly, since it contains an oversized powerplant which cannot be fully used. In addition, problems of limited flight envelope, limited component life, safety, frequent overhauls, and high maintenance costs reduce the effectiveness of the aircraft. When the structure has been greatly oversized and many structural limits are significantly beyond the flight capability, a penalty is paid through increased aircraft weight and cost. Only when a design includes structural limits, power available, and flight envelope that are matched can the best aircraft be obtained.

To obtain the ideal design, rotor loads for any proposed design must be accurately known throughout the flight envelope for both maneuvers and level flight. To obtain these loads requires a mixture of test and analysis. Analysis is the most efficient approach, since parameter variations, flight envelope investigations, and tradeoff studies can be performed with a minimum of time and cost. However, wind tunnel tests must also be performed to check the analytical results, establish confidence, and account for the unknowns of actual hardware without the scatter of flight data. Some flight data for a similar aircraft is needed to determine actual load scatter in the real environment.

The rotor loads that can limit the aircraft flight envelope include blade loads, control loads, and hub loads. Hub loads directly cause fuselage vibration, which can become so severe that specifications are exceeded or pilot effectiveness is reduced. Blade loads include flapwise and chordwise blade bending moments and blade torsional moments which are used to determine blade life. Control loads determine pitch link, swashplate, and control actuator life and can affect aircraft controllability. All these loads are required at critical points of the flight envelope, including level flight, maneuvers, and emergency conditions, to effectively design the rotor.

However, rotor analysis will have a critical role in the selection and design of advanced prop/rotor aircraft. The Vertol Division of The Boeing Company has an operational steady-state rotor loads analysis that has shown good agreement with measured helicopter flight data. However, the Vertol rotor program is intended to analyze helicopter rotors and must be further developed to correctly analyze propeller-type rotors.

For highly twisted blades, the principal axes in the chordwise and flapwise directions change their orientation relative to the rotor shaft at each spanwise location. The helicopter analysis does not consider this principal axis rotation. To accurately calculate the blade deflections, including principal axis rotation, requires that either all calculations be performed in a local-axis system coincident with the local principal axis orientation, or in a fixed-axis system with all the cross-inertia terms included. In either case, the analysis is best performed if the chordwise and flapwise deflections are coupled. In addition, since the chordwise mass center is not coincident with the shear center, coupling with torsion will also result. Therefore, to properly analyze rotors with large twist (propellers), a coupled chordwise-flapwise-torsion analysis is required.

The present helicopter rotor analysis assumes that the pitch axis, vertical neutral axis, and shear center are coincident. This assumption was fairly accurate when applied to long, slender rotor blades with spar-type construction. However, recent developments in composite materials, new construction techniques, and the larger chord-to-radius ratio of propellers have made the difference between the pitch axis and shear center more important. Control input (cyclic and collective), as well as flexible control input resulting from control loads, are input about the pitch axis while elastic twist resulting from blade torsional loads pitches about the shear center. When the difference between the pitch axis and shear center is significant, both axis systems must be taken into account when calculating the rotor loads.

In light of the need for improved knowledge of prop/rotor behavior, contract number RFPF 33615-71-R-1075, "Airload Predictions for the Avoidance of Dynamic Problems on Rotor/Prop Powered Military V/STOL Aircraft," was awarded. A portion of this contract provided for the continued development of the Vertol rotor loads program (C-60) to be expanded to allow analysis of propellers. These improvements included the effect of large twist, shear center chordwise location, vertical neutral axis chordwise location, and fully coupled blade deflections. This section outlines the prop/rotor methodology and provides user's instructions for the computer programs developed under this contract.

HISTORY OF DEVELOPMENT

This program has undergone continual modification and improvement since its inception. The original analysis, which used 10 mass and elastic bays, 4 harmonics of loads and deflections, uniform inflow, and linear aerodynamics, was developed by the Vertol Division Dynamics Group for their study of helicopter rotor hub vibratory forces under Navy Bureau of Weapons Contract NOa(s) 60-6112c. The program development and parameter study results are given in Reference 6. Following the completion of this contract, the analysis was expanded to include 15 mass and elastic bays, 10 harmonics of loads and deflections, and nonlinear aerodynamics, including stall and compressibility effects. As programmed on the IBM 650, the actual computing time of the expanded analysis was approximately 2 hours and required hand assembly of subprogram inputs. With the replacement of the IBM Model 650 computer by the faster computers and subsequent reprogramming into a continuous chain, the unit running time was reduced to approximately 10 minutes.

Taking advantage of the faster computer, the Research and Development Group extended the rotor analysis to include special input formats, aerodynamic performance calculations, and an internal nonuniform downwash calculation. Since downwash is a major source of higher harmonic rotor and hub loads, the development of an internal nonuniform downwash computation significantly improved rotor load prediction capability (7). These improvements are reported in the program description and users instructions (8).

In subsequent years, further improvements have been made in the thrust routine, pitch and elastic matrices, flap boundary conditions, and downwash representation. Special problems, such as mechanical flap-pitch coupling (δ_3), linear hub motion, and flap dampers can now be analyzed. The engineer has the option to perform either a flexible or rigid blade analysis. Either linear or nonlinear aerodynamics may be employed and additional options are available to represent downwash. The program's aerodynamic theory was expanded to include an approximation for the unsteady shed wake of an oscillating airfoil (described in Reference 9) which significantly improved pitch link load prediction capability (10). Any airfoil section may be used in the load calculations by inputting two-dimensional static airfoil data tables. Only representative stall and compressibility effects were accounted for previously. In addition, blades with variable airfoil sections that change thickness ratio or camber with blade span can be accounted for by defining up to three airfoil sections along the blade and linearly interpolating between them. A description of the program with all the above changes has been documented in Reference 11. A comparison of predicted loads with test is

presented in Reference 12 and the effect of linear hub motion is given in Reference 13.

Since 1967 the theory has been further improved to consider blade tab and trailing-edge bends, an increased number of mass stations (from 15 to 20), an increased number of aero stations (from 10 to 15), viscous damping in the pitch links, angular hub motion in the blade load calculations (14), hub loads for rotors with 2 to 9 blades, and a 3-point or 4-point swashplate actuator system for the lower control load calculations. In addition, there were two major improvements: 1 - the development of a nonuniform downwash theory that includes compatibility between vortex strength, downwash, and the airload distribution (15), and 2 - the inclusion of a newly developed nonlinear, unsteady aerodynamic theory (16). The downwash modifications improved blade loads (17) and probably hub loads. The new unsteady aerodynamics provide a significant improvement in rotor performance prediction (18) and can now predict the sharp increase in control loads that occur at the high C_T/σ or high airspeeds associated with blade stall (16).

PROGRAM FLOW DIAGRAM

A flow diagram of this analysis is shown in Figure 33. The solutions for the nonlinear aerodynamic loads and the coupled flap-lag-pitch blade response are performed in series and up to 10 iterations between the airloads and blade response are used to obtain the final solution. An iterative solution is used to account for the nonlinear coupling between the blade deflections and airloads that result from airfoil stall and compressibility. Iteration techniques are also used to obtain compatibility between the airloads, downwash, and vortex strength and to obtain a match with a specified rotor thrust. A brief outline of the computer procedure is given below, followed by a description of the methodology used in this analysis.

The prop/rotor loads program is started by calculating initial deflections and defining boundary conditions from input (i.e., collective and cyclic pitch and root flap deflections). These inputs are either known (as in the case of a model test or where these quantities were measured in flight) or are obtained from an aerodynamic trim analysis. The trim analysis calculates the rotor trim (i.e., aircraft angle of attack, thrust, collective pitch, cyclic pitch, and blade root flap angle) by considering aircraft gross weight, center of gravity, fuselage drag, rigid blade properties, quasi-linear static airfoil characteristics, nonuniform downwash correction factors, forward speed, and rotor speed to determine the airloads required to maintain the free-flight aircraft in equilibrium for a steady-state flight condition.

Next, the rotor-induced velocities are calculated to provide a downwash field for each blade (see Figure 34). First uniform downwash is determined either from input or a simple calculation. If only uniform downwash is required, the program exits from the downwash routine and proceeds to the airload routine; if nonuniform downwash is required, a complex iteration loop is initiated. The downwash field resulting from this routine is used throughout the program with no updates or modifications.

For clarity, when calculating tandem-rotor downwash, the two rotors are designated as the prime rotor and the secondary rotor. If the program is calculating aft rotor loads of a tandem helicopter, the aft rotor is the prime rotor and the forward rotor is the secondary rotor. In the case of a single-rotor aircraft, the main rotor is always the prime rotor.

For a tandem helicopter, the program first calculates a compatible self-induced downwash for the secondary rotor. Then, the resulting vortex field of this rotor is used to calculate

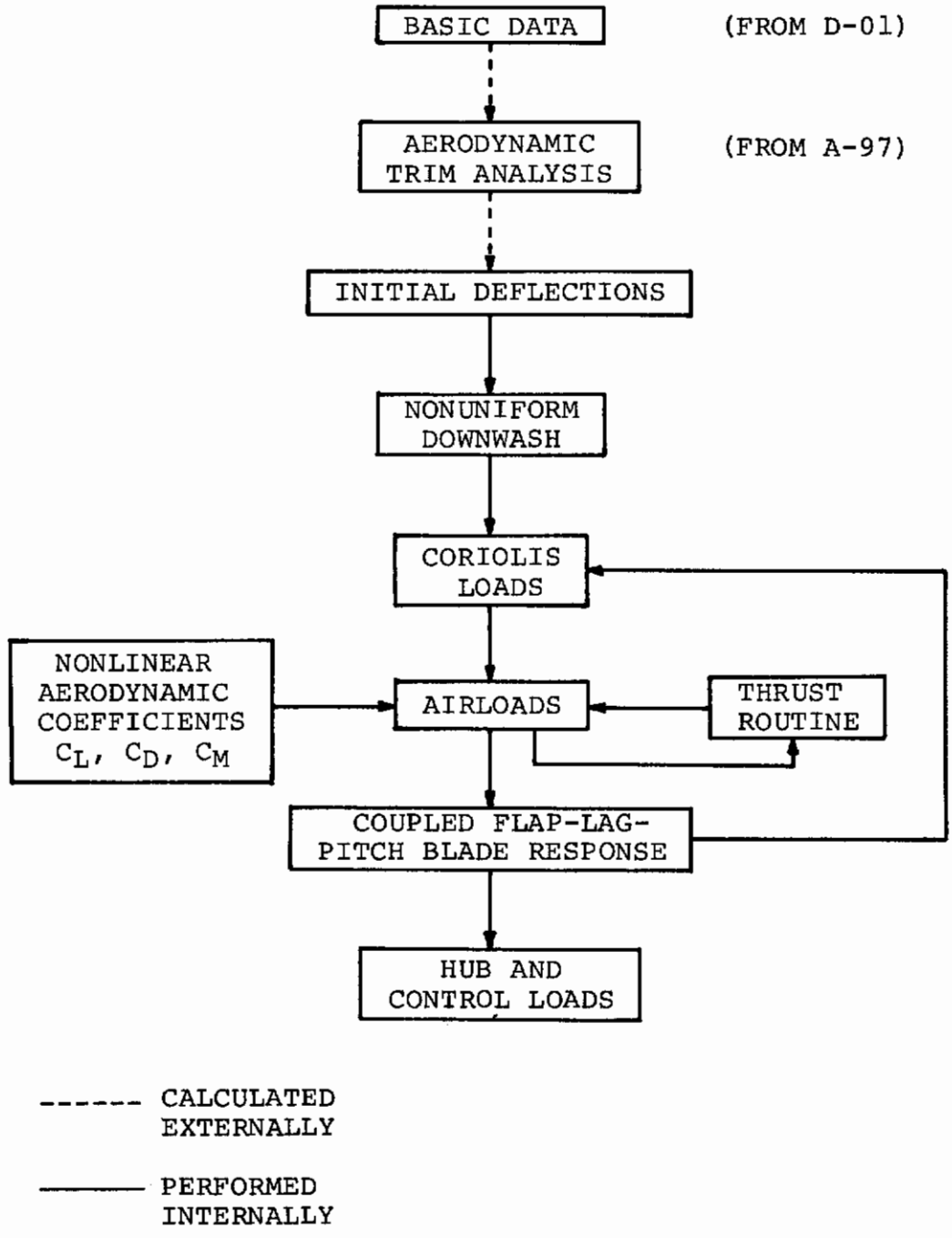

Figure 33. Flow Chart for Rotor Loads Program

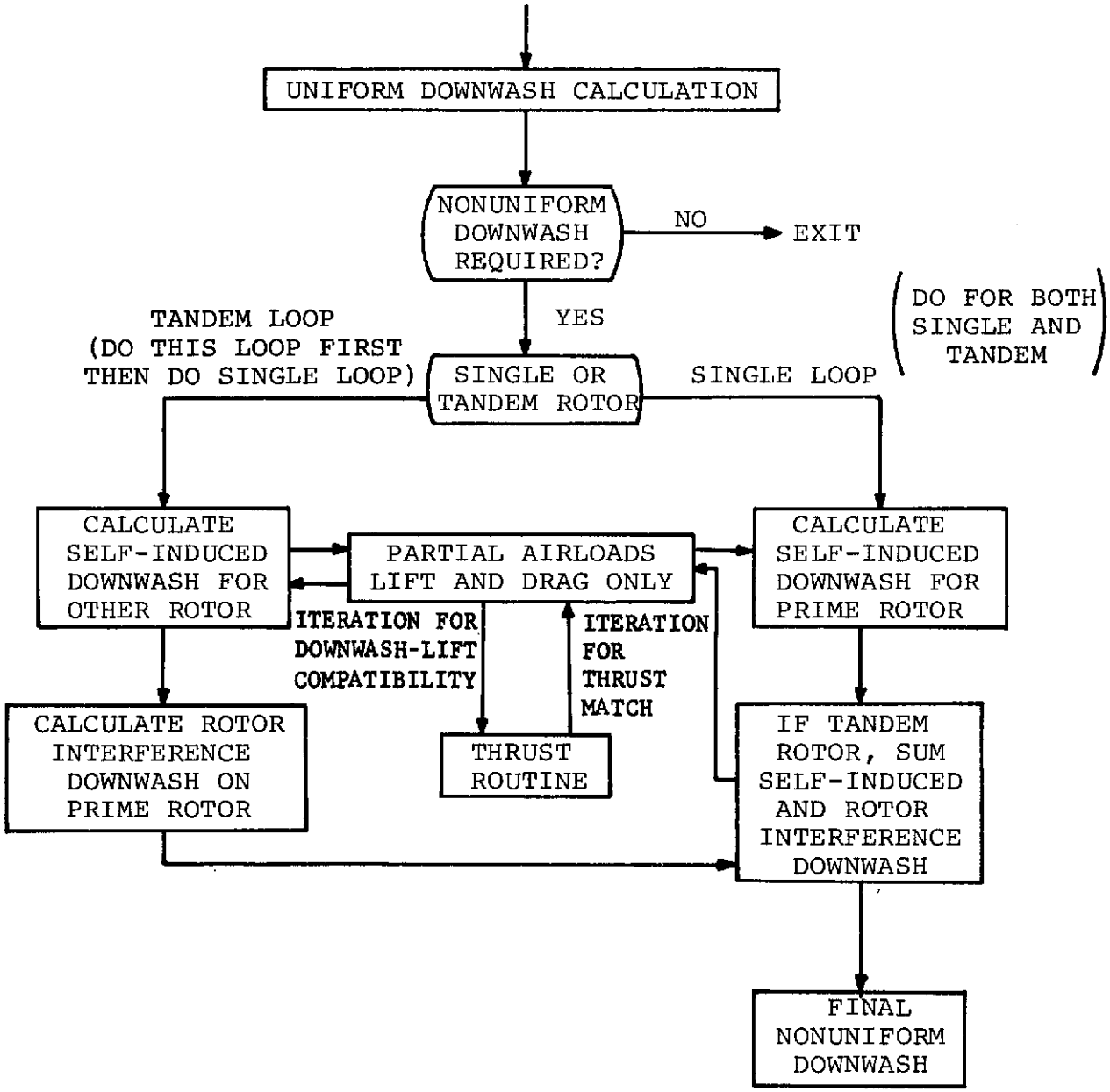

Figure 34. Schematic Diagram of Nonuniform Downwash Routine for Normal Conditions

the rotor interference downwash on the prime rotor. The prime rotor self-induced downwash is then calculated in the already-defined rotor interference downwash field. The final prime rotor downwash field is then the sum of the rotor interference downwash plus the self-induced downwash of the prime rotor. For a single-rotor aircraft, only the self-induced downwash is calculated.

Calculating the self-induced downwash requires an iteration between airloads, trailed vortex strength, and downwash. This iteration is performed up to 10 times to insure compatibility among these three quantities. As Figure 16 shows, each time the partial airload routine is entered an iteration between the thrust routine and airloads may be performed. This thrust routine iteration is performed when agreement with the thrust defined by the trim program is desired. The thrust routine should be used when analyzing a specified flight condition where rotor lift and propulsive force are defined. To obtain this constant thrust, every time the airload routine is entered an iteration process is performed on the airloads by altering the steady root collective pitch until a collective angle is found which corresponds to the required thrust. If no thrust match is required, the thrust routine iteration is not performed.

A thrust match is needed whenever the analysis of a specific aircraft flight condition is required. For any steady state flight condition, the rotor thrust and propulsive force must overcome the aircraft weight and drag (i.e., the equilibrium of the aircraft must be maintained). To analyze a steady state flight condition, a trim analysis calculates the rotor thrust required for equilibrium, assuming rigid blades and uniform downwash. In general, the value of collective defined by the trim program will not produce the same thrust with nonuniform downwash and a flexible blade. Therefore, a thrust match must be performed to guarantee that the required thrust is maintained. A thrust match is not performed when the value of collective must be held constant. This is often the case in a wind tunnel test where the collective pitch is held constant during the test and the rotor thrust is allowed to vary by changing rotor shaft tilt. The model, however, is maintained in equilibrium by the forces exerted by the test stand; there is no guarantee that an aircraft in free flight would remain in equilibrium under those conditions.

After the downwash field is calculated, the rigid blade deflections (initial deflections) are used to calculate the coriolis forces. Then, the nonuniform downwash, nonlinear aerodynamic coefficients, and rigid blade deflections are combined to calculate the airloads. Here again, a thrust routine iteration is provided to guarantee a thrust match if desired. Following the airload routine, the airloads and coriolis loads are harmonically analyzed and used as forcing functions to calculate the

coupled flap-lag-pitch dynamic response of the blade. Since the forcing airloads and coriolis loads are nonlinear functions of the forced response (due to stall, compressibility, and blade shortening), an iteration between aerodynamic loads and the blade dynamic response is required to provide feedback. To perform the iteration, the most recently calculated coupled flap-lag-pitch deflections are substituted back into the coriolis and aerodynamic analyses, the forcing functions are evaluated again, and the coupled blade response analysis repeated. The iteration is continued until a specified number of iterations (usually 10) has been completed. The number of iterations specified should be sufficient to insure a converged solution.

Next, blade radial forces are calculated by considering blade shortening resulting from flap and lag deflections. Pitch link loads are calculated by determining the blade system pitching moment and all loads are resolved from the undeflected blade system into the deflected blade system. Finally, fixed and rotating system hub and lower control loads are evaluated by combining the root shears and moments with the system geometry.

The program flow diagram shows that the aeroelastic rotor analysis is basically an aerodynamic analysis coupled by iteration to a dynamic analysis. A discussion of the dynamic and aerodynamic methodologies follows.

DYNAMIC ANALYSIS

BLADE IDEALIZATION

The rotor blade is essentially a long, flexible beam with a nonsymmetrical cross section, nonlinear mass and elastic properties, and five degrees of elastic freedom. (The five degrees of freedom are flapwise and chordwise linear translations, torsion, flap, and lag rotations. The elastic radial deflection can be neglected.) To calculate the blade's response by a classically rigorous method is certainly a waste of time and money since the blade's physical properties and aerodynamic forcing loads are only approximations. In order to obtain an accurate dynamic response at reasonable cost, an approximate blade analysis will be performed. Therefore, a simple blade idealization that lends itself to a direct-solution method is required.

Figure 35 compares the actual prop/rotor blade with the blade idealization. The actual blade has large, nonlinear twist, variable shear center and vertical neutral axis, nonlinear mass and elastic properties, variable planform, and variable cross section. The idealized blade is obtained by cutting the actual blade into sections, each section idealized to have uniform mass and geometric properties. Then, the distribution of physical properties for the idealized blade approximates the actual blade distribution with a stepwise variation of the blade properties (see Figure 36).

The blade section boundaries (see Figure 35) define the blade idealization. Each blade section acts dynamically as a rigid body and each is elastically connected to the adjacent sections through equivalent stiffness. The blade sections also act as idealized aerodynamic sections, each having constant planform and cross section and a constant distribution of velocity, angle of attack, and airloads along its length. Since each blade section is rigid with a uniform mass distribution, the blade section can be replaced by pitch inertia about the pitch axis, flap and lag inertia about the section midpoint, and a concentrated mass at the section midpoint some distance from the pitch axis (at the section center of gravity). The pitch axis is defined as a straight line about which an inelastic blade would pitch for an applied control input.

An elastic bay is defined as a weightless beam of constant stiffness between the blade masses. The constant stiffnesses are defined as the equivalent stiffness needed to match the section deflection calculated from the actual blade elastic properties. Torsional elastic twist is calculated about the shear center and chordwise bending is calculated about the

ACTUAL BLADE

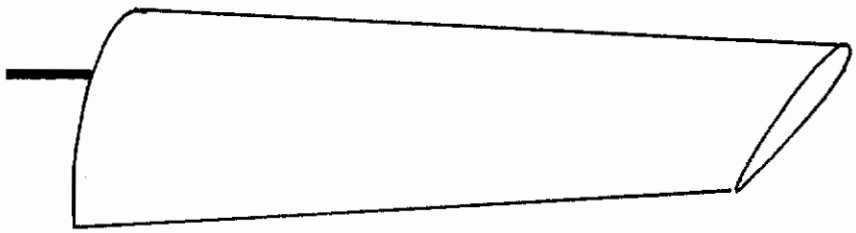

THE BLADE HAS:

- LARGE, NONLINEAR TWIST
- VARIABLE SHEAR CENTER AND VERTICAL NEUTRAL AXIS
- NONLINEAR MASS & ELASTIC PROPERTIES
- VARIABLE PLANFORM & CROSS SECTION

APPROXIMATION

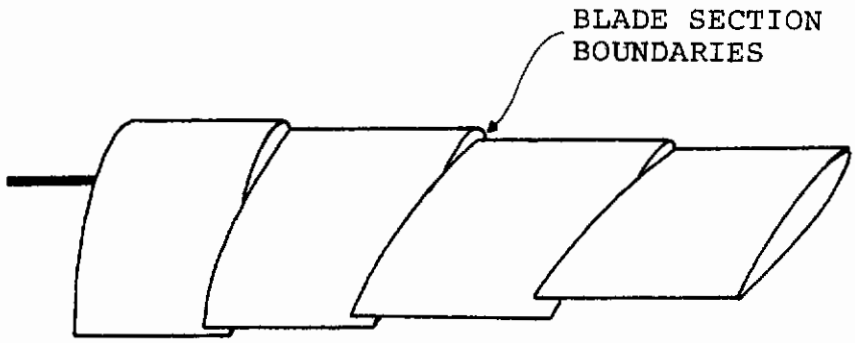

EACH SECTION HAS:

- NO TWIST
- CONSTANT SHEAR CENTER & VERTICAL NEUTRAL AXIS
- NO ELASTIC DEFLECTION BUT IS CONNECTED TO THE ADJACENT SECTION THROUGH EQUIVALENT STIFFNESS
- CONSTANT PLANFORM & CROSS SECTION

EQUIVALENT SYSTEM

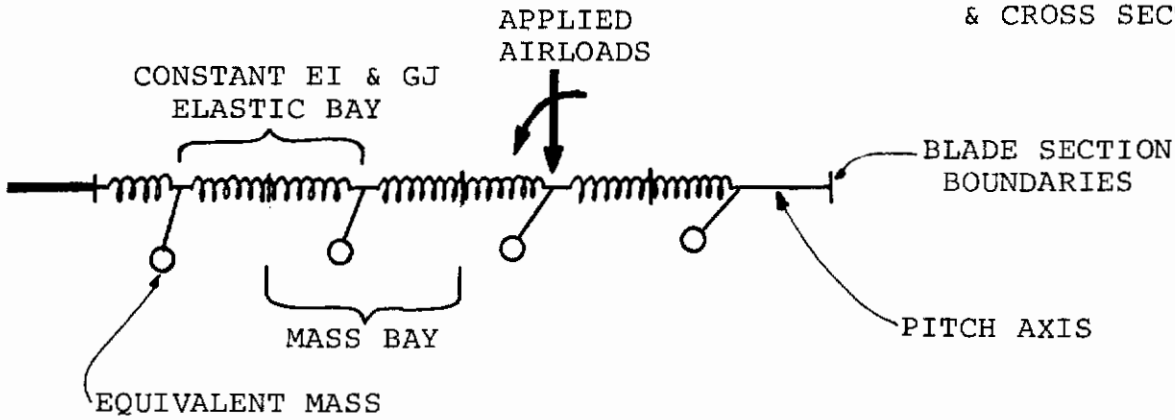

Figure 35. Comparison of Actual Blade and Idealized Blade

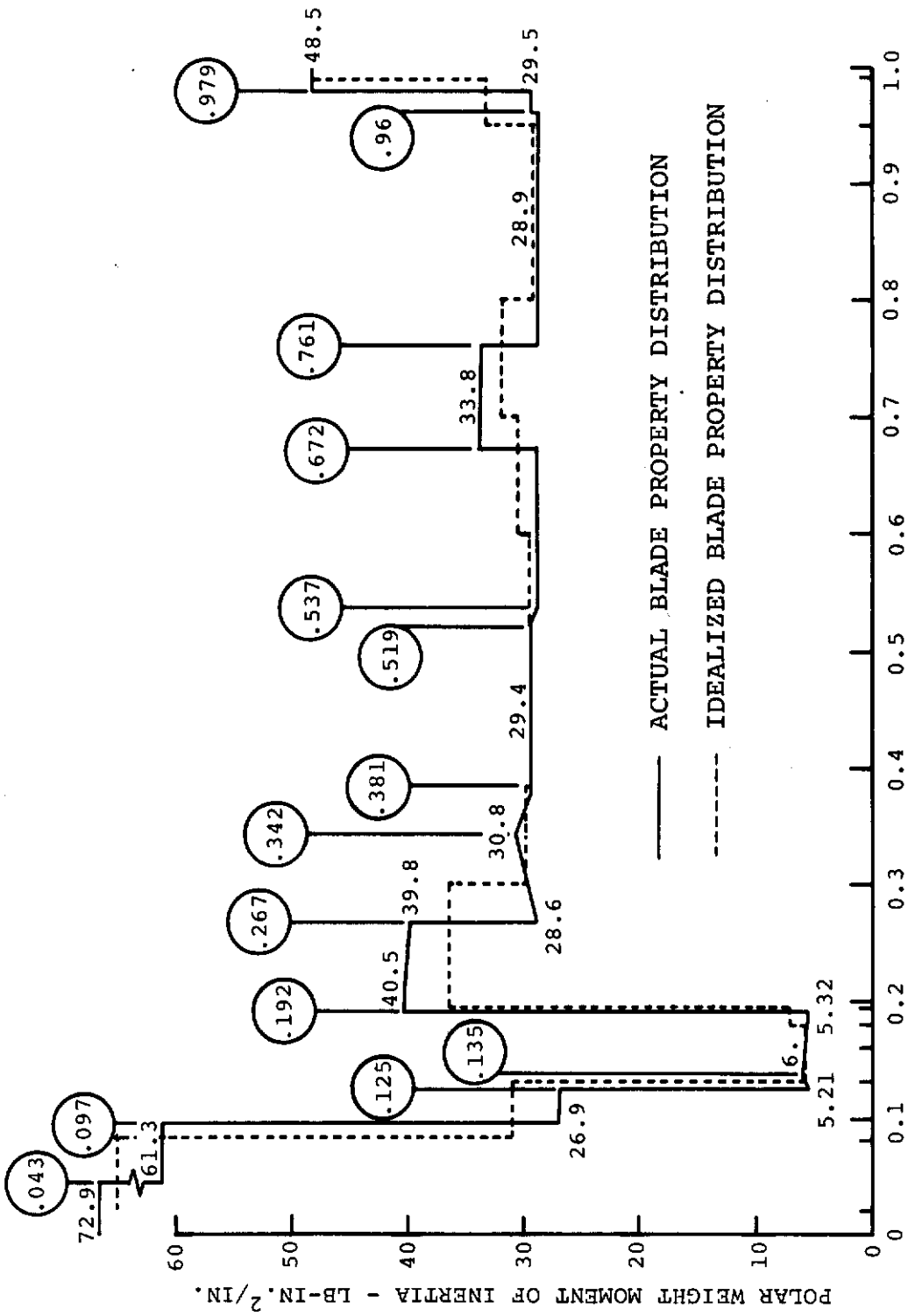

Figure 36. Spanwise Variation of Blade Physical Properties

vertical neutral axis. Flap bending can be calculated anywhere since blade thickness is neglected.

Therefore, the blade is idealized as an equivalent system composed of 20 discrete mass points possessing flap, chord, and torsional moments of inertia, connected by 20 weightless uniformly elastic beams. Associated with each mass is a rigid airfoil segment. The airloads generated by each airfoil segment are applied on the pitch axis at the middle of the segment.

DYNAMIC BLADE RESPONSE

Background

The aim of the prop/rotor loads analysis is to predict the blade and hub loads for aircraft in steady flight. The problem of predicting transient maneuver loads must wait until the steady-state loads have been obtained.

The steady-state blade response may be calculated by two methods. One approach uses a timewise extrapolation, which uses the loads and deflections at a given time to extrapolate to loads and deflections at a future time. This approach is mandatory for transient load and deflection calculations but is extremely time-consuming for steady-state calculations, since the program must start from arbitrary initial conditions and continues until the response is periodic.

The method used for this prop/rotor program is quicker and more direct. For this approach the solution is assumed to be steady-state and hence periodic. This allows the blade response to be expanded in a series and the solution is obtained by finding the series coefficients. Since a rotor has a natural period of one rotor cycle and since virtually all steady-state rotor responses are multiples of this natural period, the blade response will be represented by a Fourier series based upon multiple frequencies of the rotor speed. Each multiple of the rotor speed is defined as a separate harmonic. A deflection that occurs at the period of the rotor frequency is a first-harmonic deflection. A load that experiences three cycles in the period of a rotor cycle is a third-harmonic load.

A possible exception to the Fourier series solution based on rotor speed is the subharmonic blade response which can arise from coupling and beating of the rotor with other aircraft components, such as a wing or a feedback stability system. However, for this analysis only the rotor will be considered and subharmonic responses will be neglected.

This method of solution will be further simplified by neglecting interharmonic coupling of the blade response. Simply stated, this assumption means that moments resulting from terms like second-harmonic deflection times third-harmonic load are neglected. In fact, only steady deflections times steady loads, steady deflections times harmonic loads, and harmonic deflections times steady loads will be considered. This assumption allows each harmonic to be solved separately, requiring solution of the load and deflection coefficients for one harmonic at a time. Therefore, first the steady solution is found, then the first harmonic, second harmonic, etc. The final solution is obtained as a continuous function by reconstituting the series at 24 discrete positions around the azimuth.

To develop the equations for the dynamic analysis, a mass coordinate system was chosen and the following assumptions were made:

1. The blade idealization described above adequately represents the blade.

2. The airloads and coriolis loads are assumed to be known, continuous, and periodic.

3. The solution is steady-state and expandable in a Fourier series.

4. All angular deflections are small.

5. Steady centrifugal untwist can be calculated once and superimposed on the blade built-in twist. Live centrifugal untwist is accounted for by increasing the effective GJ.

6. Only linear terms will be considered in the dynamic response. Large nonlinear deflections such as radial deflection of the mass due to flap and lag and incremental flap, lag, and pitch deflections of the shear center are calculated separately.

The blade is analyzed by transforming the lumped mass and elastic elements of the idealized blade into a sequence of transfer matrix products by means of the associated-matrix method. This method replaces each blade element with an equivalent transfer matrix that transfers the dynamic system variables--shear, moment, deflection, and slope--inboard across the element.

Since the blade response is expanded in a Fourier series and interharmonic coupling is neglected, the blade response for each harmonic is independent of the others and can be

calculated separately. Since this program considers a steady plus 10 harmonics of blade response, 11 dynamic matrix equations must be solved, one for the steady and each harmonic. Each dynamic equation considers cosine and sine components of coupled flap-lag-pitch blade deflections and loads. The unknown loads for each harmonic are shear normal to the chord, shear in the chord direction, pitching moment, flap bending, and chord bending. The unknown deflections for each harmonic are flapwise and chordwise translation, flapwise and chordwise rotation, and pitch rotation. Therefore, the transfer matrix represents the transfer of harmonic coefficients for a single harmonic from one point on the blade to the next.

Transfer Matrices

For this method, the blade variables (the unknown loads and deflections) at each discrete point along the blade are listed in a column matrix called a state vector. If q is a state vector representation of the problem variables, [M] is the transfer matrix across discrete mass, [F] is the transfer matrix across a discrete load, and [E] is the transfer matrix across an elastic beam, then the matrix transfer equations can be written.

For a discrete mass at station n,

$\{q'\}_n \quad \{q\}_n$

{q} is the vector of loads and deflections outboard of the mass and $\{q'\}_n$ is the vector of loads and deflections inboard of the mass. The matrix transfer equation is

$$\{q'\}_n = [M]_n\{q\}_n \quad .$$

For a discrete load (forcing function) at station n,

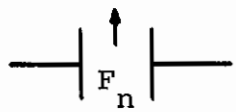

$\{q'\}_n$ is the vector of loads and deflections outboard of the load and $\{\bar{q}\}_n$ is the vector of loads and deflections inboard of the load. The matrix transfer equation is

$$\{\bar{q}\}_n = [F]_n\{q'\} \quad .$$

To obtain the discrete loads for the transfer matrix, the coriolis force, aerodynamic pitching moment, lift, and drag are harmonically analyzed and the appropriate harmonic components are inserted into the transfer matrix to represent a concentrated external load. To help the program converge, linear aerodynamic damping and coupling terms are provided in the load transfer matrix to approximate anticipated airload changes resulting from elastic deflections. Substituting $\{q'\}_n$ into the above equation,

$$\{\bar{q}\}_n = [F]_n[M]_n\{q\} \quad .$$

For the elastic beam element of length ℓ_n,

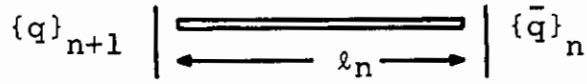

$\{\bar{q}\}_n$ is the vector of loads and deflections outboard of the elastic beam and $\{q\}_{n+1}$ is the vector of loads and deflections inboard of the elastic beam. Then:

$$\{q\}_{n+1} = [E]_n\{\bar{q}\}_n \quad ,$$

or, substituting for $\{\bar{q}\}_n$ gives:

$$\{q\}_{n+1} = [E]_n[F]_n[M]_n\{q\}_n \quad ,$$

which is a transfer equation relating a vector of the loads and deflections acting at one mass station to the loads and deflections at the next most inboard mass station.

Therefore, multiplying the state vector of a given harmonic by the transfer matrix gives the harmonic state vector inboard of the blade element. Similarly, for the next inboard station (n+1) the transfer equation becomes:

$$\{q\}_{n+2} = [E]_{n+1}[F]_{n+1}[M]_{n+1}\{q\}_{n+1} \quad ,$$

or

$$= [E]_{n+1}[F]_{n+1}[M]_{n+1}[E]_n[F]_n[M]_n\{q\}_n \quad .$$

As shown here, the state vectors can be premultiplied by a successive string of transfer matrices, each representing the change in loads and deflections across the mass, airload, and elastic sections it represents. A boundary matrix (or matrices) is added between the most inboard mass and the blade hub to account for multiple load paths (such as pitch links and lag dampers) and hub geometry (such as hinge configuration and delta three). In this way the root state vector can be equated to the tip state vector through a string of transfer matrices and the elastic blade idealization is then reduced to a sequence of transfer matrix products (see Figure 37). Collapsing the string of transfer matrices (i.e., multiplying the matrices out), a single collapsed transfer matrix is obtained and the blade equation for each harmonic becomes:

$$\{S\}_{ROOT} = [T.M.]\{S\}_{TIP} \quad ,$$

where $\{S\}_{ROOT} = \{V_{Z(KC)}, M_{Y(KC)}, \beta_{(KC)}, \bar{Z}_{(KC)}, V_{Y(KC)},$

$M_{Z(KC)}, \xi_{(KC)}, \bar{Y}_{(KC)}, M_{X(KC)}, \theta_{f(KC)}, 1 ,$

$V_{Z(KS)}, M_{Y(KS)}, \beta_{(KS)}, \bar{Z}_{(KS)}, V_{Y(KS)},$

$M_{Z(KS)}, \xi_{(KS)}, \bar{Y}_{(KS)}, M_{X(KS)}, \theta_{f(KS)}\}$

$\{S\}_{TIP}$ = a column of the same variables at $\{S\}_{ROOT}$ but defined at the blade tip.

$[T.M.] = K\ R\ E_{(20)A}\ T_{19}\ E_{(19)B}\ M_{19}\ E_{(19)A}\ T_{1B}\ E_{(18)B}$

$M_{1B}\ E_{(18)A}\ T_{17}\ E_{(17)B}\ M_{17}\ E_{(17)A}$ ----- $E_{(4)A}$

$T_3\ E_{(3)B}\ B_{18}\ E_{(18)A}\ E_{(3)A}\ T_2\ E_{(2)B}\ F_2\ M_2$

$E_{(2)A}\ T_1\ E_{(1)B}\ F_1\ M_1$

= a 21 x 21 matrix obtained from multiplying the indicated transfer matrices

V_Z = shear normal to the chord

M_Y = flap bending moment

β = flap angle

Z = translation normal to the chord

V_Y = shear in the chord direction

$$S_{ROOT} = K_{22}\ R_{21}\ E_{20A}\ T_{19}\ E_{19B}\ M_{19}\ E_{19A}\ T_{18}\ E_{18B}\ M_{18}\ E_{18A}\ \text{-----}$$

$$\text{------}\ E_{4A}\ T_3\ E_{3B}\ F_3\ M_3\ E_{3A}\ T_2\ E_{2B}\ F_2\ M_2\ E_{2A}\ T_1\ E_{1B}\ F_1\ M_1\ S_{TIP}$$

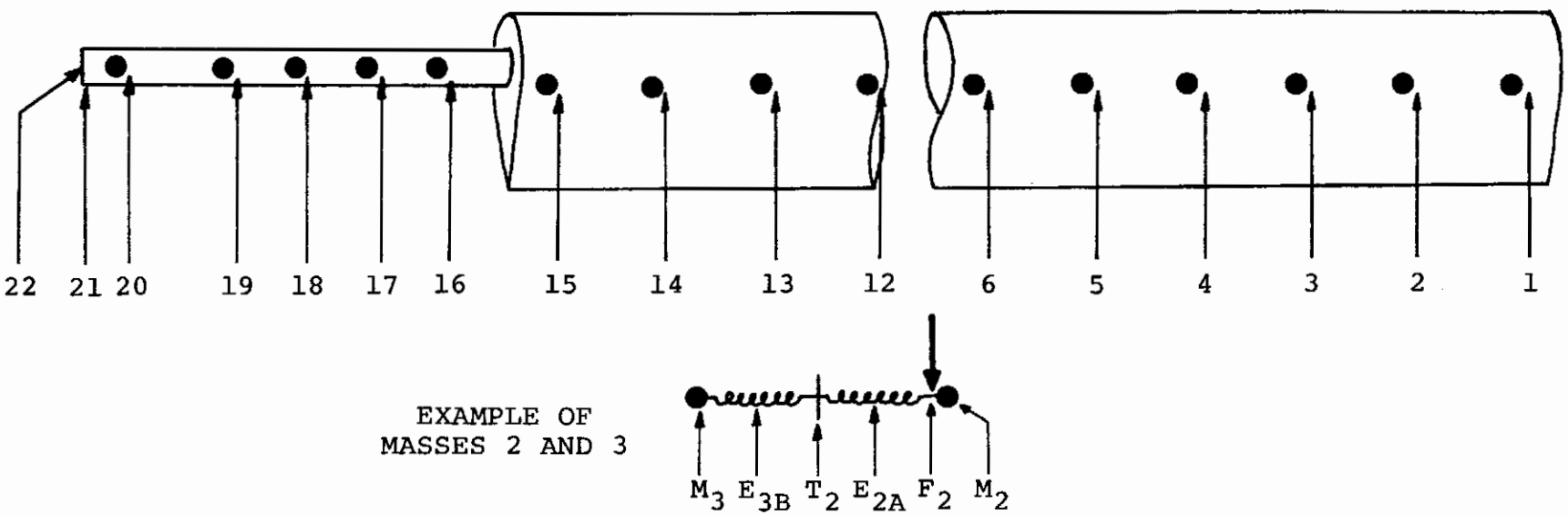

M = MASS MATRIX F = FORCE MATRIX

E = ELASTIC MATRIX T = TWIST MATRIX

Figure 37. Coupled Flap-Lag-Torsion Matrix Sequence

M_Z = chord bending moment

ξ = lag angle

$\bar{Y}$ = translation in the chord direction

M_X = torsion moment in the disc plane

θ_f = flexible torsion rotation

The subscript (KC) indicates the K^{th} harmonic cosine component and (KS) indicates the sine component.

M = mass matrix

F = aerodynamic matrix, a discrete load matrix

E = elastic matrix

T = twist matrix

K = control system matrix

R = is composed of a sequence of additional matrices which vary with the boundary configuration and hinge sequence (for articulated rotors).

The detailed definitions of each of the transfer matrices are defined in the supplemental sections of this report.

Solution of Dynamic Equations

Since there is a dynamic equation for each harmonic, the frequency of vibration is known. Therefore, the velocity and acceleration terms can be written as:

$$\dot{X} = d/dt(X_{KC} \cos K\psi + X_{KS} \sin K\psi)$$

$$= -\omega K X_{KC} \sin K\psi + \omega K X_{KS} \cos K\psi$$

$$\ddot{X} = d^2/dt^2 (X_{KC} \cos K\psi + X_{KS} \sin K\psi)$$

$$= -\omega^2 K^2 X_{KC} \cos K\psi - \omega^2 K^2 X_{KS} \sin K\psi$$

where ω is the rotational frequency of the rotor and K is the harmonic number.

Since the time derivatives are removed from the equation and replaced by parameters dependent on ω, the dynamic equation above reduces to a simple set of simultaneous algebraic

equations. To solve these equations, boundary conditions must be applied.

All loads at the blade tip are zero, so the state vector at the tip becomes:

$$\{S\}_{TIP} = \{0,\ 0,\ \beta_{(KC)},\ \bar{Z}_{(KC)},\ 0,\ 0,\ \xi_{(KC)},\ \bar{Y}_{(KC)},\ 0,\ \theta f_{(KC)},\ 1,\ 0,\ 0,\ \beta_{(KS)},\ \bar{Z}_{(KS)},\ 0,\ 0,\ \xi_{(KS)},\ \bar{Y}_{(KS)},\ 0,\ \theta f_{(KS)}\}$$

Multiplying the zeros through the collapsed transfer matrix reduces the equation to

$$\underset{21x1}{\{S\}_{ROOT}} = \underset{21x11}{[\bar{T}.M.]}\ \underset{11x1}{\{\bar{S}\}_{TIP}} \tag{93}$$

where $\{S\}_{TIP} = \{\beta_{(KC)},\ \bar{Z}_{(KC)},\ \xi_{(KC)},\ \bar{Y}_{(KC)},\ \theta f_{(KC)},\ 1,\ \beta_{(KC)}\ Z_{(KS)},\ \xi_{(KS)},\ \bar{Y}_{(KS)},\ \theta f_{(KS)}\}$

Next, apply the 10 known root boundary conditions and select the resulting 10 equations that contain the known root end conditions and the 10 unknown tip deflections. Invert the resulting reduced collapsed transfer matrix and solve the equations for the coupled flap-lag-pitch tip deflections. By progressively applying the transfer matrices to the tip deflections, the deflections and loads at each blade element are determined. Repeating the procedure for each harmonic and then superimposing the separate harmonic responses, the total coupled flap-lag-pitch coupled loads and deflections are found.

An example of this procedure will be illustrated below for a hingeless rotor boundary condition. The root end conditions for a hingeless rotor are zero flapwise and chordwise deflections, defined flap and lag angles for the zero harmonic (precone and prelag) and zero for all other harmonics, and pitch deflections defined by the control input. Therefore, β, Z, ξ, Y, and θ are known. Selecting the 10 equations for the known root end conditions (i.e., β_{KC} equation, β_{KS} equation, Z_{KC} equation, etc.) from the 21 equations of matrix equation 92 gives

$$\underset{10x1}{\{S_B\}} = \underset{10x11}{[\bar{\bar{T}}.M.]}\ \underset{11x1}{\{\bar{S}\}_{TIP}} \tag{94}$$

where $\{S_B\} = \{\beta_{(KC)}, \bar{Z}_{(KC)}, \xi_{(KC)}, \bar{Y}_{(KC)}, \theta f_{(KC)}$

$\beta_{(KS)}, \bar{Z}_{(KS)}, \xi_{(KS)}, \bar{Y}_{(KS)}, \theta f_{(KS)}\}$

$= \{0, 0, 0, 0, \theta_{B(KC)},$

$0, 0, 0, 0, \theta_{B(KS)}\}$

$\theta_{B(KC)}$ and $\theta_{B(KS)}$ are the known control inputs. Since $\{\bar{S}\}_{TIP}$ contains a unity element and $[\bar{T}.\bar{M}.]$ is not square, equation 93 can be partitioned and written as:

$$\begin{Bmatrix} S_{BC} \\ S_{BS} \end{Bmatrix} = \left[\begin{array}{c|c|c} T_{CC} & t_c & T_{SC} \\ \hline T_{CS} & t_s & T_{SS} \end{array}\right] \begin{Bmatrix} \bar{S}_C \\ 1 \\ \bar{S}_S \end{Bmatrix}_{TIP} .$$

Rearranging the equation and solving for the tip unknowns gives:

$$\{\bar{S}\}_{TIP} = \begin{Bmatrix} \bar{S}_c \\ \bar{S}_s \end{Bmatrix} = \begin{bmatrix} T_{CC} & T_{SC} \\ T_{CS} & T_{SS} \end{bmatrix}^{-1} \begin{Bmatrix} S_{BC} & -t_c \\ S_{BS} & -t_s \end{Bmatrix} .$$

Form the complete tip state vector and premultiply it by $E_{(2)A}\ T_1\ E_{(1)B}\ F_1\ M_1$ to obtain the state vector before the second mass. Repeat this process to obtain the state vector before each mass station. The state vectors for each mass station and each harmonic, along with the harmonically reconstituted loads and deflections, are printed out.

AERODYNAMIC ANALYSIS

AIRLOADS

This program's airload calculations include the effects of airfoil section geometry, compressibility, stall, three-dimensional flow, unsteady aerodynamics, and nonuniform inflow. Static airfoil tables are used to account for compressibility, static stall, and airfoil shape. The unsteady aerodynamic loads are calculated by modifying the static loads resulting from the airfoil tables to include Theodorsen's shed wake function, dynamic stall effects based on oscillating airfoil data, and yawed flow across the blade.

In the development of this theory it is assumed that the separate effects of stall, compressibility, dynamic stall hysteresis, and yawed flow can be superimposed to give a theory that adequately defines the unsteady, three-dimensional environment of helicopter rotors. Though this assumption has not been substantiated by specific tests, it has been used to demonstrate a significant improvement in rotor performance prediction in the rotor stall region (18) and control load prediction (16).

DEVELOPMENT OF THE THEORY

Theodorsen in Reference 19 developed an unsteady aerodynamic theory for airfoils pitching and plunging about a zero mean angle of attack. The theory assumed linear incompressible aerodynamics and accounted for a sinusoidal shed wake trailing from the airfoil. To update this theory to account for the helicopter aerodynamic environment, compressibility and blade stall were included and the restrictions of small angles and zero mean angle of attack were removed.

In the lift equation this was accomplished by replacing the linear aerodynamic expression $\pi\alpha$ by the static aerodynamic lift coefficient C_L as obtained from a table involving the angle of attack and Mach number. For the aerodynamic pitching moment, the static aerodynamic moment about the quarter chord (as given by the C_M coefficient) was added to the calculation. The C_M term was added since the moment equation in Reference 19 does not account for a static moment about the quarter chord.

To use the shed wake representation of Reference 19, the differences between the fixed-wing aerodynamic environment and the helicopter environment must be reconciled by making three assumptions. First, the curvature of the helicopter's shed wake pattern is neglected and a pattern parallel to the blade is assumed (see Figure 38). This assumption is reasonable,

- PARALLEL WAKE

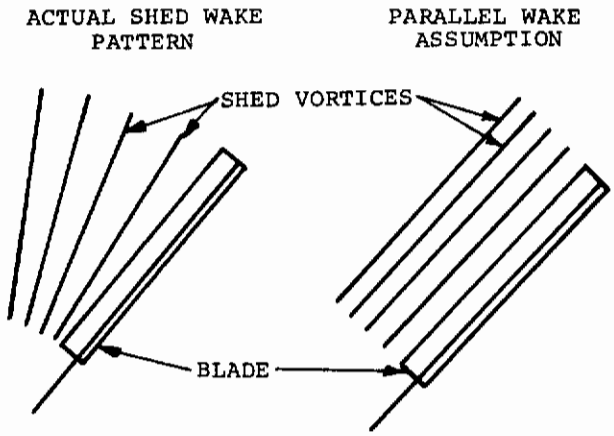

- LINEAR RELATION BETWEEN VORTEX STRENGTH AND ANGLE OF ATTACK

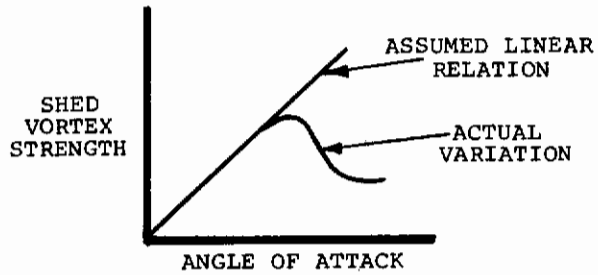

- REDUCED FREQUENCY USES THE INSTANEOUS RELATIVE VELOCITY AND ASSUMES ONLY 1/REV BLADE MOTION IS PRESENT

Figure 38. Shed Wake Assumptions

since the most important vortices are close to the blade where the effects of curvature are the smallest.

Second, a linear relationship between angle of attack and shed wake is assumed. This assumption is valid in the sub-stall region but incorrect in the stall region. However, the error introduced is minimal since the dominant characteristics of the airloads in the stall region are determined by stall hysteresis. The third requirement is to assume an instantaneous value of reduced frequency based on the one-per-revolution flap and pitching motions and the instantaneous relative wind velocity.

The expression for this pseudo-reduced frequency is

$$\bar{K} = C\Omega/2U \quad , \tag{95}$$

where U is the total, instantaneous, two-dimensional velocity relative to the airfoil and Ω is the one-per-revolution rotational frequency.

To include yawed flow (i.e., radial flow) in the theory, an empirical approximation to account for three-dimensional flow on the lift coefficient was developed in Reference 20. The equation used to define the three-dimensional C_L is given as:

$$C_{L(3D)} = C_{L(2D)}/\cos \Lambda \quad , \tag{96}$$

where Λ is the yaw angle.

The equation has the restriction that $dC_{L(3D)}/d\alpha$ may not exceed the maximum value of $dC_{L(2D)}/d\alpha$. This means that the effect of yawed flow is to delay stall to increasingly larger values of C_L with increasingly larger yawed angles. A comparison of equation 95 with test data obtained from Reference 21 is shown in Figure 39.

Therefore, Theodorsen's theory has been extended to provide an unsteady aerodynamic theory that accounts for compressibility and stall through static C_L, C_D, and C_M tables; includes unsteady shed wake induced angle of attack variations by using the Reference 19 F and G functions; and provides for three-dimensional flow with an empirical equation. However, this theory does not account for the unsteady stall effects shown in References 22, 23, and 24 and illustrated in Figure 40.

To develop a theory to include the unsteady stall effects observed above, analytical investigations, tests of oscillating airfoils, reviews of existing flight test data, and extensive wind tunnel testing of model rotors were carried out over a 3-year period. Evaluation of the oscillating airfoil test results has led to the development of an empirical

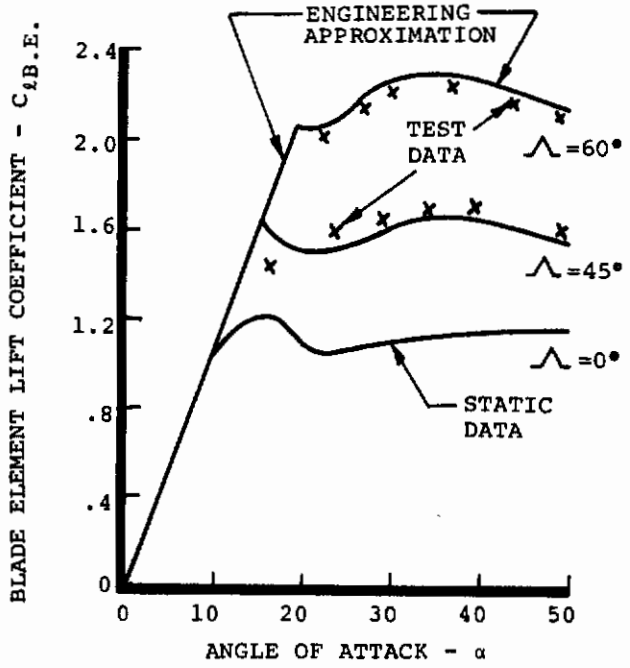

$$C_{L(3D)} = C_{L(2D)}/\cos \Lambda$$

Λ = YAW ANGLE

Figure 39. Engineering Approximation Accounting for Yawed Flow

MACH NO. = 0.4
f = 16 Hz
$\Delta\alpha$ = 5°

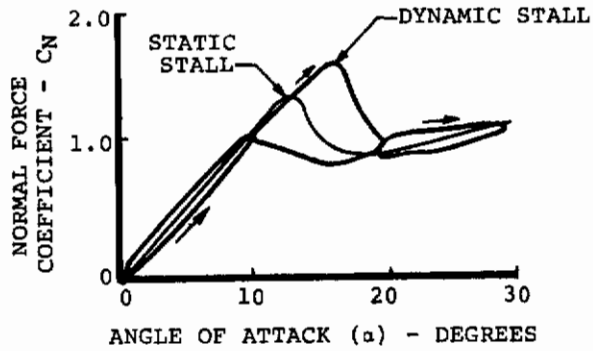

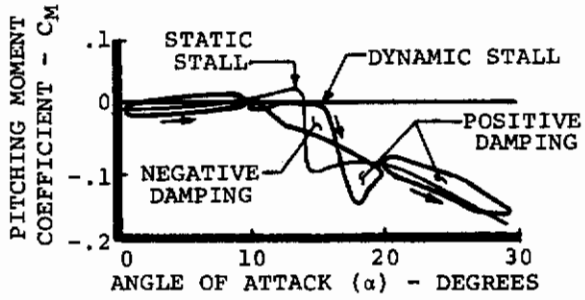

Figure 40. Typical Oscillating Airfoil Test Data for Vertol 23010-1.58 Airfoil

relationship between the static stall angle and the dynamic stall angle for lift and pitching moment. The development of this relationship is shown in Reference 25 and the resulting equation is given below:

$$\alpha_{D.S.} - \alpha_{S.S.} = \gamma[C\dot{\alpha}/2U]^{1/2} \quad . \tag{97}$$

This relationship is used as a bridge between static and dynamic stall by defining the dynamic stall angle of attack as a function of the static stall angle of attack. Therefore, with this relationship the dynamic stall can be derived from two-dimensional static airfoil data. Since dynamic and static stall can be related, a pseudo-dynamic angle of attack can be defined from the quasi-static angle of attack in the same manner. The dynamic angle of attack (α_{DYN}) can then be expressed as a combination of the quasi-static blade element angle of attack (α_{BE}) and its time derivative $d\alpha_{BE}/dt$ as:

$$\alpha_{DYN} = \alpha_{BE} - \gamma[C(d\alpha_{BE}/dt)/2V]^{1/2} \quad , \tag{98}$$

where the quasi-static angle of attack is defined in the conventional manner as

$$\alpha_{BE} = \theta + \tan^{-1} U_P/U_T \tag{99}$$

and the parameter γ is derived from the oscillating airfoil test points that exhibit dynamic stall and is experimentally dependent only on Mach number and airfoil shape (see Reference 25). The dynamic angle of attack can now be used to calculate a dynamic lift coefficient.

The static lift coefficient, C_L, can be defined as

$$C_L = (C_L/\alpha_{BE})\ \alpha_{BE} \quad , \tag{100}$$

where C_L/α_{BE} is the quasi-static lift slope. The dynamic lift coefficient can be defined using a similar equation as

$$C_{L(DYN)} = (C_{L_{(AT\alpha_{DYN})}/\alpha_{DYN}})\ \alpha_{BE} \quad , \tag{101}$$

where the quasi-static lift slope is replaced by a dynamic lift slope composed of the pseudo-dynamic angle of attack α_{DYN} and a value of C_L obtained from the static tables using the dynamic angle. With this method C_L will not show the effects of stall until α_{DYN} reaches stall, even though α_{BE} may be significantly beyond the static stall angle.

In any region of the two-dimensional static airfoil data where the dynamic lift slope equals the quasi-static lift slope, i.e.,

$$C_L/\alpha_{BE} = C_L(at\alpha_{DYN})/\alpha_{DYN} \quad , \tag{102}$$

this technique for generating a lift hysteresis is completely removed. This occurs since the region where equation 99 holds is the linear lift portion of the C_L-versus-α curve. An example of a dynamic C_L calculation using this technique is shown in Figure 41 for an airfoil at a mean angle of attack of 14 degrees oscillating with a 5-degree amplitude.

A different approach is used to calculate the dynamic C_M. Quasi-statically, C_M is obtained by looking up its value from a static C_M-versus-α curve using the quasi-static angle of attack α_{BE}. Therefore, dynamic C_M will be obtained by looking up its value using the dynamic angle of attack α_{DYN}. Note that the static stall and dynamic stall angles for C_L and C_M are not the same, and hence the pseudo-dynamic angles also differ. The subscript L and M will be used henceforth with the dynamic angle of attack to indicate whether the dynamic angle of attack was obtained from the lift or moment data. With this approach, the expression for dynamic C_M is

$$C_{M(DYN)} = C_M(at\alpha_{DYN(M)}) \quad . \tag{103}$$

The effect of this equation is shown in Figure 42 for an airfoil with a mean angle of attack of 14 degrees and an amplitude of oscillation of 5 degrees.

Superimposing the separate effects of compressibility, linear shed wake, yawed flow, and dynamic stall hysteresis gives the following equations for dynamic C_L and C_M:

$$C_{L(DYN)} = C_{LO} + \frac{C_{L_{(at\ \alpha_{DYN(L)})}} - C_{LO}}{\alpha_{DYN}\cos\Lambda}\,\alpha_{equ} + \frac{dC_{L_{(at\ \alpha_{DYN(L)})}}}{d\alpha_{DYN(L)}}\,\alpha_{DEL} + f(\ddot{H}, \ddot{\theta}) \quad , \tag{104}$$

$$C_{L(DYN)} = \frac{C_L \text{ (AT } \alpha \text{ DYN)}}{\alpha \text{ DYN}} \alpha_{B.E.}$$

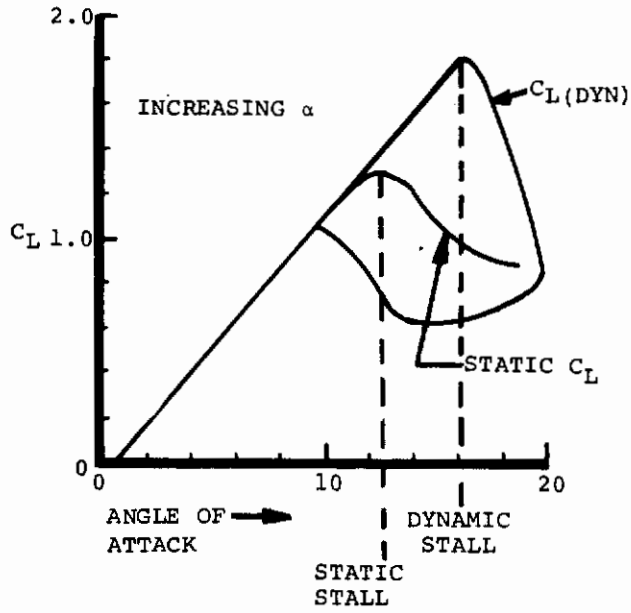

Figure 41. The Dynamic C_L Calculation in Stall Is Dependent on the Dynamic Stall Delay

$$C_{M(DYN)} = C_M[\text{AT } \alpha \text{ DYN(M)}]$$

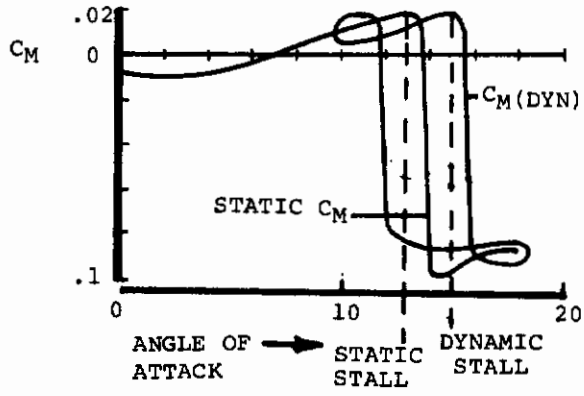

Figure 42. The Dynamic C_M in Stall Is Dependent on the Dynamic Stall Delay

$$C_{M(DYN)} = C_{M_{(at\ \alpha_{DYN(M)})}} + C_o(PA - 1/4)\ C_{L(DYN)} \cos \alpha_{BE} + C_o(PA - 1/4)\ C_{D(DYN)} \sin \alpha_{BE} - 1/2\ C_o \frac{dC_{L_{(at\ \alpha_{DYN})}}}{d\ \alpha_{DYN}} \alpha_{DEL} \cos \alpha_{BE} + F(\ddot{H}, \ddot{\theta}) \quad (105)$$

The last terms in the C_L and C_M equation can be neglected since they are generally small.

The equivalent angle of attack α_{equ} is based upon the mechanical angle of attack, flapping motion, rotor inflow from shaft tilt, and downwash. All these terms give a relative velocity that is nearly uniform across the chord. This angle is a modification of α_{BE} resulting from shed wake and can be considered as the overall angle of attack of the airfoil. The equation is

$$\alpha_{equ} = \theta_o + [F - C_o(3/4 - PA)\ G\ \frac{\omega}{V}]\ \theta_V + \tan^{-1}\ [\{\dot{H}_o + F\dot{H}_V + [C_o(3/4 - PA)F + \frac{G}{\omega} V]\ (\dot{\theta} + \Omega\ B_V) + C_o(3/4 - PA)\ \Omega\ B_o\}\ /U_T] \quad , \quad (106)$$

where $\dot{H}$ represents the relative velocity normal to the chord, θ is the mechanical pitch angle, and B is the flap angle. The delta angle of attack, α_{DEL}, results directly from the pitching velocity which gives an angle of attack that is independent of shed wake and varies directly as the chord,

$$\alpha_{DEL} = 1/4\ C_o\ \{\frac{(\dot{\theta} + \Omega B)}{U}\} \quad . \quad (107)$$

This term is treated separately since its impact on pitching moment is much larger than the other lift terms. It is arbitrarily treated as a perturbation on the angle of attack and uses the dynamic lift curve slope to determine its contribution to C_L.

The ability of this theory to predict C_L and C_M has been evaluated by comparing calculated values with test data obtained by oscillating an airfoil through a prescribed pitch motion.

The results of this comparison for test conditions below stall, at stall, and beyond stall are shown in Figure 43.

METHOD OF CALCULATION

Before airloads can be calculated, the blade deflections and downwash field must be known. The total velocity on each aerodynamic bay of the rotor blade is calculated for 15-degree azimuth positions by summing the downwash, rotational velocity, aircraft forward speed, and blade motions. The pitch angle, tangential velocity, and axial velocity are combined to calculate the blade element (α_{BE}) angle of attack (see equation 98). Next, the dynamic angle of attack for lift and pitching moment is calculated (α_{DYN}) from equation 97 by using the stall delay parameter γ and the pseudo-reduced frequency. The value of γ is found from a linear interpolation of input γ values for Mach numbers of 0, 0.2, 0.4, 0.6, 0.8, and 1.0 for both lift and pitching moment.

The static values of C_L (at α_{DYN}), C_M (at α_{DYN}), and C_D for equations 100 and 102 and the drag calculations are found from a double table. The tables define curves of the aerodynamic coefficients C_L, C_D, C_M versus airfoil angle of attack from two-dimensional static airfoil tests.

Compressibility is accounted for by providing separate aerodynamic curves for a range of Mach numbers from 0 to 1. The tables consist of punched-card decks which must be input with the job and equations which are contained in the program. A description of the card decks and equations is included in the user's instruction portion of this document.

Using the dynamic angles of attack (α_{DYN}) for both lift and pitching moments and local Mach number, a linear double interpolation with Mach number and angle of attack is used to find the static aerodynamic coefficients. Next, the equivalent angle of attack (α_{equ}) is calculated from equation 105, based upon the blade deflections and the Theodorsen F and G functions. The values of F and G are calculated in the program; the method is defined in detail in the supplemental document.

Substituting the static aerodynamic coefficients into equations 103 and 104 along with blade motions and the equivalent angle of attack defines the dynamic C_L ($C_{L(DYN)}$) and the dynamic C_M ($C_{M(DYN)}$). The dynamic C_D is set equal to the value of C_D obtained from the static tables.

The lift, drag, and pitching moment are then calculated in the conventional lifting-line approach using the dynamic aerodynamic coefficients; therefore,

DYNAMIC C_L

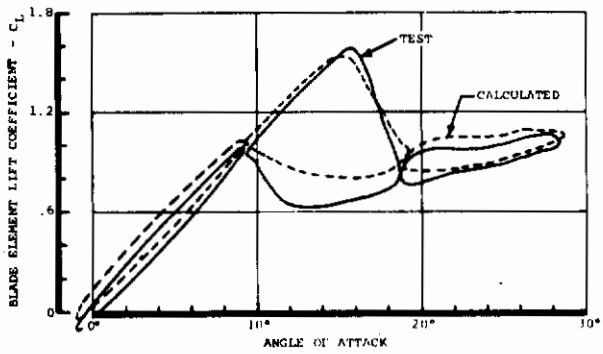

DYNAMIC C_M

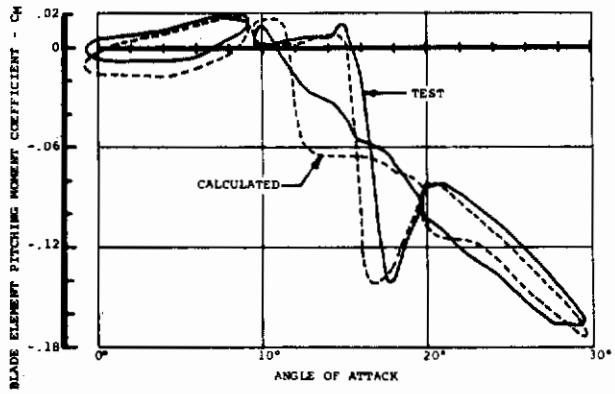

Figure 43. Comparison of Test and Theoretical Dynamic C_L and C_M for a Condition Below Stall, at Stall, and Beyond Stall

$$L = \text{Lift} = 1/2\rho V^2 C\ell C_{L(DYN)}$$

$$D = \text{Drag} = 1/2\rho V^2 C\ell C_{D(DYN)}$$

$$M = \text{Pitching Moment} = 1/2\rho V^2 C^2\ell C_{M(DYN)} \quad .$$

The wind axis airloads (L, D, and M) are then converted into blade system loads for every aero blade station at 15-degree increments. The dynamic airloads for each station are harmonically analyzed into 10 harmonics which then become part of the harmonic forcing loads applied in the response analysis.

NONUNIFORM DOWNWASH

Background

The initial effort in the representation of nonuniform downwash in the rotor loads program was made in 1960-61 with an attempt to use the theory of Reference 26. Later the work in References 27 and 28 was employed in digital computer programs. This effort was minimal and these programs were not readily adaptable for integration with the existing rotor analysis. Later, effort was extended to use the tabulated induced velocities prepared in Reference 29; but about this period of time, Davenport completed his computer analysis which was reported in Reference 30. This program can compute nonuniform induced velocities for an n-bladed rotor with prescribed loading, either to yield rotor self-induced or rotor-rotor interference velocities and was, in fact, the first source from which the downwash for a tandem could be computed.

This analysis was suited for incorporation as a subroutine for the rotor loads analysis, but it had two basic deficiencies in that:

1. With 10 trailing vortices from each blade, the computer running time was greatly increased.

2. To compute the necessary airloads for input to this routine required that it be made a part of the existing iterative loop between the airload and the blade dynamic response routines. The nonlinearities which already existed in the program from nonlinear aerodynamics considerations were therefore compounded and resulted in a highly unstable rotor analysis which would be extremely time-consuming.

To reduce the analysis computation time, the downwash analysis was modified to reduce the trailed vortices on each blade from 10 to 2 and to employ a simplified expression for the vortex strength. The analysis considered one vortex trailed at the

blade tip and the other from the root-end blade cutout. The strength of the trailed vortices was calculated by considering the blade to have a constant bound circulation along its span from the blade cutout to the tip of sufficient strength to maintain the rotor thrust. Assuming a constant bound circulation along the blade span eliminated the need to include the downwash calculations in the airload-blade response iteration, since the trailed vortex can be calculated from the assumed bound circulation without knowing the actual lift distribution. Correlation of the loads program with test data (Reference 7) verified the acceptability of this approach.

With the advent of faster computers, it became feasible to use the actual blade lift distribution to calculate the trailed vortex strength. Studies showed the principal factor perturbing the blade lift distribution near the tip and cutout was not the flexible blade deflections but the downwash itself. Figure 44 shows that the downwash alters the aerodynamic angle of attack. The altered angle of attack changes the lift distribution which modifies the trailed vortex strength. Therefore, as a first approximation, the effect of downwash on the lift will be included and the blade flexibility neglected in the calculation of the trailed vortex strength.

Therefore, a downwash distribution that is directly a function of the blade tip and cutout lift distribution is obtained by iterating among lift, downwash, and vortex strength until there is compatibility among the three. Comparisons of the currently used compatibility method with the earlier constant circulation method show a significant improvement in load prediction ability with the current method (see References 15 and 17).

Method of Calculation

The nonuniform downwash is calculated by considering the blade lift distribution at 15-degree increments around the rotor azimuth. At each increment, a vortex is assumed to trail from the blade cutout and blade tip circulation discontinuities of strength determined by the lift of the adjacent aerodynamic bay (see Figure 45). The lift and hence the vortex strength are assumed to vary linearly from azimuth position to azimuth position. Since the vortices are trailed from all blades on both rotors (for a tandem helicopter), a complex pattern of vortex spirals is formed in space. By summing the effects of all the vortex segments on a given blade element, the nonuniform downwash for each blade element is determined.

Next, the blades are rotated 15 degrees and the previously trailed vortices drift relative to the hub with a velocity composed of the aircraft forward speed and the uniform

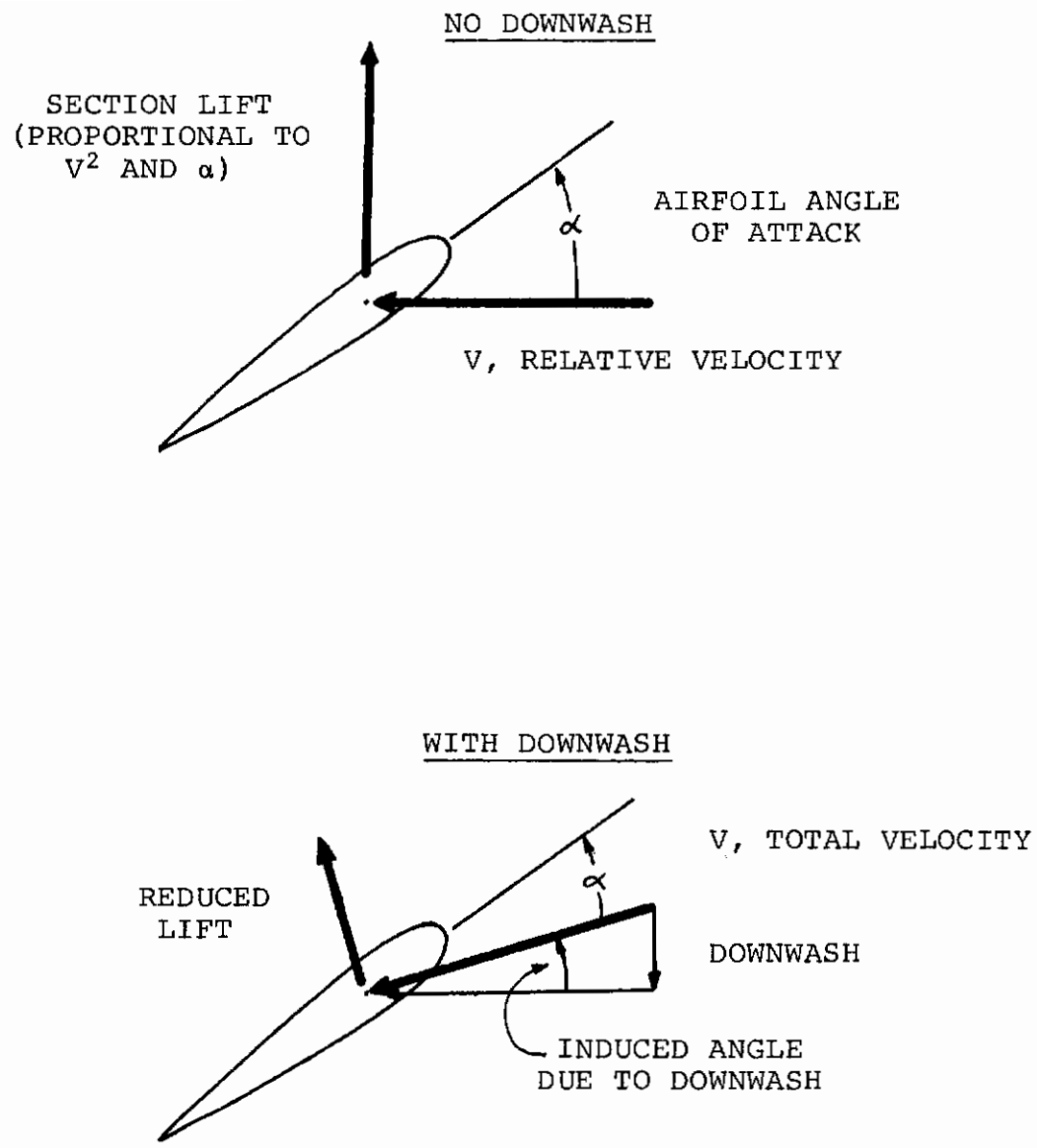

THE DOWNWASH FROM THE TRAILED VORTICES REDUCES THE ANGLE OF ATTACK. THE REDUCTION IN ANGLE OF ATTACK REDUCES THE LIFT (LIFT DEFICIENCY) AND HENCE REDUCES THE STRENGTH OF THE TRAILED VORTEX SINCE THE TRAILED VORTEX STRENGTH IS PROPORTIONAL TO THE BLADE SECTION LIFT.

Figure 44. Effect of Downwash

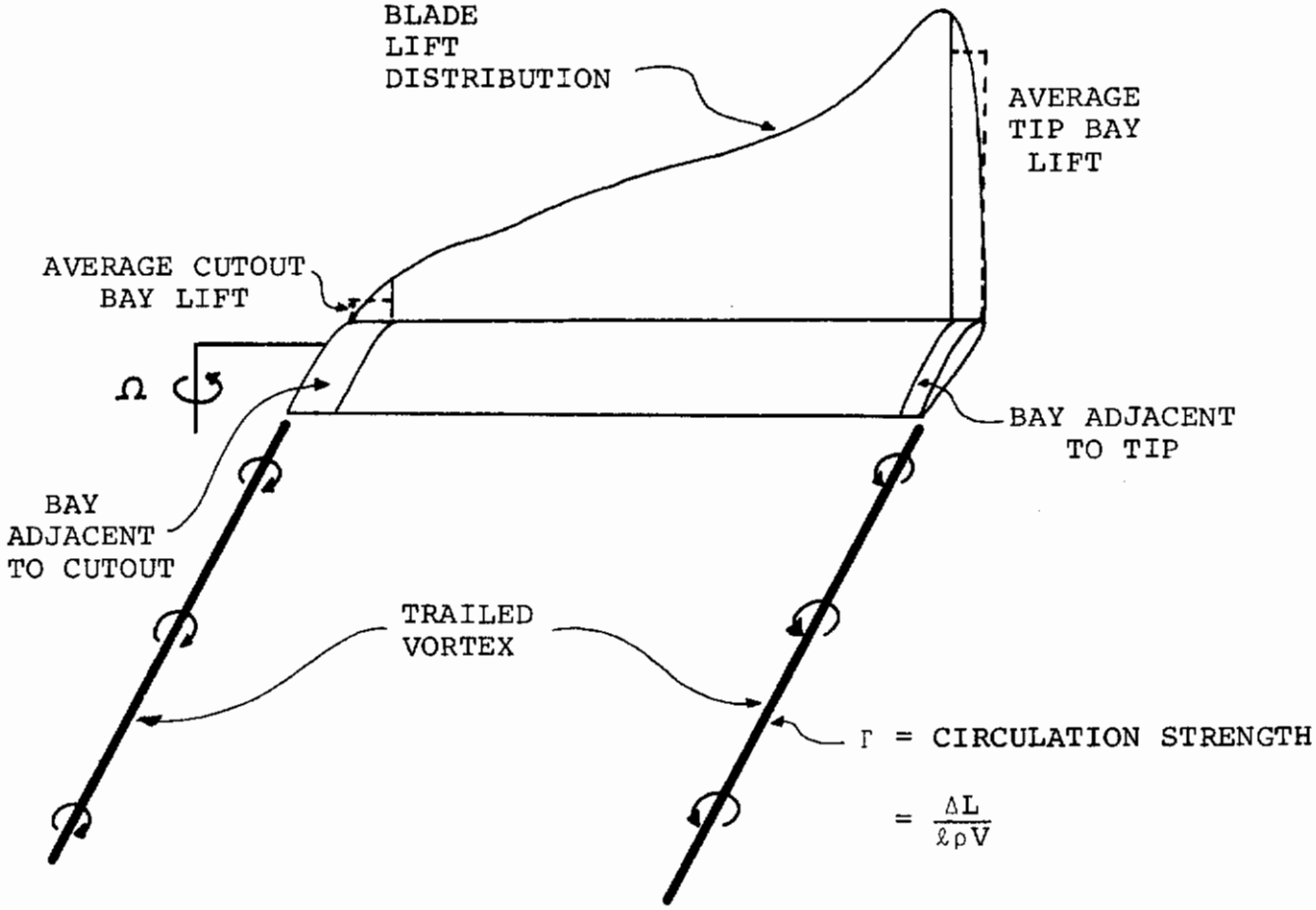

ΔL = AVERAGE ADJACENT BLADE LIFT

ℓ = BAY LENGTH

ρ = AIR DENSITY

V = LOCAL VELOCITY

Figure 45. Calculation of Trailed Vortex Strength

downwash. New trailed vortices are calculated for this azimuth position and the downwash of all the vortex segments is again summed on each blade element. Then the blades are incremented another 15 degrees to the next azimuth position.

When the whole rotor azimuth has been covered by this stepwise procedure, a nonuniform downwash field has been defined by a downwash value at each blade airfoil section all around the azimuth at 15-degree increments. A description of the downwash calculations follows.

Theory

Reference 30 presents a detailed description of the analytical method which is based on the assumption of a rigid wake. The essential steps involved in the computation of rotor-induced velocities are summarized below.

Considering the origin as the center of rotation of the rotor trailing the vortex, the position of the vortex filament is established from the vector diagram in Figure 46.

It is shown that:

$$Q_x = r \cos \beta(\theta) \cos \theta + \mu_x(\psi-\theta)$$

$$Q_y = -r \cos \beta(\theta) \sin \theta + \mu_y(\psi-\theta)$$

$$Q_z = -r \sin \beta(\theta) + \mu_z(\psi-\theta)$$

where r = radial distance along blade

R = rotor radius

$\vec{Q}$ = vortex filament position vector with components Q_x, Q_y, and Q_z

Ω = rotor angular velocity

β = rotor blade flapping angle

ψ, θ = rotor blade azimuth angles

μ_x, μ_y, μ_z = ratio of components of vortex system drift velocity to $R\Omega$

Computing the $\vec{Q}$ vector components for a series of points spaced at equal increments in time (i.e., equal increments in ϕ), the geometry of the complete vortex filament is defined. Between successive computed points the filament is represented by straight line segments. A linear variation of the circulation strength along the filament is assumed.

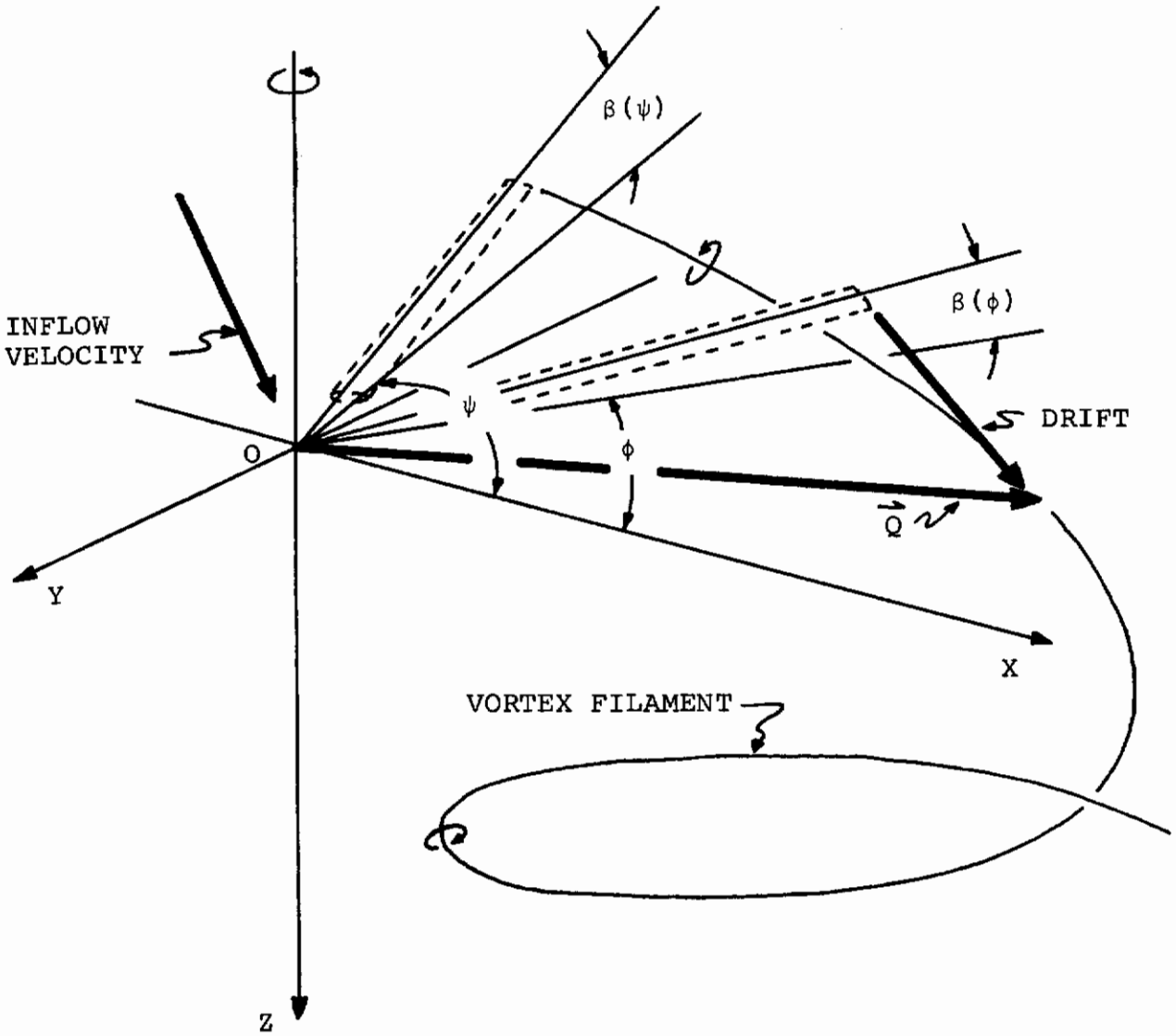

Figure 46. Vortex Vector Diagram

The segment between successive points A and B along the filament is given by

$$\vec{T} = \vec{Q}_B - \vec{Q}_A \ .$$

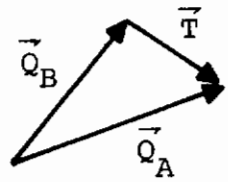

Then, let P be the vector from the origin to the point at which it is desired to compute the velocity. The vectors between the points A and B on the vortex filament and the point at which the downwash is to be obtained are

$$\vec{S_A} = \vec{Q_A} - \vec{P}$$

$$\vec{S_B} = \vec{Q_B} - \vec{P} \ .$$

For defining circulation along the filament, the positive direction is a vector pointing from A toward B (i.e, downstream along the filament) using the right-hand rule for the sense of rotating. Positive circulation would therefore induce a velocity coming out of the paper as shown below.

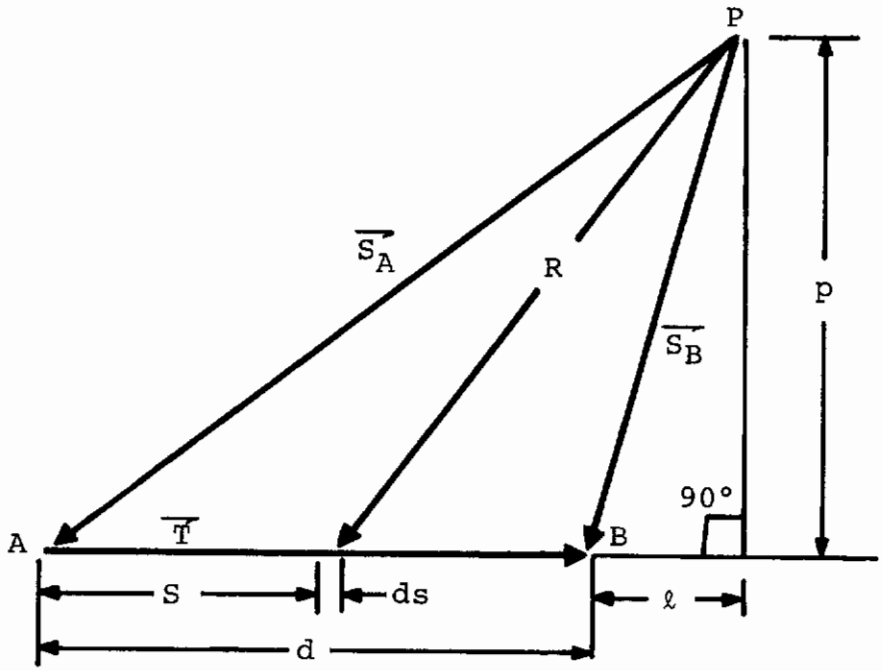

A unit vector in the direction of the velocity induced by the segment is given by

$$\vec{U} = \frac{\vec{S}_A \times \vec{S}_B}{|\vec{S}_A \times \vec{S}_B|} \quad .$$

Using the Biot-Savart law, the magnitude of the induced velocity can be written

$$V = \int_A^B \frac{\Gamma P}{4\pi R^3} ds \quad .$$

Integrating the above expression for a linear variation of the circulation,

$$V = \frac{\Gamma_A}{4\pi Pd}\left[\sqrt{\ell^2 + P^2} - \frac{\ell d + \ell^2 + P^2}{\sqrt{(\ell + d)^2 + P^2}}\right] + \frac{\Gamma_B}{4\pi Pd}\left|\sqrt{(\ell + d)^2 + P^2} + \frac{\ell d + \ell^2 + P^2}{\sqrt{\ell^2 + P^2}}\right| \quad .$$

Velocity components induced at P by the filament A B are those of the vector,

$$\vec{V} = V\vec{U} \quad .$$

The circulation value at the corners A and B of each filament is defined from the spanwise lift distribution at the ψ values corresponding to the corners. Bound circulation at any radial station on the blade for a particular ψ can be found by the Kutta-Joukowski law:

$$\text{Lift} = (\text{density})(\text{speed})(\text{circulation}) = \rho V \Gamma \quad .$$

From the above, the nondimensional bound circulation is

$$\Gamma = C/R \frac{C_L}{2}\left(\frac{r}{R} + \mu \cos \alpha_s \sin \psi\right) \quad ,$$

where the term in parentheses is an approximation to the blade element velocity and

C_L = blade element lift coefficient

C = blade chord length

μ = ratio of helicopter flight speed to ΩR

α_s = shaft angle of attack

r = radial distance along blade

R = rotor radius

ψ = rotor blade azimuth angle

Using the above expression, the strength of each trailed vortex is established from the lift distribution along the blade at each ψ position. The velocity at point P is then obtained by successive additions of the contribution from each segment of each vortex, going back along the filament spirals far enough to include all substantial contributions.

Part IV. Prop/Rotor Loads Analysis Correlation

R. B. Taylor

INTRODUCTION

Extensive loads correlation was performed with the C-70 analysis to determine its prediction capability for a wide range of rotors and test conditions. For correlation of the analysis with highly twisted prop/rotors, model test data from 3 prop/rotor wind tunnel tests was used. The test data range included hover, transition, and cruise for the tilt-wing and tilt-rotor aircraft, in addition to windmilling cruise for the stowed-rotor aircraft. Blade flap and chord bending, in addition to blade torsion, were of primary concern for this part of the correlation. In addition, steady rotor forces and moments were also correlated with the prop/rotor test data. That portion of the analysis which predicts loads for low-twisted rotors for which flapwise and lagwise motions are largely uncoupled (C-60) was used for helicopter loads correlation. For correlation of the analysis with low-twisted articulated rotors, flight test data for the CH-47 and Model 347 was used in addition to CH-34 full-scale wind tunnel test data. Correlation of pitch link loads, blade flap, and chord bending was of primary concern for this part of the correlation. Also, airloads were correlated with CH-34 airloads test data.

PROP/ROTOR LOADS CORRELATION

INTRODUCTION

Blade loads and rotor loads test data from three hingeless prop/rotor wind tunnel models was used for correlation with the C-70 analysis to determine its prediction capability for highly twisted prop/rotors. The wind tunnel models selected provided a wide range of flight conditions and also a large variation of blade dynamic properties. Two of the models were stiff in plane (first chordwise bending frequency greater than operating rotor speed), and the other model was soft in plane (first chordwise bending frequency less than operating rotor speed). Due to the high twist, all three model rotors had highly coupled flapwise and lagwise motions and therefore provided a good test of the flap-chord coupling capabilities of the C-70 analysis.

Table I is a brief summary of the prop/rotor models used for correlation. The 160 performance model is a 1/10-scale, full-span powered wind tunnel model of the Model 160 tilt-rotor aircraft, a current Boeing-Vertol tilt-rotor design. The wind tunnel model has stiff-in-plane blades; and since the model is intended to obtain primarily performance data, the blades are geometrically scaled only. The 1/3-scale LIT model is a powered, 4-bladed rotor mounted on a wing. The blades are Froude-scaled and are stiff in plane. The 1/9-scale conversion model is a half-span, unpowered windmilling model of the Model 213 stowed-rotor aircraft which is a current Boeing-Vertol stowed-rotor design. The 4-bladed rotor and the wing are Froude-scaled and the blades are soft in plane.

The test data obtained from these models covered the 3 main flight regimes of the tilt-rotor and tilt-wing aircraft: hover, transition, and cruise. In addition, as shown in Table II, data was obtained for correlation in windmilling cruise, an important flight regime of the stowed-rotor aircraft.

Table III is a summary of the prop/rotor model test data used for correlation. As shown, blade loads and steady rotor hub moments for all three models were correlated with the analysis.

CORRELATION RESULTS

Hover

Test data from two prop/rotor models was used for correlation with the analysis in hover: the 1/3-scale LIT rotor and the Model 160 performance model. Both models were tested out of ground effect to reduce interference effects; cyclic application with the rotor disc plane in a horizontal position produced the blade loads and hub moments for the hover

TABLE I
SUMMARY OF PROP/ROTOR MODELS USED FOR CORRELATION

Model	Blade Radius (ft)	Number of Blades	Twist (deg)	$\frac{\omega_{1Flap}}{\Omega}$*	$\frac{\omega_{1Chord}}{\Omega}$*	Brief Description
160 Performance	2.75	3	36	1.5	2.5	tilt-rotor, full-span, powered
1/3-Scale LIT	4.403	4	40	2.1	3.5	tilt-wing, wing-rotor, powered
1/9-Scale Conversion	2.73	4	25	1.25	0.75	stowed-rotor conversion, half-span, unpowered windmilling

*NOTE: First-flap and first-chord frequency ratios are given for operating rotor speed.

TABLE II
SUMMARY OF TEST CONDITIONS OF PROP/ROTOR
MODELS USED FOR CORRELATION

Model	Hover	Transition	Powered Cruise	Windmilling Cruise
160 Performance	X	-	-	-
1/3-Scale LIT	X	X	X	-
1/9-Scale Conversion	-	-	-	X

TABLE III
SUMMARY OF PROP/ROTOR MODEL TEST DATA USED FOR CORRELATION

Model	Blade Flap Bending	Blade Chord Bending	Blade Torsion	Steady Rotor In-Plane Moments
160 Performance	X	X	X	X
1/3-Scale LIT	X	X	X	X
1/9-Scale Conversion	X	X	X	X

correlation. The correlation is presented as a comparison of predicted and measured alternating blade moments, first- and second-harmonic blade moments, and blade moment waveforms. Wind tunnel testing experience with prop/rotors has shown that alternating bending moments are nearly all 1- and 2-per-rev, with the exception of blade torsion near stall flutter and chord bending in conditions where pitch-lag coupling is evident. For a condition such as this, the waveforms clearly show the higher harmonic content. Since the prediction of steady rotor moments due to hover cyclic is closely related to and as important as the prediction of blade bending moments, correlation is also performed with steady rotor in-plane moments.

Figures 47 through 56 are the hover cyclic correlation results for the 1/3-scale LIT rotor. As mentioned in the introduction, this 4-bladed rotor was mounted on a wing and the blades are stiff in plane with 40 degrees of twist. Correlation with alternating blade root flap bending (one half peak-to-peak) in Figure 47 is very good, with the analysis slightly over-predicting flap bending sensitivity to cyclic. Correlation of the first two flap bending harmonics, which are the prime harmonics of the alternating moment, is shown in Figure 48. The analysis correlates very well with the first-harmonic flap bending sensitivity to cyclic but overpredicts second-harmonic flap bending. The flap bending waveform in Figure 49 shows that the predicted first harmonic agrees well in phase and magnitude with the measured data, but inclusion of the predicted second harmonic shifts the total waveform peak to 150 degrees azimuth. The alternating blade root chord bending correlation is shown in Figure 50, and the prediction again agrees very well with the test data. Correlation of the first two chord bending harmonics in Figure 51 shows the analysis overpredicts first-harmonic chord bending by 13 percent and agrees very well with the measured low value of 2-per-rev chord bending. Figure 52 shows the predicted chord bending waveform has a large 3-per-rev contribution; this can be traced to the over-prediction of 2-per-rev flap bending combined with the large 1-per-rev flap bending, since 1- and 2-per-rev flapping produce 3-per-rev and 4-per-rev lag motion. Note that the predicted first-harmonic waveform agrees well in magnitude and fairly well in phase with the measured waveform. Correlation results for alternating blade root torsion are presented in Figures 53 and 54. The analysis overpredicts alternating torsion by 14 percent in Figure 53 and the predicted waveform in Figure 54 shows a large 3-per-rev contribution. This indicates a strong coupling in the analysis between blade pitching and lag motion, probably due to the aft shear center location (35 percent chord) for this blade. The Model 160 performance model blade loads test data showed this type of coupling in hover; these results will be discussed later in this section. Correlation with the steady rotor pitching and yawing moments

is shown in Figures 55 and 56. A steady pitching moment pitches the aircraft nose up and the yawing moment rolls the aircraft in hover. The results show the analysis agrees very well with the test data for both moments. These results are important since they demonstrate the capability of the analysis to predict the ratio of rotor hub moment-to-blade bending moment amplitude in hover. This ratio is critical to prop/rotor design since the bending fatigue design loads are those produced by hover cyclic to produce required steady rotor forces and moments for aircraft control in hover.

Figures 57 through 66 are the hover cyclic correlation results for the Model 160 performance model. As mentioned in the introduction, this model has a 3-bladed rotor and the blades are stiff in plane. The cyclic pitch was phased to yield pure longitudinal blade flapping so that the total steady hub moment would pitch the aircraft with little aircraft roll. In terms of prop/rotor nomenclature, the desired effect was to produce a rotor pitching moment with little or no yawing moment. The blade root flap bending correlation in Figures 57, 58, and 59 shows the analysis agrees well with the test data, both in alternating value (one-half peak-to-peak) and the first harmonic. The measured second harmonic is very low compared to the first harmonic, and the prediction for the second harmonic agrees well with the measured data above 2,200 rpm. Correlation with the measured flap bending waveform in Figure 59 is very good, both in amplitude and phase. The good phase correlation demonstrates that the blade dynamic response, in terms of phase lag, to a 1-per-rev cyclic input is correctly accounted for in the analysis. This is an important result since the first flapping mode deflection at the blade root is nearly perpendicular to the blade major principal axis, which is inclined nearly 40 degrees with the disc plane at the blade root due to blade twist and collective pitch. Thus, in- and out-of-plane motion are coupled for blade root flap bending and the analysis has shown the capability to predict this coupling effect on flap bending moment.

The results of the hover cyclic chord bending correlation for the Model 160 performance model are presented in Figures 60, 61, and 62. Predicted alternating chord bending agrees well with the test data. Both prediction and test data are relatively insensitive to changes in rotor speed. Correlation for the first and second harmonics in Figure 61 shows overprediction of the first harmonic and underprediction of the second harmonic. Poor correlation of the first harmonic can be due to the blade lag root boundary in the analysis. The blade was modeled as a cantilevered beam such that the lag deflection slope at the root boundary was zero. A detailed analysis of the blade root retention, including bearings, indicated that significant lag motion in the bearing would be present; and therefore, the blade lag root retention would be more

accurately defined as pinned with a stiff angular spring instead of cantilevered. The effect of changing the root boundary condition from cantilevered to pinned with an angular spring would be small on first chord frequency and also small on lag dynamic response, but the effect on chord bending moment radial distribution could be significant. For a rotating cantilevered beam, the first modal bending moment distribution in a vacuum steadily increases from zero at the end of the beam to a maximum value at the cantilevered boundary. The effect of pinning the beam and applying an angular spring is to decrease the bending moment value at the root boundary from that for the cantilevered condition, even though tip deflections for both conditions are equal. Therefore, modeling the blade lag root retention in the analysis as a pin with angular spring should decrease the predicted first-harmonic chord bending, with little effect on second-harmonic chord bending.

The waveform correlation for chord bending in Figure 62 shows that both prediction and measured data have significant higher-harmonic contributions. A large 6-per-rev contribution is evident, particularly between 90 and 210 degrees azimuth. Blade lag motion is coupling with blade pitching motion, as shown by a comparison of the chord bending and torsional waveforms in Figures 62 and 63, respectively. The measured data shows that chord bending and torsion are oscillating in phase at 6 per rev. The blade first torsional frequency ratio is near 6 per rev at this rotor speed and the rotor is probably on the verge of stall flutter at this point. Stall flutter inception is characterized by a large growth in alternating blade torsion oscillating at the torsional natural frequency. Coupling of the torsional 6-per-rev motion with the lag mode can be traced to the aft shear center location for this blade (at 38 percent chord). Pitching moment at 6 per rev induces 6-per-rev airloads which in turn force the chord mode at 6 per rev due to induced drag. When the shear center is offset from the aerodynamic center, the oscillating airloads increase the blade angle of attack at the same frequency, thus amplifying 6-per-rev airloads and therefore 6-per-rev chord bending. The analysis shows the same tendency to oscillate at 6 per rev, both in chord bending and torsion. In Figure 62, note that the phasing of the predicted 6-per-rev component is in phase with the measured data, but the analysis has gone into premature stall flutter as shown by the large 6-per-rev spiking in the second quadrant. Note that the sixth harmonic in the predicted chord bending waveform (Figure 63) is in phase with the predicted 6 per rev in the torsional waveform. This result is important since it shows the capability of the analysis to predict pitch-lag coupling. A comparison of predicted and measured alternating blade torsion in Figure 64 shows good correlation with the analysis slightly overpredicting. The overprediction is due to premature stall flutter inception in the analysis.

Correlation results for the steady rotor in-plane moments due to hover cyclic for the Model 160 performance model are shown in Figures 65 and 66. Correlation for both pitching and yawing moments is good, with the analysis overpredicting the pitching moment by 10 percent at 2,300 rpm.

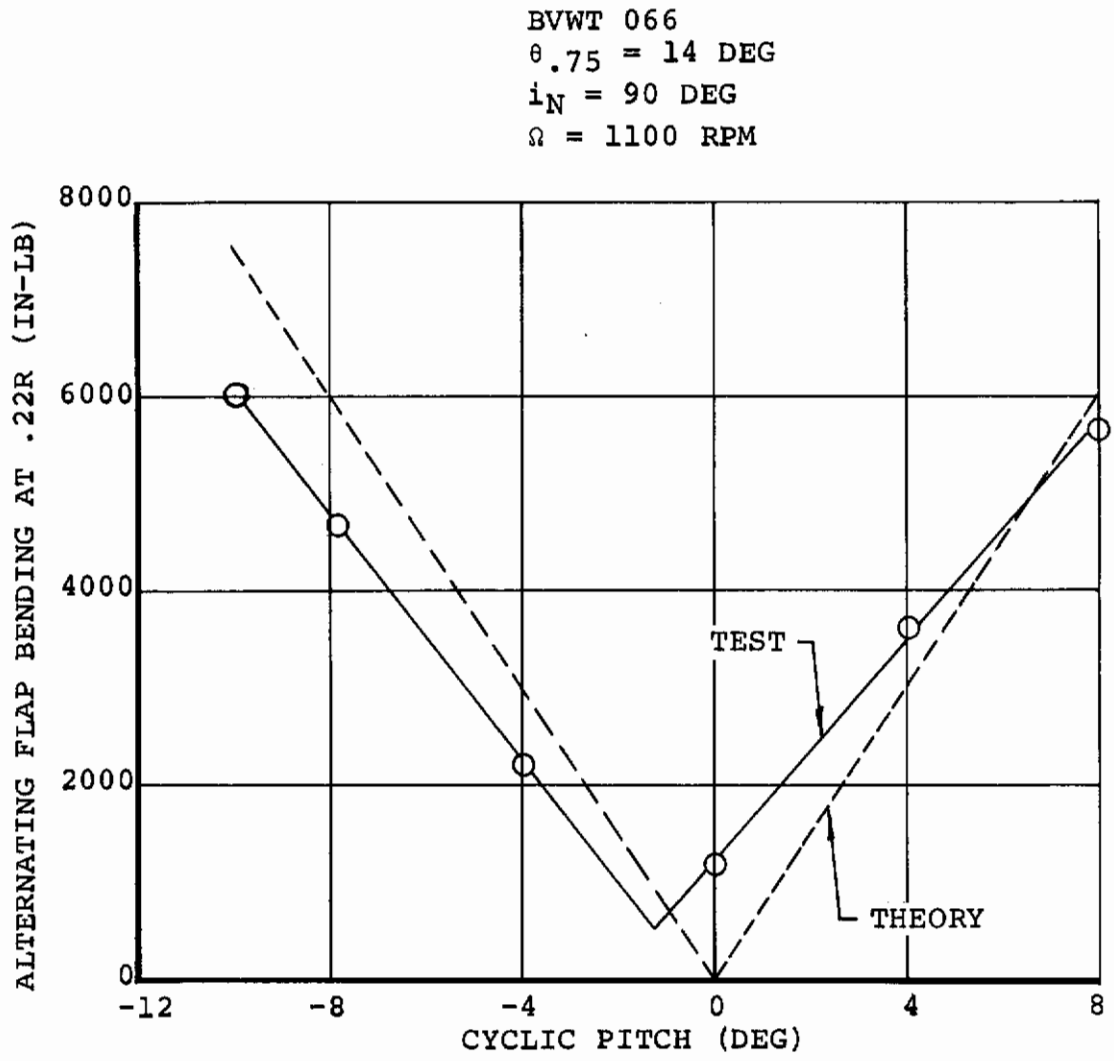

Figure 47. 1/3-Scale LIT Blade, Predicted and Measured Alternating Flap Bending in Hover Due to Cyclic Pitch

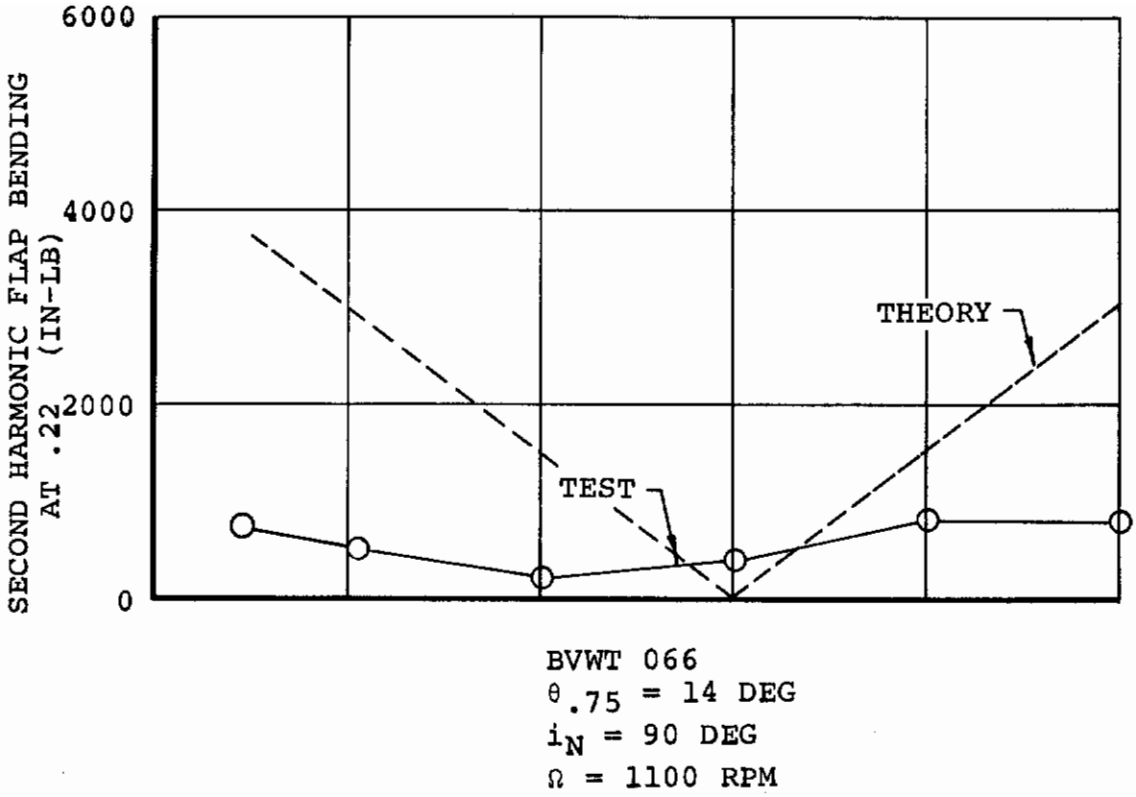

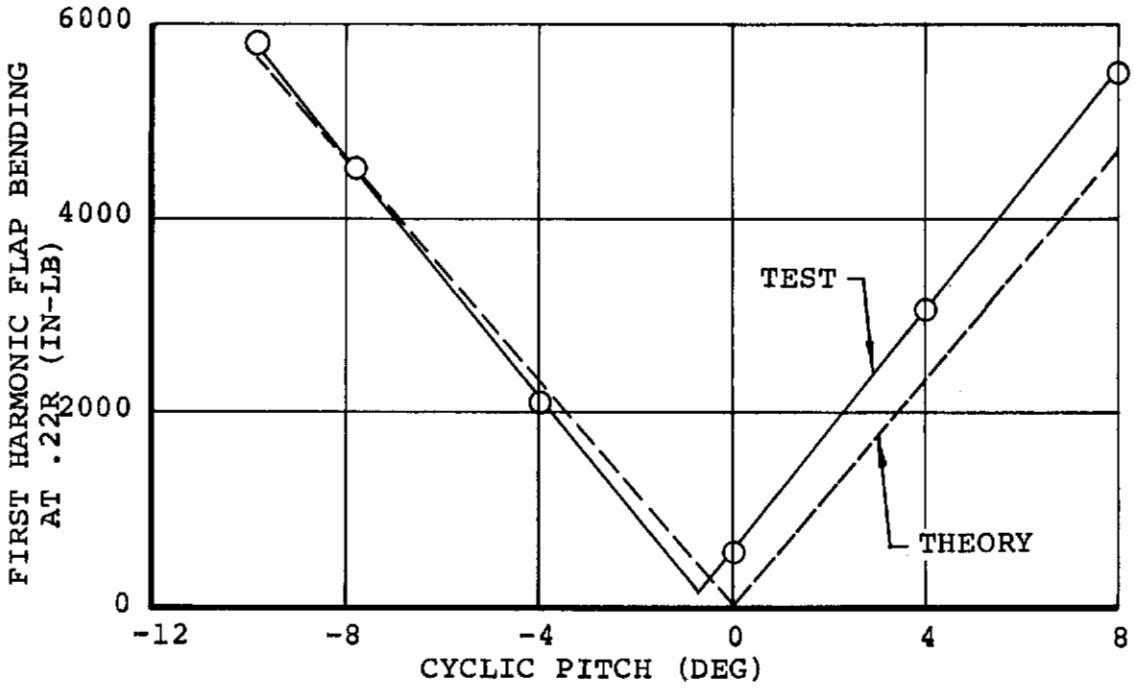

Figure 48. 1/3-Scale LIT Blade, Predicted and Measured First- and Second-Harmonic Flap Bending in Hover Due to Cyclic Pitch

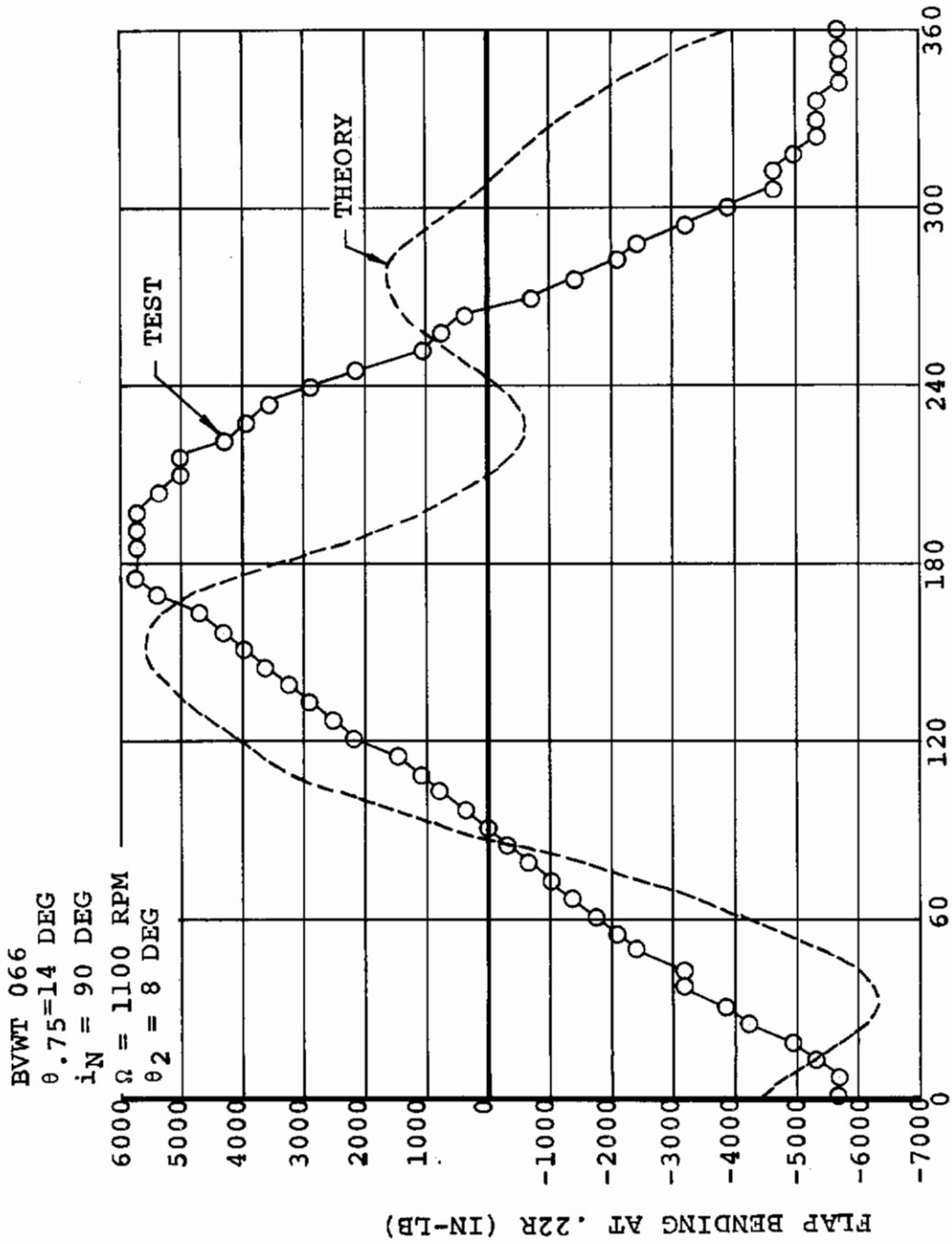

Figure 49. 1/3-Scale LIT Blade, Predicted and Measured Flap Bending Waveform in Hover for 8 Degrees Cyclic Pitch

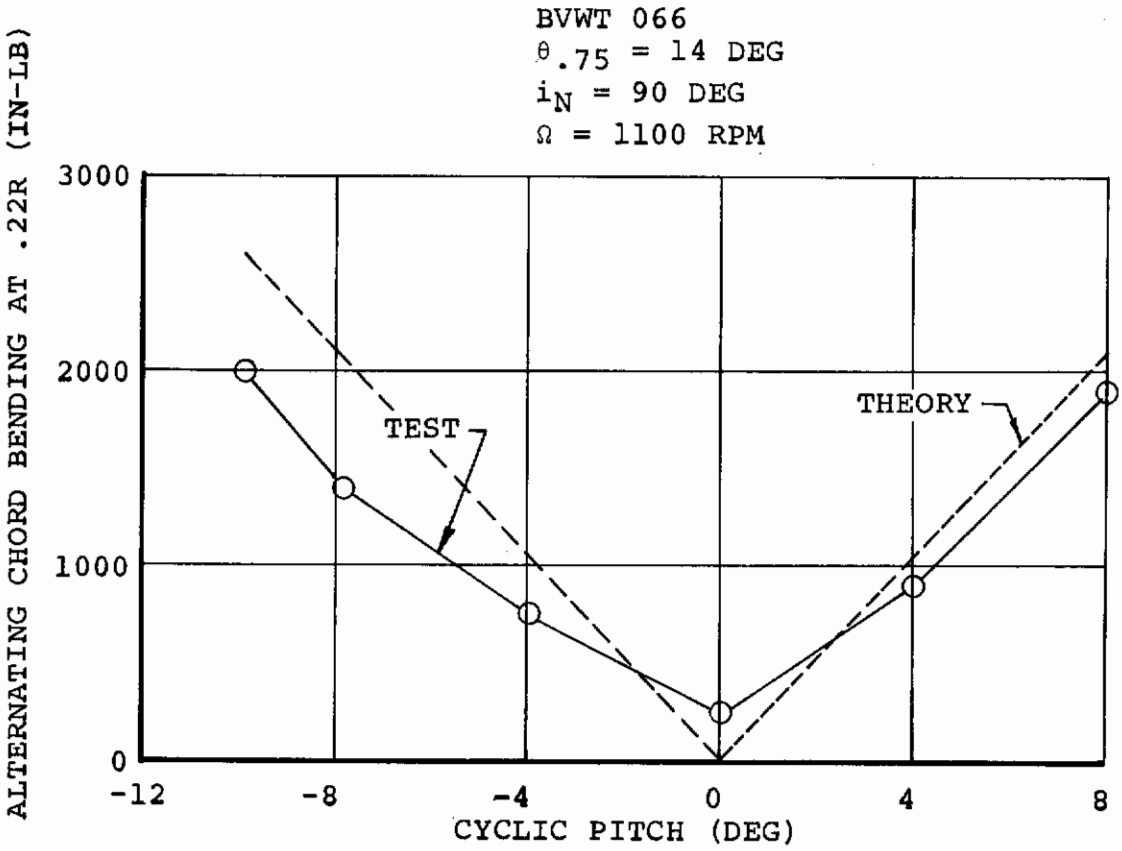

Figure 50. 1/3-Scale LIT Blade, Predicted and Measured Alternating Chord Bending in Hover Due to Cyclic Pitch

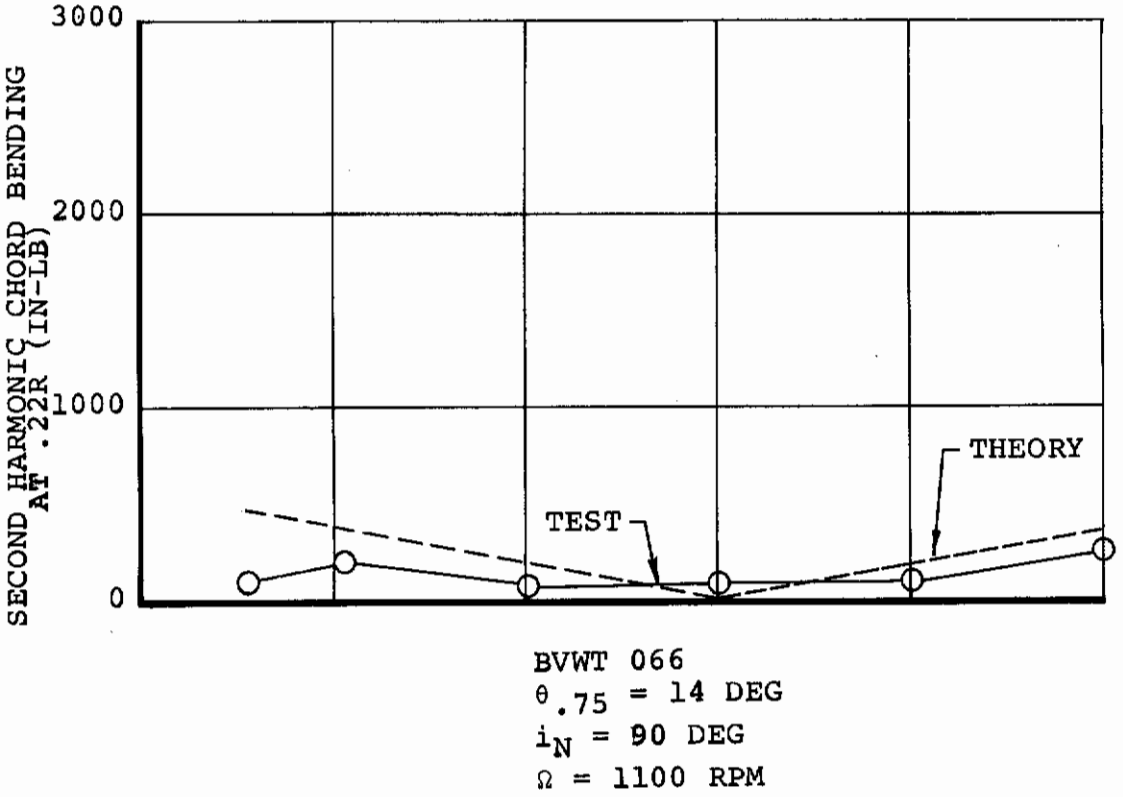

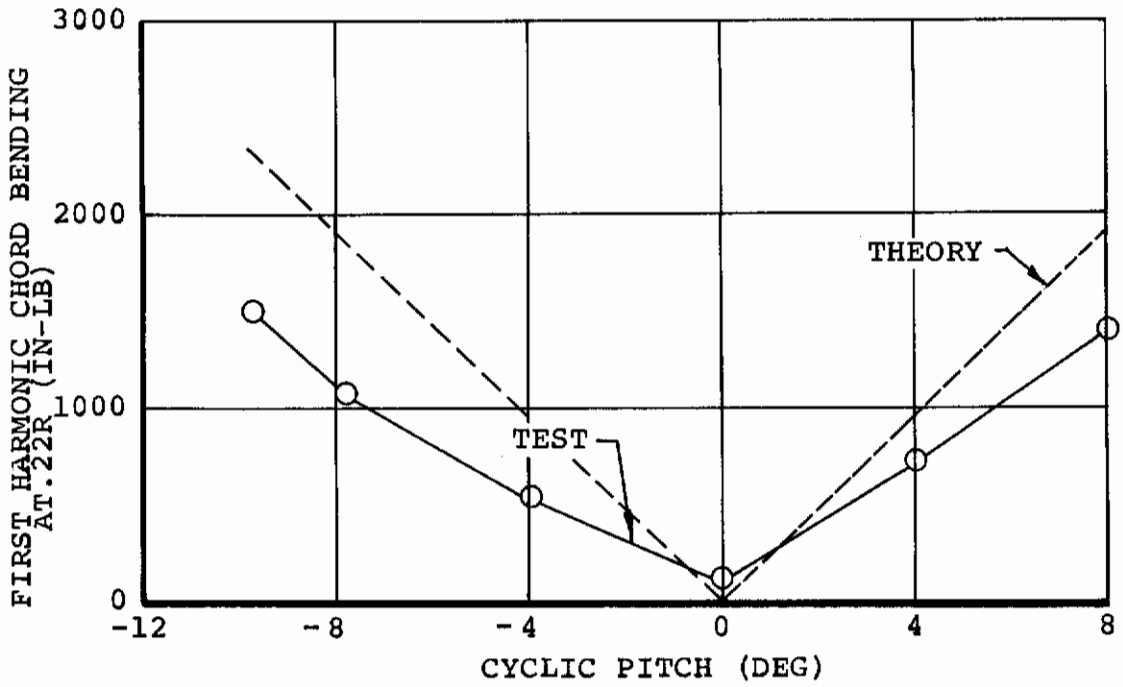

Figure 51. 1/3-Scale LIT Blade, Predicted and Measured First- and Second-Harmonic Chord Bending in Hover Due to Cyclic Pitch

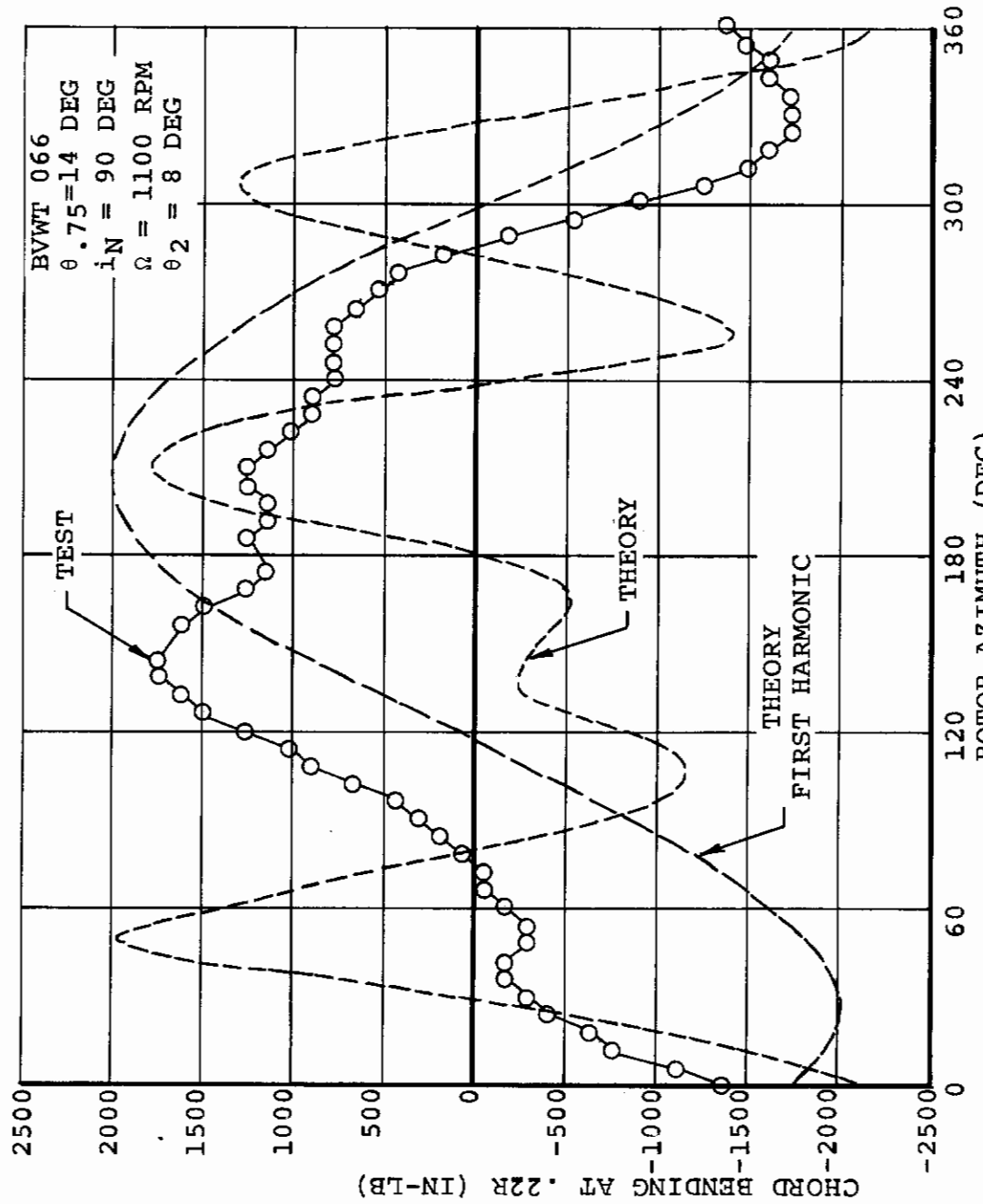

Figure 52. 1/3-Scale LIT Blade, Predicted and Measured Chord Bending Waveform in Hover for 8 Degrees Cyclic Pitch

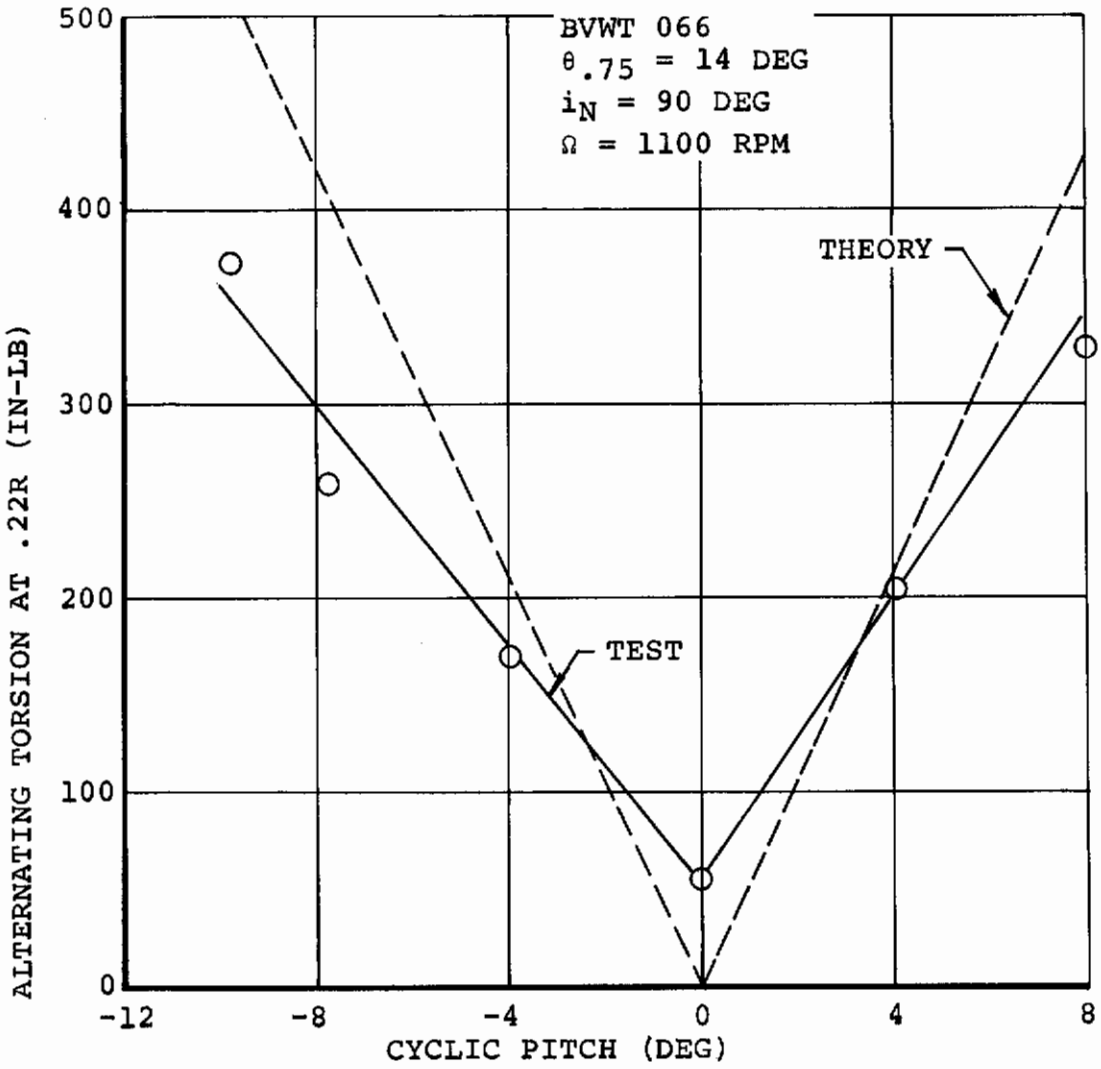

Figure 53. 1/3-Scale LIT Blade, Predicted and Measured Alternating Torsion in Hover Due to Cyclic Pitch

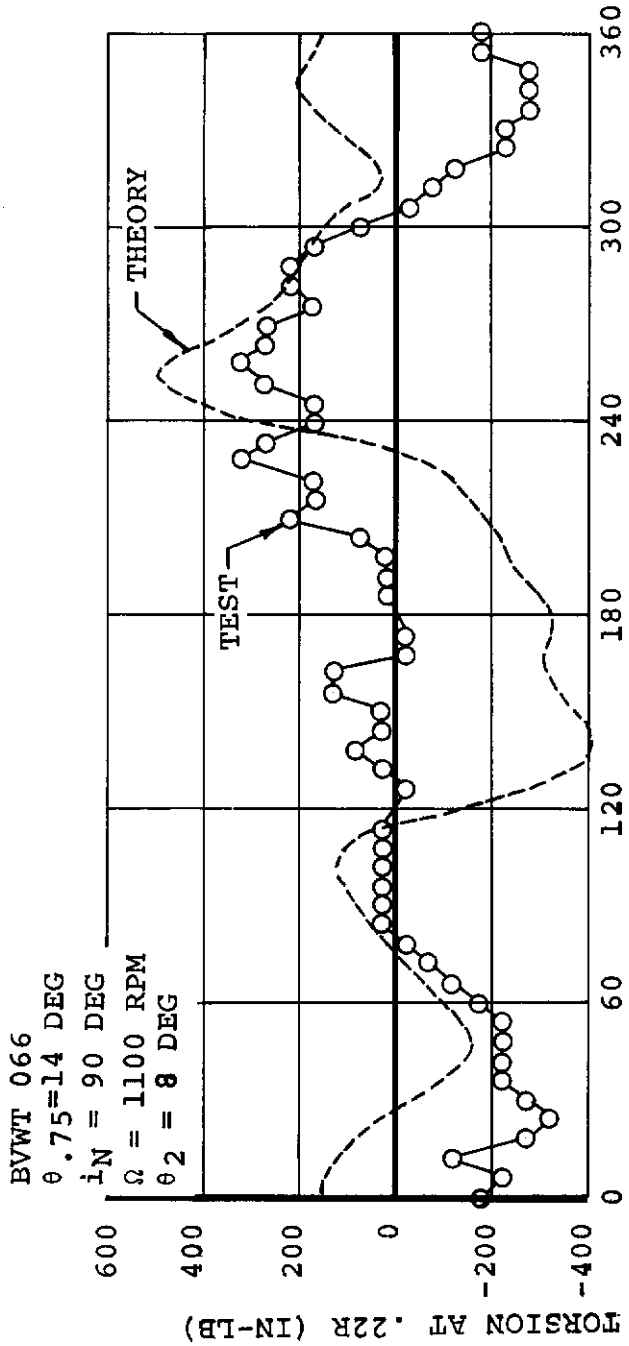

Figure 54. 1/3-Scale LIT Blade, Predicted and Measured Torsional Waveform in Hover for 8 Degrees Cyclic Pitch

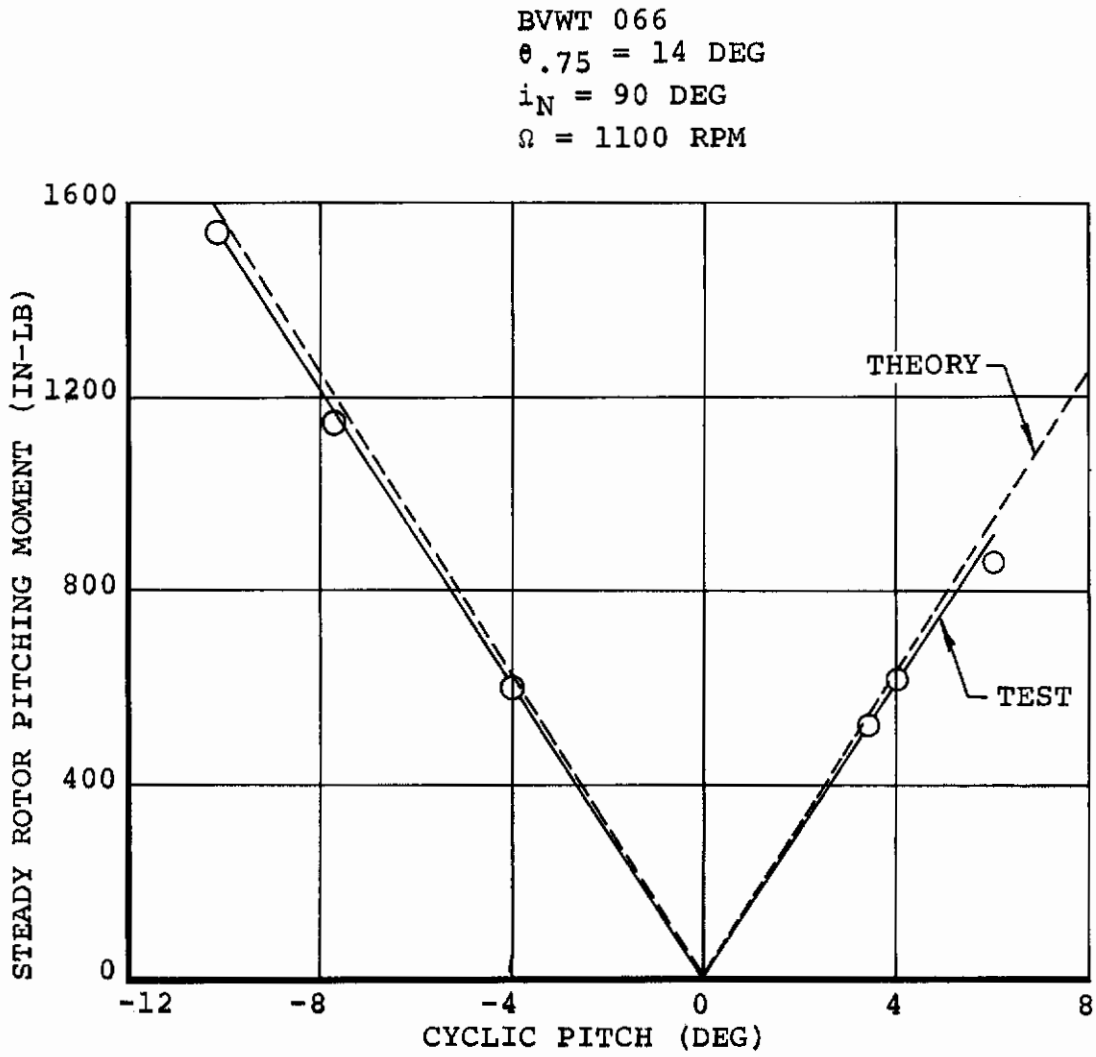

Figure 55. 1/3-Scale LIT Blade, Predicted and Measured Steady Rotor Pitching Moment in Hover Due to Cyclic Pitch

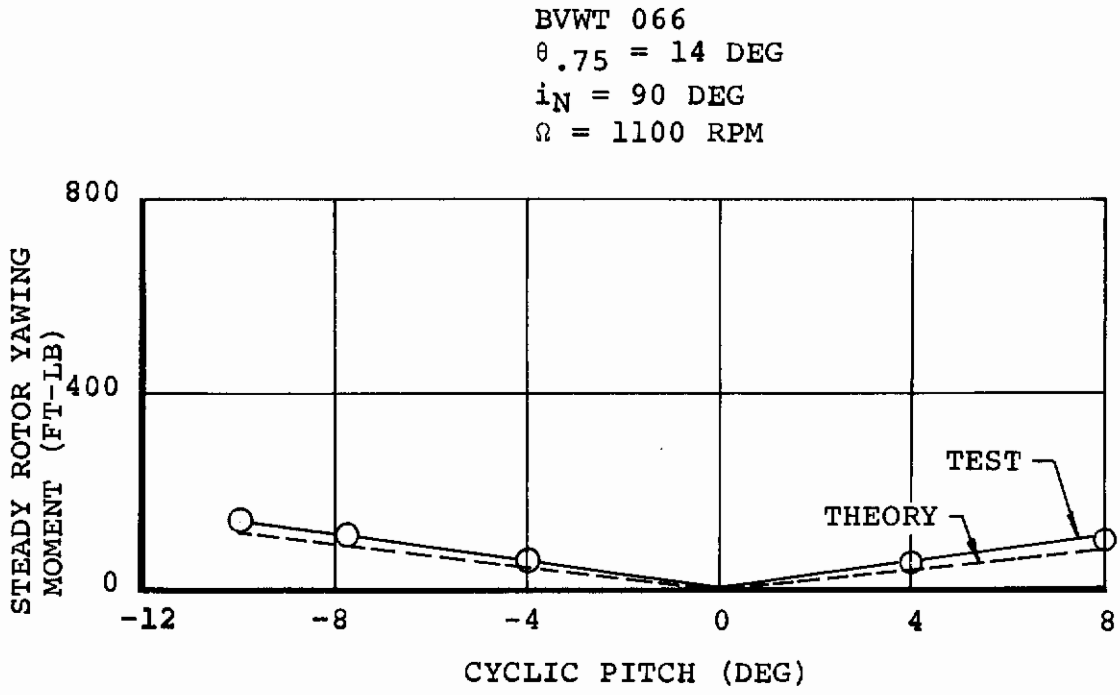

Figure 56. 1/3-Scale LIT Blade, Predicted and Measured Steady Rotor Yawing Moment in Hover Due to Cyclic Pitch

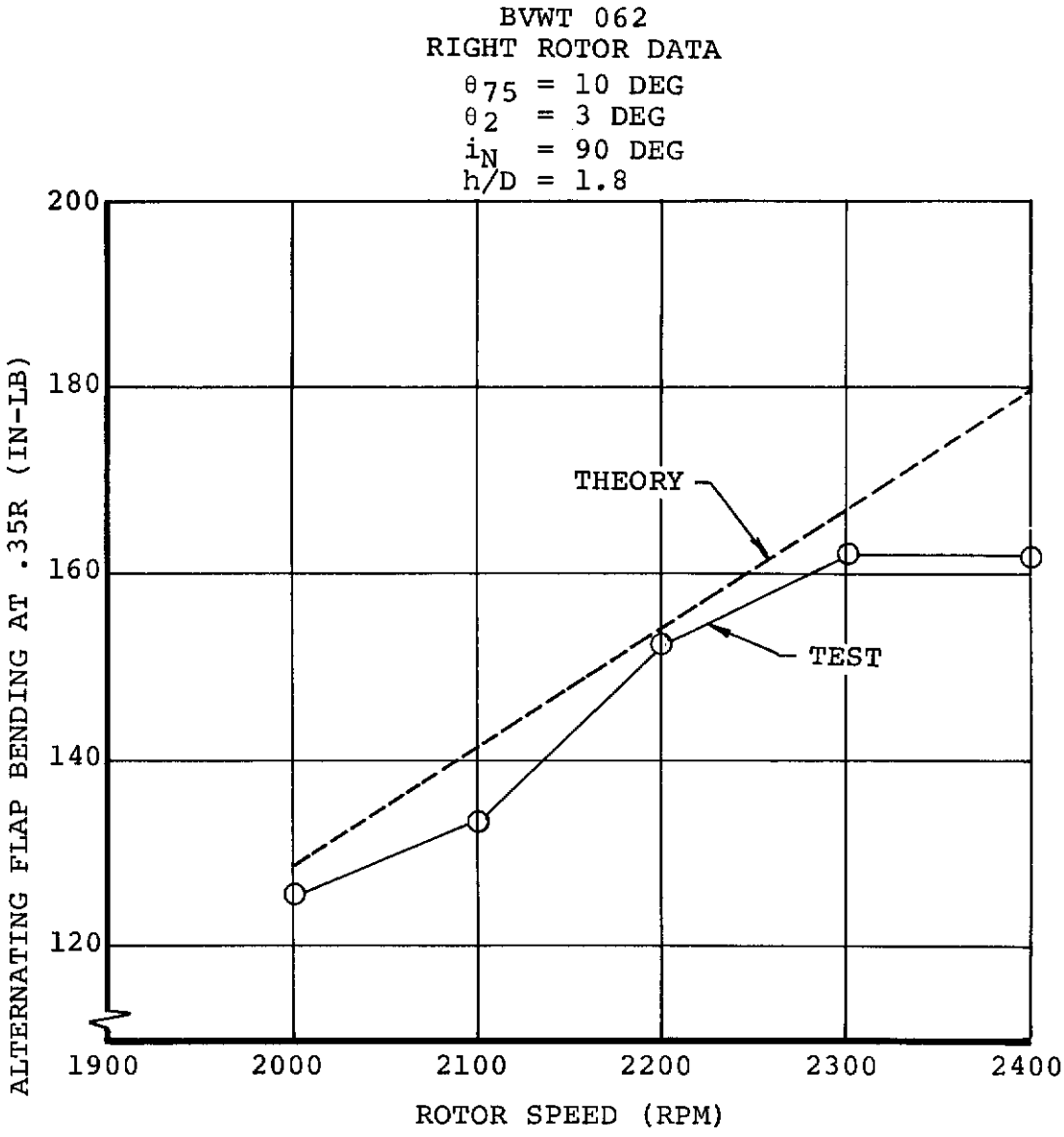

Figure 57. Model 160 Performance Model, Predicted and Measured Alternating Flap Bending Moment in Hover for 3 Degrees Cyclic Pitch

BVWT 062
RIGHT ROTOR DATA
θ_{75} = 10 DEG
θ_2 = 3 DEG
i_N = 90 DEG
h/D = 1.8

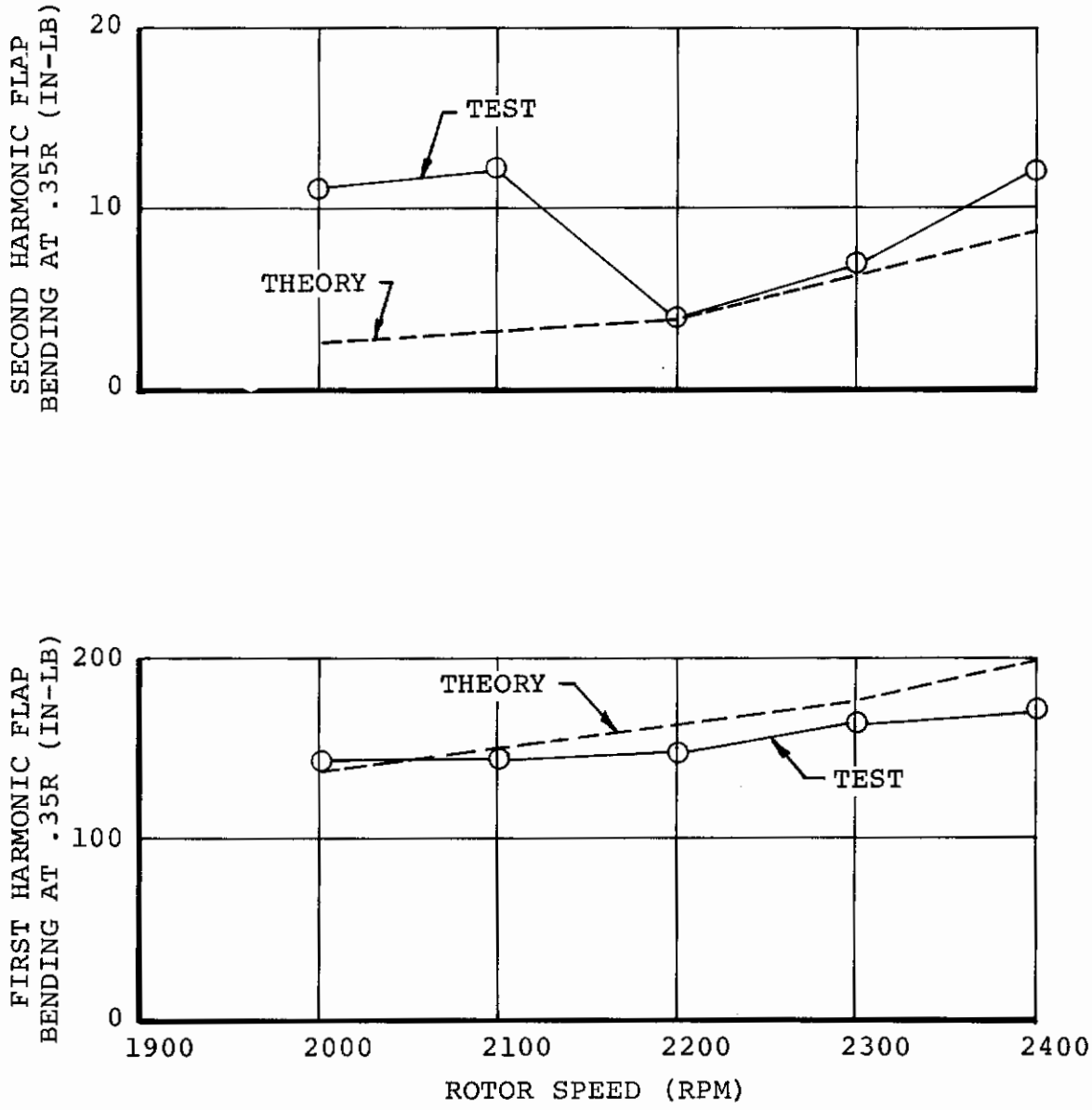

Figure 58. Model 160 Performance Model, Predicted and Measured First- and Second-Harmonic Flap Bending Moment in Hover for 3 Degrees Cyclic Pitch

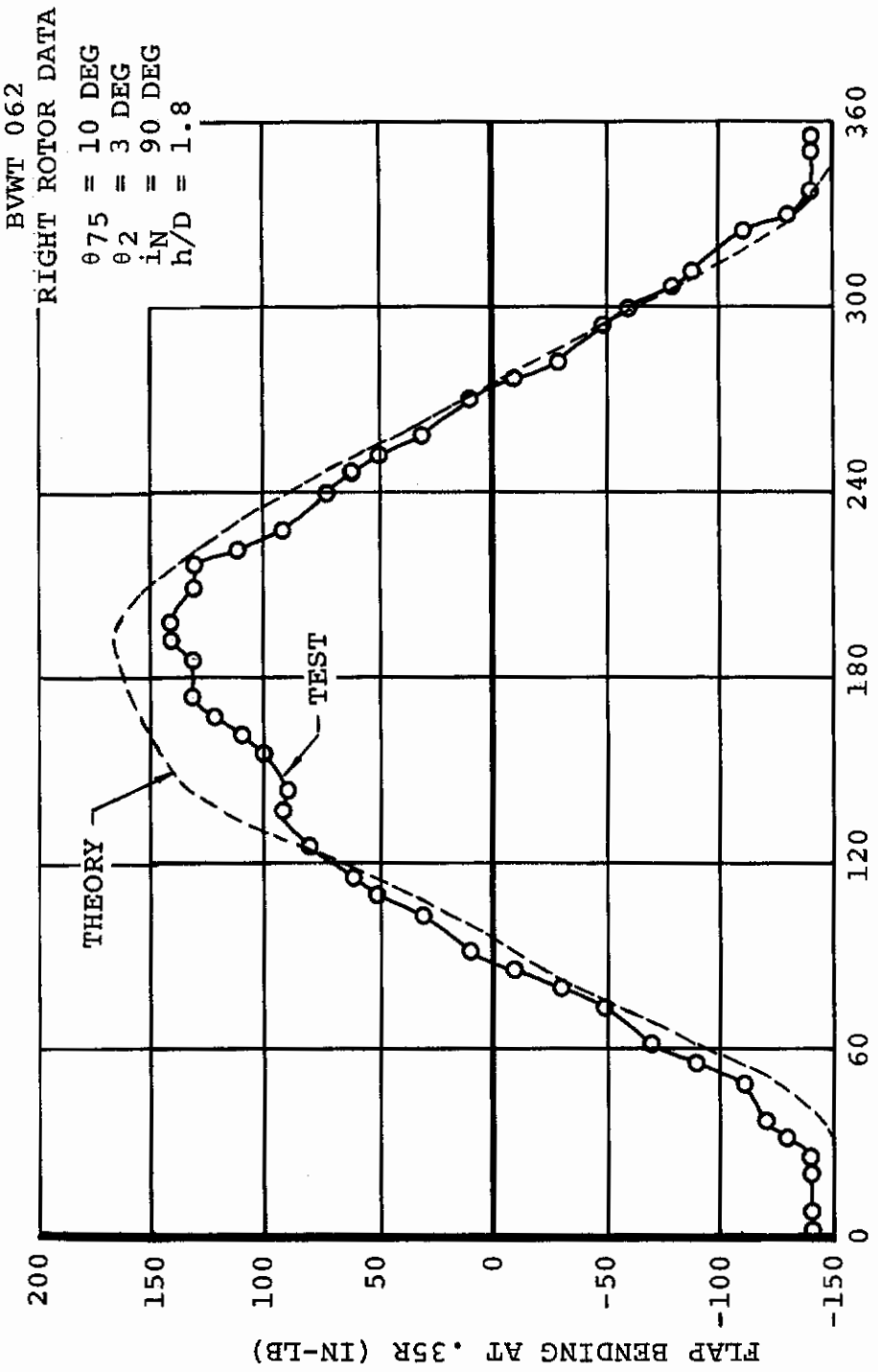

Figure 59. Model 160 Performance Model, Predicted and Measured Flap Bending Waveform in Hover for 3 Degrees Cyclic at 2,300 RPM

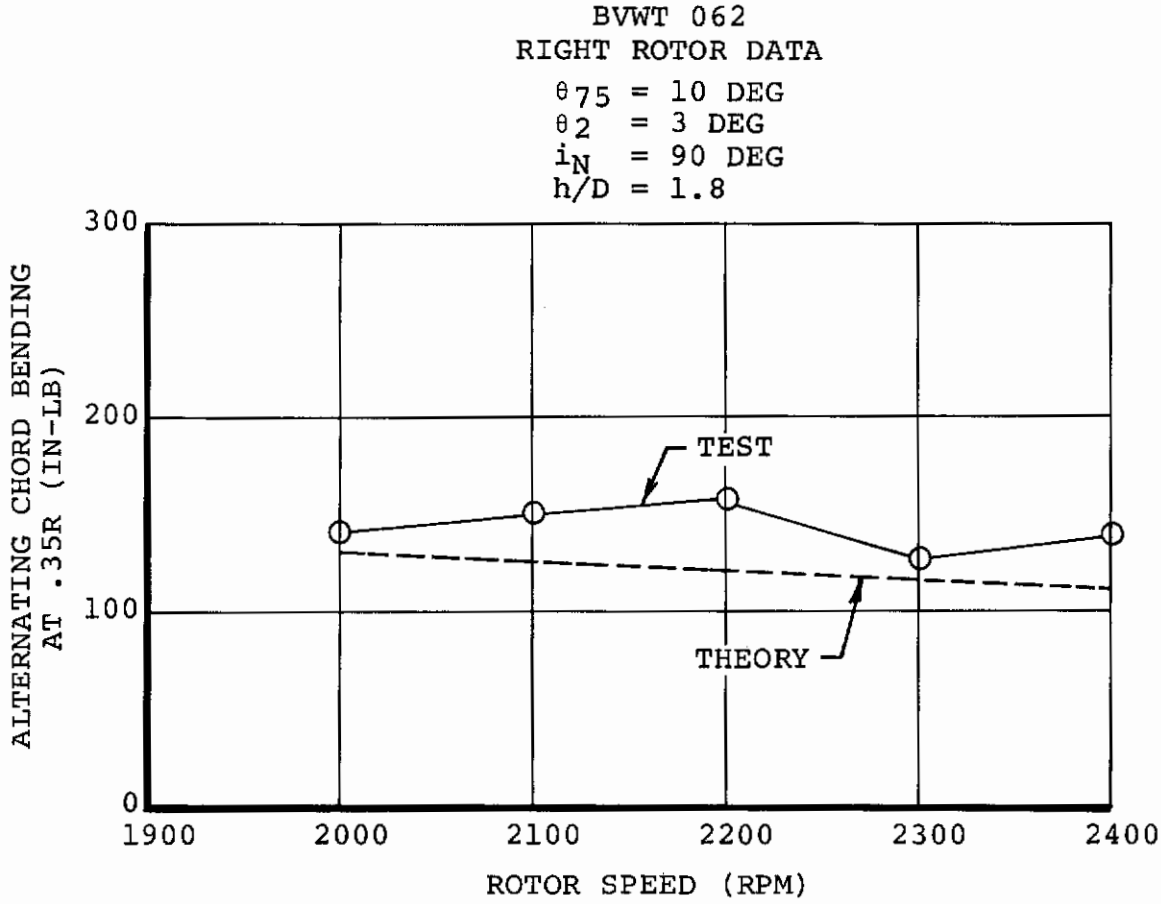

Figure 60. Model 160 Performance Model, Predicted and Measured Alternating Chord Bending Moment in Hover for 3 Degrees Cyclic Pitch

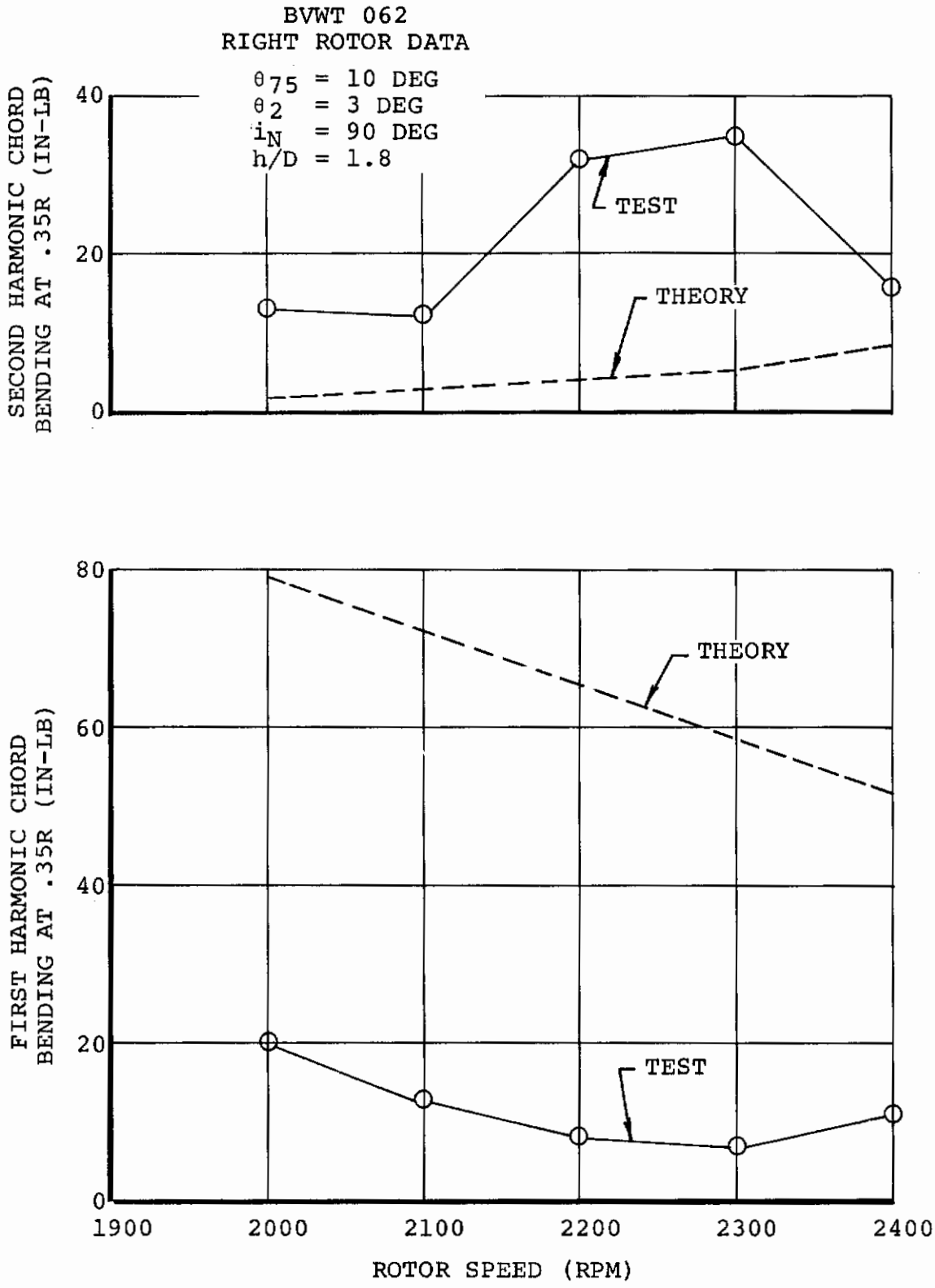

Figure 61. Model 160 Performance Model, Predicted and Measured First-and Second-Harmonic Chord Bending Moment in Hover for 3 Degrees Cyclic Pitch

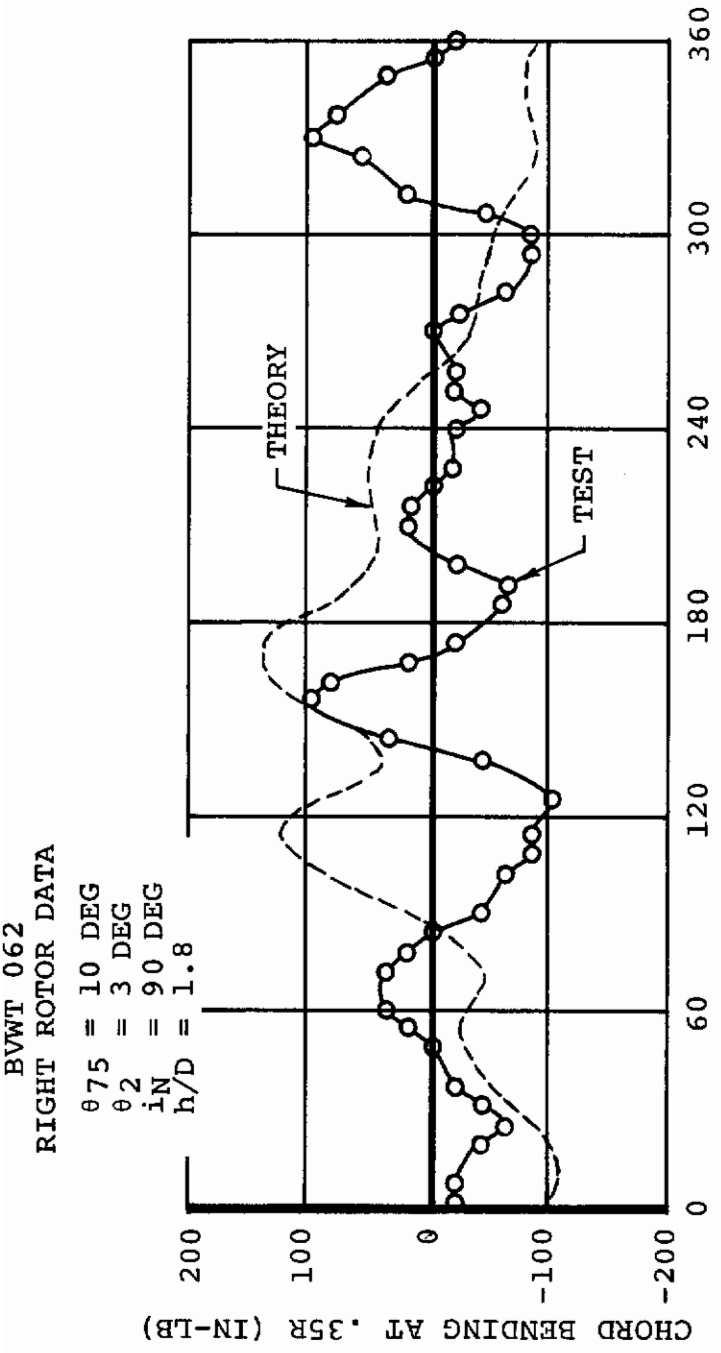

Figure 62. Model 160 Performance Model, Predicted and Measured Chord Bending Waveform in Hover for 3 Degrees Cyclic at 2,300 RPM

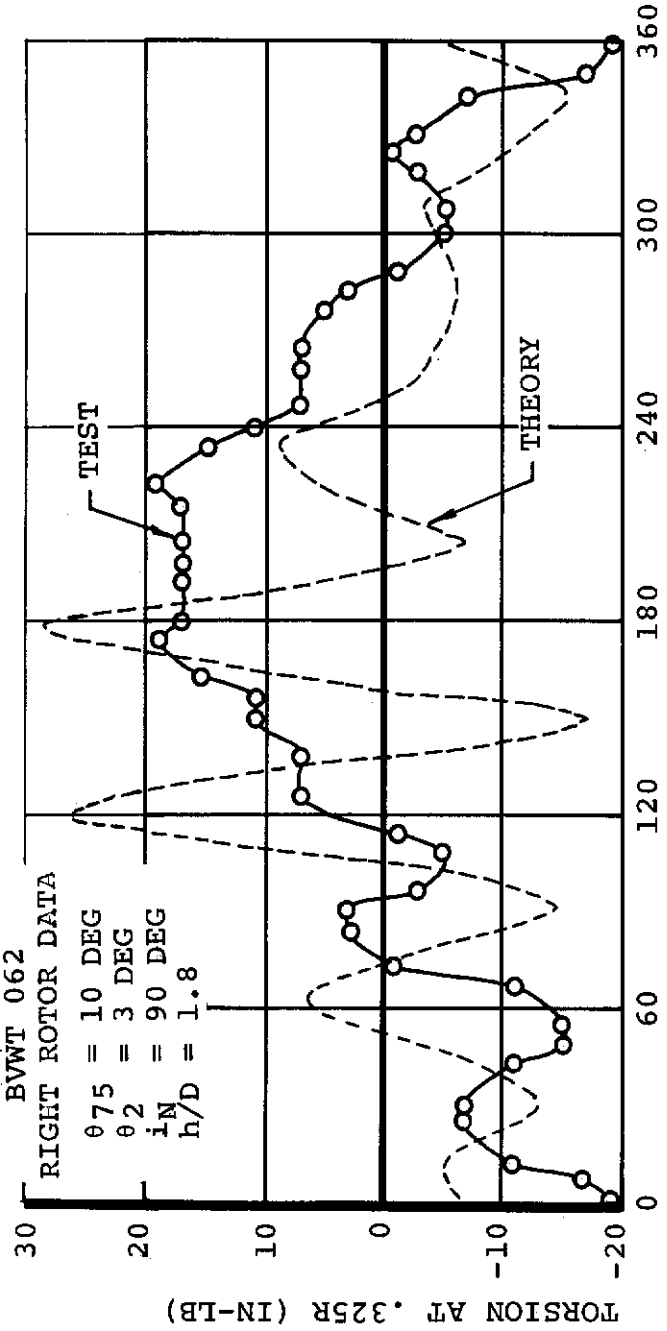

Figure 63. Model 160 Performance Model, Predicted and Measured Blade Torsional Waveform in Hover for 3 Degrees Cyclic at 2,300 RPM

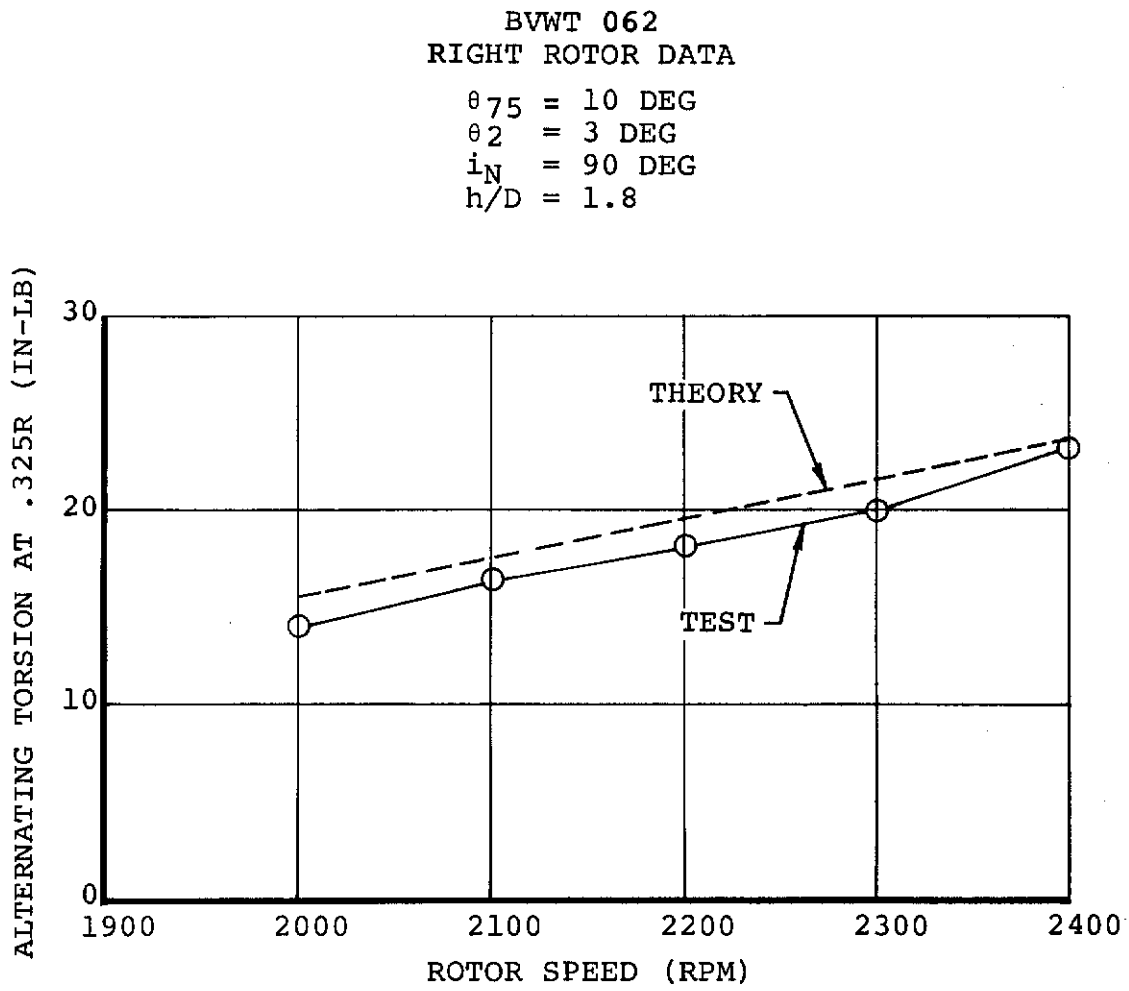

Figure 64. Model 160 Performance Model, Predicted and Measured Alternating Torsion in Hover for 3 Degrees Cyclic Pitch

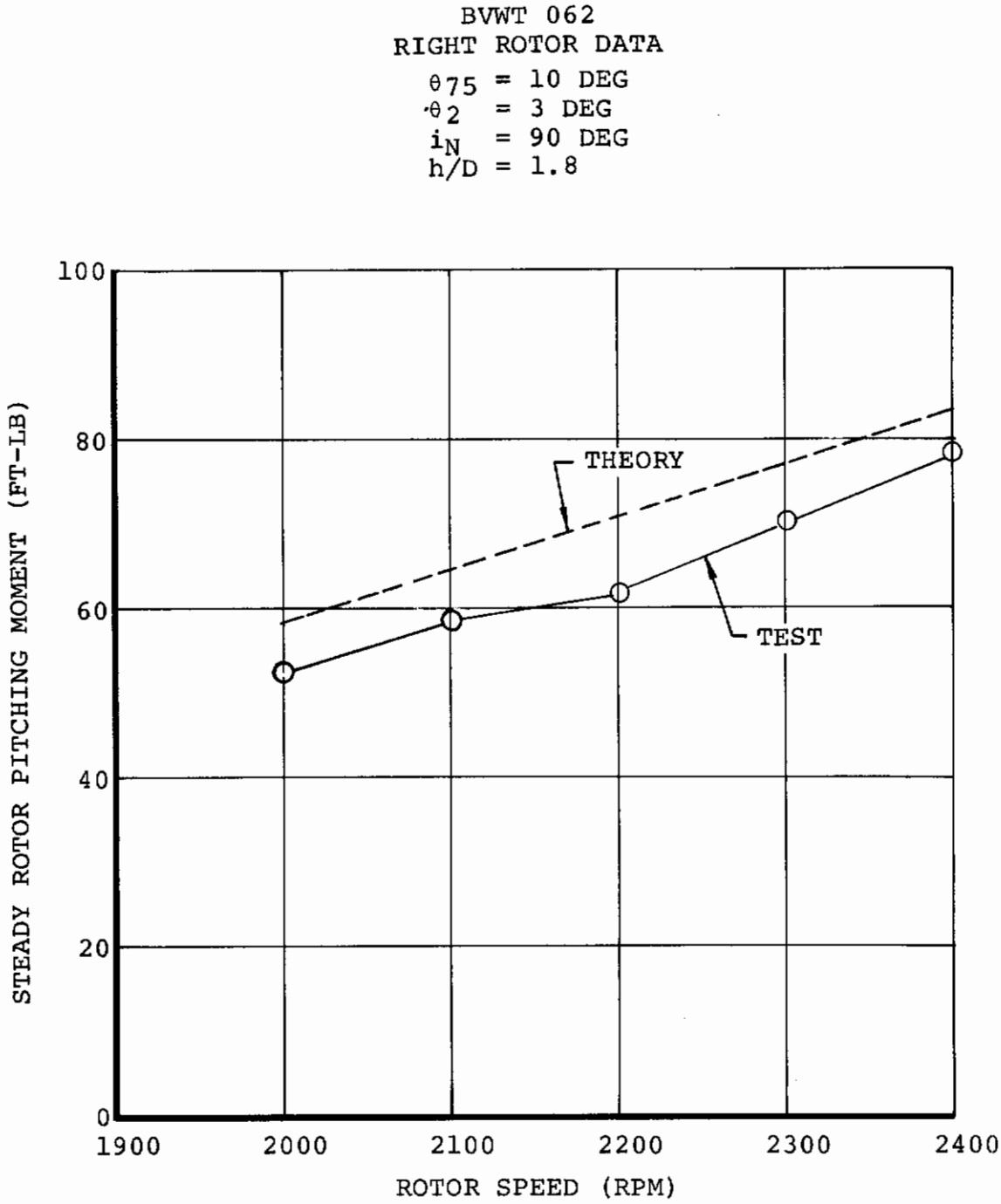

Figure 65. Model 160 Performance Model, Predicted and Measured Steady Rotor Pitching Moment in Hover for 3 Degrees Cyclic Pitch

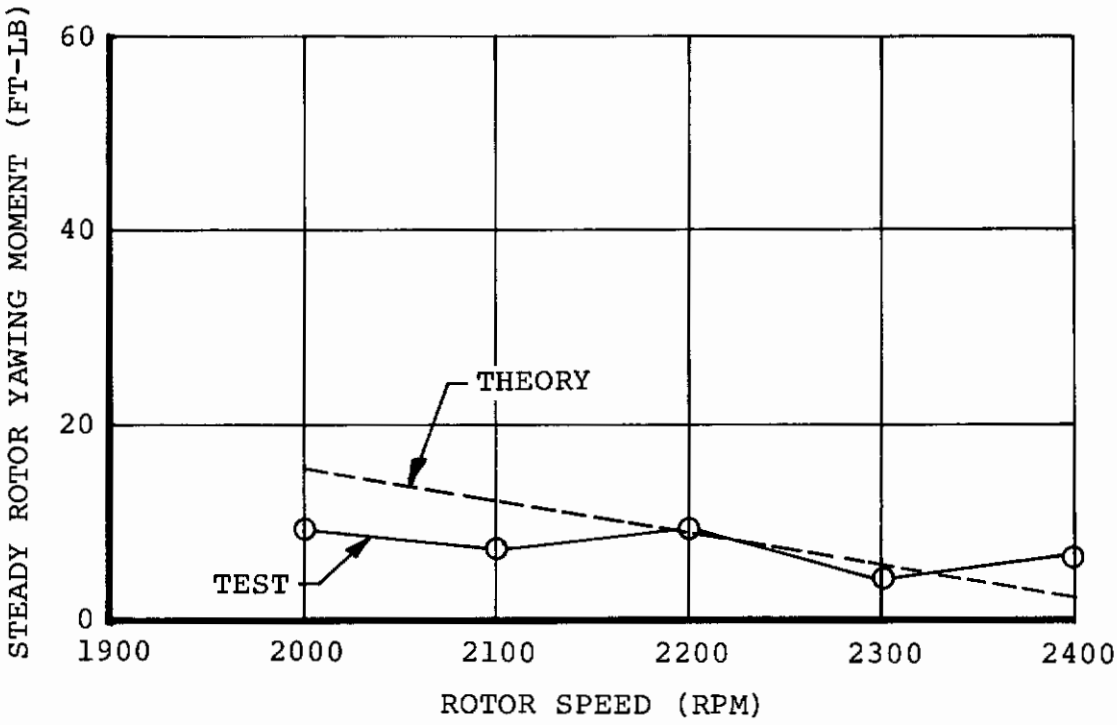

Figure 66. Model 160 Performance Model, Predicted and Measured Alternating Flap Bending Moment in Hover for 3 Degrees Cyclic Pitch

Powered Cruise

Test data from the 1/3-scale LIT rotor was used for correlation in powered cruise. The rotor shaft was horizontal in a propeller configuration with rotor thrust producing the total propulsive force. Rotor angle of attack was varied with all other parameters remaining constant. The results of the powered cruise correlation are shown in Figures 67 through 76. Alternating blade root flap bending, chord bending, and torsion correlation (Figures 67, 68, and 69) are very good, with the analysis predicting within at least 5 percent of the measured bending moment data and within 15 percent of the measured blade root torsion. Correlation with the first and second bending moment harmonics (Figures 70 and 71) is also very good for first-harmonic flap and chord bending. The analysis underpredicts second-harmonic flap and chord bending. Interference due to wing circulation probably induced measured higher-harmonic bending moments, and this effect was not included in the analysis predictions. Correlation results for bending moment and blade torsion waveforms (Figures 72, 73, and 74) are very good. The analysis predicts the correct amplitude for flap, chord, and torsion, but the phase of the predicted first-harmonic contribution is shifted by about 30 degrees. The analysis predicts peak moments to occur at 90 degrees, whereas test data peaks at about 120 degrees. The impact of the phase shift on steady hub moments is large as shown in the hub moment correlation in Figures 75 and 76. The analysis underpredicts steady rotor pitching moment by a large margin but correlates very well with rotor yawing moment. A steady pitching moment pitches the aircraft nose up and a yawing moment yaws the aircraft in cruise.

The poor pitching moment correlation can be traced to the source of its forcing. The sources of rotor pitching moment and yawing moment are independent of each other due to the dynamic response characteristics of the blades. Since the blade first-flapping frequency ratio is so high ($\omega/\Omega = 2.7$), the flapping phase lag is only 10 degrees. Therefore the blade response to 1-per-rev forcing is nearly in phase with the force. This implies that rotor inflow induced by rotor angle of attack will produce only lateral 1-per-rev flapping and therefore a pure rotor yawing moment. Likewise, cyclic phased 170 degrees from downwind will produce only longitudinal flapping and therefore a pure rotor pitching moment; therefore the source of the poor pitching moment correlation must be due to cyclic. The very good pitching moment correlation in hover due to cyclic for this rotor demonstrated the capability of the analysis to predict rotor pitching moment due to cyclic, and therefore the measured cyclic which was input in the analysis is suspected to be incorrect. This is plausible since a small amount of cyclic has a large impact on rotor pitching moment. As shown in Figure 55, one degree of cyclic produces

150 foot-pounds of steady pitching moment and moment sensitivity to cyclic is even greater in cruise.

Summarizing the powered cruise correlation, the results are very encouraging since the analysis demonstrated a very good capability to predict rotor loads for a condition in which the flapwise and chordwise modes are highly coupled. Due to the high collective pitch required for cruise flight (in this case, 38 degrees), the modes become more highly coupled and aerodynamic damping plays a greater roll in the response of both flapping and lagging. Use of an uncoupled analysis for rotor loads predictions would provide at best crude approximations in cruise, particularly for chord bending, and the cruise correlation results demonstrate the quality of predictions that can be obtained when the modes are fully coupled.

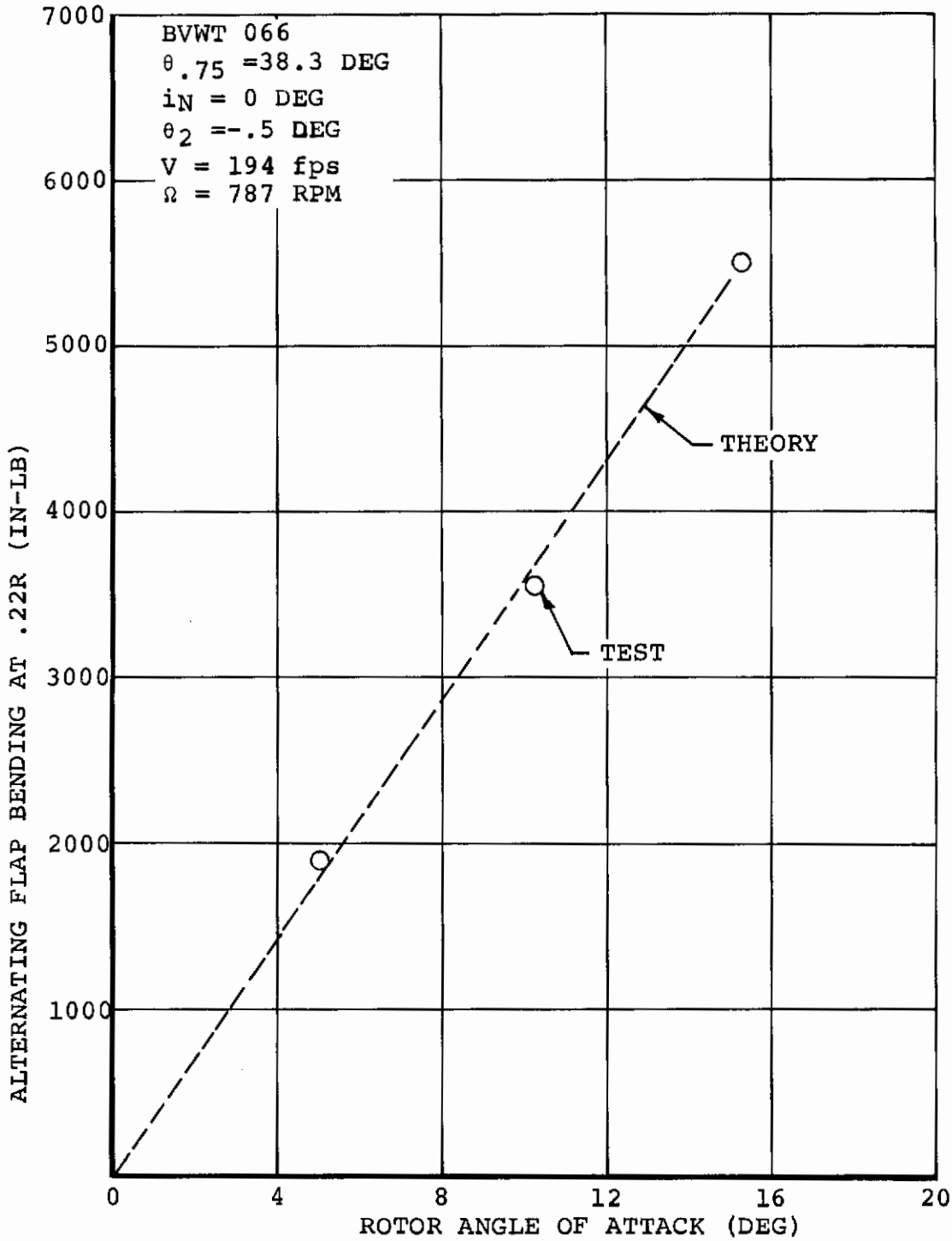

Figure 67. 1/3-Scale LIT Blade, Predicted and Measured Alternating Flap Bending Due to Rotor Angle of Attack in Cruise

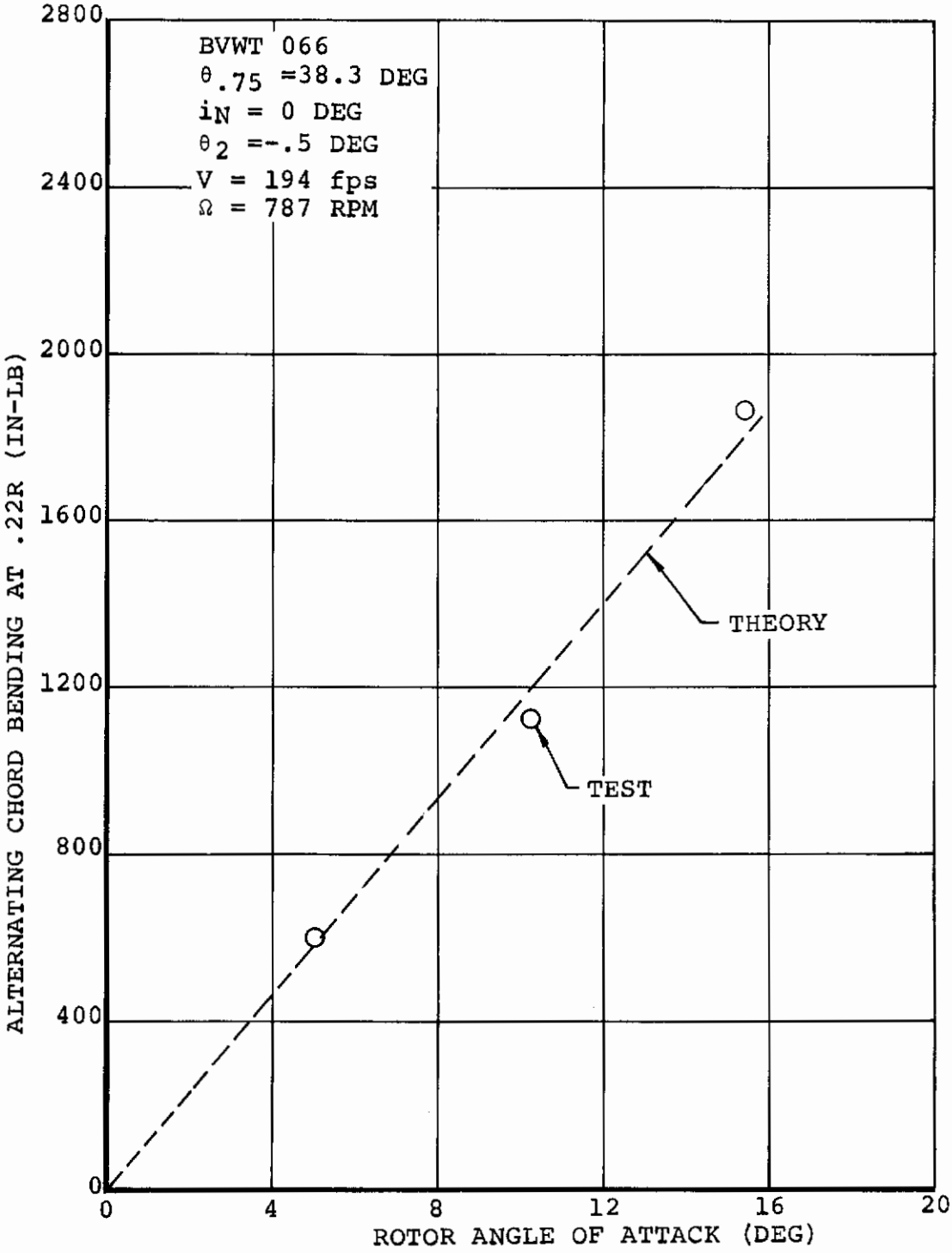

Figure 68. 1/3-Scale LIT Blade, Predicted and Measured Alternating Chord Bending Due to Rotor Angle of Attack in Cruise

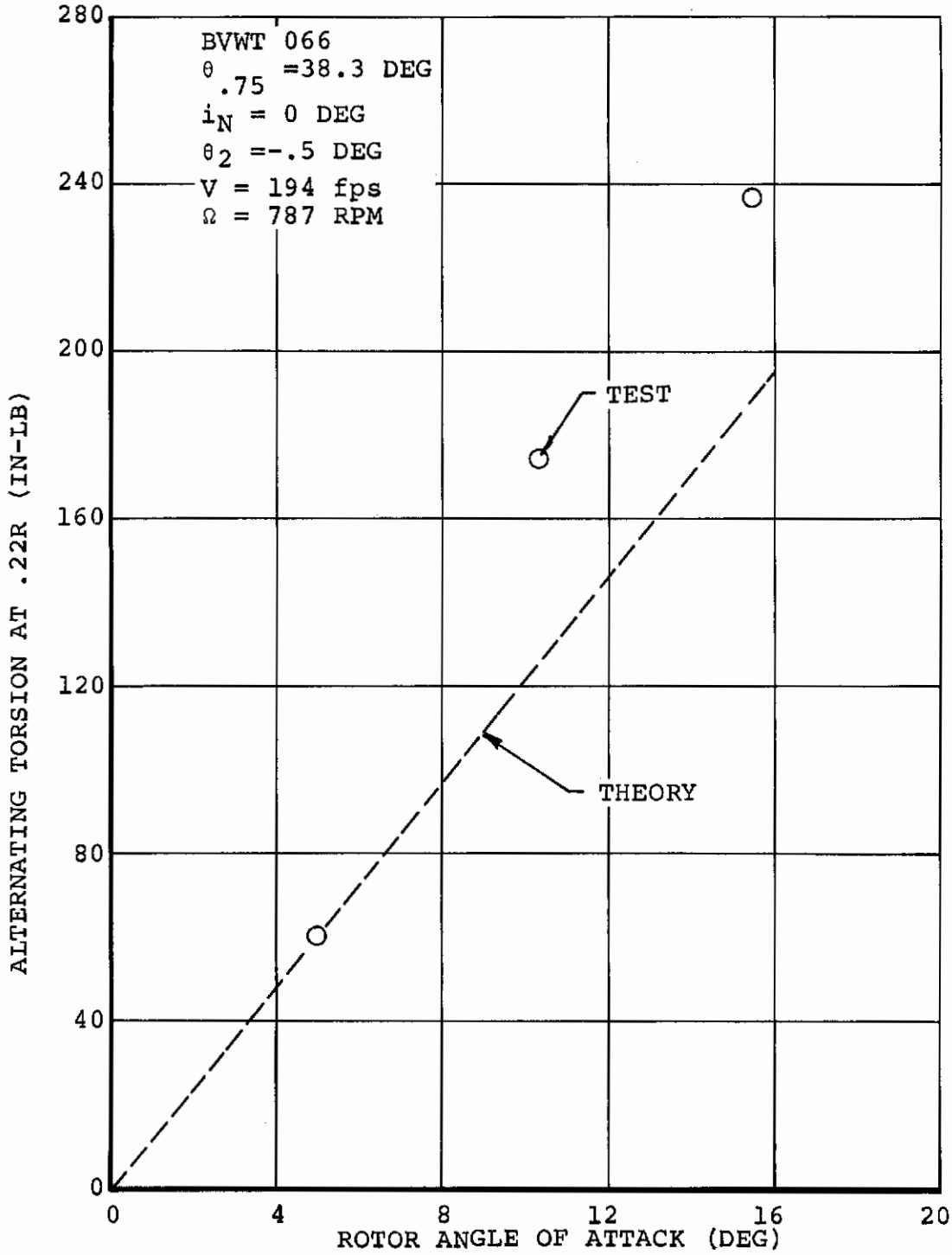

Figure 69. 1/3-Scale LIT Blade, Predicted and Measured Alternating Torsion Due to Rotor Angle of Attack in Cruise

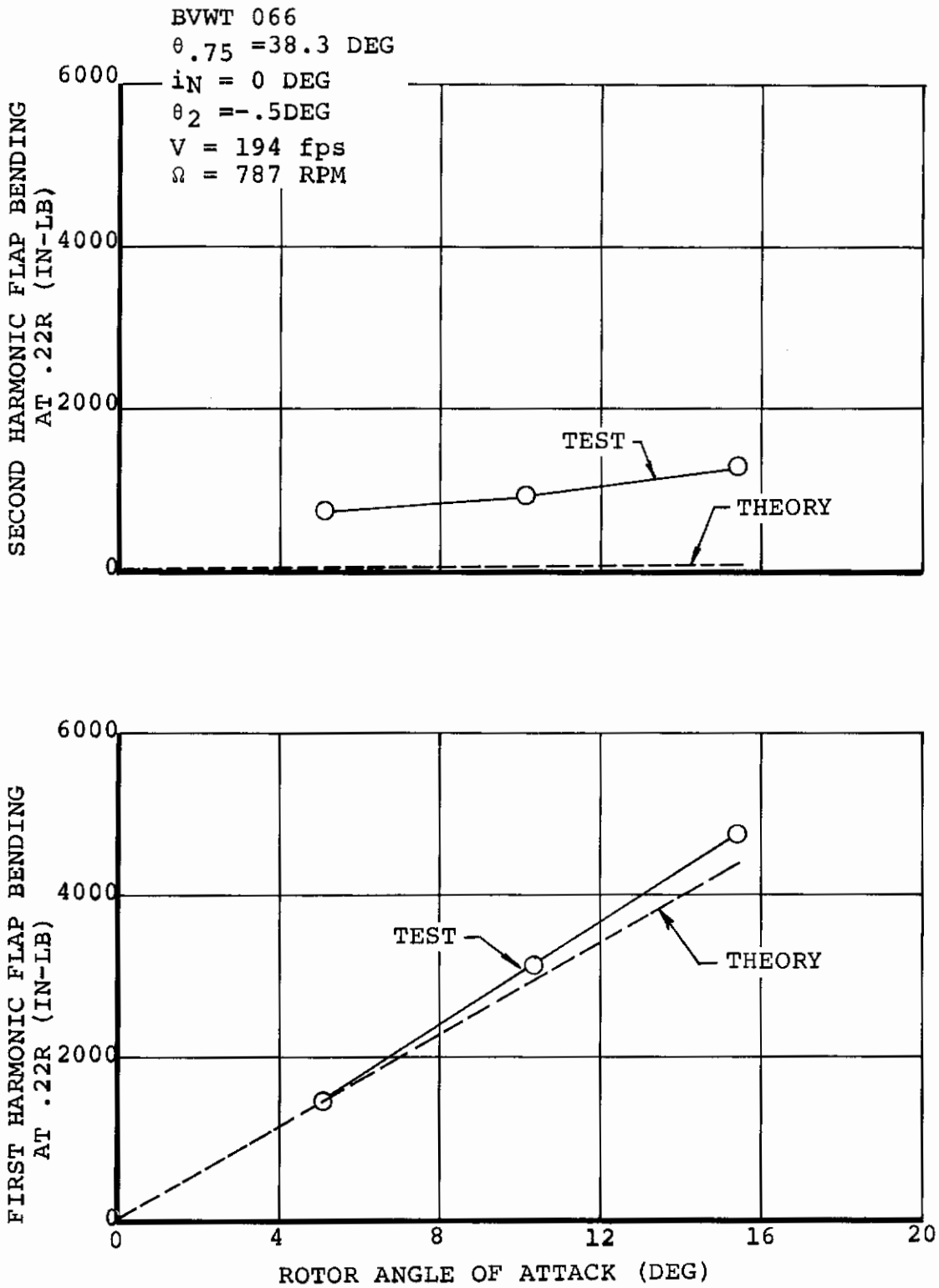

Figure 70. 1/3-Scale LIT Blade, Predicted and Measured First- and Second-Harmonic Flap Bending Due to Rotor Angle of Attack in Cruise

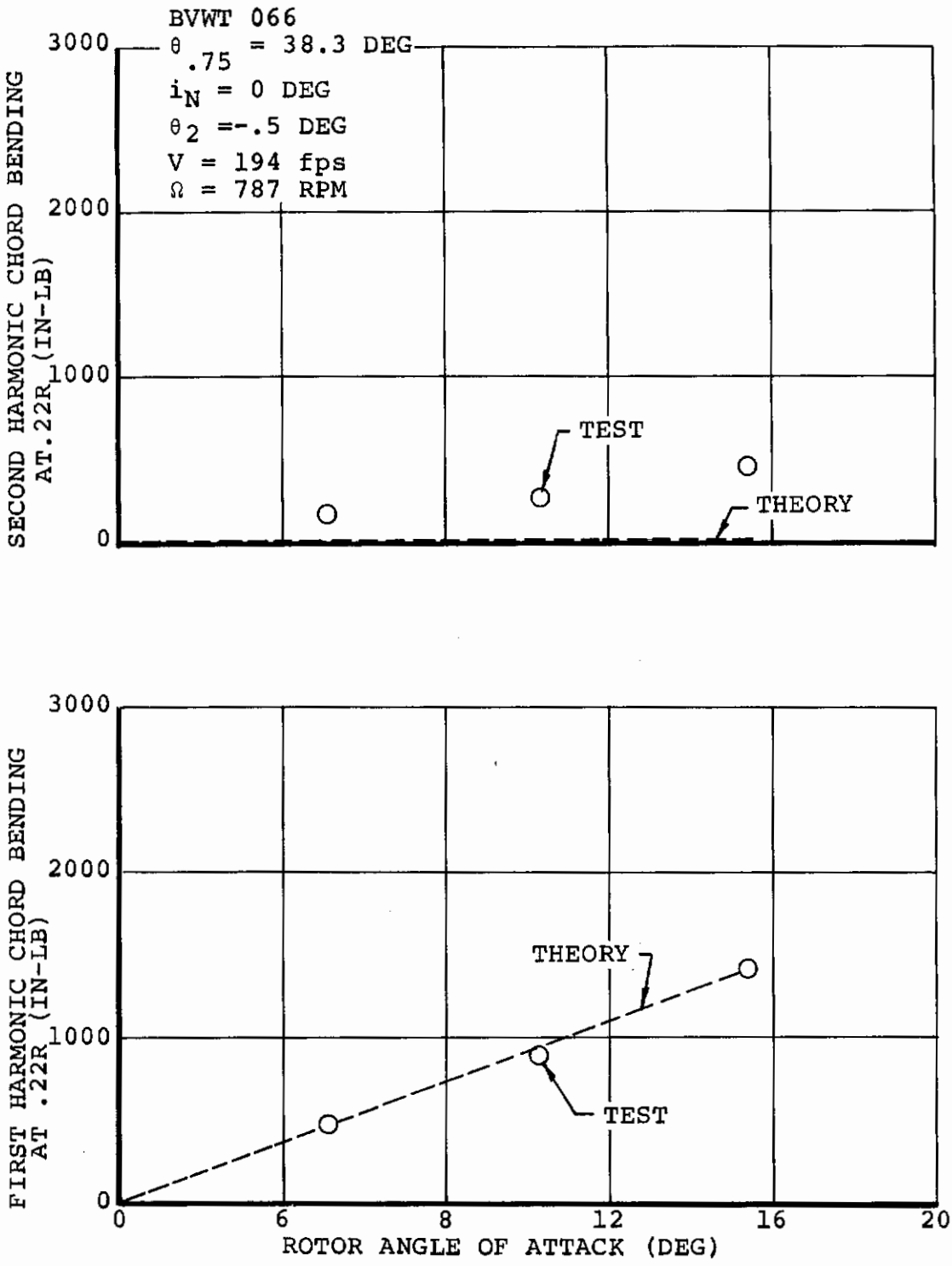

Figure 71. 1/3-Scale LIT Blade, Predicted and Measured First- and Second-Harmonic Chord Bending Due to Rotor Angle of Attack in Cruise

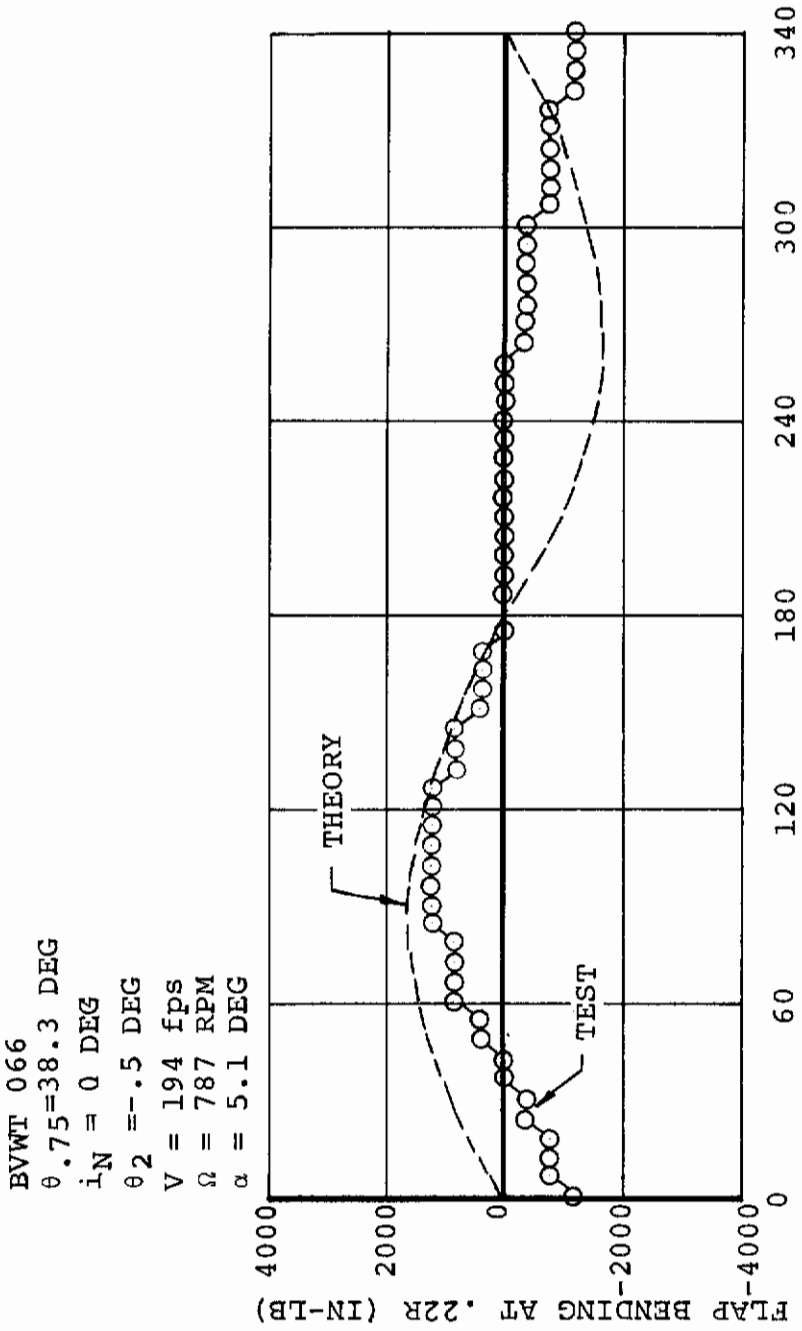

Figure 72. 1/3-Scale LIT Blade, Predicted and Measured Flap Bending Waveform for 5.1 Degrees Angle of Attack in Cruise

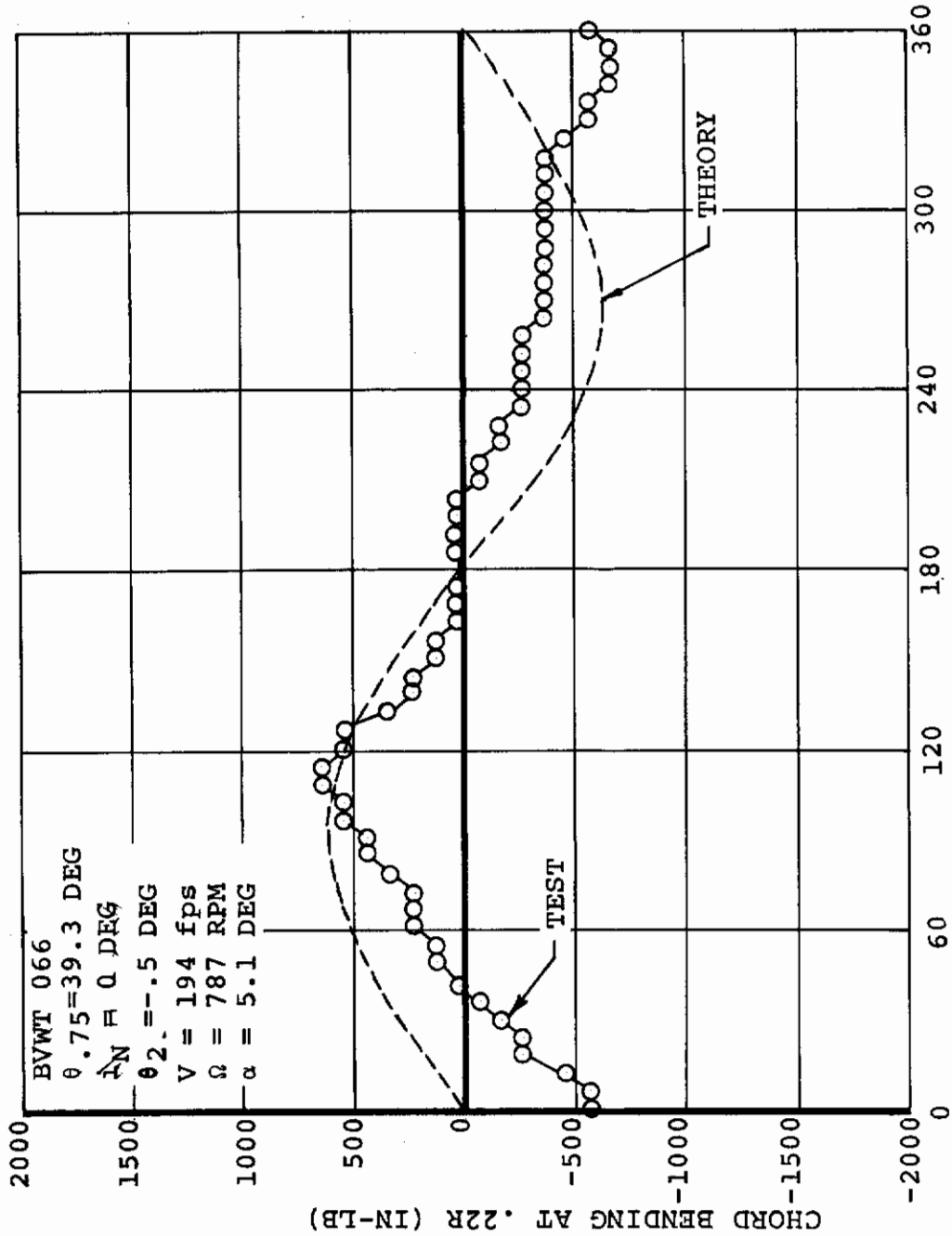

Figure 73. 1/3-Scale LIT Blade, Predicted and Measured Chord Bending Waveform for 5.1 Degrees Angle of Attack in Cruise

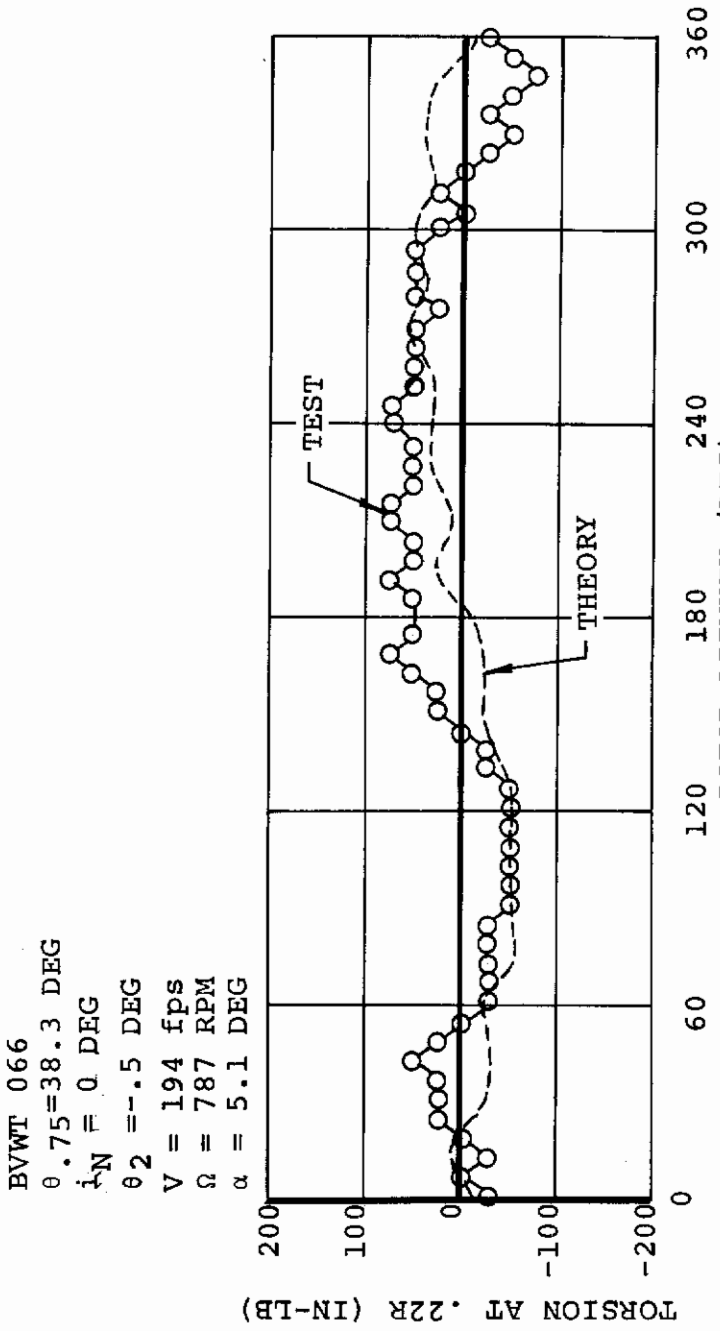

Figure 74. 1/3-Scale LIT Blade, Predicted and Measured Torsional Waveform for 5.1 Degrees Angle of Attack in Cruise

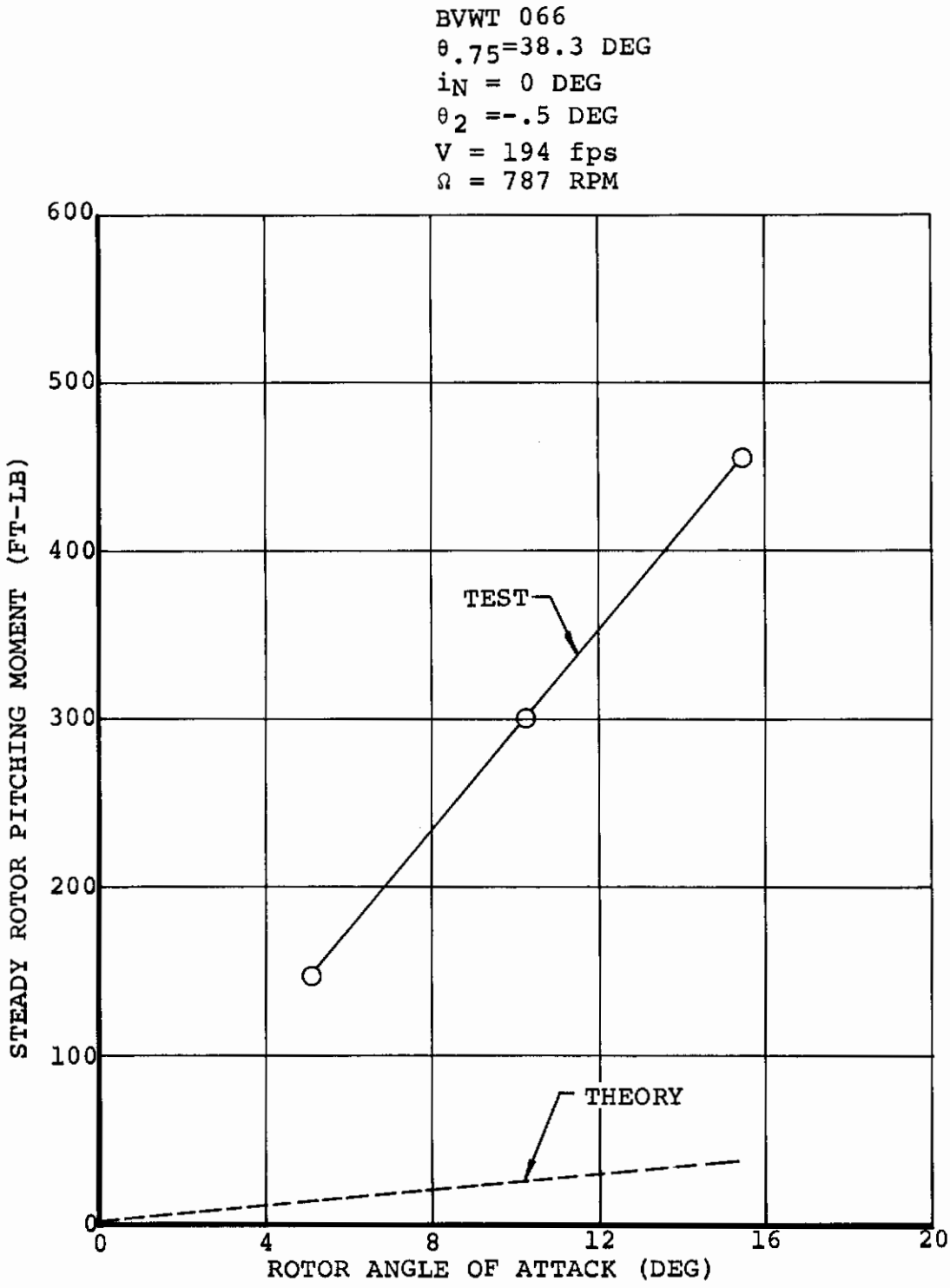

Figure 75. 1/3-Scale LIT Blade, Predicted and Measured Steady Rotor Pitching Moment Due to Rotor Angle of Attack in Cruise

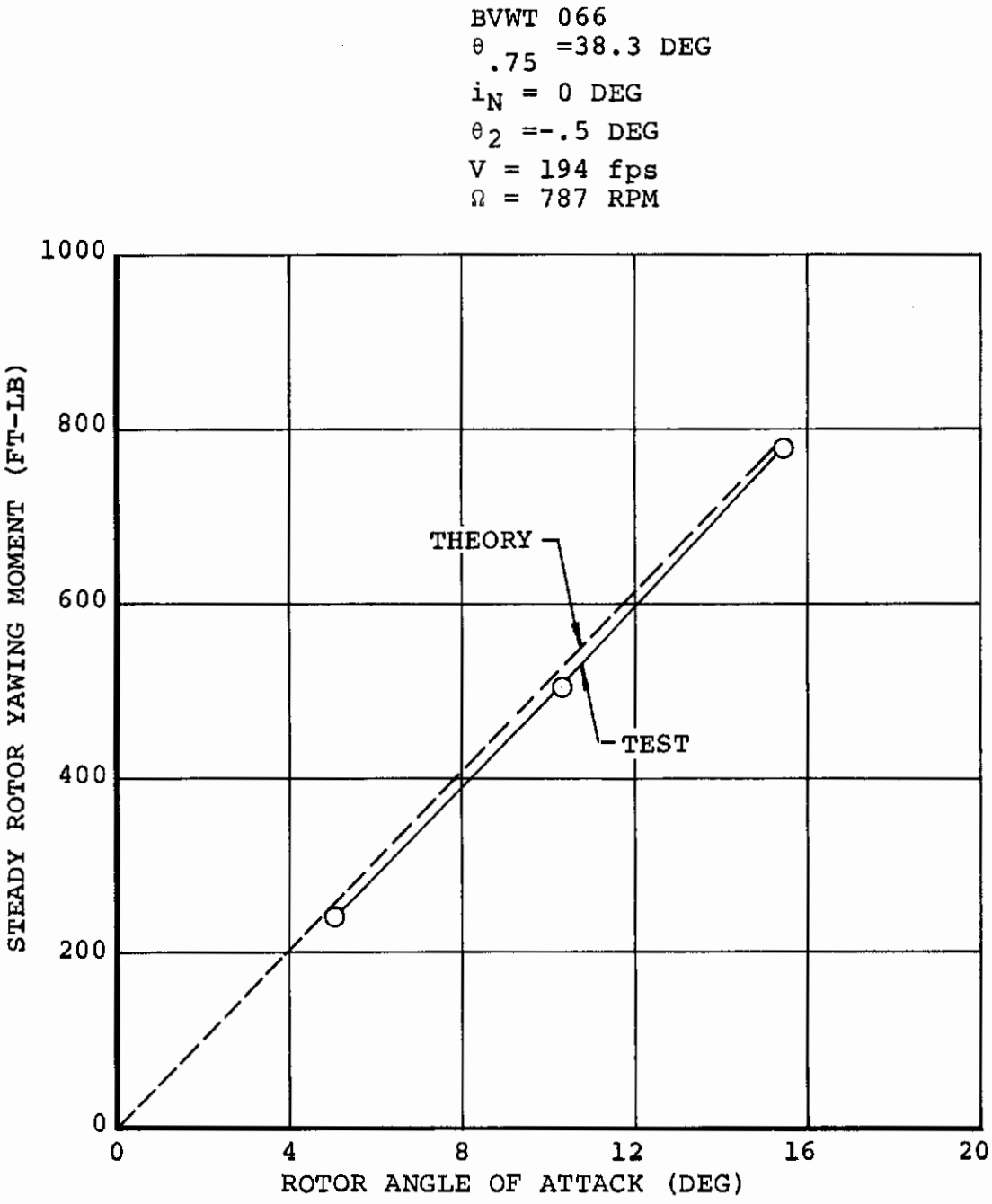

Figure 76. 1/3-Scale LIT Blade, Predicted and Measured Steady Rotor Yawing Moment Due to Rotor Angle of Attack in Cruise

Windmilling Cruise

Figures 77 through 83 are the cruise correlation results for the 1/9-scale conversion model. As mentioned in the introduction, this model is a 1/9-scale, half-span model of a Boeing-Vertol stowed-rotor aircraft design. The 4-bladed rotor is Froude-scaled, as is the wing, and the rotor is unpowered. The blades are soft in plane with a first chordwise frequency ratio of 0.75 ω/Ω at cruise rpm. Windmilling is produced by changing blade collective pitch. Rotor loads data were taken at a cruise condition which simulated the end of transition flight. On a full-scale design, the aircraft would now be jet-powered with the rotors windmilling and ready for stowing. The model rotor angle of attack was varied, with tunnel speed and rotor speed being held constant.

The blade root flap bending correlation in Figure 77 shows that the analysis correctly predicts the slope of first-harmonic flap bending with rotor angle of attack, but the predicted magnitude is high on a point-to-point correlation basis. No explanation can be given for the overprediction, but the good correlation of flap bending moment per degree of angle of attack is encouraging. The analysis underpredicts second-harmonic flap bending, showing very little 2-per-rev response. Second-harmonic flap bending was also underpredicted for the 1/3-scale LIT rotor in cruise and, as for that rotor, the large measured value of 2-per-rev flap bending is suspected to be due to wing interference effects. Correlation with the flap bending waveform in Figure 78 shows the analysis overpredicts in amplitude but agrees well in phase with the measured first-harmonic content. Chord bending correlation results are presented in Figure 79. The analysis correctly predicts the trend of first-harmonic chord bending with rotor angle of attack but overpredicts the magnitude. The reason for this is not known. Like the flap bending correlation, the analysis also underpredicts second-harmonic chord bending; this is attributed to wing interference effects on the measured chord bending. Correlation with the measured chord bending waveform in Figure 80 is good, both in amplitude and phase.

Correlation with alternating blade root torsion is shown in Figure 81. The analysis overpredicts by a large margin, probably due to an incorrect torsional root spring description. Blade pitch on this rotor was controlled by a worm gear in the center of the hub to which all 4 blades were geared. This type of pitch control was used instead of the standard swashplate configuration to attain a rapid and equal rate of change of collective on the rotor. The torsional root spring due to the gearing could not be accurately calculated and therefore an estimation was made.

Correlation with steady rotor in-plane moments due to rotor angle of attack is shown in Figures 82 and 83. Both pitching moment and yawing moment correlate well with the measured data.

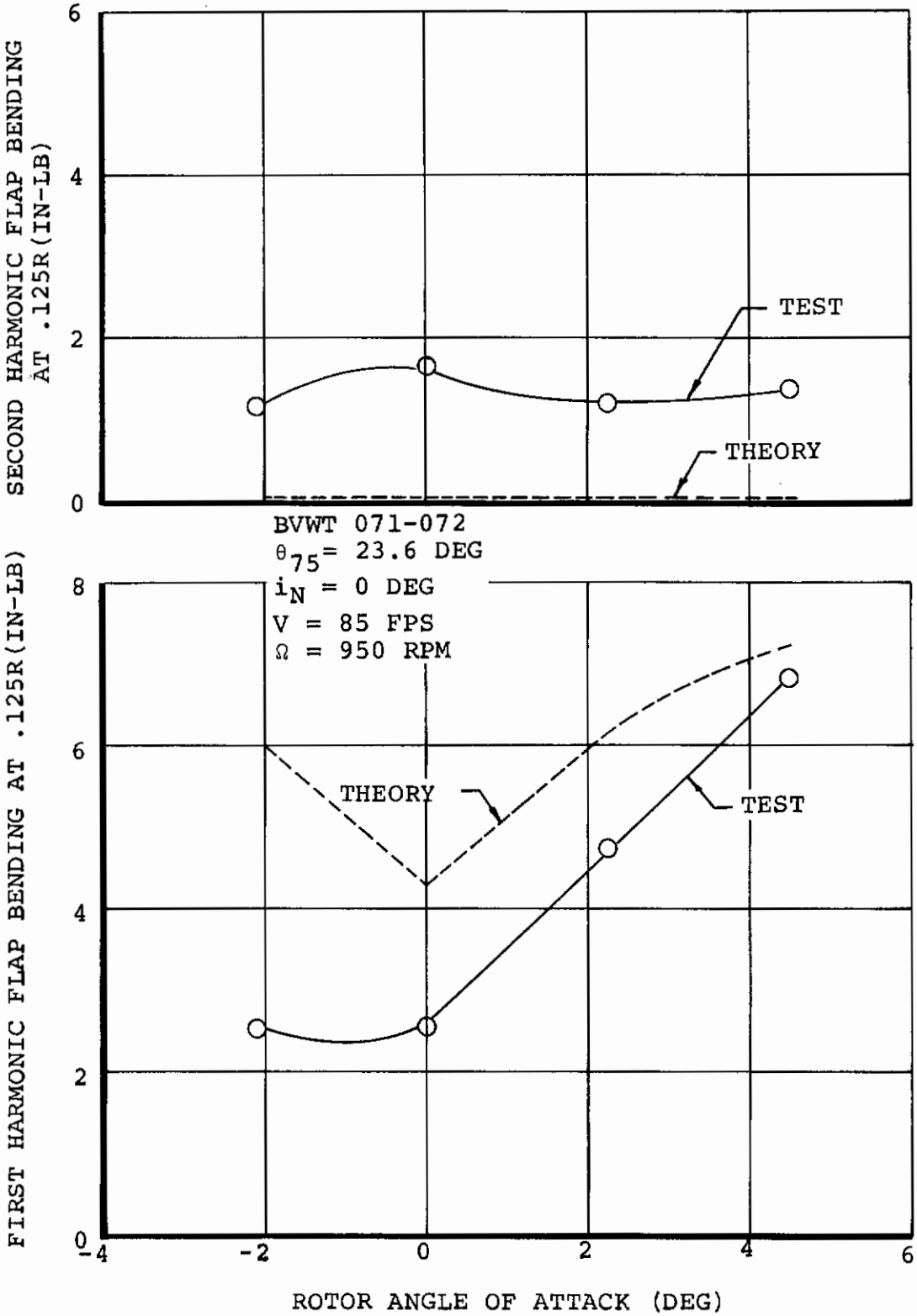

Figure 77. Model 213 1/9-Scale Conversion Model, Predicted and Measured First- and Second-Harmonic Flap Bending at 0.125R Due to Rotor Angle of Attack in Cruise

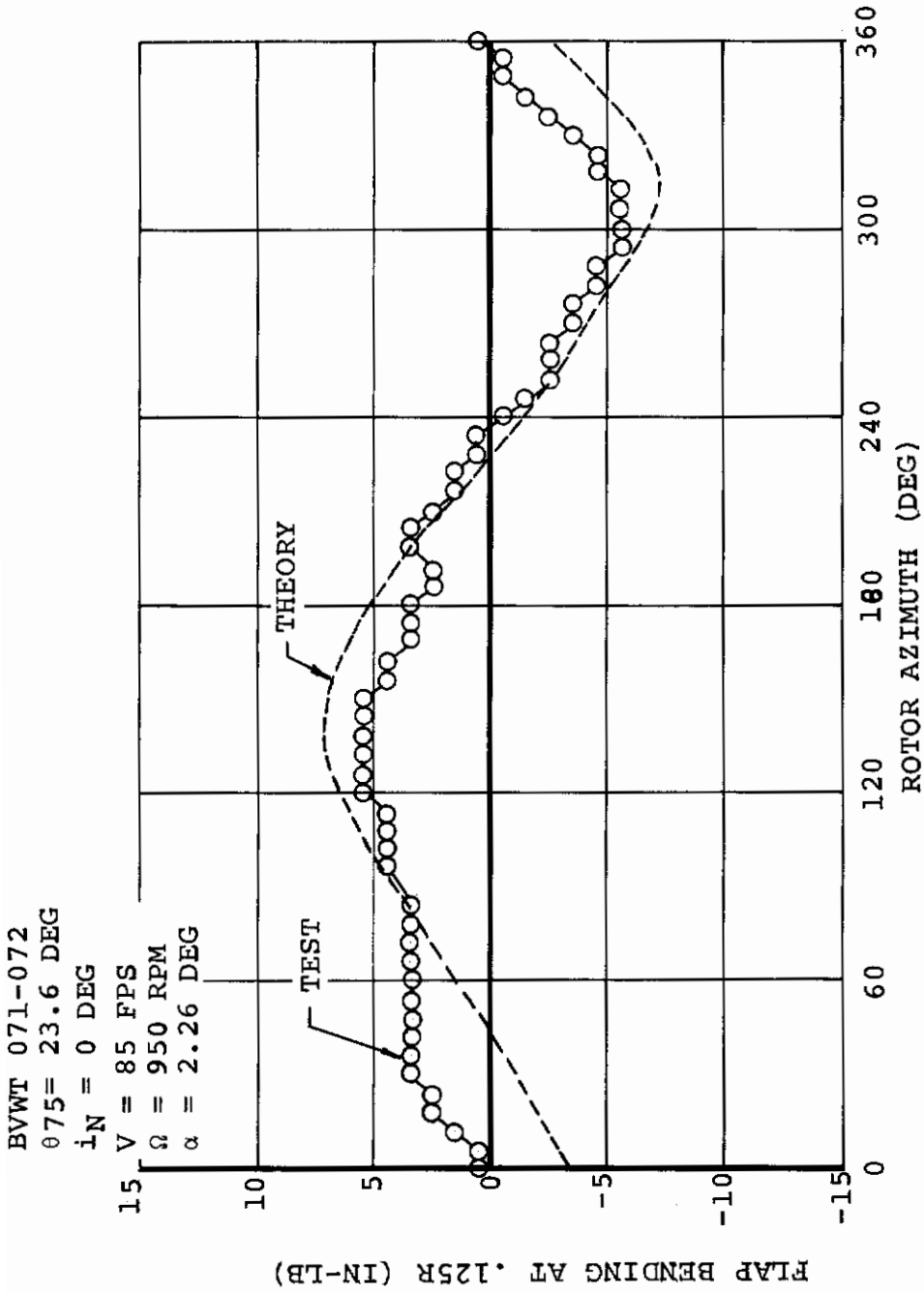

Figure 78. Model 213 1/9-Scale Conversion Model, Predicted and Measured Flap Bending Waveform at 0.125R for 2.26 Degrees Rotor Angle of Attack in Cruise

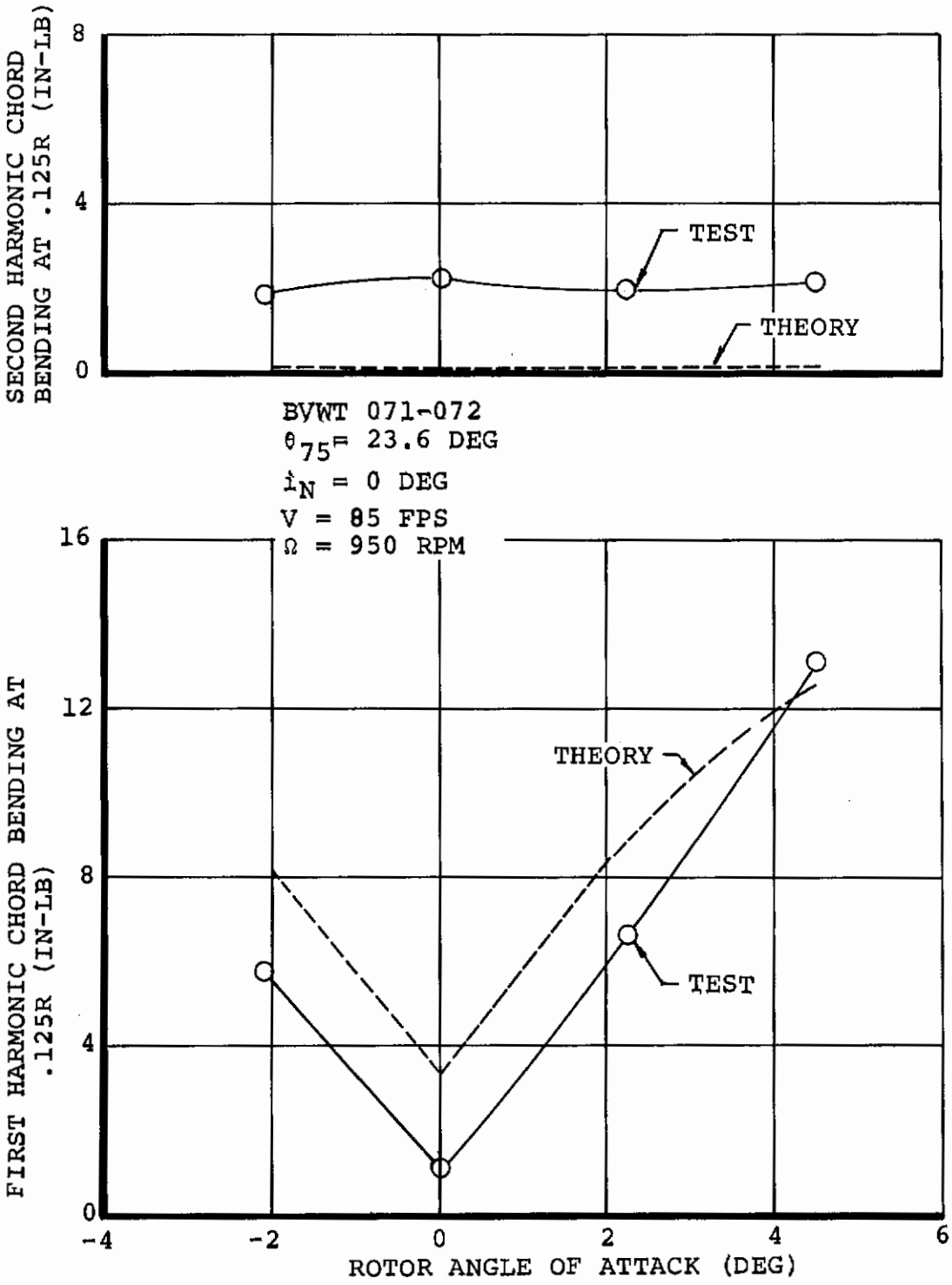

Figure 79. Model 213 1/9-Scale Conversion Model, Predicted and Measured First- and Second-Harmonic Chord Bending at 0.125R Due to Rotor Angle of Attack in Cruise

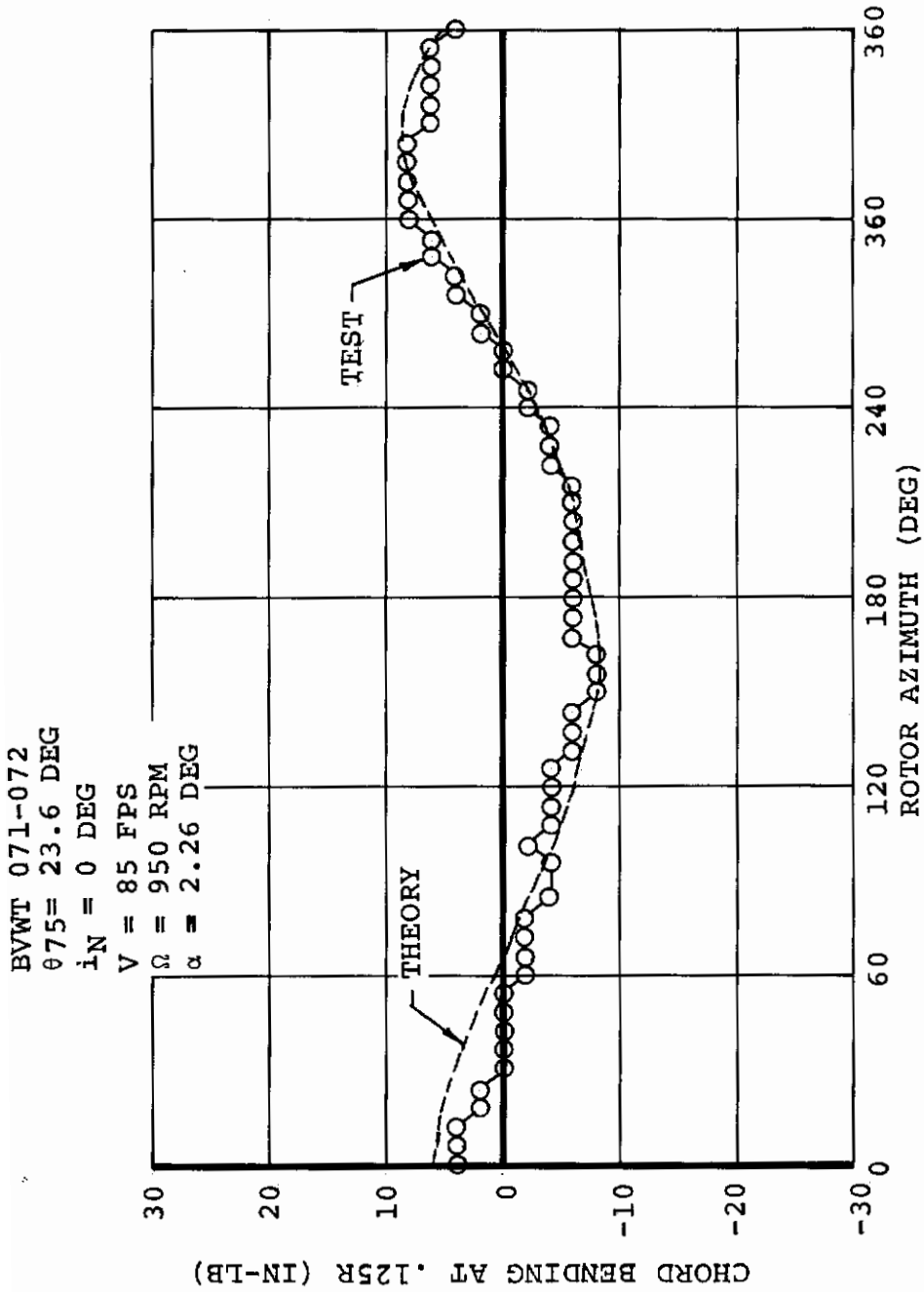

Figure 80. Model 213 1/9-Scale Conversion Model, Predicted and Measured Chord Bending Waveform at 0.125R for 2.26 Degrees Rotor Angle of Attack in Cruise

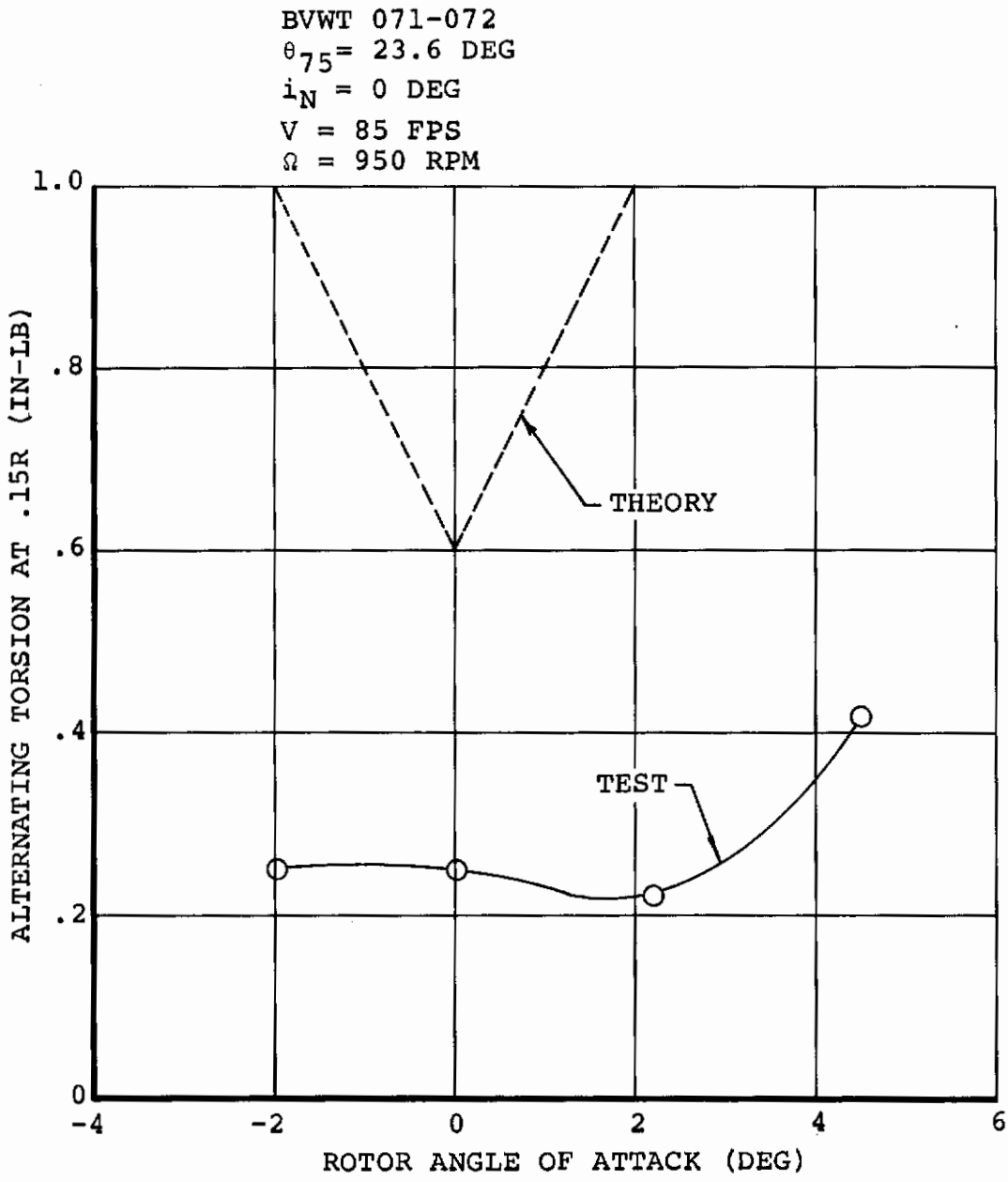

Figure 81. Model 213 1/9-Scale Conversion Model, Predicted and Measured Alternating Torsion at 0.150R Due to Rotor Angle of Attack in Cruise

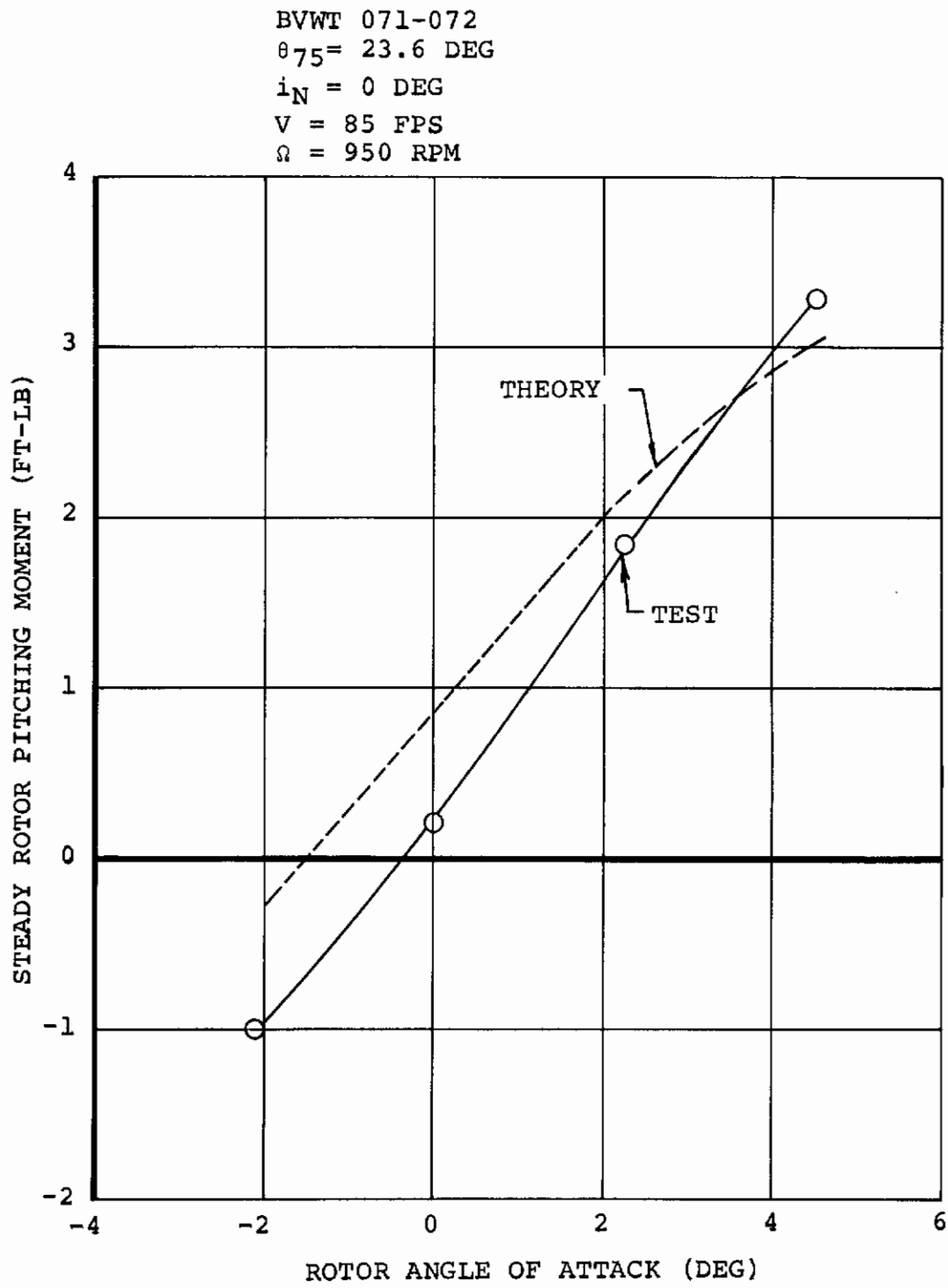

Figure 82. Model 213 1/9-Scale Conversion Model, Predicted and Measured Steady Rotor Pitching Moment Due to Rotor Angle of Attack in Cruise

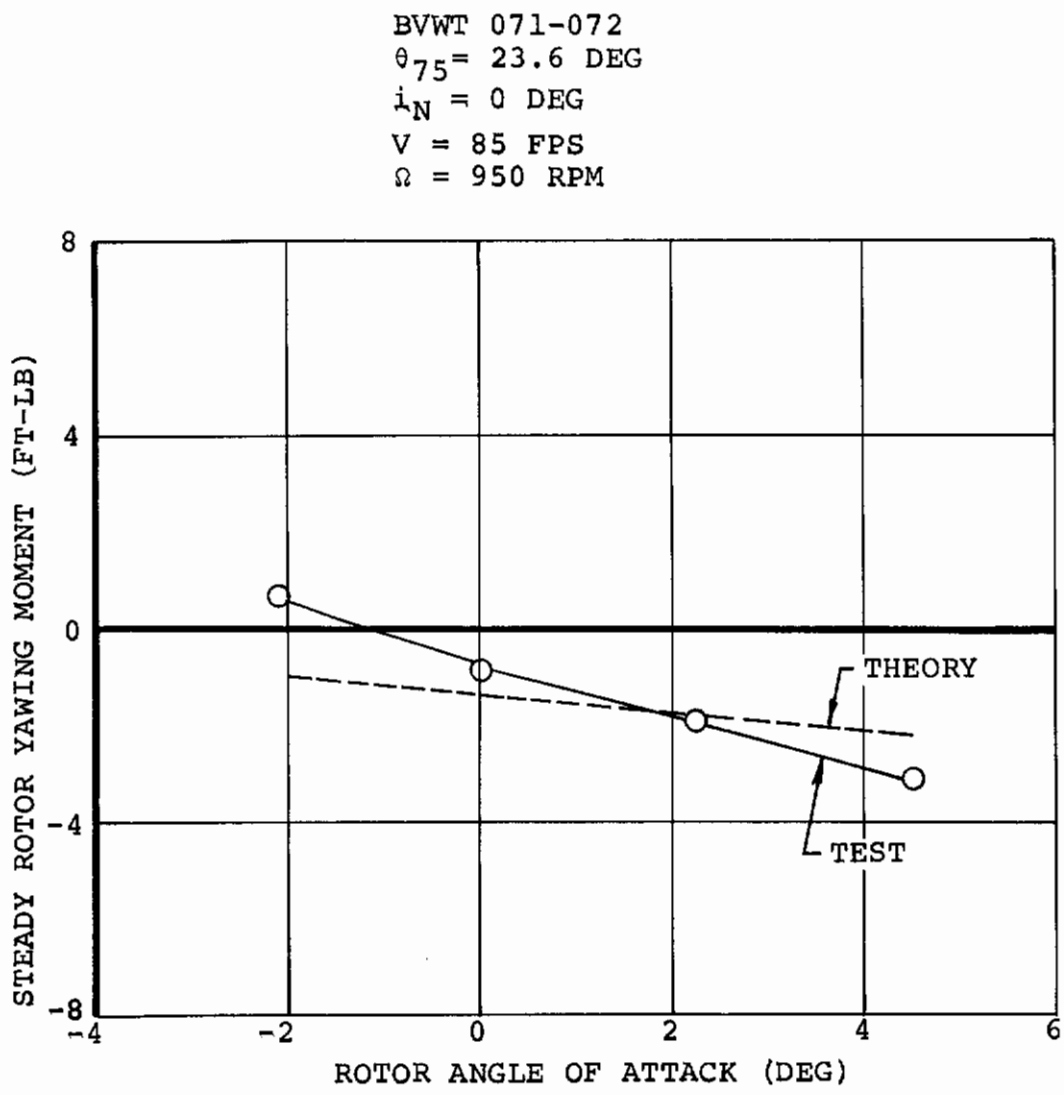

Figure 83. Model 213 1/9-Scale Conversion Model, Predicted and Measured Steady Rotor Yawing Moment Due to Rotor Angle of Attack in Cruise

Transition

Test data obtained from the 1/3-scale LIT rotor was used for transition correlation. With the rotor shaft angle held constant at 30 degrees from the horizontal, cyclic pitch was varied. Results of the blade root flap bending correlation are shown in Figures 84 through 86. The prediction correlates well with alternating flap bending up to 2 degrees cyclic pitch, but the analysis does not reflect the nonlinear increase in flap bending above 2 degrees cyclic. For negative cyclic pitch, the analysis predicts minimum flap bending at minus 1 degree cyclic compared with a measured minimum at minus 2 degrees. However, the analysis does correlate well with the sensitivity of flap bending to negative cyclic. Correlation with the first two flap bending harmonics in Figure 85 shows the same trend for the first harmonic as the alternating value in Figure 84, and underprediction of second harmonic flap bending for positive cyclic. The flap bending waveform correlation in Figure 86 is good in amplitude but the predicted maximum value is at 120 degrees azimuth compared with a measured value of 165 degrees; the analysis is underpredicting longitudinal flapping for this condition. In light of the small phase lag response (about 10 degrees) of the flapping mode for this rotor speed, the measured longitudinal flap bending is abnormally large. The forcing producing the flap bending moment in Figure 86 is all due to a 1-per-rev variation of rotor inflow, since cyclic pitch is zero for this test point. Since aerodynamic forcing due to rotor angle of attack is a maximum on the advancing blade and a minimum on the retreating blade and the flapping phase lag is 10 degrees, the blade flapping response and therefore flap bending moment would be expected to be predominately in the lateral direction. Downwash nonuniformity due to a strong tip vortex interaction could cause a shift in airloads but, since uniform downwash was used in the analysis for this part of the correlation, any such effects would not be reflected in the predictions presented herein.

The transition chord bending correlation results are shown in Figures 87 through 89. The analysis correlates well for positive cyclic pitch but predicts the same sensitivity of chord bending for negative cyclic. The measured data shows little sensitivity to negative cyclic for this condition. Correlation results for the first two chord bending harmonics in Figure 88 show the same trend, with the analysis correlating well for positive cyclic pitch values but overpredicting for negative cyclic pitch. The predicted chord bending waveform in Figure 89 shows the same correlation trends as the flap bending waveform. The predicted amplitude correlates well with the measured data but the phase of the predicted first-harmonic content is shifted 45 degrees, with the maximum value occurring at 120 degrees azimuth.

Correlation with alternating blade root torsion is shown in Figures 90 and 91. The analysis underpredicts by 50 percent but correlates well with the trend of alternating torsion with cyclic pitch. Correlation with the torsional waveform in Figure 91 shows the analysis underpredicts the first-harmonic content, which dominates the measured waveform. Note that the analysis reflects excitation at the first torsional frequency (nearly 8 per rev), as does the measured data. The measured high-harmonic content on the retreating side of the disc indicates that the rotor is on the verge of stall flutter inception. The analysis predicts this trend toward stall flutter but with appreciably more damping.

Figures 92 through 94 are the correlation results for steady rotor in-plane moments in transition. The correlation is presented as the gradient of pitching and yawing moment per degree of cyclic and also the gradient of total hub moment with cyclic pitch. The test data shows a linear sensitivity of pitching and yawing moment with increasing cyclic and the analysis correlates very well with the gradient of both in-plane moments. Note that the predicted and measured pitching moments are more sensitive to cyclic than yawing moment. Cyclic input was phased with maximum cyclic angle occurring at 170 degrees azimuth so that the flapping phase lag response of 10 degrees would produce nearly pure longitudinal flapping and therefore a large pitching moment contribution. The analysis correctly predicts the high sensitivity of pitching moment and the low sensitivity of yawing moment to cyclic pitch. The analysis correlates well with the measured total hub moment for positive cyclic values, but overpredicts hub moment sensitivity for negative cyclic. This is to be expected since the flap bending predictions showed the same trend and steady hub moments are highly dependent upon blade flapping.

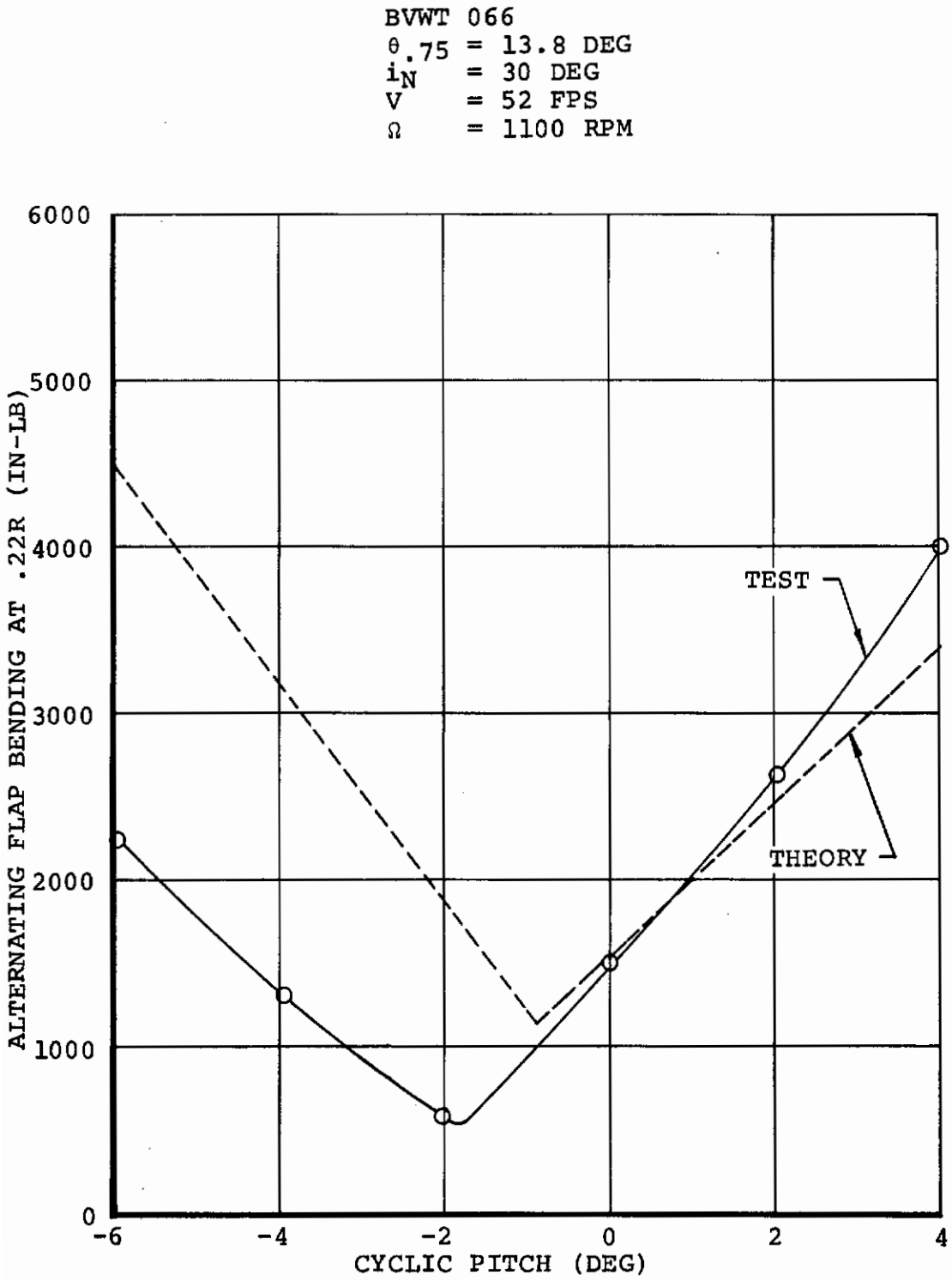

Figure 84. 1/3-Scale LIT Blade, Predicted and Measured Effect of Cyclic Pitch on Alternating Flap Bending in Transition

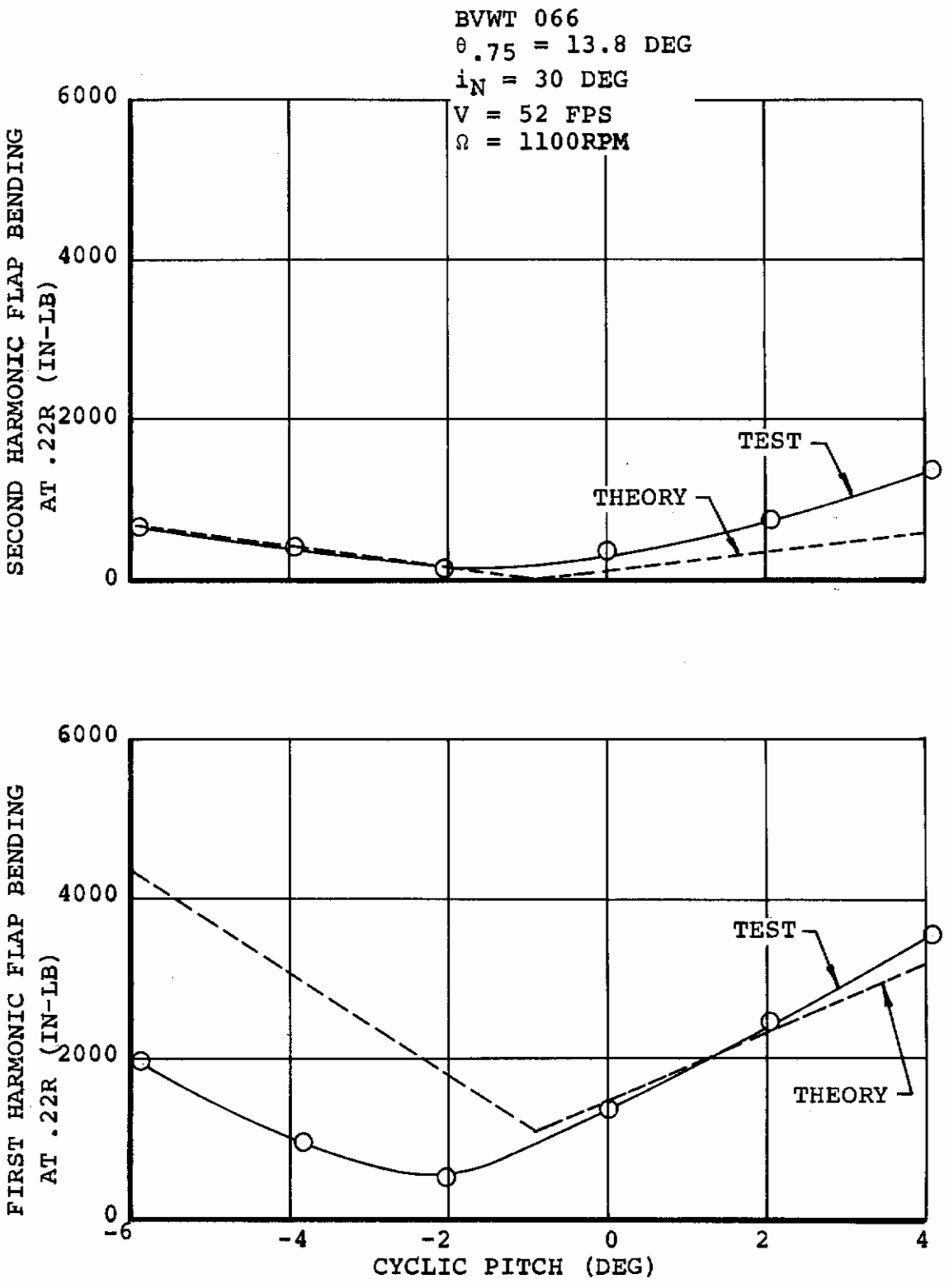

Figure 85. 1/3-Scale LIT Blade, Predicted and Measured First- and Second-Harmonic Flap Bending Due to Pitch in Transition

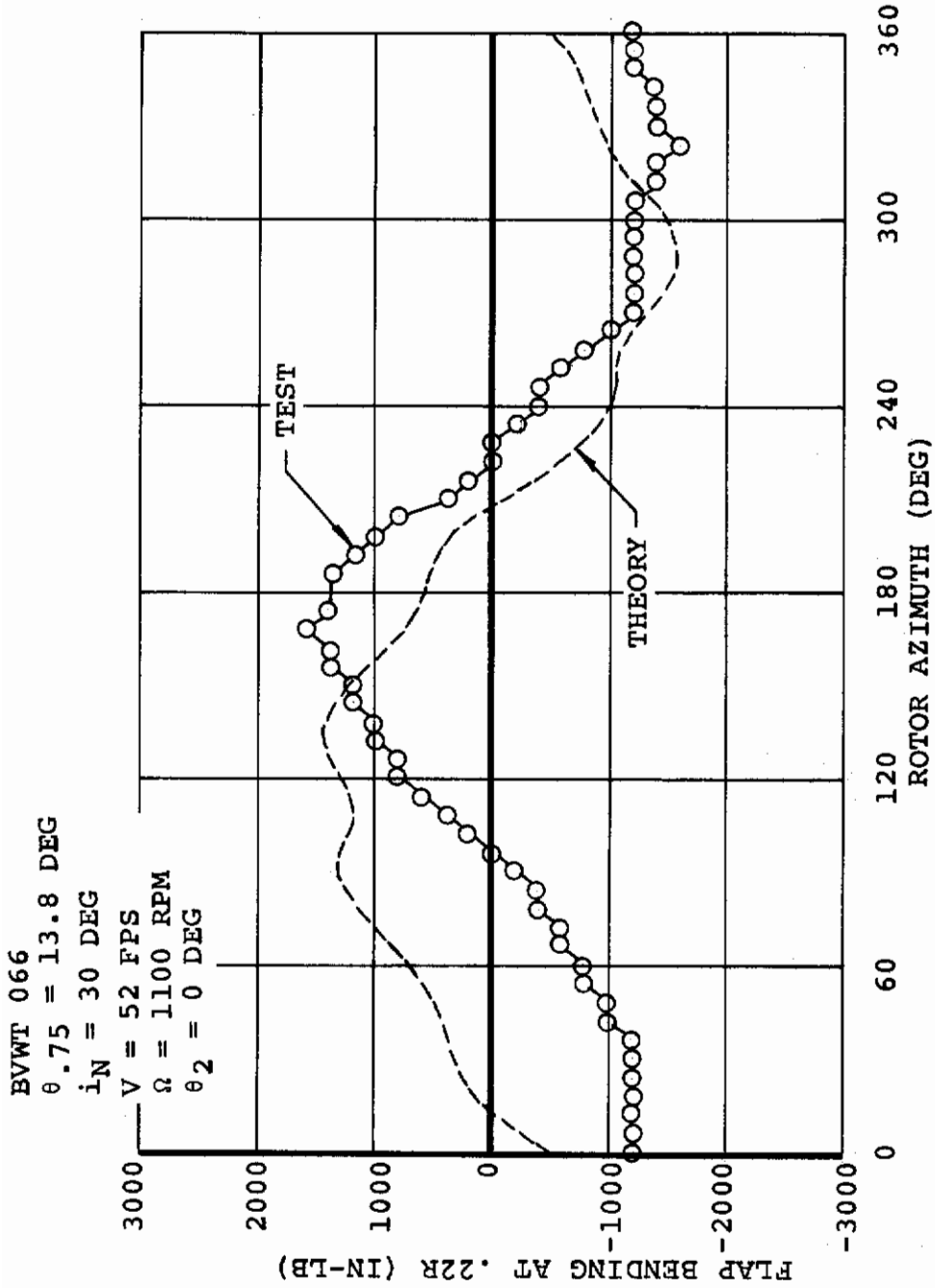

Figure 86. 1/3-Scale LIT Blade, Predicted and Measured Flap Bending Waveform for 0 Degrees Cyclic Pitch in Transition

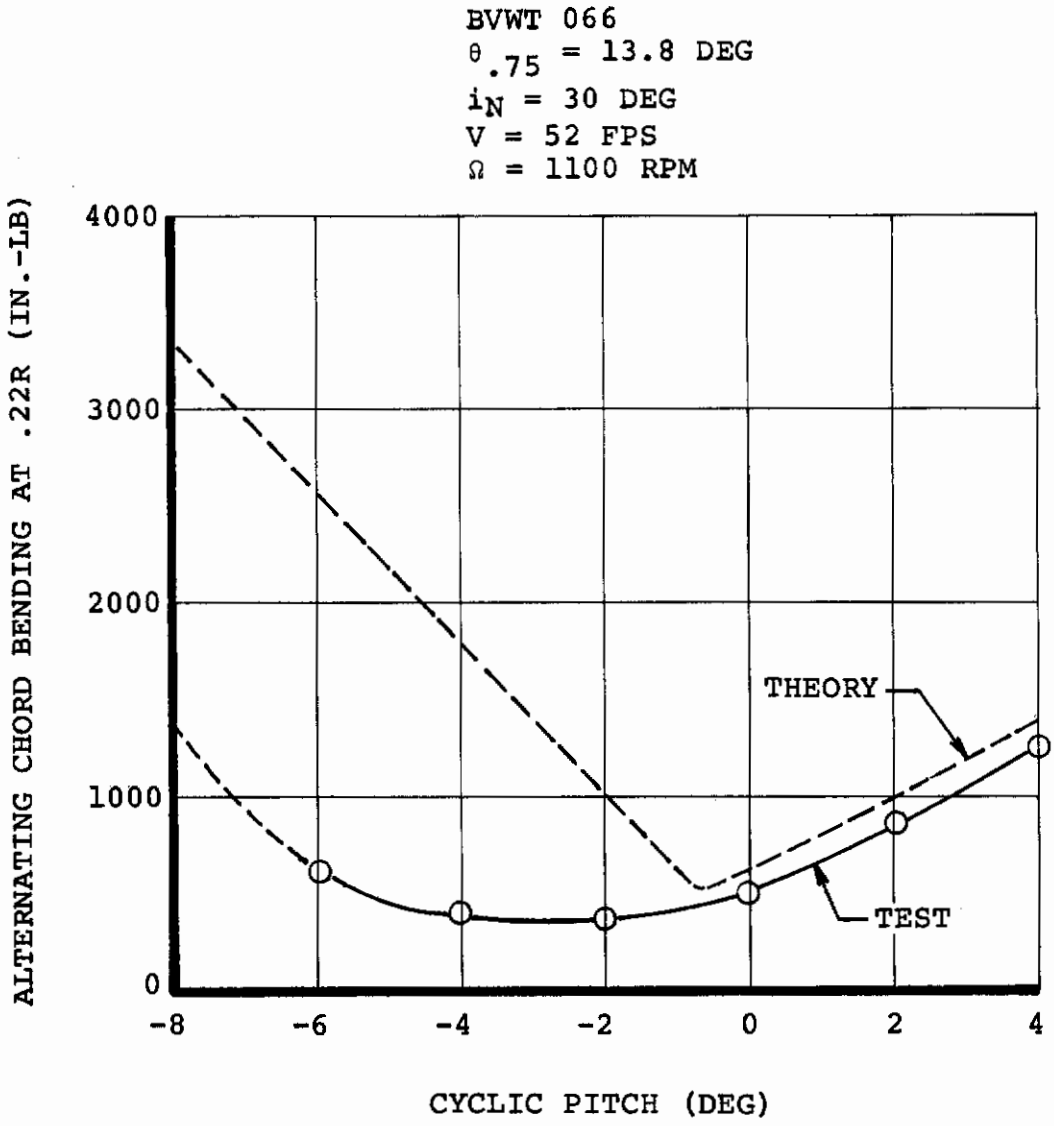

Figure 87. 1/3-Scale LIT Blade, Predicted and Measured Alternating Chord Bending Due to Cyclic Pitch in Transition.

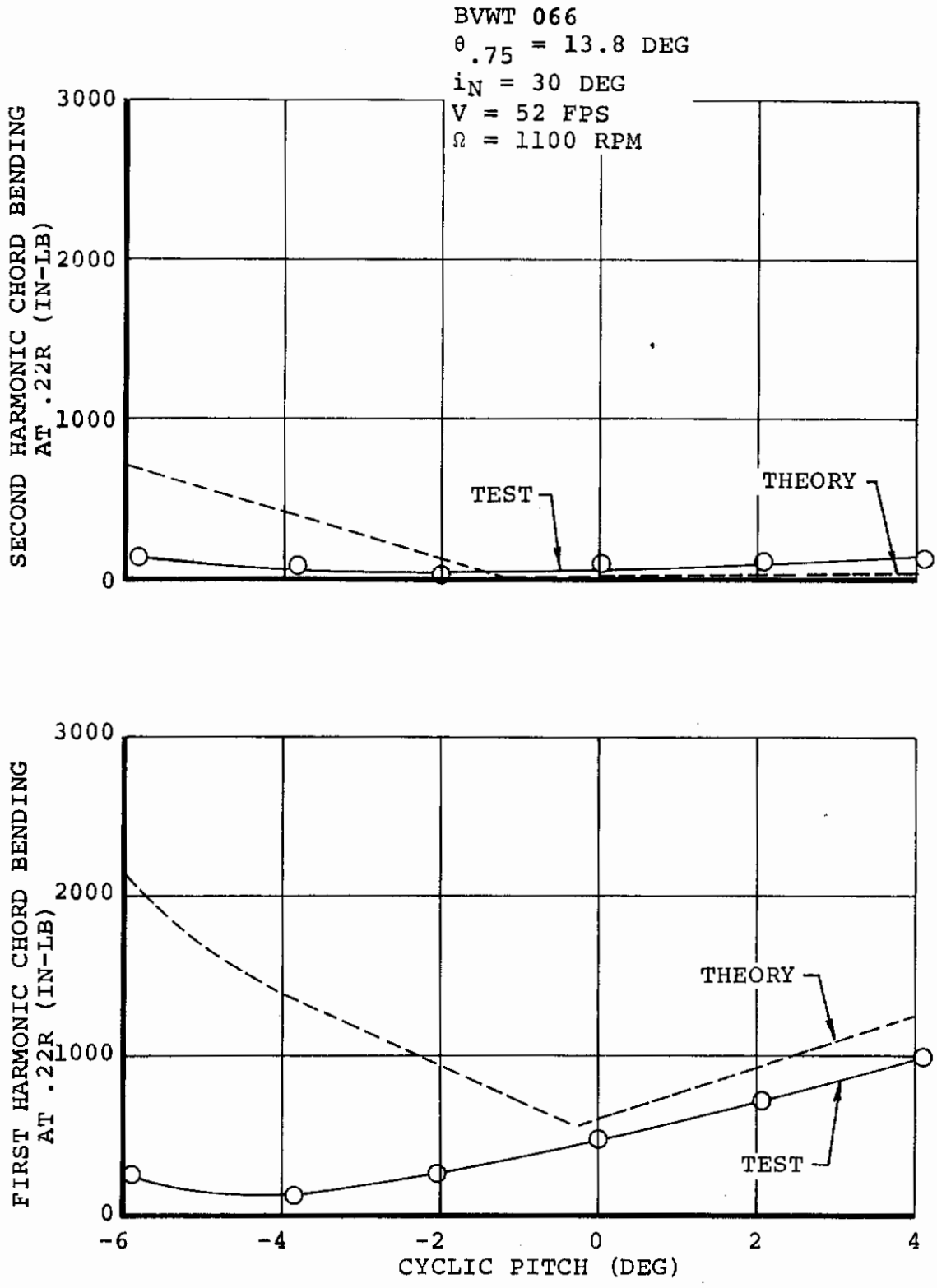

Figure 88. 1/3-Scale LIT Blade, Predicted and Measured First- and Second-Harmonic Chord Bending Due to Cyclic Pitch in Transition

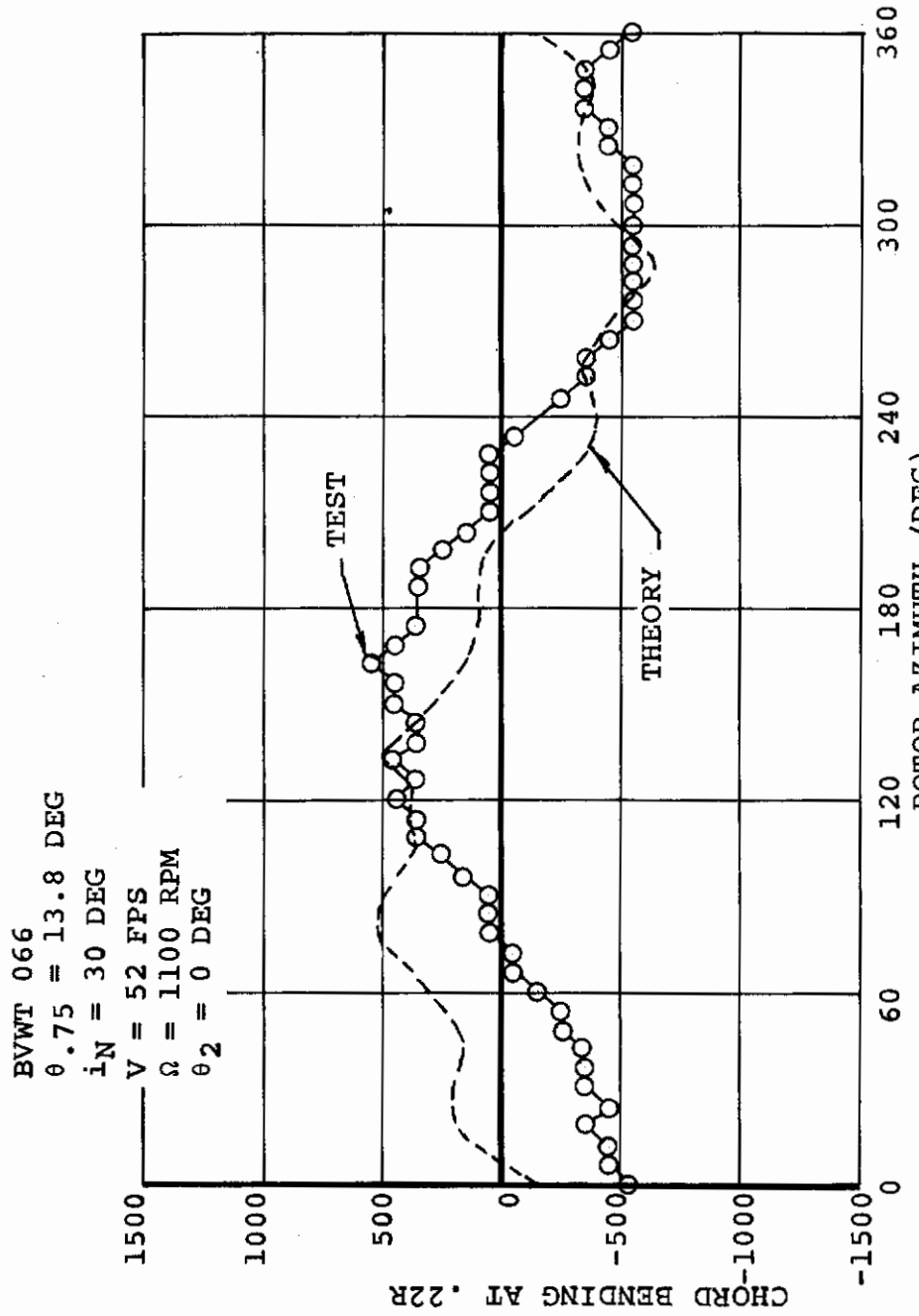

Figure 89. 1/3-Scale LIT Blade, Predicted and Measured Chord Bending Waveform for 0 Degrees Cyclic Pitch in Transition

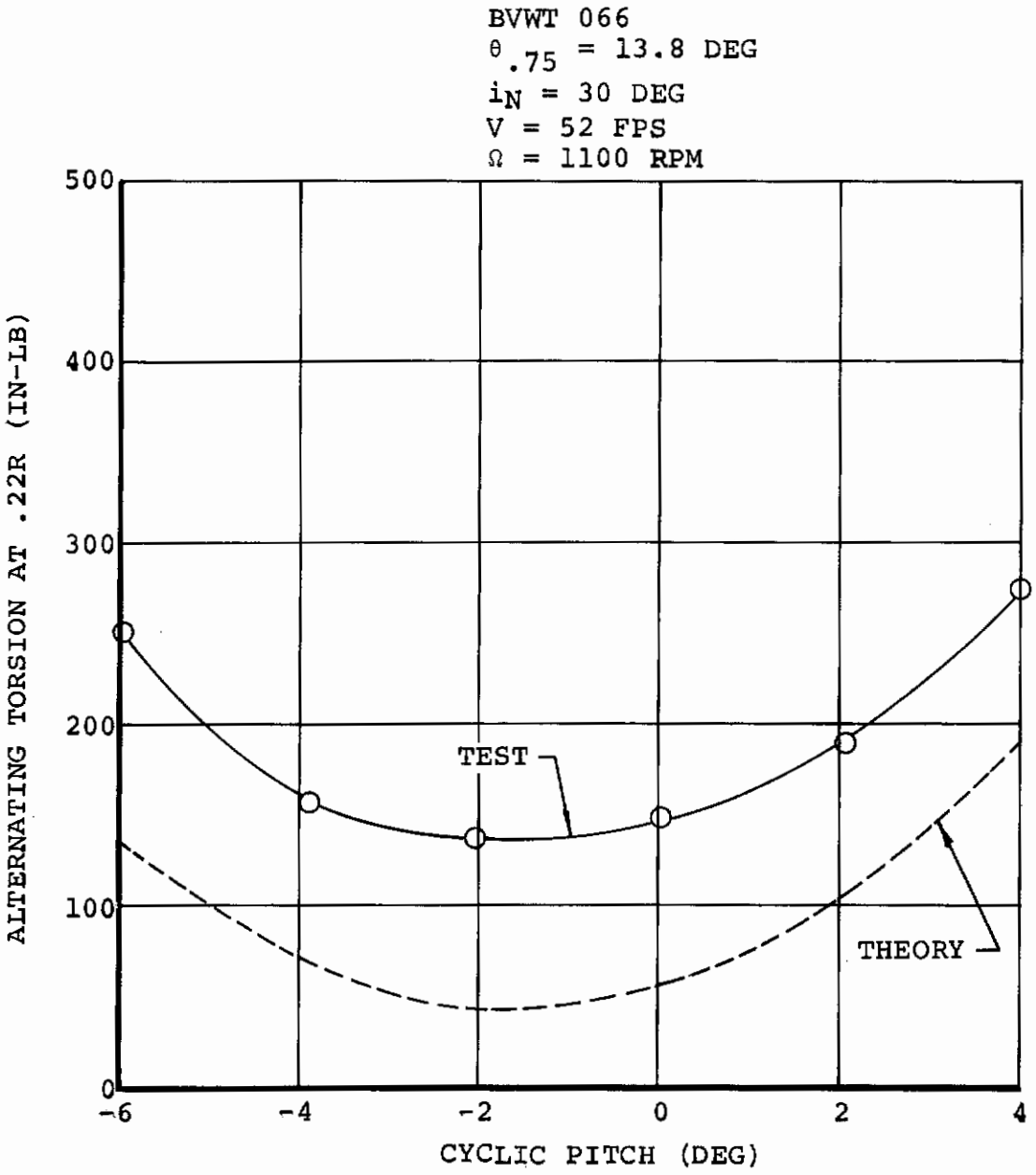

Figure 90. 1/3-Scale LIT Blade, Predicted and Measured Alternating Torsion Due to Cyclic Pitch in Transition

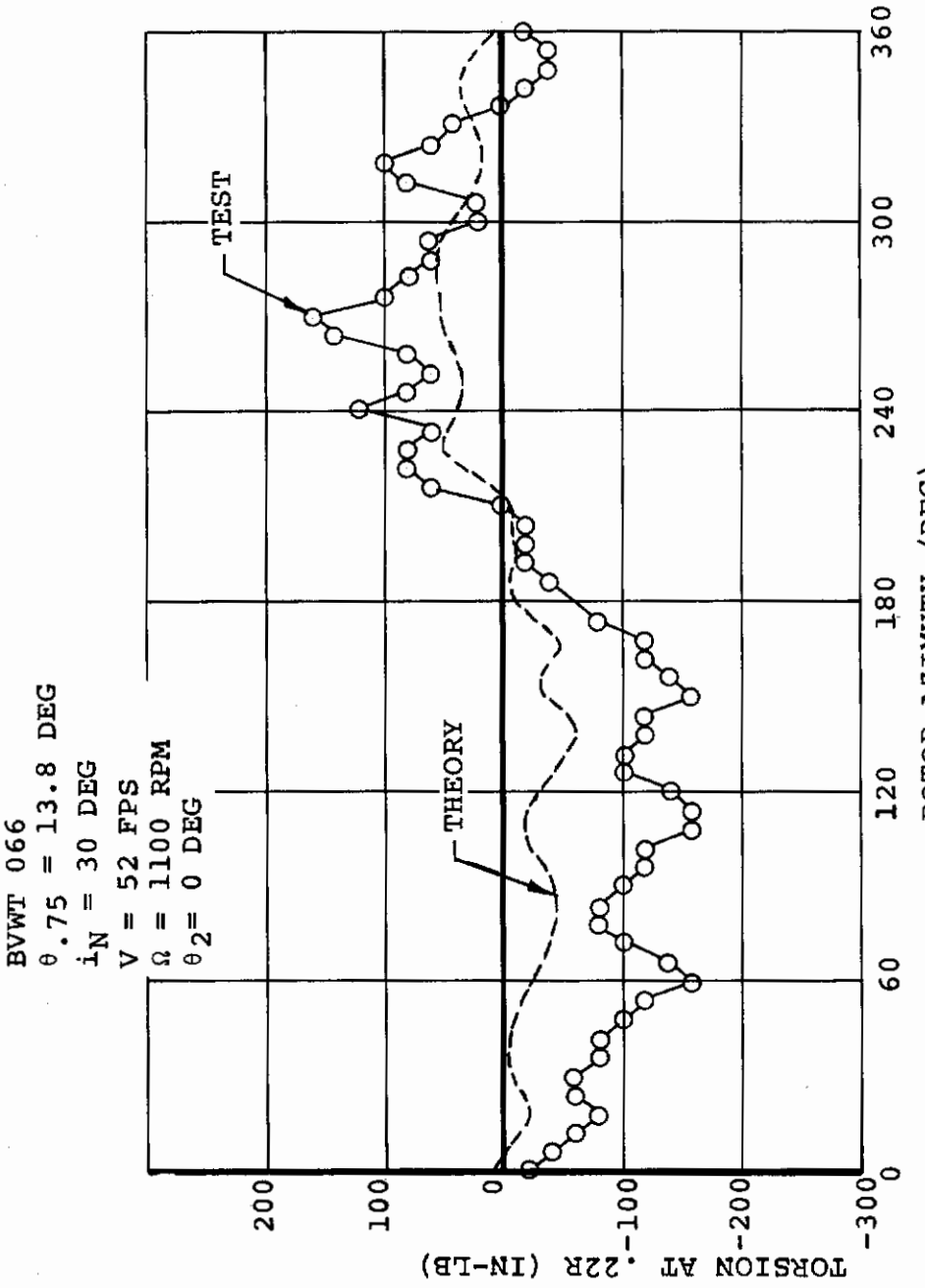

Figure 91. 1/3-Scale LIT Blade, Predicted and Measured Torsional Waveform for 0 Degrees Cyclic Pitch in Transition

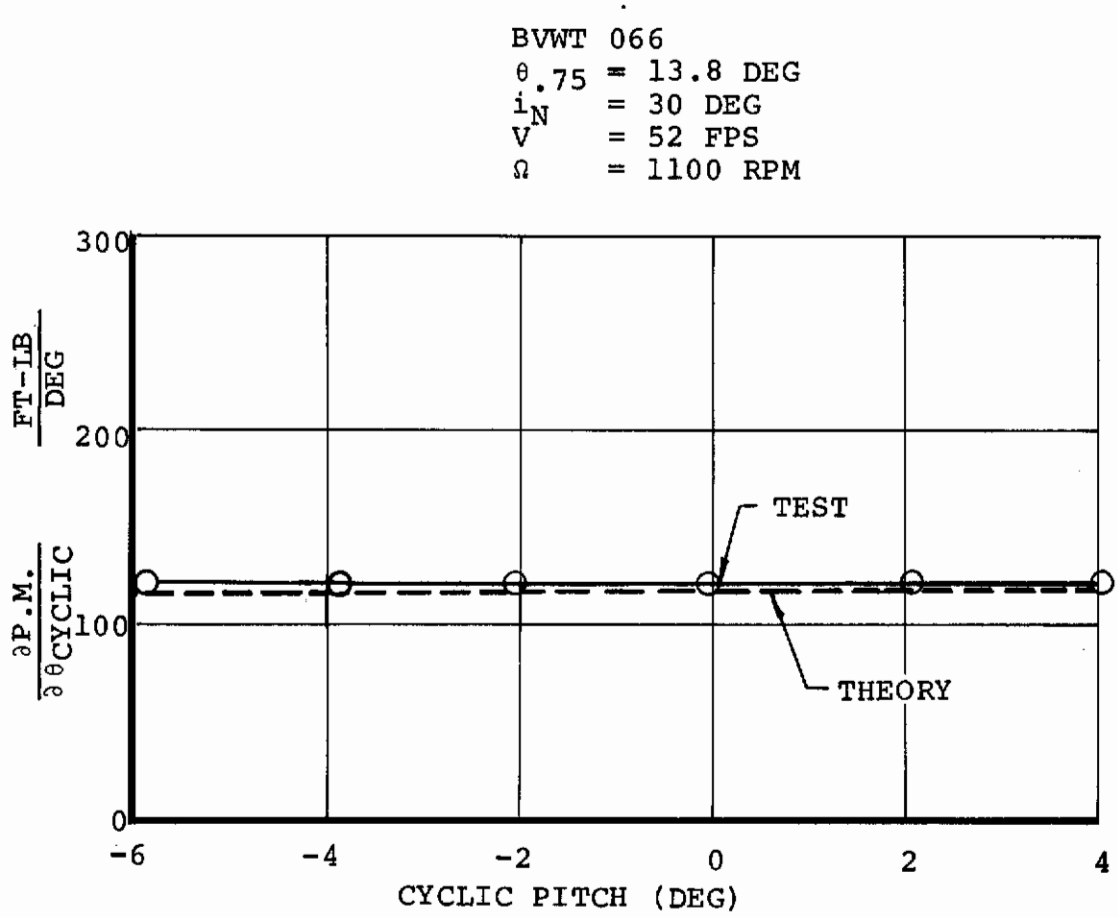

Figure 92. 1/3-Scale LIT Blade, Predicted and Measured Rate of Change of Steady Rotor Pitching Moment With Cyclic in Transition

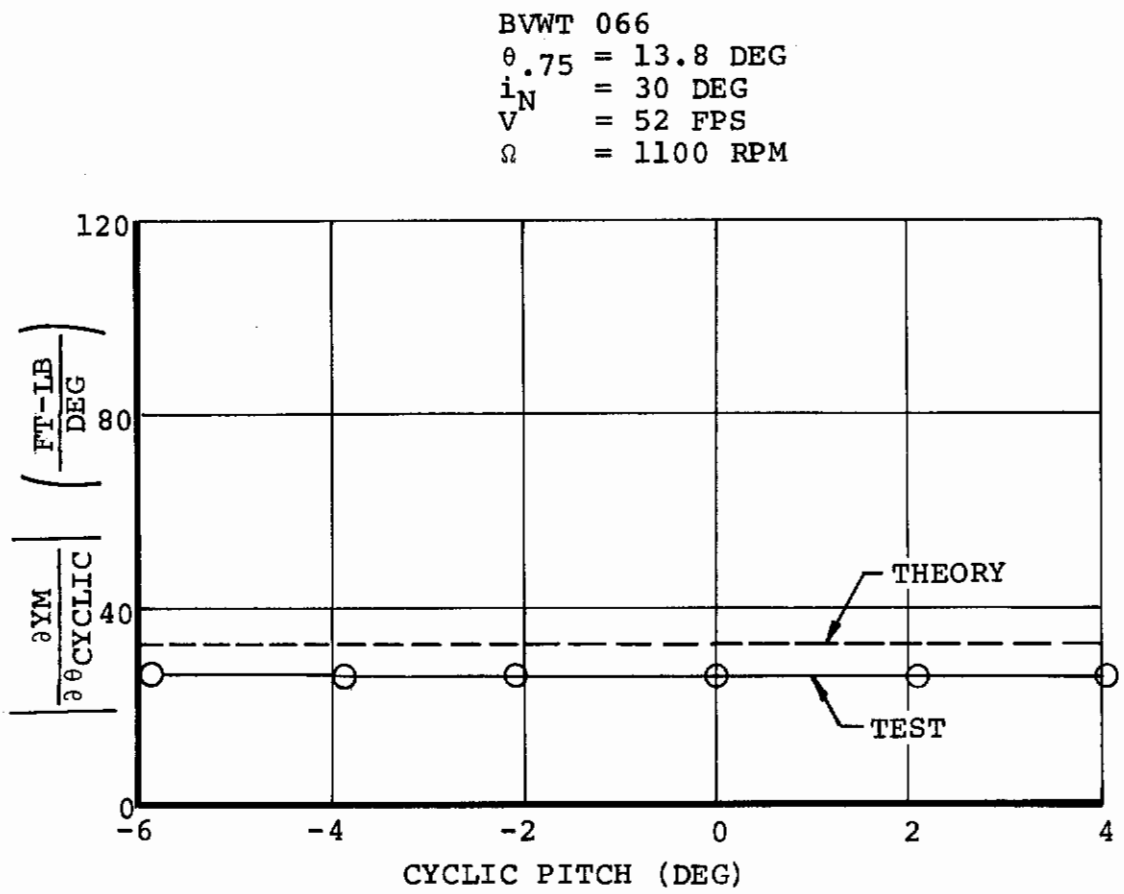

Figure 93. 1/3-Scale LIT Blade, Predicted and Measured Rate of Change of Steady Rotor Yawing Moment With Cyclic in Transition

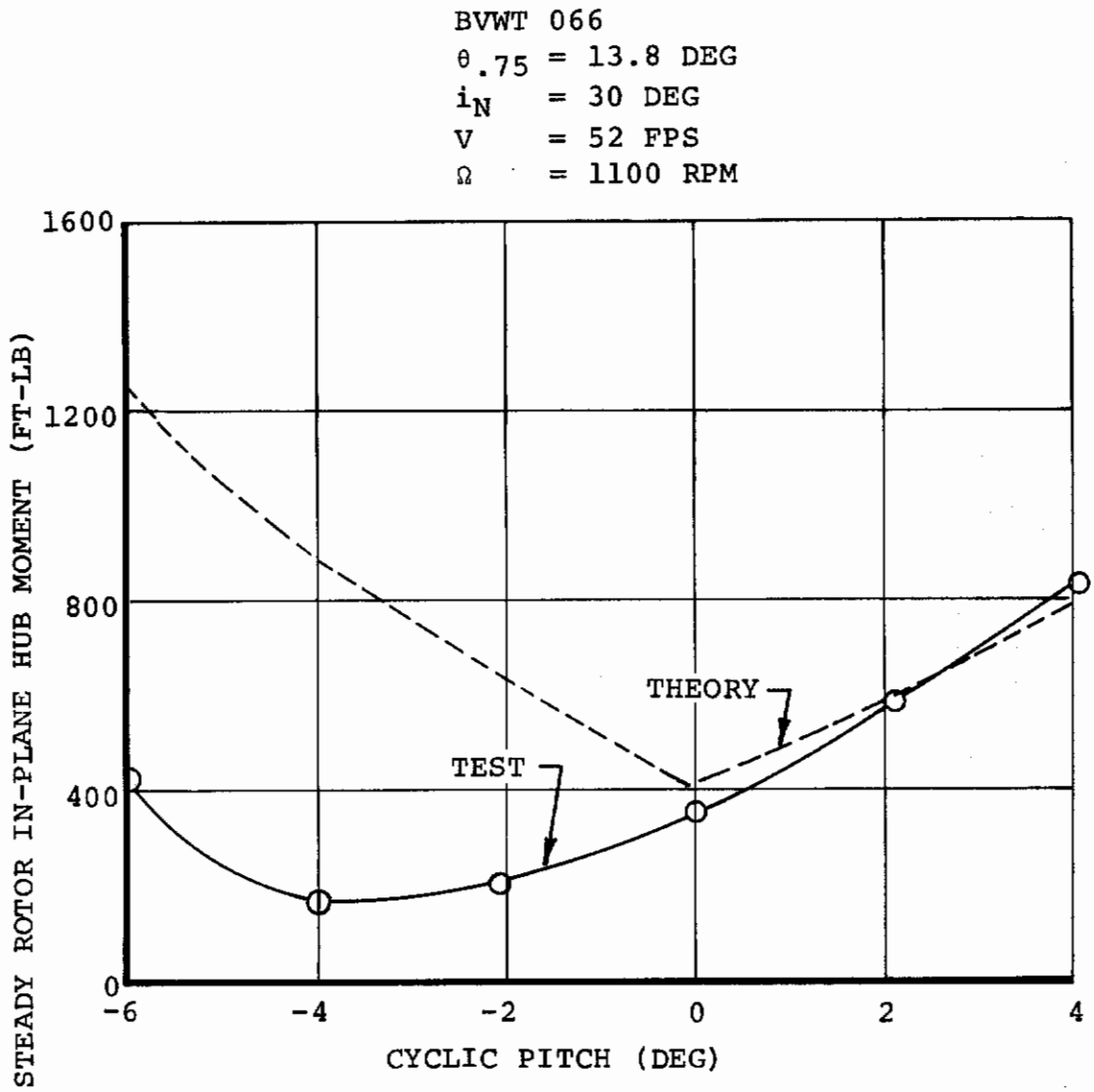

Figure 94. 1/3-Scale LIT Blade, Predicted and Measured Total Steady Rotor In-Plane Hub Moment With Cyclic in Transition

HELICOPTER LOADS CORRELATION

INTRODUCTION

Three tandem-rotor helicopter flights were chosen for blade loads correlation: one flight of the CH-47 with CH-47C blades; one flight of the CH-47 with advanced-geometry blades (AGB); and one flight of the Model 347 with CH-47C blades. These flights were chosen since they offered a wide range of steady level-flight conditions (particularly rotor loading and advance ratio), as well as having varied rotor configurations. The CH-47C has a 3-bladed, constant-chord, constant-thickness rotor of steel and fiberglass construction; the CH-47 AGB configuration has a 3-bladed, tapered-chord, tapered-thickness rotor of fiberglass construction. Test data from the Model 347 with 4 CH-47C blades provided a 3-bladed/4-bladed rotor comparison. Wind tunnel test data from the CH-34 isolated full-scale rotor (Reference 31) provided airloads data for correlation. Table IV is a summary of the helicopters and flight conditions used for correlation. All flight test data is for steady, level, forward flight. Table V is a summary of the helicopter test data used for correlation.

CORRELATION RESULTS

Pitch Link Loads

CH-47 and Model 347 tandem-rotor helicopter test data were used for pitch link load correlation. The test data includes pitch link loads for predominately unstalled and predominately stalled rotor conditions, the deepest stalled condition being the aft rotor of the CH-47C, flight X-83, at 133 knots. The aft rotor for this condition was operating at $\mu = 0.306$ and $C_T/\sigma = 0.1147$, which is the highest C_T/σ encountered for the total helicopter correlation.

The pitch link loads measured from flight test data are presented as one-half of the peak-to-peak value for one rotor cycle. Most test data points are the average value of 25 to 120 rotor cycle values. The symbol represents the arithmetic average value of all the cycles, while the vertical line through the symbol represents the highest and lowest values of all the cycles in that run. This is a convenient means of plotting flight test data where data scatter is expected due to pilot handling or turbulent conditions but it also can be misleading, especially in or near a stalled condition. In some cases the value of the most typical cycle (the value that occurred most often during the run) is not the same as the arithmetic mean of the data. A good example of this is the aft rotor pitch link load of CH-47C, flight X-83, at 123 knots, shown in Figure 95. The pitch link load test data at this speed has a scatter from 2,070 to 600 pounds with an arithmetic

TABLE IV
SUMMARY OF HELICOPTERS AND FLIGHT CONDITIONS USED FOR CORRELATION

Helicopter	Number of Blades	Blade Radius (ft)	Flight No.	Gross Weight (lb)	Density Altitude (ft)	RPM	CG (in.)	Max C_T/σ	Max μ
CH-47C	3	30	83	39,000	3,000	230	5 aft	0.1147	0.307
Model 347 CH-47C Blades	4	30	313	42,000	1,600	220	6 aft	0.0873	0.373
CH-47(AGB)	3	30	272	46,000	6,000	245	4 aft	0.0890	0.299
CH-34	4	28	-	-	-	222	-	0.0819	0.450

NOTE: The advanced-geometry blades (AGB) are tapered in chord and thickness.

TABLE V
SUMMARY OF HELICOPTER TEST DATA USED FOR CORRELATION

Helicopter	Flight No.	Pitch Link Loads	Blade Flap Bending	Blade Chord Bending	Airloads Lift/Span
CH-47C	83	X	X	X	-
Model 347 CH-47C Blades	313	X	X	X	-
CH-47 (AGB)	272	X	X	X	-
CH-34	wind tunnel test	-	-	-	X

mean of 1,540 pounds. But, as shown in Figure 96, the value of the cycle that occurs most often is between 1,800 and 1,900 pounds, an increase of 300 pounds over the arithmetic mean. This indicates that the aft rotor was normally in a stalled condition, shown by the large number of occurrences of high pitch link loads, but due to pilot techniques or turbulent conditions the rotor briefly went into an unstalled condition. Therefore, caution must be taken not to weigh the arithmetic mean too heavily when correlating pitch link loads in or near a stalled condition.

Figures 95 through 107 are the aft rotor pitch link load correlation results for CH-47C and Model 347 tandem-rotor helicopter test data. Figures 95, 97, and 98 show the analysis correlates well with the pitch link load data with increasing airspeed; the prediction for CH-47C flight X-83 (Figure 95) is especially good in predicting stall inception and the growth of loads as airspeed increases. As mentioned before, the most typical value of pitch link load is significantly different than the arithmetic mean load for this flight in stall. The most typical value is plotted for the two highest airspeeds for a more meaningful correlation with the analysis.

As shown by the correlation results in Figure 95, the analysis with uniform downwash correlates very well with pitch link loads in deep stall at 123 and 133 knots. Uniform downwash was used primarily in the analysis for two reasons. Use of uniform downwash instead of nonuniform downwash results in substantial savings in computer time. The second reason for using uniform downwash was to avoid the problems associated with a high C_T/σ condition such as that shown in Figure 95 at 123 and 133 knots. For a condition such as this, predicted pitch link loads when nonuniform downwash is used in the analysis have been found to be sensitive to rotor interference. Presumably, blade moment stall, and therefore pitch link loads, are highly dependent upon the analysis description of blade tip vortex proximity to a passing blade. As shown in the figure, after stall inception at 123 and 133 knots where moment stall is significant, the nonuniform downwash predictions are erratic. Since use of uniform downwash in the analysis correlates well with measured pitch link loads in and out of stall, uniform downwash is recommended for pitch link load prediction.

Figures 99, 100, and 101 are the aft rotor pitch link load waveform correlation results for CH-47C flight X-83. The three highest airspeeds in the flight are shown and the test data at each airspeed was chosen from a cycle near the most typical alternating value for that airspeed. At 111 knots the analysis shows definite stall indications, as does the test

data, and at 123 and 133 knots the analysis predicts the large spike on the retreating side of the disc plane. The analysis not only correlates well with the amplitude of the spike but also predicts within 30 degrees the phasing of the spike in the rotor azimuth.

For the aft rotor pitch link load correlation for the CH-47 with advanced-geometry blades, Figure 97 shows the analysis correlates well with increasing airspeed. As mentioned before, the aft rotor for this flight attained a maximum C_T/σ of 0.0890, a predominately unstalled condition. The analysis correctly predicts this predominately unstalled trend as shown by the smooth increase in predicted load with airspeed. Figures 102, 103, and 104 show the waveform correlation results at 116, 125, and 131 knots. The test data is predominately 1-per-rev, indicating that the rotor is operating below stall. The analysis correctly predicts the amplitude of the 1-per-rev load and the absence of a spike in the prediction shows that the analysis correctly predicts that the rotor is operating out of stall. The higher harmonics in the test data are due to rotor interference and cannot be reflected in the analysis results when uniform downwash is used. These correlation results are important since they demonstrate the capability of the analysis to predict aft rotor pitch link loads for blades that are tapered in chord and thickness.

Figure 98 shows the aft rotor pitch link load correlation results with airspeed for the Model 347 with CH-47C blades. The analysis correlates very well with the test data, with both test data and analysis showing the rotor is operating predominately unstalled. The waveform correlation in Figures 105, 106, and 107 show that both test data and prediction are primarily 1-per-rev and correlation is good in amplitude and phase. The test data also contains 2-per-rev and higher harmonics due to rotor interference. Use of uniform downwash neglects higher harmonic forcing due to interference and the predicted waveform does not show any significant higher harmonics. But since the first harmonic dominates the measured pitch link load, this correlates well with the test data.

Figures 108 through 119 are the forward rotor pitch link load correlation results. For the CH-47C forward rotor in Figure 108, the prediction increases sharply at 123 knots. The analysis is showing premature stall inception, as demonstrated in the pitch link load waveforms in Figures 109, 110, and 111. At 111 and 123 knots, both test data and prediction are primarily 1-per-rev with the analysis showing a slight stall indication in the fourth quadrant at 123 knots. At 133 knots the analysis shows definite stall characteristics as demonstrated by the large spikes in the fourth quadrant. The test data at 133 knots is showing a slight indication of stall in the fourth quadrant but is still primarily 1-per-rev. The

rotor is operating at a C_T/σ of 0.0987, which is on the verge of stall inception, and the analysis has predicted stall to occur prematurely by about 10 knots. Figures 112 through 119 are the forward rotor pitch link load correlation results for the CH-47 AGB and the Model 347 with CH-47C blades. The predictions and test data for both aircraft flights show the forward rotor is unstalled and the waveforms show that the pitch link load is primarily 1-per-rev. The analysis overpredicts the growth of pitch link load with airspeed for the CH-47 AGB (Figure 112) and the analysis correlates well with the growth of pitch link load for the Model 347 (Figure 116). As in the case for the CH-47C forward rotor, the pitch link load waveforms for both of these aircraft show higher harmonics due to interference. But note that the first harmonic dominates the amplitude of the measured waveforms. The capability of the analysis to predict pitch link loads before stall (primarily 1-per-rev loads) and in stall (impulsive loading in the fourth quadrant) demonstrates that the use of uniform downwash in the analysis, thereby neglecting rotor interference, is justified.

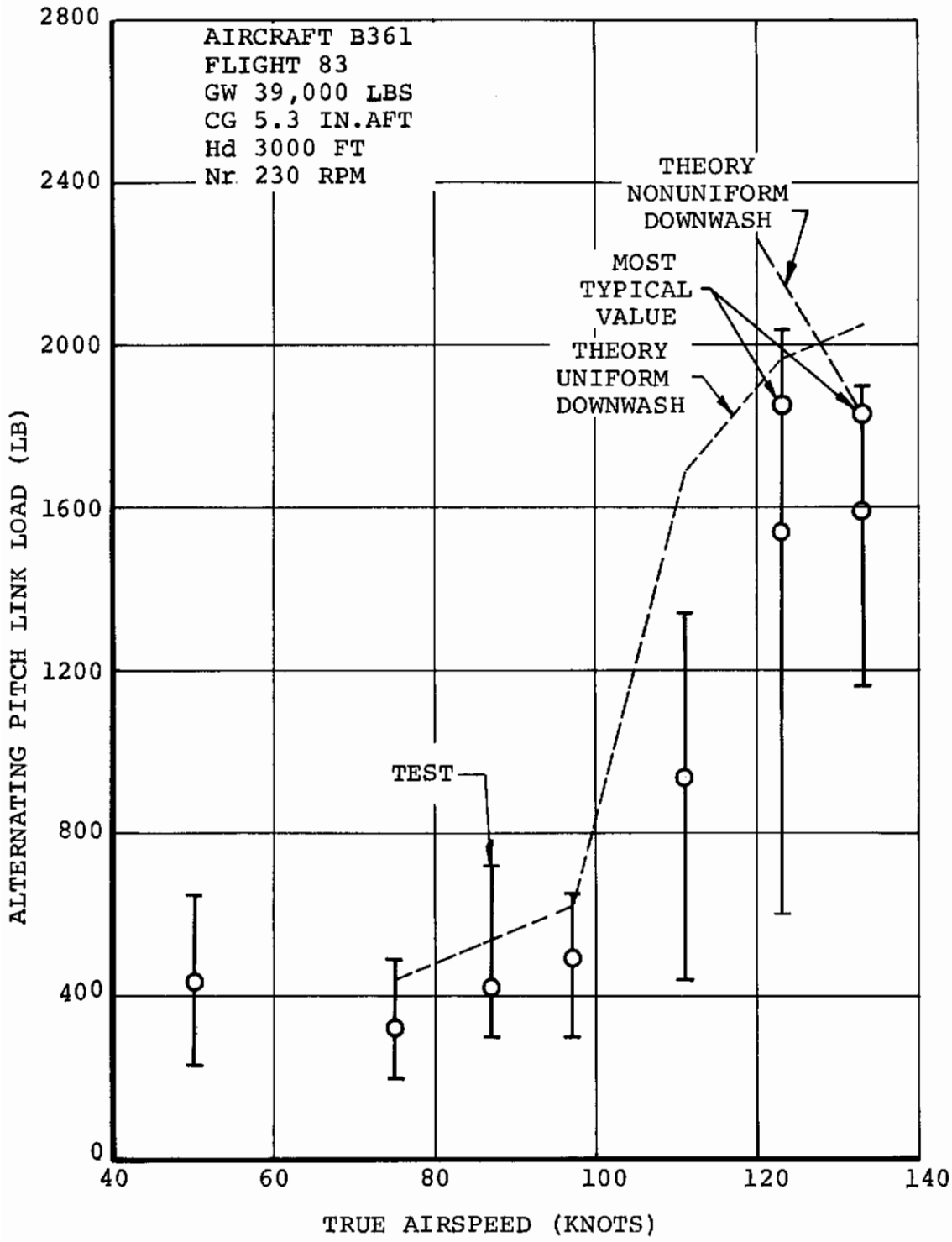

Figure 95. CH-47C Aft Rotor, Predicted and Measured Alternating Pitch Link Loads With Airspeed

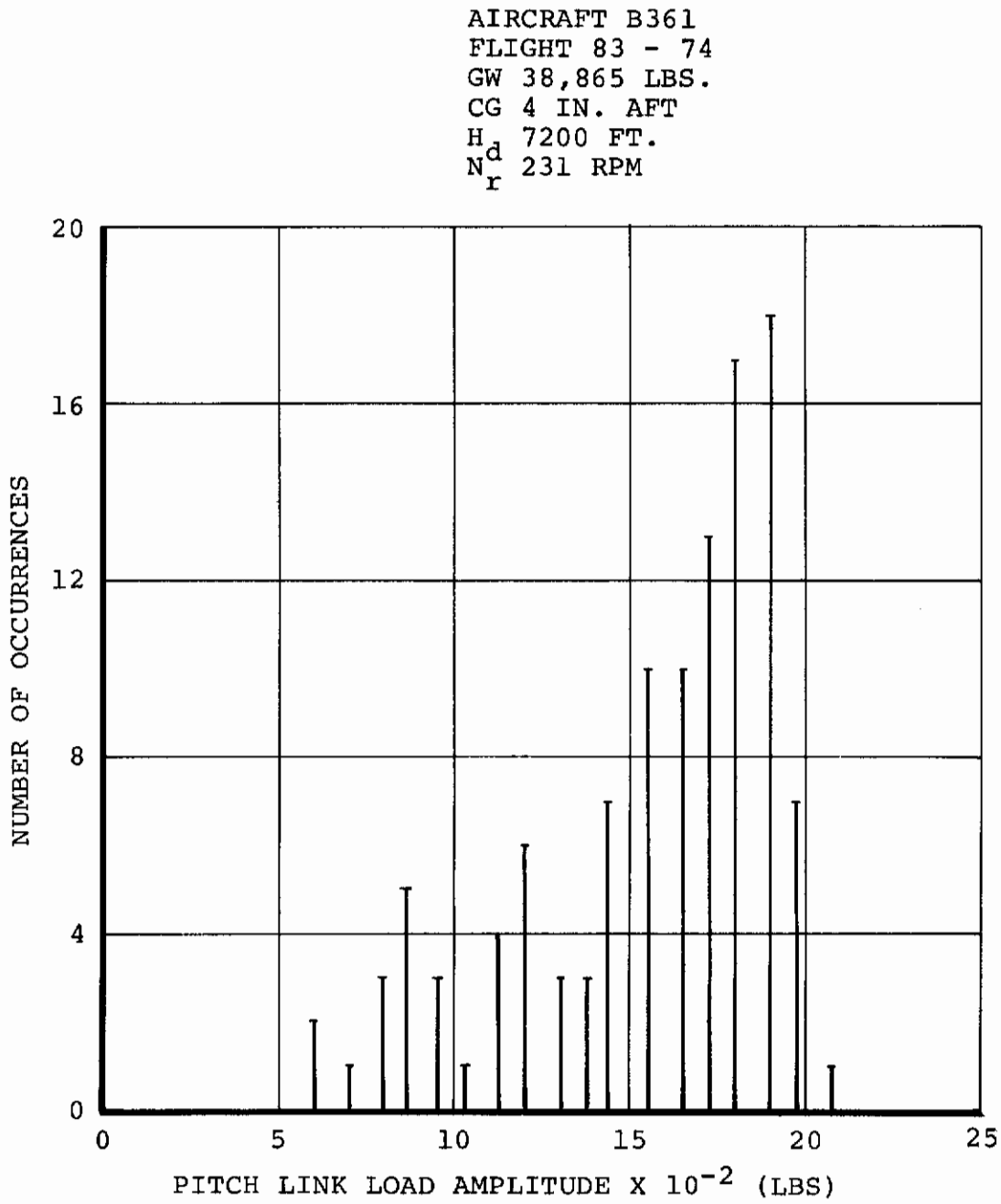

Figure 96. CH-47C Aft Rotor Pitch Link Load Amplitude Distribution for 114 Data Cycles at 123 Knots

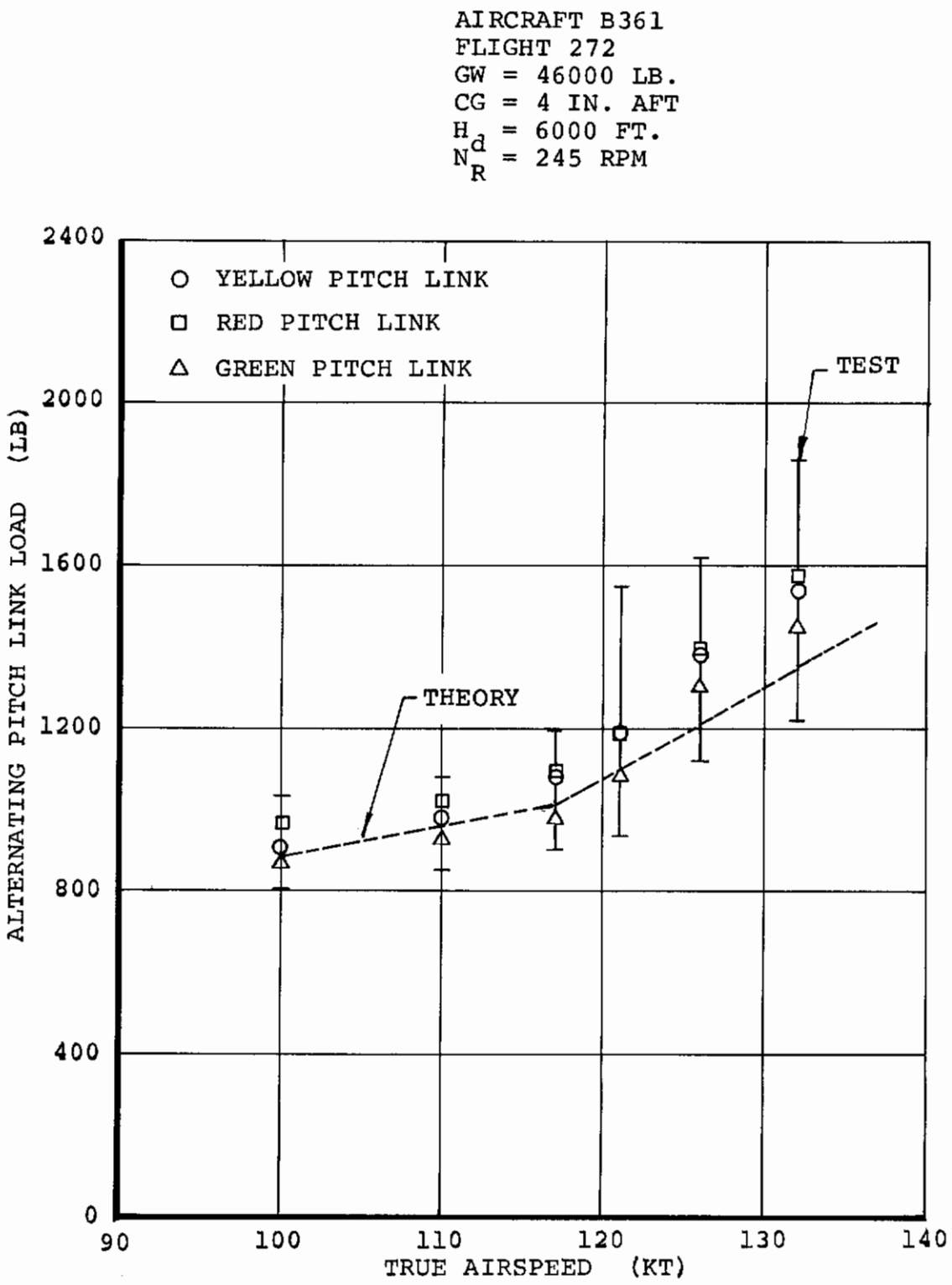

Figure 97. CH-47C With Advanced-Geometry Blades, Aft Rotor Predicted and Measured Alternating Pitch Link Loads With Airspeed

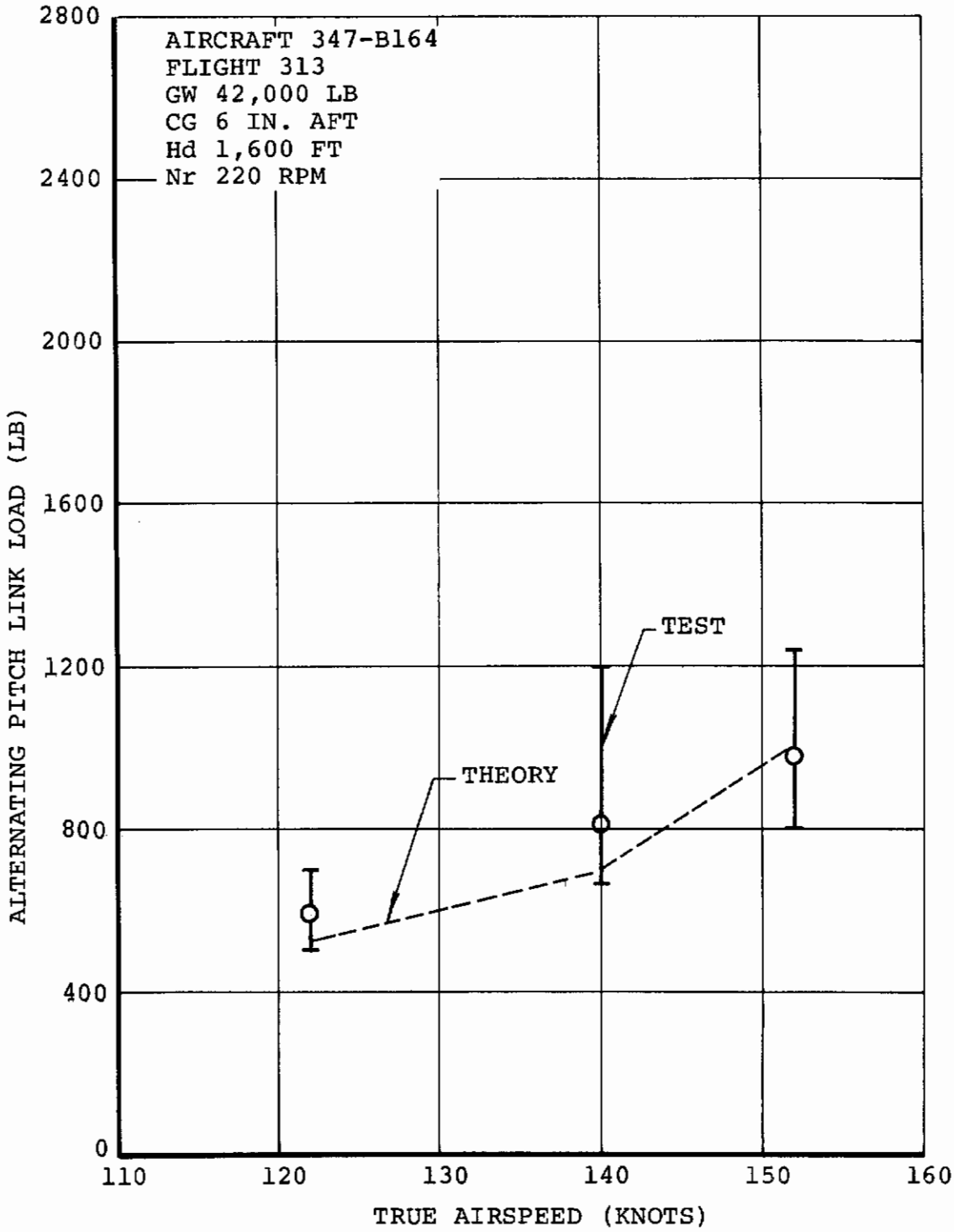

Figure 98. Model 347 With CH-47C Blades, Aft Rotor Predicted and Measured Alternating Pitch Link Loads With Airspeed

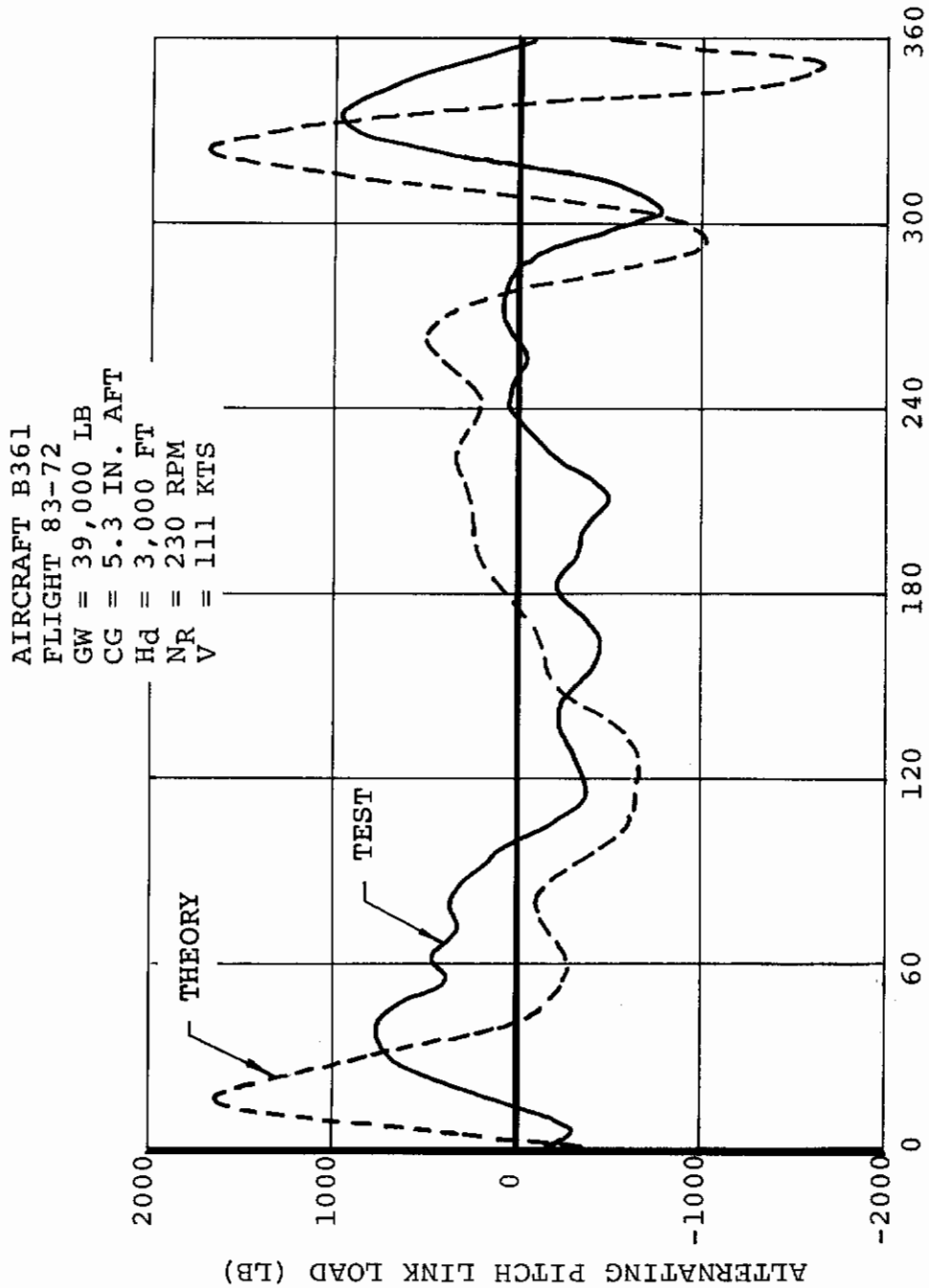

Figure 99. CH-47C Aft Rotor, Predicted and Measured Pitch Link Load Waveform at 111 Knots

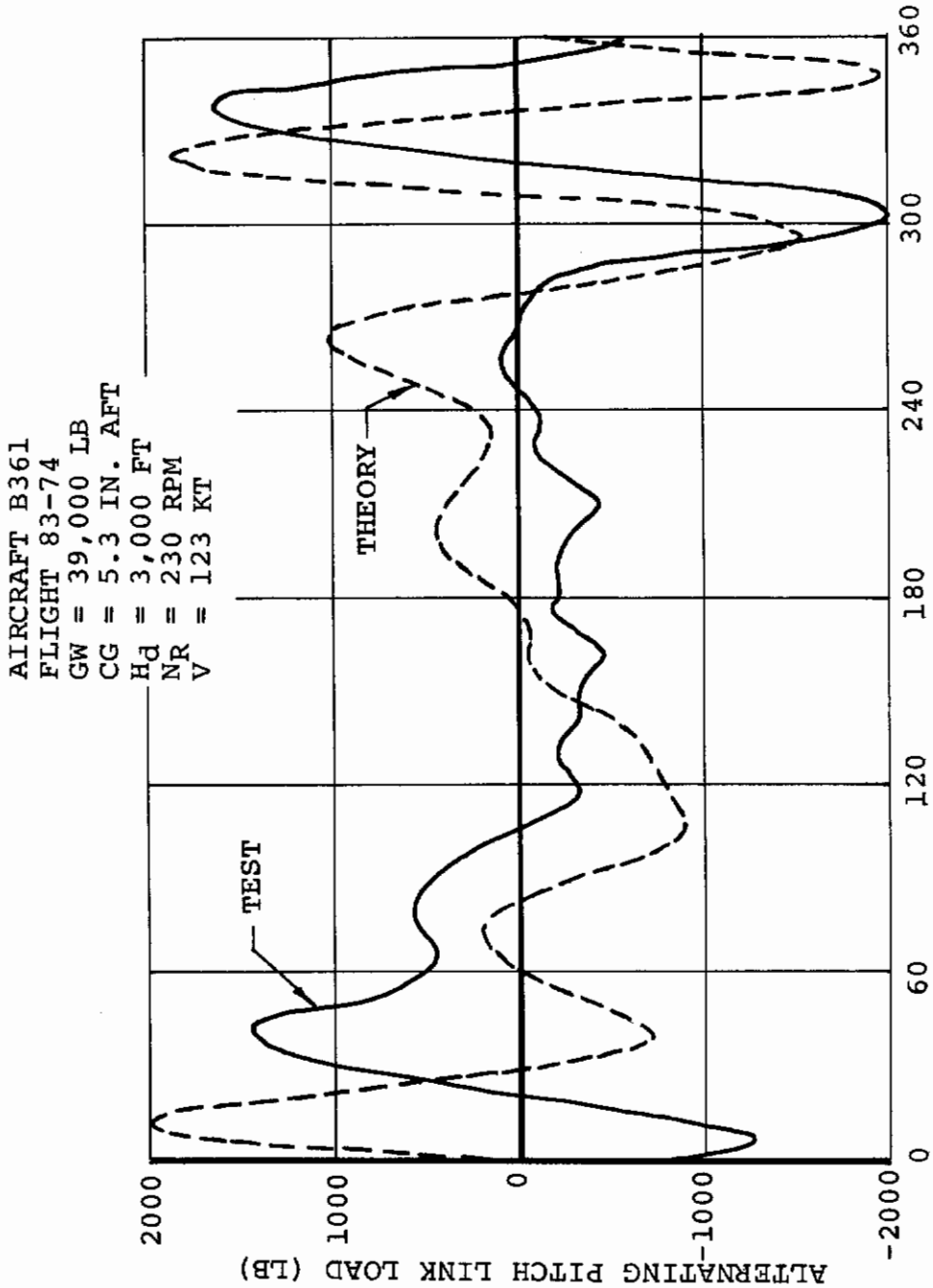

Figure 100. CH-47C Aft Rotor, Predicted and Measured Pitch Link Waveform at 123 Knots

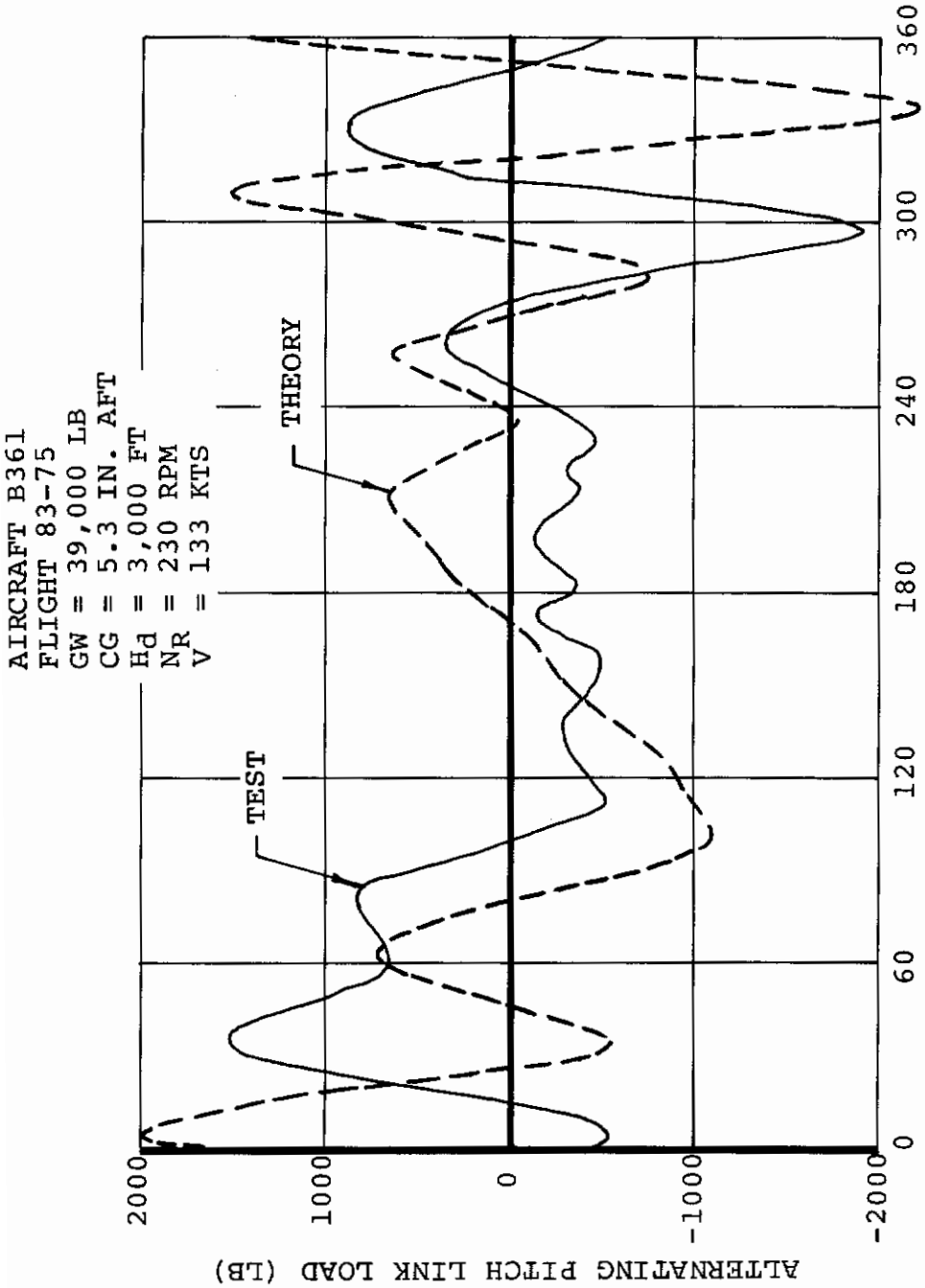

Figure 101. CH-47C Aft Rotor, Predicted and Measured Pitch Link Load Waveform at 133 Knots

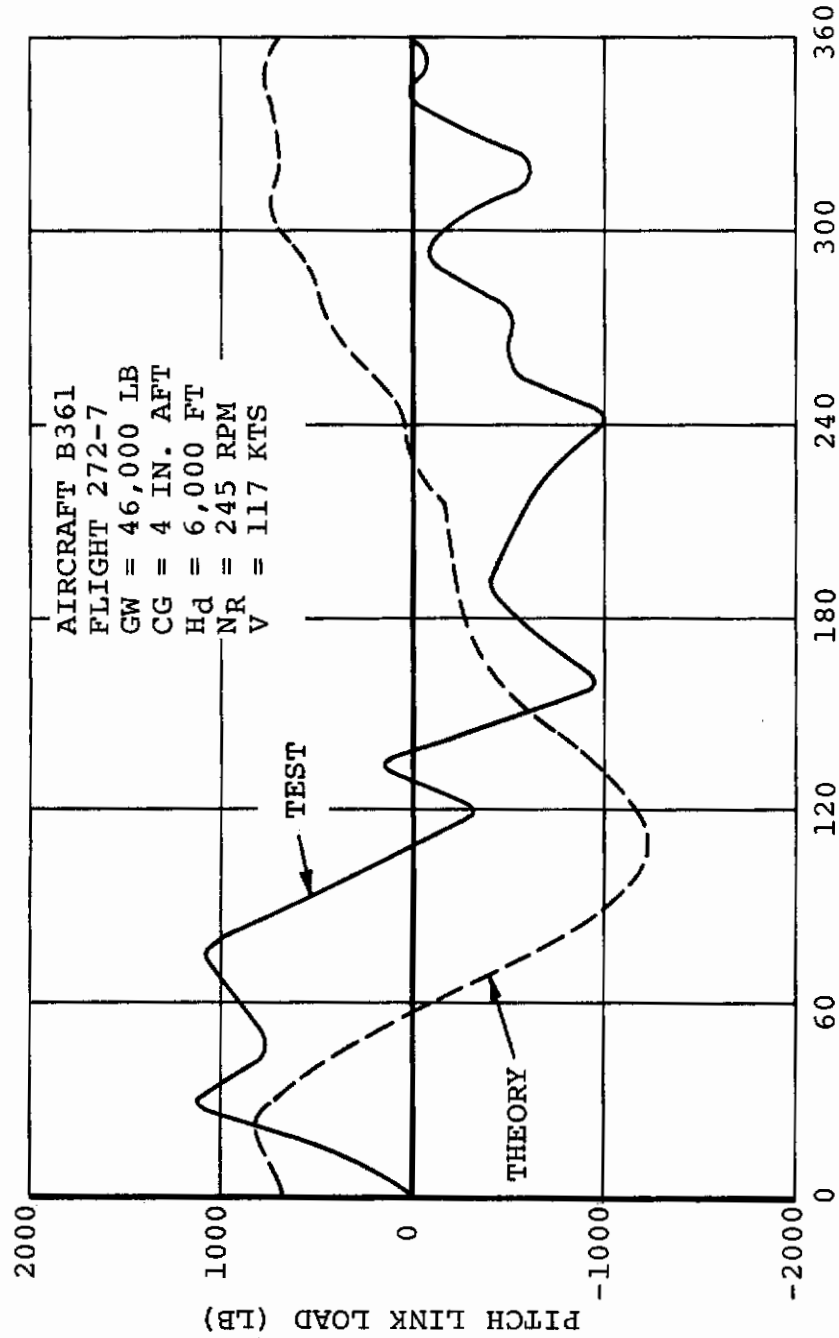

Figure 102. CH-47C With Advanced-Geometry Blades, Aft Rotor Predicted and Measured Pitch Link Waveform at 117 Knots

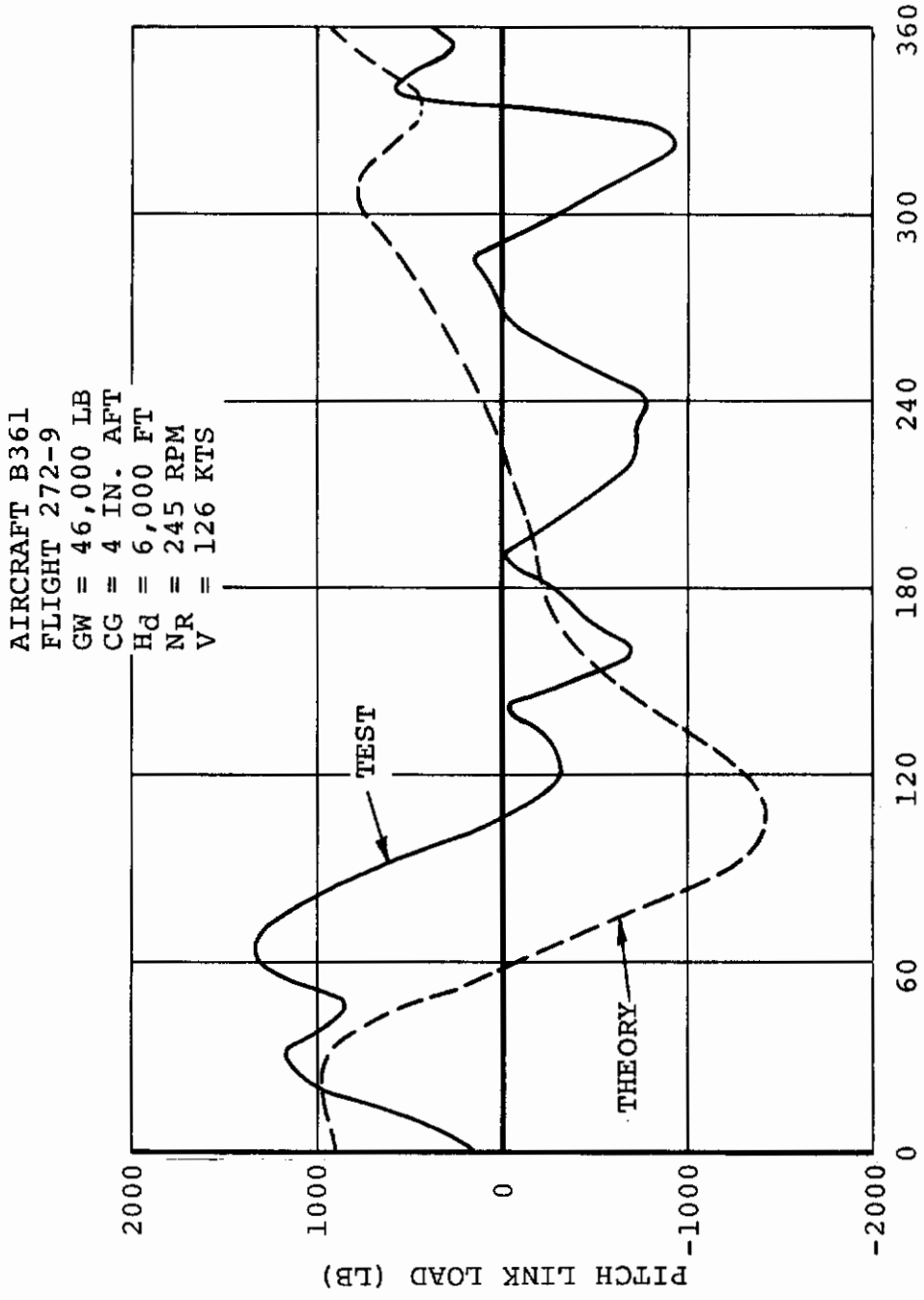

Figure 103. CH-47C With Advanced-Geometry Blades, Aft Rotor Predicted and Measured Pitch Link Waveform at 126 Knots

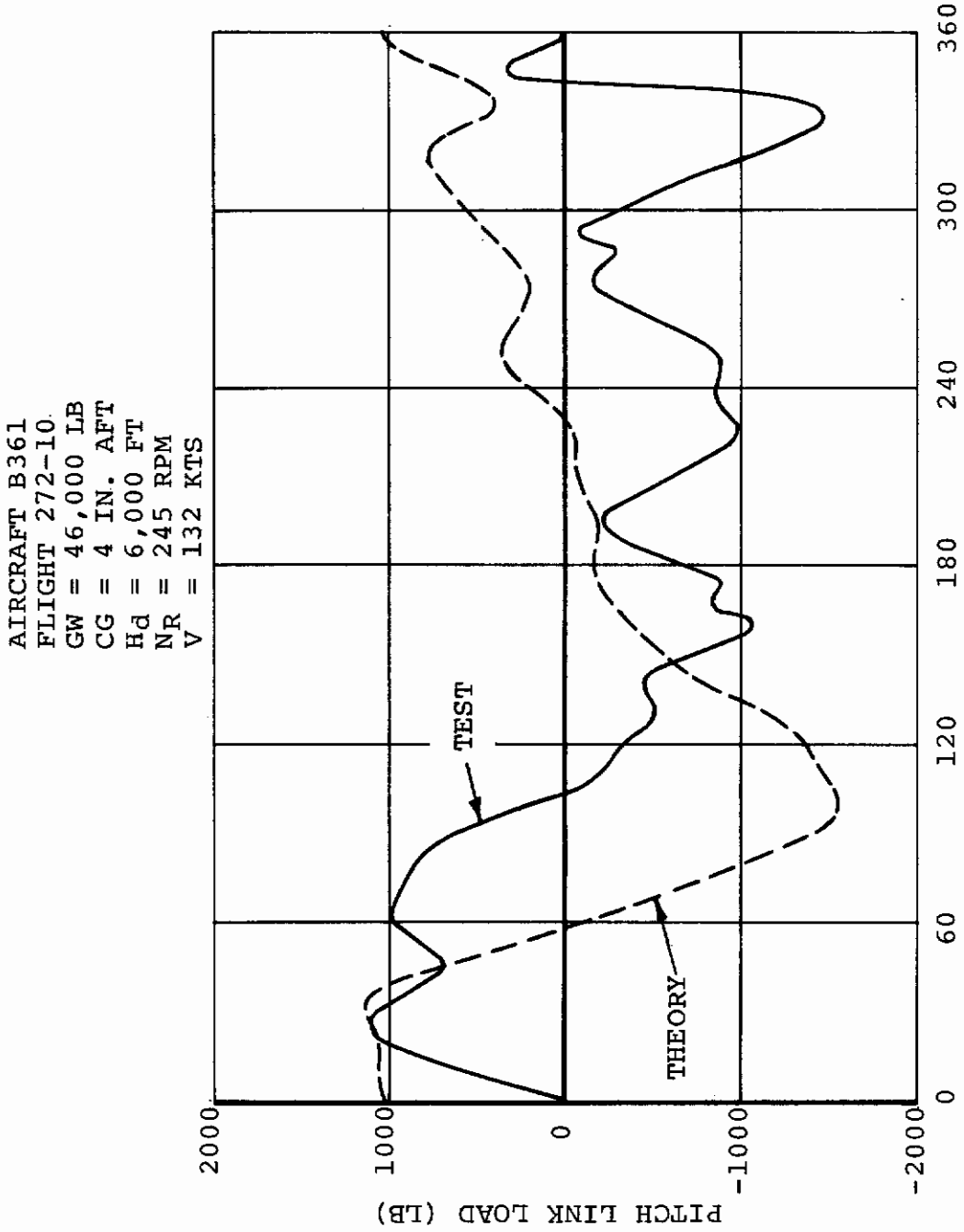

Figure 104. CH-47C With Advanced-Geometry Blades, Aft Rotor Predicted and Measured Pitch Link Waveform at 132 Knots

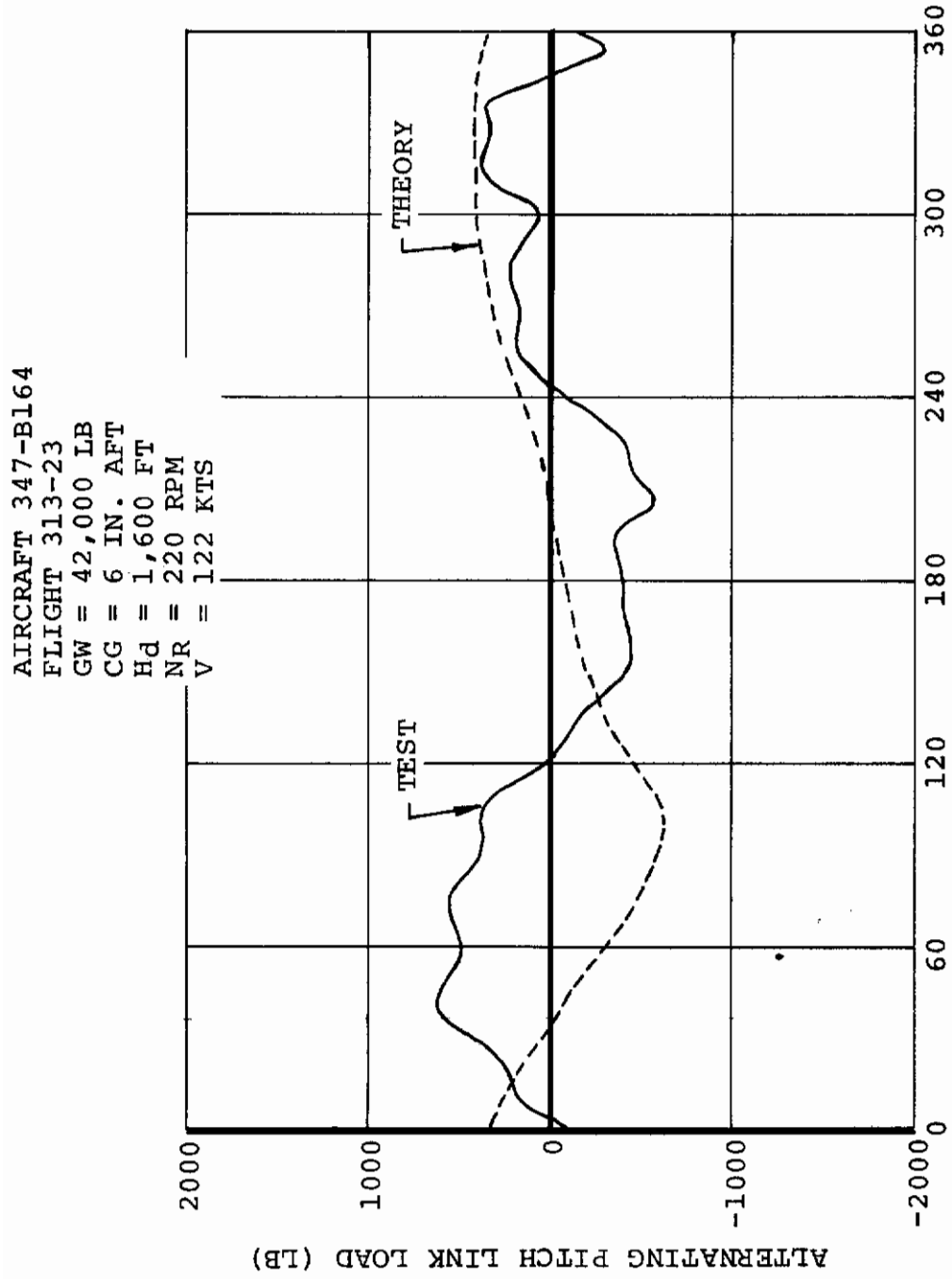

Figure 105. Model 347 with CH-47C Blades, Aft Rotor Predicted and Measured Pitch Link Load Waveform at 122 Knots

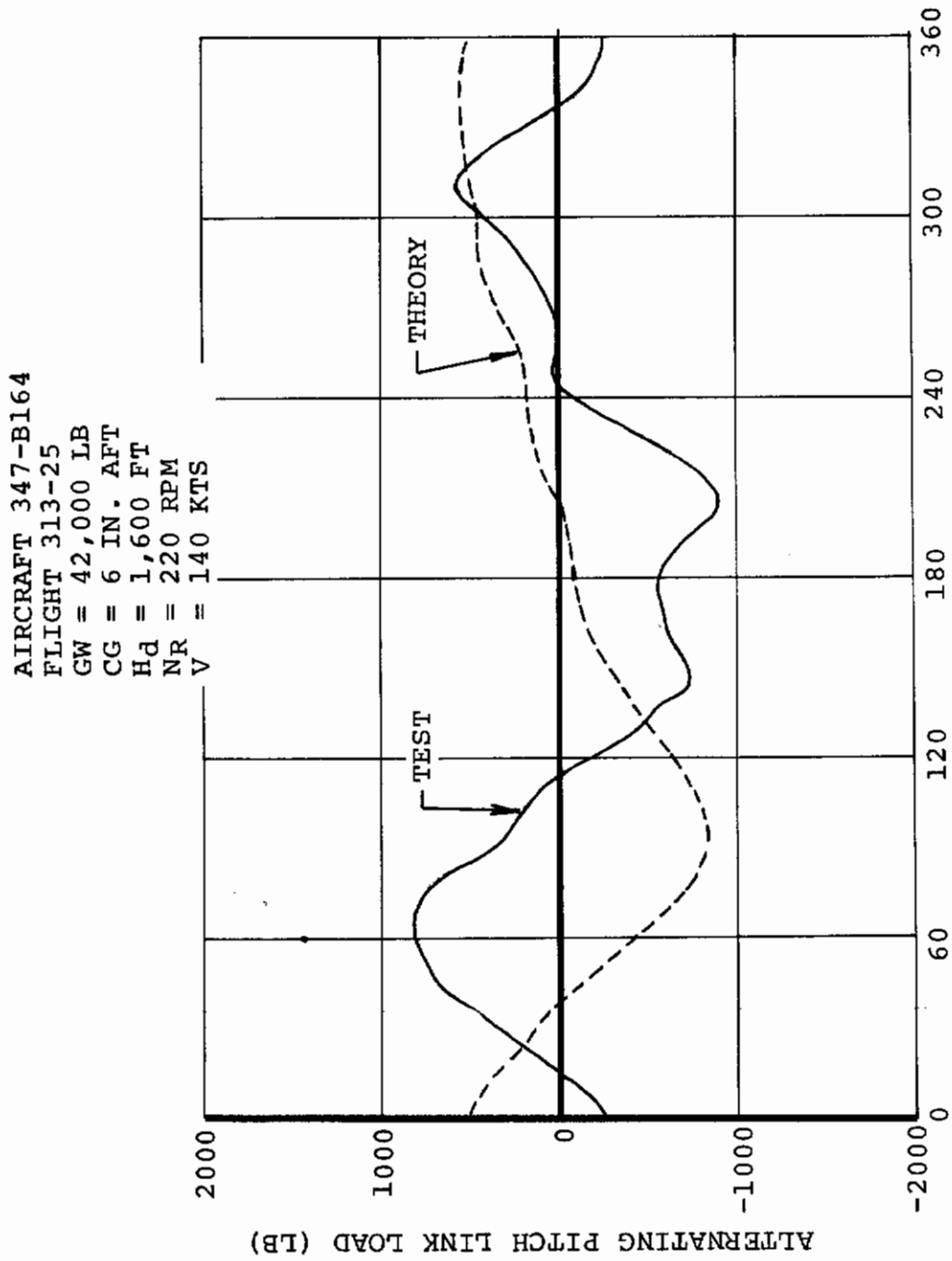

Figure 106. Model 347 With CH-47C Blades, Aft Rotor Predicted and Measured Pitch Link Load Waveform at 140 Knots

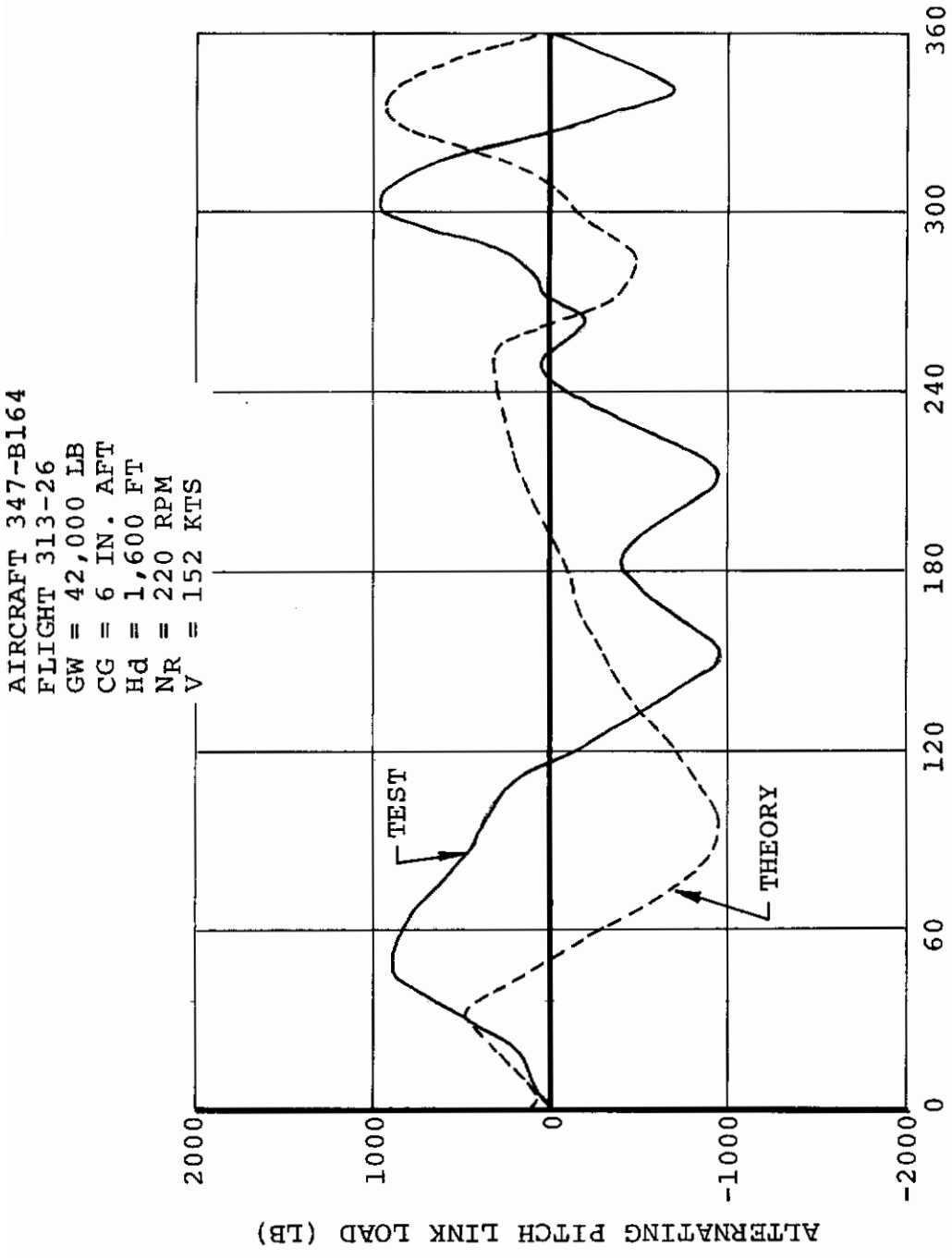

FIGURE 107. Model 347 With CH-47C Blades, Aft Rotor Predicted and Measured Pitch Link Load Waveform at 152 Knots

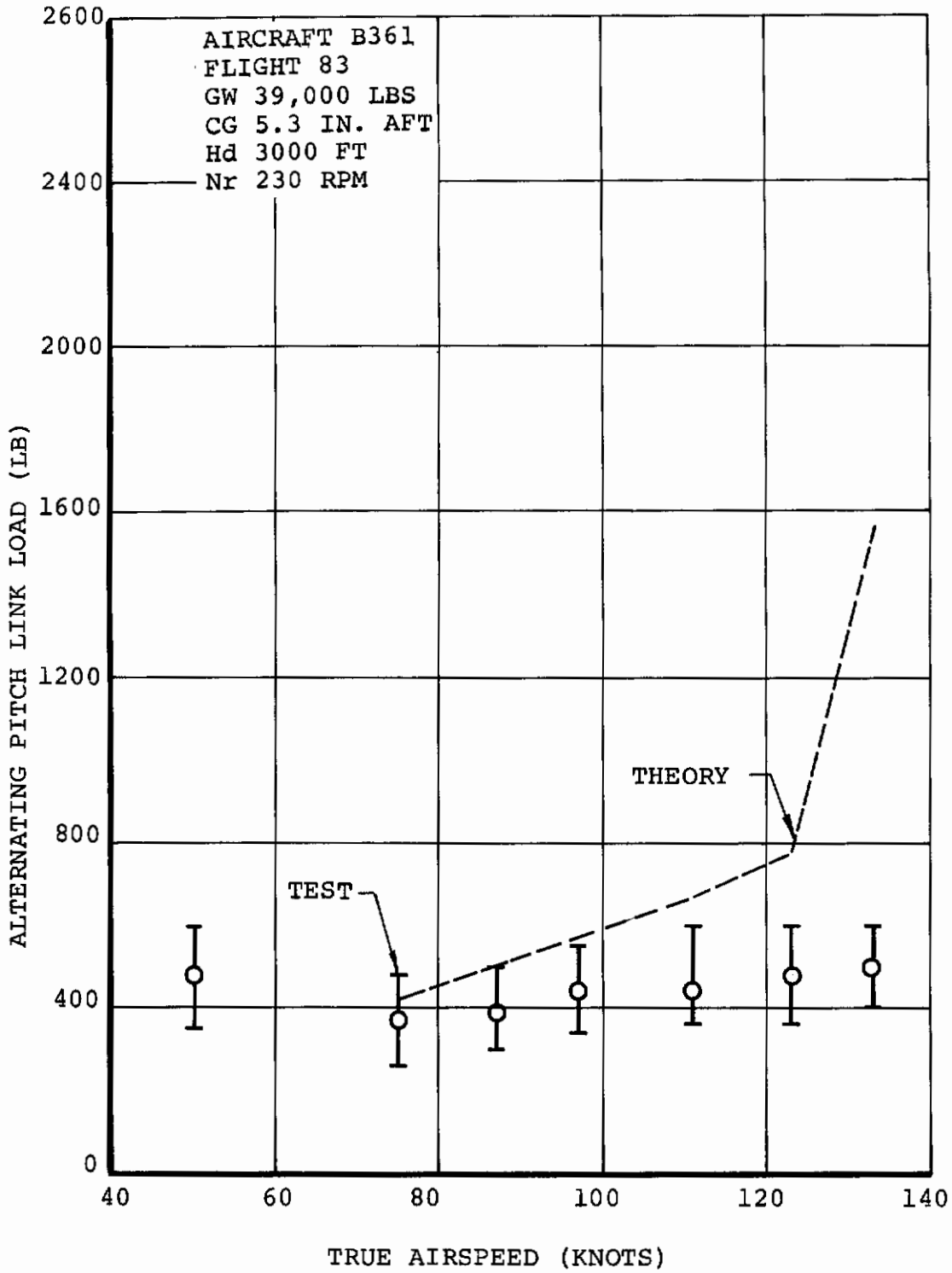

Figure 108. CH-47C Forward Rotor, Predicted and Measured Alternating Pitch Link Loads With Airspeed

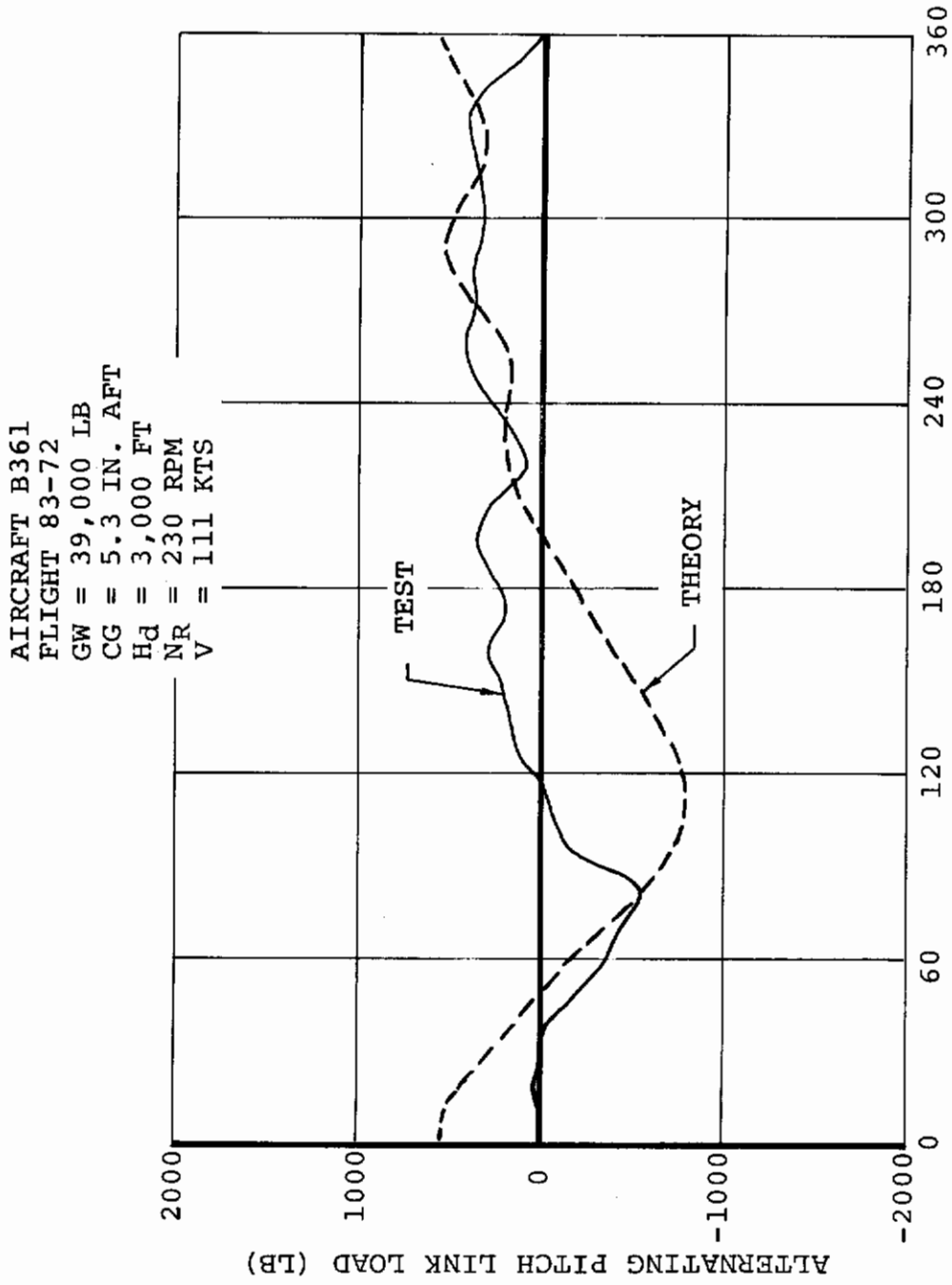

Figure 109. CH-47C Forward Rotor, Predicted and Measured Pitch Link Load Waveform at 111 Knots

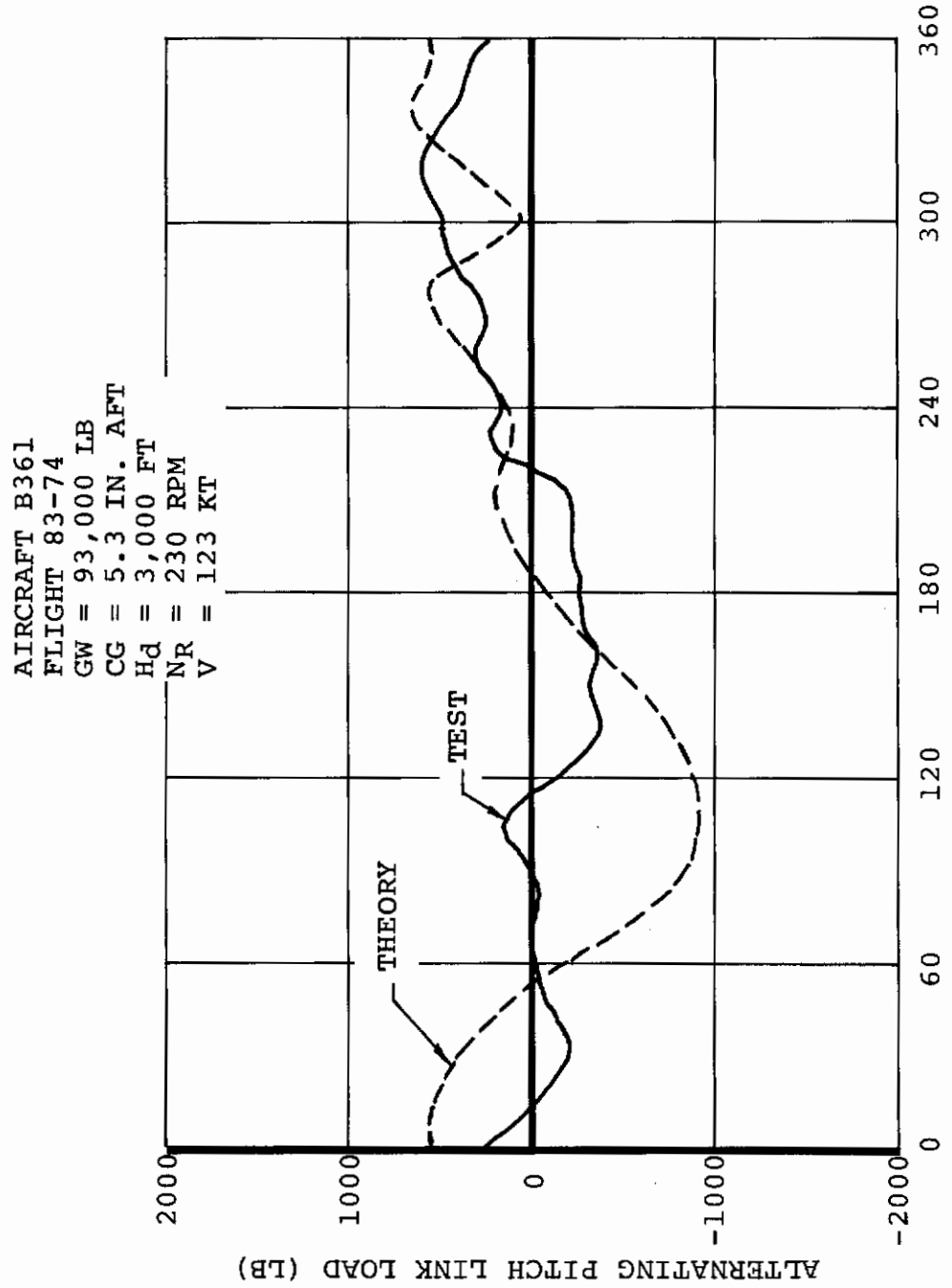

Figure 110. CH-47C Forward Rotor, Predicted and Measured Pitch Link Load Waveform at 123 Knots

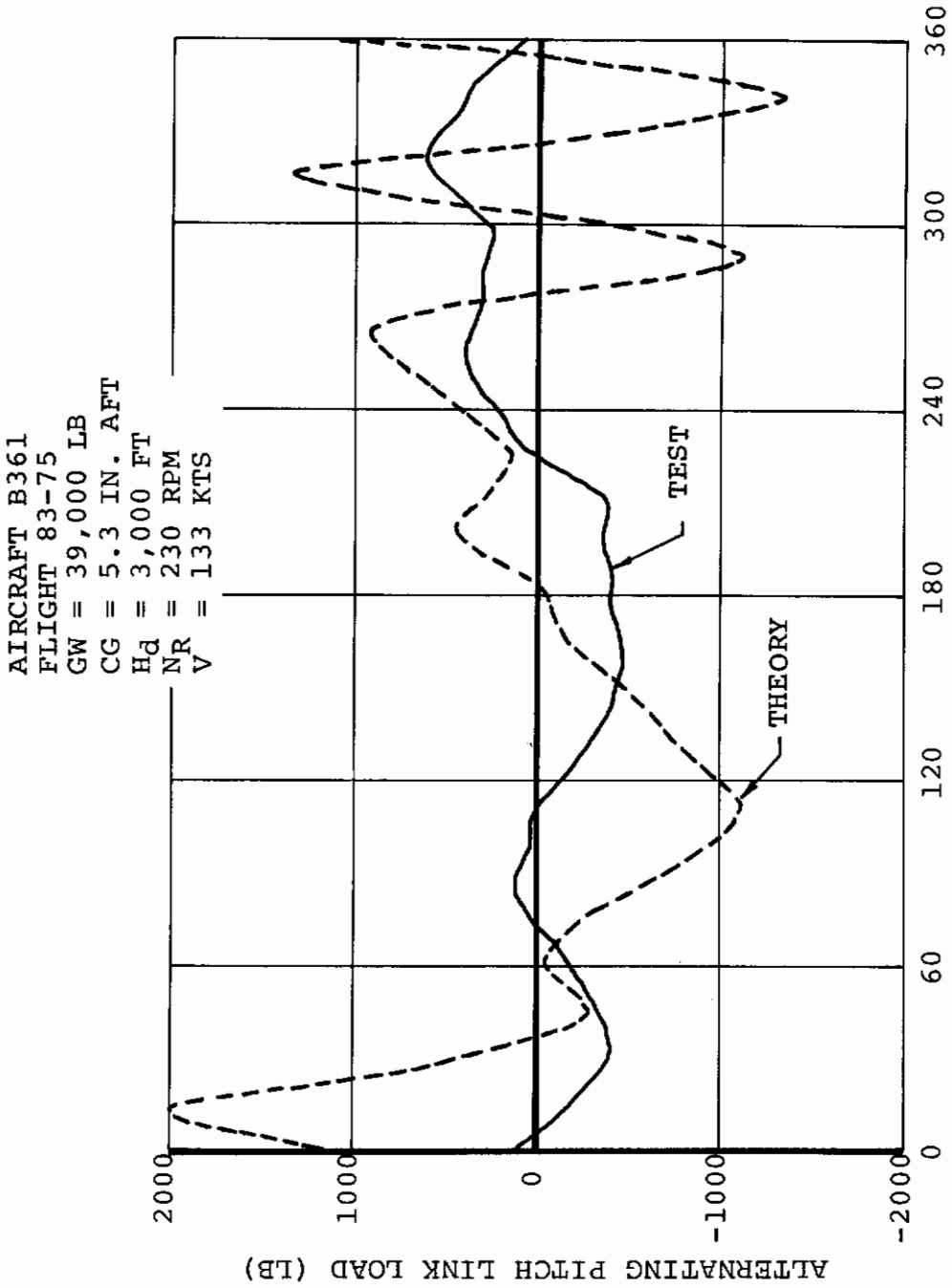

Figure 111. CH-47C Forward Rotor, Predicted and Measured Pitch Link Load Waveform at 133 Knots

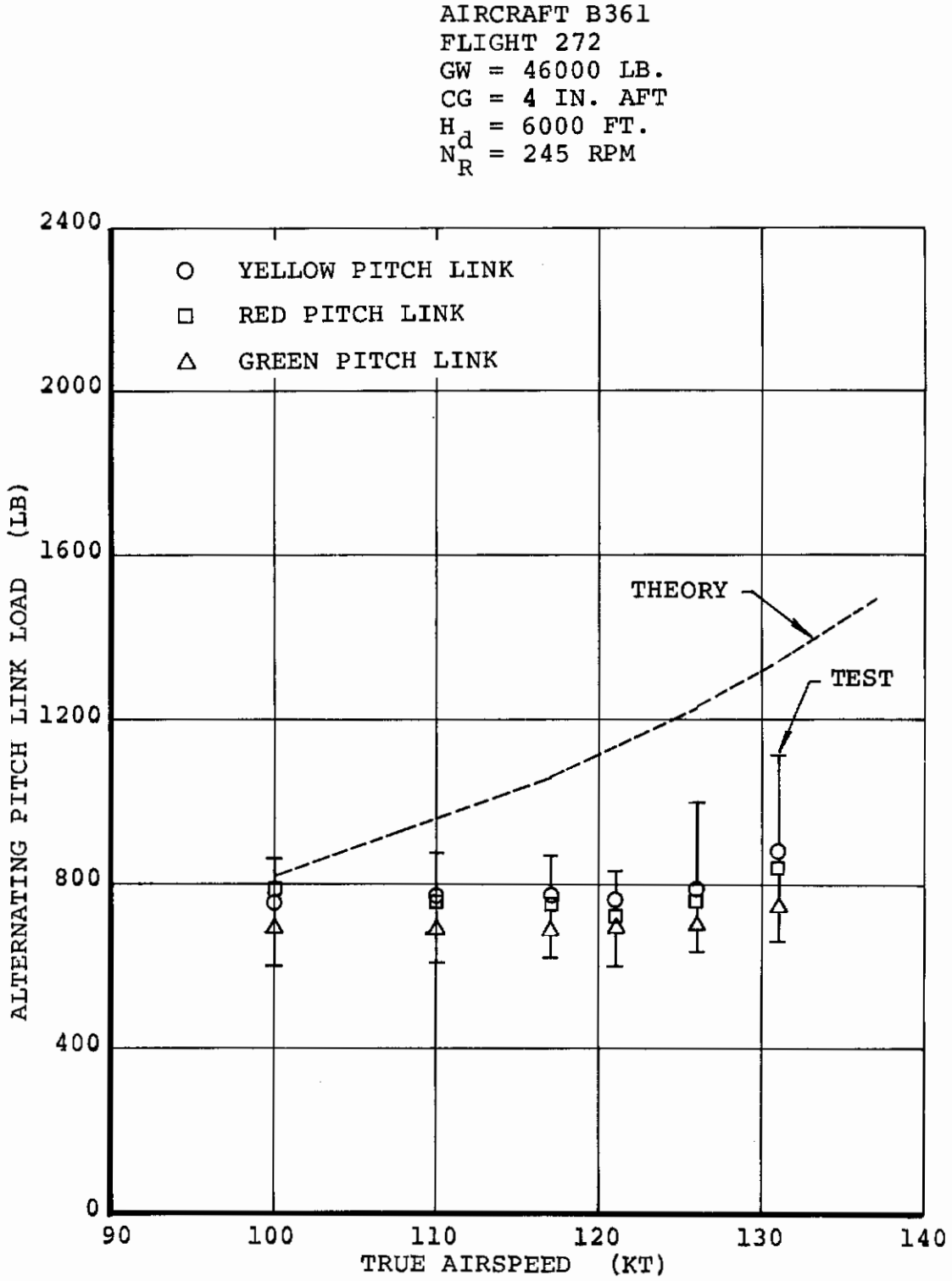

Figure 112. CH-47C With Advanced-Geometry Blades, Forward Rotor Predicted and Measured Alternating Pitch Link Loads With Airspeed

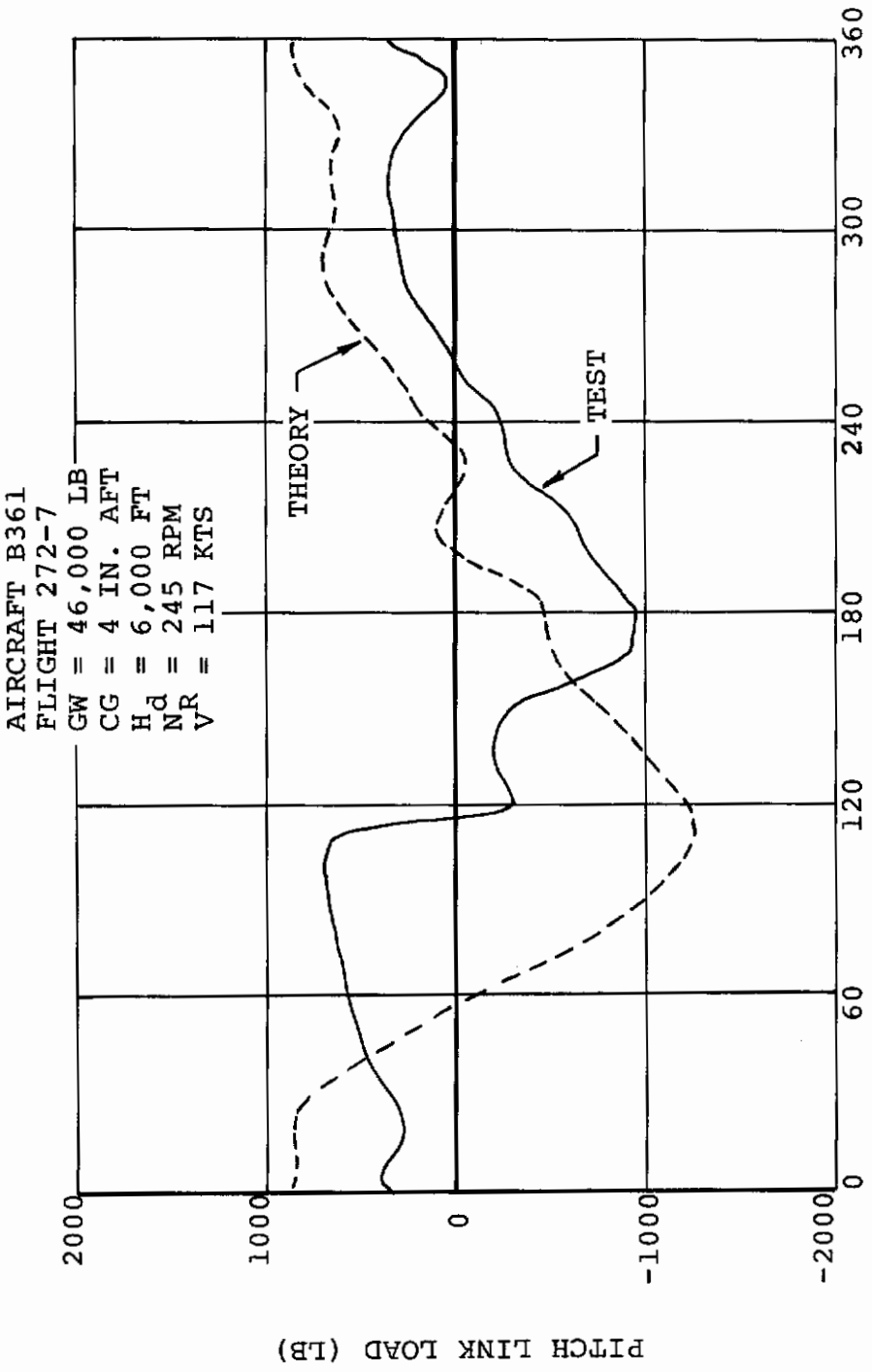

Figure 113. CH-47C With Advanced-Geometry Blades, Forward Rotor Predicted and Measured Pitch Link Waveform at 117 Knots

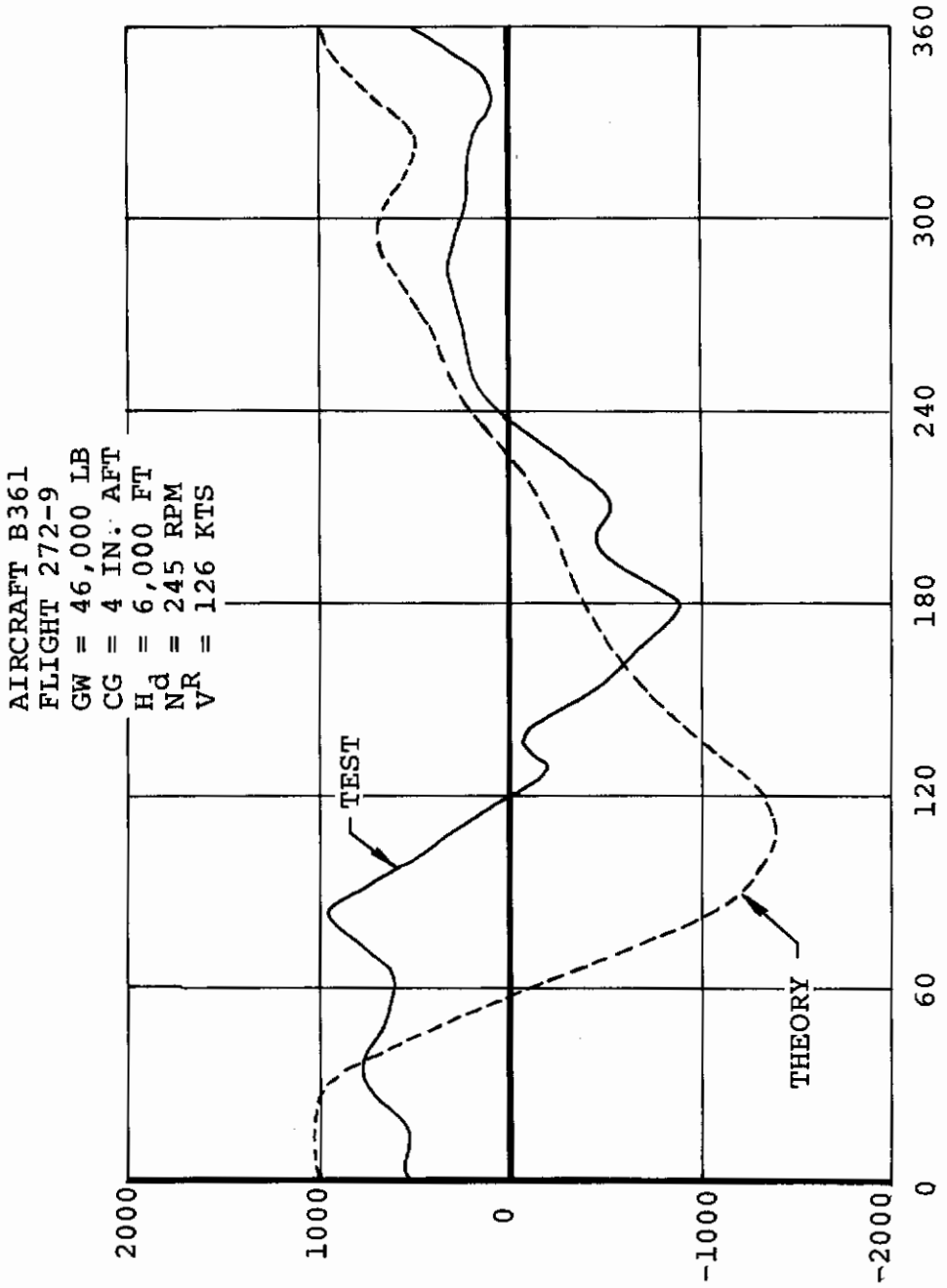

Figure 114. CH-47C With Advanced-Geometry Blades, Forward Rotor Predicted and Measured Pitch Link Waveform at 126 Knots

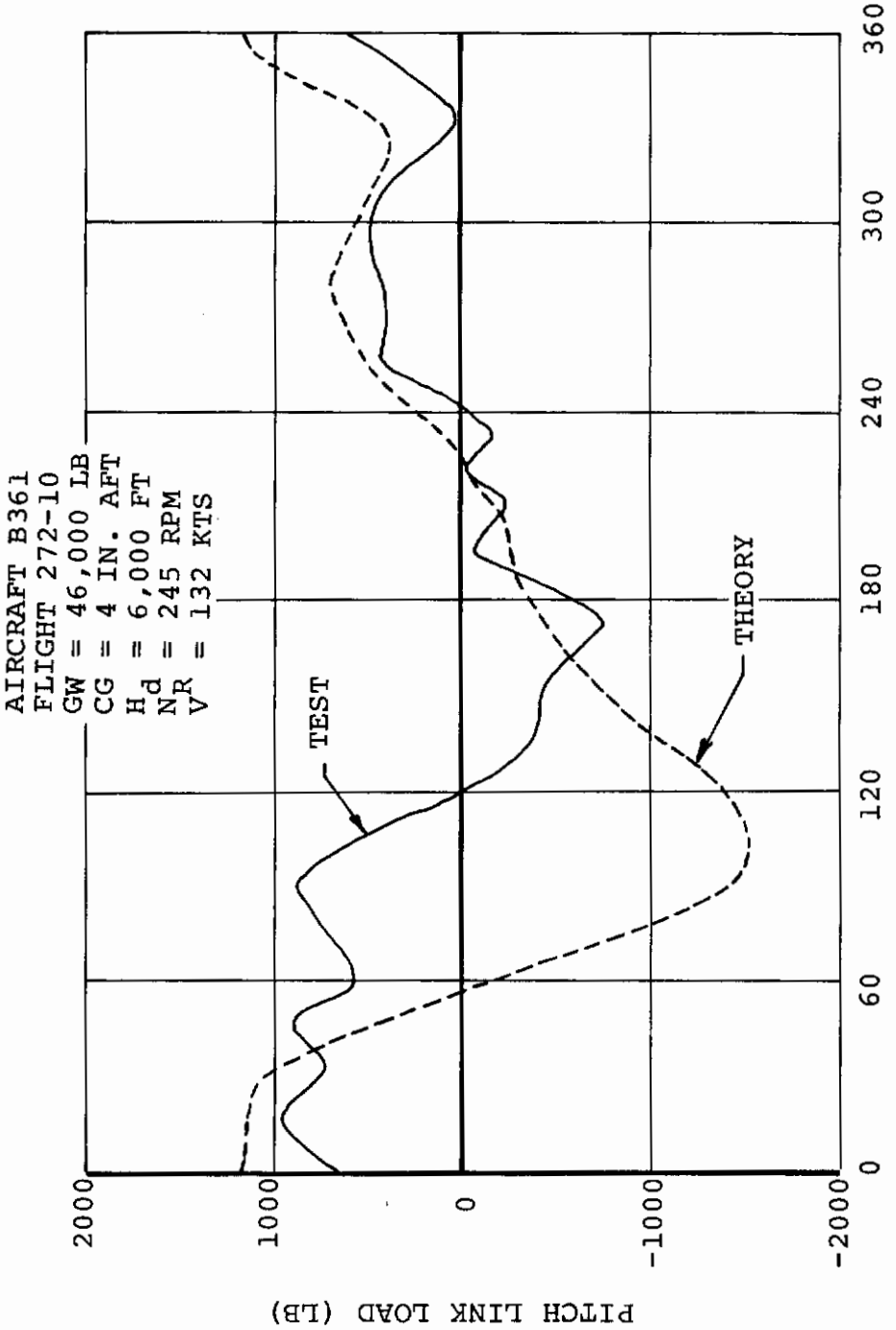

Figure 115. CH-47C With Advanced-Geometry Blades, Forward Rotor Predicted and Measured Pitch Link Waveform at 132 Knots

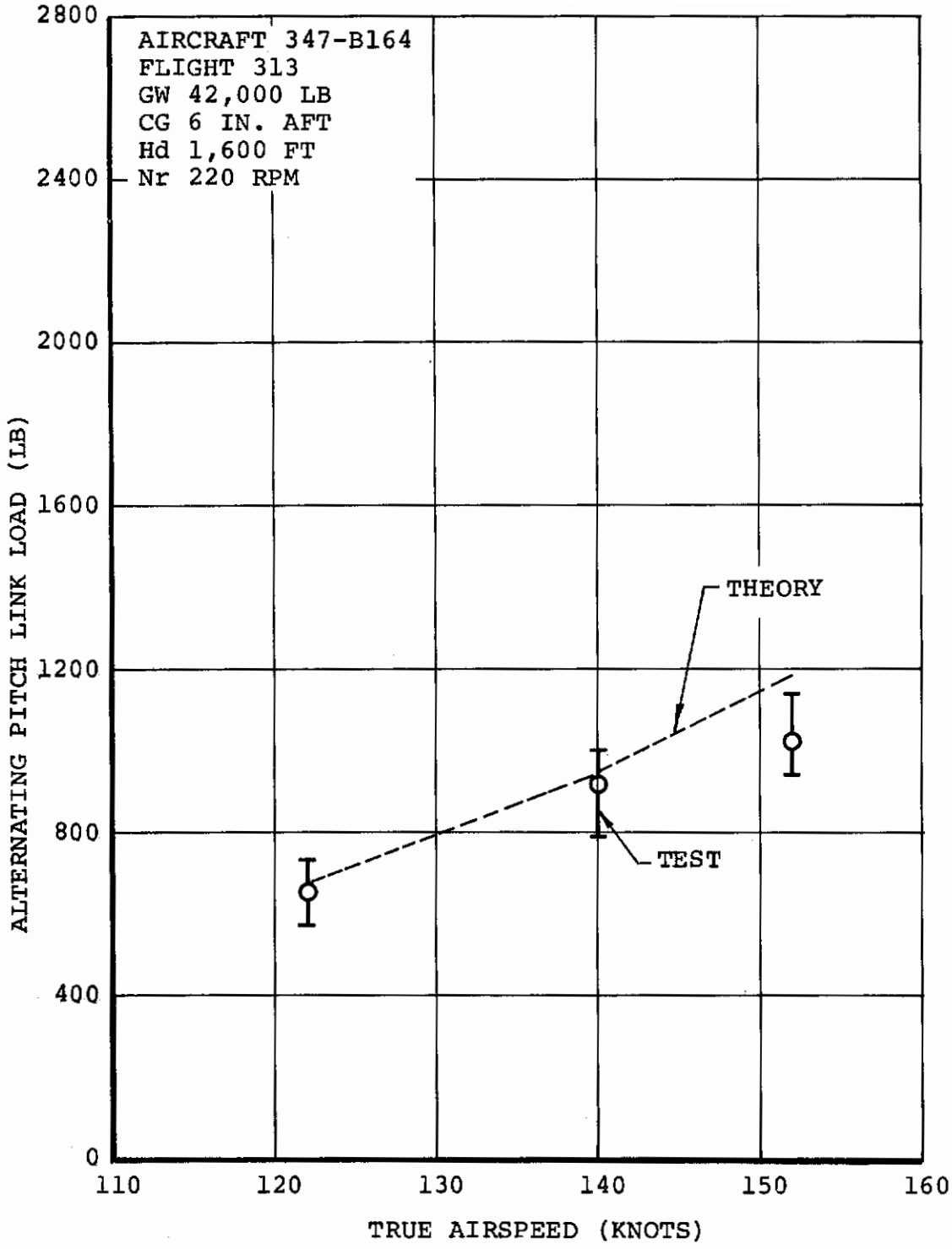

Figure 116. Model 347 With CH-47C Blades, Forward Rotor Predicted and Measured Alternating Pitch Link Loads With Airspeed

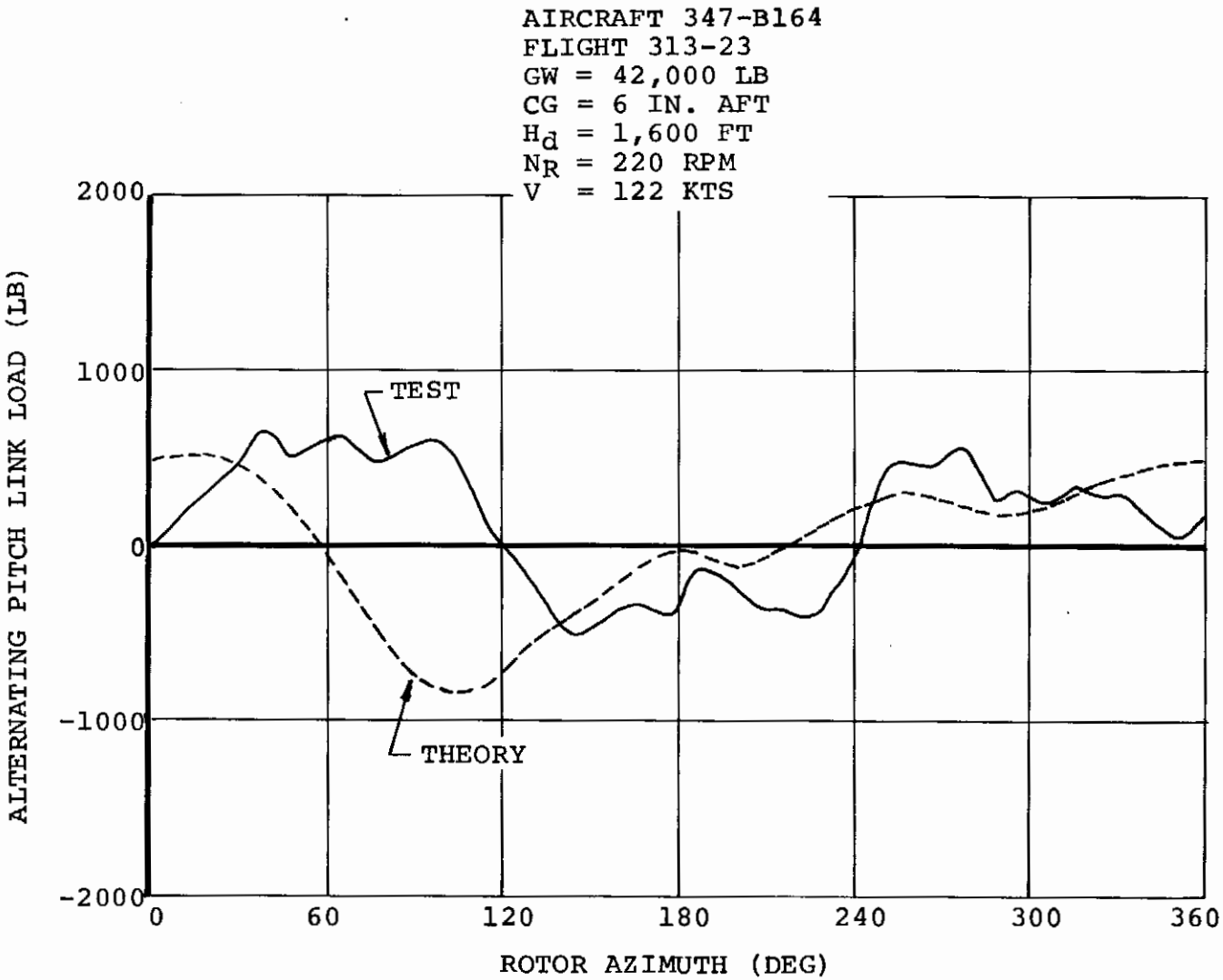

Figure 117. Model 347 with CH-47C Blades, Forward Rotor Predicted and Measured Pitch Link Load Waveform at 122 Knots

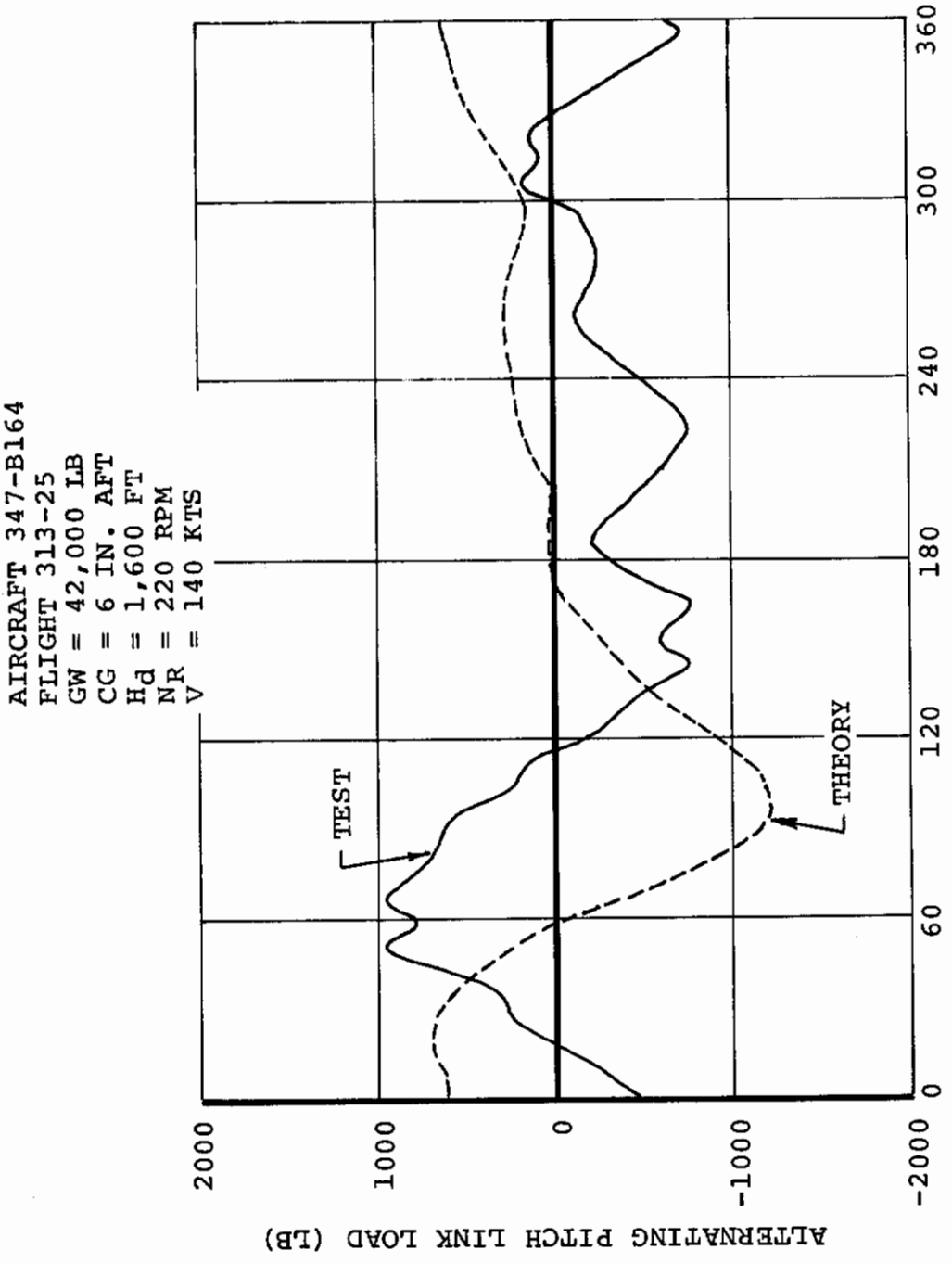

Figure 118. Model 347 with CH-47C Blades, Forward Rotor Predicted and Measured Pitch Link Load Waveform at 140 Knots

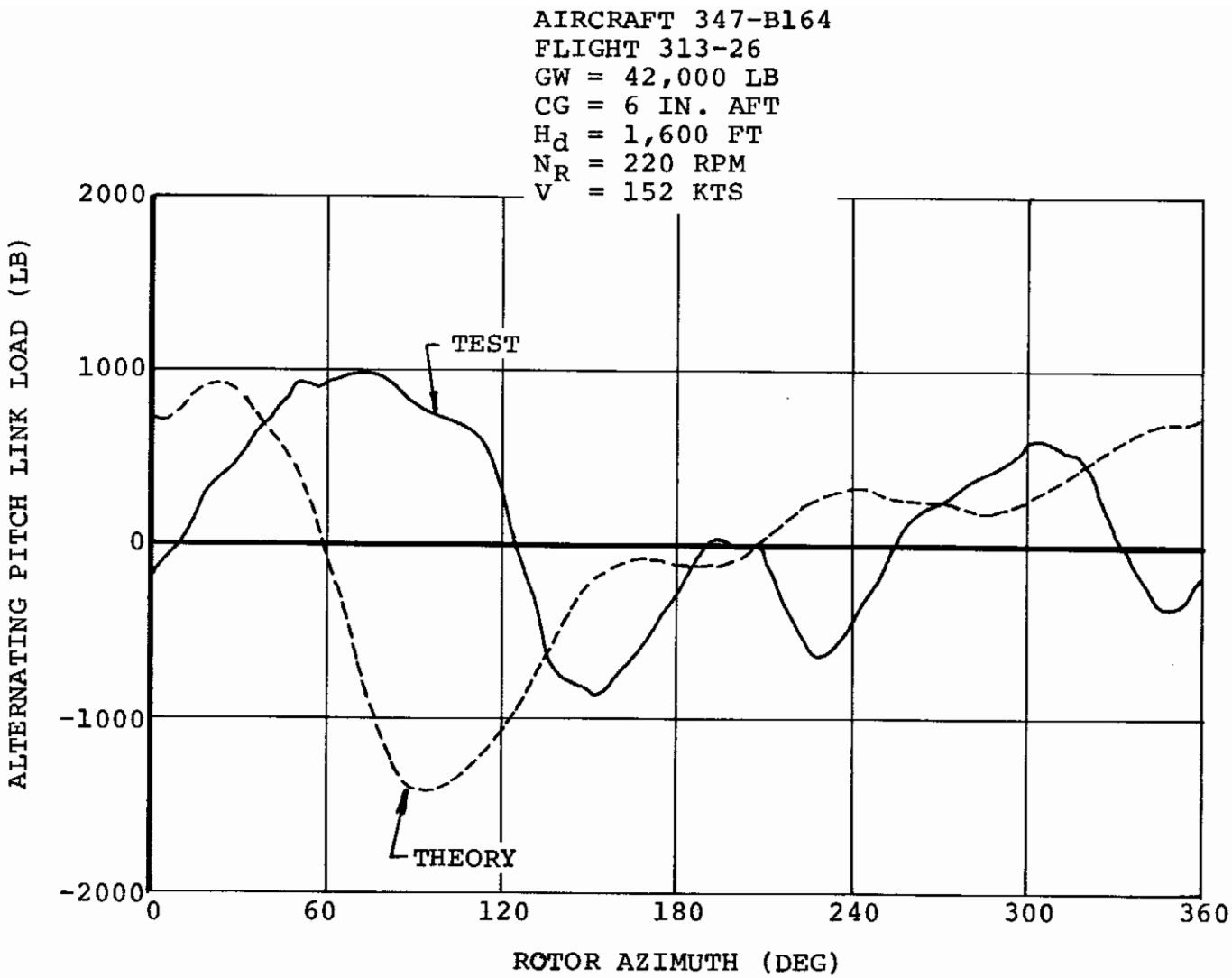

Figure 119. Model 347 with CH-47C Blades, Forward Rotor Predicted and Measured Pitch Link Load Waveform at 152 Knots

Flap Bending

Figures 120 through 131 are the correlation results for aft rotor alternating flap bending. The test data presented in these figures is for the CH-47 and Model 347 (both tandem-rotor configuration). The alternating bending moments shown are one-half of the peak-to-peak value for one rotor cycle. The symbol represents the arithmetic average value of all the cycles in the run while the vertical line through the symbol represents the highest and lowest value of all the cycles for that run.

The analysis with uniform downwash shows a consistent trend to increase mid-span and outboard alternating flap bending with airspeed. This predicted trend is consistent with the test data, but the analysis overpredicts with increasing airspeed. Model 347 flight 313 shows the best outboard bending moment correlation, while inboard bending moment correlation for both the Model 347 and the CH-47 tends to be underpredicted. The primary reason for overprediction outboard of mid-span and underprediction inboard is the use of uniform downwash in the analysis. When uniform downwash is used, downwash strength on the retreating side of the rotor azimuth is overpredicted, thereby creating a smaller blade section angle of attack and reduced lift on the retreating side of the rotor disc. This results in overprediction of 1-per-rev forcing which in turn results in overprediction of 1-, 2-, and 3-per-rev flap bending moments. Figure 120 shows why 1-, 2-, and 3-per-rev flap bending are overpredicted when uniform downwash is used in the analysis. This figure shows the predicted flap mode shapes in a vacuum for the CH-47C rotor blade. Note that the first flexible mode with a frequency ratio of 2.57 at 230 rpm is roughly symmetrical about its peak bending moment at mid-span. Any 1-per-rev forcing will result in 1-, 2-, and 3-per-rev flap bending moments with a radial distribution similar to the first flexible mode. Note that all the flap bending predictions with uniform downwash have this same radial distribution, reflecting dominant excitement of the first flexible mode.

Use of nonuniform downwash in the analyses more closely predicts blade lift radial distribution around the azimuth and also introduces blade tip vortices lying in or near the disc plane. For the forward rotor of a tandem-rotor configuration, blade vortices are predominantly due to that of a preceding blade of the same rotor (called blade-to-blade interference), while for the aft rotor of a tandem-rotor helicopter blade vortex interference is predominantly due to tip vortices from the forward rotor trailing downstream (called rotor-on-rotor interference). Vortex strikes or near-strikes tend to impart impulsive forcing to the blade due to the high velocities associated with tip vortices, therefore exciting the higher flap bending modes. These modes (primarily second flexible

through fourth flexible modes) are lightly damped and therefore contribute significantly to the flap bending moment when vortex interference is involved. Note from Figure 120 that the second, third, and fourth flexible modes for the CH-47C, 4.75 ω/Ω, 7.90 ω/Ω, and 12.19 ω/Ω, respectively, all peak at 10 to 13 percent radius and 80 to 85 percent radius. This indicates that rotor blade flap bending moments, when operating with significant vortex disturbances, would have a large outboard and inboard peak mainly due to higher harmonics (4 to 12 per rev). Also note that the third flexible mode suppresses bending moments near mid-span due to the first flexible mode, thus indicating that use of nonuniform downwash in the analysis would tend to suppress first-, second-, and third-harmonic bending at mid-span. The analysis was run with nonuniform downwash for the highest speed condition for each helicopter to show the impact of higher harmonics due to vortex interference on predicted blade flap bending. The results, shown in Figures 122, 123, 127, and 131, reflect the outboard and inboard peak and correlate better with the flap bending test data than the predictions with uniform downwash. A sharper inboard peak and outboard peak would be predicted with nonuniform downwash if the analysis had 12-harmonic capability instead of 10 harmonics. Note that the fourth flexible mode in Figure 120 has a frequency ratio of 12.19 per rev; and therefore, 12-per-rev bending moment contributions due to this mode at 10 and 80 percent span will not be reflected in the analysis.

Figures 132 through 142 are the correlation results for the forward rotor alternating flap bending on the tandem-rotor helicopters. The uniform downwash predictions for these data follow the same trend as the uniform downwash predictions for the aft rotor. Mid-span and outboard flap bending increases with increasing airspeed and overpredicts. As with the aft rotor predictions, use of uniform downwash overpredicts 1-per-rev forcing and neglects vortex interference. The only difference is that forward rotor interference is mainly blade-to-blade while aft rotor interference is predominantly rotor-on-rotor. Figures 134, 138, and 142 show nonuniform downwash predictions for the highest speed case for each helicopter rotor. The predictions with nonuniform downwash correlate better than those with uniform downwash, reflecting the outboard and inboard peak due to higher harmonics induced by interference.

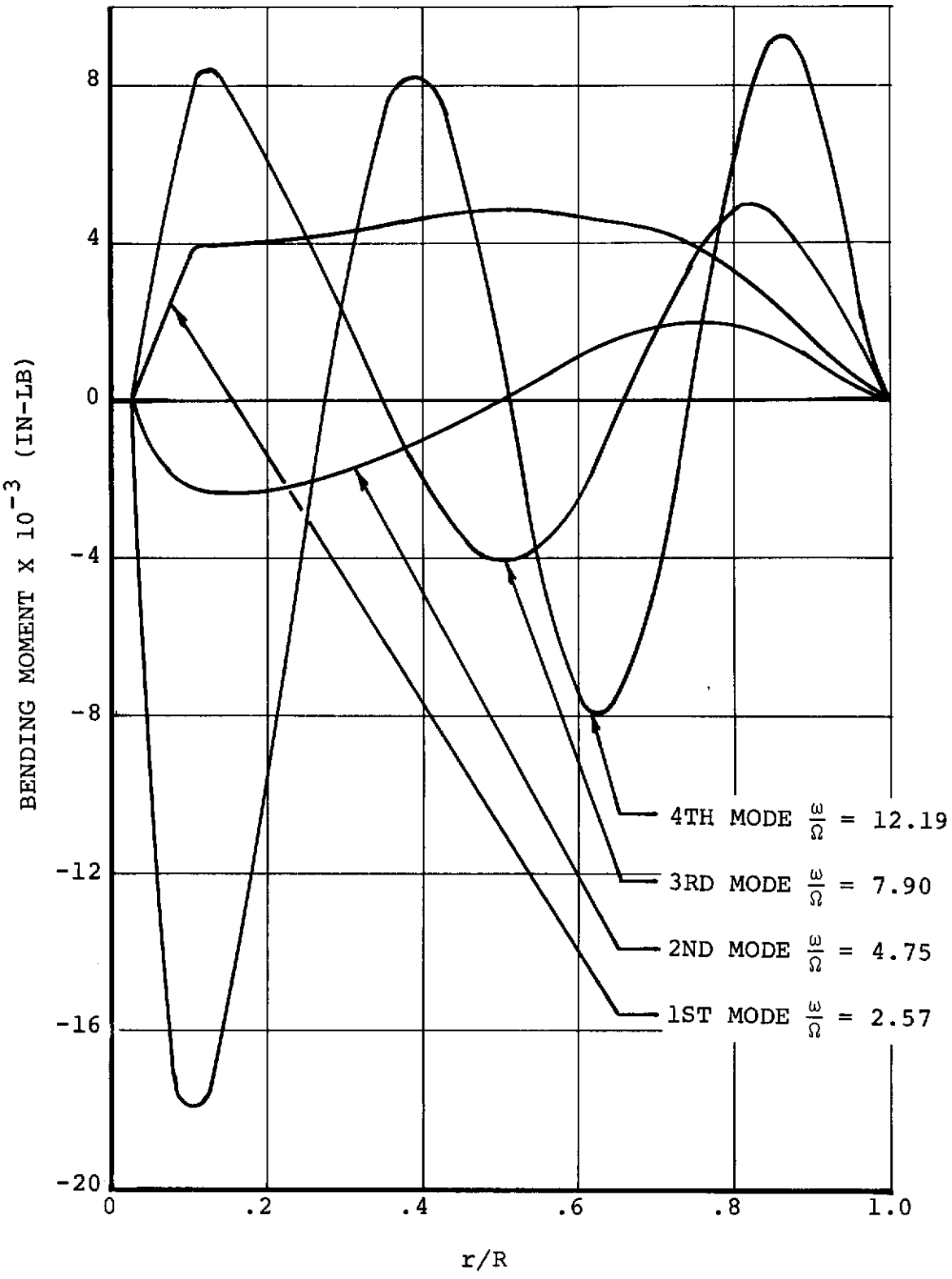

Figure 120. CH-47C L-01, Predicted Flap Bending Moment Mode Shapes in a Vacuum at 230 RPM

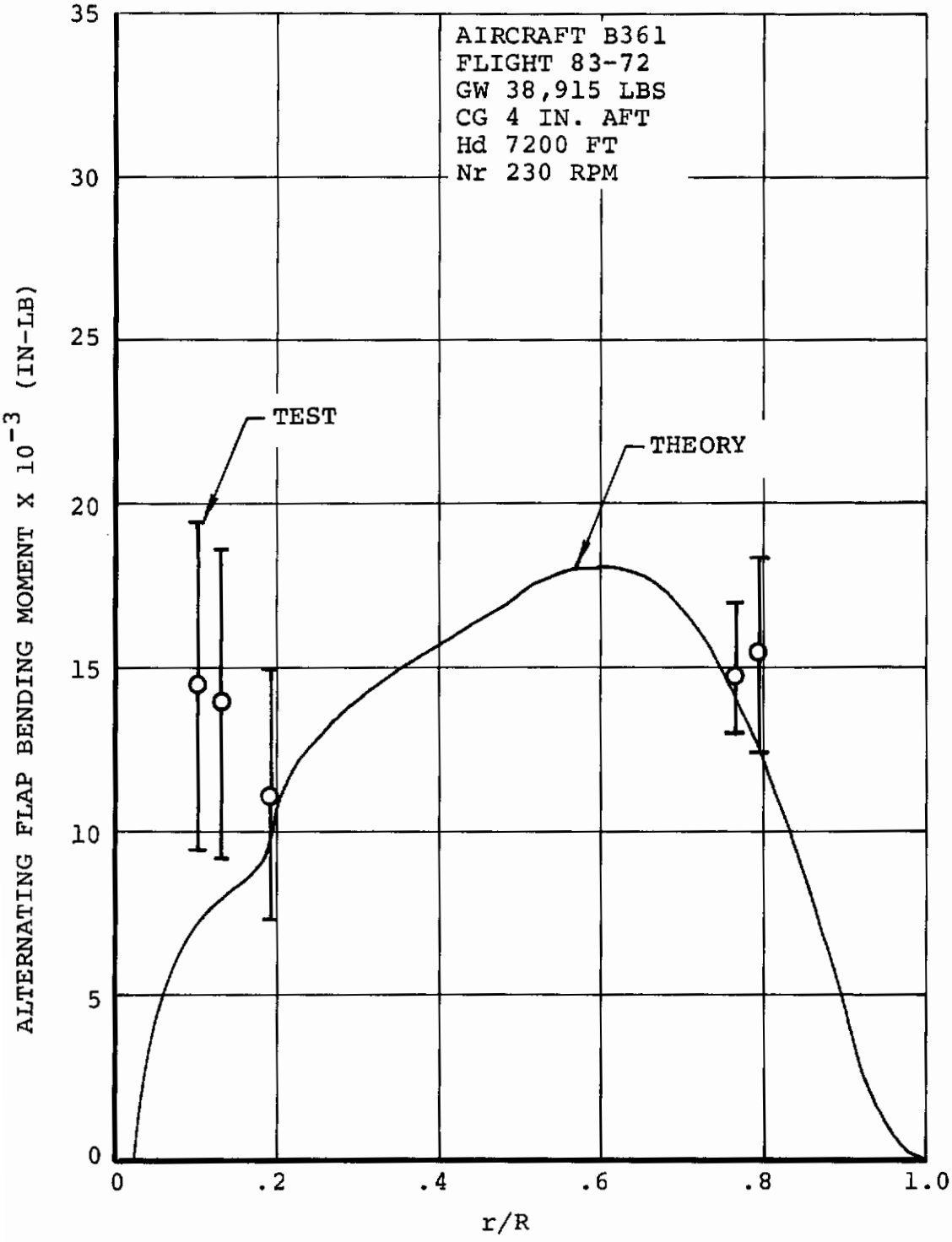

Figure 121. CH-47C Aft Rotor, Predicted and Measured Alternating Flap Bending Moment at V = 111 Knots

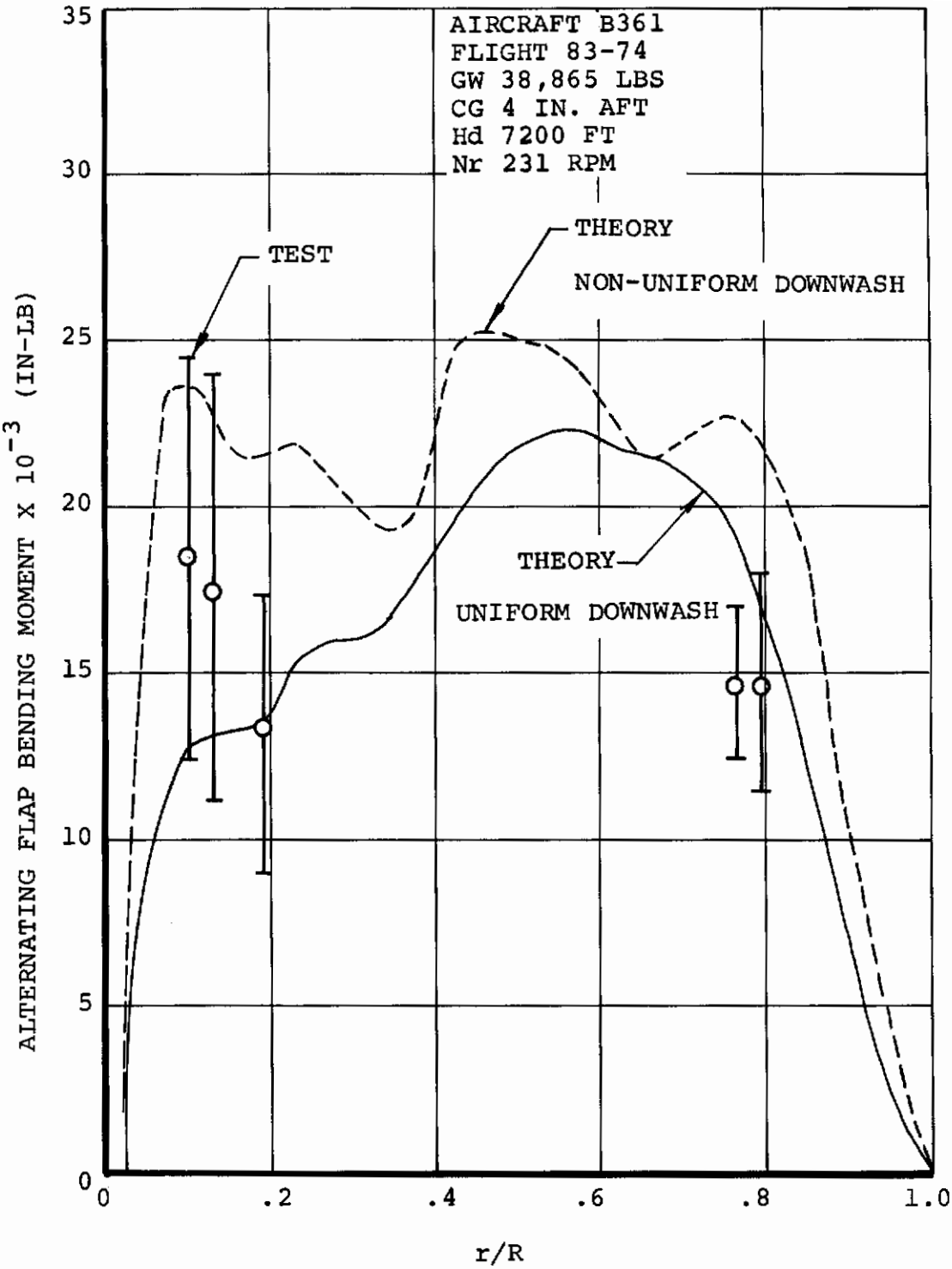

Figure 122. CH-47C Aft Rotor, Predicted and Measured Alternating Flap Bending Moment at V = 123 Knots

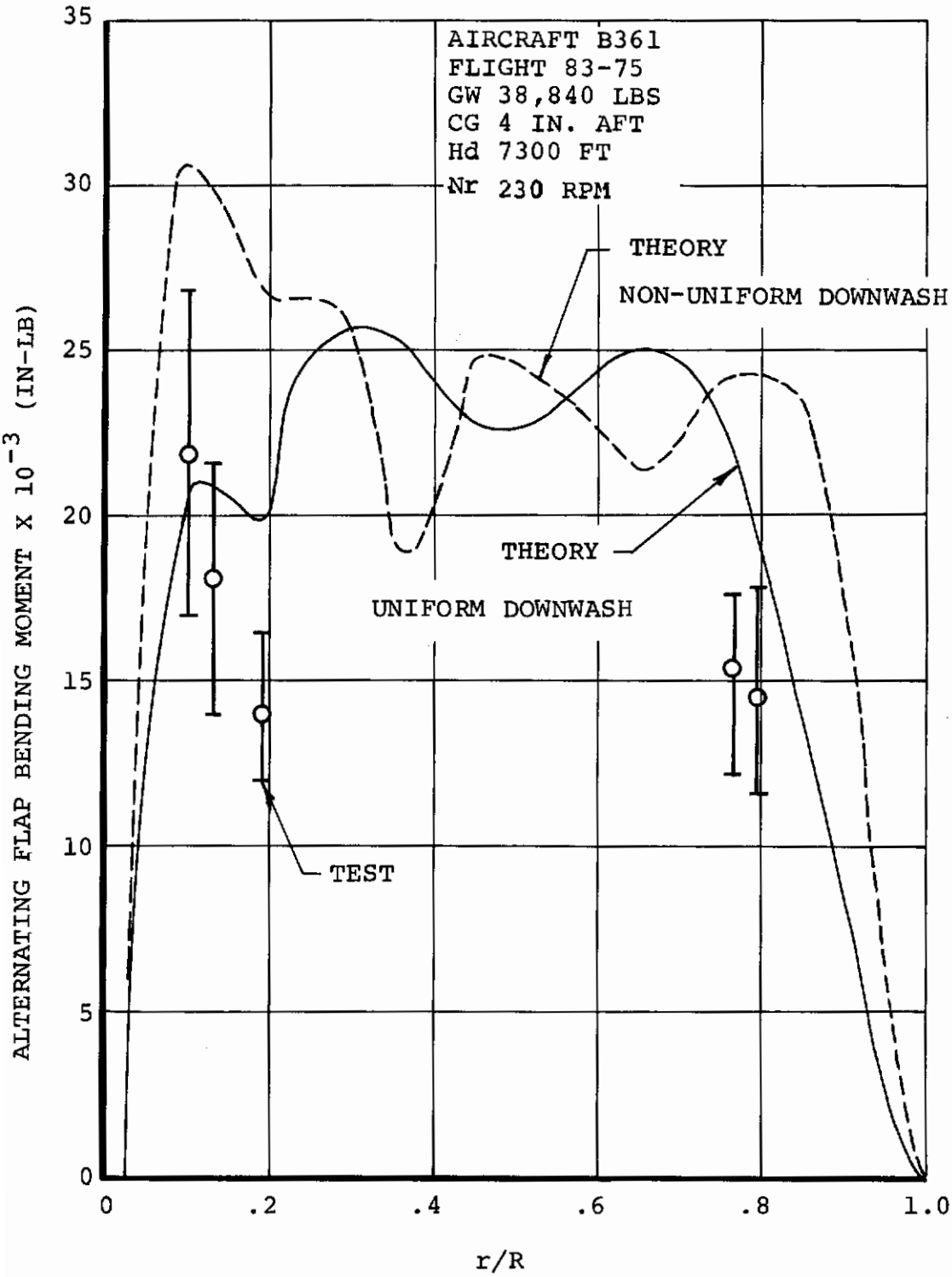

Figure 123. CH-47C Aft Rotor, Predicted and Measured Alternating Flap Bending Moment at V = 133 Knots

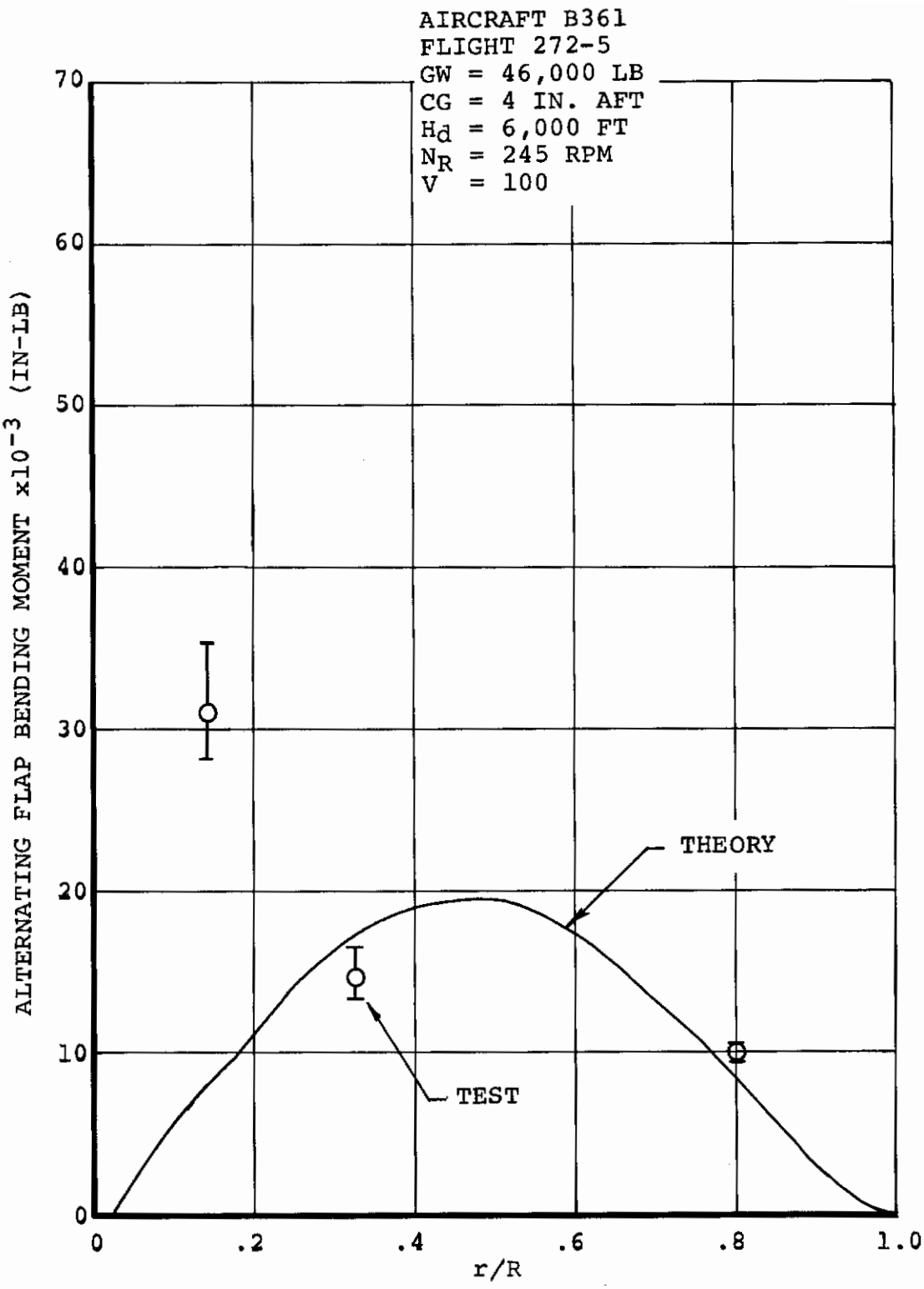

Figure 124. CH-47C With Advanced-Geometry Blades, Aft Rotor Predicted and Measured Alternating Flap Bending Moment at 100 Knots

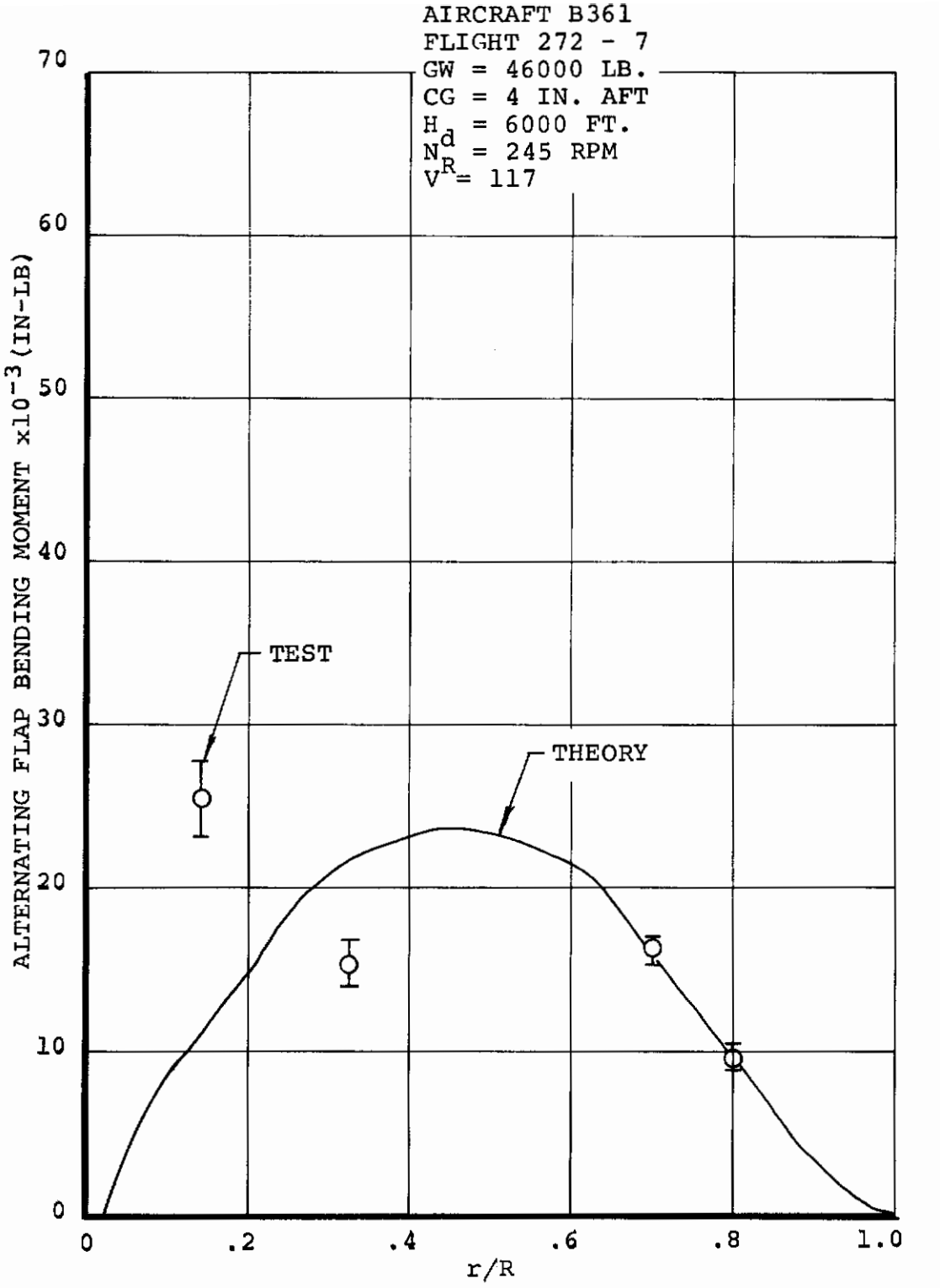

Figure 125. CH-47C With Advanced-Geometry Blades, Aft Rotor Predicted and Measured Alternating Flap Bending Moment at 117 Knots

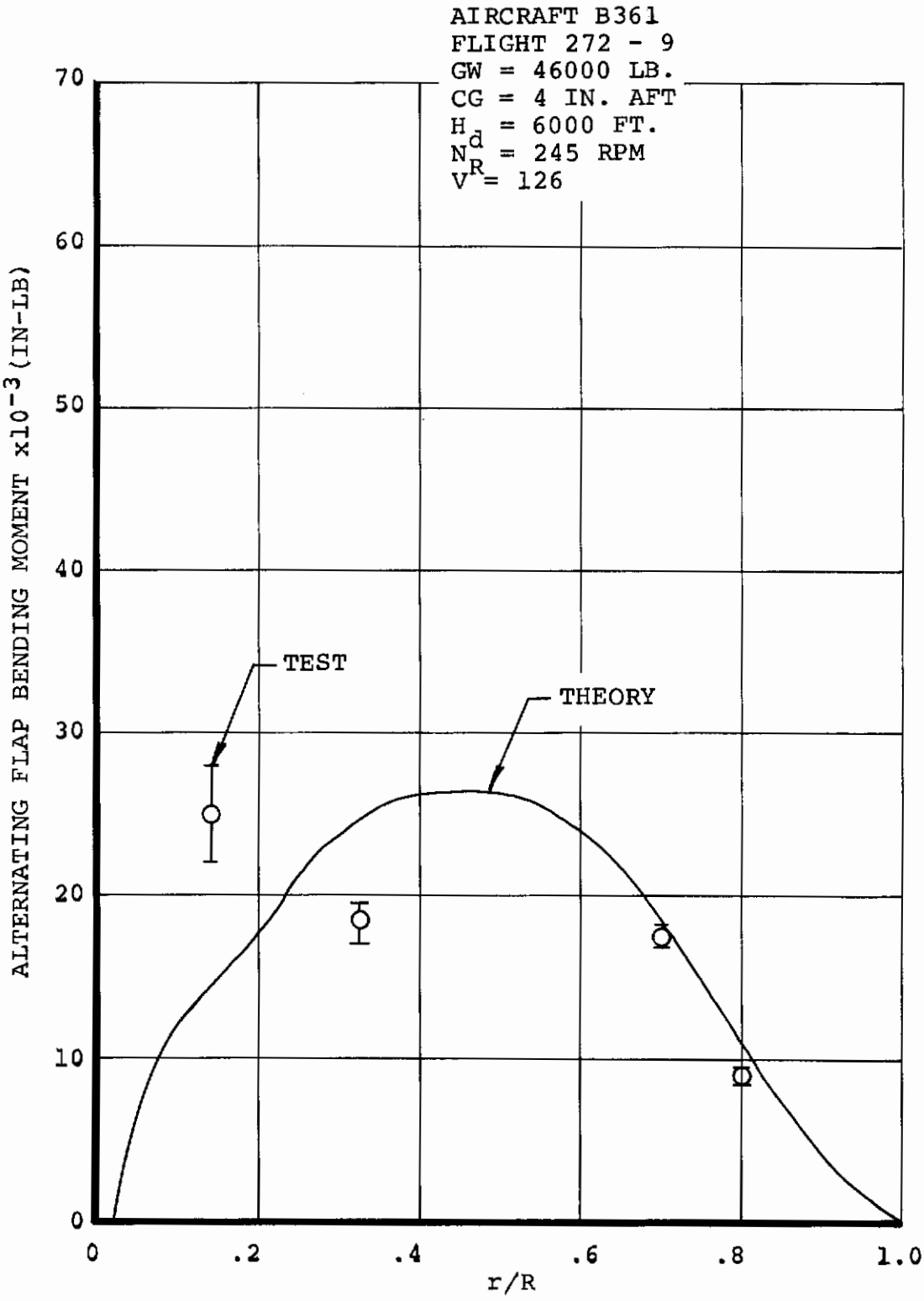

Figure 126. CH-47C With Advanced-Geometry Blades, Aft Rotor Predicted and Measured Alternating Flap Bending Moment at 126 Knots

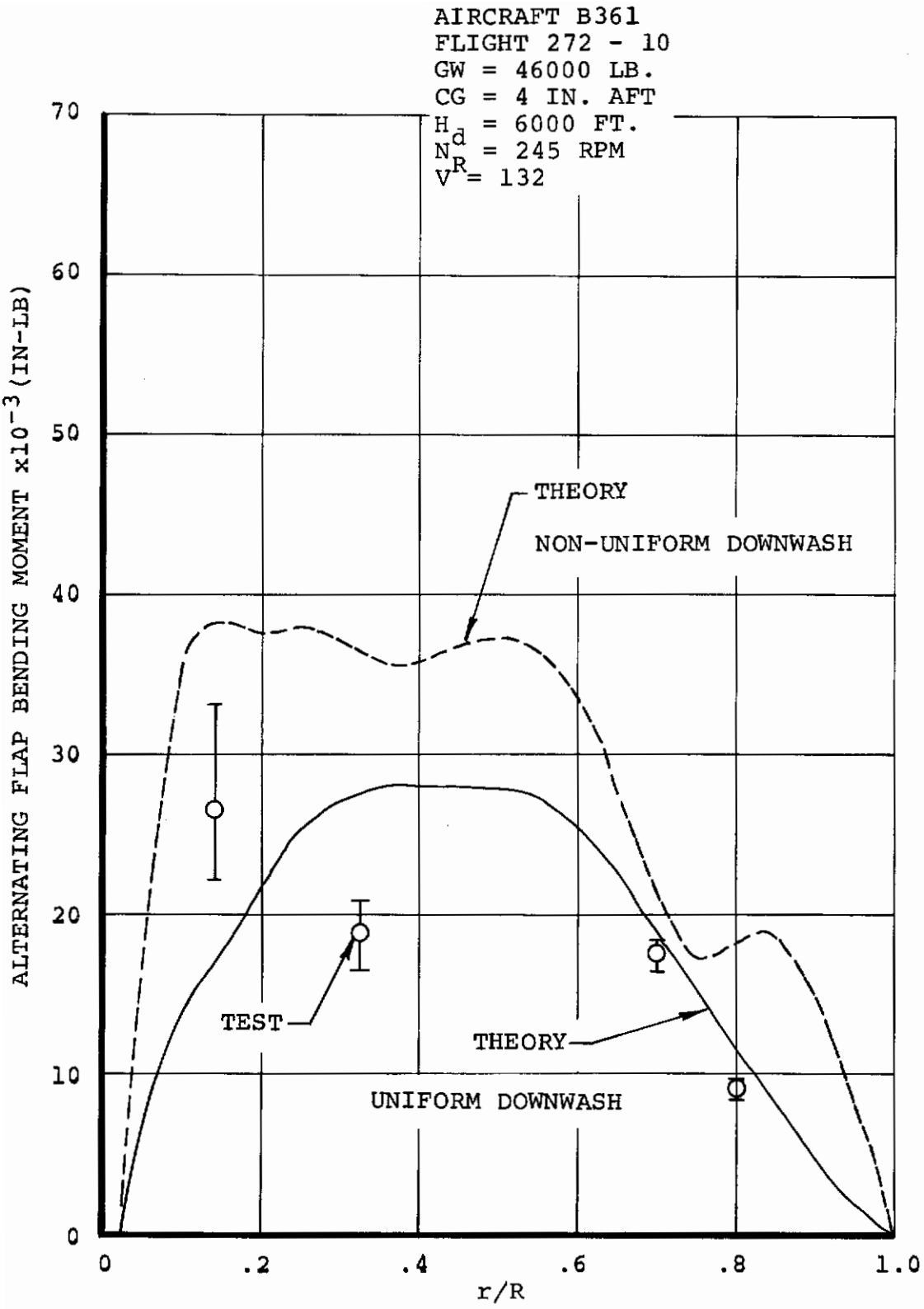

Figure 127. CH-47C With Advanced-Geometry Blades, Aft Rotor Predicted and Measured Alternating Flap Bending Moment at 132 Knots

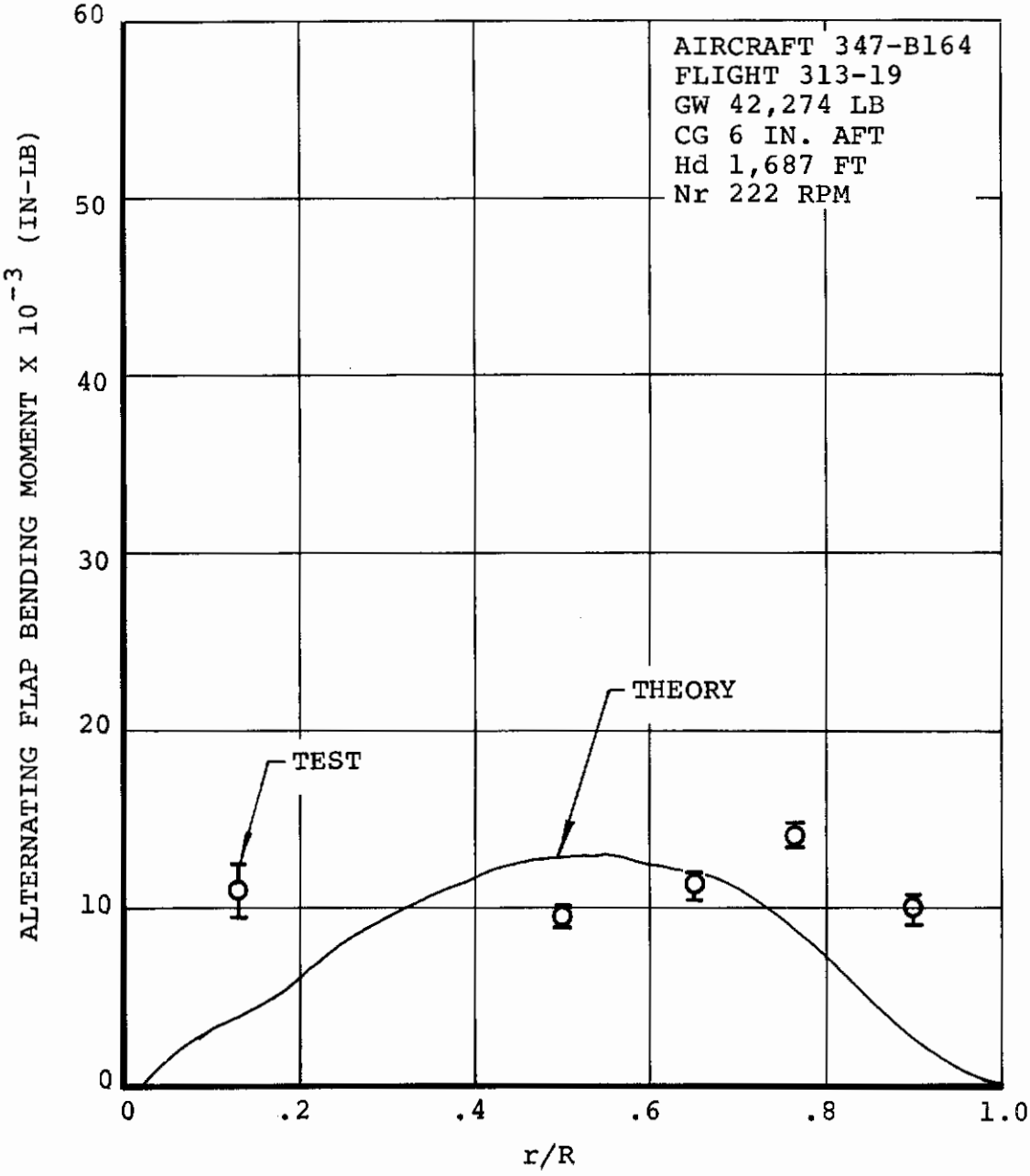

Figure 128. Model 347 With CH-47C Blades, Aft Rotor Predicted and Measured Alternating Flap Bending Moment at V = 87 Knots

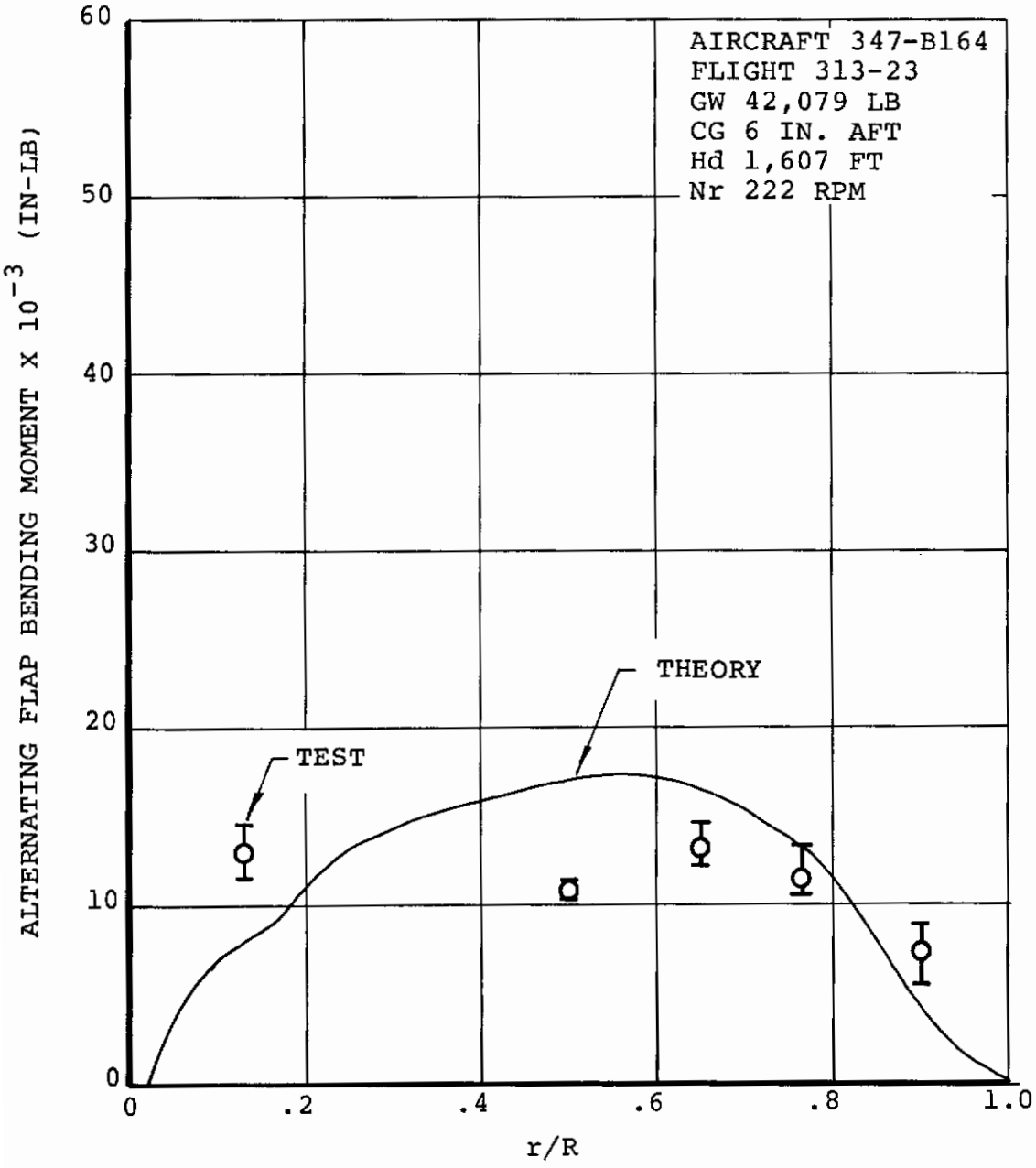

Figure 129. Model 347 With CH-47C Blades, Aft Rotor Predicted and Measured Alternating Flap Bending Moment at V = 122 Knots

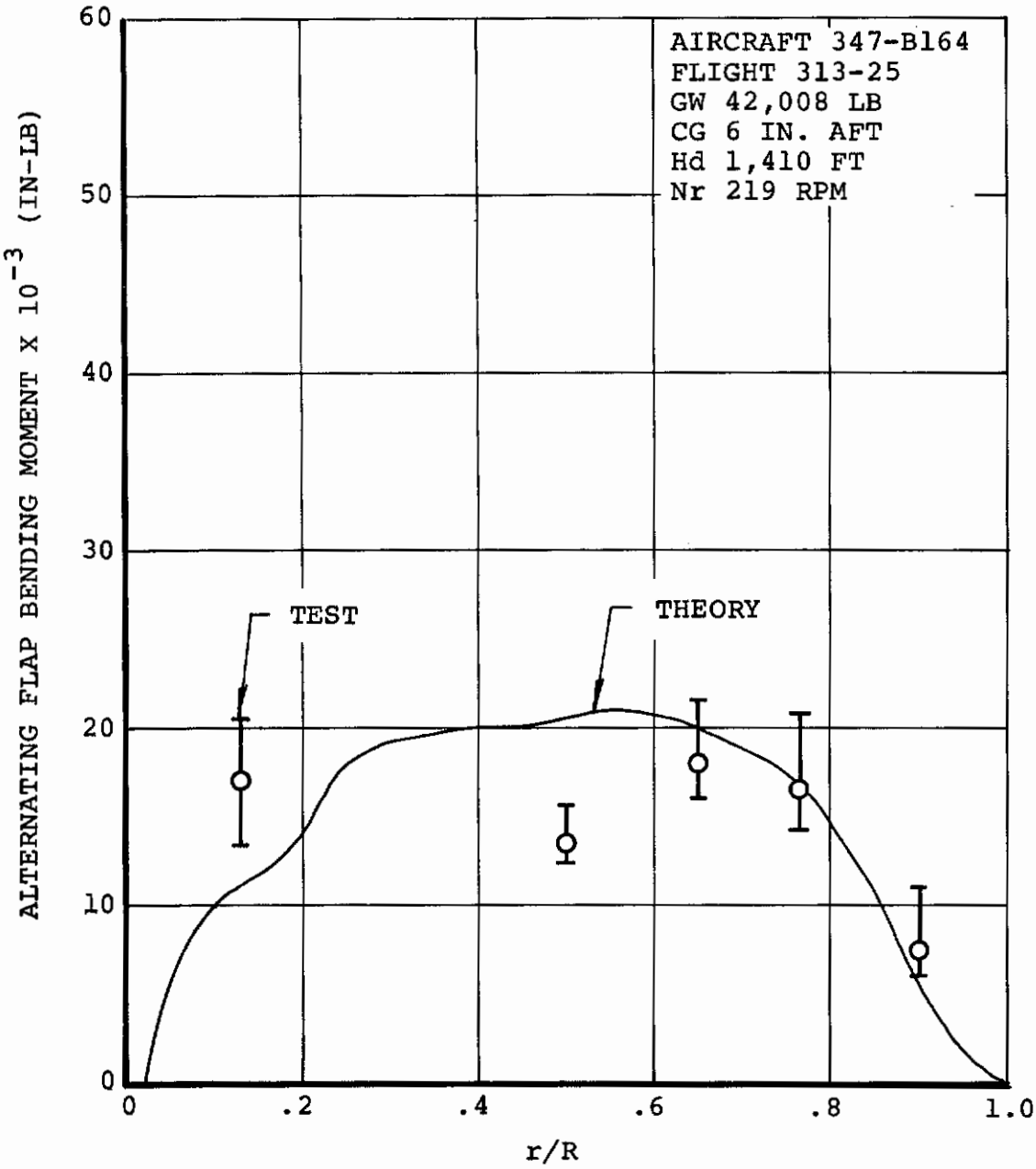

Figure 130. Model 347 With CH-47C Blades, Aft Rotor Predicted and Measured Alternating Flap Bending Moment at V = 140 Knots

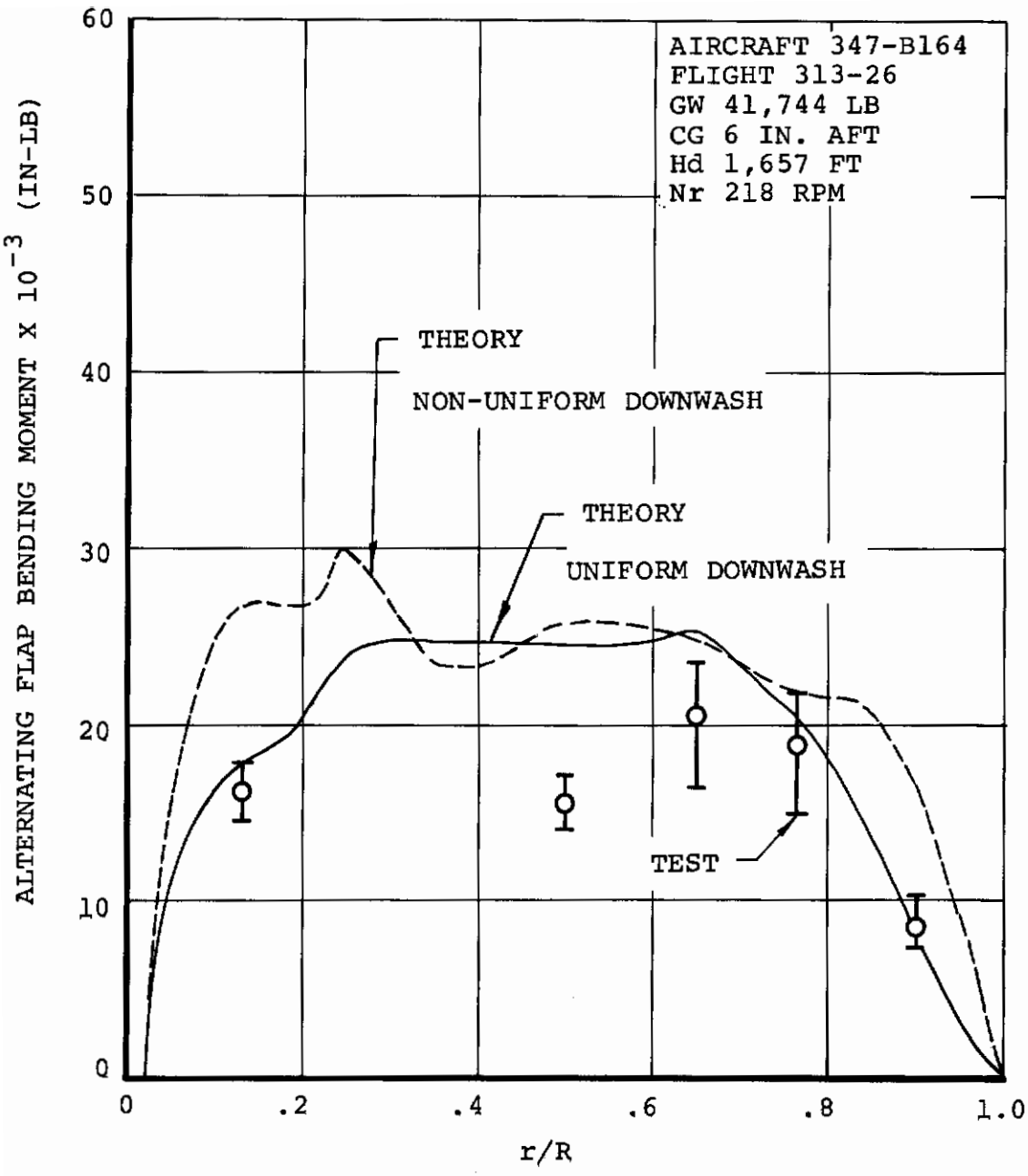

Figure 131. Model 347 With CH-47C Blades, Aft Rotor Predicted and Measured Alternating Flap Bending Moment at V = 152 Knots

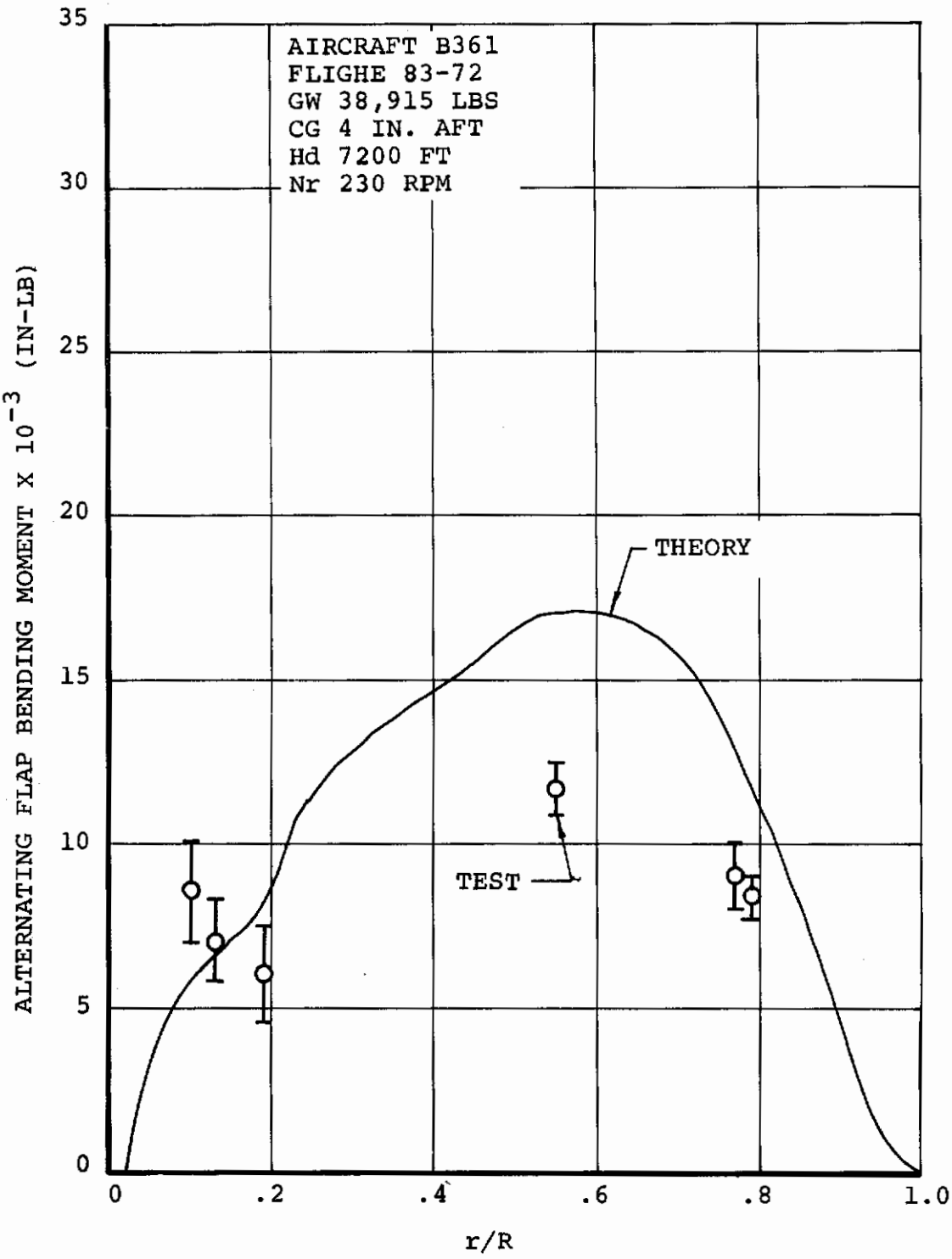

Figure 132. CH-47C Forward Rotor, Predicted and Measured Alternating Flap Bending Moment at V = 111 Knots

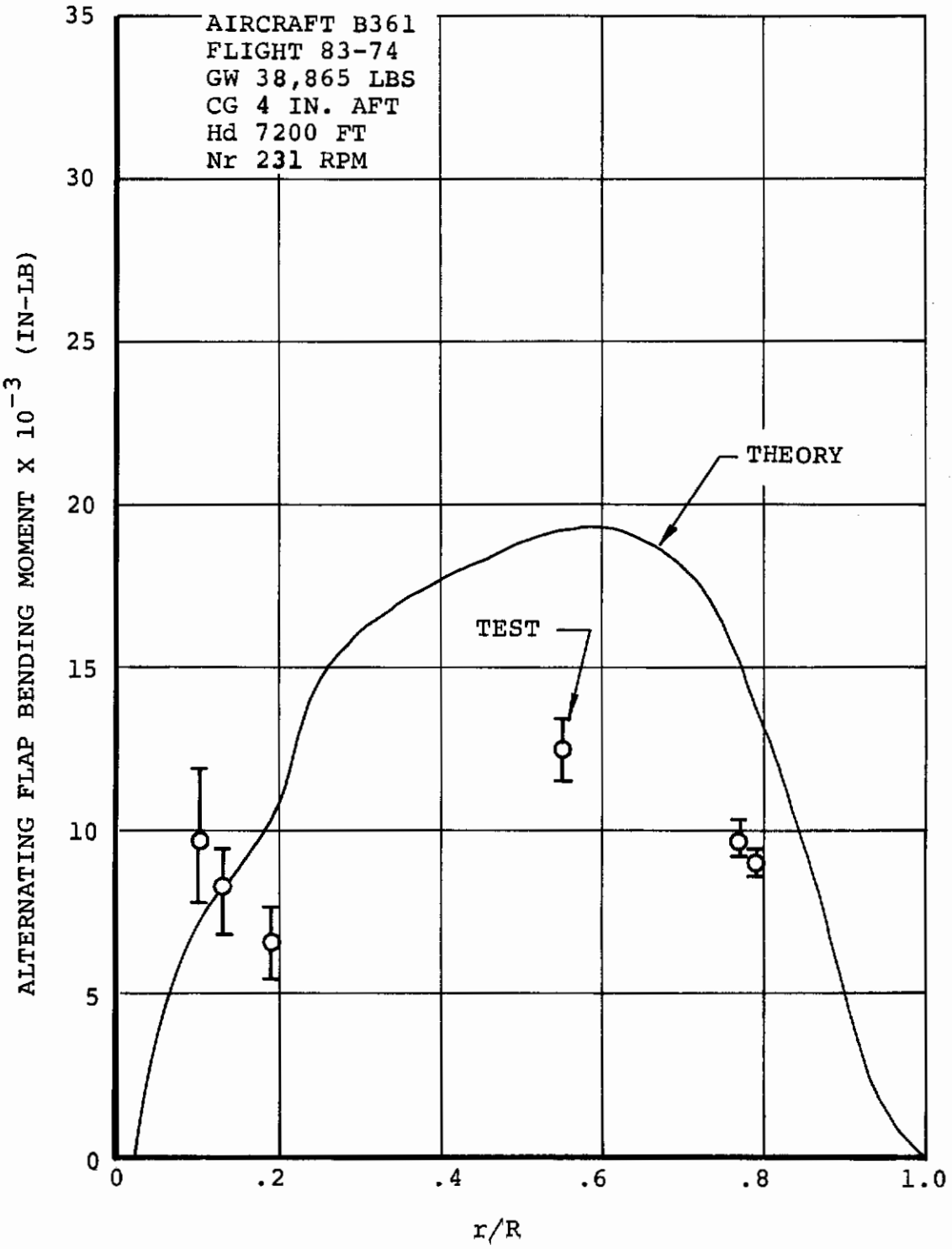

Figure 133. CH-47C Forward Rotor, Predicted and Measured Alternating Flap Bending Moment at V = 123 Knots

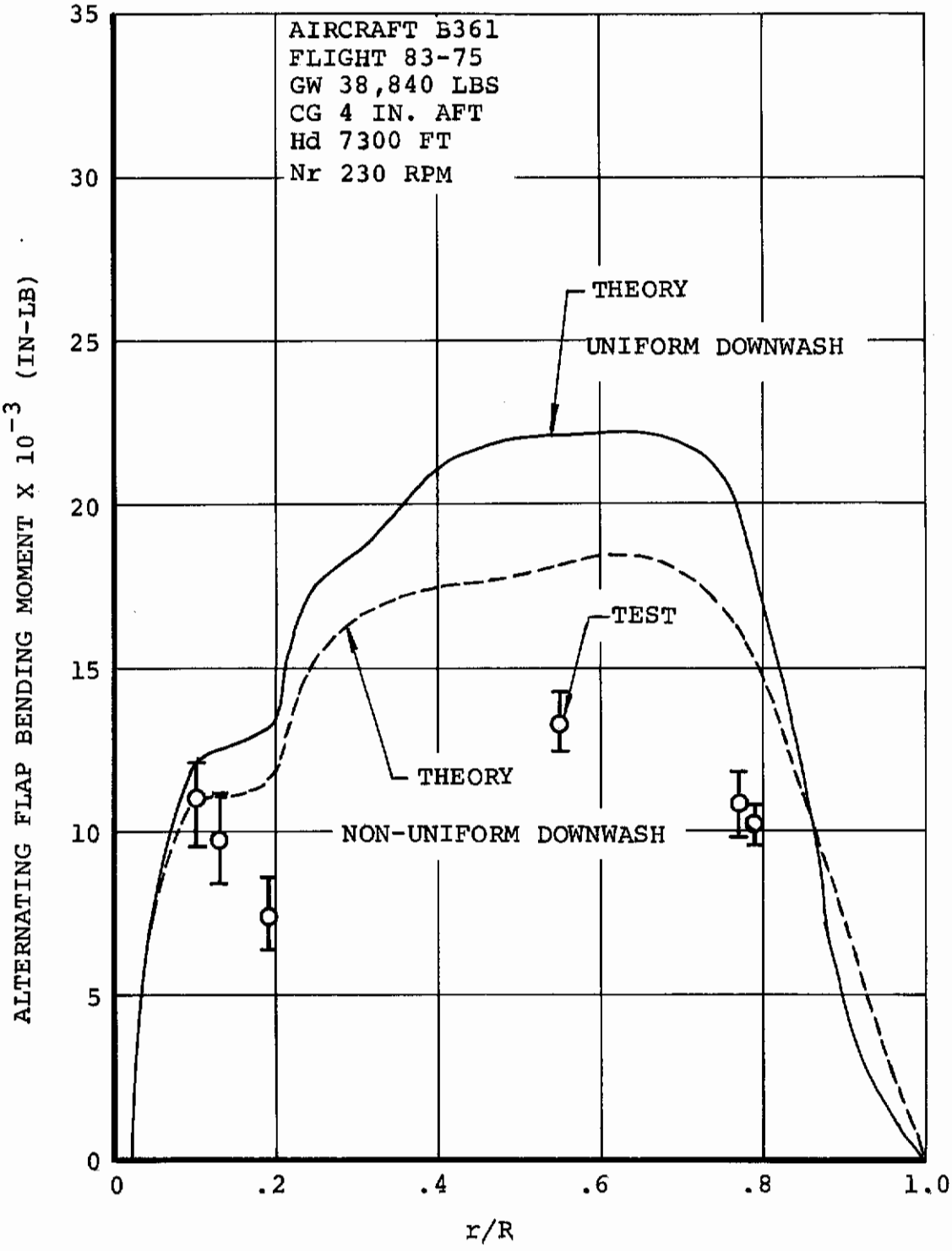

Figure 134. CH-47C Forward Rotor, Predicted and Measured Alternating Flap Bending Moment at V = 133 Knots

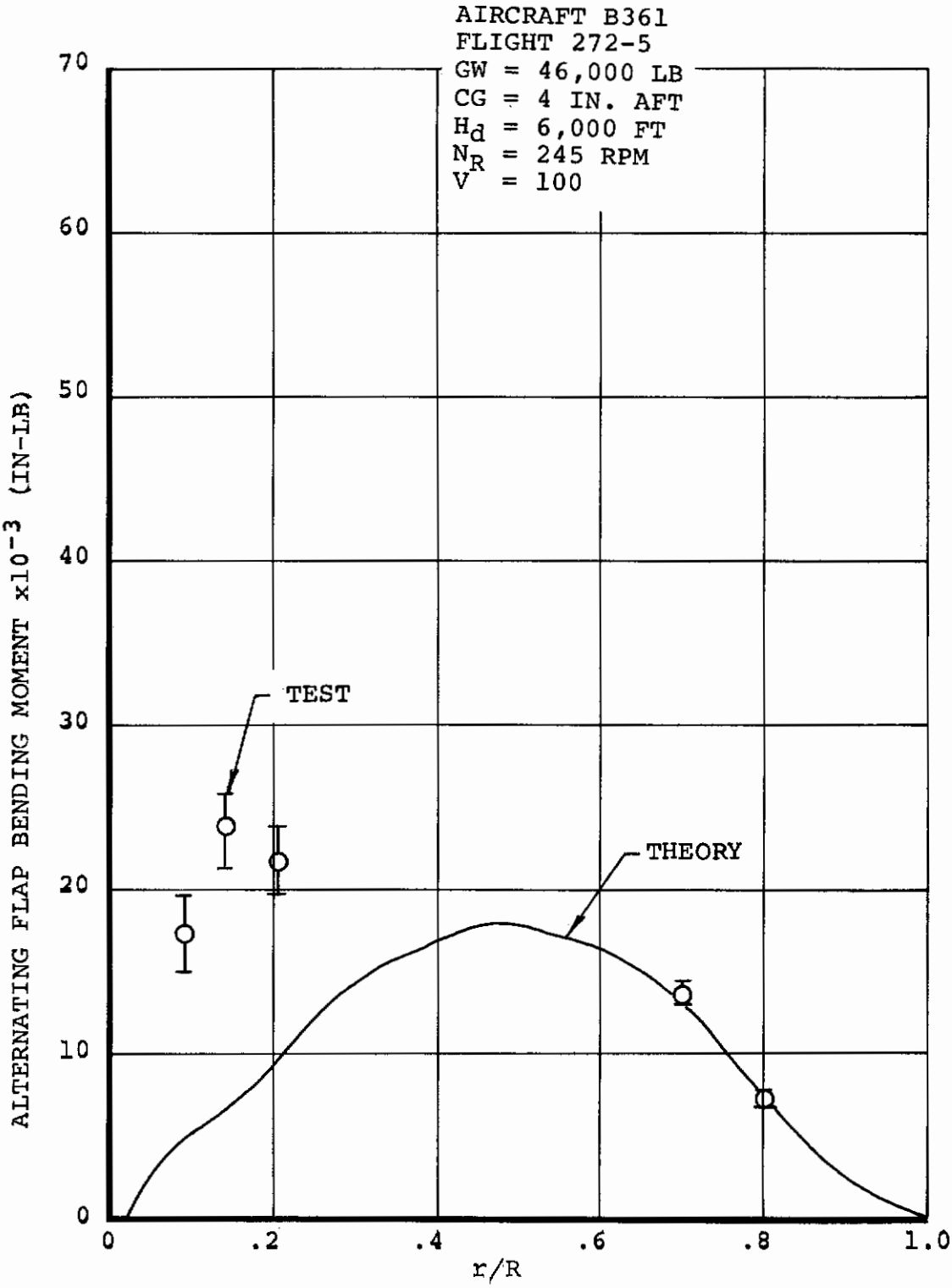

Figure 135. CH-47C With Advanced-Geometry Blades, Forward Rotor Predicted and Measured Alternating Flap Bending Moment at 100 Knots

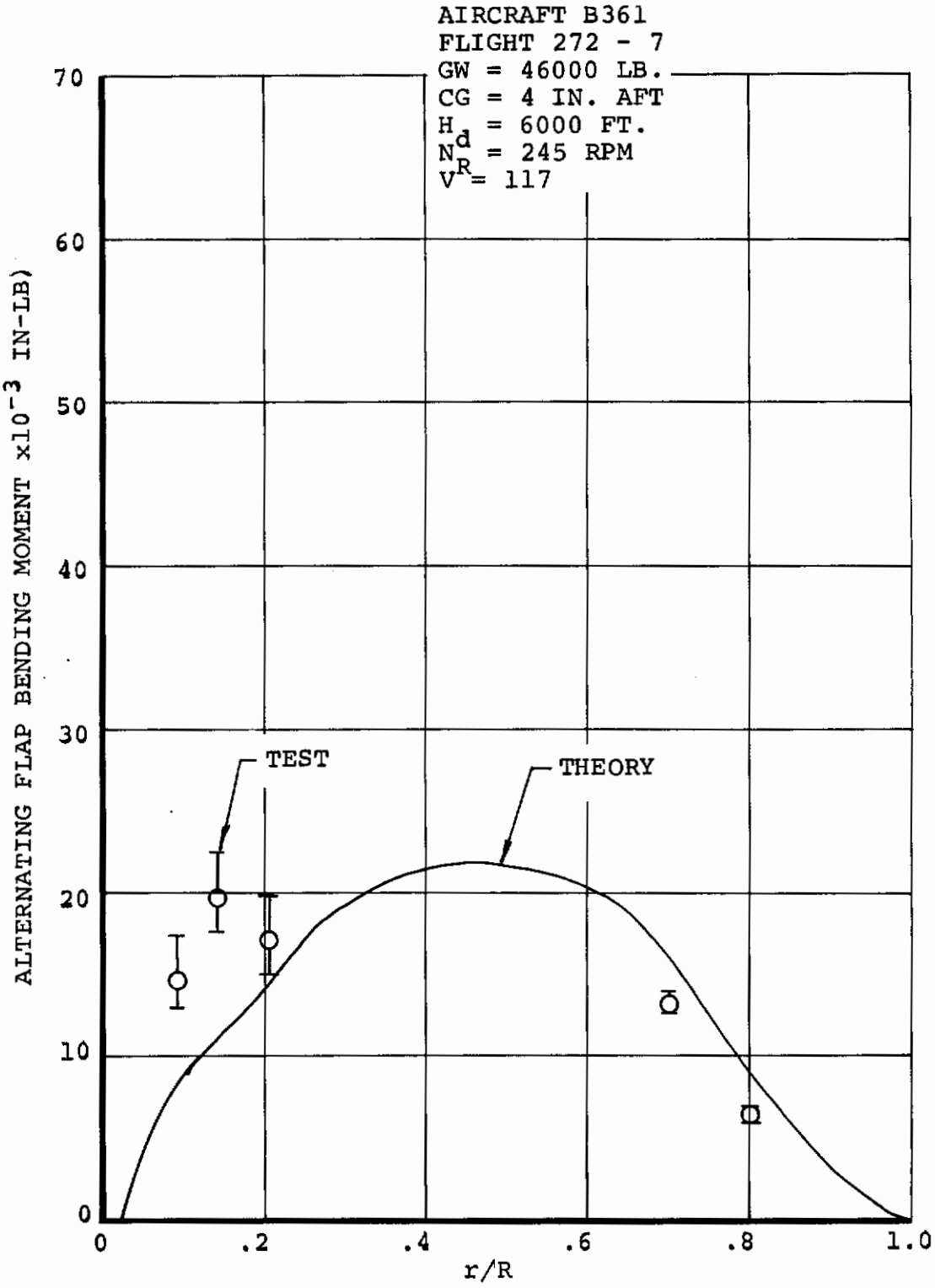

Figure 136. CH-47C With Advanced-Geometry Blades, Forward Rotor Predicted and Measured Alternating Flap Bending Moment at 117 Knots

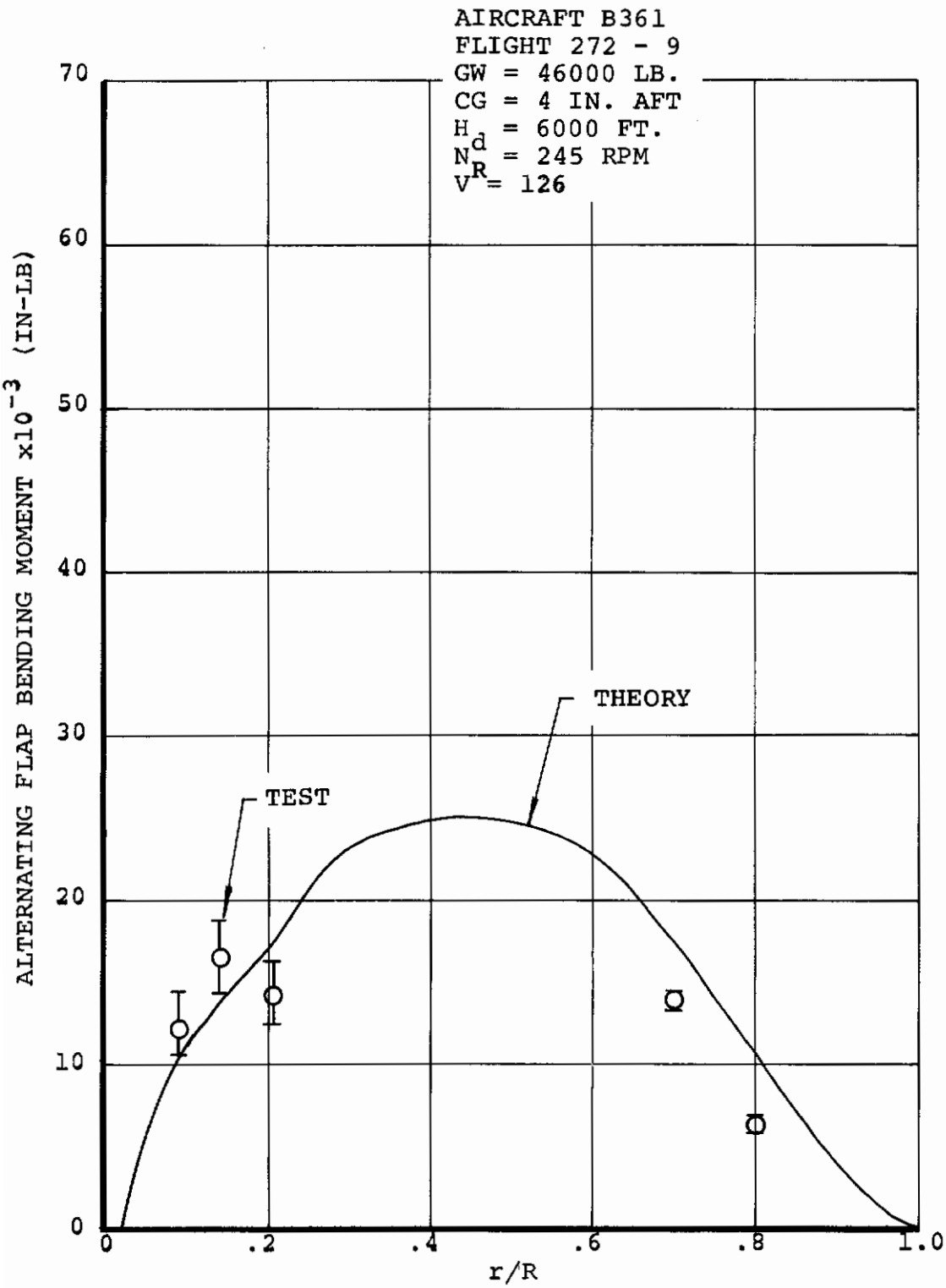

Figure 137. CH-47C With Advanced-Geometry Blades, Forward Rotor Predicted and Measured Alternating Flap Bending Moment at 126 Knots

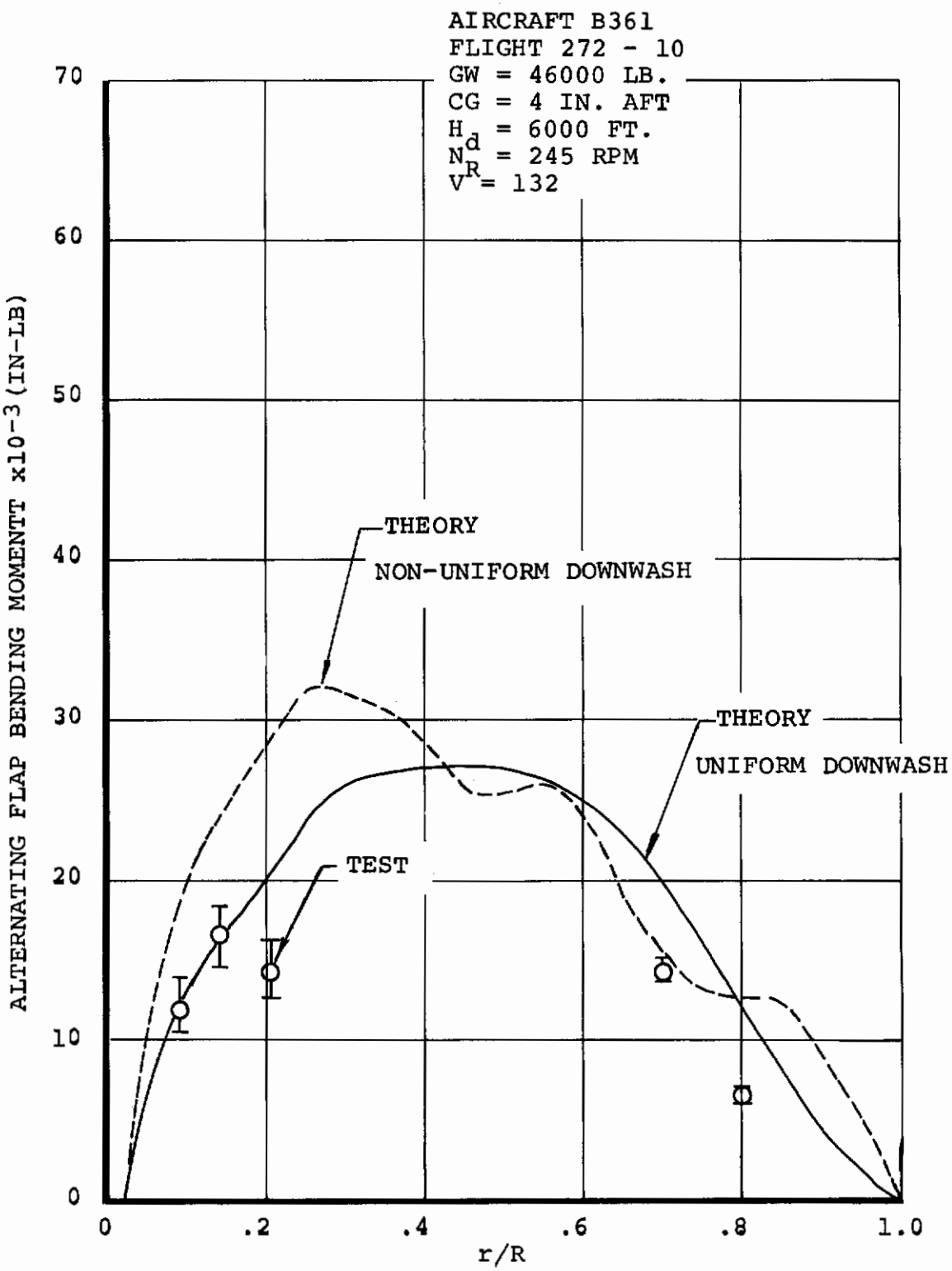

Figure 138. CH-47C With Advanced-Geometry Blades, Forward Rotor Predicted and Measured Alternating Flap Bending Moment at 132 Knots

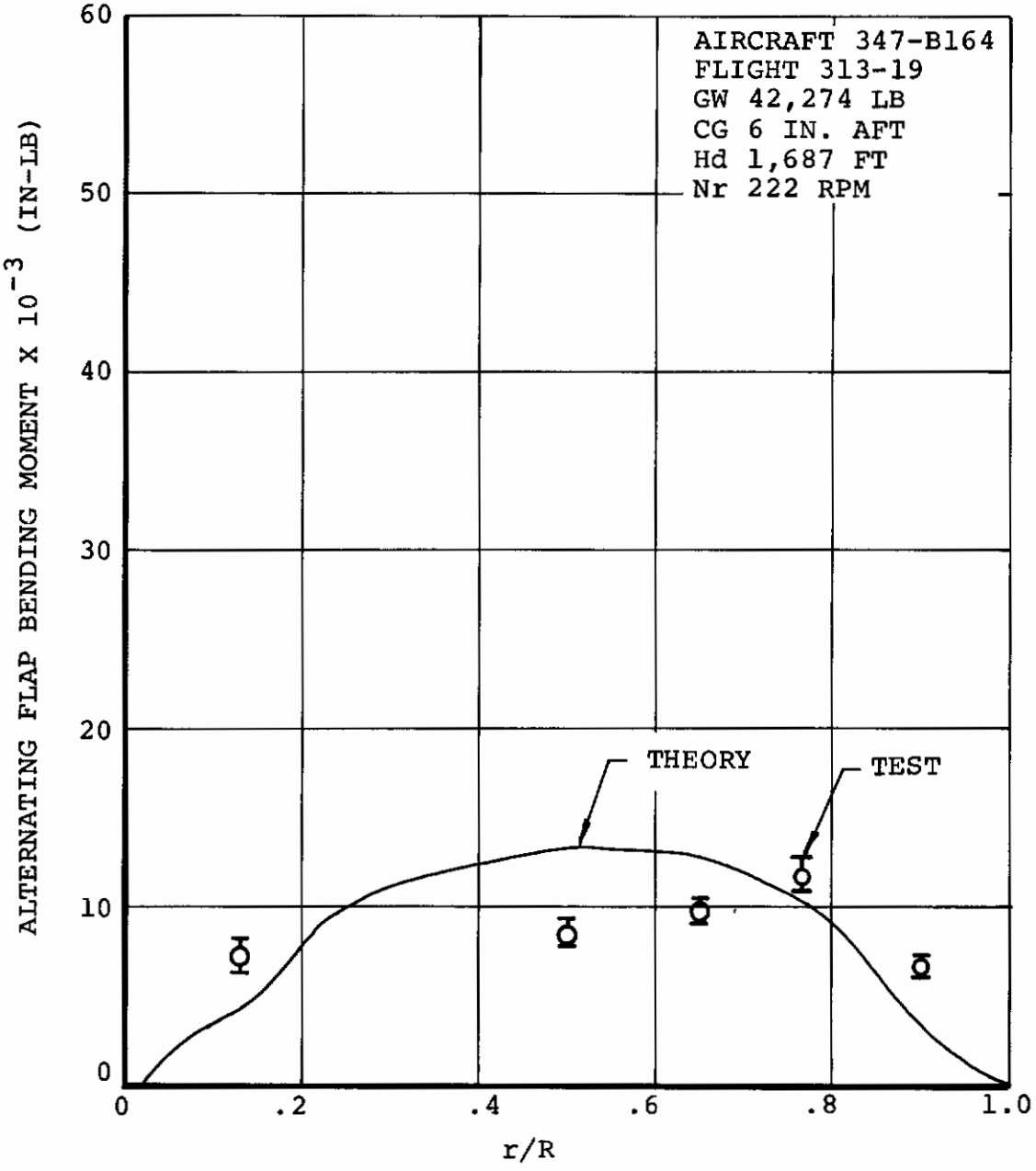

Figure 139. Model 347 With CH-47C Blades, Forward Rotor Predicted and Measured Alternating Flap Bending Moment at V = 87 Knots

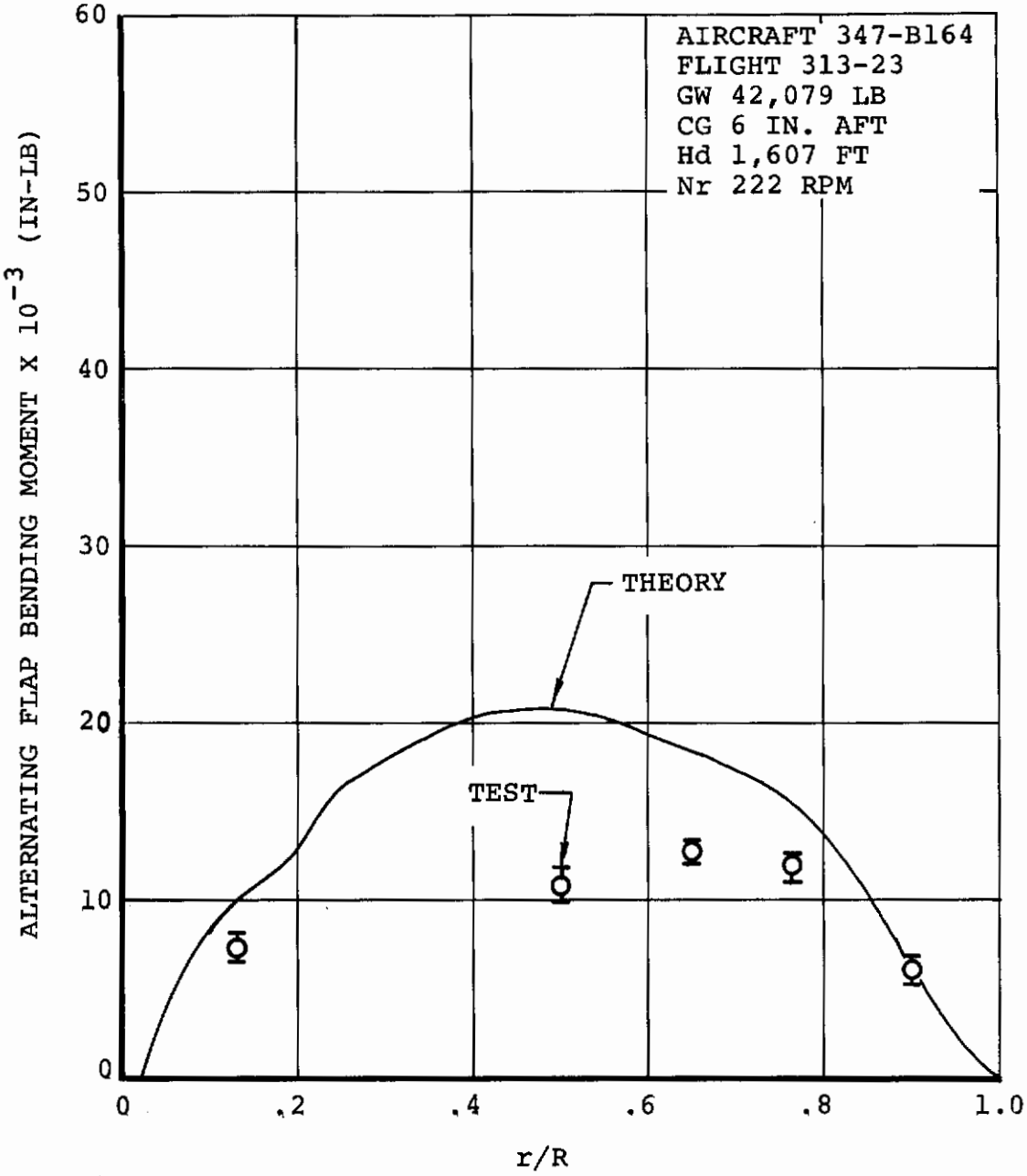

Figure 140. Model 347 With CH-47C Blades, Forward Rotor Predicted and Measured Alternating Flap Bending Moment at V = 122 Knots

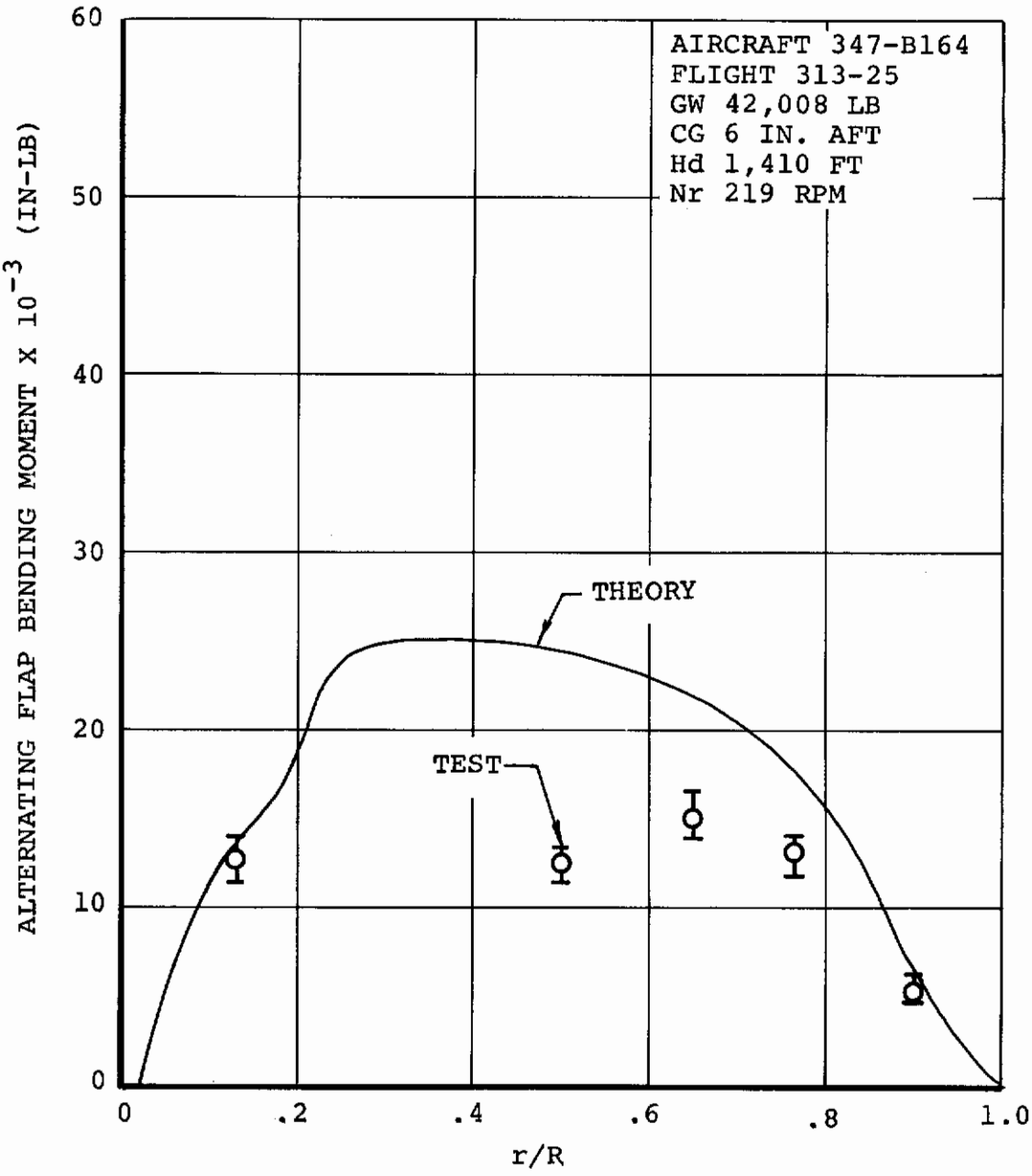

Figure 141. Model 347 With CH-47C Blades, Forward Rotor Predicted and Measured Alternating Flap Bending Moment at V = 140 Knots

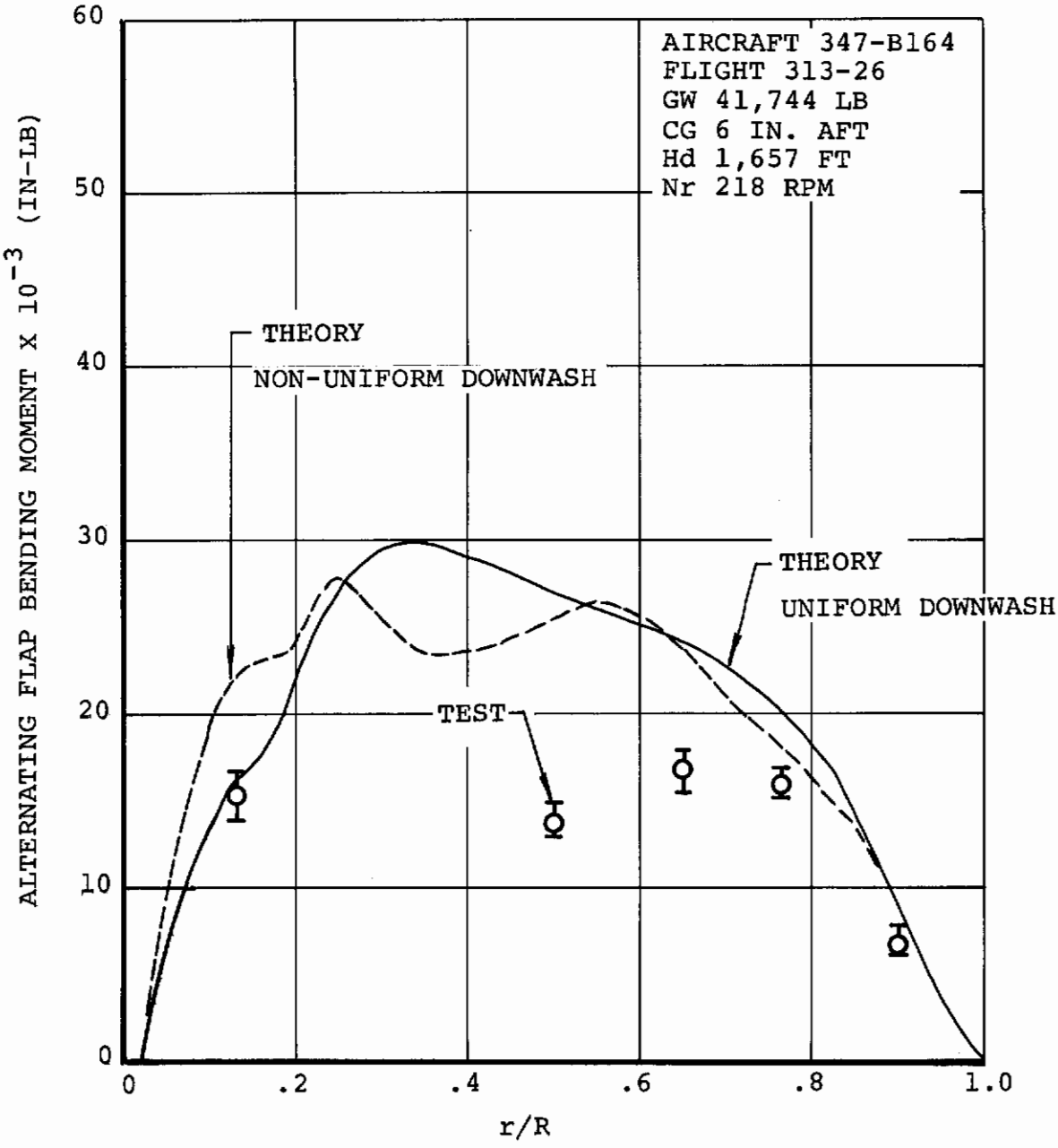

Figure 142. Model 347 With CH-47C Blades, Forward Rotor Predicted and Measured Alternating Flap Bending Moment at V = 152 Knots

Chord Bending

Figures 143 through 154 are the correlation results for helicopter aft rotor chord bending. CH-47 and Model 347 flight test data was used for correlation. Uniform downwash was used primarily in the analysis for chord bending predictions to reduce computer time. However, one nonuniform downwash prediction was made for each flight to show the impact of downwash representation on chord bending.

The aft rotor correlation results show that the analysis consistently underpredicts when uniform downwash is used. This is to be expected due to the lag damper representation in the analysis. The lag damper in the analysis is an ideal torsional viscous damper and therefore the energy absorbed by the damper is dependent upon the lag velocity. The lag damper on the CH-47 and Model 347 is a torsional viscous damper with a constant coulomb (preload) damper superimposed. As shown in Figure 155, the CH-47C lag damper has a large preload which is independent of lag velocity except for valve leakage. Therefore, to equate the lag damper value in the analysis to the actual lag damper, a 1-per-rev lag angle is assumed and the lag damper value in the analysis is determined by equating energy. The energy absorbed by the lag damper in the analysis is forced to be equal to that absorbed by the actual lag damper by the following equation:

$$C_{\zeta_{ANALYSIS}} = \frac{4M_P}{\pi\omega\zeta_{MAX}} + \overline{C}$$

where $C_{\zeta_{ANALYSIS}}$ = viscous torsional damping rate in the analysis
$\overline{C}$ = actual viscous torsional damping rate
M_P = preload moment in damper
ω = lag natural frequency
ζ_{MAX} = 1-per-rev amplitude of lagging motion

This method of representing a lag damper with a preload would yield a fair approximation of the amplitude of the lag bending moment if the lag motion was nearly all 1 per rev. But even then the phasing would be incorrect since the force exerted by the actual damper preload (acting like a spring) is 90 degrees out of phase with the force exerted by the viscous torsional damper. In addition, the use of uniform downwash in the analysis partially neglects 1-, 2-, and 3-per-rev airloading induced by blade tip vortex proximity to a passing blade, thus in part neglecting 1-, 2-, and 3-per-rev lagging due to induced drag. Therefore use of nonuniform downwash in the analysis to account for airloading due to vortex proximity should increase 1-, 2-, and 3-per-rev lag motion and yield

higher chord bending motion, even though the rate at which the damper is doing work in the analysis is based on 1-per-rev lag motion.

As shown in Figures 144, 145, and 149, use of nonuniform downwash in the analysis substantially increases predicted chord bending and the results correlate well with bottom-of-scatter data. It should be noted that the effect of rotor interference on chord bending moment is limited to excitation of the first flexible mode, primarily due to the high frequency ratio of the second flexible mode as shown in Figure 156. Comparing this figure to the flap bending moment mode shapes in Figure 120, chord bending for the CH-47C has only one flexible mode with a frequency between 1 and 12 per rev, while flap bending has four flexible modes up to 12 per rev. Flight test experience has shown that the frequency spectrum of rotor interference, as reflected in bending moments, is between 1 and 12 per rev. Thus the second flexible mode is lightly forced and high-harmonic (6- through 12-per-rev) chord bending is low in amplitude. The aft rotor chord bending correlation for the Model 347 in Figures 150 through 153 shows the analysis underpredicts by a large margin even with nonuniform downwash in the analysis.

Comparing Figures 145 and 152, the test data for the Model 347 is 1.5 times as large as the CH-47C at 50 percent span at nearly the same airspeed. The high chord bending moments on the Model 347 are due to a resonant condition between 4-per-rev in-plane forcing and the third and fourth flexible modes of the coupled rotor/drive system which are nearly 4 per rev. This condition is discussed extensively in Reference 32. As shown in Figure 154, alternating chord bending is dominated by the fourth-harmonic contribution. Since the analysis does not have the capability to input hub motion and simulate the rotor/drive system coupling, the predicted 4-per-rev chord bending is much lower than measured test data.

Figures 157 through 168 are the correlation results for helicopter forward rotor chord bending. These figures show prediction trends similar to that for the aft rotor. The analysis underpredicts when uniform downwash is used due to the lack of higher-harmonic lagging induced by blade-to-blade interference. When nonuniform downwash is used in the analysis the chord bending prediction increases substantially and correlates better with the test data (Figures 159 and 163). The higher-harmonic lag motions are now included and the lag damper is absorbing more energy per rotor cycle, thus increasing chordwise bending moments. Note the small increase in predicted chord bending in Figure 163 when nonuniform downwash is used; this indicates that predicted interference effects are small and the predicted lag motion is primarily 1 per rev. The Model 347 forward rotor correlation results in Figures 164 through

167 show the analysis to be underpredicting by a large margin with uniform and nonuniform downwash. As shown in Figure 168, the test data has a large 4-per-rev contribution due to the rotor/drive system coupling, as discussed earlier, and the analysis does not have the capability to simulate drive system coupling.

In summary, the chord bending predictions, especially for the aft rotor with nonuniform downwash, correlate well with the test data when it is considered that the lag damper representation in the analysis does not have the capability to simulate damper preload. It is extremely difficult to represent the lag damper effect on chord bending by equating energy as discussed earlier, especially when the lag motion contains higher harmonics. Inputting a lag damper rate into the analysis for a preloaded-type damper is at best an approximation. A parametric study of the effect of lag damper value on predicted chord bending would be helpful, but the study would be complicated by the dependence of lagwise motion (amplitude, harmonic contribution, and phasing) on specific aircraft and flight conditions. Interference, which contributes to higher-harmonic lagwise motion, is highly dependent upon tandem-rotor separation, C_T/σ, advance ratio, and tip path plane tilt. The most promising solution for chord bending prediction is to treat the lag damper in the analysis as a torsional viscous damper and a constant coulomb damper in the form of two table lookup routines. One table would account for the preload (constant coulomb damper) shown in Figure 155 and the other table would account for the viscous damper. With this method, the force exerted by the damper when the blade is in a specific azimuth position will be entirely dependent upon aerodynamic forcing and dynamic response at that instant instead of being dependent upon an average lag damper value for the entire rotor cycle.

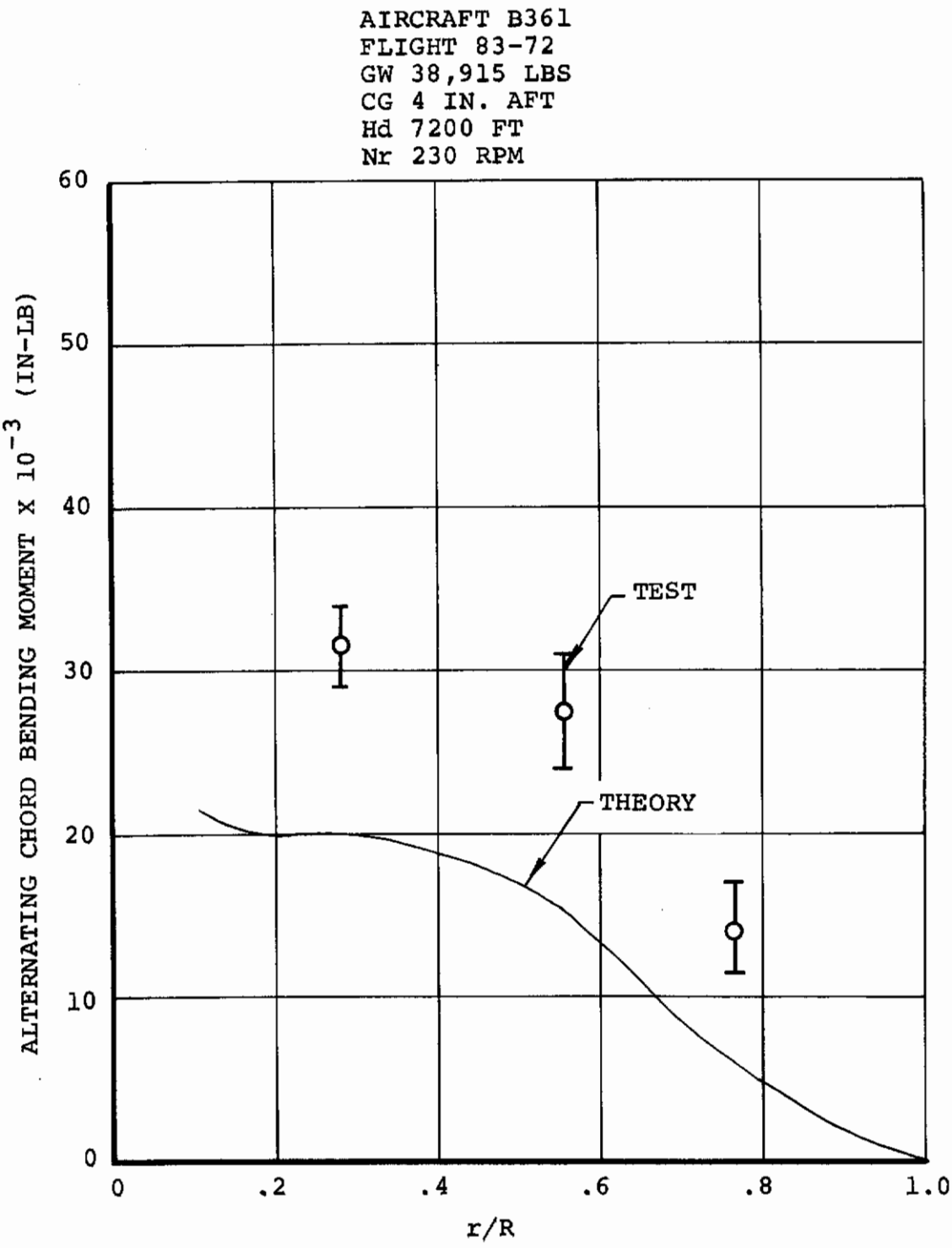

Figure 143. CH-47C Aft Rotor, Predicted and Measured Alternating Chord Bending Moment at V = 111 Knots

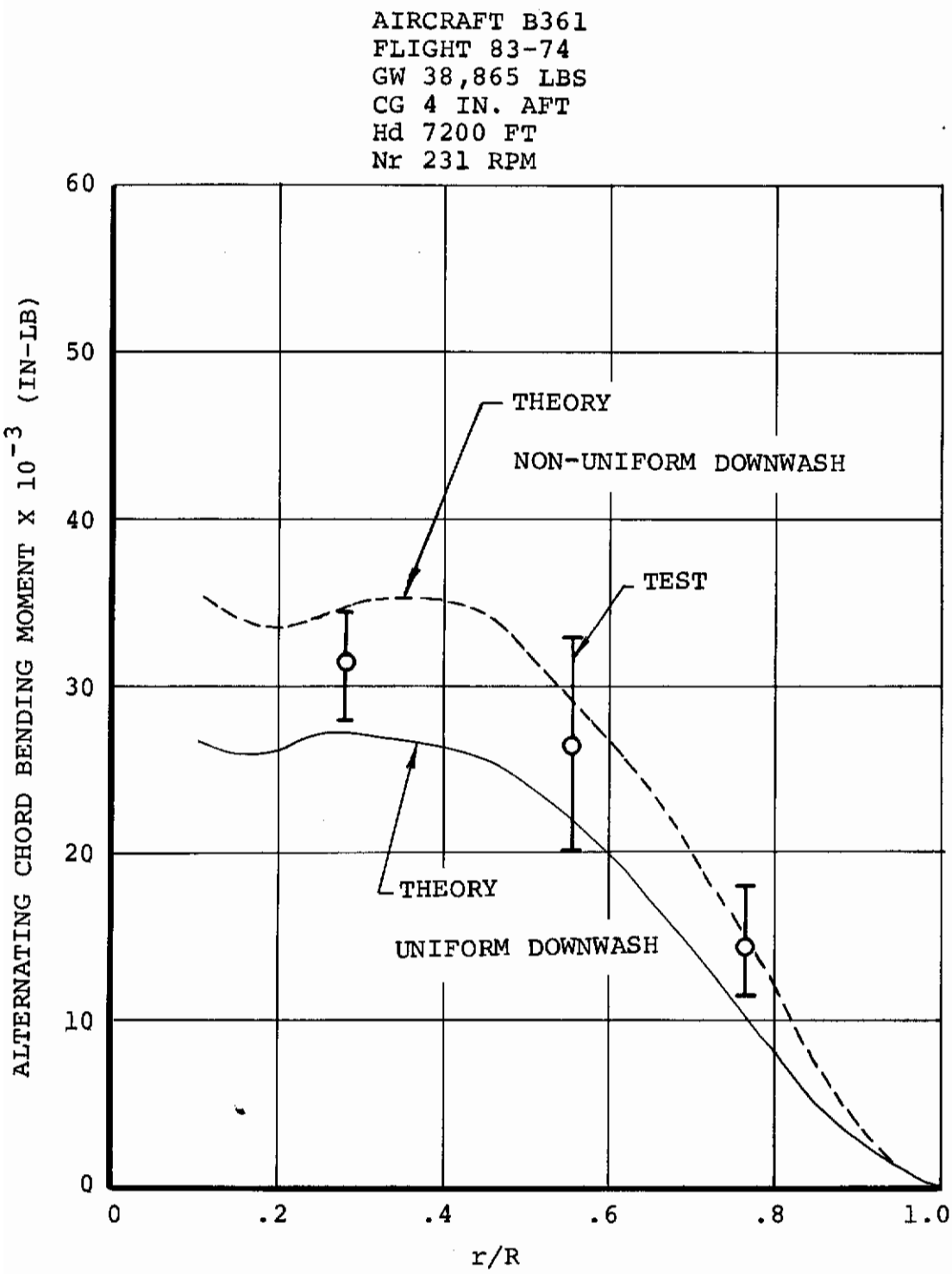

Figure 144. CH-47C Aft Rotor, Predicted and Measured Alternating Chord Bending Moment at V = 123 Knots

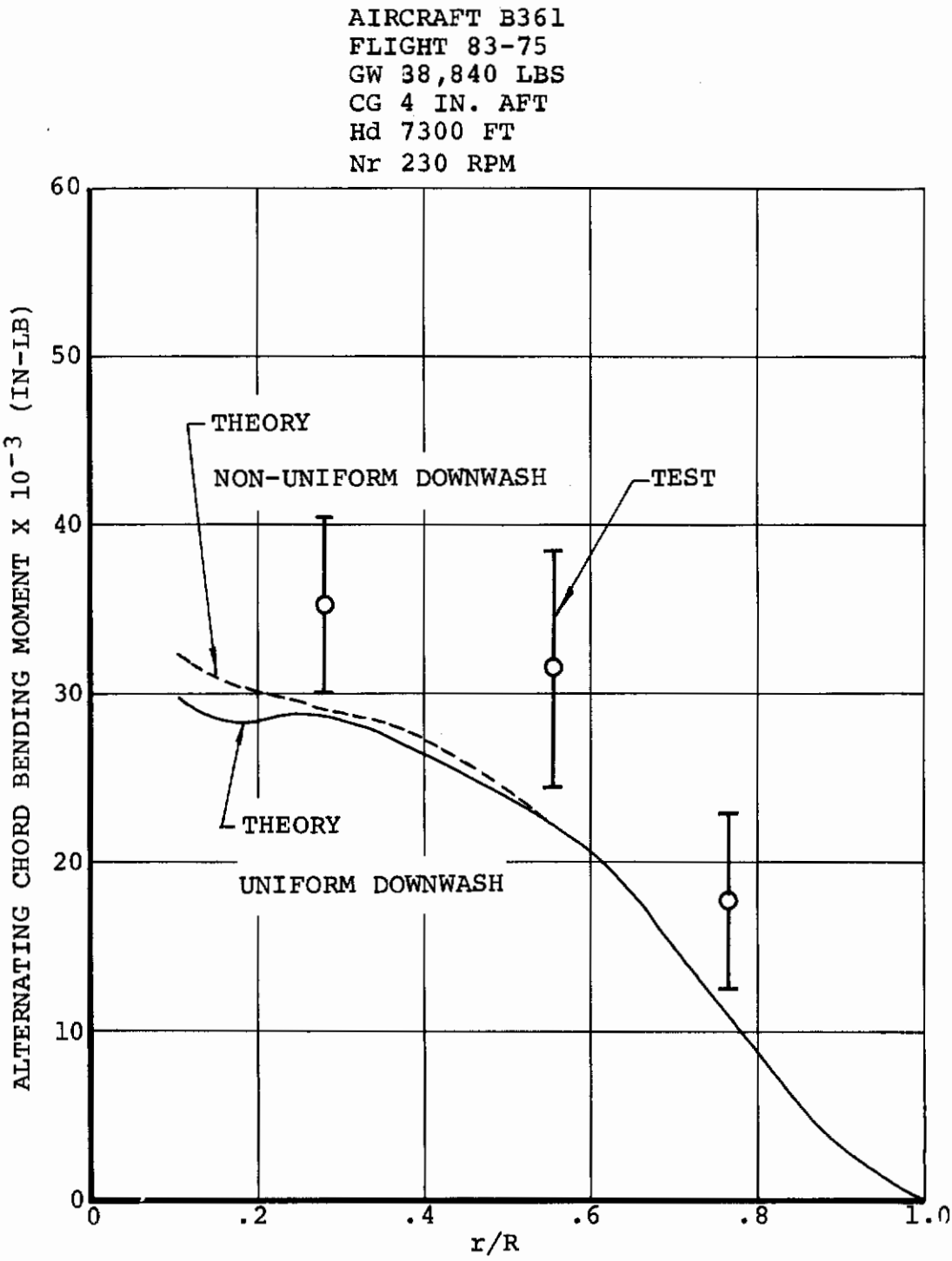

Figure 145. CH-47C Aft Rotor, Predicted and Measured Alternating Chord Bending Moment at V = 133 Knots

AIRCRAFT B361
FLIGHT 272-5
GW = 46,000 LB
CG = 4 IN. AFT
H_d = 6,000 FT
N_R = 245 RPM
V = 100

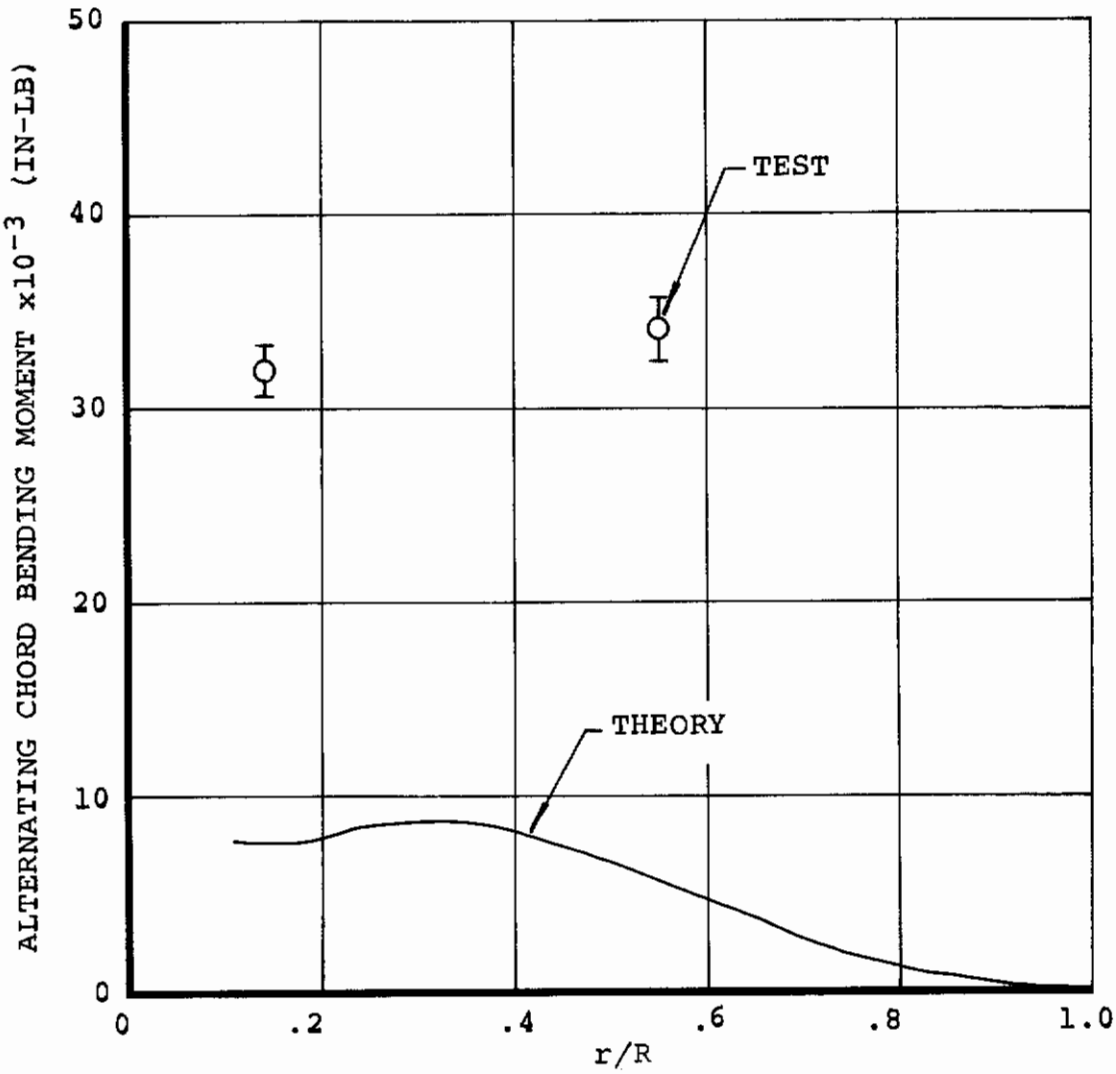

Figure 146. CH-47C With Advanced-Geometry Blades, Aft Rotor Predicted and Measured Alternating Chord Bending Moment at 100 Knots

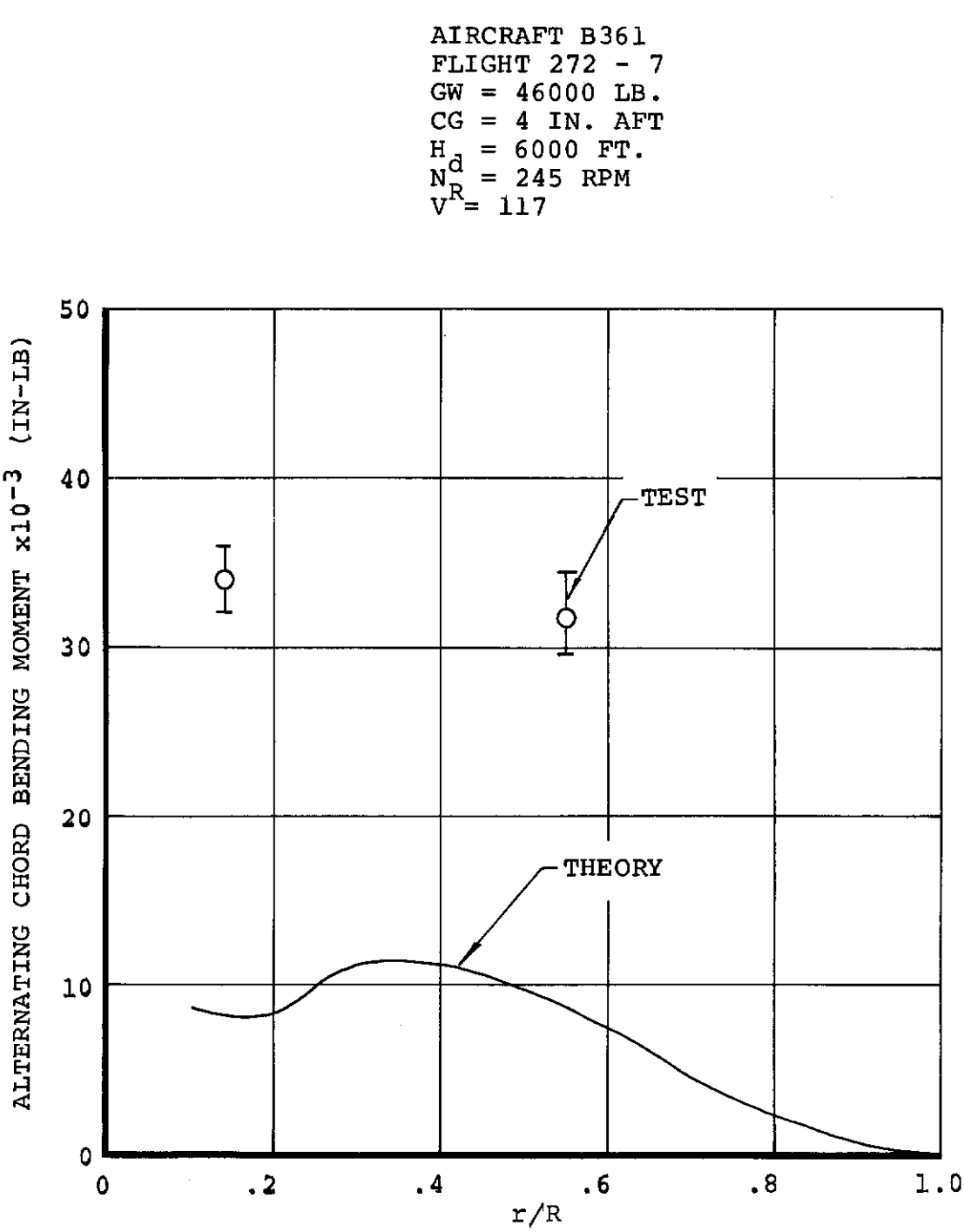

Figure 147. CH-47C With Advanced-Geometry Blades, Aft Rotor Predicted and Measured Alternating Chord Bending Moment at 117 Knots

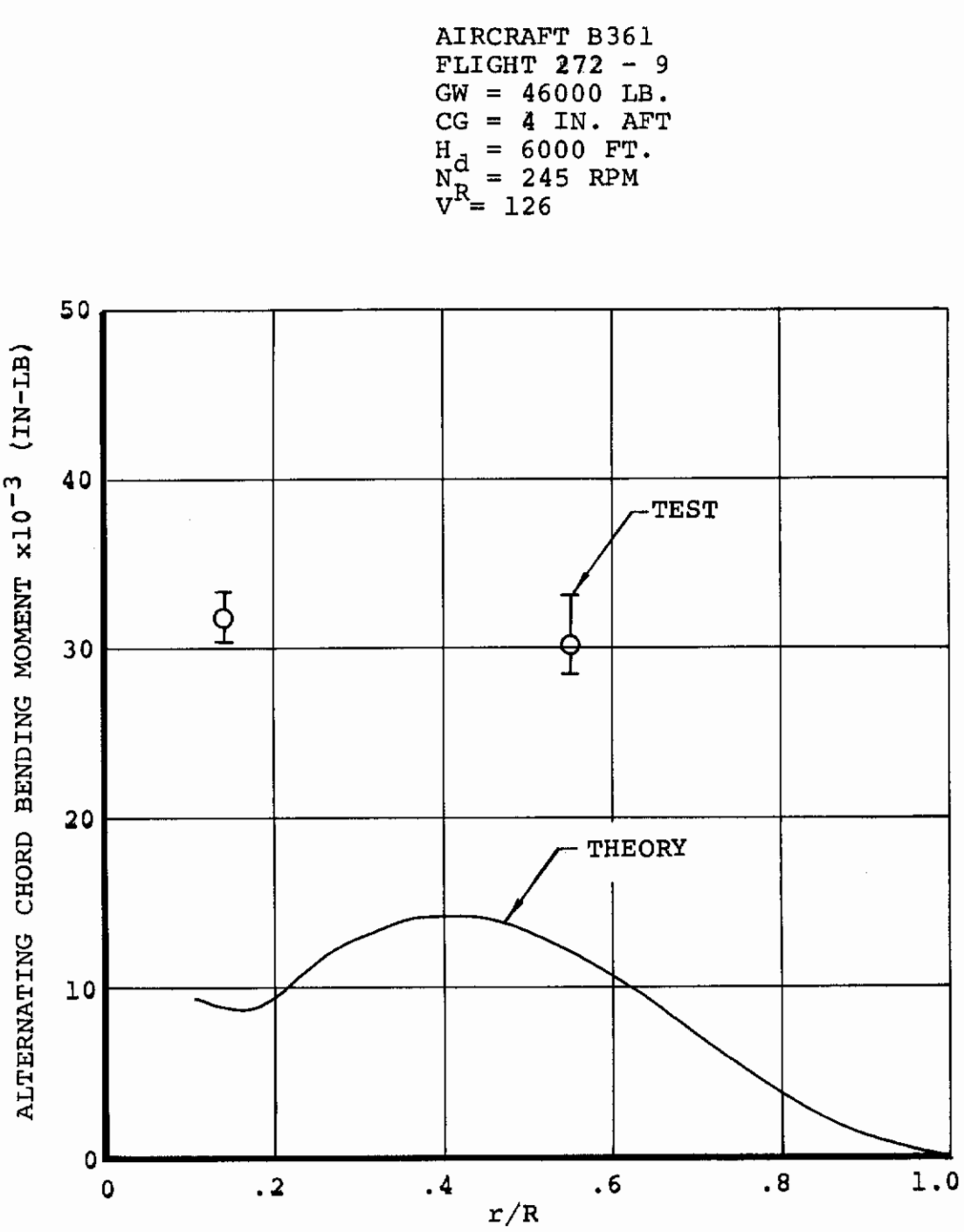

Figure 148. CH-47C With Advanced-Geometry Blades, Aft Rotor Predicted and Measured Alternating Chord Bending Moment at 126 Knots

AIRCRAFT B361
FLIGHT 272 - 10
GW = 46000 LB.
CG = 4 IN. AFT
H_d = 6000 FT.
N_R = 245 RPM
V = 132

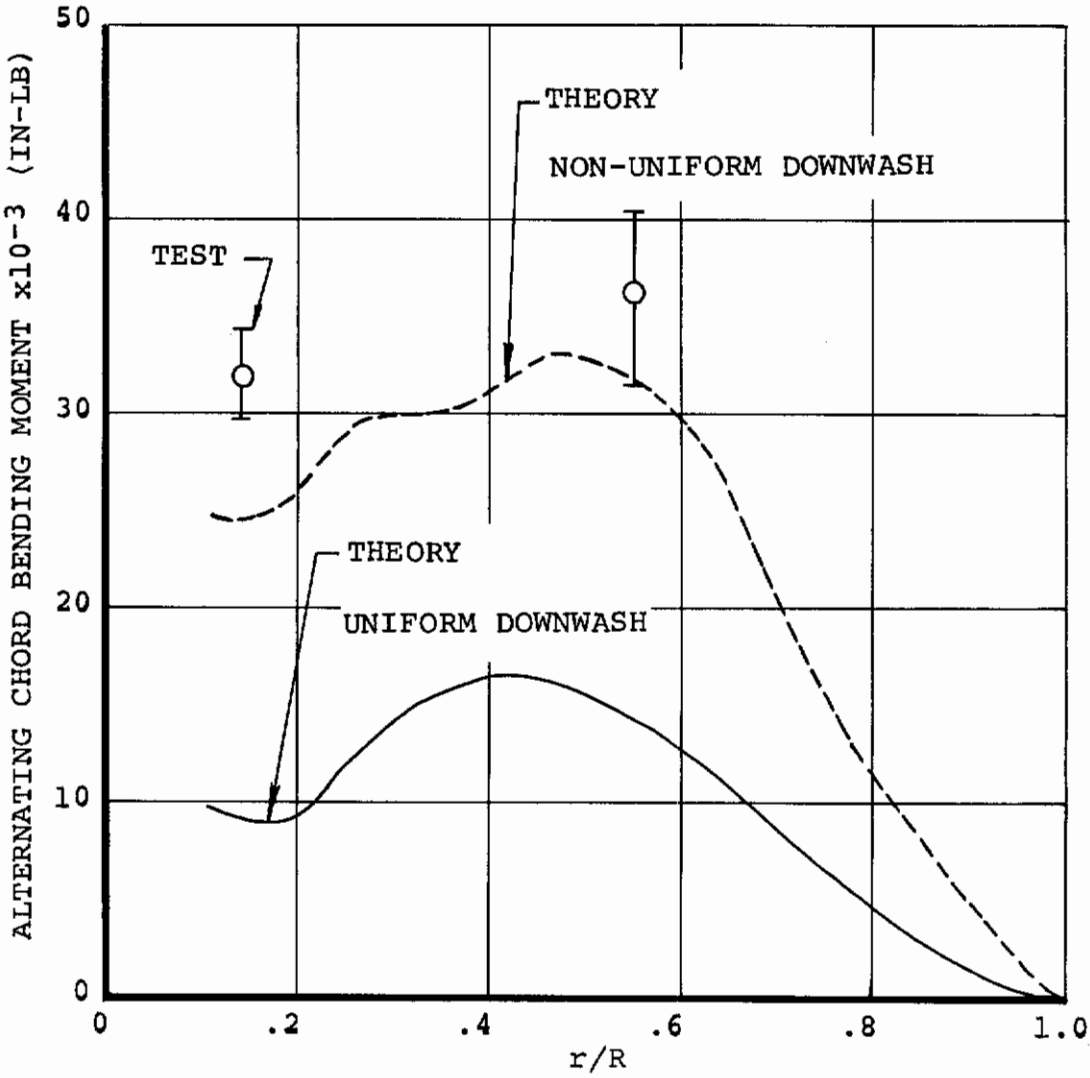

Figure 149. CH-47C With Advanced-Geometry Blades, Aft Rotor Predicted and Measured Alternating Chord Bending Moment at 132 Knots

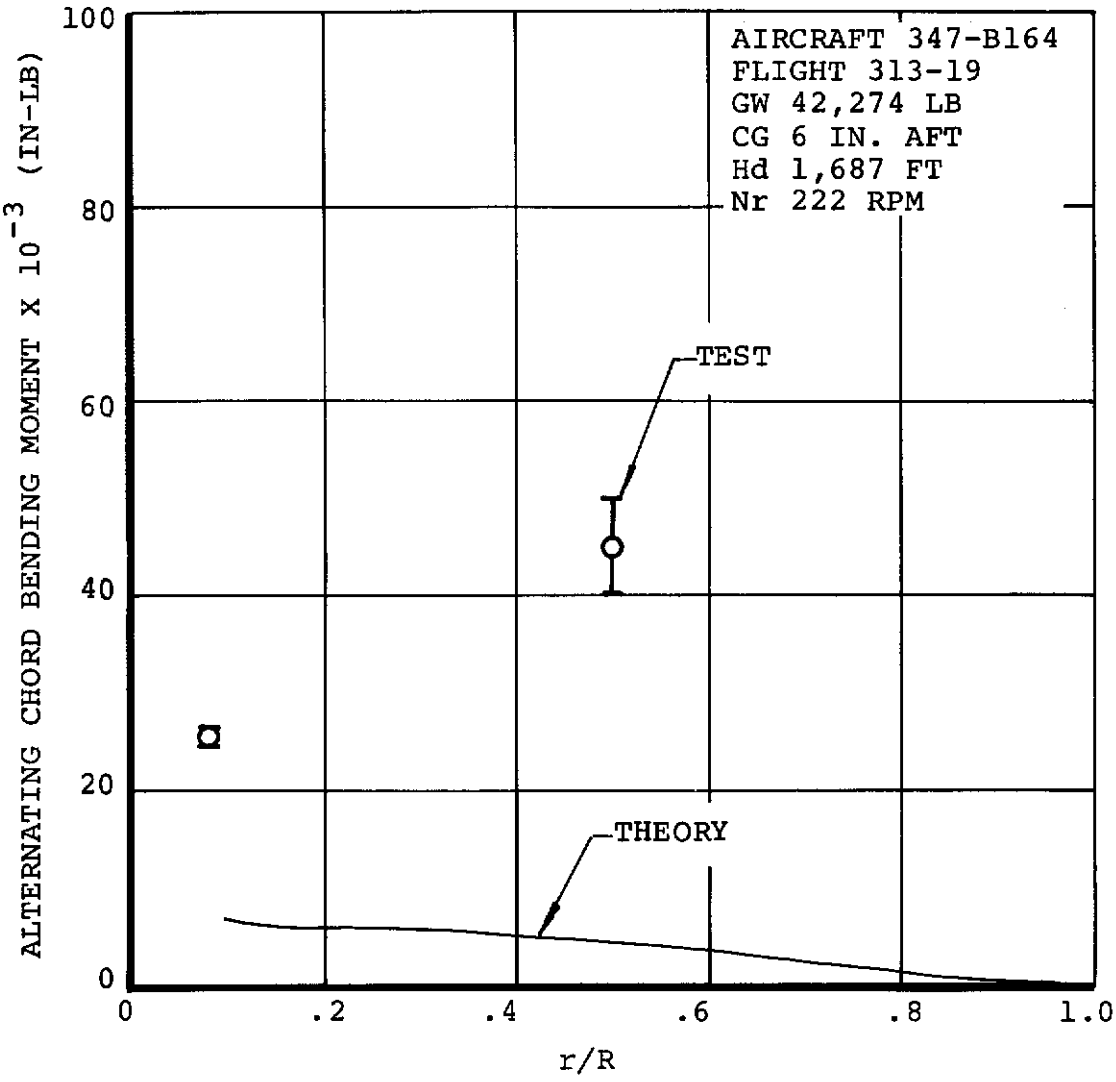

Figure 150. Model 347 With CH-47C Blades, Aft Rotor Predicted and Measured Alternating Chord Bending Moment at V = 87 Knots

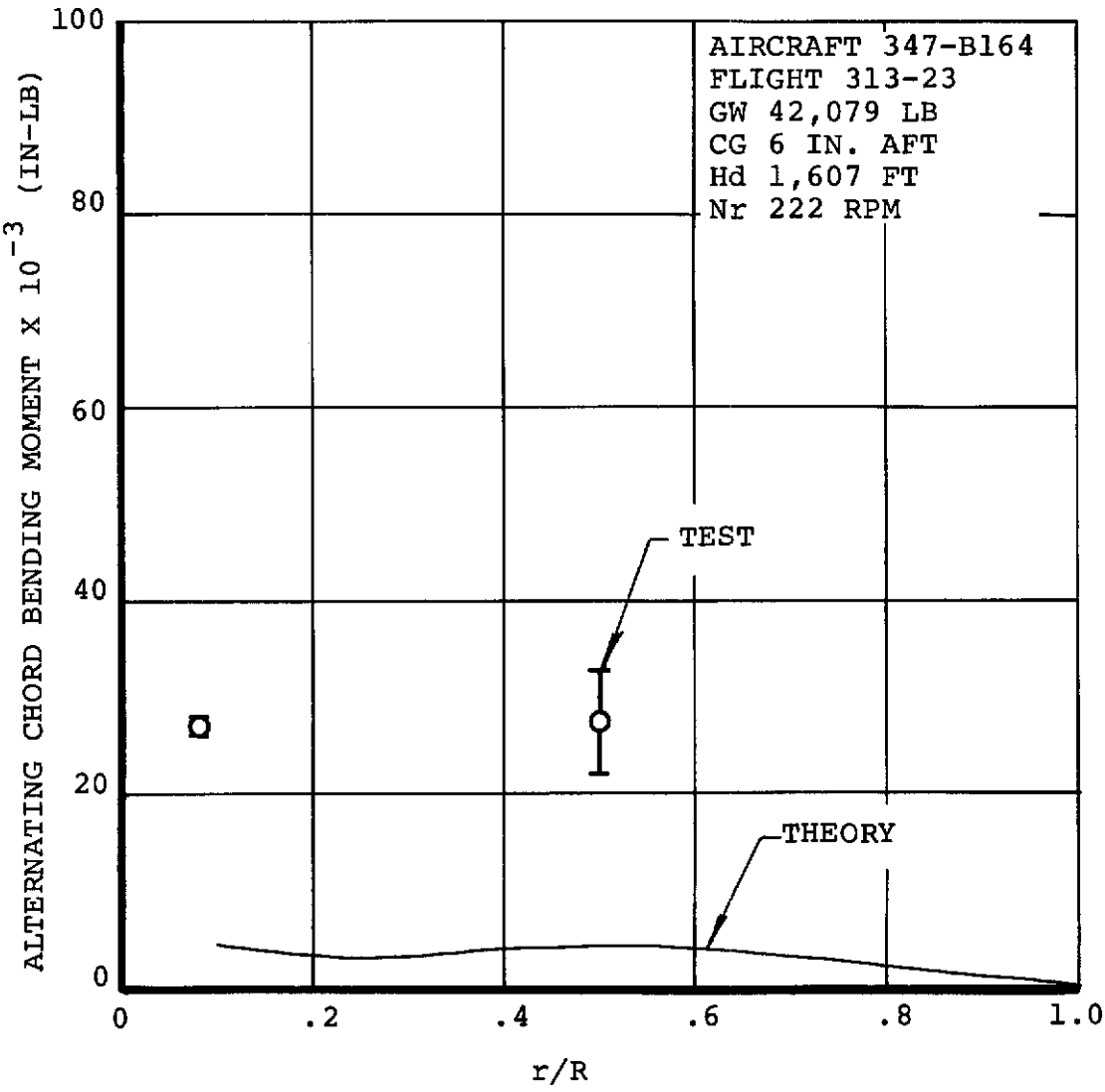

Figure 151. Model 347 With CH-47C Blades, Aft Rotor Predicted and Measured Alternating Chord Bending Moment at V = 122 Knots

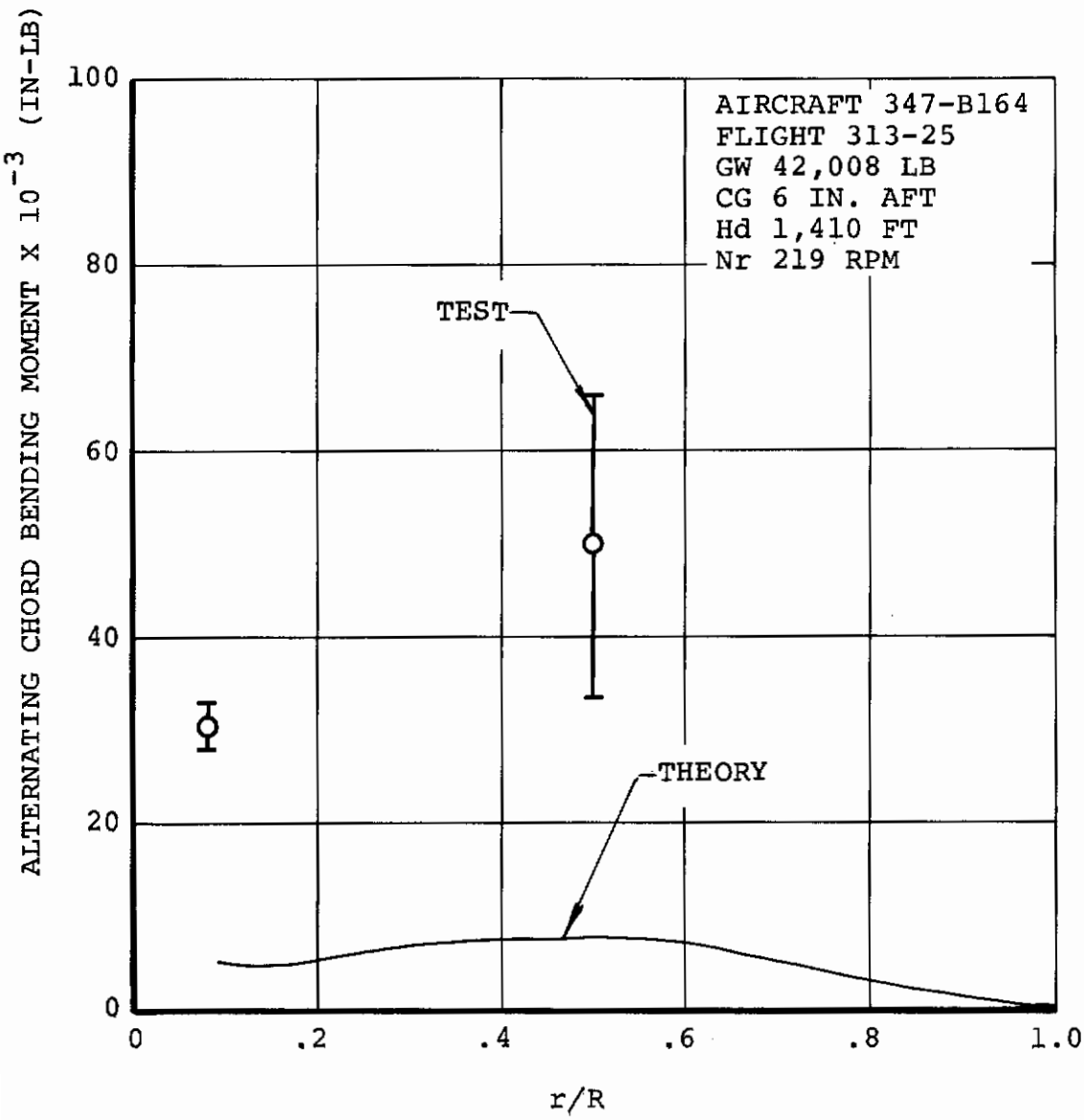

Figure 152. Model 347 With CH-47C Blades, Aft Rotor Predicted and Measured Alternating Chord Bending Moment at V = 140 Knots

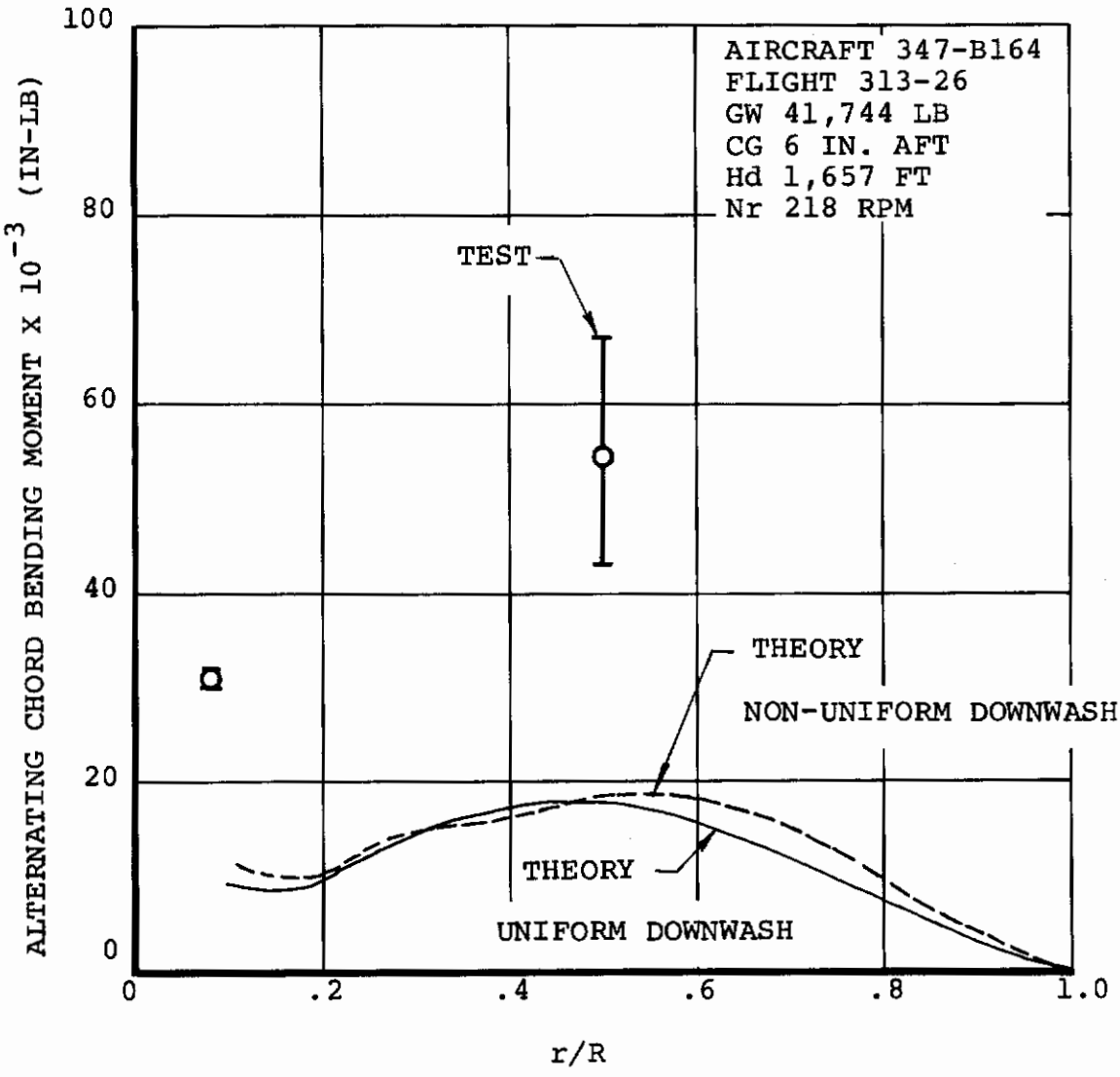

Figure 153. Model 347 With CH-47C Blades, Aft Rotor Predicted and Measured Alternating Chord Bending Moment at V = 152 Knots

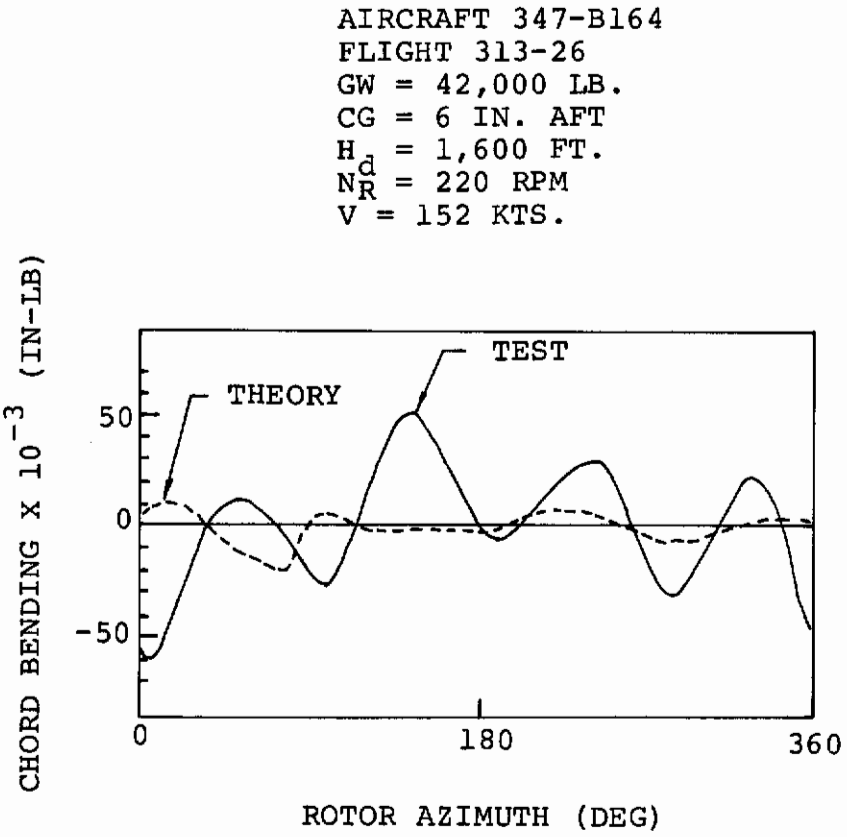

Figure 154. Model 347 With CH-47C Blades, Aft Rotor Predicted and Measured Chord Bending Waveform at 152 Knots

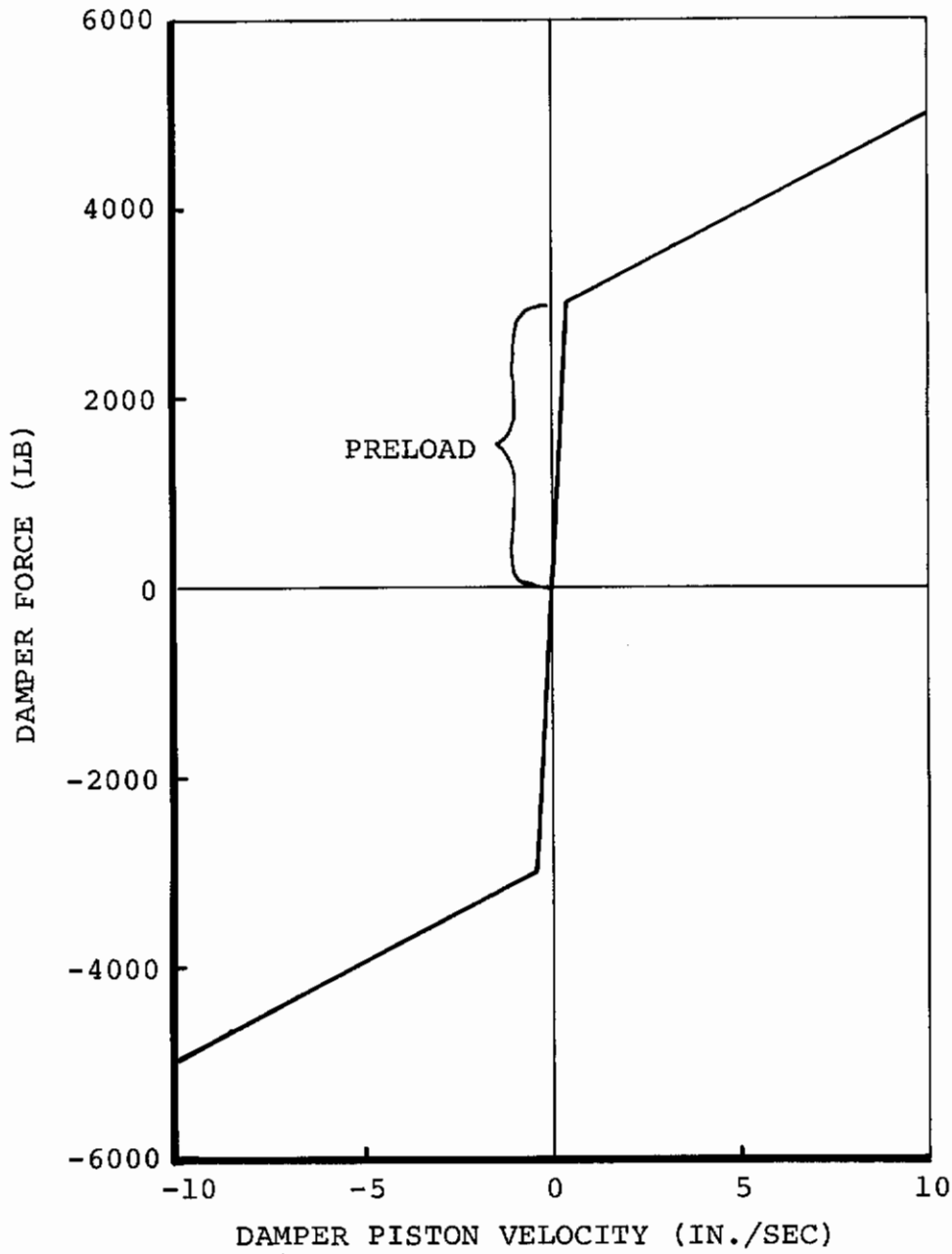

Figure 155. CH-47C Rotor Blade Lag Damper Force Versus Piston Velocity

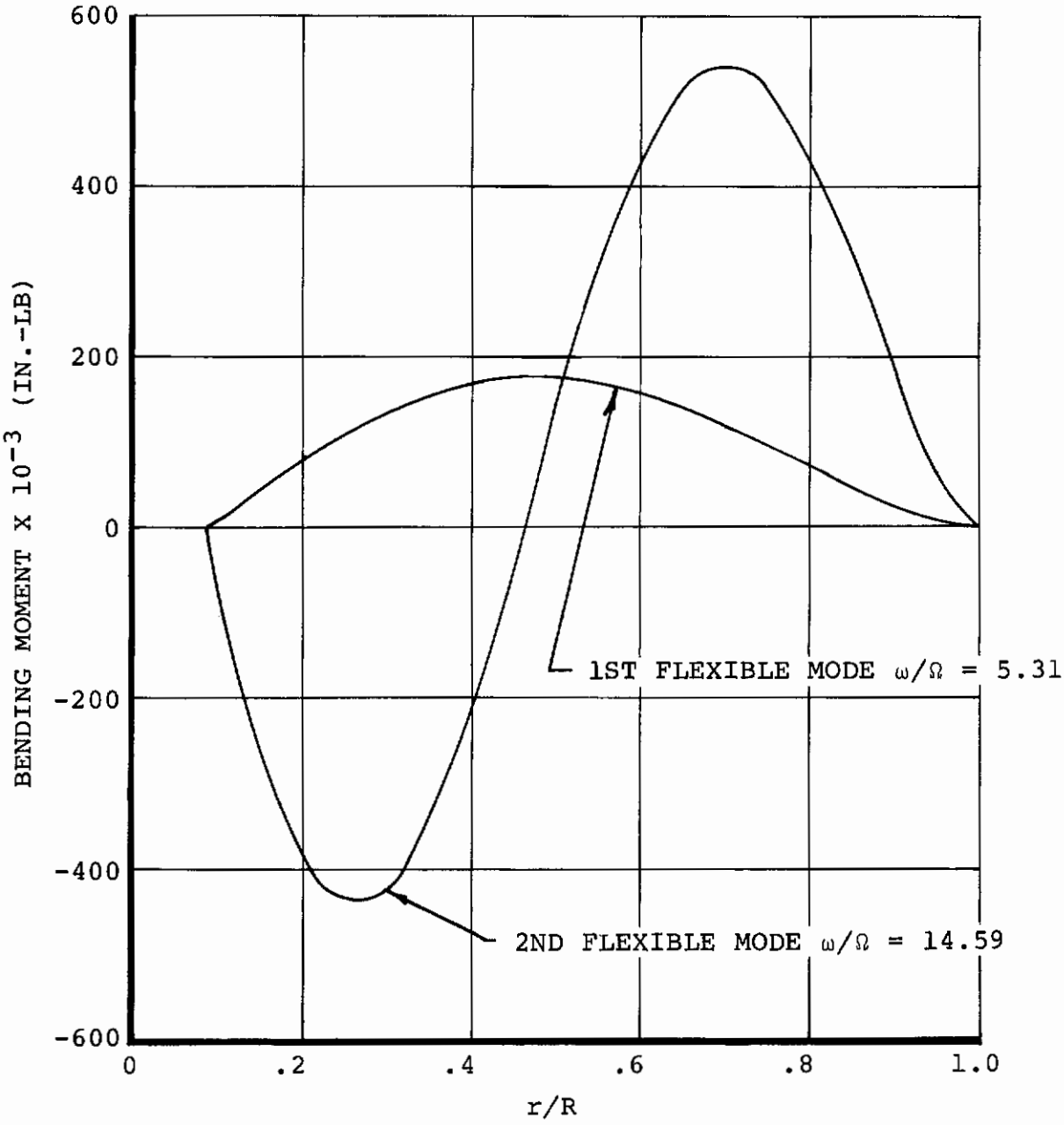

Figure 156. CH-47C L-01, Predicted Chord Bending Moment Mode Shapes in a Vacuum at 230 RPM

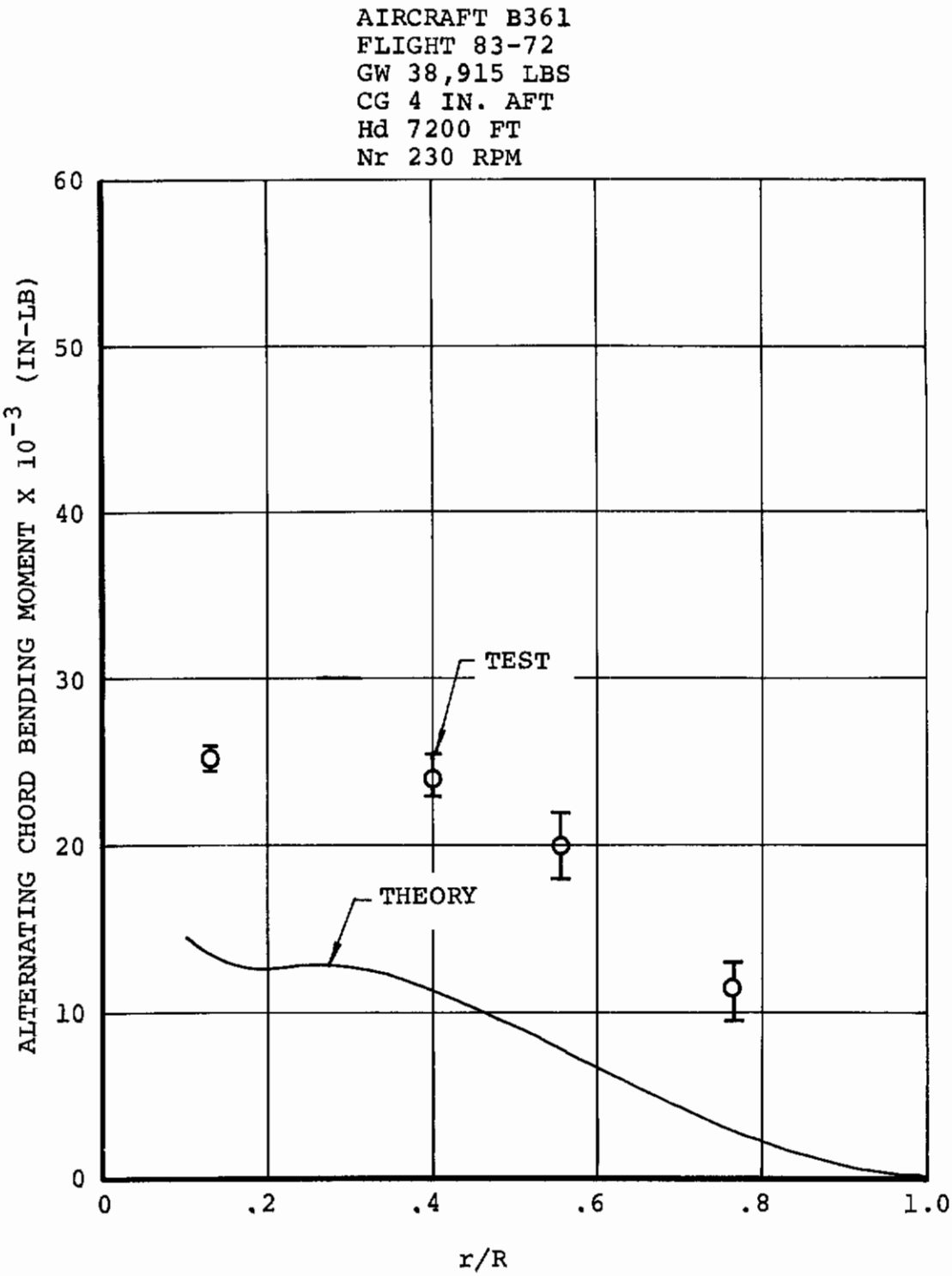

Figure 157. CH-47C Forward Rotor, Predicted and Measured Alternating Chord Bending Moment at V = 111 Knots

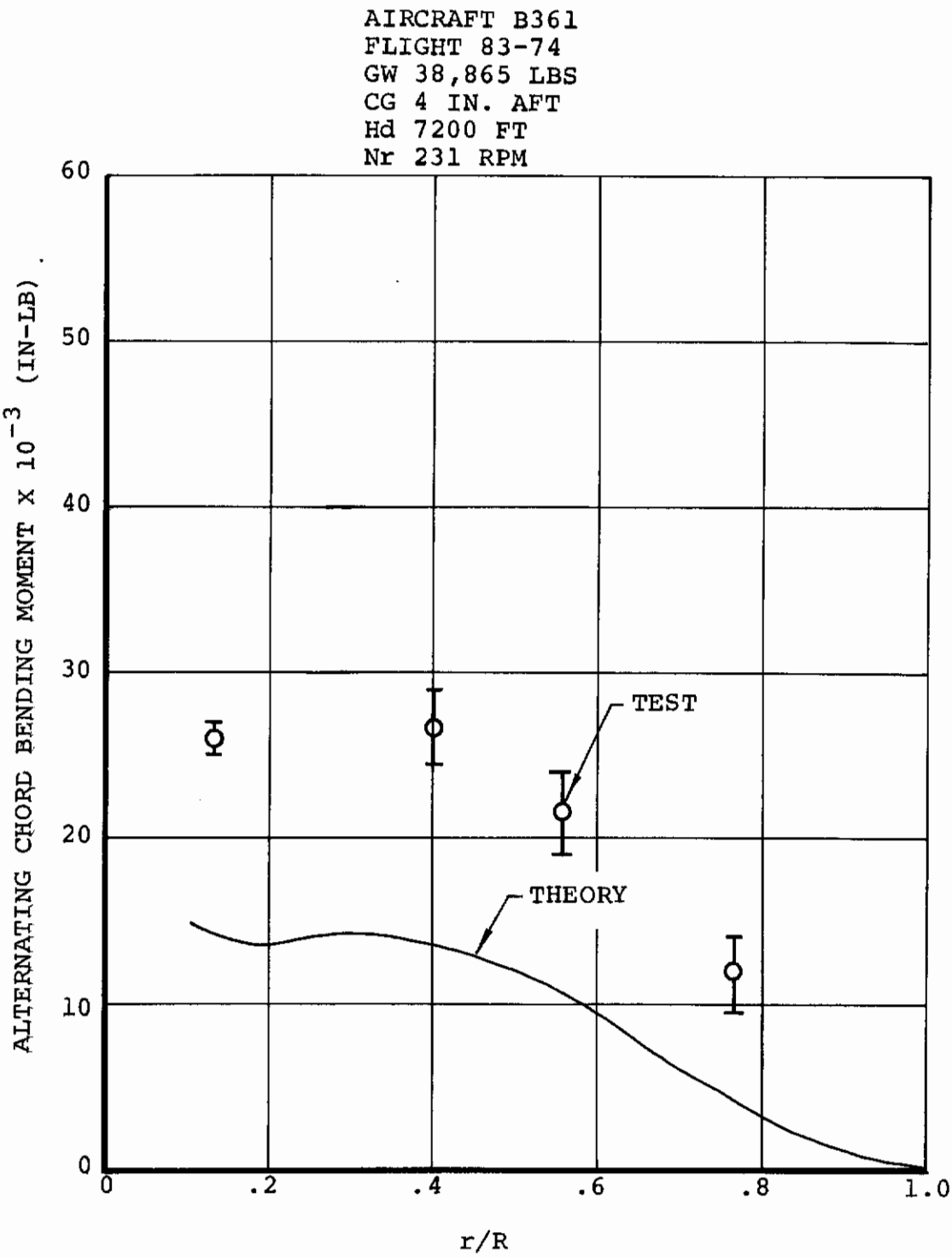

Figure 158. CH-47C Forward Rotor, Predicted and Measured Alternating Chord Bending Moment at V = 123 Knots

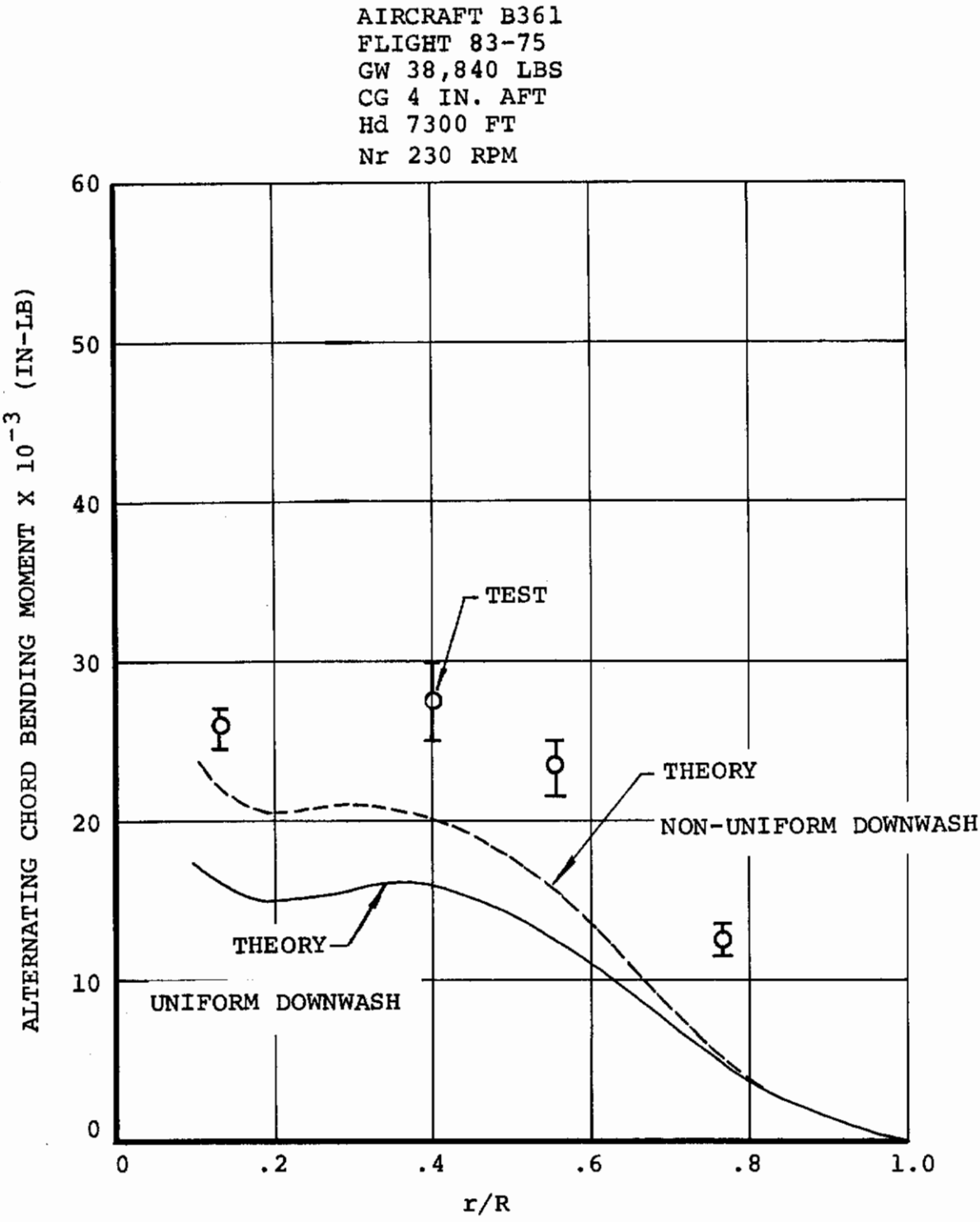

Figure 159. CH-47C Forward Rotor, Predicted and Measured Alternating Chord Bending Moment at V = 133 Knots

AIRCRAFT B361
FLIGHT 272-5
GW = 46,000 LB
CG = 4 IN. AFT
H_d = 6,000 FT
N_R = 245 RPM
V = 100

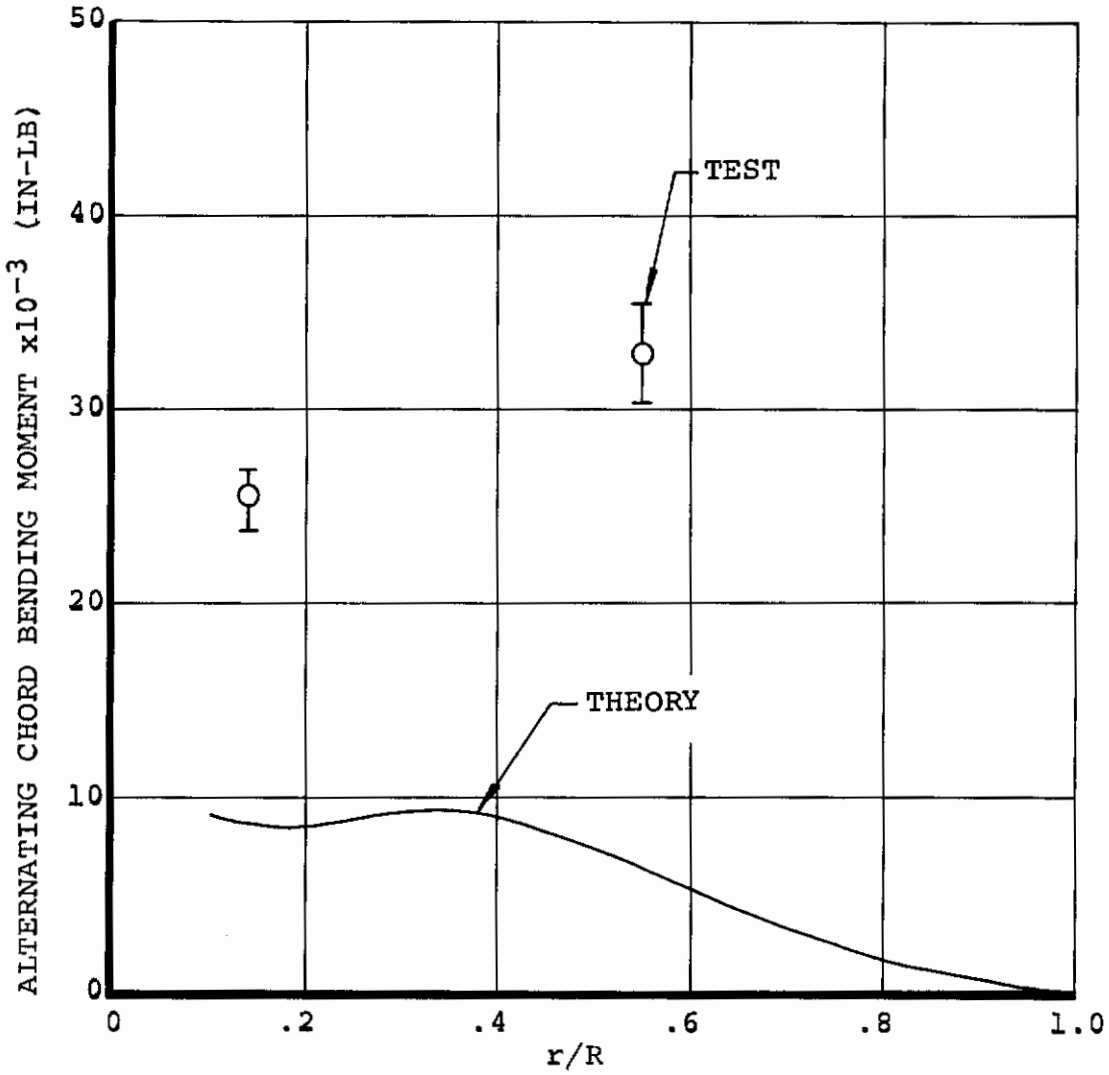

Figure 160. CH-47C With Advanced-Geometry Blades, Forward Rotor Predicted and Measured Alternating Chord Bending Moment at 100 Knots

AIRCRAFT B361
FLIGHT 272 - 7
GW = 46000 LB.
CG = 4 IN. AFT
H_d = 6000 FT.
N_R = 245 RPM
V = 117

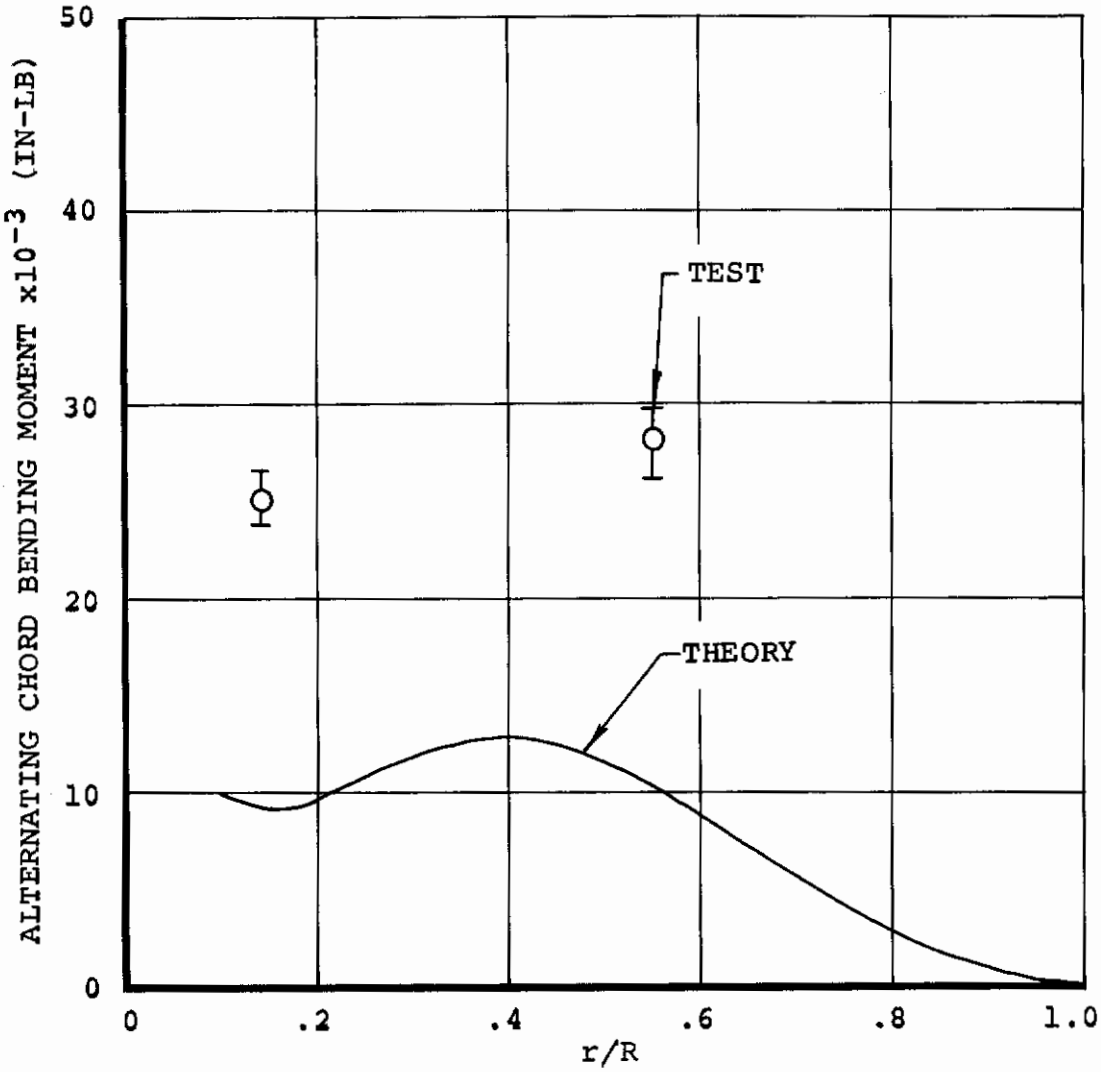

Figure 161. CH-47C With Advanced-Geometry Blades, Forward Rotor Predicted and Measured Alternating Chord Bending Moment at 117 Knots

AIRCRAFT B361
FLIGHT 272 - 9
GW = 46000 LB.
CG = 4 IN. AFT
H_d = 6000 FT.
N_R = 245 RPM
V_R = 126

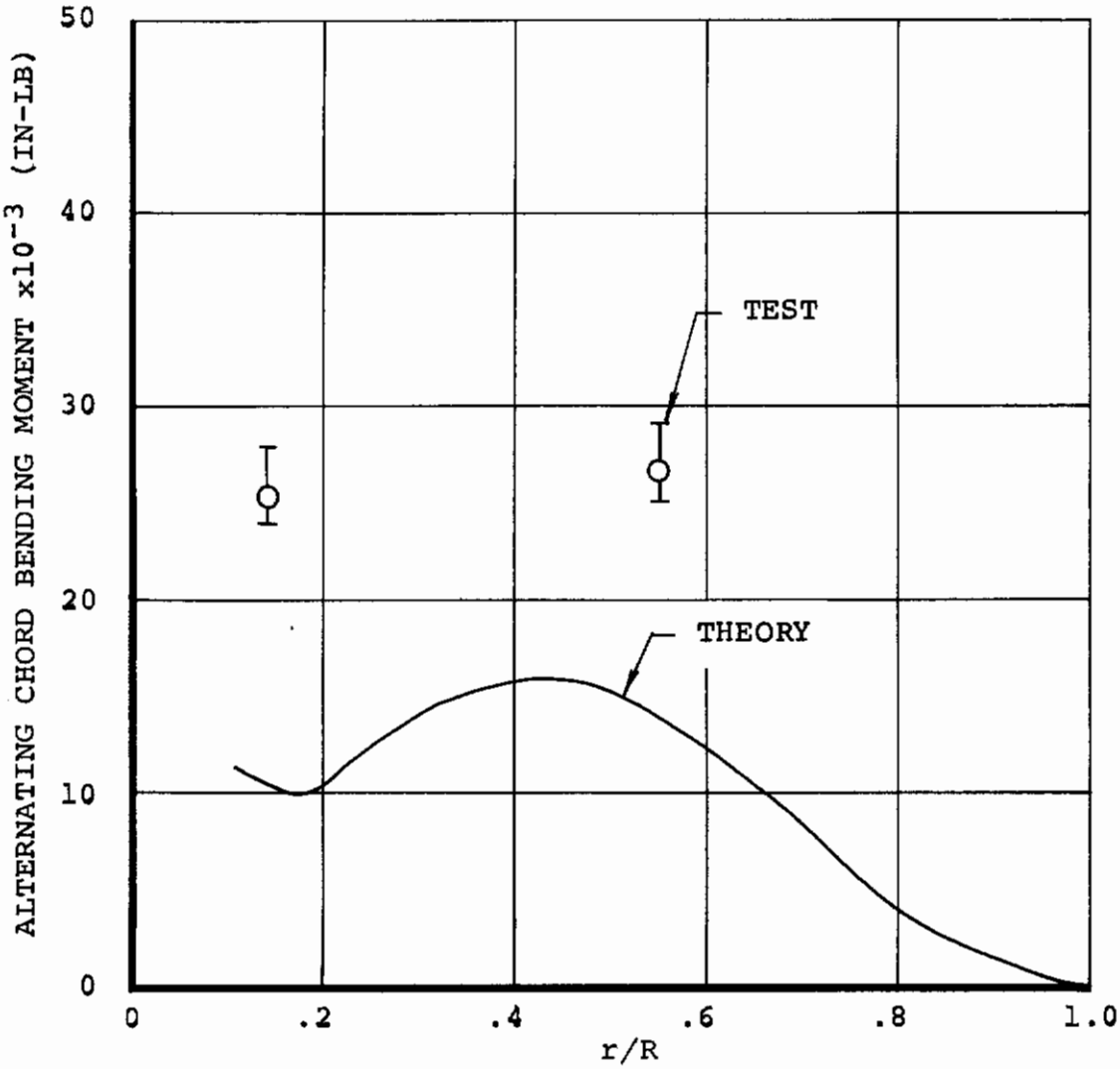

Figure 162. CH-47C With Advanced-Geometry Blades, Forward Rotor Predicted and Measured Alternating Chord Bending Moment at 126 Knots

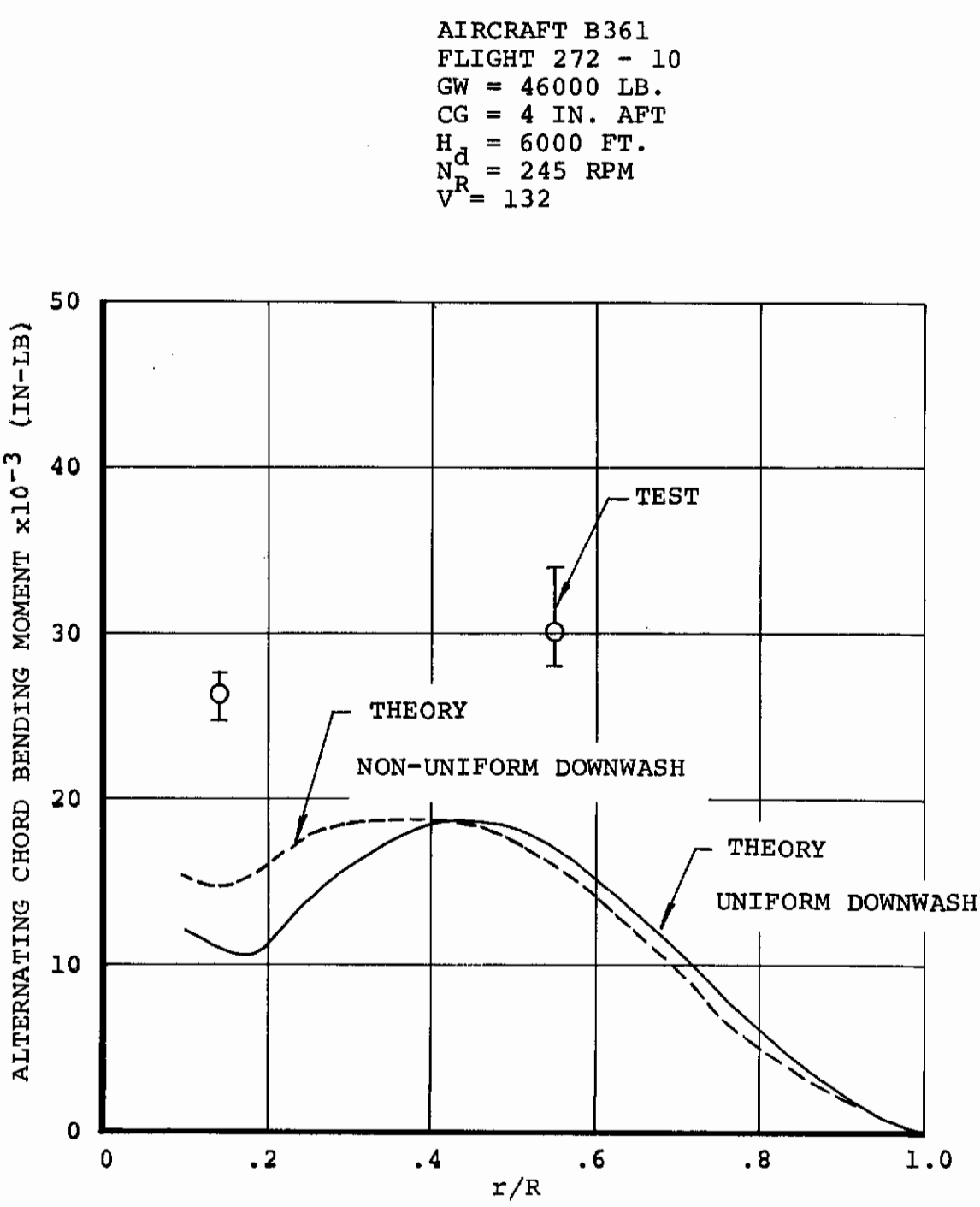

Figure 163. CH-47C With Advanced-Geometry Blades, Forward Rotor Predicted and Measured Alternating Chord Bending Moment at 132 Knots

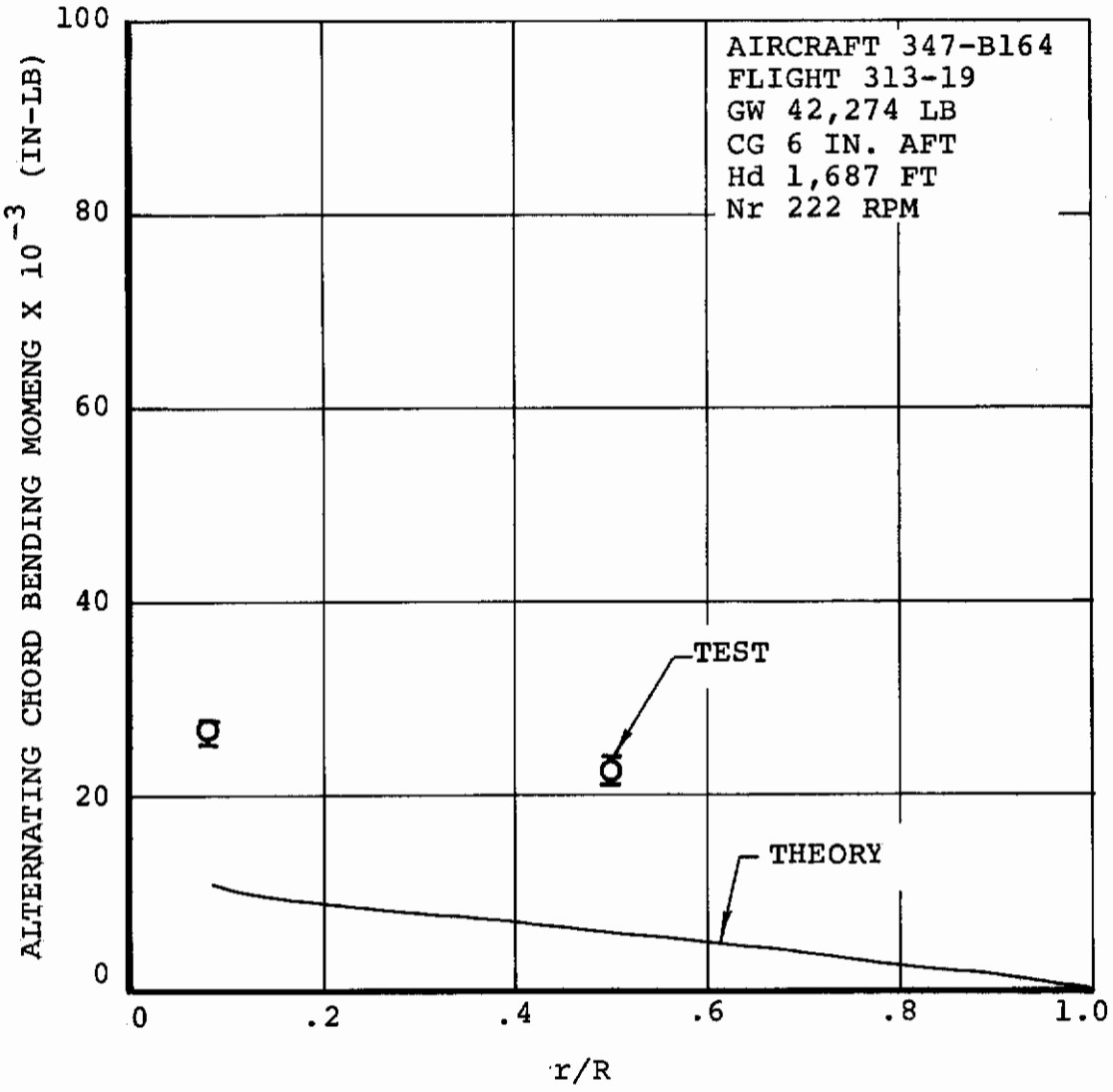

Figure 164. Model 347 With CH-47C Blades, Forward Rotor Predicted and Measured Alternating Chord Bending Moment at V = 87 Knots

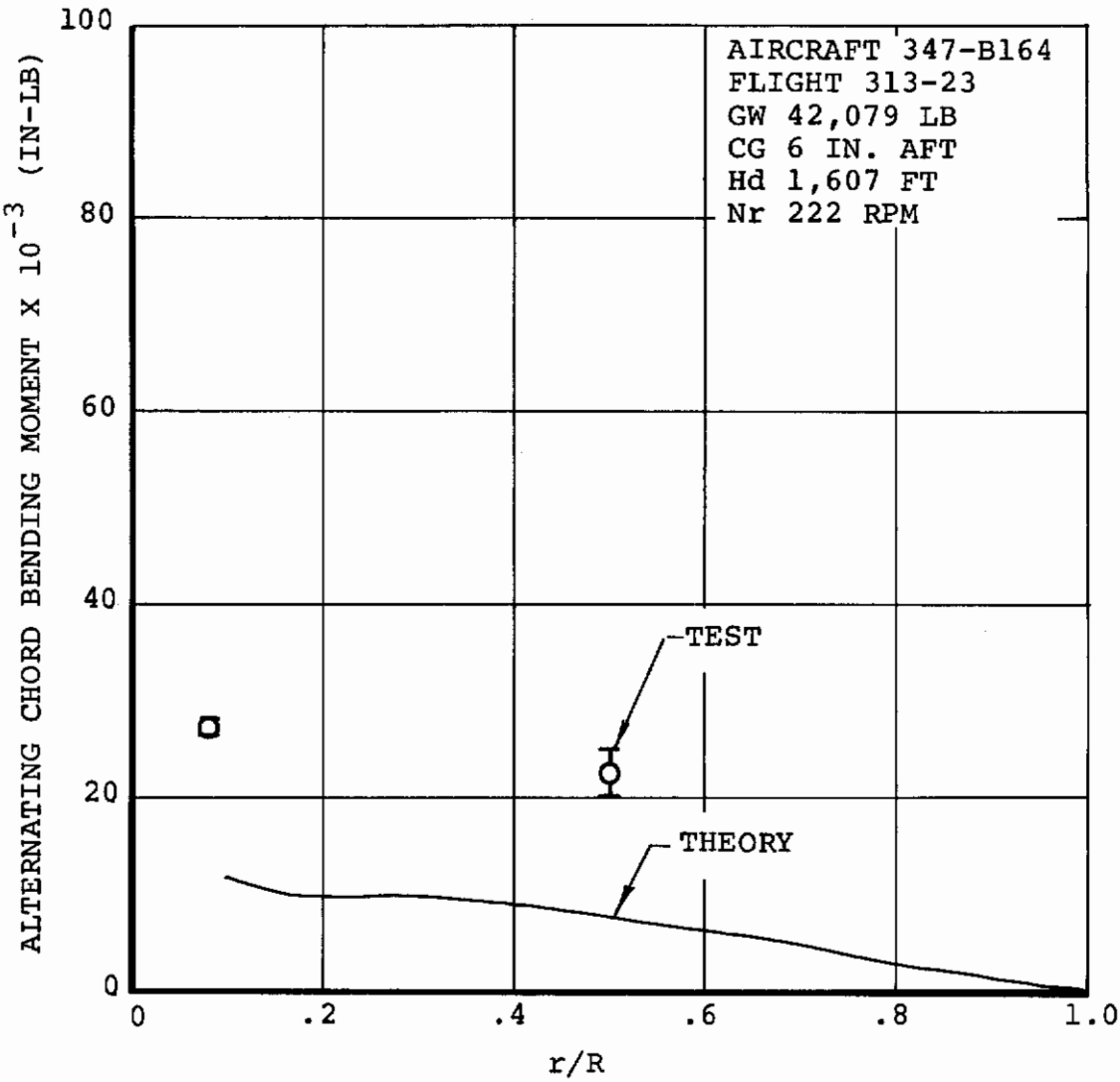

Figure 165. Model 347 With CH-47C Blades, Forward Rotor Predicted and Measured Alternating Chord Bending Moment at V = 122 Knots

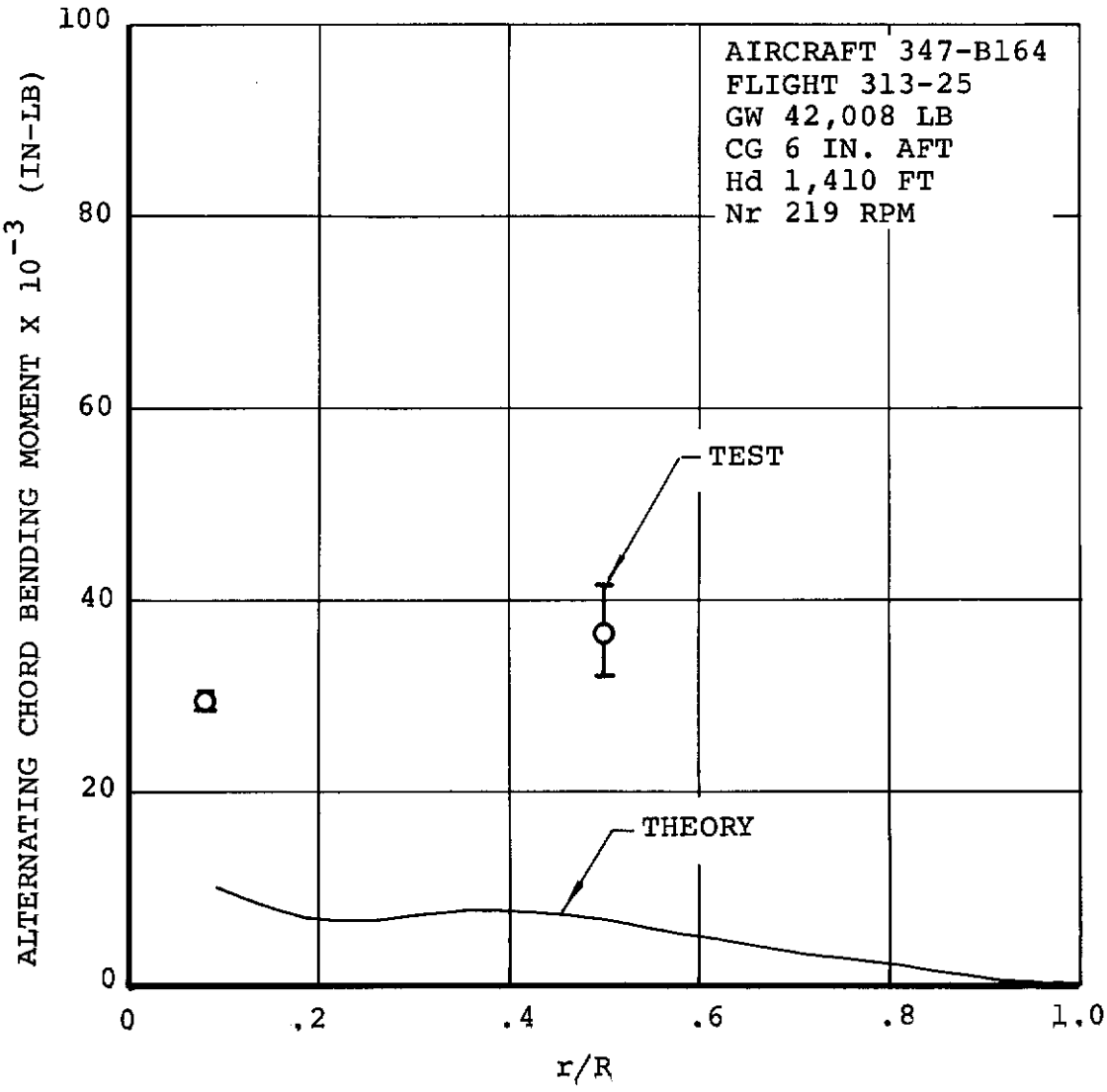

Figure 166. Model 347 With CH-47C Blades, Forward Rotor Predicted and Measured Alternating Chord Bending Moment at V = 140 Knots

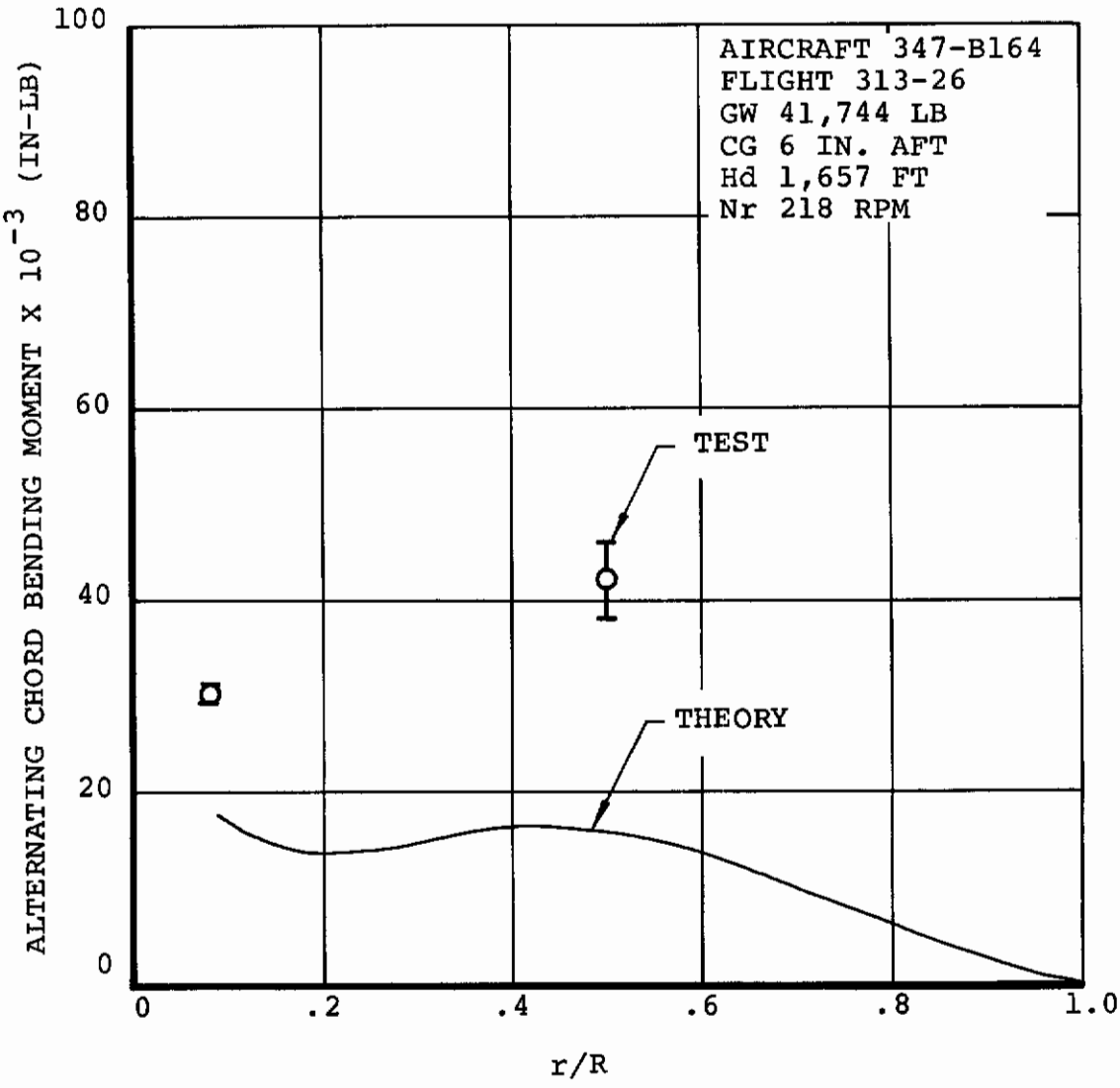

Figure 167. Model 347 With CH-47C Blades, Forward Rotor Predicted and Measured Alternating Chord Bending Moment at V = 152 Knots

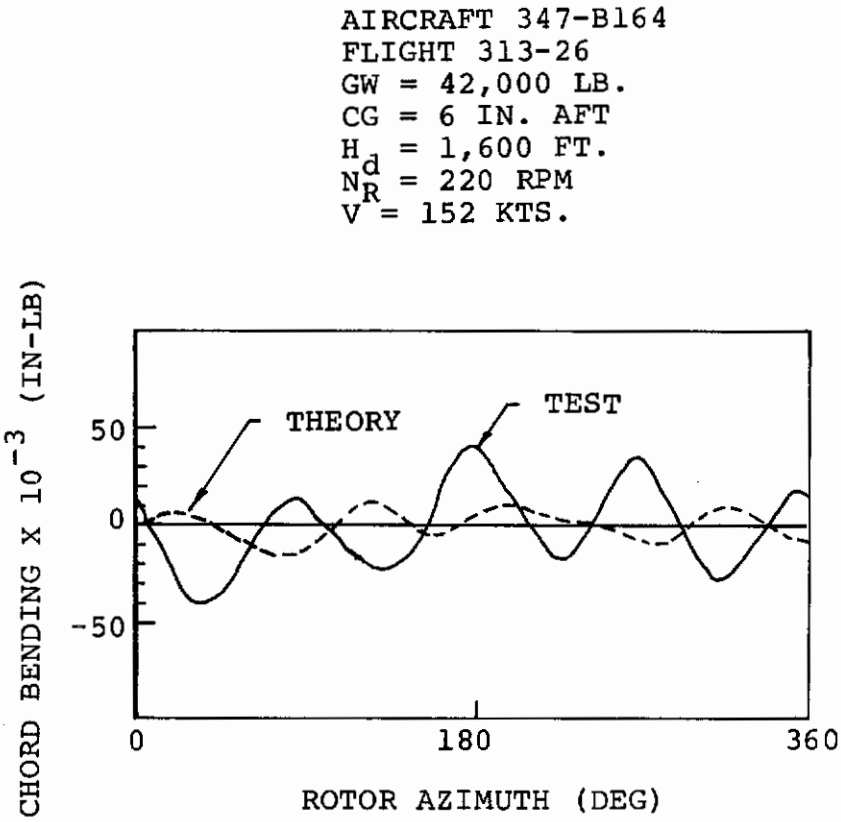

Figure 168. Model 347 With CH-47C Blades, Forward Rotor Predicted and Measured Chord Bending Waveform at 152 Knots

Airloads

Airloads correlation was performed with measured differential chordwise pressure distributions obtained from a test of a CH-34 full-scale rotor conducted in the NASA-Ames 40-foot by 80-foot wind tunnel. Blade physical and geometric properties and the airloads test data were obtained from Reference 31. The predicted and measured airloads are presented as lift-per-unit-span time histories for one rotor cycle. Correlation with uniform downwash is made at 5 radial stations spaced from mid-span to the blade tip. Test data for three airspeeds (110, 150, and 175 knots) at a constant shaft tilt of 5 degrees forward was used for correlation to show the effect of airspeed. In addition, test data at a 110-knot condition with 10 degrees forward shaft tilt was used to show the effect of shaft tilt.

Results of the correlation, presented in Figures 169 through 188, show the analysis correlates with the steady and peak-to-peak measured airloads. The correlation is particularly good at 0.55R (Figures 169, 174, 179, and 184) and 0.75R (Figures 170, 175, 180, and 185). At 85 percent and 95 percent span at 175 knots (Figures 186 and 187), the analysis underpredicts the peak-to-peak airloads. Underprediction is probably due to a strong blade-to-blade interference effect which cannot be simulated when uniform downwash is used in the analysis. Note that the analysis overpredicts airloads by a large margin at 99 percent span for all airspeeds (Figures 173, 178, 183, and 188). The effect of the tip vortex on airloads is very strong over the outboard 5 percent of the blade and washout of the blade tip cannot be simulated with uniform downwash. Figures 169 through 173 can be compared with Figures 174 through 178 for correlation with forward shaft tilt at 110 knots. The analysis correlates well at 0.55R and 0.75R but overpredicts at 0.85R and 0.95R, as well as at the blade tip. Overprediction at 0.85R and 0.95R is surprising since increasing forward shaft tilt lessens blade-to-blade interference, therefore suggesting that uniform downwash predictions should be better at higher shaft tilts. Just the opposite is shown to be true at 0.95R (Figures 172 and 177); correlation is better at the lower shaft tilt.

A comparison of the predicted and measured azimuthal variation of airloads shows that both the analysis and measured data show a large decrease in lift on the advancing blade. However, the analysis shows a phase shift of about 30 degrees--the predicted minimum lift occurring 30 degrees before the measured minimum at 120 degrees. The uniform downwash representation in the analysis is not sufficient to describe the downwash nonuniformity in the region of rapidly changing vortex strength. In this region of the azimuth, the measured airloads also show evidence of tip vortex interference from the preceding blade. Note in Figures 171 and 172 the high harmonic

airloading at about 90 degrees azimuth for 5 degrees shaft tilt and 110 knots. As mentioned before, vortex interference is expected to decrease as forward shaft tilt is increased, and this trend is evident when Figures 171 and 172 are compared with Figures 176 and 177. In the last two figures, the forward shaft tilt has been increased to 9 degrees, and the high-harmonic airloading at 90 degrees azimuth is no longer present.

In summary, the good peak-to-peak airloads correlation indicates that the analysis with uniform downwash is adequate for predicting peak-to-peak bending moments on a single-rotor helicopter. However, the higher harmonic content of bending moments will not be reflected in the peak-to-peak value if blade-to-blade interference effects are significant (near zero or aft shaft tilt). It also should be remembered that rotor-on-rotor interference effects are significant even at large forward shaft tilts for tandem-rotor configurations and therefore, use of uniform downwash is not recommended for bending moment predictions for tandem-rotor configurations. Use of nonuniform downwash in the analysis should improve airloads and bending moment predictions for both single-rotor and tandem-rotor helicopters.

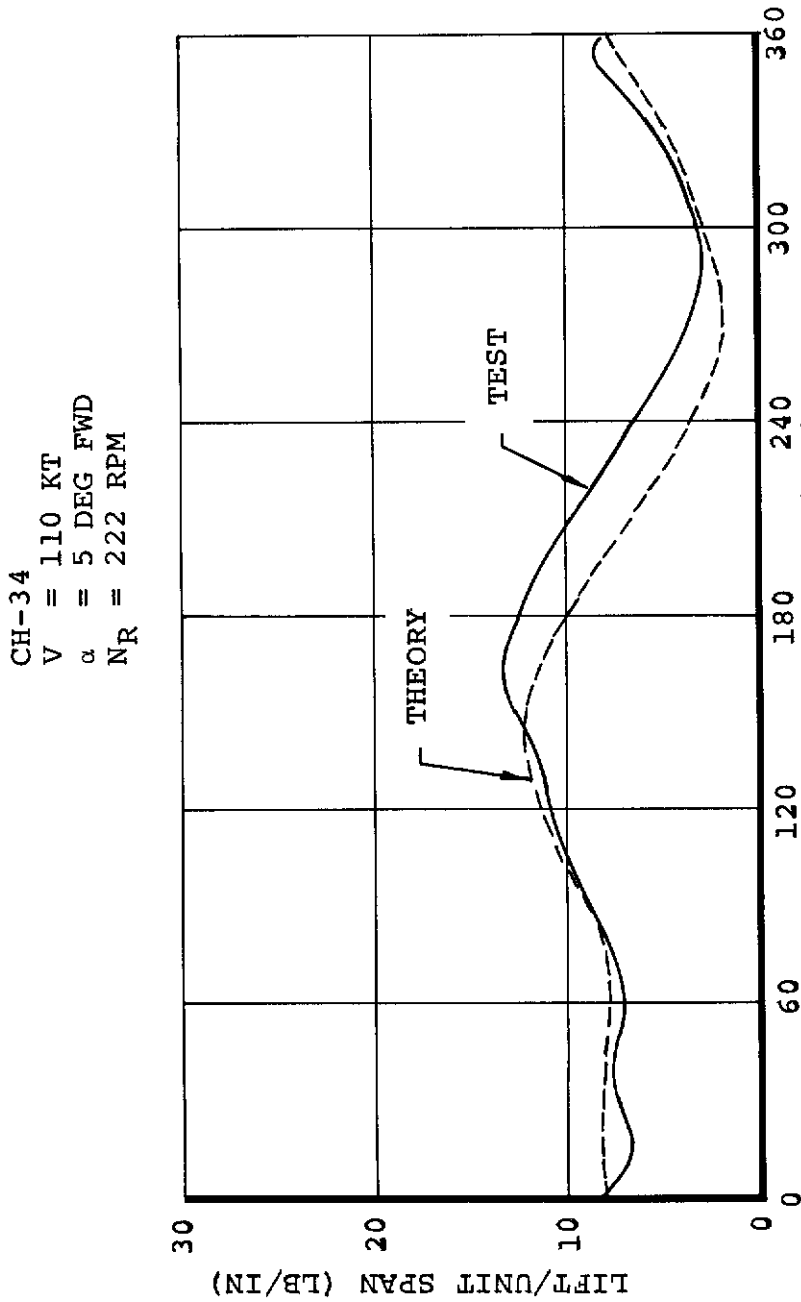

Figure 169. CH-34 Predicted and Measured Lift/Unit Span at 0.55R at 110 Knots

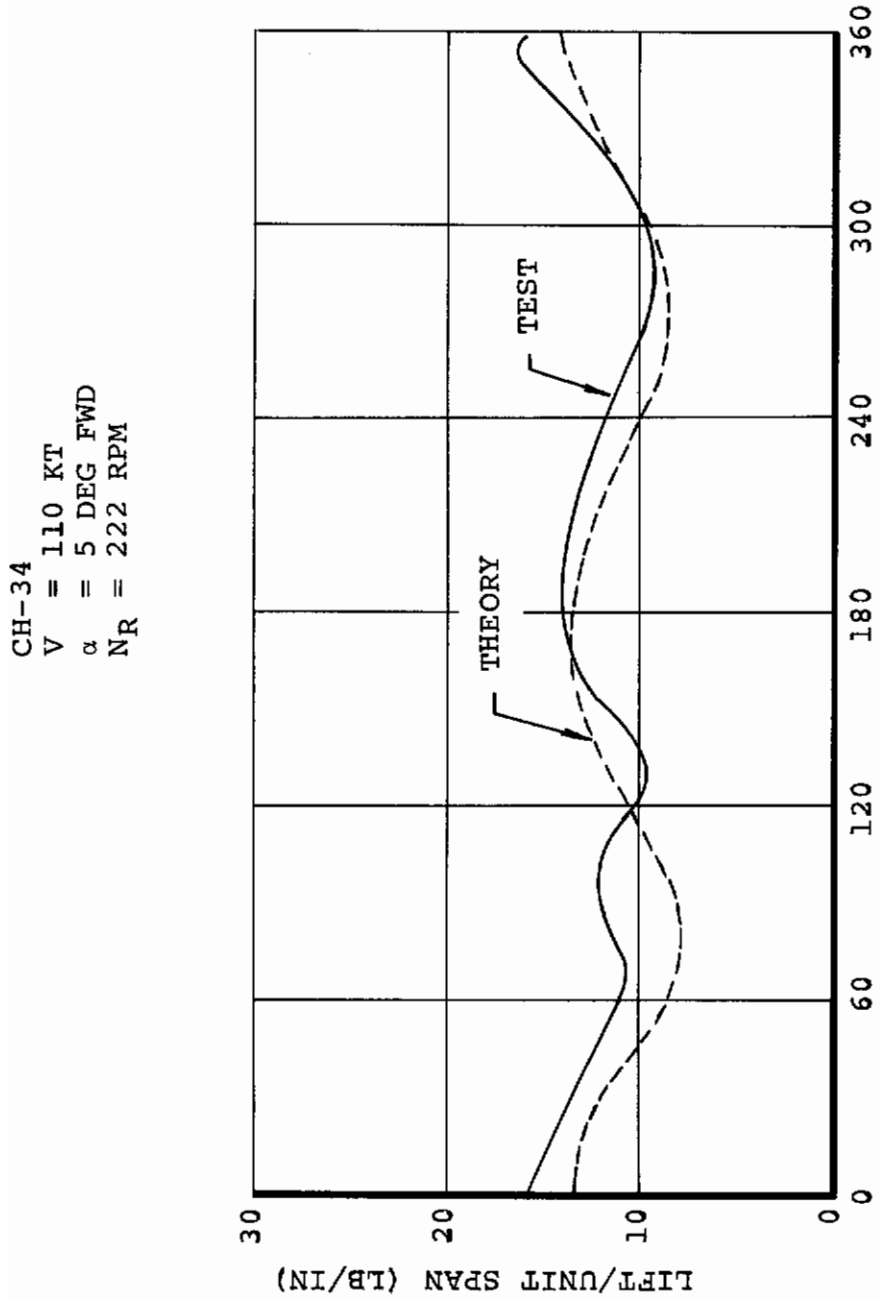

Figure 170. CH-34 Predicted and Measured Lift/Unit Span at 0.75R at 110 Knots

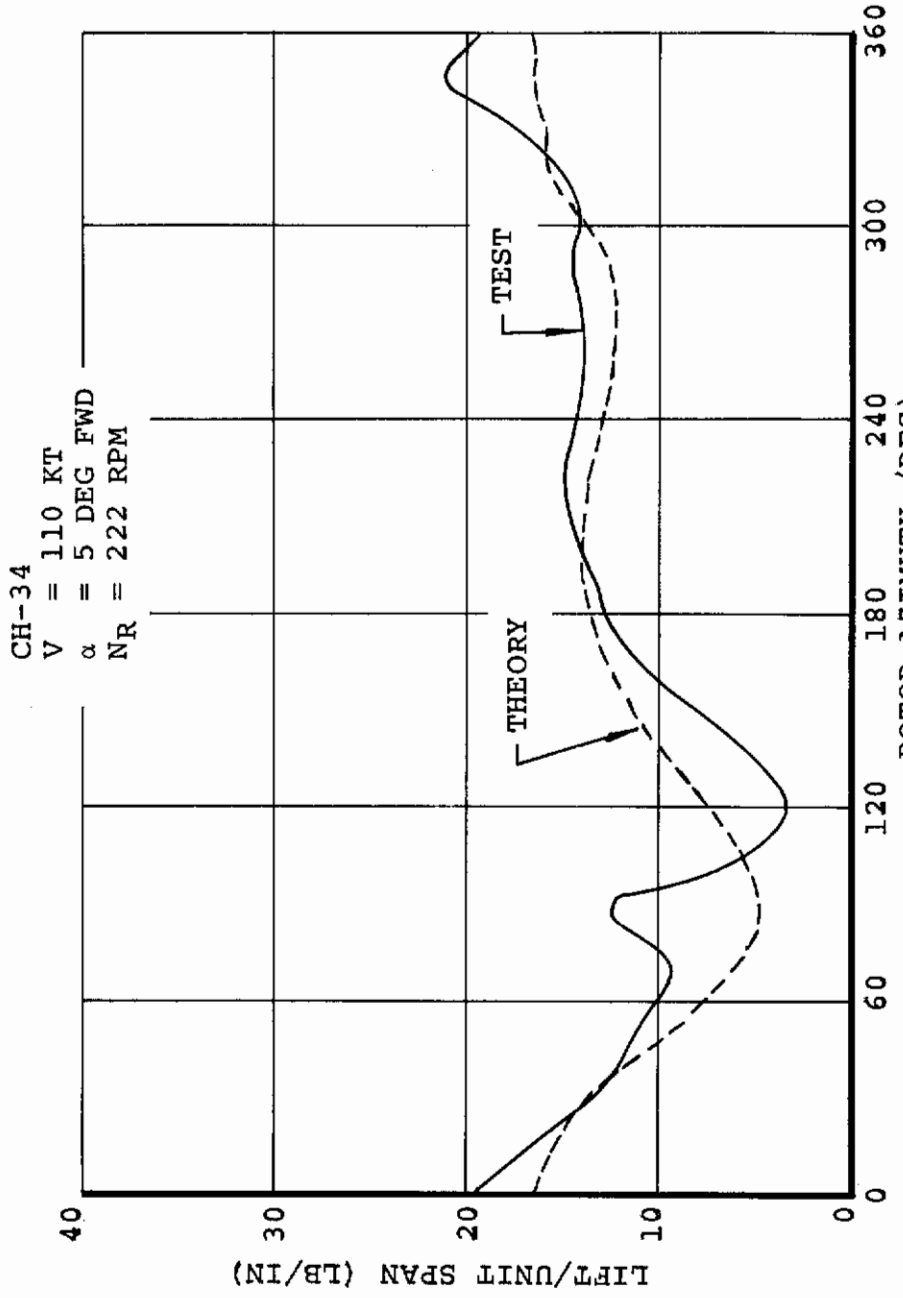

Figure 171. CH-34 Predicted and Measured Lift/Unit Span at 0.85R at 110 Knots

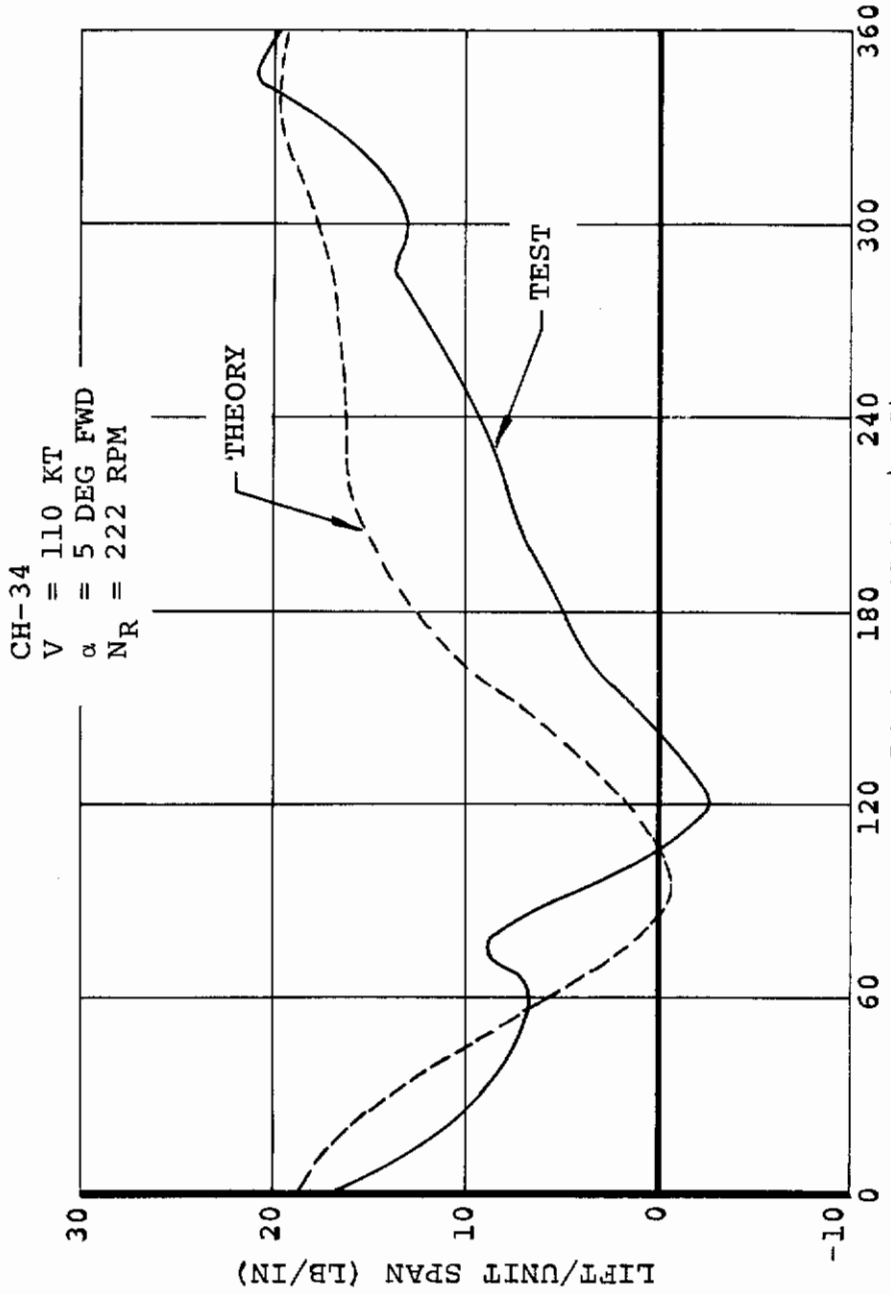

Figure 172. CH-34 Predicted and Measured Lift/Unit Span at 0.95R at 110 Knots

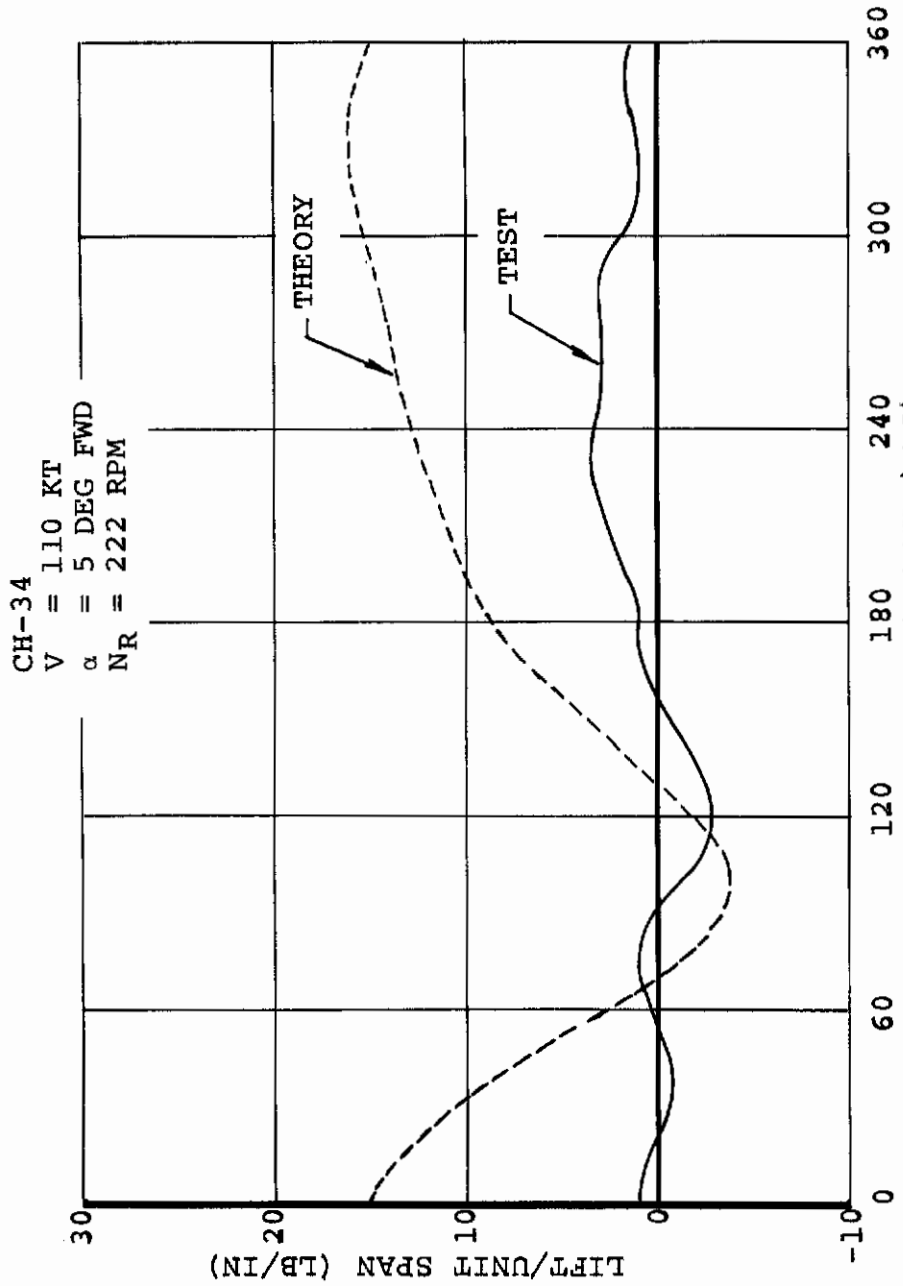

Figure 173. CH-34 Predicted and Measured Lift/Unit Span at 0.99 R at 110 Knots

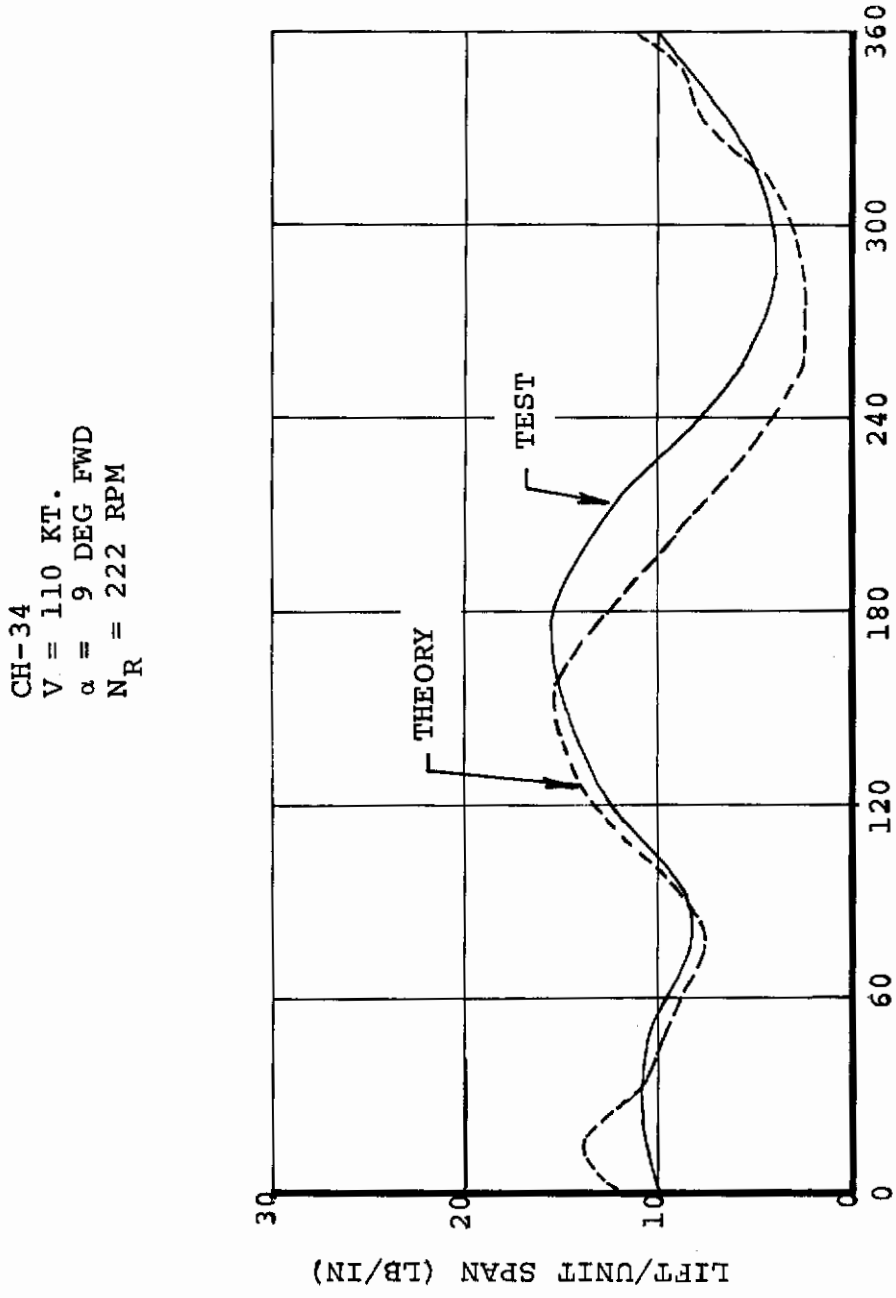

Figure 174. CH-34 Predicted and Measured Lift/Unit Span at 0.55R at 110 Knots

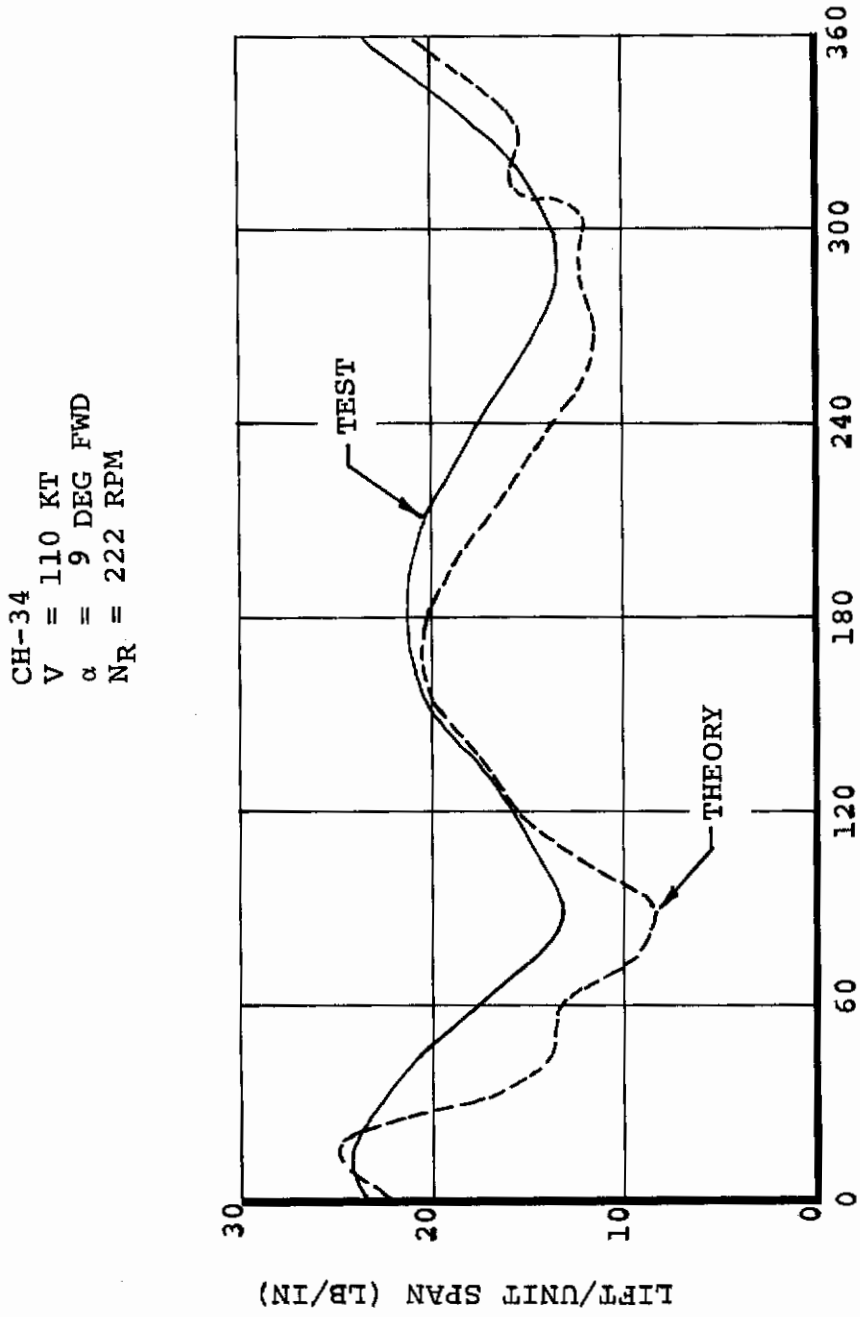

Figure 175. CH-34 Predicted and Measured Lift/Unit Span at 0.75R at 110 Knots

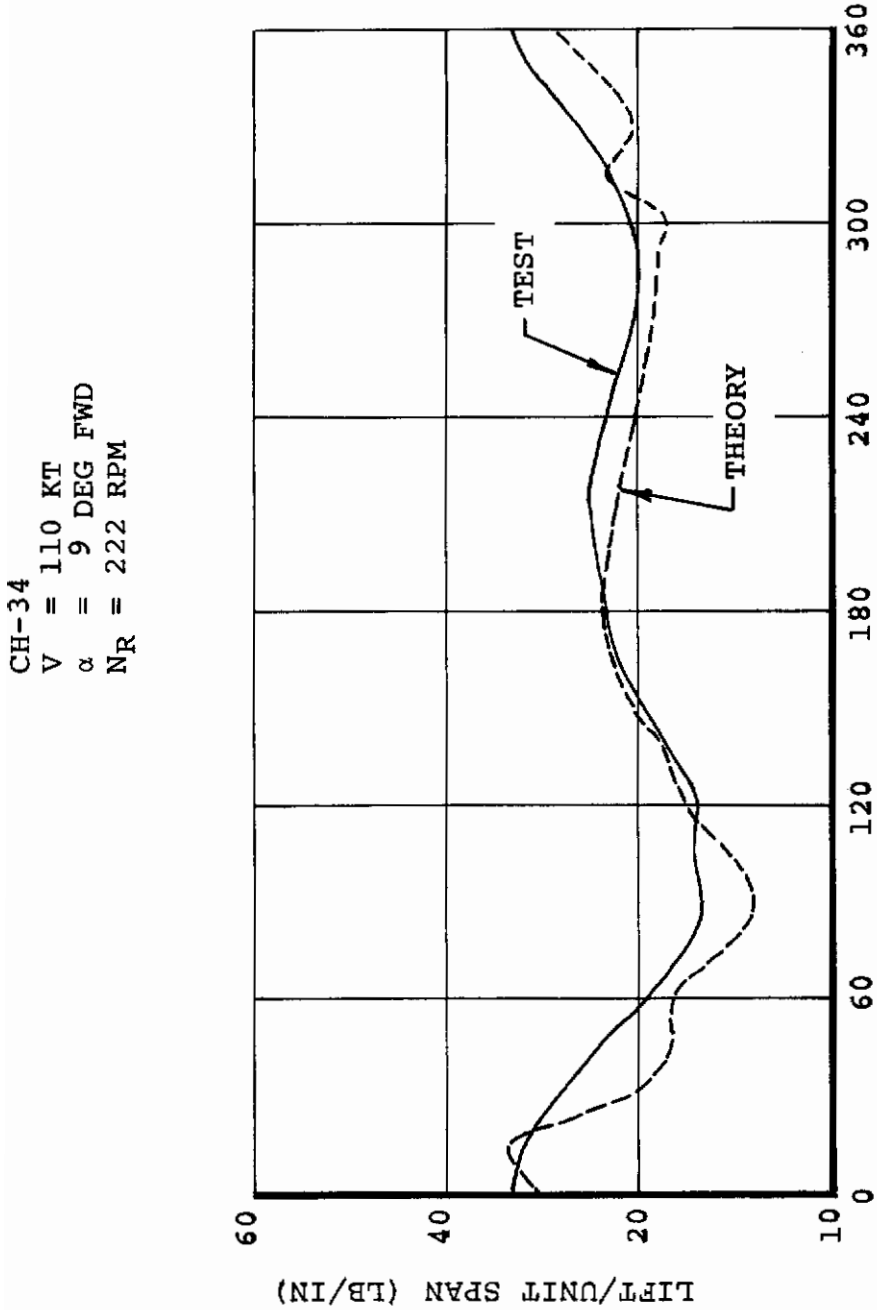

Figure 176. CH-34 Predicted and Measured Lift/Unit Span at 0.85R at 110 Knots

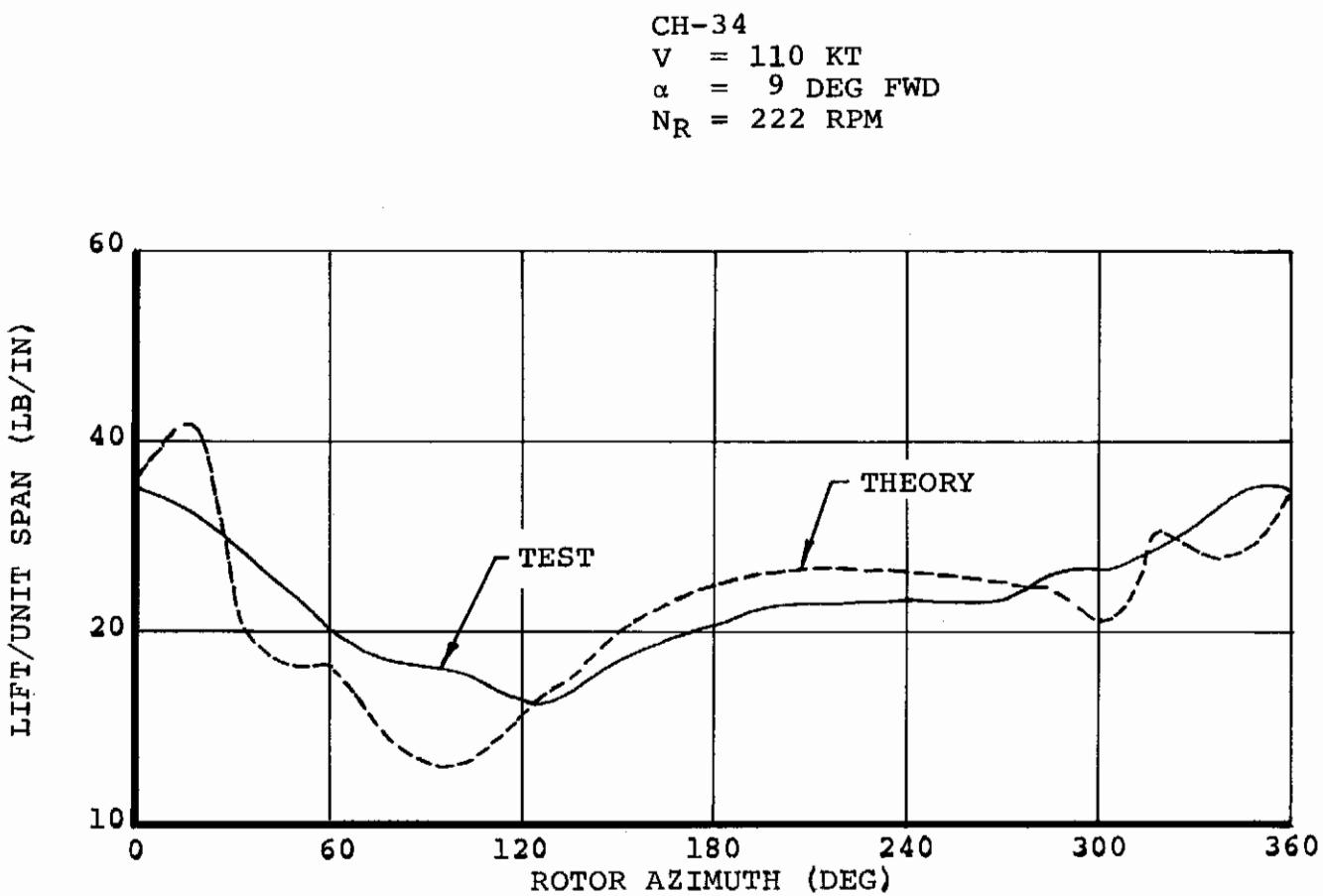

Figure 177. CH-34 Predicted and Measured Lift/Unit Span at 0.95R at 110 Knots

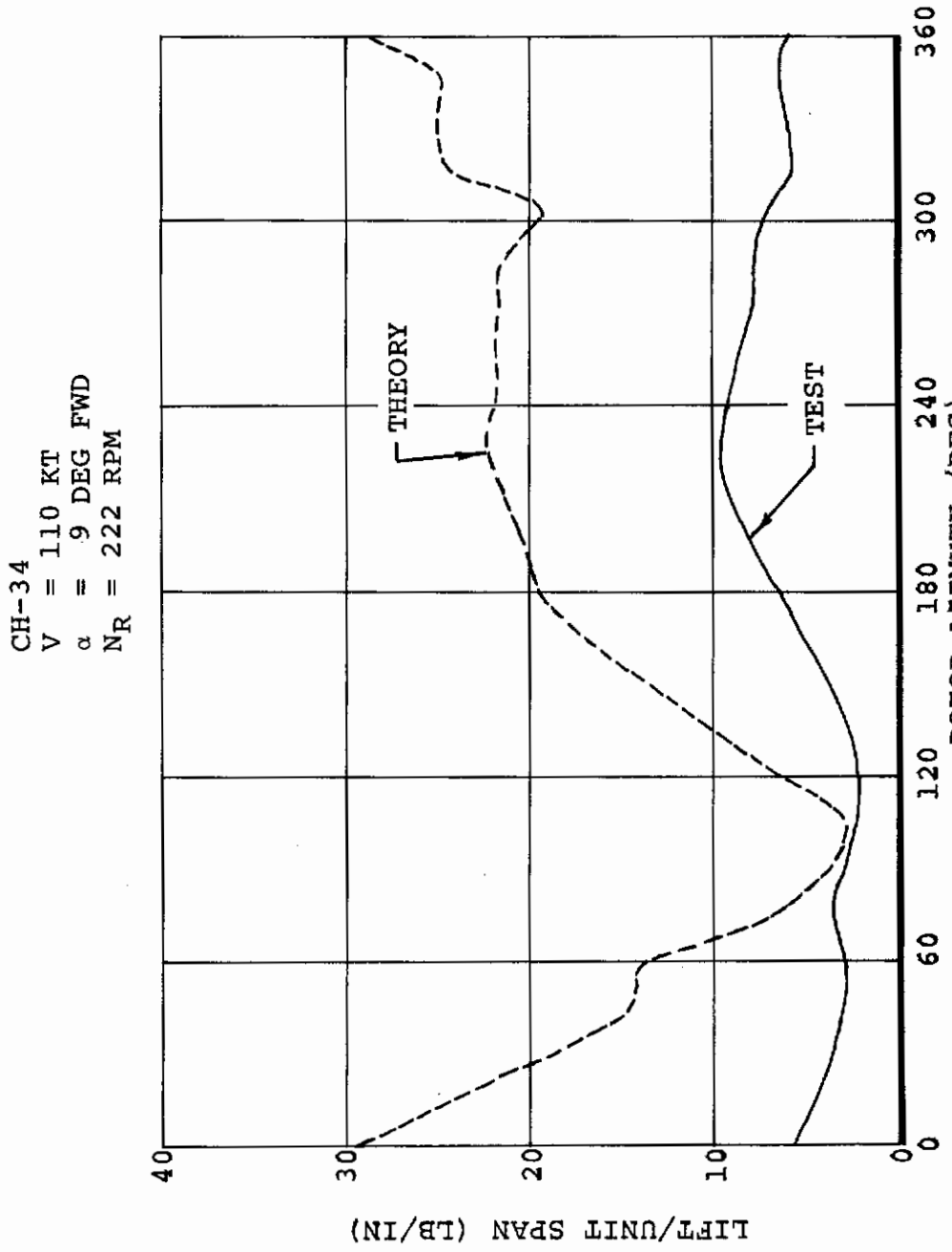

Figure 178. CH-34 Predicted and Measured Lift/Unit Span at 0.99R at 110 Knots

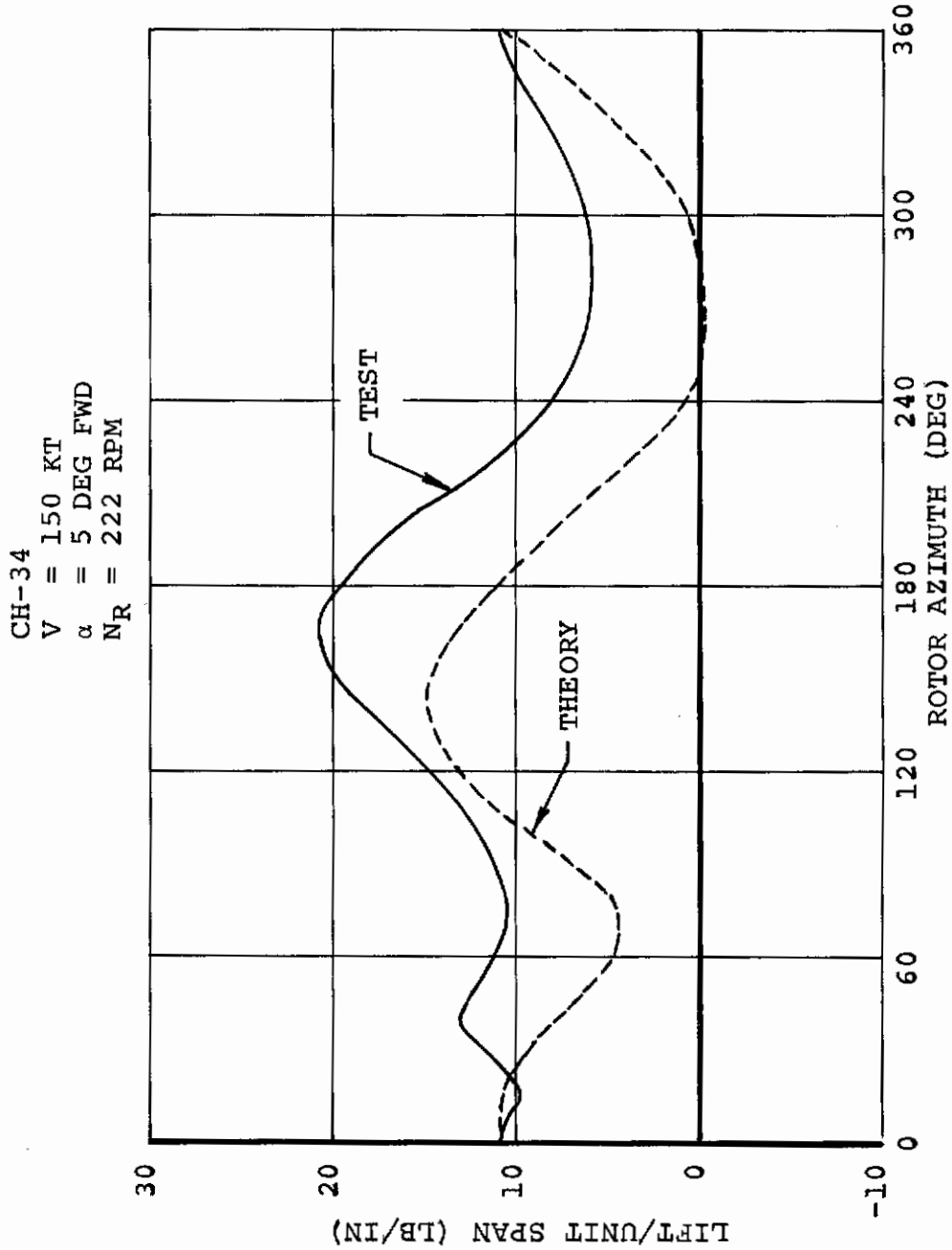

Figure 179. CH-34 Predicted and Measured Lift/Unit Span at 0.55R at 150 Knots

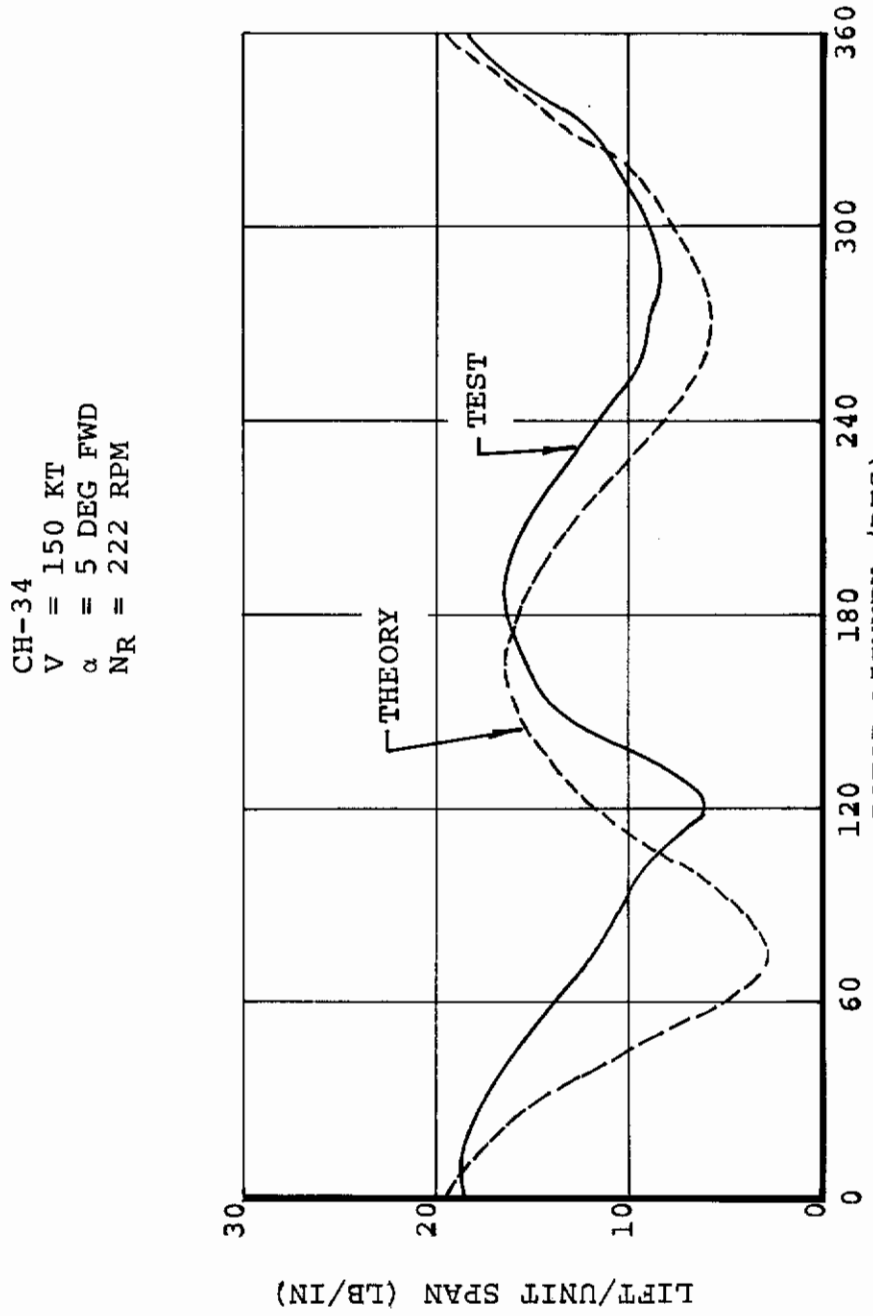

Figure 180. CH-34 Predicted and Measured Lift/Unit Span at 0.75R at 150 Knots

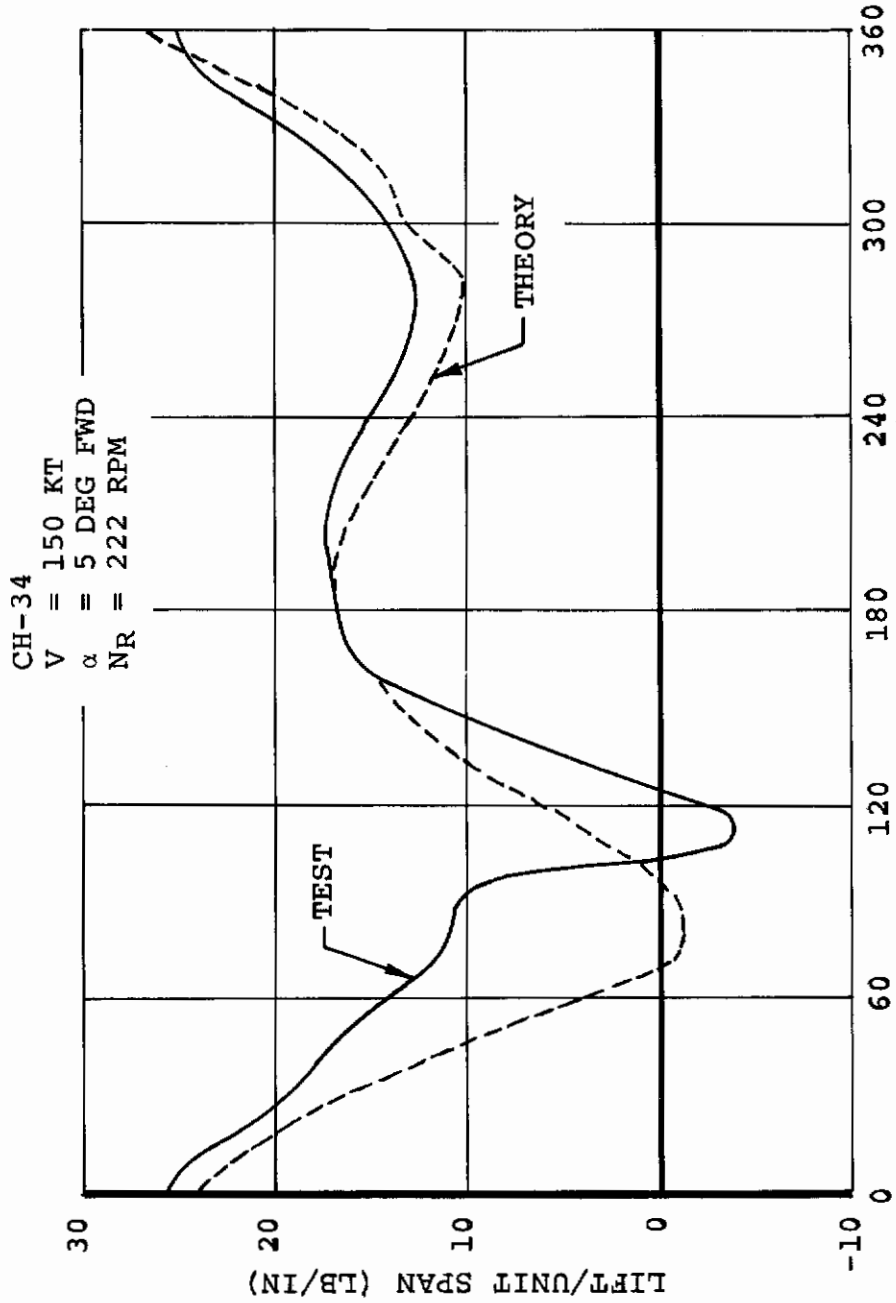

Figure 181. CH-34 Predicted and Measured Lift/Unit Span at 0.85R at 150 Knots

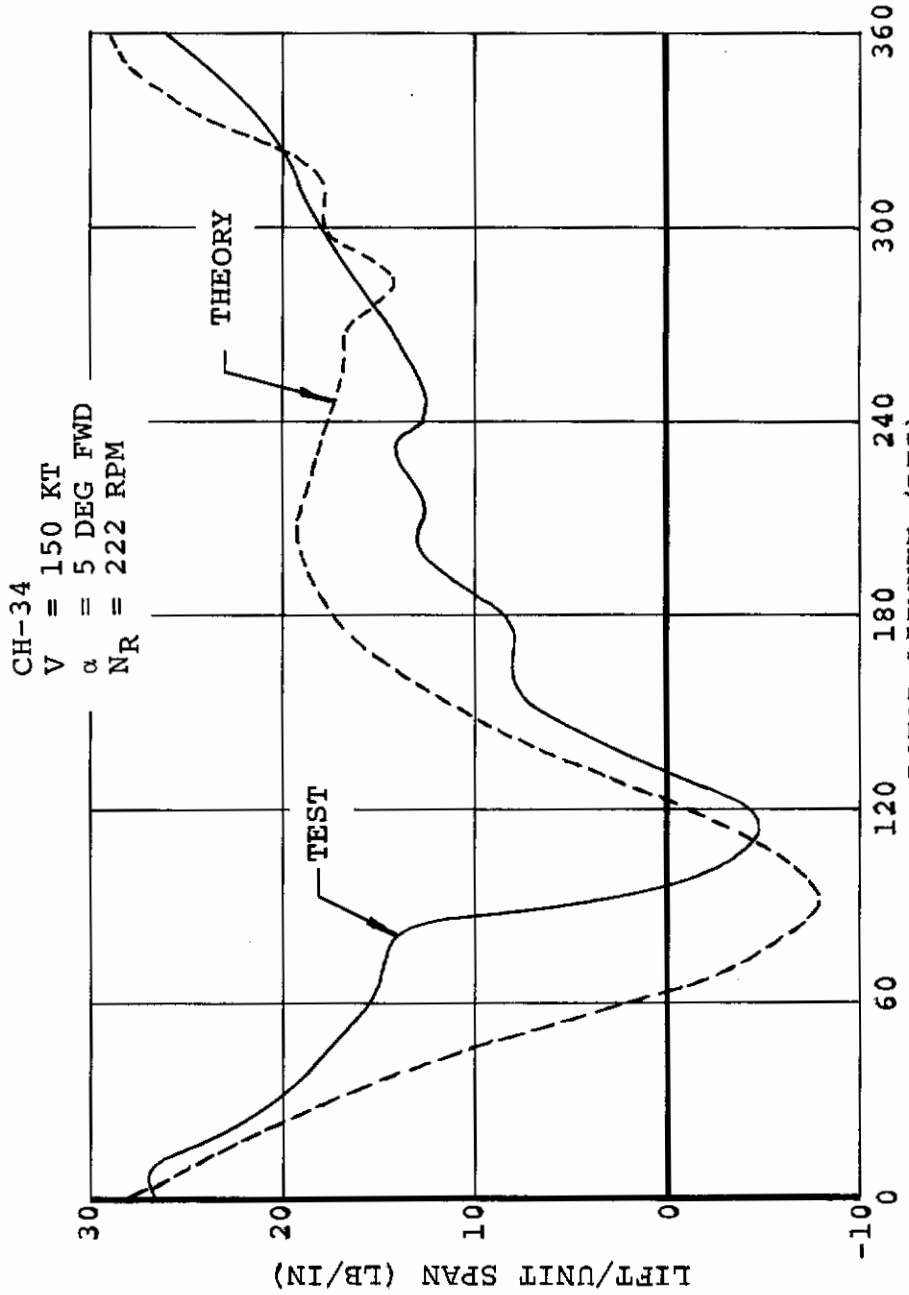

Figure 182. CH-34 Predicted and Measured Lift/Unit Span at 0.95R at 150 Knots

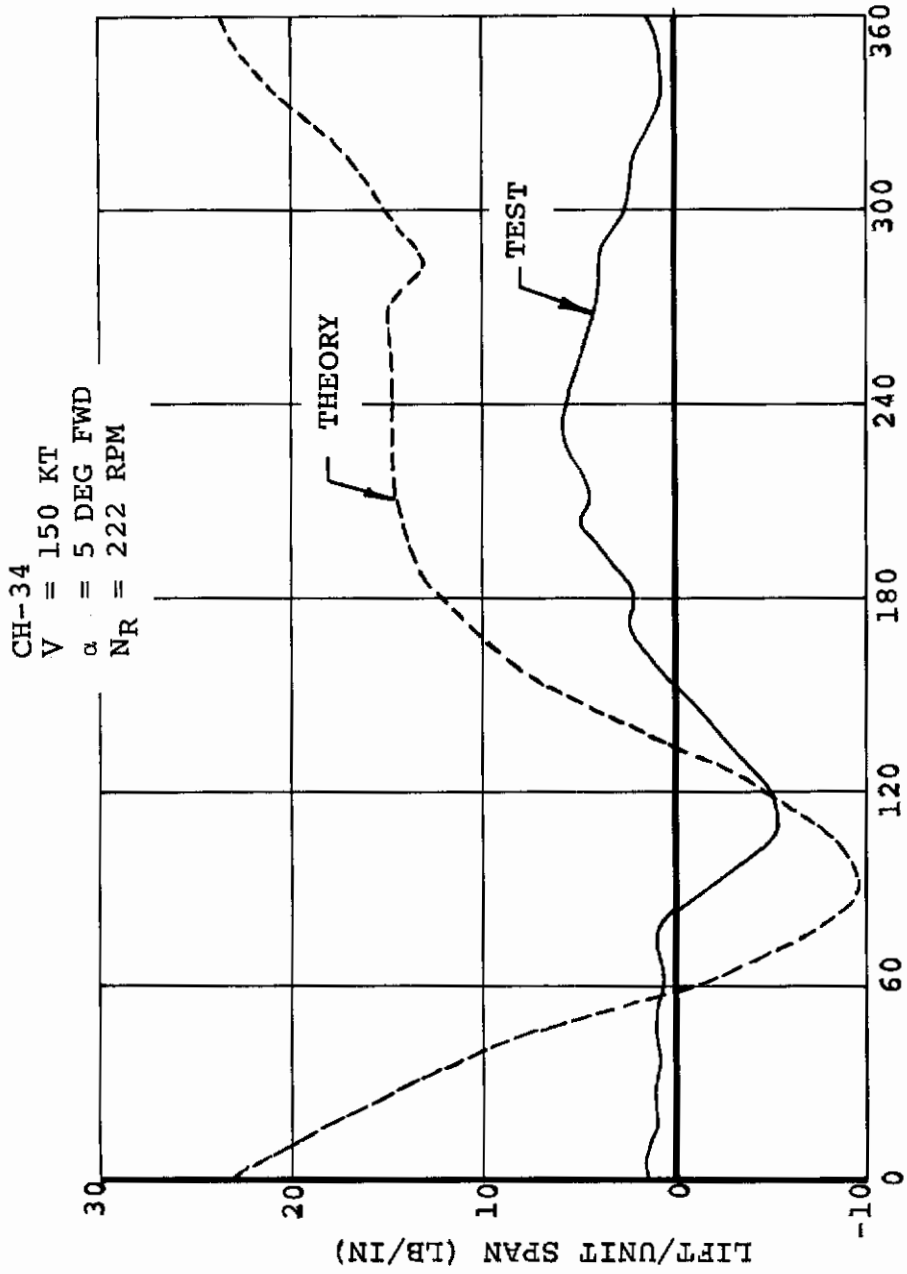

Figure 183. CH-34 Predicted and Measured Lift/Unit Span at 0.99R at 150 Knots

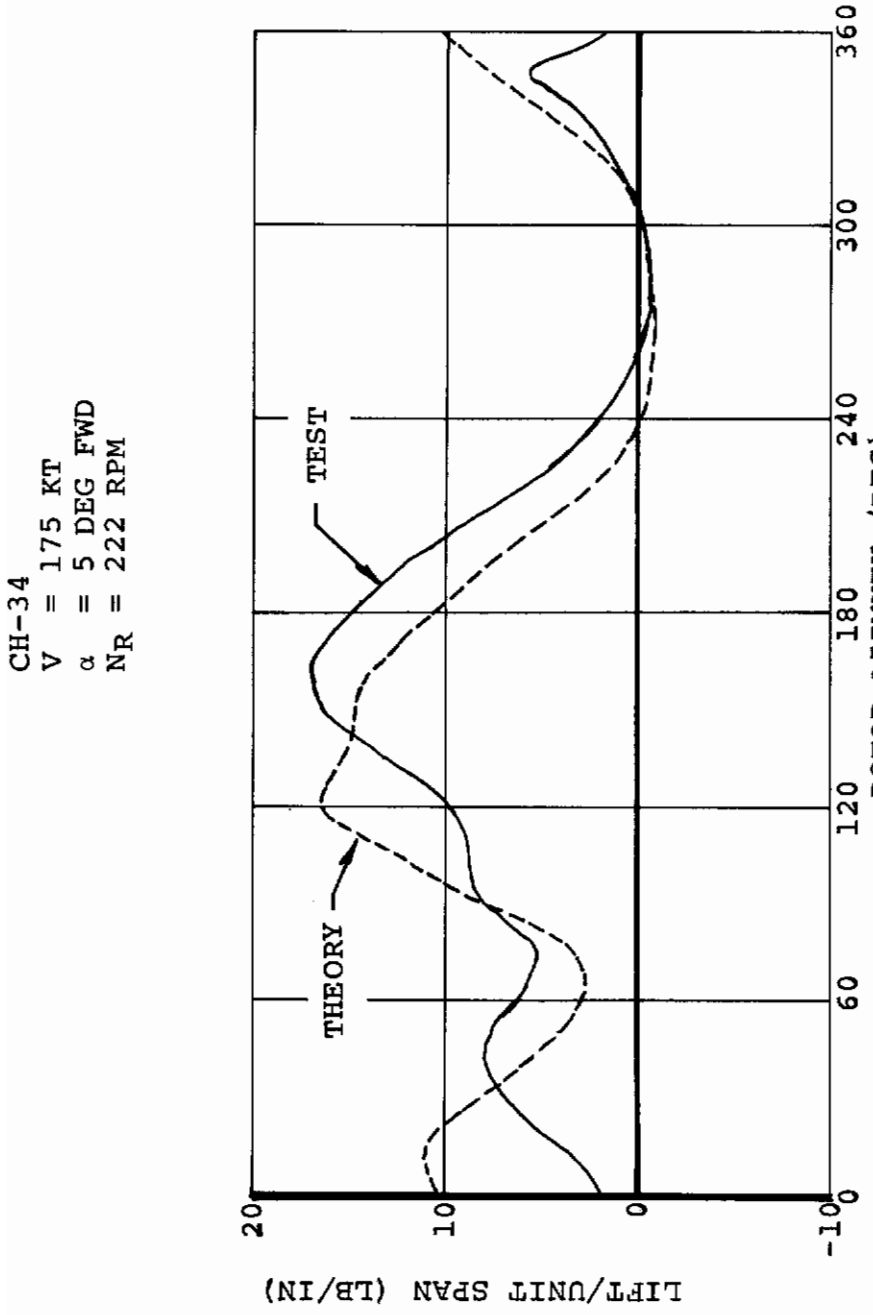

Figure 184. CH-34 Predicted and Measured Lift/Unit Span at 0.55R at 175 Knots

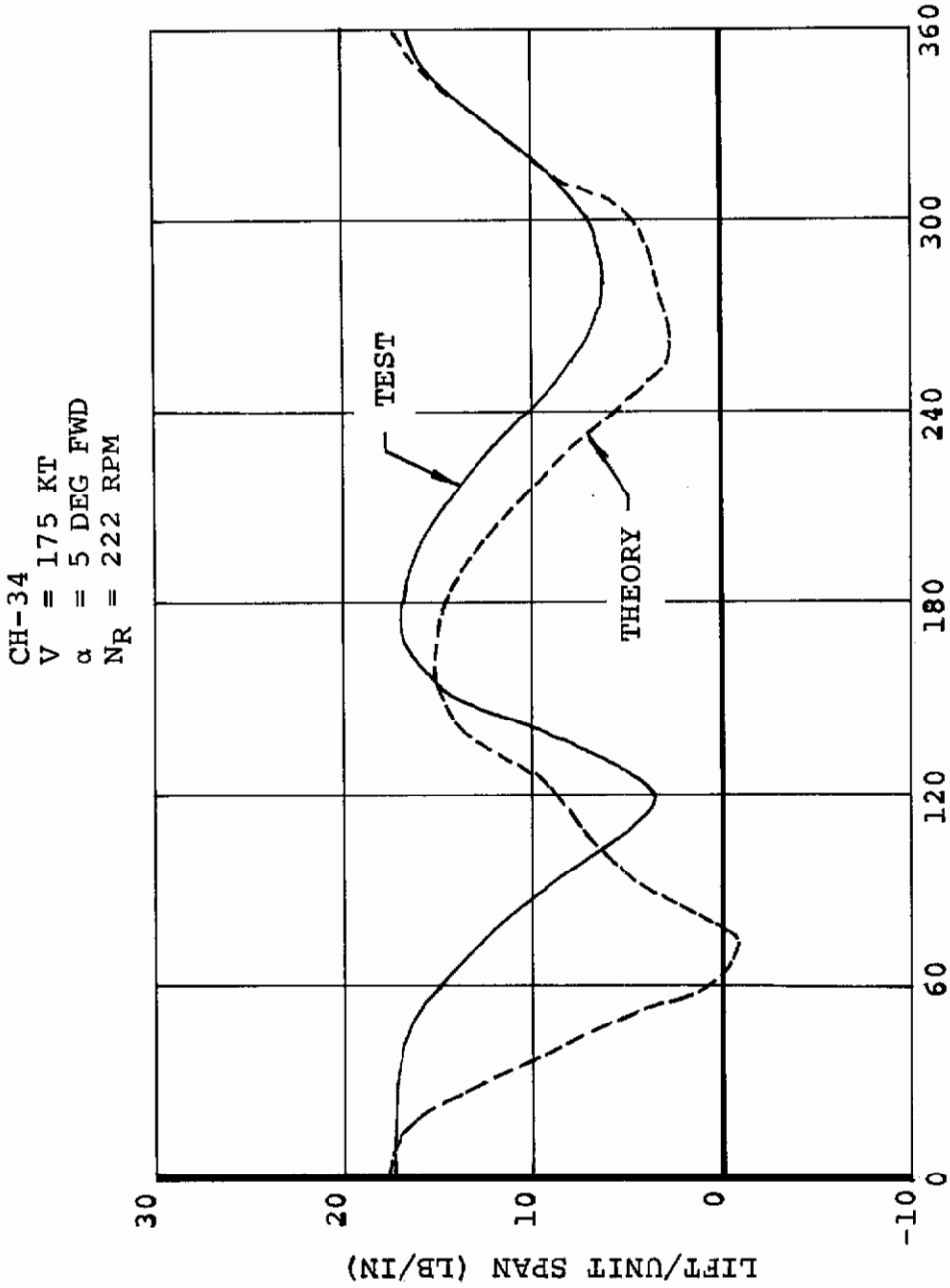

Figure 185. CH-34 Predicted and Measured Lift/Unit Span at 0.75R at 175 Knots

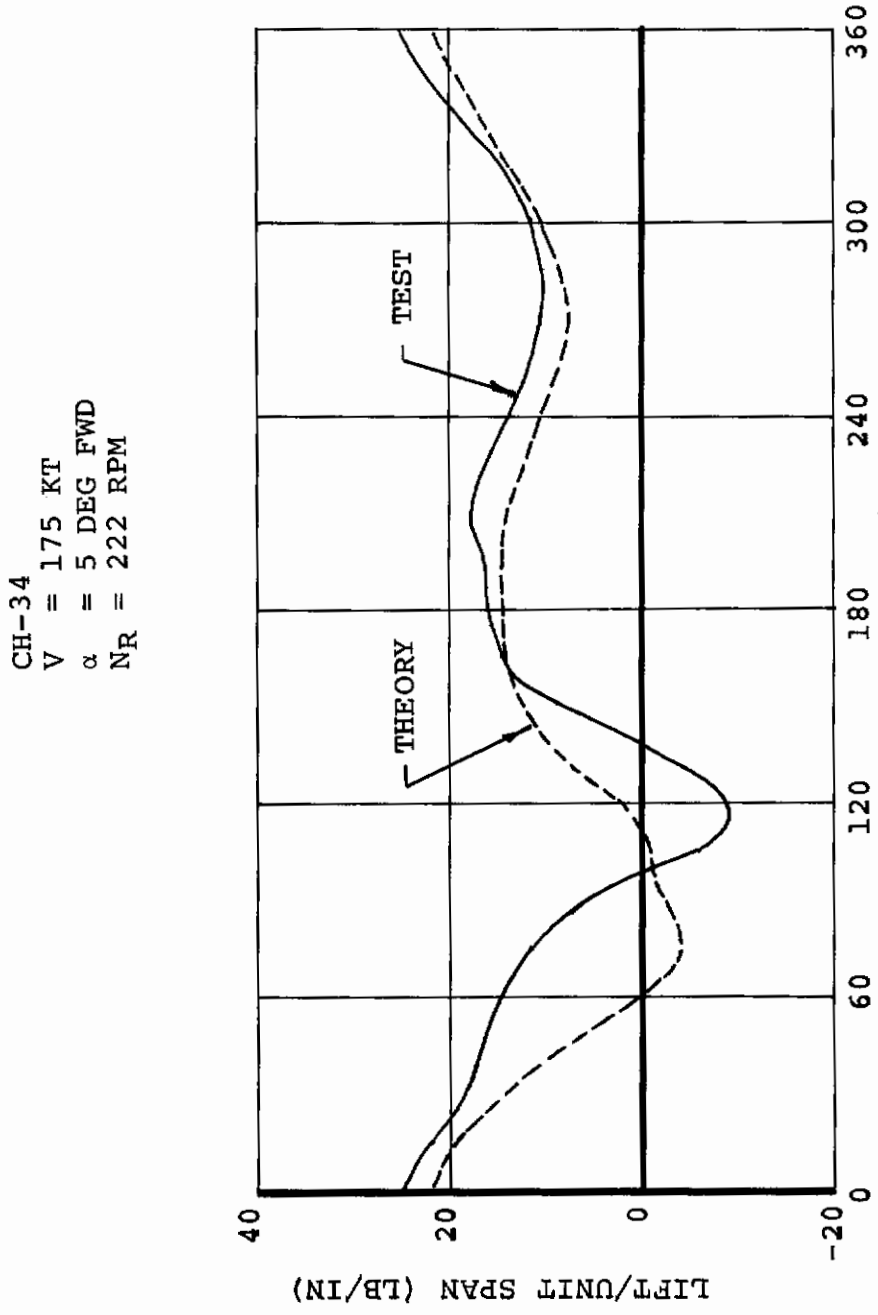

Figure 186. CH-34 Predicted and Measured Lift/Unit Span at 0.85R at 175 Knots

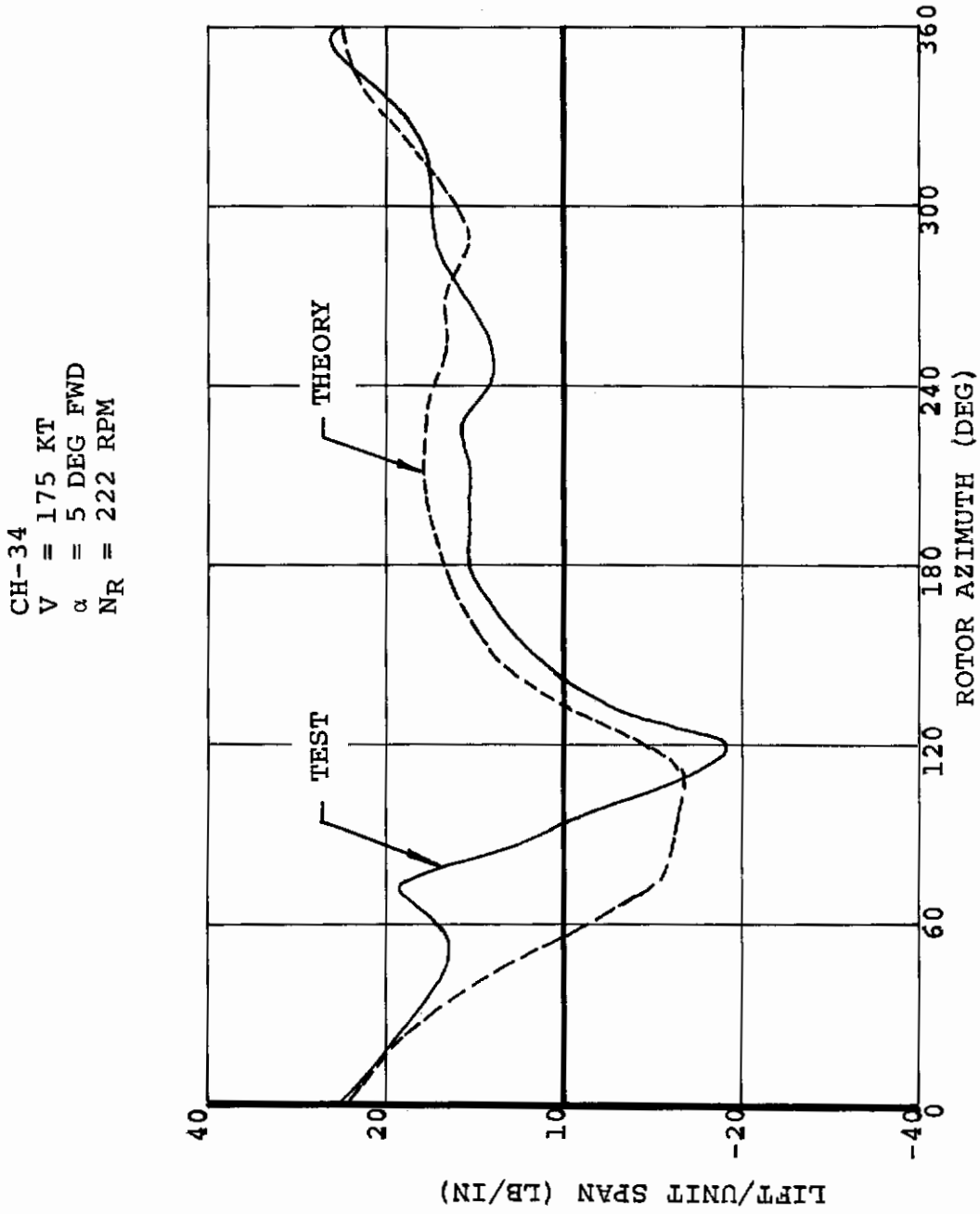

Figure 187. CH-34 Predicted and Measured Lift/Unit Span at 0.95R at 175 Knots

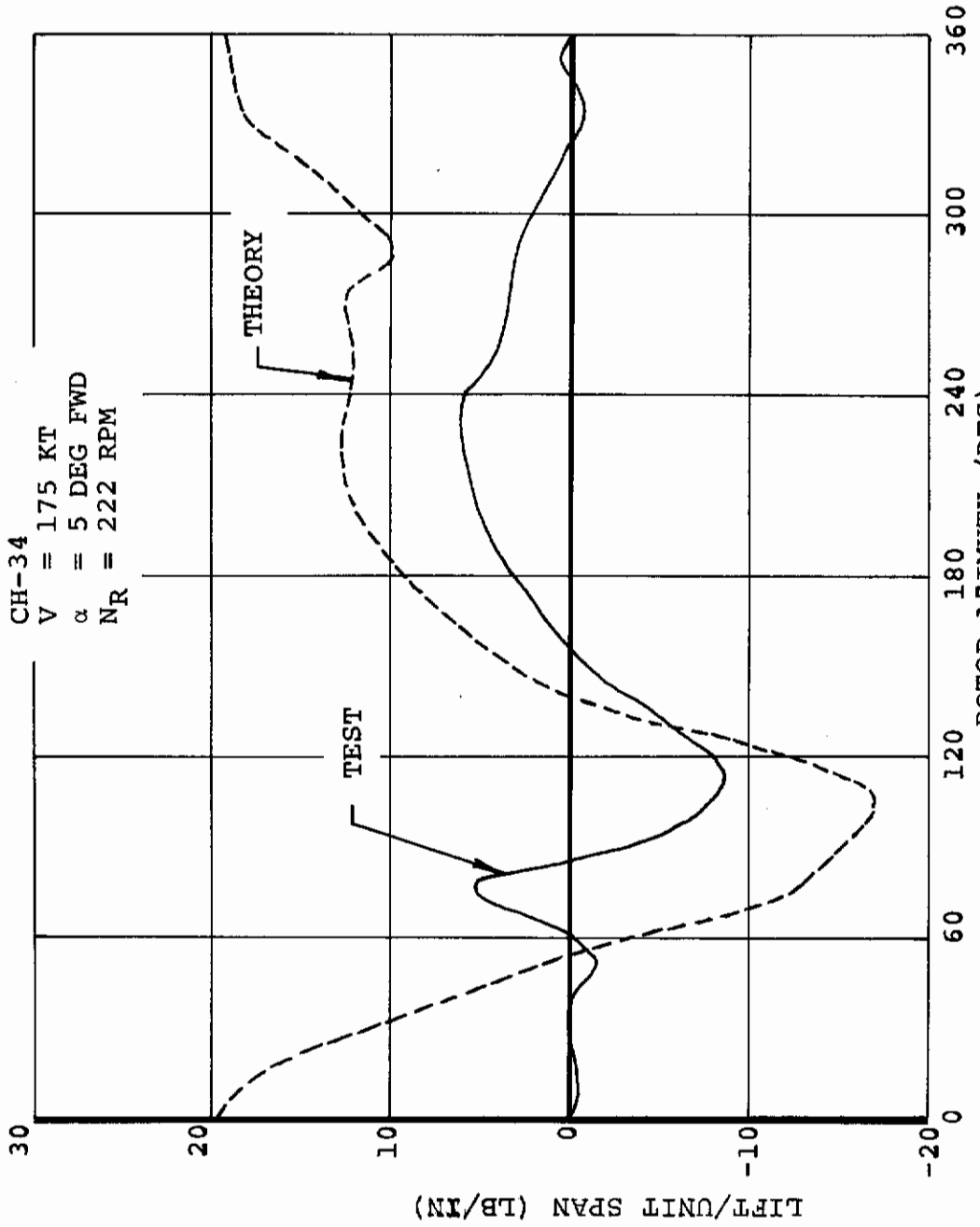

Figure 188. CH-34 Predicted and Measured Lift/Unit Span at 0.99R at 175 Knots

Part V. Impact and Potential of New Methods

H. R. Alexander
R. B. Taylor

IMPACT OF NEW METHODOLOGY ON PREDICTION CAPABILITY

AEROELASTIC STABILITY

The stability methodology featured in Part I differs from that of earlier programs in several important aspects. These fall into two categories:

(a) The new capability to analyze a deflected hingeless rotor blade fully coupled in the flap, lag, and pitch degrees of freedom.

(b) An upgraded aerodynamic representation which will treat nonaxial flow through the rotor without the usual small angle.

The effectiveness of this new capability has been demonstrated in correlation with a number of difficult cases which had not previously been correlated satisfactorily. Success in these areas lends credibility to design predictions which will be made using the C-39 program and to the parametric trend studies already accomplished and presented in Part II of this volume.

There is now good reason to believe that nonclassical as well as classical instability mechanisms can be analyzed in the design phase of aircraft featuring large rotors. In particular the stability of wing-rotor combinations may be addressed in all phases of flight from hover through transition to high-speed cruise.

ROTOR LOADS

Results of the rotor loads correlation with the fully coupled loads analysis clearly showed an improvement in prediction capability over loads analyses used in the past. Correlation over a large range of flight conditions with a number of rotor blades whose geometric and dynamic characteristics differ widely demonstrated that coupling of the pitch-flap-chord modes and the use of unsteady aerodynamics, in addition to nonuniform downwash representation, are the primary sources of improved prediction capability. Specific results and implications of the correlation as applied to prop/rotor and helicopter loads predictions are discussed below.

In the area of prop/rotor loads, the coupled analysis showed the capability to predict blade bending moments with a much greater accuracy than previously experienced with uncoupled analyses. A summary of the prop/rotor bending moment correlation results is shown in Table VI. The results are presented as a ratio of predicted-to-measured bending moment sensitivity to cyclic pitch rotor angle of attack or rotor rpm, whichever

is applicable to the particular model and flight condition. First-harmonic bending moments are used for the comparison since prop/rotor bending moments are predominantly 1 per rev. The analysis predicts flap bending within +5 percent and -11 percent and chord bending within +23 percent and -6 percent. The quality of this correlation is important to prop/rotor design since it implies that the coupled analysis can be used to accurately predict fatigue design bending loads. Past predictions of prop/rotor design loads have been a mixture of uncoupled analysis results coupled with test data and a large amount of engineering judgment. Use of the coupled analysis for prop/rotor fatigue design loads should considerably reduce the amount of engineering judgment required.

In the area of helicopter loads correlation, the analysis showed the importance of nonuniform downwash and unsteady aerodynamics on loads predictions. Use of nonuniform downwash increased the higher-harmonic content of blade flap bending due to rotor interference and improved the flap bending moment radial distribution predictions. Use of nonuniform downwash also improved chord bending correlation, but the consistent underprediction implies poor representation of the lag damper in the analysis. The chord bending correlation results show that lag damper preload is not properly accounted for by using an analytical torsional viscous damper in the analysis. Additional work should be done with the analysis to include lag damper preload effects.

The highlight of the helicopter loads correlation was the significant improvement of pitch link load predictions for predominantly unstalled and predominantly stalled conditions. Use of unsteady aerodynamics in the analysis to include hysteresis effects on blade section lift and pitching moment enabled the analysis to accurately predict pitch link load amplitude at the onset of stall and the growth of pitch link loads as stall increased. Correlation results when nonuniform downwash was used in the analysis were erratic for predominantly stalled conditions, indicating strong interference effects. Since pitch link load predictions were good both in and out of stall when uniform downwash was used in the analysis, use of uniform downwash is recommended for pitch link load predictions. The quality of the pitch link load correlation indicates that the analysis can be used to determine fatigue design pitch link loads for stalled and unstalled conditions for helicopter blade design.

TABLE VI
SUMMARY OF PROP/ROTOR BENDING MOMENT CORRELATION RESULTS
(RATIO OF PREDICTED TO MEASURED BENDING MOMENT SENSITIVITY TO A FORCING FUNCTION)

Model	Flight Condition	Forcing Function	Predicted/Measured 1st Harmonic	
			Flap Bending	Chord Bending
1/3-Scale LIT	hover	cyclic	0.97	1.0
160 Performance	hover	rpm	1.05	1.16
1/3-Scale LIT	cruise	angle of attack	0.89	1.0
1/9-Scale Conversion	cruise	angle of attack	0.89	0.94
1/3-Scale LIT	transition	cyclic	0.92	1.23

POTENTIAL EFFECTS OF NEW CAPABILITY ON DESIGN PRACTICE AND CRITERIA

AEROELASTIC STABILITY

The impact of the new methodology on design practices may be expected to arise from increasing confidence in our capability to predict and prevent instabilities that had previously been beyond the range of routine analysis. Thus rotor-airframe designs of advanced configurations may now be investigated with confidence. This may be expected to lead to a gradual relaxation of conservative conventions currently applied in blade design since novel ideas may be investigated parametrically to select those which are sufficiently promising to initiate hardware programs or test investigations. Currently, certain designs which may appear attractive peripherally will be aborted at the analysis stage without the expense of extensive test programs.

In particular, the new analysis provides a tool for investigating and understanding pitch-lag-flap flutter which is currently a matter of concern in hingeless rotor designs. It may be expected that, with additional understanding, design criteria and procedures will be developed which will reduce this type of mechanism to the same status as other forms of aeroelastic behavior.

ROTOR LOADS

The results of the loads correlation indicated two areas of significant improvement of rotor loads predictions for which the analysis can be used to develop design criteria. In the area of prop/rotor design, correlation of alternating flap and chord bending moments and steady rotor moments in hover due to cyclic pitch showed significant improvement over predictions made in the past with uncoupled analyses. Since hover cyclic produces fatigue design blade loads for prop/rotor design, the analysis can be used as a tool to develop an improved prop/rotor design criteria.

In the area of helicopter loads, the good correlation of pitch link loads indicates that the analysis can be used to develop a sounder pitch link design criterion for both unstalled and stalled conditions. The analysis can be used in conjunction with, or possibly replace, pitch link load flight test data for pitch link design. As the amount of correlation of flight test data with the analysis increases, confidence in the pitch link load prediction capability of the analysis should also increase, and the analysis can then be used to replace the extrapolation of existing flight test data for pitch link load design of heavier and faster helicopter designs.

REFERENCES

1. Alexander, H. R., and Leone, P. F., STATE-OF-THE-ART REVIEW OF V/STOL ROTOR TECHNOLOGY, VOLUME I, The Boeing Company, Vertol Division, Philadelphia, Pennsylvania; U.S. Air Force Flight Dynamics Laboratory, Air Force Systems Command, Wright-Patterson Air Force Base, Ohio, February 1972.

2. Amos, A. K., and Alexander, H. R., ANALYTICAL DEVELOPMENT OF AEROELASTIC STABILITY PROGRAM FOR PROP/ROTOR AIRCRAFT, The Boeing Company, Vertol Division, Philadelphia, Pennsylvania, Document D210-10411-1, February 1972.

3. Fu, F. C. L., and Nemal-Nasser, S., STABILITY OF SOLUTION OF SYSTEMS OF LINEAR EQUATIONS WITH HARMONIC COEFFICIENTS, Journal of the American Institute of Aeronautics and Astronautics, Vol. 10, No. 1, January 1972.

4. Gessow, A., and Myers, G. C., Jr., AERODYNAMICS OF THE HELICOPTER, Frederick Ungar Publishing Company, New York, New York, 1967.

5. Lytwyn, R. T., and Schagrin, E., AIRBORNE AEROMECHANICAL STABILITY OF CH-46 HELICOPTER, The Boeing Company, Vertol Division, Philadelphia, Pennsylvania, Document D210-10164-1, June 1971.

6. Yntema, R., Gabel, R., and Capurso, V., HELICOPTER ROTOR HUB VIBRATORY FORCES, The Boeing Company, Vertol Division, Philadelphia, Pennsylvania, Document R-244, May 1961.

7. Henderson, B., ROTOR LOAD CORRELATION REPORT, The Boeing Company, Vertol Division, Philadelphia, Pennsylvania, Document DYMR-9, December 1965.

8. Tarzanin, F., and Henderson, B., ROTOR ANALYSIS PROGRAM D-82, The Boeing Company, Vertol Division, Philadelphia, Pennsylvania, Document DYMR-5, September 1965.

9. Tarzanin, F., D-94 ROTOR AEROELASTIC ANALYSIS, PREDICTION OF PITCH LINK LOADS, The Boeing Company, Vertol Division, Philadelphia, Pennsylvania, Interoffice Memorandum 8-7453-1-1073, May 1966.

10. Henderson, B., CAPABILITY OF D-95X FOR THE PREDICTION OF PITCH LINK LOADS, The Boeing Company, Vertol Division, Philadelphia, Pennsylvania, Interoffice Memorandum 8-7453-1-2028, November 1966.

11. Tarzanin, F., and Thomas, E., AEROELASTIC ROTOR ANALYSIS D-94/95, The Boeing Company, Vertol Division, Philadelphia, Pennsylvania, Document D8-0614, May 1967.

12. Gross, D., and Csoboth, F., TANDEM HELICOPTER ROTOR LOAD CORRELATION STUDY, The Boeing Company, Vertol Division, Philadelphia, Pennsylvania, Document D8-1023, January 1968.

13. Milo, J., HUB MOTION TEST CASE AT 140 KNOTS, The Boeing Company, Vertol Division, Philadelphia, Pennsylvania, Interoffice Memorandum 8-7453-1-2124, February 1968.

14. Milo, J., ROTATIONAL HUB MOTION, The Boeing Company, Vertol Division, Philadelphia, Pennsylvania, Interoffice Memorandum 8-7454-1-042, September 1970.

15. Tarzanin, F., IMPROVEMENT OF D-95 ROTOR ANALYSIS PREDICTION CAPABILITY, The Boeing Company, Vertol Division, Philadelphia, Pennsylvania, Interoffice Memorandum 8-7458-1-162, August 1968.

16. Tarzanin, F., PREDICTION OF CONTROL LOADS DUE TO BLADE STALL, 27th Annual National V/STOL forum of the American Helicopter Society, Preprint No. 513, May 1971.

17. Tarzanin, F., and Ranieri, J., THE CH-34 CORRELATION STUDY, The Boeing Company, Vertol Division, Philadelphia, Pennsylvania, Document D8-2328-1, May 1969.

18. Harris, F., Tarzanin, F., and Fisher, R., ROTOR HIGH-SPEED PERFORMANCE, TEST VS. THEORY, Journal of the American Helicopter Society, July 1970.

19. Theodorsen, T., GENERAL THEORY OF AERODYNAMIC INSTABILITY AND THE MECHANISM OF FLUTTER, National Aeronautics and Space Administration, Washington, D.C., NACA Report 496.

20. Harris, F., PRELIMINARY STUDY OF RADIAL FLOW EFFECTS ON ROTOR BLADES, Journal of the American Helicopter Society, July 1970.

21. Purser, P., and Spearman, M., WIND TUNNEL TESTS AT LOW SPEED OF SWEPT AND YAWED WINGS HAVING VARIOUS PLANFORMS, National Aeronautics and Space Administration, Washington, D.C., NACA TN 2445, December 1951.

22. Halfman, R., Johnson, H., and Haley, B., EVALUATION OF HIGH-ANGLE-OF-ATTACK AERODYNAMIC DERIVATIVE DATA AND STALL FLUTTER PREDICTION TECHNIQUE, National Aeronautics and Space Administration, Washington, D.C., NACA TN 2533.

23. Carta, F., AN ANALYSIS OF THE STALL FLUTTER INSTABILITY OF HELICOPTER ROTOR BLADES, 23rd Annual National Forum of the American Helicopter Society, May 1967.

24. Liiva, J., Davenport, F., et al., TWO-DIMENSIONAL TESTS OF AIRFOILS OSCILLATING NEAR STALL, USAAVLABS Technical Report 68-13A, Eustis Directorate, U.S. Army Air Mobility Research and Development Laboratory, Fort Eustis, Virginia, 1968.

25. Gross, D., and Harris, F., PREDICTION OF INFLIGHT STALLED AIRLOADS FROM OSCILLATING AIRFOIL DATA, 25th Annual National Forum of the American Helicopter Society, May 1969.

26. Mangler, K. W., and Squire, H. B., THE INDUCED VELOCITY FIELD OF A ROTOR, R&M No. 2642, Ministry of Supply, Aeronautical Research Council, Reports and Memoranda, London, England, May 1950.

27. Miller, R. H., ROTOR BLADE HARMONIC AIR LOADING, IAS Paper No. 62-82, Institute of the Aerospace Sciences, New York, New York, January 1962.

28. Miller, R. H., UNSTEADY AIRLOADS ON HELICOPTER ROTOR BLADES, Journal of the Royal Aeronautical Society, London, England, October 1963.

29. Castles, W., Jr., and Durham, H. L., Jr., TABLES FOR COMPUTING THE INSTANTANEOUS VELOCITIES INDUCED AT THE BLADE AXES OF A LIFTING ROTOR IN FORWARD FLIGHT BY THE SKEWED HELICAL WAKE VORTICES AND A METHOD FOR CALCULATING THE RESULTANT BLADE AIR LOADS, Georgia Institute of Technology, Atlanta, Georgia, VER-2585, June 1962.

30. Davenport, F., A METHOD FOR COMPUTATION OF THE INDUCED VELOCITY FIELD OF A ROTOR IN FORWARD FLIGHT, SUITABLE FOR APPLICATION TO TANDEM CONFIGURATIONS, Journal of the American Helicopter Society, Vol. 9, No. 3, July 1964.

31. Rabbott, J. P., et al., A PRESENTATION OF MEASURED AND CALCULATED FULL-SCALE ROTOR BLADE AERODYNAMIC AND STRUCTURAL LOADS, USAAVLABS Technical Report 66-31, U.S. Army Air Mobility Research and Development Laboratory, Fort Eustis, Virginia, July 1966.

32. PROPOSAL FOR THE AVOIDANCE OF ROTOR/DRIVE SYSTEM N/REV TORSIONAL FORCED RESPONSE, The Boeing Company, Vertol Division, Philadelphia, Pennsylvania, Document D347-10092-1, October 1971.

BIBLIOGRAPHY

Bradbury, T. C., THEORETICAL MECHANICS, John Wiley and Sons, Inc., New York, New York, 1968.

Goldman, R. L., VIBRATION ANALYSIS BY DYNAMIC PARTITIONING, RM-305, Martin Company, Baltimore, Maryland, May 1966.

Hurty, W. C., and Rubinstein, M. F., DYNAMICS OF STRUCTURES, Prentice Hall, Inc., New York, New York, 1964.

Hurty, W. C., DYNAMIC ANALYSIS OF STRUCTURAL SYSTEMS USING COMPONENT MODES, Journal of the American Institute of Aeronautics and Astronautics, Vol. 3, No. 4, April 1965.

Scanlan, R. H., and Rosenbaum, R., AIRCRAFT VIBRATION AND FLUTTER, Dover Publications, Inc., New York, New York, 1968.

UNCLASSIFIED

Security Classification

DOCUMENT CONTROL DATA - R & D

(Security classification of title, body of abstract and indexing annotation must be entered when the overall report is classified)

1. ORIGINATING ACTIVITY (Corporate author)	2a. REPORT SECURITY CLASSIFICATION
THE BOEING COMPANY, Vertol Division Boeing Center, P.O. Box 16858 Philadelphia, Pennsylvania 19142	Unclassified 2b. GROUP

3. REPORT TITLE

V/STOL DYNAMICS AND AEROELASTIC ROTOR - AIRFRAME TECHNOLOGY
VOLUME II. DESCRIPTION AND CORRELATION OF NEW METHODOLOGIES

4. DESCRIPTIVE NOTES (Type of report and inclusive dates)

Final Report, February 1971 - February 1972

5. AUTHOR(S) (First name, middle initial, last name)

H. R. Alexander
A. K. Amos
F. J. Tarzanin
R. B. Taylor

6. REPORT DATE	7a. TOTAL NO. OF PAGES	7b. NO. OF REFS
September 1972	300	32

8a. CONTRACT OR GRANT NO.	9a. ORIGINATOR'S REPORT NUMBER(S)
F33615-71-C-1310 b. PROJECT NO. 1370	D210-10464-2
c. Task No. 137005 d.	9b. OTHER REPORT NO(S) (Any other numbers that may be assigned this report) AFFDL-TR-72-40, Volume II

10. DISTRIBUTION STATEMENT

Distribution limited to U. S. Government agencies only; test and evaluation; statement applied 18 April 1972. Other requests for this document must be referred to the AF Flight Dynamics Laboratory, (FY), Wright-Patterson AFB, Ohio 45433.

11. SUPPLEMENTARY NOTES	12. SPONSORING MILITARY ACTIVITY
Volume II of a 3-volume report	Air Force Flight Dynamics Laboratory Air Force Systems Command Wright-Patterson Air Force Base, Ohio

13. ABSTRACT

The blade loads analysis calculates rotor blade flapwise, chordwise, and torsional deflections and loads, together with rotor performance, control system forces, and vibratory hub loads. Articulated and hingeless rotors with 2 to 9 blades and large twist may be analyzed. The analysis considers coupled flapwise-chordwise-torsion deflections of the rotor blades. Boundary conditions for either articulated or hingeless rotors are applied and the solution is obtained by expanding the variables in a 10-harmonic Fourier series. Airload calculations include the effects of airfoil section geometry, compressibility, stall, 3-dimensional flow, unsteady aerodynamics, and nonuniform inflow. In the area of rotor loads, correlation of prop/rotor and helicopter rotor loads test data has been made with the fully coupled rotor loads and steady in-plane hub moments for prop/rotors and for alternating blade loads, pitch link loads, and airloads for helicopters. An unexpected discovery of this study was the sensitivity of the rotor derivatives to blade lead-lag motion when the frequency of this mode is near 1 per rev. This result was subsequently confirmed by test. The impact of the new prediction capabilities and possible refinement or development of design criteria through use of the analysis are discussed. The methods contained in this report are intended to be used by designers to calculate with improved accuracy, the dynamic and aeroelastic response characteristics of rotor powered V/STOL aircraft. The essential new feature of these methods is that the coupled flap-pitch-lag blade deflections are taken into account. These calculations are essential if a high level of confidence is to be had in the results.

DD FORM 1 NOV 68 1473

UNCLASSIFIED

Security Classification

14. KEY WORDS	LINK A		LINK B		LINK C	
	ROLE	WT	ROLE	WT	ROLE	WT
Aeroelastic stability analysis						
Articulated rotors						
Blade design						
Blade idealization						
Blade loads						
Fixed coordinates						
Flapwise, chordwise, and torsional deflections						
Fourier series						
Helicopter airloads						
Hingeless rotors						
Lead-lag motion						
Limit-cycle wing rotor flutter						
Nonuniform downwash						
Pitch-lag-flap coupling						
Pitch link loads						
Prop/rotor loads analysis						
Rotor loads						
Spatial coordinates						
V/STOL dynamics						
Model 160 tilt-rotor						
ONERA 13-foot diameter propeller						

☆U.S.Government Printing Office: 1972 — 759-486/131